Muon-neutrino disappearance with multiple liquid argon time projection chambers in the Fermilab Booster neutrino beam

Thesis submitted in accordance with the requirements of the
University of Liverpool for the degree of Doctor in Philosophy by

Rhiannon Susan Jones

October 2021

Abstract

The Short Baseline Neutrino (SBN) program consists of three liquid argon time projection chamber (LArTPC) experiments: SBND, MicroBooNE and ICARUS, with 110 m, 470 m and 600 m baselines respectively. The detectors are located in the Booster Neutrino Beam (BNB) at Fermilab which has a peak energy around 0.7 GeV and contains predominantly muon neutrinos. The baseline and energy range of the SBN program is conducive to measuring neutrino oscillation parameters under various sterile neutrino hypotheses. Sterile neutrinos have been proposed as a possible solution to the numerous short baseline anomalies. The proposed particles must be sterile in nature such that they do not interact via the weak force, however they may undergo oscillations with the active neutrino flavours. Their existence may consequently be confirmed through measurements of the appearance and disappearance of the active flavours. The analyses presented in this thesis aimed to calculate and understand the sensitivity of the SBN program to measuring the ν_μ disappearance parameters under the (3+1) sterile neutrino oscillation hypothesis.

The sensitivity of SBN to measuring the ν_μ disappearance sterile oscillation parameters, $\sin^2 2\theta_{\mu\mu}$, Δm^2_{41}, was calculated through semi-exclusive joint fits of the ν_μ CC 0π and ν_μ CC Other reconstructed neutrino energy spectra. The first iteration used truth-level Monte Carlo (MC) events, and determined that the 5σ SBN sensitivity is comparable to the 90% MINOS/MINOS+ confidence level and supersedes the 90% MiniBooNE confidence level across entire phase space. Semi-exclusive joint fits of the aforementioned sample spectra were performed between the MC and multiple mock data sets in SBND. This analysis assessed the accuracy with which the near detector can disentangle systematic from physics effects in the oscillation analysis. The result was a 5.49% discrepancy between the ICARUS Monte Carlo and mock data event rates, when the systematic constraints from the near detector fit were extrapolated to the far detector. The second iteration of the SBN sensitivity analysis involved the application of an event selection procedure developed in SBND, following the full reconstruction chain. ν_μ CC 0π events were selected from sample of neutrinos with 84.5% efficiency and 84.3% purity. The sterile neutrino sensitivity was determined once more at the near detector with these samples, and was shown to be consistent with the truth-level studies.

Declaration

The content of this thesis was written in its entirity by me, with references to material adapted from external sources clearly defined. The document has not been submitted for any other qualification to this or any other institution. The research content combines literature reviews and my own original work. Any content taken from literature is always clearly referenced. A summary of the contributions to each chapter is as follows.

Chapter 1 contains a general overview of the subject and the contents of the thesis. Chapter 2 is a literature review of the theoretical contributions to the field of neutrino oscillation physics, which motivate and substantiate my research. Chapter 3 comprises a description of the experiments which make up the Short Baseline Neutrino program, with sources from internally and externally-published SBN documentation. Chapter 4 outlines the methodology of the simulation and reconstruction software through reviews of the available documentation and source code.

Chapter 5 contains entirely my own work using inputs from chapter 4. Chapter 6 summarises the inputs to the neutrino oscillation analyses which were developed in the SBNCode and VALOR analysis frameworks. The VALOR neutrino fitting framework was under active development for the SBN experiment by myself, Costas Andreopoulos, Steve Dennis, Dom Barker and Tom Ham throughout my PhD. SBNCode was also under development by myself, Andy Mastbaum and Gray Putnam. The content of chapter 6 therefore combines independent and collaborative work performed as part of the VALOR and SBNCode analysis groups.

Chapters 7 and 8 contain original neutrino physics analyses using the work outlined in chapter 6 as input, performed entirely by me. Chapter 9 contains an original neutrino physics analysis using the inputs outlined in chapter 4, developed and performed entirely by me. Finally, chapter 10 is a summary of the presented research.

Acknowledgements

First and foremost, to Costas, you have been a phenomenal guide and have taught me **so** much. None of this would have been possible without your support. More importantly though, thank you for convincing me to get up at 5am so we could watch the sunrise over Mount Rushmore. That was a pretty unforgettable introduction to the US, and a perfect taste of the adventures we'd all have throughout the following years.

The VALOR, GENIE and Liverpool groups have been at the core of my entire PhD experience. Not only in helping with the working side of things, but with the solo long-haul flights, meeting new people, and of course, introducing me to all the **exquisite** food. In particular, I owe a colossal debt of gratitude to both Marco and Steve, you are both a PhD student's dream. Thank you for the late-night and always instantaneous answers, no matter how stupid the question. I could not have done any of this without you both.

I also have to mention Júlia, we have had the most fun all over the world, and one day I hope we can make $\nu_{\text{♀}}$ into something amazing. And Dom (Barker), I didn't know whether to mention you with the VALOR group, the SBN(D) group or the friend group, but you've been everywhere. It blows my mind that I only met you 5 years ago. Thank you for the teamwork, the endless hilarity and of course for providing us all with the beautiful Desmond. And thank you to every other memeber of the VALOR, GENIE and Liverpool groups I have worked and played with over the years, you have all helped make this worthwhile.

Thank you to the SBN and SBND collaborations for all your support and guidance, and to every collaborator who I spent time with in and around the workshops, meetings and conferences. To Dom (Brailsford), you have been completely invaluable in so many ways. I have offered you multiple pints and even a vegan cake at some point, so here is a written declaration that I will get those to you ASAP. Also to Ornella, thank you for all your invaluable guidance and to Andrzej for putting up with my painfully long presentations. To Gray and Ed, thank you for generating and regenerating the samples whenever I needed. Finally to Joseph and Nicola, you guys let me play with the real detector and taught me so much about the hardware side of neutrino life, I had the most fun in DAB with you both.

It would be impossible to list all of the people I met while at Fermilab, but to the Butterfield, Batavia and Taco Tuesday guys and gals, thank you for making that year the best I've ever had, and for providing all of the animal content since I left. Thank you to every single person that visited site 56 while we all lived there. To Iker, Jack and Nicola, thank you for being such awesome housemates during the teeny tiny time we had together. And last, but by no means least, thank you Tom. I can't mention all of fun we had here, but I loved every moment of it. The road trips, pool games, parties, hungover burger deliveries, Tour de Goodwill... The list seriously is endless. That year would have been half as epic without you there.

I have honestly met countless incredible people from all around the world over the last few years, and every single new friend I have made and old friend I have spent time with has contributed to the most unforgettable experiences of my life so far. If I haven't mentioned you by name, it's likely only due to you not being inflicted with the working side of my PhD life. But to all friends, old and new, this would not have been remotely enjoyable without you.

To my whole family, thank you for your unwavering support over the many, many years it has taken me to get here. Mum, you are the strongest woman I have ever met, and have just been the biggest and greatest role model all the way through my life. I would not have made it here without you. Dad, you have really helped me get to know myself in the last few years, and of course have provided some excellent content to while away the hours. Rowan, you made the last few weeks of writing up more fun than stressful, I cannot thank you enough for that. To my grandparents, thank you for listening to me tell you all about my research.

To Pam and Rob, thank you for giving us a home and such wonderful company for so long during the pandemic, and for the endless supply of cheese and wine. One person who blurs the line between friend and family is Nic. You were the first person I knew in Liverpool, and your music and the amazing We Want Women helped me feel so at home in this fantastic city, thank you. To the Allens, Goffs, Davieses and McWilliams, thank you for being the best extended family a girl could ask for.

Finally, to Andy. There are simply not enough words to truly express how grateful I am. Thank you, for **everything**.

Time for a kebab and a pint of wine.

Glossary

Abbreviations

ADC Analog-to-Digital Converter

APA Anode Plane Assembly

ARAPUCA Argon R&D Advanced Program at UniCAmp

ATF Assembly and Transport Fixture

BDT Boosted Decision Tree

BNB Booster Neutrino Beam

BSM Beyond the Standard Model

CC Charged-Current

CC QE Charged-Current Quasi-Elastic

CNGS CERN Neutrinos to Gran Sasso

Coh Coherent

CRT Cosmic Ray Tagger

DAQ Data Acquisition

DaR Decay-At-Rest

DiF Decay-In-Flight

DIS Deep Inelastic Scattering

DUNE Deep Underground Neutrino Experiment

FCA Field Cage Assembly

FEM Front End Motherboard

FHC Forward Horn Current

FKR Feynman-Kislinger-Ravndal

FSI Final State Interactions

ICARUS Imaging Cosmic And Rare Underground Signals

IMB Irvine-Michigan-Brookhaven

J-PARC Japan Proton Accelerator Research Complex

LAMPF Los Alamos Meson Physics Facility

LArTPC Liquid Argon Time Projection Chamber

LFG Local Fermi Gas

LRC Long-Range Correlations

LSND Liquid Scintillator Neutrino Detector

MC Monte Carlo

MCS Multiple Coulomb Scattering

MCT Monte Carlo Template

MEC Meson Exchange Current

MINOS Main Injector Neutrino Oscillation Search

MIP Minimum Ionising Particle

MSW Mikheyev-Smirnov-Wolfenstein

NC Neutral-Current

NC El Neutral-Current Elastic

npnh N-Particle N-Hole

NuMI Neutrinos at the Main Injector

OOFV Out Of Fiducial Volume

PID Particle Identification

PMNS Pontecorvo–Maki–Nakagawa–Sakata

PMT Photo Multiplier Tube

POT Protons On Target

RENO Reactor Experiment for Neutrino Oscillation

Res Resonant

RFG Relativistic Fermi Gas

RHC Reverse Horn Current

R&D Research and Development

SBL Short Baseline

SBN Short Baseline Neutrino

SBND Short Baseline Near Detector

SiPM Silicon Photo Multiplier

SM Standard Model

SNO Sudbury Neutrino Observatory

SNR Signal-to-Noise Ratio

SRC Short-Range Correlations

SuperK Super Kamiokande

TPB Tetraphenyl Butadiene

TPC Time Projection Chamber

VUV Vacuum Ultra-Violet

Contents

List of Figures

List of Tables

"I can feel pieces of my brain falling away like a wet cake."

— Bernard Black

For Andy.

Chapter 1.

Introduction

Neutrino physics is at the core of current high energy physics research, having accelerated throughout the decades following the discovery of the electron neutrino by Reines and Cowan in 1956 [1]. One of the most profound discoveries made in recent years was that neutrinos are massive particles, refuting their depiction in the Standard Model (SM) of particle physics to provide the first evidence of Beyond the Standard Model (BSM) physics. This discovery was made through the observation of neutrino flavour oscillations by the Super Kamiokande [2] (1998) and SNO [3] (2001) experiments and was awarded the 2015 Nobel Prize in physics [4]. Current and future neutrino physics research continues to be pertinent in answering fundamental questions about the nature of the universe, along with probing some of the existing experimental anomalies in high energy physics, such as:

- Do sterile neutrinos exist?
- What is the magnitude of the CP-violating phase in the lepton sector?
- What are the mass ordering and absolute masses of the 3 active neutrinos?

The Short Baseline Neutrino (SBN) program is under construction at Fermilab and will consist of three liquid argon time projection chamber (LArTPC) detectors situated along the Booster Neutrino Beam (BNB) [6]. The Short Baseline Near Detector (SBND), at 110m, MicroBooNE, 470m, and ICARUS T600, 600m, will act as a research and development (R&D) projects in both construction and operation for the future long baseline Deep Underground Neutrino Experiment (DUNE) through the implementation of unique and novel technological features in a similar beamline [6] [7].

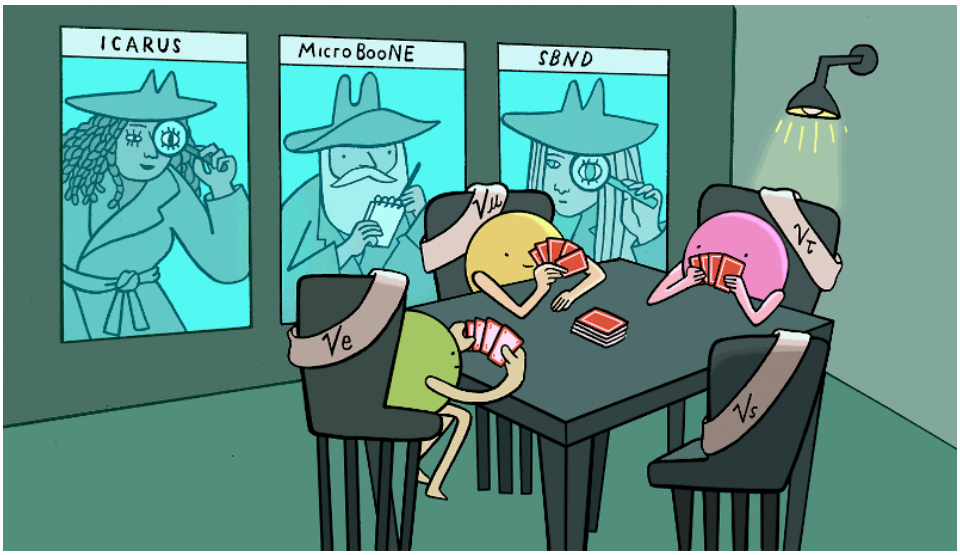

Searching for sterile neutrinos in the SBN program, cartoon [5].

Coupled with the R&D goals, the joint physics program includes measuring neutrino oscillations in the search for sterile neutrinos. In addition, each of the three SBN detectors will investigate the behaviour of neutrino interactions with argon at energies around 1 GeV, along with searches for other new physics beyond the standard model.

The baseline of the SBN program and peak operational energy, 0.7 GeV, of the Booster neutrino beam (BNB) were chosen in order for the experiment to be maximally sensitive to measuring short-baseline neutrino oscillations driven by values of the squared mass splitting on the order of $\sim$1 eV^2. Such studies will be performed by calculating the rate of $\nu_\mu \rightarrow \nu_e$ ($\bar{\nu}_\mu \rightarrow \bar{\nu}_e$) appearance and $\nu_\alpha \rightarrow \nu_\alpha$ ($\bar{\nu}_\alpha \rightarrow \bar{\nu}_\alpha$), $\alpha = e, \mu$, disappearance between the near and far detectors [6].

Neutrino interactions have historically been measured on both heavy and light nuclei, however high-precision cross-section measurements of their interactions with argon have recently become extremely interesting due to technological advances in the field. As a result, neutrino-argon interaction phenomenology is not yet well-understood, such that the interaction-based systematic uncertainties have not been constrained in oscillation measurements. Neutrino interaction cross-section measurements on argon will therefore be critical to fully exploiting the physics capabilities of DUNE, in order to minimise the interaction systematic uncertainties in oscillation measurements [6].

SBND is the near detector in the SBN program. Its proximity to the neutrino source introduces a huge flux of neutrinos in the detector, from which millions per year will have a sufficient probability of interacting, due to the volume and density of argon, and

will be observable in SBND. These high statistics coupled with the imaging capability of the LArTPC detector technology will allow SBND to make high-precision cross-section measurements with many possible kinematic states in a multi-dimensional phase space.

The first part of this thesis will begin with an outline of the theory and current status of experimental and theoretical neutrino oscillation physics in chapter 2. An in-depth description of the LArTPC operation principles and their implementation in the SBN program will be given in chapter 3. A description of the procedure for simulating and processing events in the SBN detectors will then be given in chapter 4.

The second part of the thesis will discuss the analysis procedures and results, each of which will be performed in the context of both the entire muon neutrino charged-current (ν_μ CC) event rate and the exclusive subset of the ν_μ CC events which have no pions in the final state (ν_μ CC 0π). The main reasons for focussing on these channels are,

- The substantial expected rate of such events at the near detector, see section 5.1. This abundance, $\mathcal{O}(10^6)$ events/year, coupled with the LArTPC detector technology, see section 3.2, will allow us to place unprecedented constraints on ν_μ-Ar interaction models and their uncertainties.
- Probing the complexity of neutrino interactions within the heavy argon nucleus with the simplicity of the 0π final state will provide the clearest understanding of the unobservable intranuclear behaviour of ν_μ-Ar interaction products.
- Not only is the CC 0π final state the most simple, it is also the most direct way to make targeted studies of the highly-prevelant '2 particle 2 hole' (2p2h) interaction, in which the neutrino interacts with bound nucleons inside the nucleus to produce 2 or more nucleons in the final state of the interaction [8]. Theoretical models of this process on heavy nuclei have only recently been developed, and there is currently insufficient global neutrino-nuclear scattering data to constrain them. Measurements of CC 0π final states in SBND will directly address this issue.
- Making neutrino oscillation measurements through joint-fits to many exclusive channels will improve our sensitivity to observing new physics. This is primarily because interaction-based systematic variations will affect individual final states in unique ways, therefore separating the samples into exclusive channels will give the fits a better chance of discriminating between systematic and physics-based variations in data.

Before presenting the analyses themselves, samples of ν_μ CC 0π events in SBND, generated with multiple neutrino interactions models, will be explored in order to understand the model-dependent contributions to the event rate in chapter 5. As a result, the analyses which follow will be better-suited to identifying kinematic and topological model-dependencies, such as the effect of applying interaction-dependent systematic parameters to each sample. The construction and parametrisation of the oscillation analysis inputs will then be discussed in chapter 6.

The sensitivity of SBN to measuring the ν_μ-disappearance oscillation parameters, $\sin^2 2\theta_{\mu\mu}$, Δm^2_{41}, in the context of a 3+1 (active+sterile) neutrino hypothesis will then be explored in chapter 7. Contributions to the sensitivity from each SBN detector, multiple model configurations and various sets of systematic parameters will be investigated through inclusive and semi-exclusive joint fits of the ν_μ CC 0π and ν_μ CC 'Other' reconstructed neutrino energy spectra across the ν_μ disappearance sterile oscillation parameter space. The 'Other' component of the sample refers to all CC events in which 1 or more pions are emitted, such that the total event rate in the CC 0π+CC Other samples is equal to that of the CC Inclusive sample.

The impact of flux and interaction systematic uncertainties on neutrino interactions in SBND will be explored through a 'mock data analysis' in chapter 8. This study aims to assess the performance of the near detector in constraining the systematic parameters within the SBN sterile neutrino oscillation analysis. This will be investigated through fits of the ν_μ CC Inclusive reconstructed neutrino energy spectra along with joint fits of the ν_μ CC 0π and ν_μ CC 'Other' spectra.

The analyses outlined above will be performed using a truth-level sample of neutrino interaction events with detector effects and reconstruction limitations applied through predictive smearing and threshold cuts. In reality, the detector effects will be simulated as part of the production chain, followed by the application of real reconstruction techniques to determine the final state particle content and kinematics of every neutrino interaction event. Both of these components are currently under development in SBND and ICARUS. Chapter 9 presents the final analysis in this thesis and will utilise a sample of SBND neutrino events which have undergone all stages of the production chain, including the current versions of the detector simulation and reconstruction. A topological selection procedure has been developed to identify events with the ν_μ CC 0π final state from this sample. Although the reconstruction procedure has not yet been finalised, developing the selection at this early stage can inform areas for improvement in the reconstruction, which will in turn incite updates to the selection.

Chapter 2.

Neutrinos

This chapter will begin with an exploration of the origin of the neutrino, before outlining key historical moments which would help shape the current field of research in section 2.1. Neutrino interactions in the Standard Model of particle physics will be discussed in section 2.2. Active neutrino flavour oscillations and modern experimental results will then be discussed in section 2.3, followed by an extension to include the possible existence of sterile neutrinos along with existing measurements in section 2.4.

2.1. Discovery and early developments

The neutrino physics story began with the proposal laid out briefly, and somewhat timidly, by Wolfgang Pauli in the 1930 letter to his radioactive colleagues [9]. It is in this letter that he addresses the unexpected shape of the energy spectrum of electrons emitted from the nucleus during the β-decay of 'Radium-E' (now known to be Bismouth-210) observed three years earlier, in 1927, by Ellis and Wooster [10]. If the well-understood law of energy conservation was to be upheld, such a spectrum was expected to be a delta peak at the kinetic energy of the outgoing electron. Pauli therefore proposed to his colleagues the 'neutron': a neutral fermion with a mass around the same size as the electron and the ability to propagate 10 times further through Earth than a photon [9].

The neutron itself was discovered in 1932, resulting in the pivotal renaming of Pauli's 'neutron' to the 'neutrino'. In 1933, Enrico Fermi constructed a theory of β decay which involved a neutron decaying to a proton to produce an electron and a neutrino in order to directly address the aforementioned electron energy spectrum issue [11]. Soon after, Bethe and Peierels attempted to define a neutrino interaction cross-section

using the assumptions required by Fermi's β decay theory and determined that, if these assumptions held true, 'one can conclude that there is no practically possible way of observing the neutrino' [12].

26 years passed before any evidence of the neutrino was found experimentally. During this time a huge amount of work was done to build the theoretical groundwork and determine how it could be possible to observe this seemingly 'undetectable' particle. Finally, in 1956, Reines and Cowan made a measurement which confirmed the observation of the 'free neutrino' [1]. They had previously indicated that these particles had been found in 1953 through the detection of positrons and neutrons following fission-fragment decay in a large reactor experiment,

$$\bar{\nu} + p \rightarrow \beta^+ + n, \tag{2.1}$$

but their reactor-induced and cosmic backgrounds were too large to be confident in the results obtained [13]. Following this, the experiment was updated to incorporate significant background mitigation techniques such as moving the experiment underground. In 1956 they were finally able to announce the discovery of the 'neutrino', now known to have been the electron antineutrino, at an observed signal rate 20 times higher than that of the reactor-based background [1].

In 1957, the Wu experiment determined that parity is not conserved in the weak interaction. This was demonstrated through the observation of ^{60}Co undergoing β-decay in a magnetic field which polarises the nucleus through its intrinsic magnetic moment. If the number of electrons emitted in a given direction was identical to the number emitted in the opposite direction, then parity would have been conserved in the process. However the count rates were not equivalent, thereby demonstrating the parity-violating nature of the weak interaction [14].

A further verification of this parity violation was exhibited through the determination of the helicity of neutrinos in the Goldhaber experiment later that year. Helicity, h, corresponds to the component of a particle's spin, $\mathbf{S}$, the direction of its momentum, $\mathbf{p}$,

$$h = \frac{\mathbf{S} \cdot \mathbf{p}}{|\mathbf{p}|}, \tag{2.2}$$

which is identical to the chirality in a massless particle. Processes which conserve parity would observe particles with equal rates of positive and negative helicity states.

In the Goldhaber experiment, measurements of orbital electron capture in the decay of Europium to Samarium were made as per,

$$\begin{aligned} {}^{152m}Eu + e^- \quad &\longrightarrow {}^{152}Sm^* + \nu_e \\ &\qquad \big\llcorner\!\!\longrightarrow {}^{152}Sm + \gamma. \end{aligned} \tag{2.3}$$

Photons are emitted at the end of the decay chain, and it is possible to measure their helicity in order to infer the helicity of the neutrino. Contrary to parity-conservation requirements, the helicity of the neutrino was found to be entirely negative [15].

During the years leading up to the experimental confirmation of the existence of the neutrino, the muon was discovered [16]. The question was then raised by Pontecorvo in 1959 about whether neutrinos produced alongside electrons were the same as those produced with muons: Does $\nu_e = \nu_\mu$ or $\nu_e \neq \nu_\mu$? [17].

Only 3 years later, in 1962, Lederman, Schwartz and Steinberger successfully confirmed the existence of the ν_μ as a by-product of confirming its flavour independence with respect to the electron neutrino [18]. This experiment involved firing 15 GeV beam of protons at a beryllium target to produce pions and kaons, which decay in-flight to muons and muon neutrinos. The muon neutrino interaction products were then detected in a spark chamber and the topological signature of outgoing muons was distinguished from that of electrons. If the muon neutrino interactions had produced equal rates of outgoing muons and electrons, then the ν_μ could not be differentiated from the ν_e. However, they observed no electron-like events. Thus proving the existence of a second type of neutrino [18].

The ν_τ was first postulated following the discovery of the τ lepton in 1975. The DONUT experiment discovered the ν_τ through the detection of τ leptons produced following charged-current ν_τ interactions using nuclear emulsion targets [19].

In 1989, the ALEPH detector at the Large Electron Positron (LEP) collider had ruled out the possibility of there being a fourth active neutrino flavour at the 98% C.L. through measurements of the Z-boson decay width [20] [21].

2.2. Neutrino interactions in the Standard Model

Neutrinos interact via the weak and gravitational forces, and cannot undergo electromagnetic or strong interactions. Within the standard model, the two possible formulations of the weak interaction are charged-current (CC) through the exchange of a massive $W^{\pm}$ boson, and neutral-current (NC) through the exchange of a massive Z^0 boson.

All interaction matrix elements ($\mathcal{M}_{ij}$) must be Lorentz invariant. The currents that contribute to the matrix elements are only Lorentz invariant when defined in 5 distinct ways. The distinction is made according to how they transform under parity: *scalar*, **pseudoscalar**, **vector**, *axial vector* and tensor, where those in italics remain unchanged under the parity transformation and those in bold change sign under parity. Furthermore, the exchange of a spin-1 boson in weak interactions limits the possible forms of the weak currents, j^{μ}, to be either **vector** or *axial vector* [22].

When the matrix element of an interaction is constructed with one of the aforementioned current structures, parity is always conserved in the interaction since, $\mathcal{M}_{ij} \propto j_i^{\mu}.j_j^{\nu}$, where μ and ν denote separate interaction vertices and i, j represent the particles involved. Given that the weak interaction does not conserve parity, the weak currents must be defined in another way. Extensive theoretical and experimental studies have confirmed that the weak currents are instead defined with a vector-axial, V-A, structure, which necessarily violates parity in $\mathcal{M}_{ij}$ [22].

Another critical feature of the weak force corresponds to its relationship with the chirality, or 'handedness', of a particle: a Lorentz-invariant quantum-mechanical property related to spin. In the case of massless or highly-energetic particles, the physical interpretation of this quantity is identical to helicity, wherein a massless particle whose spin is (anti)aligned with its direction of motion is said to have (negative)positive helicity and (left)right-handed chirality. In contrast, the helicity of massive particles corresponds to a superposition of both left and right-handed chiral states. The W-boson couples only with (right)left-handed (anti)particles, and only (right)left-handed (anti)neutrinos have ever been observed [23].

The charged current interaction is represented in the standard model Lagrangian as follows,

$$\mathcal{L}_{CC} = \frac{g}{2\sqrt{2}}\{j_W^{\mu} W_{\mu}^{+} + h.c\}, \tag{2.4}$$

where W^+_μ is the W^+-boson field and g is the weak coupling constant, which defines the strength of the weak force. j^μ_W is the leptonic component of the charged weak current,

$$j^\mu_W = \sum_{\alpha=e,\mu,\tau} \bar{\nu}_\alpha \gamma^\mu \left(1-\gamma^5\right) l_\alpha, \tag{2.5}$$

where the neutral leptonic field is denoted by ν and the charged leptonic field by l. γ^μ corresponds to one of the 4 gamma matrices where, $\mu = \{0,1,2,3\}$ [24] [25].

The left-handed nature of the charged weak current arises naturally from the V-A structure since the left and right-handed projection operators are defined as,

$$P_L = \frac{1}{2}\left(1-\gamma^5\right); \qquad P_R = \frac{1}{2}\left(1+\gamma^5\right), \tag{2.6}$$

$$\tag{2.7}$$

where $\gamma^5 = i\gamma^0\gamma^1\gamma^2\gamma^3$. When applied to generic left and right-handed particle and antiparticle bi-spinors, u and v respectively, $P_L u = u_L$ and $P_L v = v_R$ [22].

The Z-boson can couple to right-handed particles and left-handed anti-particles, however the neutrino itself is entirely left-handed, therefore the neutral current is depicted in the Standard Model as per,

$$\mathcal{L}_{NC} = \frac{g}{2\cos\theta_W} j^\mu_Z Z_\mu, \tag{2.8}$$

where Z_μ is now the Z-boson field, and $\cos\theta_W$ the weak mixing angle. j^μ_Z is now the neutral leptonic weak current,

$$j^\mu_Z = \sum_{\alpha=e,\mu,\tau} \left[\bar{l}_\alpha \gamma^\mu \left(g^l_V - g^l_A\gamma^5\right) l_\alpha + \bar{\nu}_\alpha \gamma^\mu \left(g^\nu_V - g^\nu_A\gamma^5\right) \nu_\alpha\right], \tag{2.9}$$

with additional fermionic couplings for the neutral vector and axial components, $g^\nu_V = g^\nu_A = 1/2$ and charged vector and axial components, $g^l_V = -1/2 + 2\sin^2\theta_W, g^l_A = -1/2$ respectively [24]. The additional factor of $2\sin^2\theta_W$ in the charged axial component of the weak neutral current allows the weak current to couple to right-handed charged fermions. θ_W is the Wienberg angle or weak mixing angle and relates the masses of the $W^\pm$ and Z^0 bosons as per, $\cos\theta_W = M_W/M_Z$ as well as being defined by the weak coupling constant, g, and the fine-structure constant, α, as per, $\sin\theta_W = \sqrt{4\pi\alpha}/g$.

2.3. Neutrino oscillations

Expanding the definition of the neutrino to include multiple flavours opened up the field to wider possibilities, the most prominent of which involved the oscillation between such flavours. In 1957 Pontecorvo had sought to determine that the neutrino and antineutrino were not the same particle, and proposed that mixing between the neutrino and antineutrino may not be strictly forbidden [26]. Similarly, following the discovery of the muon neutrino, in 1967 he expanded this proposal of neutrino oscillations to include the transition between flavours [27].

Neutrino oscillation measurements are made using two analysis procedures, the 'disappearance' method and the 'appearance' method. A disappearance search involves monitoring the change in event rate of a single neutrino flavour over a defined distance. An appearance search involves determining the event rate of flavour β given an initial sample of flavour α with known β contamination. Depending on their sensitivity to each flavour eigenstate, a given experiment can make one or both of these measurements [28]. Having a comprehensive understanding of the neutrino flux and interaction cross-sections is also deterministic of the sensitivity an experiment has to each of these analysis procedures.

This section will begin with an overview of the first experimental hints and evidence for the existence of neutrino oscillations in sections 2.3.1 and 2.3.2 respectively. An introduction to the three-flavour active neutrino oscillation phenomenology will then be given in section 2.3.3 respectively, followed by a description of two modifications to this framework in section 2.3.4. A summary of the global active neutrino oscillation dataset will then be given in section 2.3.5. An extension to the active paradigm involving the introduction of a single eV-scale sterile neutrino will be discussed in section 2.4.

2.3.1. Origin of solar and atmospheric neutrino anomalies

In 1968, Ray Davis, Don Harmer and Kenneth Hoffman observed a deficit in the expected rate of neutrinos from the decay of ^{8}B in the sun [29]. Their detector was located 4850 ft underground at the Homestake mine in Lead, SD, and contained $3.9{\times}10^5$ litres of liquid tetrachloroethylene with the aim of observing $\sim$10 MeV neutrinos through the ν_e capture reaction,

$$\nu_e + {}^{37}\mathrm{Cl} \rightarrow e^- + {}^{37}\mathrm{Ar}. \tag{2.10}$$

The rate of solar neutrinos measured in the Homestake experiment was 7 times lower than expected, having taken into account all known sources of background [29]. This was the first occurrence of a neutrino-based anomaly since their discovery 22 years prior.

Several years after finding the first indications of the solar neutrino anomaly, the Kamiokande, GALLEX and SAGE experiments each measured their own deficit, none of which matched the rate recorded by the Homestake experiment. GALLEX and SAGE primarily measured neutrinos emitted from pp fusion at energies around 0.7 MeV, whilst Kamiokande measured high energy solar neutrinos, between 4 and 18.7 MeV [30] [31] [32]. The implication from the four differing results was then that the solar neutrino problem was energy dependent.

A further anomaly was indicated by the Irvine-Michigan-Brookhaven (IMB) and Kamiokande experiments in 1986 who were primarily looking for proton decay and could observe higher energy, ∼1 GeV, atmospheric electron and muon neutrinos [33] [34]. Atmospheric neutrinos are produced via the decay of pions, kaons and muons in the atmosphere of the Earth. The dominant decay modes are,

$$\begin{aligned} \pi^+ &\rightarrow \mu^+ + \nu_\mu \\ &\qquad \big\lfloor\!\!\longrightarrow e^+ + \nu_e + \bar{\nu}_\mu, \end{aligned} \tag{2.11}$$

and their corresponding charge conjugates, resulting in an expected ratio of electron to muon neutrinos in the atmospheric flux of approximately $(\nu_e+\bar{\nu}_e) : (\nu_\mu+\bar{\nu}_\mu)$=1:2 [35] [36]. IMB and Kamiokande observed a lower rate of muon neutrinos than expected, and although they could not confidently conclude that there was a deficit at the time, it was the first indication of an atmospheric neutrino anomaly [33] [34].

2.3.2. Resolving the solar and atmospheric neutrino anomalies

The atmospheric anomaly was the first to be solved by the Super Kamiokande (SuperK) experiment in 1998 [36]. The SuperK detector is a 50 kiloton water Čherenkov detector with a 22.5 kiloton fiducial volume surrounded by ∼11,000 photomultiplier tubes (PMTs).

SuperK aimed to measure the $\Phi = \nu_\mu/\nu_e$ flux ratio by looking for the final state particles of neutrino interactions in ultra-pure water. A ν_e interaction produces a characteristic Čherenkov ring known as 'electron-like', which is more blurred-out than the well-defined 'muon-like' Čherenkov ring [36].

SuperK calculated the ratio of the neutrino flux in data with that of the expected MC, $R \equiv \Phi_{Data}/\Phi_{MC}$, to determine if it deviated from the nominal value of $R = 1$. They recorded a value around $R \approx 0.6$ and the data was consequently in good agreement with two-flavour atmospheric neutrino oscillations and presented the first limits on the atmospheric oscillation parameters: $\sin^2 2\theta_{23} > 0.82$ and $5\times10^{-4} < \Delta m^2_{32} < 6\times10^{-3}$ eV^2 at a 90% confidence level [36] these parameters will be defined in section 2.3.3.

The solar neutrino anomaly was resolved in 2001 by the Sudbury Neutrino Observatory (SNO)[3]. SNO is a spherical water Čherenkov detector containing 1×10^6 kgs of ultra-pure D_2O. The Čherenkov light is collected by the 9456 PMTs surrounding the detector volume and can be reconstructed as one of the following interactions,

$$\nu_e + d \rightarrow p + p + e^- \tag{2.12}$$
$$\nu_x + d \rightarrow \nu_x + p + n \tag{2.13}$$
$$\nu_x + e^- \rightarrow \nu_x + e^-. \tag{2.14}$$

The charged current interaction in equation 2.12 is sensitive only to the electron neutrino, but the elastic scattering and neutral current interactions in equations 2.13 and 2.14 are sensitive to all 3 neutrino flavours [3]. SNO could therefore measure both the total flux of the incoming solar neutrinos along with the flux of only the electron neutrinos, which is the predominant flavour produced by ^8B in the sun. They confirmed that the total flux was consistent with theoretical models, but the comparison between the total and electron neutrino-only flux returned a lower rate than expected, implying that the component of the total flux from a different neutrino flavour was higher than the models suggested [3]. The first measurement recorded by SNO was a 3.3σ variation from expectation of non-electron solar neutrino interactions and set the first limits on the solar mass splitting: $\Delta m^2_{12} < 10^{-3}$ eV^2. Alongside this first limit, SNO also presented an updated estimate of the atmospheric mass splitting at $\Delta m^2_{32} \simeq 3.5 \times 10^{-3}$ eV^2 [3].

The Kamioka Liquid scintillator antineutrino Detector (KamLAND) experiment was built to detect antineutrinos from nuclear reactors at baselines of about 180km. $\bar{\nu}_e$'s with energies above 1.8 MeV were detected through the selection of positrons from

inverse β decay reactions ($\bar{\nu}_e + p \rightarrow e^+ + n$) and the gamma ray following neutron capture. The energy and baseline of KamLAND was able to set the first limits on the solar neutrino angle (θ_{12}) using man-made reactor, rather than solar, neutrinos in 2002: $0.86 < \sin^2 2\theta_{12} < 1.0$ [37].

By 2003, SNO had collected data in three distinct phases of the experiment,

1. The pure D_2O phase, described above
2. Day/night phase, sensitive to measuring neutrinos which traverse the Earth and are therefore subject to possible matter effects
3. Salt phase, with an enhanced sensitivity to neutral-current interactions over charged-current and elastic-scattering interactions.

With the two additional datasets, the SNO experiment was consequently able to further-constrain the solar mass splitting limit to $\Delta m^2_{21} = 7.1^{+1.0}_{-0.3}$ eV^2 as well as set a new limit on the solar mixing angle, $\theta_{12} = 32.5^{+1.7}_{-1.6}$ [38].

Additional three-flavour neutrino oscillation parameter limits, including updates to the solar and atmospheric parameters, from modern neutrino oscillation experiments will be discussed in section 2.3.5.

2.3.3. The three-flavour active neutrino paradigm

In the active paradigm neutrinos exist in two forms, each with 3 variants: Flavour eigenstates, ν_e, ν_μ, ν_τ, and mass eigenstates, ν_1, ν_2, ν_3. The flavour eigenstates undergo weak interactions and are experimentally detectable whilst the mass eigenstates dictate the propagation of neutrinos in space and time. The mass-state composition of the flavour states evolves along the trajectory of the neutrino due to the differences in momenta of the mass eigenstates, it is this formulation which results in neutrino flavour oscillations [39].

In order to determine the probability of oscillations occurring between neutrino flavour states in space, it is necessary to define their behaviour in time. The neutrino flavour eigenstates will be referred to using the Greek alphabet, for instance $\alpha, \beta, \gamma = (e, \mu, \tau)$. The mass eigenstates will be referred to using the Latin alphabet, for instance $i, j, k = (1, 2, 3)$. Using this construction, the flavour eigenstates are defined by the flavour of

the lepton which is involved in the interaction process, while the mass eigenstates are defined as follows,

$$\mathscr{H}|\nu_k\rangle = E_k|\nu_k\rangle = \sqrt{m_k^2 + \mathbf{p}^2}|\nu_k\rangle, \tag{2.15}$$

where $\mathscr{H}$ is the Hamiltonian operator [39] and the time-independent mixing between the flavour and mass states is defined as,

$$|\nu_\alpha\rangle = \sum_{k=1}^{3} U_{\alpha k}^* |\nu_k\rangle \tag{2.16}$$

$$|\nu_k\rangle = \sum_{\alpha} U_{\alpha k} |\nu_\alpha\rangle, \tag{2.17}$$

where each of $U_{\alpha k}$ are elements of the unitary Pontecorvo–Maki–Nakagawa–Sakata (PMNS) matrix such that $U^{-1} = U^\dagger \equiv (U^*)^T$ [22].

U can be decomposed as the product of 3x3 matrices [40]:

$$\begin{aligned} U_{\alpha k} &= \begin{pmatrix} U_{e1} & U_{e2} & U_{e3} \\ U_{\mu 1} & U_{\mu 2} & U_{\mu 3} \\ U_{\tau 1} & U_{\tau 2} & U_{\tau 3} \end{pmatrix} \\ &= \begin{pmatrix} 1 & 0 & 0 \\ 0 & c_{23} & s_{23} \\ 0 & -s_{23} & c_{23} \end{pmatrix} \begin{pmatrix} c_{13} & 0 & s_{13}e^{-i\delta} \\ 0 & 1 & 0 \\ -s_{13}e^{i\delta} & 0 & c_{13} \end{pmatrix} \begin{pmatrix} c_{12} & s_{12} & 0 \\ -s_{12} & c_{12} & 0 \\ 0 & 0 & 1 \end{pmatrix}, \end{aligned} \tag{2.18}$$

in which $c_{ij} = \cos\theta_{ij}$ and $s_{ij} = \sin\theta_{ij}$. The matrix is parametrised by three real mixing angles, $\theta_{12}, \theta_{23}, \theta_{13}$ and a single CP-violating complex phase, $e^{i\delta}$ [40]. Similarly,

$$U_{\alpha k}^* = \begin{pmatrix} U_{e1}^* & U_{\mu 1}^* & U_{\tau 1}^* \\ U_{e2}^* & U_{\mu 2}^* & U_{\tau 2}^* \\ U_{e3}^* & U_{\mu 3}^* & U_{\tau 3}^* \end{pmatrix}. \tag{2.19}$$

The time evolution of the mass eigenstates can be defined by a plane wave solution and propagated to the flavour states as per equations (2.20) and (2.21) [41]:

$$i\frac{\partial}{\partial t}|\nu_k(t)\rangle = \mathscr{H}|\nu_k(t)\rangle = E_k|\nu_k(t)\rangle \Longrightarrow |\nu_k(t)\rangle = e^{-iE_k t}|\nu_k(0)\rangle, \tag{2.20}$$

where $t \neq 0$. From this point on $|\nu\rangle = |\nu(0)\rangle$. The flavour eigenstates then evolve as,

$$|\nu_\alpha(t)\rangle = \sum_{k=1}^{3} U^*_{\alpha k} e^{-iE_k t}|\nu_k\rangle = \sum_{\gamma}\left(\sum_{k=1}^{3} U^*_{\alpha k} e^{-iE_k t} U_{\gamma k}\right)|\nu_\gamma\rangle, \tag{2.21}$$

where $|\nu_\alpha(t)\rangle$ is a superposition of neutrino flavour states having initially been in the definite flavour state $|\nu_\alpha\rangle$.

The probability of measuring a neutrino in the definite flavour state, $|\nu_\beta\rangle$, at a given time, t, having been in the definite initial state, $|\nu_\alpha\rangle$, is:

$$P_{\alpha\to\beta}(t) = |\langle\nu_\beta|\nu_\alpha(t)\rangle|^2 = \left|\sum_{\gamma}\left(\sum_{k=1}^{3} U^*_{\alpha k} U_{\gamma k} e^{-iE_k t}\right)\langle\nu_\beta|\nu_\gamma\rangle\right|^2, \tag{2.22}$$

where $\langle\nu_\beta|\nu_\gamma\rangle = \delta_{\beta\gamma}$. Expanding the squared amplitude of the $|\nu_\alpha\rangle \to |\nu_\beta\rangle$ transitions after a time, t gives,

$$P_{\alpha\to\beta}(t) = \left|\sum_{k=1}^{3} U^*_{\alpha k} U_{\beta k} e^{-iE_k t}\right|^2 = \sum_{k=1}^{3}\sum_{j=1}^{3} U^*_{\alpha k} U_{\beta k} U_{\alpha j} U^*_{\beta j} e^{-i(E_k - E_j)t}. \tag{2.23}$$

It is then the ultra-relativistic nature of the neutrino that is used to translate the energy of the eigenstates into the squared mass differences, which are the final parameters of interest in the calculation of the active neutrino oscillation probabilities. In this context, $\mathbf{p_k} \gg m_k$ therefore $\mathbf{p}$ is constant for all values of k and in natural units $t \to L$ since $c = 1$.

Given,

$$E_k = \sqrt{\mathbf{p}^2 + m_k^2} = \mathbf{p}\left[1 + \left(\frac{m_k}{\mathbf{p}}\right)^2\right]^{\frac{1}{2}}, \tag{2.24}$$

using a Taylor expansion and the definition $\lim_{m\to 0} E = \mathbf{p}$, the squared mass difference of the mass eigenstates, $\Delta m^2_{ij} = m^2_i - m^2_j$, can be used in place of the energy of the mass eigenstates as per:

$$E_k = E + \frac{m_k^2}{2E} \Longrightarrow E_k - E_j = \frac{\Delta m^2_{kj}}{2E}, \tag{2.25}$$

in which the mass splittings are not independent, $\Delta m^2_{12} + \Delta m^2_{23} = \Delta m^2_{13}$. Therefore, the probability of a neutrino with initial flavour, $|\nu_\alpha\rangle$, to be in the flavour state, $|\nu_\beta\rangle$, after travelling a distance $L(= t)$ is [41]:

$$P_{\alpha\to\beta}(t) = \sum_{k,j=1}^{3} U^*_{\alpha k} U_{\beta k} U_{\alpha j} U^*_{\beta j} \exp\left(-i\frac{\Delta m^2_{kj} L}{2E}\right). \tag{2.26}$$

Parametrising this probability in terms of the mass splittings and the mixing angles can be done by expanding equation (2.26) into its real and imaginary components and considering the Hermitian and Unitarity nature of the PMNS matrix definitions [42]. The probability then becomes,

$$\begin{aligned} P_{\alpha\to\beta} = \delta_{\alpha\beta} &- 4\sum_{k>j} \Re\left[U^*_{\alpha k} U_{\beta k} U_{\alpha j} U^*_{\beta j}\right] \sin^2\left(\frac{\Delta m^2_{kj} L}{4E}\right) \\ &+ 2\sum_{k>j} \Im\left[U^*_{\alpha k} U_{\beta k} U_{\alpha j} U^*_{\beta j}\right] \sin\left(\frac{\Delta m^2_{kj} L}{2E}\right). \end{aligned} \tag{2.27}$$

The first term corresponds to no oscillations at all. The middle term corresponds to three-flavour oscillations, in which the component defined by the real parts of the PMNS matrix elements defines the amplitude of the oscillation and the component driven by the mass splitting defines the phase. The final term accounts for the impact of CP-violation. The probability as a whole is used by experiments to determine the expected rate of neutrino oscillations occurring in a vaccuum [41]. When $\alpha = \beta$, $\mathrm{P}(\nu_\alpha \to \nu_\beta)$ is the ν_α survival probability.

2.3.4. Modifications to the active neutrino oscillation picture

Modifications can be made to the three-flavour neutrino oscillation framework in order to either simplify the model according to a valid physical assumption, or to add in complexities which arise in nature. Examples of such revisions will be discussed here.

2.3.4.1. Two-flavour oscillations

An alternative demonstration of neutrino oscillation phenomenology involves the approximation in which there are only 2 mass and flavour eigenstates. In this simplified model, the flavour and mass eigenstate labels will remain general $\gamma = (\alpha, \beta)$ and $k = (i, j)$. The first implication of this approximation is that there is only a single mass splitting, $\Delta m^2 = m_i^2 - m_j^2$. The second is that the parametrisation of a unitary matrix of order 2 only requires a single, real, mixing angle, θ:

$$\begin{pmatrix} \nu_\alpha \\ \nu_\beta \end{pmatrix} = \begin{pmatrix} \cos\theta & \sin\theta \\ -\sin\theta & \cos\theta \end{pmatrix} \begin{pmatrix} \nu_i \\ \nu_j \end{pmatrix}. \tag{2.28}$$

Consequently, the probability of a neutrino in the initial flavour state, $|\nu_\alpha\rangle$ to be found in the flavour state $|\nu_\beta\rangle$ after travelling a distance L becomes,

$$P_{\alpha\to\beta} = \sin^2(2\theta)\sin^2\left(\frac{\Delta m^2 L}{4E}\right), \tag{2.29}$$

Typically, an experiment will be sensitive to a mass splitting around [40],

$$|\Delta m^2| \sim \frac{E}{L}, \tag{2.30}$$

where E is the energy of the detected neutrinos and L is the distance travelled before reaching the detector, the 'baseline'. These two parameters are therefore the main considerations when designing a neutrino oscillation experiment to ensure maximum sensitivity to the physics.

Substituting these relations into equation (2.29) and defining sensible units for the measured parameters [40], results in this oscillation probability in the two-flavour case:

$$P_{\alpha\to\beta} = \sin^2(2\theta)\sin^2\left(1.27\frac{\Delta m^2[\mathrm{eV}^2]L[\mathrm{km}]}{E[\mathrm{GeV}]}\right), \tag{2.31}$$

where

$$L^{Max}[\mathrm{km}] = \frac{\pi}{2}\frac{1}{1.27}\frac{E[\mathrm{GeV}]}{\Delta m^2[\mathrm{eV}^2]}, \tag{2.32}$$

is the location of the first oscillation maximum [28].

Although this two-flavour approximation is not sufficient to describe the entire active neutrino oscillation picture, there are a few circumstances in which it can be used as an informative representation of neutrino oscillation behaviour. These include,

1. If one of the 3 mixing angles approaches 0, slow oscillations become undetectable
2. If the approximation $\Delta m^2_{32} = \Delta m^2_{31}$ holds true, fast oscillations become undetectable
3. Sterile neutrino oscillations

In reality, although the value of $\theta_{13} < 10^\circ$ is very small, it is too large to satisfy the first approximation across long ranges. Similarly, although Δm^2_{32} and Δm^2_{31} are two orders-of-magnitude apart, long-range oscillation experiments are still capable of being sensitive to both parameters at once.

2.3.4.2. Matter effects

The neutrino oscillation mechanisms discussed in the previous sections assumed that the neutrinos are oscillating a vacuum, such that all neutrino flavour eigenstates interact equally. In order to account for the propagation of neutrinos through distances greater than around 1000km, for instance through the Earth and Sun, effects caused by neutrino interactions with matter must be considered. These matter effects primarily involve neutral and charged-current coherent scattering of neutrinos off electrons and nucleons in a medium. As is indicated in Figure 2.1, the neutral-current scattering impacts all active neutrino flavours equally, whilst the charged-current coherent scattering occurs only for electron neutrinos off electrons in matter [43].

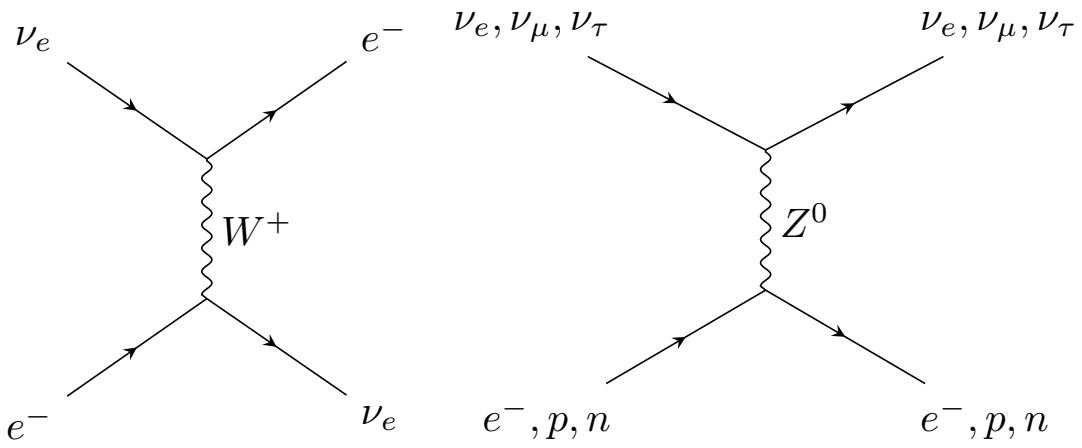

Figure 2.1.: Feynman diagrams of the charged (left) and neutral-current (right) coherent scattering processes which neutrinos are subject to as the propagate through large quantities of matter [43].

The consequences of these interactions with matter are represented by additional potentials in the Hamiltonian. The flavour-independence of the neutral-current scattering results in no change to the oscillation probability. The charged-current potential only affects electron neutrinos, and results in a modification to the time evolution of electron neutrinos in matter, compared to that of muon and tau neutrinos [40]. The corresponding charged-current potential therefore depends on the electron density of the medium, N_e,

$$V_{CC} = \sqrt{2} G_F N_e, \tag{2.33}$$

where G_F is the Fermi weak coupling constant. The neutrino oscillation mixing parameters can be modified in order to retain the form of the two-flavour oscillation probability,

$$\Delta m^2_m = \sqrt{\left(\Delta m^2 \cos 2\theta - 2E_\nu V_{CC}\right)^2 + \left(\Delta m^2 \sin 2\theta\right)^2}, \tag{2.34}$$

$$\sin 2\theta_m = \frac{\Delta m^2 \sin 2\theta}{\Delta m^2_m}, \tag{2.35}$$

where Δm^2_m and $\sin^2 2\theta_m$ are the effective, modified, mass splitting and mixing amplitude in the two-flavour neutrino oscillations in matter. The effective two-flavour oscillation probability in matter then becomes,

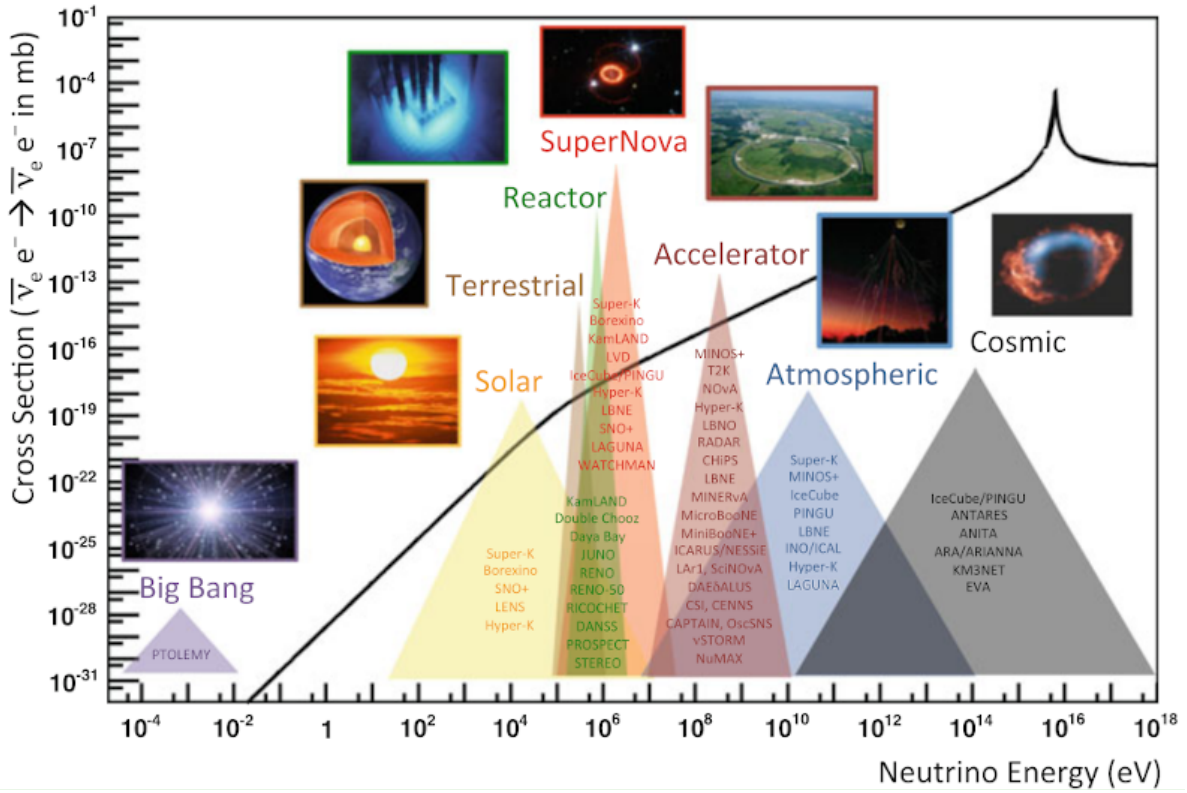

Figure 2.2.: Anti-electron neutrino scattering cross-section as a function of energy. The energy spectra is categorised into regions based on the neutrino sources which are able to produce them, along with a list of experiments built to study them [40].

$$P_{\nu_e(x)\rightarrow\nu_\mu} = \sin^2 2\theta_m \sin^2\left(\frac{\Delta m_m^2 x}{4E_\nu}\right). \tag{2.36}$$

Matter effects have some interesting implications for neutrino oscillations in both the two and three flavour framework [43],

1. A resonance exists when $2E_\nu V_{CC} = \Delta m^2 cos2\theta$ such that mixing is maximal ($\pi/4$) and total transitions between flavours are made possible, this is known as the Mikheyev-Smirnov-Wolfenstein (MSW) effect [40]

2. Matter effects depend on the sign of Δm^2, therefore they are required in the determination of the neutrino mass ordering [44].

2.3.5. Current status of the active neutrino oscillation picture

The neutrino oscillation mixing parameters are able to be constrained by neutrinos from a variety of sources, each with a characteristic energy spectra and flavour profile. Figure 2.2 depicts the anti-electron neutrino interaction cross-section across the huge range of possible interaction energies, categorised into the sources and experiments which produce and study them [40]. This section will summarise the most recent results from many neutrino oscillation experiments using a range of these sources. Table 2.1 lists the current global best fit values for the three-flavour neutrino oscillation parameters as of January 2021 [45], the values are presented for both the normal and inverted mass orderings. Contributions to this global best fit are discussed below.

2.3.5.1. Neutrino mass ordering

The parametrisation of equations (2.27) and (2.31) dictates that neutrino oscillation experiments are only sensitive to the squared mass difference of the neutrino mass eigenstates and cannot be used to directly measure the absolute neutrino masses. Determining the absolute mass of each active neutrino is a much more complex issue than measuring the mass splittings, and dedicated experiments such as KATRIN are required to measure theses quantities [46].

Existing experimental measurements have confirmed that $|\Delta m^2_{32}| \sim |\Delta m^2_{31}| \sim 10^{-3}$ eV^2 and this value is commonly referred to as the atmospheric mass splitting, $|\Delta m^2_{3l}| = |\Delta m^2_{atm}|$ whose sign is unknown. The atmospheric mass splitting is approximately 2 orders of magnitude larger than $\Delta m^2_{21} \sim 10^{-5}$ eV^2, which is referred to as the solar mass splitting, Δm^2_{sol}, whose sign is known [44]. Since the sign of Δm^2_{atm} is yet to be defined, the third neutrino mass eigenstate could be either larger or smaller than the first and second. The 'Mass Ordering' refers to the size-ordering of the absolute neutrino masses, where $m_3 > m_2 \sim m_1$ is known as the 'Normal Mass Ordering', whereas $m_3 < m_2 \sim m_1$ is known as the 'Inverted Mass Ordering' [40].

Experiments are currently trying to determine whether the neutrino masses follow that of the normal or inverted orderings. The magnitude of δ_{CP} is as yet poorly constrained in the lepton sector, and influences how much each neutrino flavour contributes to each mass eigenstate. Figure 2.3 demonstrates these characteristics of the active neutrinos in the two possible orders of the neutrino masses [44]. If the smallest neutrino mass is

Parameter	Best Fit $\pm$ 1σ	2σ Range	3σ Range
Δm^2_{21} $[10^{-5}\text{eV}^2]$	$7.50^{+0.22}_{-0.20}$	7.12-7.93	6.94-8.14
Δm^2_{31} $[10^{-3}\text{eV}^2]$ (NO)	$2.55^{+0.02}_{-0.03}$	2.49-2.60	2.47-2.63
Δm^2_{31} $[10^{-3}\text{eV}^2]$ (IO)	$2.45^{+0.02}_{-0.03}$	2.39-2.50	2.37-2.53
$\sin^2\theta_{12}$ $[10^{-1}]$	3.18 ± 0.16	2.86-3.52	2.71-3.69
θ_{12} [°]	34.3 ± 1.00	32.3-36.4	31.4-37.4
$\sin^2\theta_{23}$ $[10^{-1}]$ (NO)	5.74 ± 0.14	5.41-5.99	4.34-6.10
θ_{23} [°] (NO)	49.26 ± 0.79	47.37-50.71	41.20-51.33
$\sin^2\theta_{23}$ $[10^{-1}]$ (IO)	$5.78^{+0.10}_{-0.17}$	5.41-5.99	4.33-6.08
θ_{23} [°] (IO)	$49.46^{+0.60}_{-0.97}$	47.37-50.71	41.16-51.25
$\sin^2\theta_{13}$ $[10^{-1}]$ (NO)	$2.200^{+0.069}_{-0.062}$	2.069-2.337	2.000-2.405
θ_{13} [°] (NO)	$8.53^{+0.13}_{-0.12}$	8.27-8.79	8.13-8.92
$\sin^2\theta_{13}$ $[10^{-1}]$ (IO)	$2.225^{+0.064}_{-0.070}$	2.086-2.356	2.018-2.424
θ_{13} [°] (IO)	$8.58^{+0.12}_{-0.14}$	8.30-8.83	8.17-8.96
δ $[\pi]$ (NO)	$1.08^{+0.13}_{-0.12}$	0.84-1.42	0.71-1.99
δ [°] (NO)	194^{+24}_{-22}	152-255	128-359
δ $[\pi]$ (IO)	$1.58^{+0.15}_{-0.16}$	1.26-1.85	1.11-1.96
δ [°] (IO)	284^{+26}_{-28}	226-332	200-353

Table 2.1.: Three-flavour oscillation parameters from a fit to global data. (NO) refers to the local minima under the normal mass ordering, whilst (IO) refers to the local minima under the inverted ordering [45].

much larger than the magnitude of the mass splittings, then the neutrino masses are degenerate and the hierarchical nature of the mass ordering is diminished [47].

In order to measure both the sign of Δm^2_{atm} and the magnitude of CP violation in the lepton sector, an experiment must be sensitive to the imaginary part of equation 2.27. This requirement stems from the fact that the $\sin^2$ term in the real part of equation 2.27 removes any sensitivity to the sign of Δm^2, which is not the case in the imaginary part.

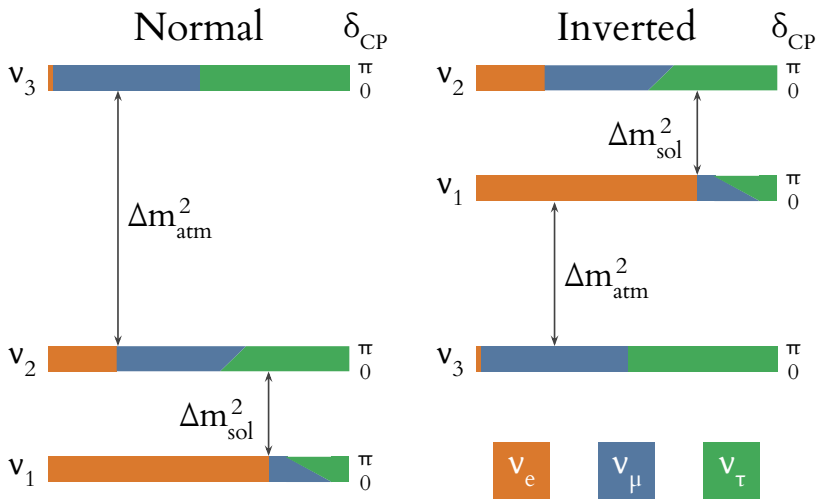

Figure 2.3.: A demonstration of how the neutrino flavour eigenstates contribute to the neutrino mass ordering in each of the normal and inverted cases. The magnitude of the as-yet-unknown CP-violating phase will impact the flavour contributions to the mass states and this is also shown [44]. The magnitude of the atmospheric mass splitting, $|\Delta m^2_{atm}|$, is approximately 300 times larger than that of the solar mass splitting, $|\Delta m^2_{sol}|$.

In order to make these measurements, large quantities of appearance data are required, since,

- In disappearance measurements, the imaginary part of equation 2.27 collapses to 0 on account of the fact that $U^*_{\alpha\beta}U_{\beta\alpha} = 1$, which is real
- Large numbers of events are required in order to be sensitive to the small contribution of the CP-violating phase to the oscillation probability.

2.3.5.2. Atmospheric neutrino oscillation experiments

Contributions to the global best fit of the atmospheric neutrino experimental data includes the ν_μ-disappearance data from all four run periods of SuperK [48] and IceCube DeepCore [49] in 2018 as well as ν_τ-appearance data from DeepCore in 2019 [50]. The allowed regions from these contributions in the $\sin^2\theta_{23}$, Δm^2_{31} parameter space are given in Figure 2.4.

In addition to the results used in the global analysis, SuperK have released an updated analysis using improved reconstruction which included ν_e-appearance data and constraints on θ_{13} and δ_{CP} [51]. The updated limits assuming normal (inverted) ordering are as follows,

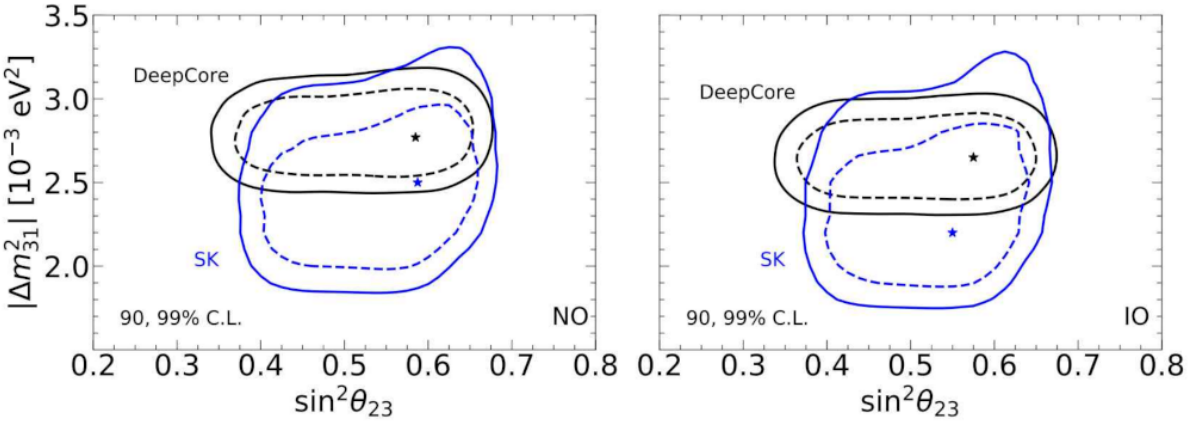

Figure 2.4.: Allowed regions of the $\sin^2\theta_{23}$, Δm^2_{31} parameter space for NO (left) and IO (right), obtained from Super-Kamiokande (SK) atmospheric (blue) and DeepCore (black) data included in the global analysis from [45]. The best fit values are indicated by stars.

$$
\begin{aligned}
|\Delta m^2_{32}| &= 2.63^{+0.10}_{-0.21}\ (2.53^{+0.14}_{-0.08}) \times 10^{-3}\ \text{eV}^2 \\
\sin^2\theta_{23} &= 0.588^{+0.030}_{-0.062}\ (0.575^{+0.034}_{-0.075})\ \text{[Second Octant, best fit]} \\
\sin^2\theta_{23} &= 0.425^{+0.051}_{-0.034}\ (0.425^{+0.075}_{-0.027})\ \text{[First Octant]} \\
\sin^2\theta_{13} &= 0.008^{+0.025}_{-0.005}\ (0.008^{+0.015}_{-0.007}) \\
\delta_{CP} &= 3.84^{+2.00}_{-2.14}\ (4.19^{+2.09}_{-4.19}).
\end{aligned}
$$

The IceCube DeepCore experiment is a new component of the IceCube neutrino observatory. DeepCore was designed to increase the sensitivity of the experiment to observing neutrinos around 10 GeV in energy, over an order-of-magnitude lower than the experiment was initially designed to detect. The total IceCube array houses 5160 PMTs, arranged as 60 PMTs per 86 vertical strings in the ice, to detect Čherenkov light. DeepCore comprises 8 such strings, corresponding to 480 PMTs with high quantum-efficiency. In order to increase the sensitivity to lower-energy neutrinos, the strings are densely packed and located in the bottom central region of the entire IceCube array at around 2100m below the ground at the South Pole, where the ice is clearest [52].

The DeepCore limits in both 2018 and 2019 use neutrinos from the full sky with reconstructed energies from 5.6 - 56 GeV [49]. Including the additional results from the ν_τ-appearance analysis, the DeepCore limits on the atmospheric parameters are,

$$
\begin{aligned}
|\Delta m^2_{32}| &= 2.55^{+0.12}_{-0.11} \times 10^{-3}\ \text{eV}^2 \\
\sin^2\theta_{23} &= 0.58^{+0.04}_{-0.13}.
\end{aligned}
$$

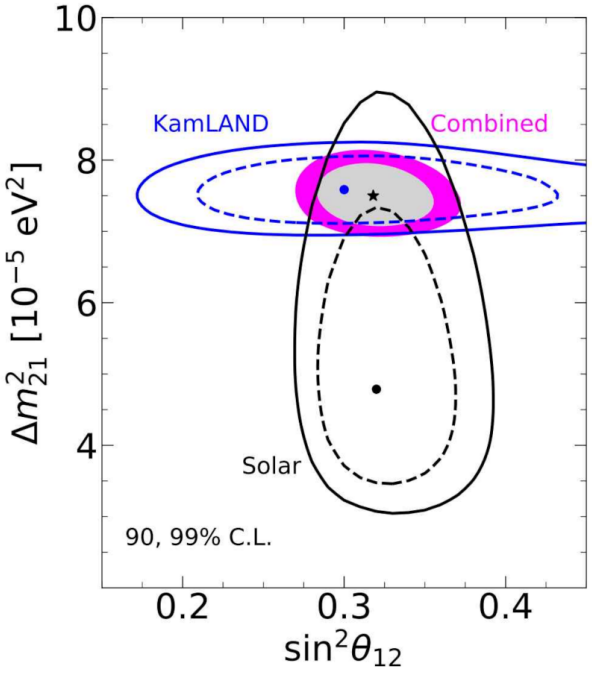

Figure 2.5.: Allowed regions of the $\sin^2\theta_{12}$, Δm^2_{21} parameter space obtained from solar neutrino experiments (black), KamLAND (blue) data and the combined analysis (shaded regions) from [45]. The individual best fit values are indicated by dots and the combined best fit point is indicated by a star.

The best fit points do not agree to within 1σ, however there is substantial overlap between the allowed regions in Figure 2.4 which indicates that the measurements are compatible with one another.

2.3.5.3. Solar neutrino oscillation experiments

The solar neutrino oscillation experiments included in the global best fit analysis include Homestake [53], SAGE [54], GALLEX [55], a combined analysis of all three SNO phases [56] and Borexino [57] [58]. In addition, the latest solar oscillation parameter limits from the KamLAND experiment were also included in the fit [59] [60].

Figure 2.5 shows the allowed regions in $\sin^2\theta_{12}$, Δm^2_{21} parameter space given by the combined solar data, the KamLAND results and finally a combined solar+KamLAND analysis which were inputs in the global fit. The combined best fit value of the solar mass splitting from the aforementioned solar experiments is $\Delta m^2_{21} = 4.8 \times 10^{-5}$ eV^2 [45]. The most-recent limits set by KamLAND used in the global analysis are [60],

$$\begin{aligned} \Delta m^2_{21} &= 7.53 \pm 0.18 \times 10^{-5} \text{ eV}^2 \\ \tan^2\theta_{12} &= 0.436^{+0.029}_{-0.025} \\ \sin^2\theta_{13} &= 0.023 \pm 0.002. \end{aligned}$$

Although not included in the global analysis, SuperK recently presented an updated set of solar neutrino oscillation parameter limits in combination with SNO [61],

$$\Delta m^2_{21} = 6.110^{+1.21}_{-0.68} \times 10^{-5}\ \text{eV}^2$$
$$\sin^2\theta_{12} = 0.306 \pm 0.014.$$

Although the two allowed regions in Figure 2.5 do overlap, and the combined result is more precise than the individual results in both the $\sin^2\theta_{12}$ and Δm^2_{21} parameters, the KamLAND allowed region confidently excludes the solar best fit point [45].

2.3.5.4. Reactor neutrino oscillation experiments

The two datasets included in the global fit come from the Reactor Experiment for Neutrino Oscillation (RENO) [62] and DayaBay [63]. RENO consists of a near and far detector placed 294 and 1383m from the central point of the antineutrino sources respectively. The sources comprise six pressurized water reactors in the Hanbit Nuclear Power Plant situated at equal distances spanning 1.3km linearly. The functionally-identical RENO near and far detectors both contain 16 tons of gadolinium-doped liquid scintillator and detect reactor $\bar{\nu}_e$ through inverse β decay. Prompt scintillation light from a pair of 0.51 MeV photons emitted following the annihilation of the positron and a plethora of photons amounting to around 8 MeV following delayed neutron capture by the gadolinium doping is detected by 354 PMT's which surround the detector [62]. The antineutrino energy spectra is used in the rate-only measurement of electron-antineutrino disappearance for the purpose of constraining the neutrino oscillation parameters.

RENO have released an updated constraint on $\sin^2\theta_{13}$ and the effective mass splitting, $\Delta m^2_{ee} = \cos^2_{12}\Delta m^2_{31} + \sin^2\Delta m^2_{32}$, following 2900 days of data-taking [64],

$$|\Delta m^2_{ee}| = 2.74 \pm 0.10\ (stat.) \pm 0.06\ (syst.) \times 10^{-3}\ \text{eV}^2$$
$$\sin^2\theta_{13} = 0.0892 \pm 0.0044\ (stat.) \pm 0.0045\ (syst.).$$

DayaBay consists of eight functionally-identical detectors, each filled with gadolinium-doped liquid scintillator, housed in 3 experiment halls. Two reactor cores located around 365m from the first near detector hall and four additional cores at around 505m from the second near detector hall produce antineutrinos which are detected through inverse

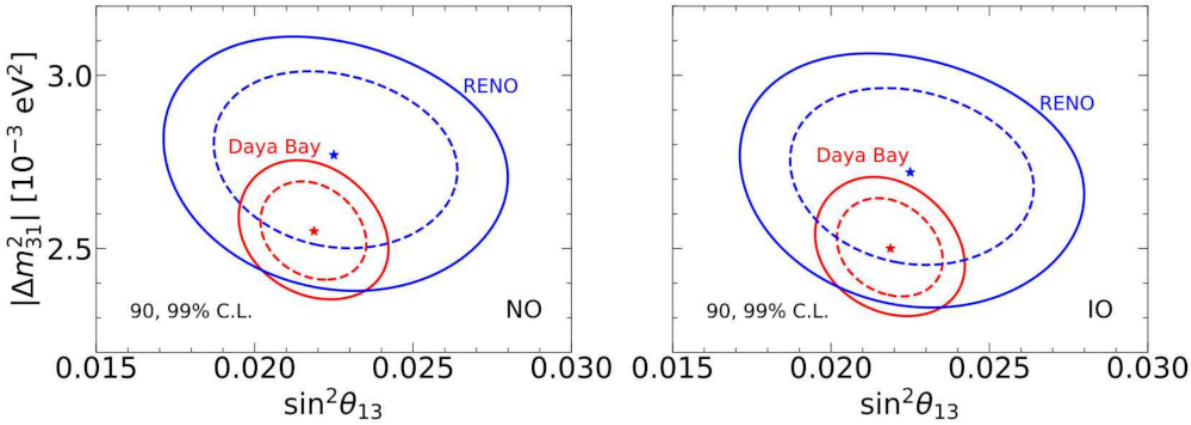

Figure 2.6.: Allowed regions of the $\sin^2\theta_{13}$, Δm^2_{31} parameter space for NO (left) and IO (right), obtained from the RENO (blue) and DayaBay (red) data included in the global analysis from [45]. The best fit values are indicated by stars.

β decay with 192 PMT's using the same detection and analysis technique as RENO [63]. DayaBay also measure the effective mass splitting, as well as $\sin^2\theta_{13}$ and Δm^2_{32}. The latest results from DayaBay following 1958 days of data-taking are,

$$
\begin{aligned}
|\Delta m^2_{ee}| &= 2.522^{+0.068}_{-0.070} \times 10^{-3}\ \text{eV}^2 \\
|\Delta m^2_{32}| &= 2.471^{+0.068}_{-0.070}\ (-2.575^{+0.068}_{-0.070}) \times 10^{-3}\ \text{eV}^2 \\
\sin^2\theta_{13} &= 0.0856 \pm 0.0029.
\end{aligned}
$$

These experiments are not sensitive to the mass ordering, therefore the results are identical under the normal and inverted hypotheses. Both the effective mass-splitting constraints do not quite agree to within the 1σ uncertainties, however Figure 2.6 shows that there is significant overlap of the allowed regions.

In addition to the constraints included in the global fit, Double Chooz have released a measurement of θ_{13} through total neutron capture following inverse β decay using their full dataset. Double Chooz also comprises functionally-identical near and far detectors, located at an average distance of 400 and 1050m from two pressurised water reactors in the N4 plant respectively. Once again, the detectors are filled with 10.3m^3 of gadolinium-doped liquid scintillator, surrounded by a gadolinium-free scintillator intended to capture the photons before they are detected by the 390 PMT's [65]. Double Chooz uses the electron antineutrino spectra in a rate+shape measurement of electron antineutrino disappearance in order to constrain the oscillation parameters, the most recent of which is $\sin^2 2\theta_{13} = 0.105 \pm 0.0014$ [66].

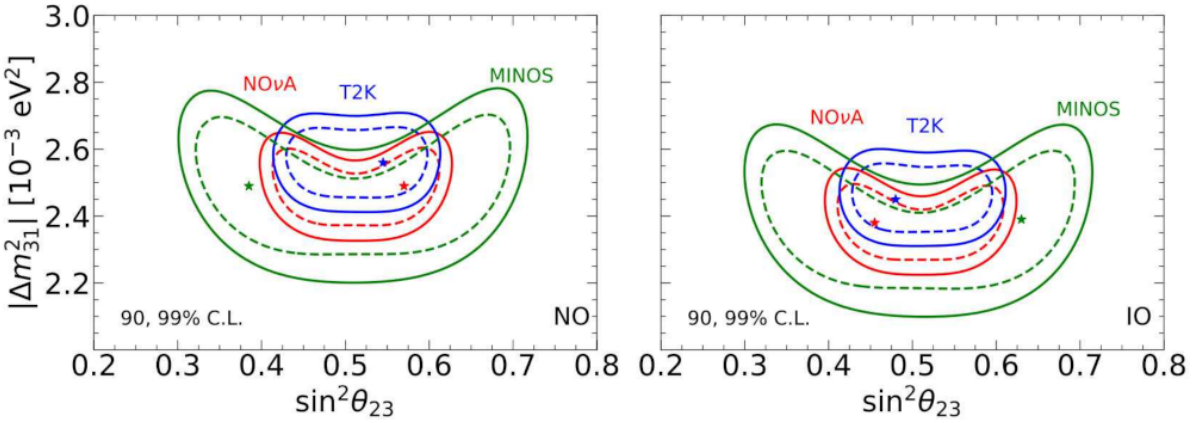

Figure 2.7.: Allowed regions of the $\sin^2\theta_{23}$, Δm^2_{31} parameter space for NO (left) and IO (right), obtained from the T2K (blue), NOνA (red) and MINOS (green) data included in the global analysis from [45]. The best fit values are indicated by stars.

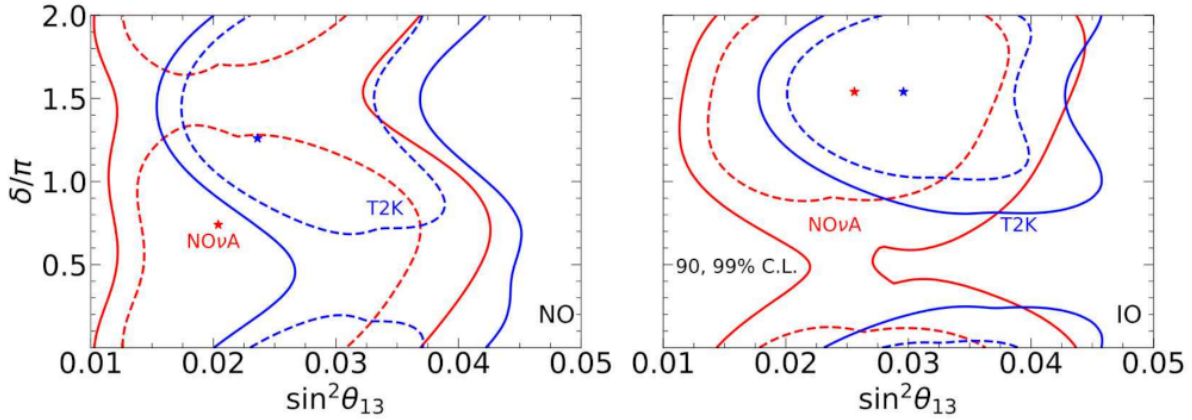

Figure 2.8.: Allowed regions of the $\sin^2\theta_{13}$, δ_{CP} parameter space for NO (left) and IO (right), obtained from the T2K (blue) and NOνA (red) data included in the global analysis from [45]. The best fit values are indicated by stars.

2.3.5.5. Accelerator neutrino oscillation experiments

This section will discuss the four long-baseline accelerator neutrino oscillation experiments whose results have been included in the global analysis. The most up-to-date neutrino oscillation parameter constraints from these accelerator experiments will also be given. Figures 2.7 and 2.8 show the allowed regions from the inputs to the global analysis in $\sin^2\theta_{23}$, Δm^2_{31} and $\sin^2\theta_{13}$, δ_{CP} parameter space respectively. These include contributions from, T2K [67], NOνA [68], MINOS [69] and K2K [70].

Beginning with the most-recent, the T2K experiment comprises two near detectors (INGRID and ND280) and a far detector (SuperK), with a 295km baseline and a primarily

ν_μ ($\bar{\nu}_\mu$) neutrino beam, sent from the Japan Proton Accelerator Research Complex (J-PARC). The J-PARC beam has been run in neutrino (antineutrino) mode and peaks at around 0.6 GeV. The INGRID near detector is an array of iron/scintillator strips, sandwiched together and arranged in a cross pattern. Both near detectors resides 280 downstream of the target, and the INGRID detector was designed to measure the beam direction and profile. The ND280 near detector was designed to constrain the $\nu_\mu, \bar{\nu}_\mu, \nu_e$ and $\bar{\nu}_e$ fluxes in the beam using three magnetised time projection chamber trackers and two fine-grained detectors surrounded by an electromagnetic calorimeter [71].

As of 2018, T2K has been exposed to 1.49×10^{21} neutrinos and 1.64×10^{21} antineutrinos. T2K has most-recently placed updated constraints on $\sin^2\theta_{23}$, Δm^2_{31} [71], through muon (anti)neutrino disappearance in neutrino (antineutrino) mode,

$$|\Delta m^2_{32}| = 2.47^{+0.08}_{-0.09}\ (2.50^{+0.18}_{-0.13}) \times 10^{-3}\ \text{eV}^2$$
$$\sin^2\theta_{23} = 0.51^{+0.06}_{-0.07}\ (0.43^{+0.21}_{-0.05}).$$

T2K have also recently given an updated set of $\sin^2\theta_{13}$ and δ_{CP} limits for the normal (inverted) mass ordering through measurements of electron (anti)neutrino appearance, and favour the normal mass ordering and the upper octant for θ_{23} [67] [72],

$$\delta_{CP},\ 3\sigma\ \text{CI} = [-3.41, -0.03]\ ([-2.54, -0.32])$$
$$\sin^2\theta_{13} = 0.0244^{+0.0021}_{-0.0064}.$$

The NOνA experiment consists of a near and far detector system located in the Fermilab NuMI beam at 1 and 810 km respectively. The NuMI beam peaks at around 2 GeV and is primarily a ν_μ ($\bar{\nu}_\mu$) beam when in neutrino (antineutrino) mode. The near and far detectors are made up of thousands of PVC cells which contain 290 and 14,000 tons of liquid scintillator respectively. Both detect many different neutrino interactions through the collection and reconstruction of energy depositions using wavelength-shifting fibres connected to photo-detectors [73].

NOνA have made ν_μ and $\bar{\nu}_\mu$ disappearance measurements as well as ν_e and $\bar{\nu}_e$ appearance measurements in order to constrain $\sin^2\theta_{23}$, Δm^2_{31} and δ_{CP}. The total neutrino (antineutrino) exposure included in making the most-recent measurements is 13.6×10^{20} (12.5×10^{20}) Protons on Target (POT) [68] and the NOνA data favours the upper octant for θ_{23} by 1.6σ and the normal mass ordering by 1.9σ [73],

$$
\begin{aligned}
|\Delta m^2_{32}| &= 2.41 \pm 0.07 \times 10^{-3}\ \text{eV}^2 \\
\sin^2\theta_{23} &= 0.57^{+0.04}_{-0.03} \\
\delta_{CP}&:\ \text{exclude } \pi/2 \text{ at } > 3\sigma \\
\delta_{CP}&:\ \text{disfavour } 3\pi/2 \text{ at } \sim 2\sigma.
\end{aligned}
$$

The Main Injector Neutrino Oscillation Search (MINOS) experiment is also a two-detector system located in the NuMI beam at Fermilab, with the detectors situated at 1 and 735 km respectively. MINOS was designed to measure ν_μ disappearance in order to constrain the atmospheric neutrino oscillation parameters, $\sin^2\theta_{23}$ and Δm^2_{32}. The MINOS detectors were designed to be functionally similar, and to detect neutrinos between with energies of around 3 GeV. The detectors are both steel-scintillator sampling calorimeters comprised of alternate planes of plastic scintillator strips and steel plates, which allows them to perform tracking, energy and particle-identification [74].

MINOS has so far been exposed to 10.71×10^{20} (3.36×10^{20}) neutrinos (antineutrinos) and the most-recent limits made assuming normal (inverted) mass ordering are,

$$
\begin{aligned}
|\Delta m^2_{32}| &= [2.28 - 2.46]\ ([2.32 - 2.53])\ \times 10^{-3}\ \text{eV}^2 \\
\sin^2\theta_{23} &= 0.35 - 0.65\ (0.34 - 0.67)\ [90\%\ \text{C.L.}].
\end{aligned}
$$

Prior to T2K, the K2K experiment combined a suite of near detectors at around 300 m from the target and used SuperK as the far detector, with a total baseline of 250 km. The EP1 neutrino beam produced primarily muon neutrinos, with some contamination from $\bar{\nu}_\mu, \nu_e$ and $\bar{\nu}_e$'s, with peak energies around 1 GeV. The near detector system was designed to characterise the unoscillated content of the beam and consisted of a kiloton water Čherenkov detector and a fine-grained detector which consisted of a scintillating-fibre/water-target tracker, a calorimeter, a fine-segmented scintillator tracker and a muon range detector [70].

K2K measured ν_μ disappearance from 0.922×10^{20} POT between 1999 and 2004. Using the two-flavour neutrino oscillation framework, K2K presented limits on the effective mass-splitting at the 90% confidence level with $\sin^2 2\theta = 1$,

$$
|\Delta m^2| = [1.9, 3.5]\ \times 10^{-3}\ \text{eV}^2.
$$

2.4. Sterile neutrinos

If there does exist a fourth type of neutrino, it must be 'sterile', such that it is unable to interact via the weak force. This requirement is necessary to maintain consistency with the three-flavour active neutrino picture defined by LEP. Given that they do not couple to the weak bosons, sterile neutrinos are unobservable both directly and indirectly in current neutrino oscillation experiments and their existence can only be determined through inconsistencies with the active-only neutrino oscillation picture.

This section will begin with an overview of the experimental anomalies which hinted towards the existence of one or more sterile neutrinos in section 2.4.1. The phenomenology of neutrino oscillations with the addition of a single sterile neutrino will be discussed within the two-flavour oscillation framework in sections 2.4.2. Finally, a summary of the global sterile neutrino oscillation dataset will be discussed in section 2.4.3.

2.4.1. Short-baseline anomalies and the first sterile hints

Following the observation of neutrino oscillations and the confirmation that neutrinos are massive particles, many experiments have taken advantage of the numerous sources of neutrinos to learn more about their behaviour, particularly in the context of flavour oscillations. Conflicting results have since emerged between existing oscillation data and the three flavour neutrino framework in short-baseline experiments, and are consequently under investigation. The anomalies hint towards the existence of an additional mass eigenstate at around $\Delta m^2 = 1$ eV^2 such that the oscillations of active neutrinos to this new state are fast, and consequently undetectable by long-baseline experiments. The first experimental hints towards the existence of one or more sterile neutrinos are as follows.

Up-to-date results from atmospheric, solar, reactor and accelerator experiments will be discussed in section 2.4.3.

2.4.1.1. Gallium neutrino oscillation anomaly

The radioactive neutrino experiments SAGE and GALLEX, who were built to detect solar neutrinos emitted in *pp* fusion, consistently observed a 40% deficit in electron neutrino events when searching for $\overset{(-)}{\nu}_e$ disappearance with ^{37}Ar and ^{51}Cr electron cap-

ture [75]. The statistical significance of this deficit was initially 3σ [76] and has since been reduced to 2.3σ [77]. Uniquely, both experiments have been able to assess their detection efficiency through the measurement of neutrino emission from radioactive sources placed within the detector volume, through inverse β decay $\nu_e + {}^{71}\mathrm{Ga} \longrightarrow {}^{71}\mathrm{Ge} + e^+$, and have consequently confirmed that the recorded solar neutrino deficit can not be caused by any such inefficiencies [30] [31] [75]. The result was found to be consistent with $\bar{\nu}_e$-disappearance due to active-sterile neutrino mixing with an eV^2-scale mass-splitting [77].

2.4.1.2. Reactor neutrino oscillation anomaly

Reactor neutrino experiments recently updated their flux model for neutrinos emitted by nuclear reactors and determined that the initial prediction of the reactor neutrino event rate had been too low. The reactor neutrino data which matched well with the initial flux prediction for $\overset{(-)}{\nu}_e$ disappearance searches was suddenly in tension with the up-to-date flux model with an overall rate difference of approximately 3% [78] [79] as well as an overall shape difference [78].

2.4.1.3. Accelerator neutrino oscillation anomaly

The accelerator-based experiments, MiniBooNE and the Liquid Scintillator Neutrino Detector (LSND) observed an excess of electron neutrinos in $\overset{(-)}{\nu}_\mu \rightarrow \overset{(-)}{\nu}_e$ appearance searches. LSND was located 30 m from the neutrino source at the Los Alamos Meson Physics Facility (LAMPF) and ran between 1993 and 1998 during which time the collaboration made ν_μ and $\bar{\nu}_\mu$ oscillation measurements with both decay-at-rest (DaR) and decay-in-flight (DiF) $\pi^\pm$'s. LSND was designed to search for $\bar{\nu}_\mu \rightarrow \bar{\nu}_e$ oscillations in the 20-50 MeV antineutrino beam from DaR pions and has since made measurements of $\nu_\mu \rightarrow \nu_e$ with the 60-200 MeV neutrino content of the beam from DiF pions [80].

LSND was designed to detect electron antineutrinos through inverse β decay from the positron-produced Čherenkov and photon-produced scintillation light. The dominant $\bar{\nu}_e$ backgrounds came from intrinsic $\bar{\nu}_e$ in the beam and low-energy μ^+ mis-identification when produced following the re-interaction of the muon antineutrino from DiF π^-'s. LSND reported an overall excess of events at the 3.8σ level, corresponding to possible oscillations at $\Delta m^2 \sim 1\ \mathrm{eV}^2$ [81].

MiniBooNE is a spherical detector filled with pure mineral oil (CH_2) located at a 541 m baseline in the Booster neutrino beam at Fermilab and collected data from 2002 until

2019. The detector is surrounded by 1520 PMTs which detect both Čherenkov and scintillation light from the charged particles produced in neutrino interactions, predominantly from charged-current quasi-elastic (CC QE) processes, in the detector. MiniBooNE also searched for ν_e and $\bar{\nu}_e$ appearance with a peak ν_μ ($\bar{\nu}_\mu$) energy of 0.6 GeV (0.4 GeV). Although this peak is substantially larger than that of LSND, the peak value of baseline/energy (L/E) is the same across the two experiments, which allows for identical sterile neutrino oscillation parameter searches.

The background contributions to the MiniBooNE results are also substantially different to those in LSND, the dominant backgrounds include $\pi^0 - e^-$ mis-identification, intrinsic ν_e's, single photon production. MiniBooNE was subject to 18.75×10^{20} (11.27×10^{20}) POT in neutrino (antineutrino) mode and observed an excess of neutrinos with energies below 1.25 GeV with a significance of 4.7σ. When interpreted as oscillations, the corresponding mass splitting is consistent with the one reported by LSND [82]. The combined significance of the LSND and MiniBooNE excesses is 6σ [82].

The strongest candidate explanation for all of the short baseline (SBL) anomalies is the existence of one or more 'Sterile' neutrinos, which will be discussed in the following sections. In addition, a summary of some of the other possible explanations for the anomalous results is given in section 2.4.4.

2.4.2. Sterile neutrino oscillations

In most short baseline neutrino experiments, a sterile neutrino oscillation measurement is made via one of the three channels,

- $\nu_\mu \to \nu_\mu$ (ν_μ disappearance)
- $\nu_\mu \to \nu_e$ (ν_e appearance)
- $\nu_e \to \nu_e$ (ν_e disappearance)

where the sensitivity of the measurement is dependent on the energy, baseline and neutrino source of the experiment. Measurements may also be made through the analogous channels with antineutrinos. In each disappearance case, a deficit in the observed event rate relative to predictions given by the three-flavour neutrino model could indicate that the active neutrino flavour eigenstate oscillated to a sterile flavour eigenstate. Similarly, in the electron neutrino appearance case, an excess of observed electron neutrinos could be due to the oscillation of a sterile flavour eigenstate into the active flavour state.

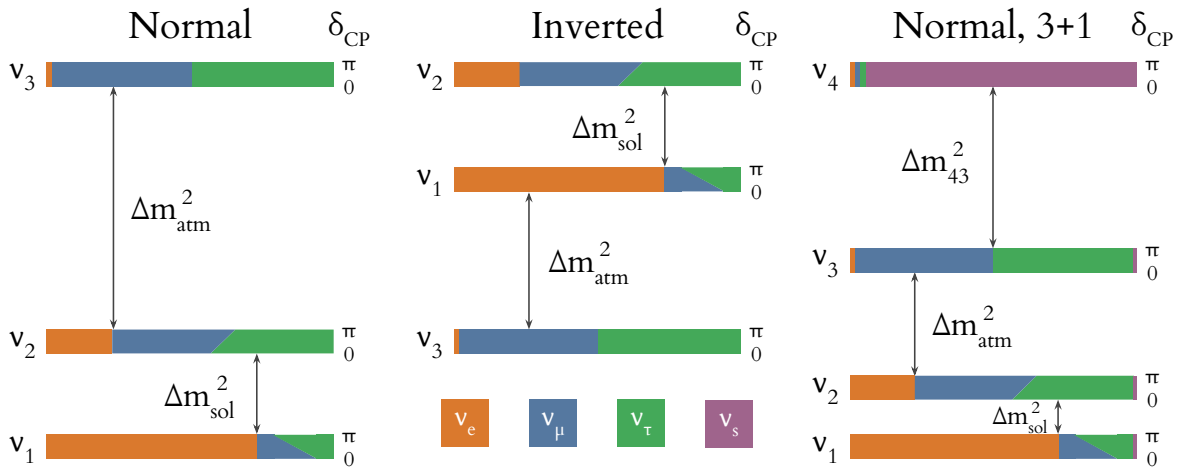

Figure 2.9.: A demonstration of how the neutrino flavour eigenstates contribute to the neutrino mass hierarchy in each of the normal, inverted and (3+1) sterile cases. The sterile neutrino mass splitting, Δm^2_{43} is included in the normal-ordering scheme to demonstrate the (3+1) model amendment to the active neutrino picture. The sterile splitting is likely to be more than 10 times larger than the active splittings [28].

Following the determination of an excess or deficit in the expected rate of three-flavour neutrino oscillations and the subsequent postulation of an additional neutrino flavour eigenstate, it is necessary to update the parametrisation of neutrino oscillations to incorporate this additional member of the neutrino family.

The simplest extension to the active neutrino picture which has been proposed to explain these short baseline anomalies is the 3+1 (active+sterile) hypothesis. The sterile component of each active neutrino must be small enough to minimise conflict with the LEP three-flavour constraint, but still allow for oscillations to occur between active and sterile flavour eigenstates. Adding in a single sterile neutrino to the mass hierarchy is shown for normal-ordering in Figure 2.9.

The constraints set by existing anomalous neutrino oscillation data suggest that the third mass splitting is at least 10 times larger than the active mass splittings. The approximation $\Delta m^2_{41} = \Delta m^2_{21,sol} + \Delta m^2_{32,atm} + \Delta m^2_{43}$ is therefore assumed to be true and allows for the assumption that, $\Delta m^2_{sol} \approx \Delta m^2_{atm} \approx 0$ [28], reducing the parametrisation of a sterile neutrino oscillation measurement in the (3+1) framework to only include the single mass splitting, Δm^2_{41}.

Incorporating the (3+1) sterile neutrino model into the mixing matrix in order to determine the probability of oscillations between the active and sterile flavours involves the addition of a single row and column to the PMNS matrix [28],

$$U_{\alpha k} = \begin{pmatrix} U_{e1} & U_{e2} & U_{e3} & U_{e4} \\ U_{\mu 1} & U_{\mu 2} & U_{\mu 3} & U_{\mu 4} \\ U_{\tau 1} & U_{\tau 2} & U_{\tau 3} & U_{\tau 4} \\ U_{s1} & U_{s2} & U_{s3} & U_{s4} \end{pmatrix}. \tag{2.37}$$

Parametrised by the sterile mixing angles and mass splitting, the probability of each of the short baseline ν_μ and ν_e appearance and disappearance oscillations occurring in the (3+1) picture is as follows [83],

$$P_{\mu\to\mu} = \sin^2(2\theta_{\mu\mu}) \sin^2\left(1.27\frac{\Delta m^2 L}{E}\right) \tag{2.38}$$

$$P_{e\to e} = \sin^2(2\theta_{ee}) \sin^2\left(1.27\frac{\Delta m^2 L}{E}\right) \tag{2.39}$$

$$P_{\mu\to e} = \sin^2(2\theta_{\mu e}) \sin^2\left(1.27\frac{\Delta m^2 L}{E}\right), \tag{2.40}$$

where the effective sterile mixing angles are defined as [28],

$$\sin^2(2\theta_{\mu\mu}) = 4(1 - |U_{\mu 4}|^2)|U_{\mu 4}|^2 \tag{2.41}$$

$$\sin^2(2\theta_{ee}) = 4(1 - |U_{e4}|^2)|U_{e4}|^2 \tag{2.42}$$

$$\sin^2(2\theta_{\mu e}) = 4|U_{e4}|^2|U_{\mu 4}|^2. \tag{2.43}$$

2.4.3. Global neutrino oscillation data in the search for eV-scale sterile neutrinos

A summary of existing neutrino oscillation experiments in the context of the (3+1) sterile hypothesis is given in Table 2.2 along with the channels measured and the most-recent publications in the context of sterile neutrino searches from each experiment. Only the most-recent/important results will be discussed throughout this section, the summary is compiled in large-part from [28] [83] [7] [84]. Figure 2.10 shows the energy and baseline distributions for a number of experiments which will contribute to the discussion in this section.

Experiment	References	Comments
$\nu_e, \bar{\nu}_e$ disappearance channel		
Gösgen, Rovno, SRP	[85, 86, 87]	
Bugey-3,4	[88, 89]	Spectra at 3 baselines
NEOS-II	[90]	Combined with Daya Bay
DANSS	[91]	Two baselines
Double Chooz, RENO	[92, 93]	Near detector, reactor
Daya Bay	[94]	Spectral ratios and fluxes for each isotope
KamLAND	[59]	Long-baseline reactor (L $\gg$ 1 km)
Homestake	[53]	
GALLEX/GNO	[55]	Solar and Radioactive (^{51}Cr) sources
SAGE	[54, 95]	Solar and Radioactive (^{51}Cr, ^{37}Ar) sources
SuperK	[96]	Accelerator $\nu_\mu, \bar{\nu}_\mu, \nu_e, \bar{\nu}_e$ CC and NC
Borexino	[97]	
KARMEN	[98]	ν_e scattering on carbon
PROSPECT, Neutrino-4, STEREO	[99, 100, 101]	Presented latest results at ν2020
LSND	[102]	ν_e scattering on carbon
$\nu_e, \bar{\nu}_e$ appearance channel		
LSND	[81]	$\bar{\nu}_\mu$ from stopped pion source (DaR) and combined (DaR+DiF) data
MiniBooNE	[103, 104, 105]	ν_μ and $\bar{\nu}_\mu$ from BNB
KARMEN	[98]	$\bar{\nu}_\mu$ from stopped pion source
E776	[106]	ν_μ from Brookhaven beam
NOMAD, ICARUS, OPERA	[107, 108, 109]	ν_μ from CERN beam
JSNS^2	[110]	Direct test of LSND
$\nu_\mu, \bar{\nu}_\mu$ disappearance channel		
IceCube	[111, 112, 113]	MSW resonance in high-E_ν atmospheric $\bar{\nu}_\mu$
CDHS	[114]	Accelerator ν_μ
CCFR84	[115]	Accelerator ν_μ and $\bar{\nu}_\mu$
MiniBooNE	[105]	Accelerator $\nu_\mu, \bar{\nu}_\mu$
SuperK, DeepCore	[96]	Low-E_ν atmospheric ν_μ
NOνA	[116]	NC data
MINOS/MINOS+	[117]	Accelerator ν_μ, two-detector fit

Table 2.2.: Global sterile neutrino oscillation measurements in each of the dominant channels with references to the latest publications on the subject in each experiment. Those which are referenced in text and plots throughout the section are highlighted in bold. Data compiled from [84].

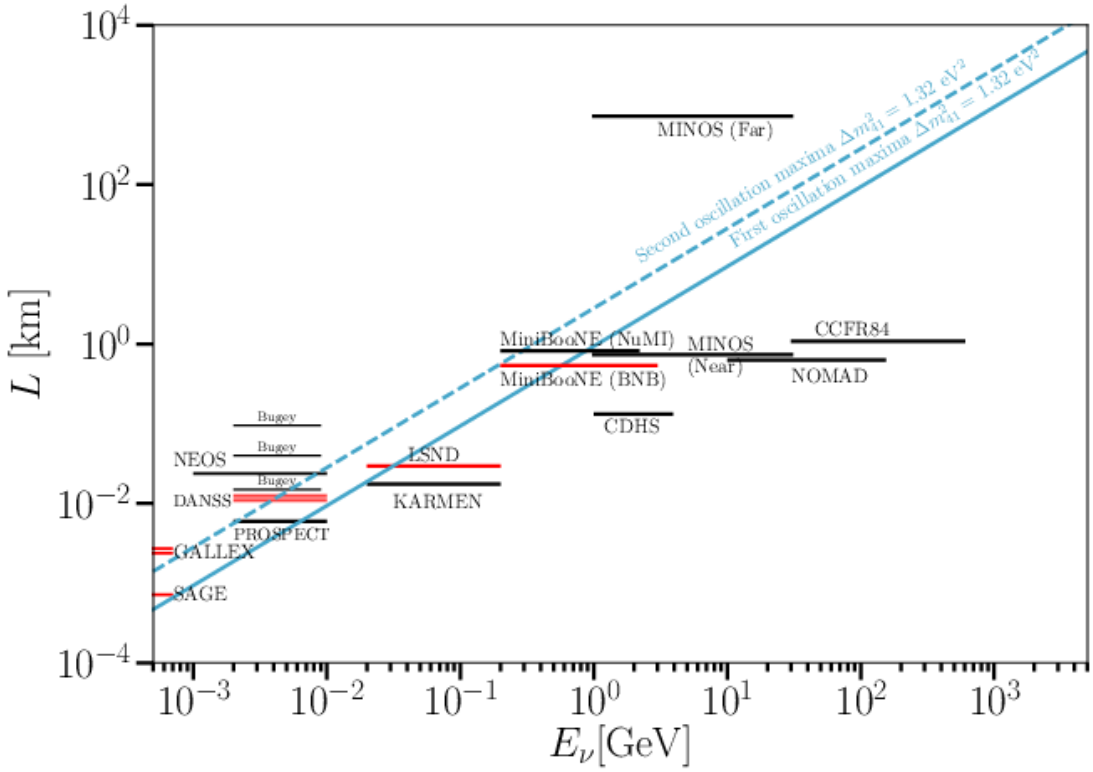

Figure 2.10.: The energy and baseline distributions from many experiments involved in the discussion. Those underlined in red indicate the experiments for which the results indicate a preference for an additional neutrino state with greater than 2σ confidence. The blue dashed and solid lines depict the second and first oscillation maxima at Δm^2_{41} respectively. Figure and caption taken from [28].

2.4.3.1. ν_e and $\bar{\nu}_e$ disappearance measurements

The first oscillation channel is dominated primarily by reactor and solar neutrino oscillation experiments, with smaller contributions from accelerator and atmospheric neutrino oscillation experiments. Figure 2.11 compiles many of the existing constraints on $\nu_e/\bar{\nu}_e$-disappearance under the (3+1) sterile neutrino hypothesis. See Table 2.2 for references to the experiments quoted in this section.

In summary, the ratio of the NEOS and Daya Bay spectra are taken in order to minimise systematic uncertainties. In doing so, they were able to determine that $\sin^2 2\theta_{14} < 0.1$ is excluded for $0.2 < \Delta m^2_{41} < 2.3$ eV^2. DANSS also excludes $\sin^2 2\theta_{14} < 0.1$ and has recorded a preference for oscillations at $\Delta m^2_{41} = 1.4$ eV^2, $\sin^2 2\theta^2_{14} = 0.05$. Furthermore, the solar experiments using radioactive sources, GALLEX and SAGE, have recorded a 2σ deficit in the expected event rate through the measurement of $R = N_o/N_e = 0.87 \pm 0.5$, where N_o and N_e are the observed and expected event rates respectively.

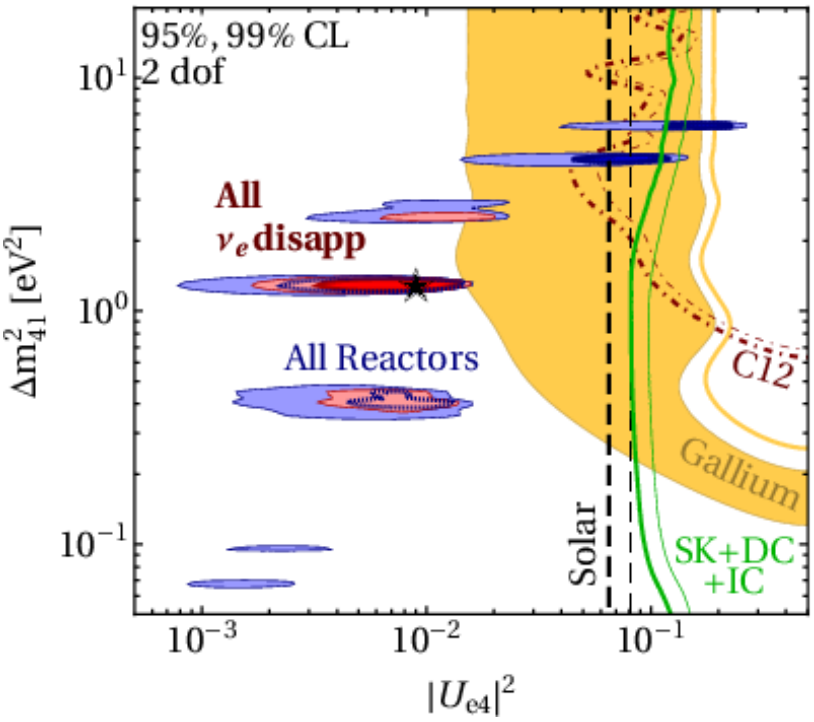

Figure 2.11.: A compilation of many of the existing constraints on $\nu_e/\bar{\nu}_e$-disappearance under the (3+1) sterile neutrino hypothesis from [84]. The experiments included are combined limits from all of the aforementioned reactor and solar experiments who have released $\nu_e/\bar{\nu}_e$ disappearance results, as well as LSND/KARMEN (C12), GALLEX/SAGE, SuperK, IceCube and DeepCore. See Table 2.2 for the most-recent publications from these experiments.

In contrast, Bugey and PROSPECT have seen no oscillation signal, and the joint LSND/KARMEN (^{12}C) analysis saw no signal whilst excluding a large portion of the gallium allowed region. In addition, it can be seen from Figure 2.11 that a number of the combined reactor allowed regions do not agree with the solar allowed region.

2.4.3.2. ν_e and $\bar{\nu}_e$ appearance measurements

The second oscillation channel is dominated primarily by short baseline accelerator neutrino oscillation experiments. Figure 2.12 compiles many of the existing constraints on $\nu_e/\bar{\nu}_e$-appearance under the (3+1) sterile neutrino hypothesis. See Table 2.2 for references to the experiments quoted in this section. As mentioned previously, LSND observed $87.9 \pm 22.4 \pm 6.0$ events above background, which corresponds to a 3.8σ excess, while MiniBooNE observed a 4.7σ signal consistent with the LSND result in the BNB whilst observing a small, 1.2σ, excess from off-axis events in the NuMI beam. In contrast, NOMAD found no signal and excludes the region above $\Delta m^2_{41} = 10$ eV^2 whilst KARMEN also found no oscillation signal and can exclude a small portion of the LSND allowed region, albeit with a lower confidence.

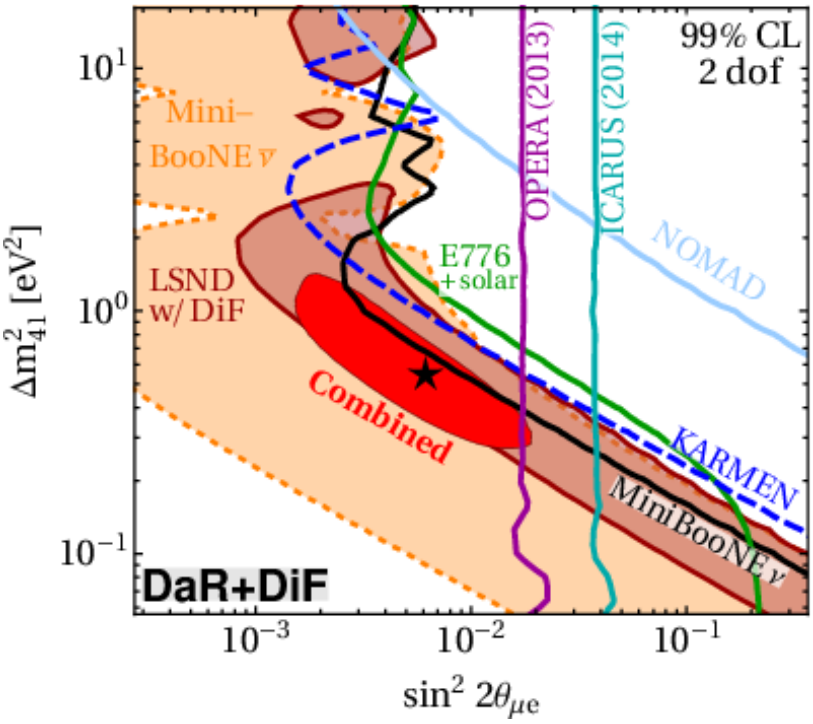

Figure 2.12.: A compilation of many of the existing constraints on $\nu_e/\bar{\nu}_e$-appearance under the (3+1) sterile neutrino hypothesis from [84]. The experiments included are combined limits from E766 and all of the aforementioned solar experiments who have released $\nu_e/\bar{\nu}_e$ appearance results, as well as LSND DaR+DiF, MiniBooNE, OPERA, ICARUS, NOMAD and KARMEN. See Table 2.2 for the most-recent publications from these experiments.

2.4.3.3. ν_μ and $\bar{\nu}_\mu$ disappearance measurements

The third and final oscillation channel is again dominated primarily by short baseline accelerator neutrino oscillation experiments with contributions from long baseline accelerator and atmospheric neutrino oscillation experiments. Figure 2.13 compiles many of the existing constraints on $\nu_\mu/\bar{\nu}_\mu$-disappearance under the (3+1) sterile neutrino hypothesis. See Table 2.2 for references to the experiments quoted in this section.

In this channel, no possible oscillation signals have been observed thus far. Instead, parameter limits have been set by multiple experiments. CCFR84 set the first limits on the ν_μ-disappearance oscillation parameters in 1984, $15 < \Delta m^2_{41} < 1000$ eV^2 and $\sin 2\theta_{14} > 0.02$. Since then, MiniBooNE, CDHS and MINOS/MINOS+ have set the limits shown in Figure 2.13, with MINOS/MINOS+ providing the most substantial constraints. MINOS/MINOS+ also have a preference for $\sin\theta_{14} = 0$, which would not allow for ν_e appearance and disappearance oscillations. Finally, SuperK, IceCube and DeepCore have contributed atmospheric neutrino results to substantially increase the constraints in the $\Delta m^2_{41} < 1$ eV^2 region of the parameter space. IceCube searches for an enhancement of the MSW resonance when antineutrinos travel upwards through the Earth, due to contributions from sterile neutrinos [113].

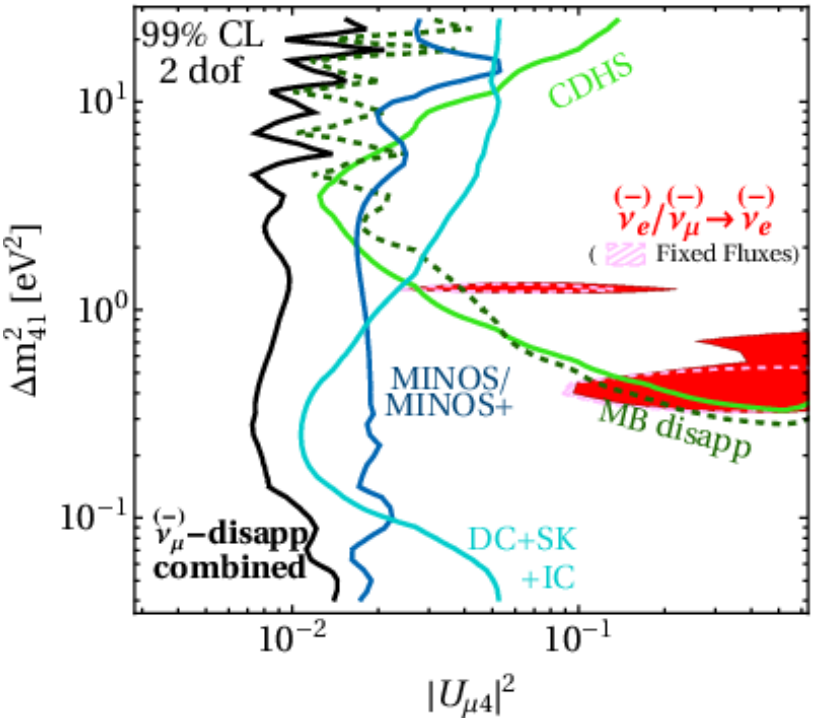

Figure 2.13.: A compilation of many of the existing constraints on $\nu_\mu/\bar{\nu}_\mu$-disappearance under the (3+1) sterile neutrino hypothesis from [84]. The experiments included are MINOS/MINOS+, MiniBooNE, CDHS, DeepCore, IceCube and SuperK. A combined limit from all experiments is shown in black, see Table 2.2 for the most-recent publications from these experiments.

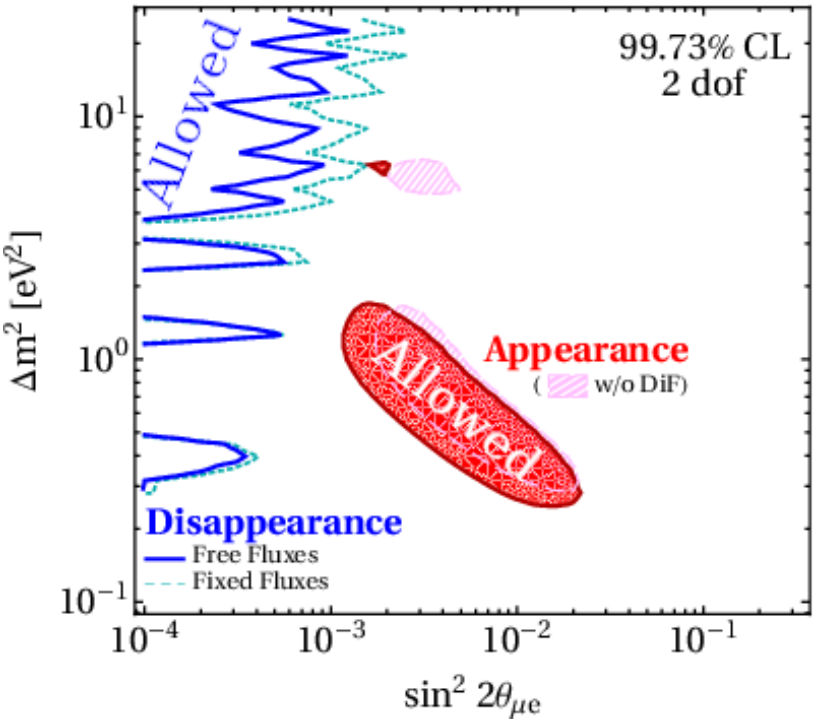

Figure 2.14.: All appearance and disappearance constraints combined in the $\sin^2 2\theta_{\mu e}, \Delta m^2_{41}$ parameter space. The blue curves show limits from the disappearance data sets using free reactor fluxes (solid) or fixed reactor fluxes (dashed), while the shaded contours are based on the appearance data sets using LSND DaR+DiF (red) and LSND DaR (pink hatched). All contours are at 99.73% CL for 2 dof. Figure and caption taken from [84].

Finally, the full appearance and disappearance datasets are combined and compared to one another in Figure 2.14. The combination of possible sterile oscillation signals from the appearance measurements and null results from disappearance and appearance experiments results in the complete exclusion of the allowed region from appearance measurements by the disappearance data. Future precision experiments such as SBN will substantially improve the global confidence in these results such that the existence of sterile neutrinos can be confirmed or ruled out once and for all.

2.4.4. Alternative explanations for the SBL anomalies

I addition to the hypothesised existence of sterile neutrinos, the short baseline neutrino anomalies have resulted in the emergence of a number of new theories which attempt to explain them. For instance,

- Charged current non-standard interactions as an additional mechanism for neutrino flavour transitions [118]
- Resonant $\nu_e \rightarrow \nu_\mu$ oscillations in the presence of a new light scalar boson which couples only to neutrinos [119]

In addition to new physics explanations for the short baseline anomalies on the global scale, systematic effects which arise on an experiment-by-experiment basis may be a candidate explanation for some of the individual anomalies. MicroBooNE has been built with the same L/E distribution as MiniBooNE and LSND in order to probe the systematic effects which are correlated across the experiments, such as those which arise from neutrinos interaction cross-sections (correlated across all 3 detectors) and the neutrino flux (correlated between MiniBooNE and MicroBooNE).

Chapter 3.

The Short Baseline Neutrino program

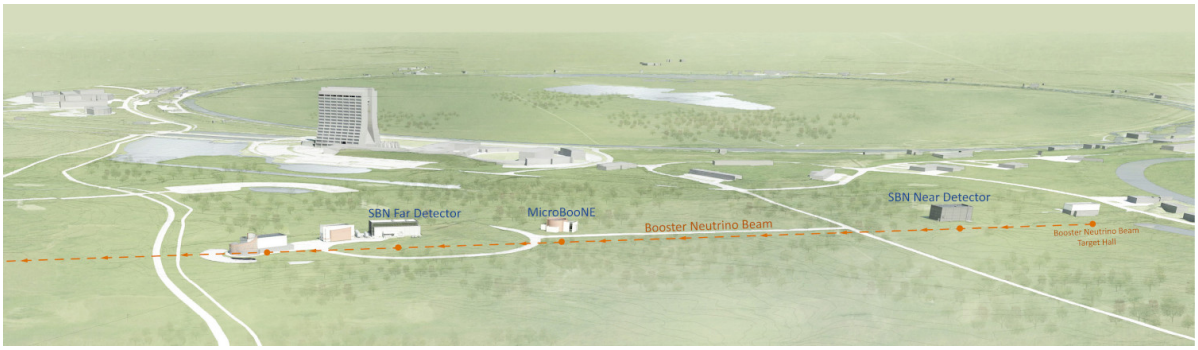

Figure 3.1.: A map of the Short Baseline Neutrino program in the Booster Neutrino Beam at Fermilab. The near detector, SBND, intermediate detector, MicroBooNE, and far detector, ICARUS, have baselines of 110 m, 470 m and 600 m respectively [6].

The Short Baseline Neutrino, SBN, program consists of three LArTPC experiments located at 110 m, 470 m & 600 m baselines in the Booster Neutrino Beam (BNB) at Fermilab. A map of these detector locations is shown in Figure 3.1 [6]. The experimental program consists of the Short Baseline Near Detector (SBND), the intermediate detector, MicroBooNE, and the far detector, ICARUS T600.

All three experiments will collaboratively search for sterile neutrinos by measuring neutrino oscillations across the short baseline of the program. These measurements will be made with unprecedented precision by virtue of the considerable functional uniformity between detectors [7]. In addition to the oscillation physics program, each experiment will conduct its own, independent search for new physics utilising both novel and unique

detection techniques. There will also be an extensive amount of research into the complex nature of neutrino interactions on heavy nuclei in each of the three detectors.

The SBN program will collectively accumulate high resolution data from millions of neutrino interactions in the few-GeV energy regime. This is made possible by many features of the experimental setup, including the dense nature and large quantities of argon, the intensity of the neutrino beam and many critical attributes of the LArTPC detector technology. All three detectors feature several prototype components for the purpose of ameliorating our understanding of this technology.

This chapter will outline the core principles of operation of the BNB in section 3.1 and general LArTPC detector technologies in section 3.2. Experiment-specific features of SBND will be described in section 3.3.1 and unique features of the two other SBN program detectors, MicroBooNE and ICARUS will be added in sections 3.3.2 and 3.3.3. An outline of the SBN physics program will be given in 3.4 followed by a summary of the current status of the SBN program construction will be given in section 3.5.

3.1. The Booster Neutrino Beam

Understanding the complex nature of neutrino interactions in any medium requires a thorough understanding of the neutrino source. The large statistics present in the SBN datasets result in systematically-dominated uncertainties on all measurements and one of the major contributions will be from the flux, which must therefore be well constrained in order to produce the required precision of the SBN physics measurements [120].

The BNB was first utilised by the MiniBooNE experiment in their effort to study the neutrino anomalies previously indicated by the Liquid Scintillator Neutrno Detector (LSND) experiment [80]. MiniBooNE therefore conducted in-depth studies of the spectrum and composition of the BNB and compared external data to the existing flux prediction to constrain the corresponding uncertainties [120]. A detailed simulation of the flux was produced by the MiniBooNE collaboration using the results of these studies [7].

Figure 3.2 depicts the BNB within the Fermilab accelerator complex [121]. The BNB is produced by extracting protons from the 400 MeV Linac, accelerating them to 8 GeV kinetic energy in the Fermilab booster synchrotron and firing them at a beryllium target [121]. Interactions between the protons and the target produces a hadronic beam

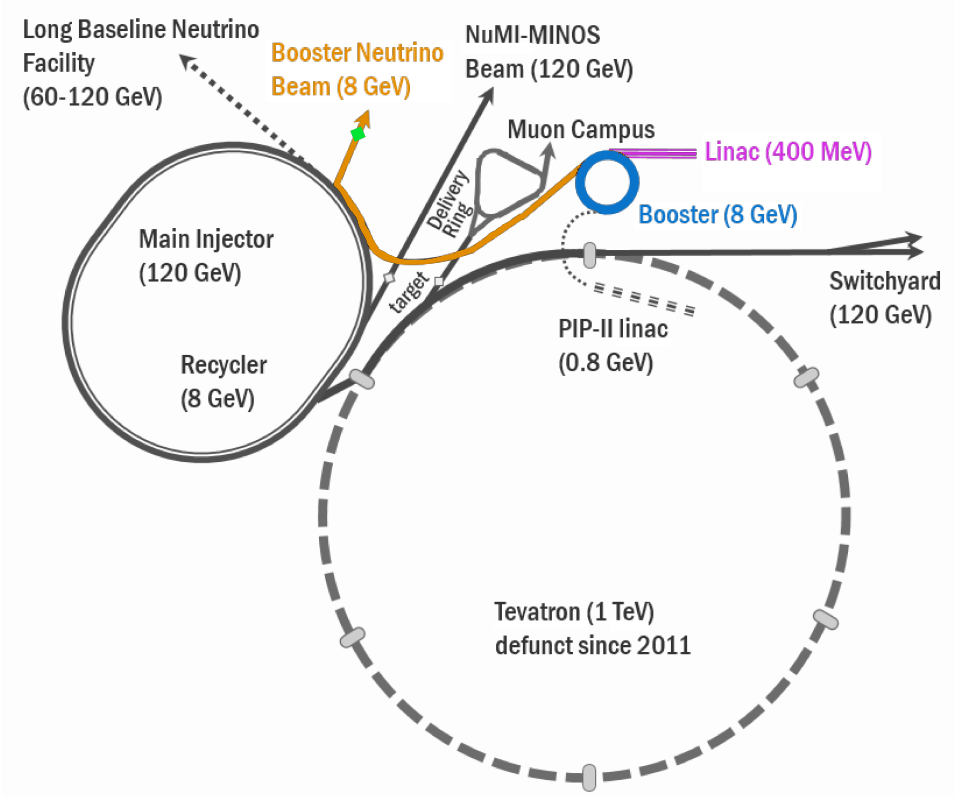

Figure 3.2.: The BNB as it occurs in the Fermilab Accelerator complex. Each component of the BNB production system is highlighted in colour [121]. Protons exiting the 400 MeV Linac (purple) are boosted to 8 GeV kinetic energy in the 8 GeV Booster synchrotron (blue) before being fired at a beryllium target (green) to produce secondary hadrons (orange) which in turn decay, producing the beam of neutrinos [7].

consisting mainly of pions, which is well understood thanks to hadron production data acquired by the HARP experiment [6] [122].

A magnetic polarising horn supplied with 174 kA in 143 μs pulses coincident with the delivery of the protons, focuses or defocuses pions based on their charge in order to steer the maximal amount of same-charge pions into a collimated beam [7]. The focussed pions then travel down a 50 m long air-filled pipe, where they decay mostly via the dominant channel,

$$\pi^{(+)}_{(-)} \longrightarrow \mu^{(+)}_{(-)} + \overset{(-)}{\nu}_{\mu}, \tag{3.1}$$

which occurs with a 99.9877% branching ratio [123].

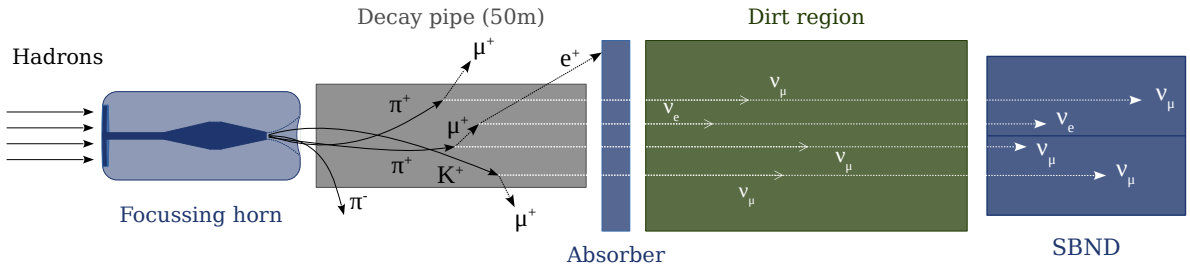

Figure 3.3.: A schematic diagram of the neutrino production procedure from the proton-Beryllium interaction products. A magnetic focussing horn collimates the hadrons based on the charge desired (positive for neutrinos, negative for anti-neutrinos), the same-charge hadrons then decay in an air-filled pipe into leptons and neutrinos. Any remaining hadrons and leptons are removed from the beam by the absorber at the end of the decay pipe. After finally travelling through some amount of dirt, the neutrinos reach the detectors.

The polarisation of the magnetic horn can be flipped in the BNB, allowing for both forward and reverse horn currents (FHC, RHC). In FHC mode, the BNB focuses π^+'s to produce a ν_μ-dominated beam, whereas in RHC mode, π^-'s are focussed to produce a $\bar{\nu}_\mu$-dominated beam [6].

The length of the decay pipe is chosen to maximise the production of ν_μ ($\bar{\nu}_\mu$) whilst minimising the chance of secondary muon decays into ν_e ($\bar{\nu}_e$) [120]. Sub-dominant pion decays, kaon decays and secondary muon decays do still occur which result in beam contributions from $\bar{\nu}_\mu$, ν_e and $\bar{\nu}_e$ [123]. The branching ratio, Γ, of pions decaying to electrons over muons is on the order of $\sim 10^{-4}$ due to helicity suppression [124],

$$\frac{\Gamma(\pi^+ \to e^+\nu_e)}{\Gamma(\pi^+ \to \mu^+\nu_\mu)} = \left(\frac{m_e}{m_\mu}\right)^2 \left(\frac{m_\pi^2 - m_e^2}{m_\pi^2 - m_\mu^2}\right)^2 \sim 10^{-4}. \tag{3.2}$$

An 'absorber' is placed at the end of the decay pipe where any remaining hadrons, electrons and muons are absorbed to ensure no further weak decays occur which may contaminate the beam. Neutrinos can then propagate through the earth and finally reach the TPC volume [6]. A schematic diagram of this neutrino production from the proton-Beryllium interaction products is shown in Figure 3.3.

The Booster beam spill window contains $\sim 5 \times 10^{12}$ protons and lasts approximately 1.6 μs with a spill delivery rate to the BNB of 5 Hz. The resulting flux of neutrinos observed in each SBN experiment is shown in Figure 3.4 for the abundant neutrino flavours [6]. These distributions emphasise the huge dominance of ν_μ's in the beam. The neutrinos produced in the BNB peak at around ~0.7 GeV and range between 0 and

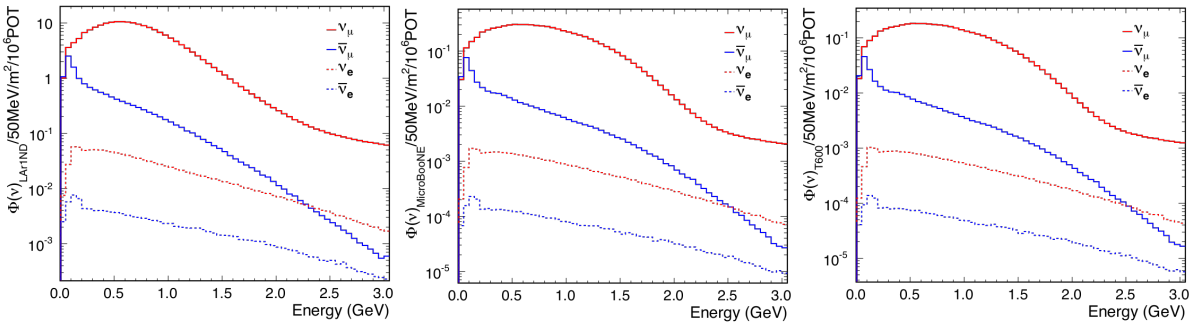

Figure 3.4.: The ν_μ, $\bar{\nu}_\mu$, ν_e & $\bar{\nu}_e$ components of the flux distributions for each SBN experiment [6]. On the left is SBND, MicroBooNE is in the middle and ICARUS is on the right. The solid red and blue lines are ν_μ & $\bar{\nu}_\mu$ respectively and the dashed lines are analogously ν_e and $\bar{\nu}_e$. Note the logarithmic scale.

3 GeV across the spectrum. The neutrino beam consists almost entirely of ν_μ (and $\bar{\nu}_\mu$) with only a 0.5% $\nu_e/\bar{\nu}_e$ component.

3.2. The LArTPC detector technology

3.2.1. History and motivation for the technology

The Liquid Argon Time Projection Chamber technology was proposed by Carlo Rubbia in 1977 as a solution to a long-standing issue in experimental neutrino physics wherein the existing technological climate limited the possible composition, and consequently the output, of a detector. Up to that point one had to decide whether their experiment were to record a small number of high resolution neutrino interactions, or record a large number of neutrino interactions at the cost of observing very little detail within them. The proposed solution was defined as an 'electronic bubble chamber' in which the entire, highly detailed, image of the products of every neutrino interaction would be collected electronically and reconstructed computationally [125].

The ICARUS collaboration were the first to successfully utilise this technology in the detectors they proposed in 1989. Their initial, ambitious goals included the study of solar neutrinos in the low-MeV energy regime, proton decay in the ∼1 GeV energy regime and cosmic neutrino interactions in the much higher energy regime [126]. Such physics goals were to be realised through a 2-step experimental process involving multiple iterations of the detector, the second of which would be a large-scale LArTPC constructed to measure proton decay, cosmic neutrino interactions and accelerator neutrinos from the

CERN Neutrinos to Gran Sasso (CNGS) beam [127]. This was known as the ICARUS T600 detector and would later be transported to Fermilab to become the far detector in the Short Baseline Neutrino program.

Following the success of the ICARUS experiment, the LArTPC technology has consistently been improving through its use in experiments designed to perform research and development (R&D), in conjunction with making groundbreaking physics measurements. For instance, the 550 L ArgoNeuT detector was positioned along the Neutrinos at the Main Injector (NuMI) beam and was the first LArTPC used in a Fermilab experiment, the first to study neutrinos in a 'low-energy' (0.5-10.0 GeV) beam and the first to make a ν_μ-Ar cross-section measurement [128]. The NuMI beam is described here [129] and can be seen as part of the Fermilab accelerator complex in Figure 3.2. To further the success story of the LArTPC detector technology, MicroBooNE began operation at its location 470m downstream of the BNB in 2015 and finished taking beam data in 2020.

3.2.2. Principle operations of a LArTPC

When a neutrino from the BNB traverses a detector in the SBN program and interacts in the liquid argon as described in section 2.2, the final state particles which exit the nucleus ionise the argon atoms as they travel through the detector medium producing ionisation electrons and scintillation photons. These electrons are then subject to an electric field which causes them to drift through the detector medium towards the Anode Plane Assemblies (APA) for collection and analysis, see section 3.2.2.2 for further details.

3.2.2.1. The target material: Liquid argon

Liquid argon was chosen as the target material in these neutrino-based TPC detectors on account of it having a number of desirable properties [125]:

1. The liquid form of argon has a high density, 1.39 gcm^{-3}, and high atomic mass
    - The probability of a neutrino interacting increases with the number of nucleons present in the detector active volume
2. Argon is a noble gas, therefore the energy absorbed from charged particles traversing the detector can only be used to ionise the argon and produce scintillation photons. As a result, minimal energy is absorbed in the argon and not re-emitted,

maximising the efficiency of the electron production. Similarly, the drift lifetime of the ionisation electrons is capable of being large enough for them to cross the entire TPC without being recaptured by the liquid argon atoms, provided a high purity of the detector medium is achieved [130]

- Purifying the argon was identified as the largest technological issue at the time the LArTPC was proposed [125]
- The MicroBooNE collaboration have recently demonstrated that it is possible to achieve and maintain the required purity of liquid argon to allow for a sufficiently large electron drift lifetime [131]

3. The electron mobility, μ, is high which allows them to be drifted quickly under an electric field, E, since the drift velocity is defined as [132],

$$v = \mu \cdot E \tag{3.3}$$

4. Liquid argon is a reasonably cheap material, the most abundant noble gas [132] and can be liquefied by liquid nitrogen [125]
   - This is ideal for use in large-scale detector volumes

A summary of the physical properties of liquid argon is given in Table 3.1 [123] [133].

3.2.2.2. The Time Projection Chamber

The (charged) particles observed following a neutrino interaction in a LArTPC are reconstructed by collecting the ionisation electrons and scintillation photons produced along the trajectory of the particles. Such trajectories take the form of either a track or an electromagnetic shower depending on the behaviour of the particles during their passage through the detector medium, this will be discussed in section 4.12. Together, these tracks and showers can be used to build composite images of the final state topology of the neutrino interaction and perform both geometric and calorimetric analyses. A general purpose LArTPC diagram is given in Figure 3.5. A description of its functionality is as follows [134].

An electric field is induced across the TPC by applying a potential difference between the cathode and anode planes causing the ionisation electrons to drift in the x-direction. At the anode end of the TPC, there are three sense planes, the inner two are known as the induction planes and the outermost is known as the collection plane. A current

Property		**Value**	**Unit**
Boiling point,	T_B	87.30	K
Density at 87K,	ρ	1.397	g cm^{-3}
When held in a 500 V cm^{-1} electric field and at 87 K			
Electron mobility,	μ	329.7	cm^2 V^{-1} s^{-1}
Electron drift velocity,	v	1.648 $\times 10^6$	cm s^{-1}
Effective longitudinal electron energy,	ϵ_L	0.02070	eV
Longitudinal diffusion coefficient,	D_L	6.823	cm^2 s^{-1}
Transverse diffusion coefficient,	D_T	13.16	cm^2 s^{-1}
Critical energy, $e^{\pm}$	$E_{c,e}$	32.8	MeV
Critical energy, $\mu^{\pm}$	$E_{c,\mu}$	485	GeV
Molière radius,	R_M	9.04	cm
Radiation length,	X_0	14.0	cm
Nuclear interaction length,	λ_i	85.7	cm
Minimum specific energy loss,	$\frac{dE}{dx}_{MIP}$	2.12	MeV cm^{-1}

Table 3.1.: Important physical properties of liquid argon. All values taken from [123] and [133].

is induced on each wire passed by a drift electron in the induction planes, which have an additional potential difference between them to ensure they are transparent to the electron and instead drive it towards the collection plane where the induced current is collected and recorded. On each electron-struck wire, the waveform of the induced current is analysed and detector effects, such as noise, are removed. In addition, deconvolution is used to separate individual waveform signals on a single wire. Algorithms have been defined to then search for local maxima and minima in the waveforms, to which Gaussian distributions are fitted and 'Hit' objects are constructed. The corresponding charge deposited by a Hit is calculated from the amplitude of the Gaussian Hit object. These Hits are then used as input to the pattern recognition at the reconstruction stage, which will be discussed in section 4.10.

The 3 dimensional position at which an ionisation electron was produced in the detector is determined by first finding which wires were hit in each plane. For example, the inner two induction planes are situated at $\pm 60^\circ$ to the vertical wires in the collection plane

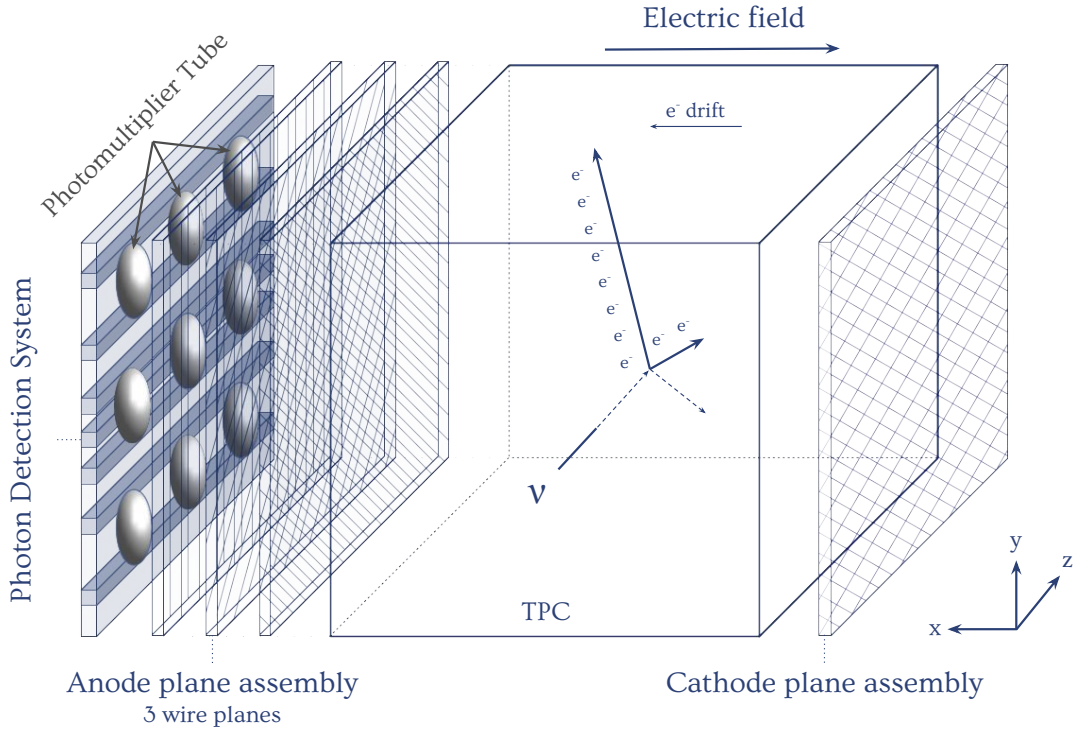

Figure 3.5.: A cartoon of a general-purpose LArTPC. The diagram includes a depiction of: The of Anode Plane Assembly, APA, which sits at the edge of the TPC in the x-plane and consists of 3 wire planes; The Cathode Plane Assembly (CPA) which lives at the opposite side of the TPC to the APA in the x-plane; A Photon Detection System (PDS) consisting of 9 PMTs, which resides behind the APA. The x-axis is defined to be positive in the drift direction. An example neutrino interaction is included to clarify the detector orientation and demonstrate how the ionisation electrons are produced along the trajectory of charged tracks in the detector. The neutral tracks are shown as dashed lines, these are not directly visible in the detector as they do not ionise the argon atoms. The electric field crosses the TPC from the APA to the CPA and opposes the drift direction of the ionisation electrons.

so that together, they can provide y-z position reconstruction at sub-millimetre precision [6]. This process is depicted in Figure 3.6. The magnitude of charge induced by each Hit on the wire planes contributes to the eventual determination of the energy, momentum and identification of each particle traversing the detector and will be discussed in chapter 4 [134].

The x-position of an electron arriving at the wire planes is determined using timing information. Scintillation photons produced in conjunction with the drift electrons reach the photon detection system, PDS, which resides behind the APA and in this general case consists of a wall of photomultiplier tubes (PMT). The arrival time of the scintillation photons is instantaneous with respect to that of the electrons. Both the scintillation and

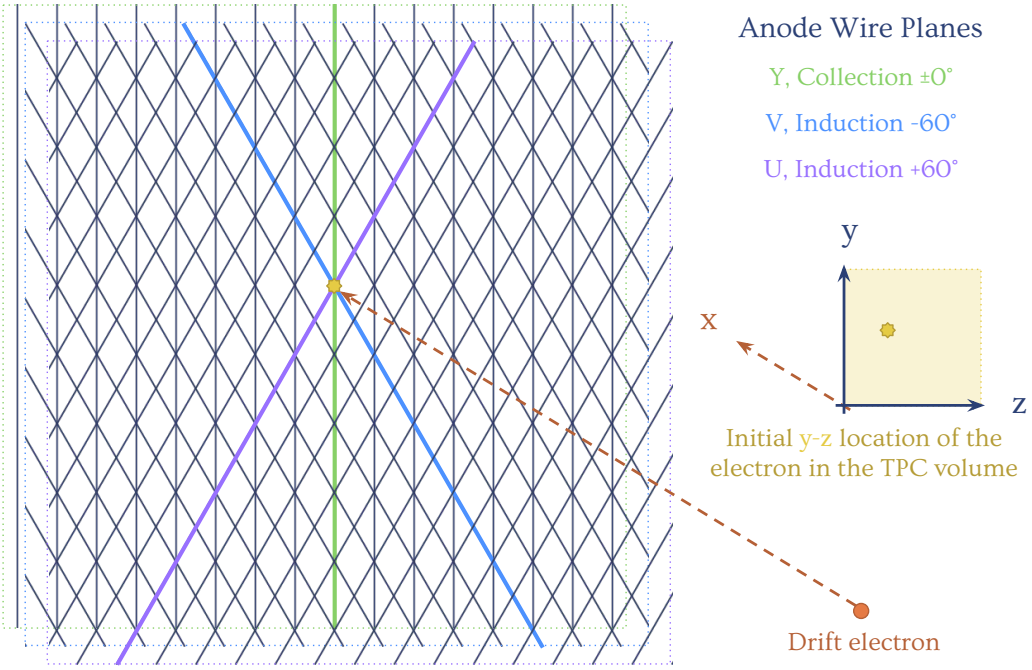

Figure 3.6.: A cartoon depicting how the y-z position of the ionisation electron is reconstructed using the Hits from the 3 wire planes. The electron drifts parallel to the x-axis towards the APA where it first hits a wire in the U (first induction) plane, followed by the V (second induction) plane and is finally collected by the Y (collection) plane. From these Hits, it is possible to find the y-z position to ∼mm precision by determining where the affected wires cross one another. The charge is acquired from the current induced on the wire planes by the electron.

beam timing information are used in conjunction with one another to give the instance at which the interaction took place, t_0, and the arrival time of the electrons at the wire planes, t, along with their drift velocity determines the distance, x, over which they travelled in the x-direction [135] [6],

$$x = v_d \times (t - t_0). \tag{3.4}$$

In the case of surface LArTPC experiments, all electrons that reach the APA during a predefined readout window are recorded, any arriving outside of this window are not. The window is therefore defined to occur in coincidence with the known beam spill time and to last for a duration equal to the maximum drift time of the ionisation electrons produced by the final state particles of neutrino interactions. This method also aims to

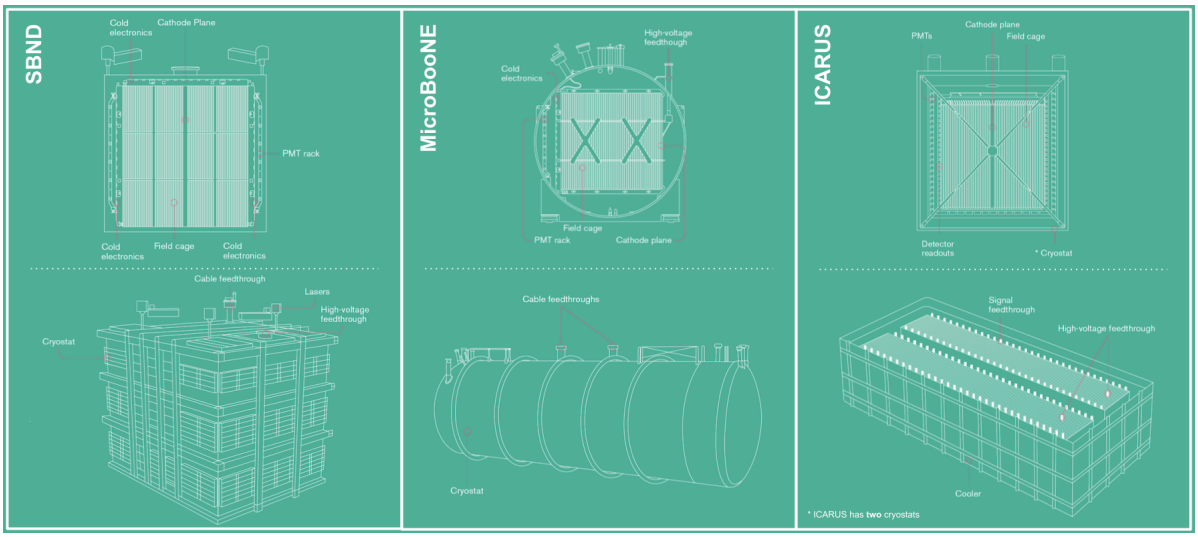

Figure 3.7.: Along the top are cross-section diagrams looking along the z-direction of each SBN detector. Along the bottom are 3D cryostat diagrams of each SBN detector. From left to right: SBND, MicroBooNE and ICARUS [5].

minimise the number of recorded cosmic ray muons which cross the detector during the readout window [6]. Since the LArTPC detectors in the SBN programme all reside on the surface of the Earth, the main background to neutrino interaction measurements will be dominated by these rays. Consequently, a huge effort to remove these backgrounds is underway. Further details on how the readout window definition assists in the tagging and removal of cosmic rays from events containing a neutrino interaction is discussed in section 3.3.1.4. The methods for removing cosmic rays computationally will be discussed in section 4.11.2.

The combined data collected by the APA and PDS provides three dimensional and calorimetric information about every recorded drift electron. Each final state particle is then reconstructed by studying all the drift electrons collected within the total readout time and particle hierarchies are constructed using highly-refined pattern recognition software, described in section 4.10.1. The resolution capability of a LArTPC due to the wire plane configuration (wire and plane spacing [6]) is sufficient to produce images of neutrino events which are comparable to that of the bubble chamber experiments [130].

3.2.2.3. Particle transportation through argon

During the electron's transportation through the argon, their mobility will be predominantly characterised by the temperature and density of the argon. The electric field

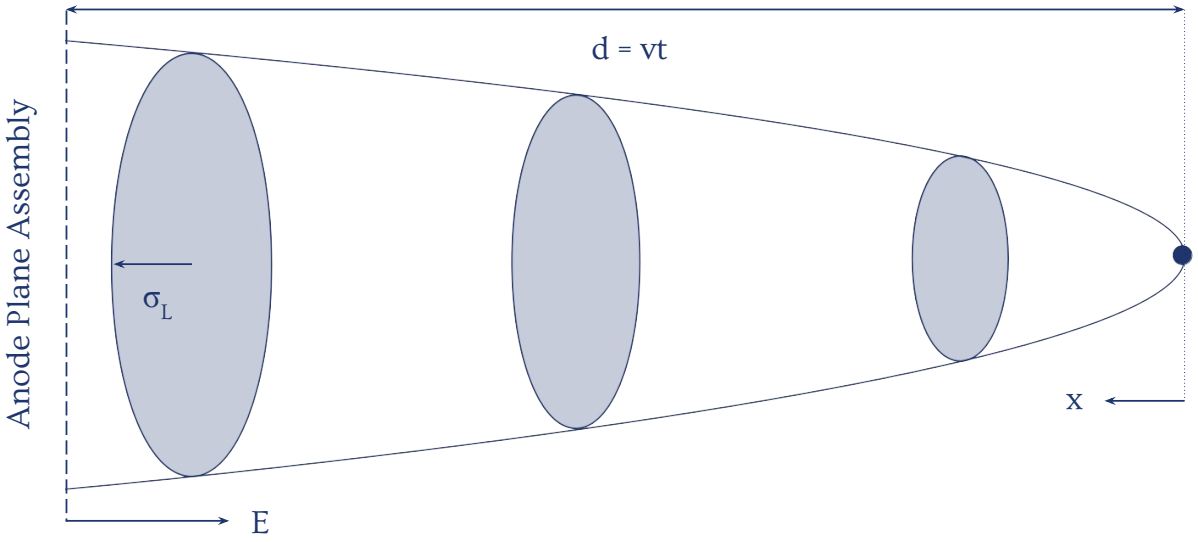

Figure 3.8.: The general behaviour of an electron swarm due to diffusion as it propagates the TPC when assumed to begin as a point source (dark blue circle). The ellipses at different positions in the electron's journey represent the standard deviation of the electron swarm at that particular drift time, σ_L.

within SBND will nominally run at 500 Vcm^{-1}. Together, these quantities determine the behaviour of the ionisation electrons produced by the neutrino-Argon interaction final states during their transportation though the detector medium.

In addition, the electrons are subject to a diffusion process which has components in both the longitudinal (drift) direction, D_L, and the transverse direction, D_T. Figure 3.8 depicts the behaviour of the electron diffusion between the location at which the electron is produced, somewhere along the trajectory of the final state particle, and the detection wire planes a distance $d = v \cdot t$ away [132]. The nominal electric field and dispersion due to the coefficients D_L and D_T enforces limits on the size of the drift dimension of a LArTPC. In a typical experiment with a 500 kV electric field, the drift length will be around 2 m.

The longitudinal and transverse diffusion coefficients follow the relations in equations 3.5 and 3.6 respectively [132],

$$D_L = \frac{kT}{e}\left(\mu + E\frac{\partial \mu}{\partial E}\right), \tag{3.5}$$

$$D_T = \frac{kT}{e}\mu, \tag{3.6}$$

where T is the electron temperature, k is the Boltzmann coefficient and the diffusion in the drift (longitudinal) direction is expected to be smaller than in the transverse direction at the field strength of the SBN detectors since $\partial\mu/\partial E < 0$ [132].

Neutrino interactions take place in the 'active volume' of the TPC which contains the liquid argon and is housed in a cryostat to ensure the argon is consistently held at the required temperature of 87 K at a ∼0.35 bar pressure [6]. These quantities minimise electronic noise and maintain the liquid state of the argon, whose boiling point is 87.3 K at a pressure of 1 bar. The argon is kept pure and the temperature variation is controlled to within less than 0.1 K, in order to maintain the desired drift velocity of the ionisation electrons to within ∼0.2% [134].

3.3. LArTPCs across the Short Baseline Neutrino program

The three detectors across the SBN program all utilise the LArTPC technology, however they are not identical and each exhibit a number of unique features. Detector R&D is a critical strategy in developing every feature of the technology, therefore implementing small variations in the sub-system configurations opens up huge potential for maximising the physics yield of the next-generation LArTPC experiments like DUNE.

Understanding both the subtle and distinctive differences between the detector functionality across the SBN program is a crucial step in accurately characterising the systematic uncertainties for the joint oscillation analyses. Increasing the number of features which are functionally identical allows for the cancellation of some of those uncertainties in the joint analyses, consequently increasing the sensitivity of the program to detecting new physics. The systematic parameters and uncertainties will be discussed in depth in chapter 6.

This section will discuss in detail the operation principles of SBND relative to the general functionality of a general-purpose LArTPC. Following this, there will be an explanation of some key differences between the three detectors for the purpose of understanding their systematic effects at the analysis level.

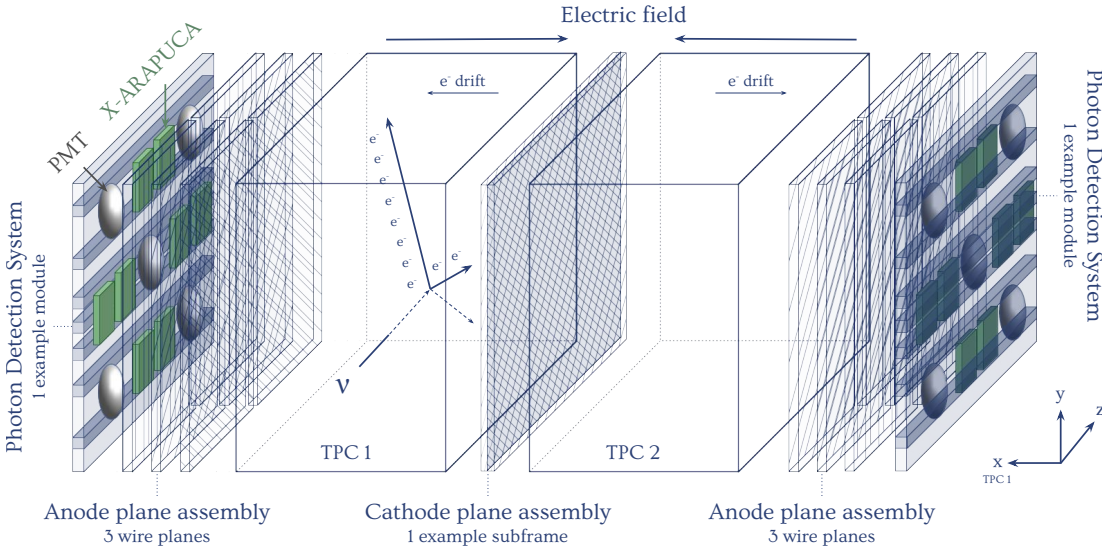

Figure 3.9.: A cartoon of the Short Baseline Near Detector TPC. The diagram includes a depiction of the 2 sets of APA pairs which sit at either end of the detector in the x-plane, a SBND CPA subframe module which includes a TPB-coated, reflective foil at the centre of the TPC in the x-plane and an example module of the SBND PDS including 5 PMTs (4 PTB-coated and 1 uncoated) and 8 X-ARAPUCAs (in 4 pairs) at either end of the TPC, behind the APA frames. The x-axis is defined to be positive in the drift direction of TPC1. An example neutrino interaction is included to clarify the detector orientation and demonstrate how the ionisation electrons are produced along the trajectory of charged tracks in the detector. The neutral tracks are shown as dashed lines, these are not visible in the detector as they do not ionise the argon atoms. The electric field crosses the two TPCs in opposite directions causing the opposing drift directions in each TPC.

3.3.1. The SBND Time Projection Chamber

The SBND detector, shown in Figure 3.9, will be 5 m long, 4 m tall and 4 m wide holding in total 112 tonnes of liquid argon in its active volume. The detector will function in mostly the same way as in the general TPC setup described in section 3.2.2.2, however there are also a number of functional uniquities, some of which are demonstrated in Figure 3.9 and described in the following sections.

Unlike the general TPC described above, SBND will have 2 cathode planes, 4 anode planes and as a result, 2 time projection chambers each with a 2m drift length. The cathode planes will lie side-by-side, positioned at the join between the two TPCs in the x-plane, the anode planes will reside in pairs on the opposite wall to the cathode plane in each TPC. This produces 2 electric fields and therefore 2 opposing drift directions. In the gaps between two adjacent anode wire planes, electrodes will divert the approaching

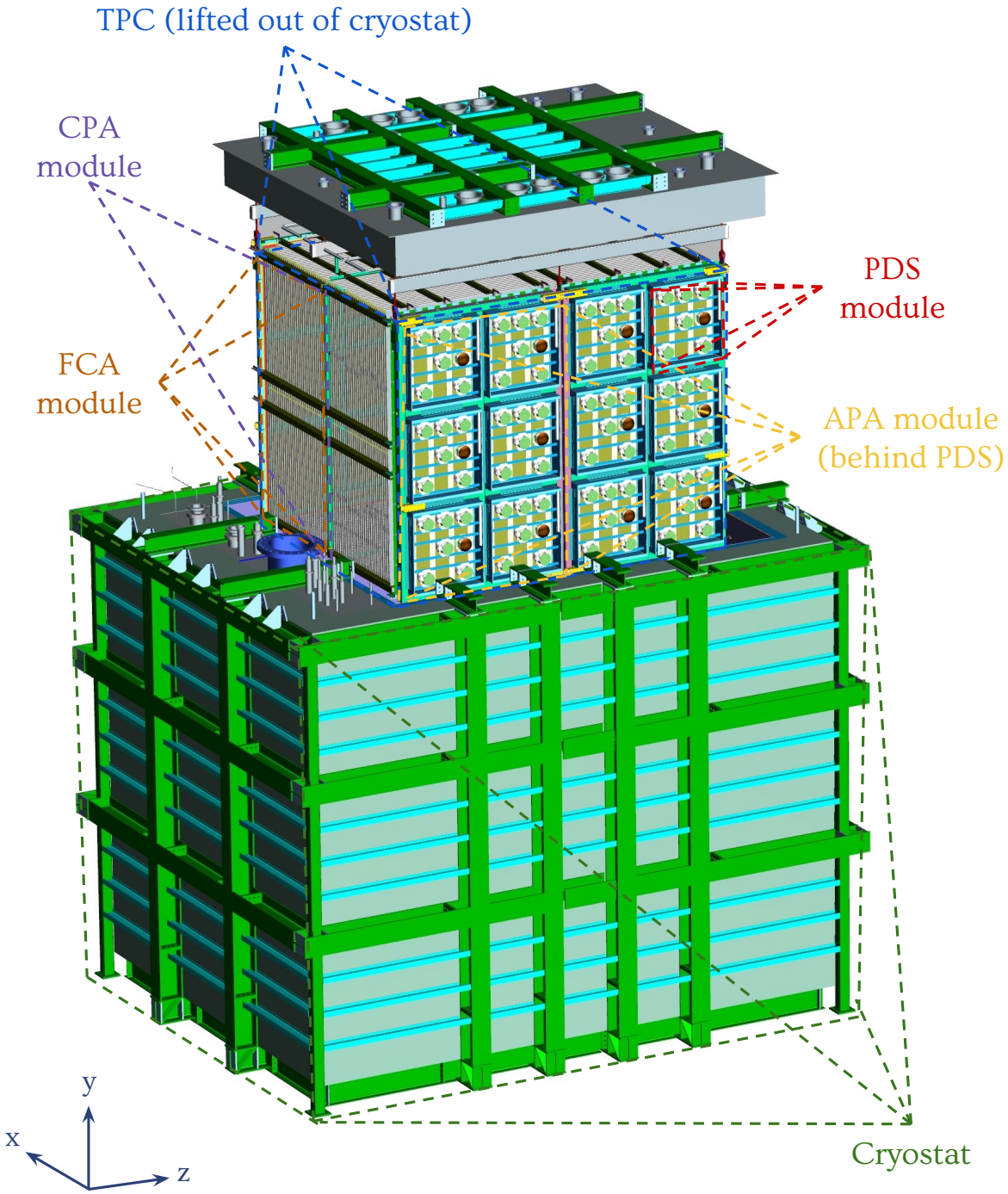

Figure 3.10.: Technical design drawing of the SBND TPC [7]. The TPC is shown lifted out of the cryostat with a wall of PDS modules in the x-plane and the FCA surrounding the remainder of the exposed detector. The CPA and APA modules cannot be seen directly but their locations are highlighted.

particles towards the nearest active wires on the plane. Limiting the distance electrons are able to drift across the TPC is necessary to prevent diffusion and attenuation due to interactions with impurities. This is why in large detector volumes such as in SBND, the solution has been to divide the detector into a multiple module system [6].

A field cage assembly (FCA) will surround the SBND TPCs between the APA and CPA modules [6]. This structure is used to maintain the constant electric field across the drift regions and is therefore a crucial component of such a large detector. Figure 3.10 demonstrates where the FCA will reside in a technical design drawing of the TPC and cryostat.

3.3.1.1. Anode Plane Assembly

A detailed description of the construction, cold-testing and quality control testing of the SBND APA modules is given in [136]. The modules will have 3 wire planes spaced 3 mm apart, with a wire separation of 3 mm in each plane. The wires themselves have a 150 μm diameter and are made of Copper-Beryllium. The SBND dimensions facilitate a total of 2816 wires across the induction (U, V) & collection (Y) planes in each APA resulting in a total of 11,264 readout channels across the entire detector [6].

The wires within the U & V planes are angled at $\pm 60^{\circ}$ to the vertical (Y) plane respectively. This wire separation and orientation allows for high resolution geometric and calorimetric reconstruction in general. Also, it matches the properties of the MicroBooNE and ICARUS detectors which ensures the efficiency of separating electromagnetic showers produced by electrons and photons is consistent across the SBN program. Photographs of one of the APA frames at Fermilab are shown in Figure 3.11 [137].

It is crucial that the wire separation is held constant across the entirety of both APA frame structures for a number of reasons. For instance, minimising the uncertainty on the geometrical reconstruction and maintaining precise uniformity of the electric field in every region of the detector. A requirement is therefore placed on the tension of the wires such that at room temperature they must be 0.5 kg [6].

Another critical feature of the TPC modular setup in maintaining the consistency of the electric field is that the pairs of APAs at each end of the detector are aligned to extremely high precision in the x-plane. A requirement is placed on the minimum 'flatness' of the planes at 0.5 mm to ensure the wire separation remains constant across the plane structure as a whole, such that the timing and spacial reconstruction of the electrons is

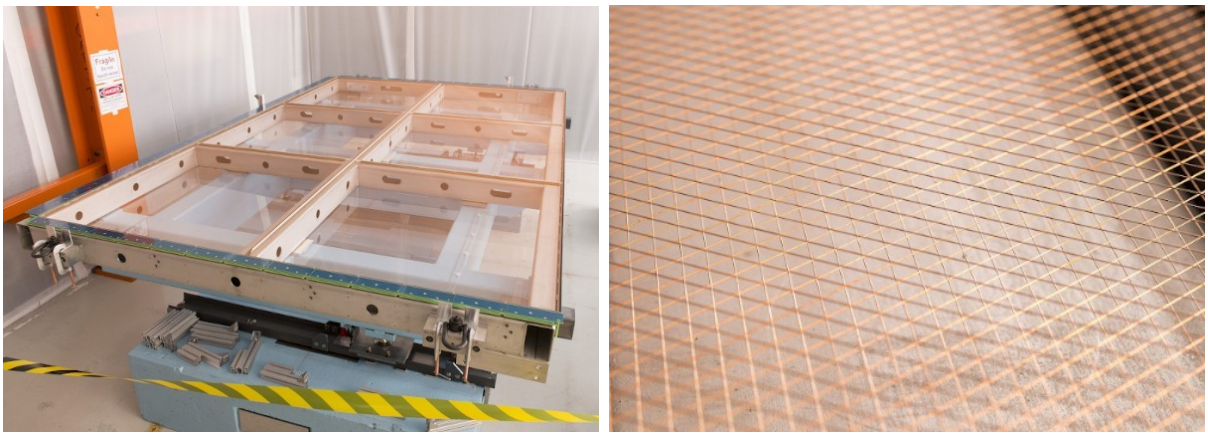

Figure 3.11.: On the left is a photograph of the APA built in the United Kingdom after being delivered to and unpacked in the D0 assembly building at Fermilab. On the right is a closer look at the wire planes, in which the angles and separation can be seen [137], December 2018.

consistent [6]. Precision measurements of the flatness ($\sim \mu$m) of the APA frame pairs are made using a laser tracking system, from which shim maps are constructed to fix any misalignment within each frame across the front (wire) faces and wrap (readout) edges. I participated in many aspects of the alignment preparatory and QC work for two of the 4 APA components during my long term attachment at Fermilab.

Each APA frame will have cold readout electronics along two edges. The U and V planes are connected electronically at the join of the APA pairs by flexible jumper cables such that the readout is only necessary along the outer sides of these wires planes. In the implementation of biased electrodes at the join of the APAs, to divert electrons away from the dead region between frames and onto the nearest wires, a distortion of the electron's path is introduced and must be corrected for. This is a straightforward procedure when the magnitude of the distortion is constant and known [6].

3.3.1.2. Cathode Plane Assembly

Each CPA will consist of a stainless steel outer frame and 8 subframes. Two CPAs will lie side-by-side in the same orientation as the APA pairs, however there is no requirement for an electronic connection between the two since the CPA does not contribute directly to the readout. The frames must still be well-aligned for the same field-shaping reasons as the APA pairs. The stainless steel outer structure of both CPA frames is shown in Figure 3.12 after installation in the assembly and transport fixture (ATF).

Figure 3.12.: The outer CPA frames with subframe spaces visible after installation in the assembly and transport fixture (ATF). The two frames are upright and have been attached together showing the scale of the detector in the y-z plane.

Figure 3.13.: Tensioning the CPA subframes. On the left is one of the subframes when submerged in the liquid nitrogen. The right hand photograph shows the screws in the slightly-defrosted mesh having been tightened whilst the surrounding frame remains extremely cold.

There have been two iterations of the CPA subframe panel design. In the first, a subset of the CPA panels have a single wire mesh layer which is transparent allowing the field to flow uniformly across the entire CPA frame whilst also allowing the argon to drift between TPCs so as to prevent there from being a physical separation between the 2 modules of the detector. The mesh must be held under high tension in order to maintain the consistency of the field across the CPA. Such tension is achieved by submerging each subframe in liquid nitrogen before tightly screwing the mesh into the stainless steel surround. This is done while the frame is still cold, so that the mesh, which warms up faster due to its finer structure, is held in place whilst being pulled tight as the frame warms up. I took part in the first iteration of this process when it was conducted at the University of Liverpool, photographs of the procedure are shown in Figure 3.13.

The remaining subset of panels within the first iteration of the CPA design along with every panel in the second iteration of the CPA design will have two mesh panels, in order to hold a reflective foil coated in wavelength-shifting tetraphenyl butadiene (TPB) between them. This version of the subframes is used to maximise the light yield of the detector by reflecting any of the scintillation photons emitted by the interacting particles which travel in the opposite direction to the PDS wall behind the APAs. This version of the subframe must also be held under high tension. A constant voltage of -100 kV will be applied to the CPA in order to provide the required 500 V/cm electric field across each of the 2 m long drift volumes. This is supplied to the CPA via a high voltage feedthrough which penetrates the cryostat.

3.3.1.3. Photon Detection System

The SBND PDS will have multiple components in its role as R&D for future LArTPC experiments. Each of the 24 modules (12 behind each APA wall) of the PDS, demonstrated in Figures 3.9 and 3.10, will have 5 PMTs (4 PTB-coated and 1 uncoated) and 4 X-ARAPUCA pairs. SBND will record both direct and indirect scintillation light, all of which is naturally produced with wavelengths in the vacuum ultraviolet (VUV) range. PMTs cannot detect VUV light, therefore detecting the direct photons requires a wavelength-shifting coating be applied to the PMTs. Indirect photons are recorded after being reflected off the CPA subframes. The reflective foils in the CPA subframes are also coated in TPB which consequently shifts the wavelengths of the scintillation photons into the visible range before they reach the PMTs. Some PMTs must therefore remain uncoated in order to make sure the reflected and direct light can be disentangled.

The ARAPUCA is a completely novel device developed for use in LArTPC experiments. Such a concept aims to record scintillation photons with extremely high efficiency by trapping them within a box that has highly reflective internal surfaces without the need for a large active photon detection system. UV scintillation light enters the ARAPUCA box through a dichroic filter which is transparent at the initial wavelengths of the light but completely reflective to other wavelengths. A further slab of material on the entry side of this filter is coated with a wavelength shifter that converts the photons travelling through it into the range which is sensitive to the filter as a highly reflective surface. Thus, the light becomes trapped and can be detected by a Silicon Photo Multiplier (SiPM) situated on the internal surface of the box [138].

Recently, an upgraded version of the ARAPUCA concept has been developed which will consequently be the system installed in the SBND experiment. The X-ARAPUCA system will blend the functionality of the original ARAPUCA design with that of a light bar. Figure 3.14 depicts the original ARAPUCA concept and demonstrates the development into the X-ARAPUCA [139]. The main difference is that the wavelength shifter which simply coated the internal slab in the initial design will instead be embedded in an acrylic slab, which is capable of capturing the photons by total internal reflection and guiding them to one end of the material where it is detected. Consequently, the number of reflections undergone by the photons on the internal surfaces of the box is greatly reduced and thus the detection efficiency of the light is increased. A further development to the design would see the photons with a high angle of incidence, such that they could not undergo total internal reflection and therefore would not be wavelength shifted by

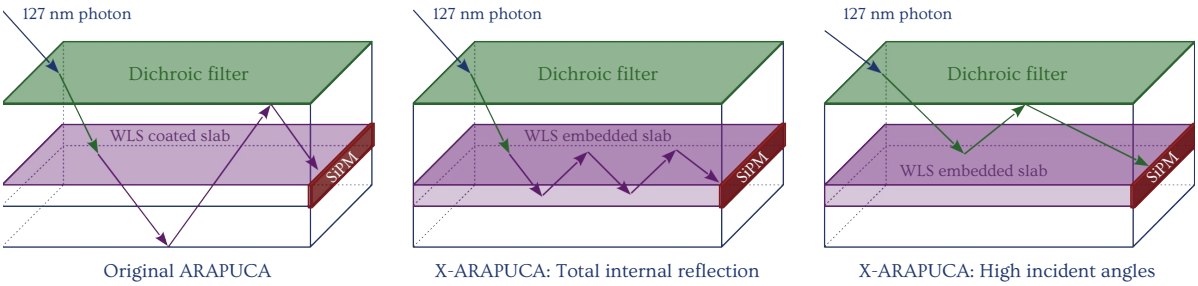

Figure 3.14.: Left is the original ARAPUCA design in which the photons enter the box, are wavelength shifted when travelling through the coated slab and are then reflected internally until they reach and are detected by the SiPM. The central diagram demonstrates the main idea behind the X-ARAPUCA, in which the photons are totally internally reflected inside the wavelength shifting slab until they reach the SiPM. The final diagram on the right demonstrates how photons with high incident angles will simply be reflected by the slab and will therefore not undergo total internal reflection or be wavelength shifted by the slab. These photons remain trapped in the upper part of the ARAPUCA and are reflected internally until they reach the SiPM [139].

the slab, be guided instead between the dichroic filter and the acrylic slab towards the SiPM due to the filter and slab's refractive indices and the photon's high angle [139].

3.3.1.4. Cosmic Ray Tagging

Since SBND will reside on the surface of the Earth, there will be a huge flux of cosmic rays entering the detector in coincidence with the neutrino beam at an estimated rate of 3 cosmic rays for every neutrino event crossing the active volume [6]. These cosmic rays will consequently be the most abundant background to the neutrino interactions and need to be addressed carefully. One major hardware feature of SBND will be a cosmic ray tagging (CRT) system comprised of a number of modular planes covering every external face of the detector.

Cosmic rays entering the detector from above will be significantly more abundant than those entering from any other side of the detector. There will therefore be 7 CRT planes in total, one covering each detector face plus an additional plane above the top face in order to help maximally mitigate the copious number of top-down rays. The two top-face modules will form a telescopic tagging system with a coordinate resolution of 1.8 cm, an angular resolution of 8 mrad and almost 4π solid angle coverage of the detector from the whole CRT system [140]. The 7 CRT planes are shown surrounding the detector on the left of Figure 3.15, with the modules of each plane shown on the right.

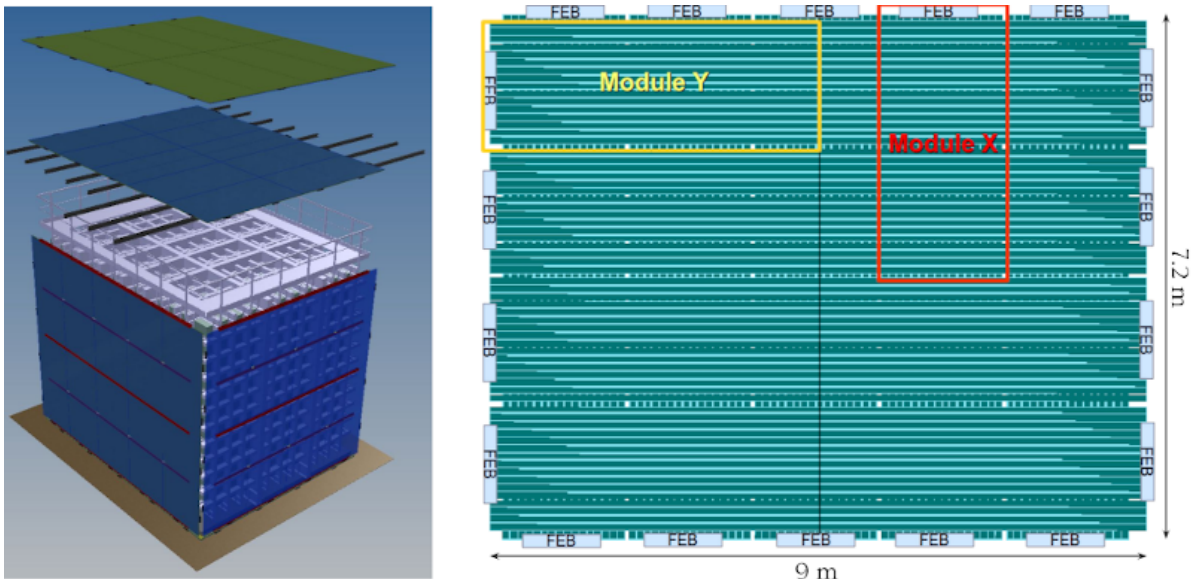

Figure 3.15.: On the left is a technical design drawing of the CRT system as it surrounds the SBND cryostat, including the additional plane above the top face of the detector. The image on the right shows the modular layout of the planes, with 2x5 modules making up the X-coordinate layer and 2x4 modules making up the Y-coordinate layer [140]. The X & Y coordinate layers are oriented at 90° to one another in order to precisely locate a CRT Hit in the X-Y coordinate system.

Each CRT plane is comprised of 2 orthogonal layers of scintillating modules lying side-by-side. The X-coordinate layer has 2x5 modules and the Y-coordinate layer has 2x4 modules as shown in the right hand side of Figure 3.15. The modules are each formed of 16 10.8 cm wide scintillating strips containing optical fibres coupled to SiPMs, the maximum distance between two adjacent strips does not exceed 0.2 mm [140]. The scintillating strip lengths depend on the coordinate layer they form a part of and the dimensions of the face of the detector they are covering, for the top and all sides of the detector this length is either 4.5 m or 3.6 m. Strips in the modules covering the bottom face will have lengths of 2.72 m to allow them to reside between the I-beams of the cryostat structure.

Figure 3.16 shows the strips within a module and how they work together to reconstruct the X-Y coordinate of a Hit in the CRT plane. This is done by first determining which SiPM was hit in each of the X and Y coordinates. Once identified, the number of photons observed by each optical fibre in the hit strip is used to find the location across the width of the strip it was struck. The relative number of photons collected by the two optical fibres at either side of the strip is characteristic of how close to each fibre that Hit was positioned.

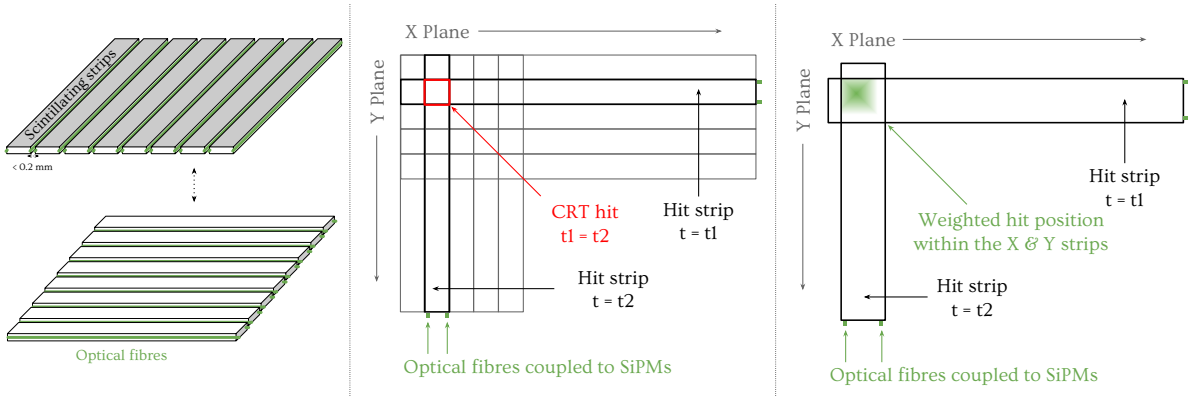

Figure 3.16.: The CRT plane modules each contain 16 scintillating strips of varying lengths. Each strip has two optical fibres located at either side of the 10.8 cm width. On the left is a 3D idea of how the strips look and how strips within 2 modules are oriented on top of one another. The central diagram shows how two orthogonal strips which lie on top of one another can be used to tag the location of a CRT Hit to within a 10.8x10.8 cm^2 square. The right hand diagram shows how the number of photons collected by the optical fibres within the hit-strips give the location of a Hit within the strip more precisely [140].

3.3.1.5. TPC and PDS readout electronics

The SBND TPC electronics are separated into three main sections: The front end cold electronics, the warm interface and the TPC readout modules. The front end electronics live and operate within the liquid argon, the warm interface and TPC readout modules live outside the cryostat and therefore do not operate at the extremely low temperature. A diagram of the electronics information flow for a single readout channel is shown in Figure 3.17 [141]. The 'front end' electronics consist of the cold electronics, the signal feedthrough and the warm interface crates. The 'back end' electronics are the TPC readout modules, also housed in crates.

There are two main reasons for using cold electronics in LArTPCs, the first is to maximise the signal-to-noise ratio (SNR) by minimising the required cable lengths between the wire planes and the pre-amplifier to reduce the capacitative load from the input wires [141]. Signal-to-noise improvements are also made in the cold by the reduction of thermal fluctuations and increase in charge carrier mobility in silicon with $\frac{kT}{e}$ [142]. The second reason for choosing to use cold electronics is to minimise the number of cables needing to be fed out of the cryostat, not only does this minimise the amount of outgassing but also allows for more independent design and configuration choices of the TPC, cryostat and readout [142] [141].

The cold electronics front end motherboards (FEM) are attached directly to the APA frames in SBND. There will be a total of 88 FEMs with 128 channels connected to each for the 11,264 total SBND wires [142]. The signal from each wire is is digitised using an analog-to-digital converter (ADC) and each are transferred via cold cable out of the cryostat to the warm interface electronics through a signal feedthrough [6]. At the warm interface stage of the TPC readout, the electrical signal is received and converted to an optical signal for passage via an optical fibre to the TPC data acquisition (DAQ) readout system. The warm interface electronics are housed in a Faraday cage to minimise external noise contributions when transferring the optical signal to the TPC readout.

Upon arrival at the TPC readout crate, the signal is processed once more before being transmitted to DAQ PCs for further storage and analysis [6]. The decision made by the readout on when to store and discard data is based on the various triggers internal and external to the detector, including the cosmic ray trigger and neutrino beam trigger. The cosmic ray removal efficiency is optimised by fully reconstructing interactions in the detector before and after the neutrino beam drift time, a readout window of 3.84 ms is therefore defined which corresponds to 3 drift windows: The neutrino beam trigger window of 1.28 ms plus 1.28 ms before and after. Determining if a ray seen in the detector started outside of the nominal neutrino interaction window gives a clear indication that it was cosmic-induced and can therefore be removed unambiguously.

The SBND PDS system is responsible for providing prompt timing information about the interactions occurring in the detector to aid in the tagging and removal of external background contributions like cosmic rays. The scintillation light is also responsible for reconstructing the x-coordinate of the neutrino interactions and can provide additional information about the reconstruction of total energy depositions and particle identification, consequently impacting the geometrical and calorimetric reconstruction precision as well [135]. The SBND PDS will be readout with a waveform digitizer which records and processes the waveforms using charge integration and pulse shape discrimination with constant fraction timing and pulse height analysis. The digitizer will provide ns timing resolution and will have a direct optical link to the computing system for analysis.

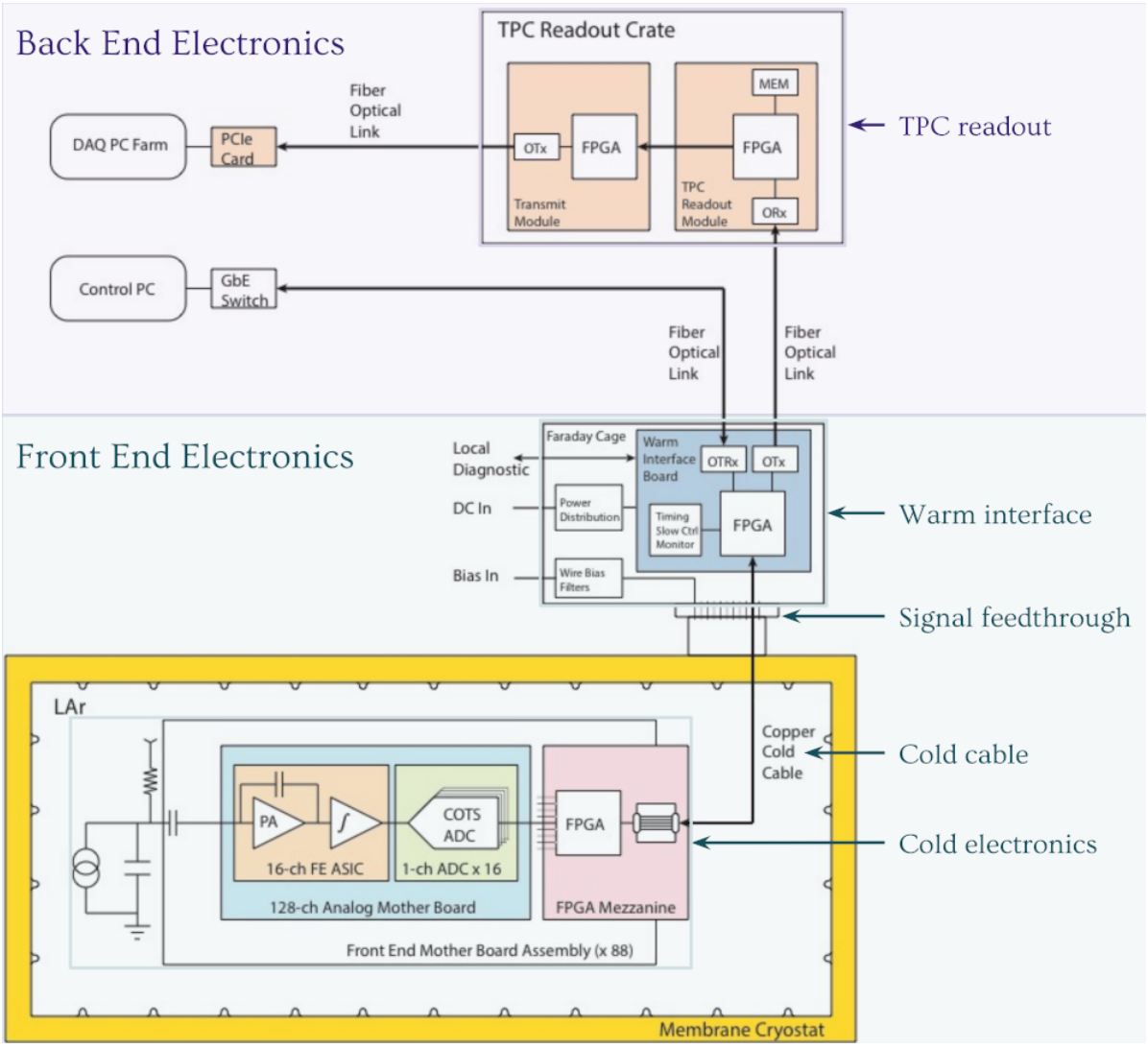

Figure 3.17.: A diagram of the SBND readout electronics. The system is made up of the front-end and the back-end electronics based on the group developing the machinery. The front-end consists of the cold electronics and the warm interface, this is being developed mainly by BNL. The back-end of the electronics system is the DAQ, developed by Nevis Labs, Columbia University for the MicroBooNE experiment [141].

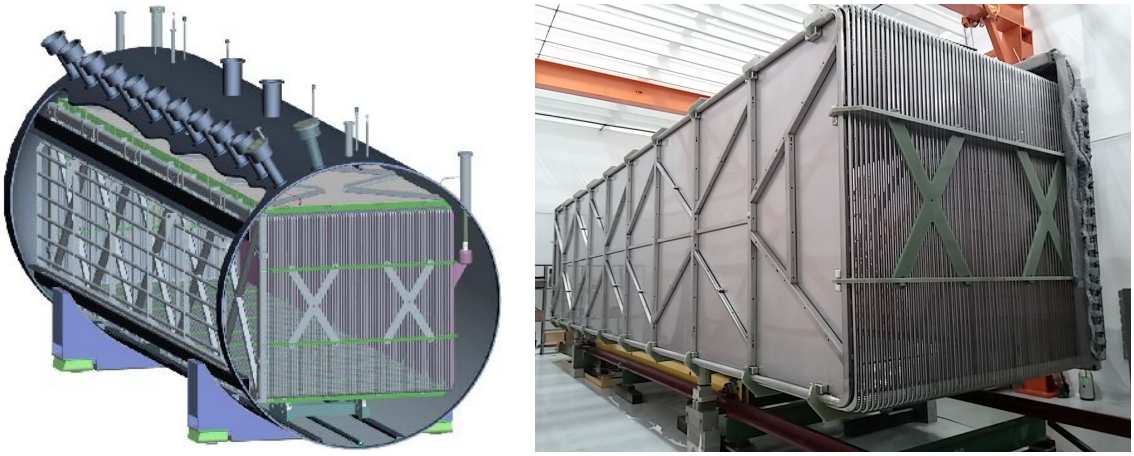

Figure 3.18.: On the left is a schematic diagram of the MicroBooNE detector inside the cylindrical cryostat, with the front and left hand side left open to show the field cage and APA frames respectively. On the right is a photograph of the MicroBooNE detector in the clean tent before it was relocated to the liquid argon test facility (LArTF) where it operates [134].

3.3.2. Unique features of the MicroBooNE detector

Unlike the other two experiments in the SBN program, MicroBooNE operates with only a single TPC in its 90 tonne detector volume surrounded by a cylindrical cryostat, see Figure 3.18 [134]. This single-TPC format is successful because of the layout of the detector volume, the horizontal and vertical (x and y) dimensions are 2.560 m and 2.325 m respectively and the beam direction dimension (z) is 10.368 m. This means that the electron drift length is still only ∼2.5 m which is acceptable when considering the attenuation of electrons in highly purified argon [134] [131]. MicroBooNE has a single set of Anode and Cathode Planes in the detector, removing the need for the electrical coupling of the planes. Rather than operating at the nominal electric field of 500 Vcm^{-2}, MicroBooNE operates at 273 Vcm^{-2} [143].

As the centrally-located experiment in the SBN program, MicroBooNE sits at a baseline of 470 m, close to the location of MiniBooNE at a 500 m baseline providing the opportunity to study neutrinos from the NuMI beam. A further technological difference between the MicroBooNE and SBND detectors is within the light collection system. In both MicroBooNE and SBND this resides behind the APA, but in MicroBooNE the system is composed of an array of PMTs and lightguide paddles in contrast to SBND's PMT & X-ARAPUCA system. The X-ARAPUCAs are a much more recent development in the world of LArTPC detector technology and were not available when MicroBooNE was being constructed [134]. The lightguide paddles were included as R&D in the MicroBooNE detector.

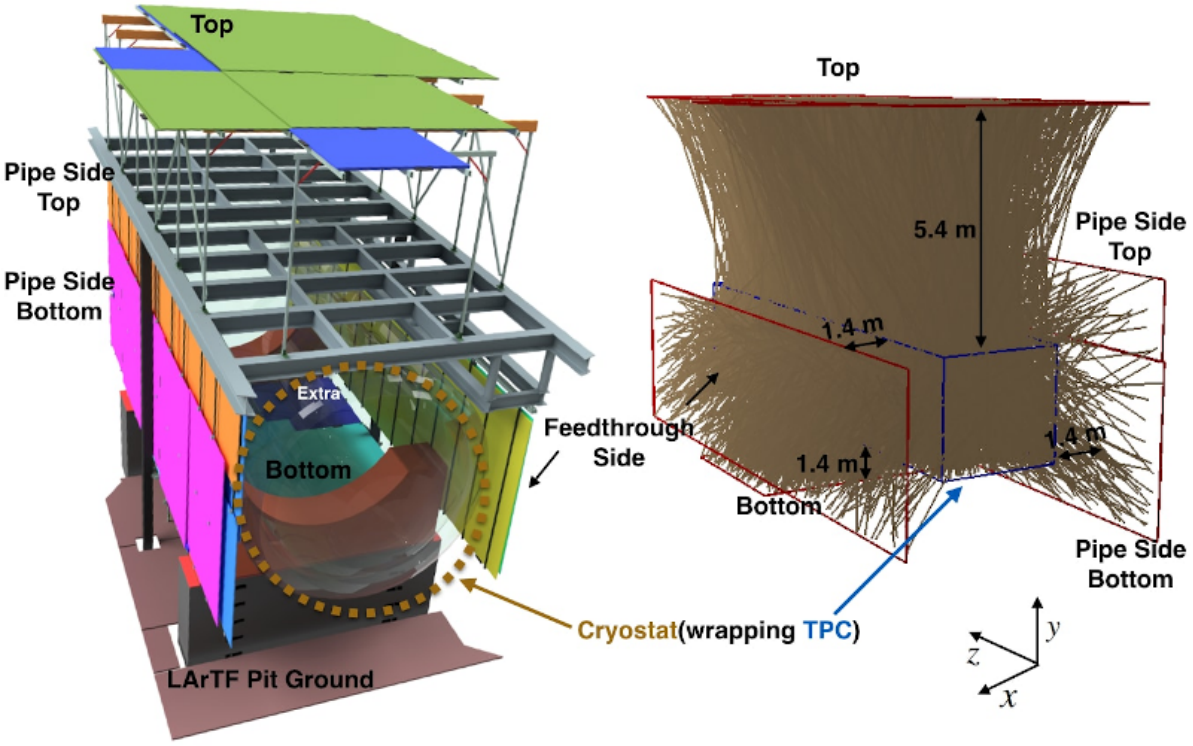

Figure 3.19.: On the left are the CRT planes surrounding the MicroBooNE cryostat along the top, bottom and both long sides. On the right are simulated cosmic ray trajectories showing their path through the detector and coincidence with the tagger planes [143].

The MicroBooNE electronics system works in a substantially different way to SBND, the analog signal is transported out of the detector rather than the digital signal and the digitising is done at the warm interface stage of the readout process [134]. The SBND DAQ PCs are based off the MicroBooNE system.

As is the case in all of the SBN detectors, MicroBooNE is housed on the surface of the Earth and will therefore be exposed to a huge flux of cosmic rays. In addition, because the electric field is lower than the nominal value, the electron drift time is longer, 2.2 ms, therefore MicroBooNE is exposed to an increased rate of cosmic rays relative to its size and position with respect to the other SBN detectors [143]. A CRT system was therefore designed for the detector, but was not put in place until after the first data run had been recorded, therefore MicroBooNE has an entire dataset whose cosmic rays cannot be mitigated by the hardware trigger. The MicroBooNE CRT system is different to that of SBND in that its detector coverage is much lower, with only 4 planes in total covering the top, bottom and both long sides of the cryostat as shown in Figure 3.19 [143]. The CRT planes themselves are constructed in the same way as in SBND.

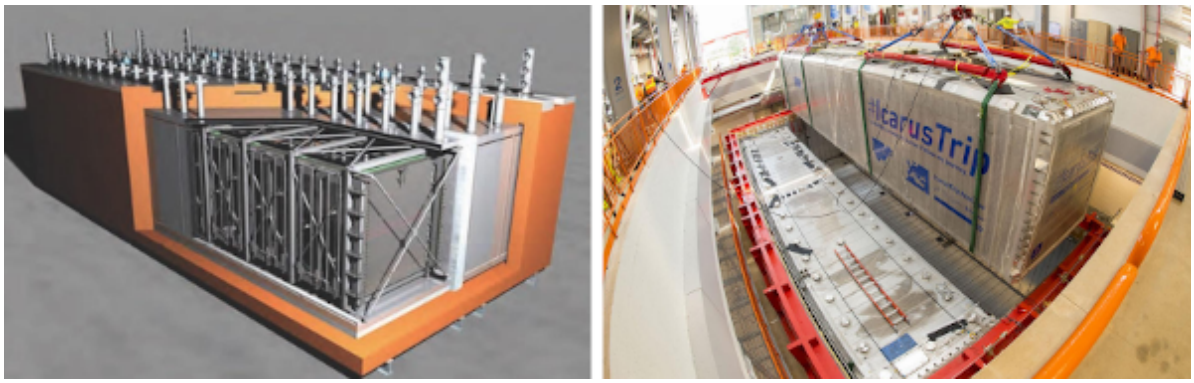

Figure 3.20.: On the left is a schematic diagram of the ICARUS detector with one cryostat open to show the orientation of the wire planes and the field cage [6]. On the right is a photograph of one of the detector modules being inserted into its home at Fermilab [137].

3.3.3. Unique features of the far detector, ICARUS

The ICARUS detector, shown as a technical design drawing and photographed entering its home in the far detector building at Fermilab in Figure 3.20, is made up of two separate identical cryostats with equal active volume dimensions of $3.2 \times 2.96 \times 18.0$ m^3. Similar to SBND, each cryostat will house two TPCs separated by the central cathode. The subframes in the cathode plane will be semi-transparent and made of pierced stainless steel sheets, rather than having mesh panels or reflective foils sandwiched between two mesh panels [6], as is the case in the centre of the SBND cryostat. Consequently, all scintillation light reaching the PDS is VUV and requires wavelength-shifting in order to be readout. The ICARUS PDS also resides behind the wire planes and consists of 74 PMTs coated in the wavelength-shifting PTB, unlike the other two SBN detectors these are not combined with another light detection system for R&D [6].

The wire planes are constructed with 53,248 wires in total across 3 sense planes placed 3 mm apart, each with wires at a 3 mm separation [6]. Although this format is identical to the SBND and MicroBooNE detectors, one key difference is that the wire angles on each sense plane are situated at 0° and ±60° to the horizontal, not the vertical. This orientation was decided upon because ICARUS was originally designed as a cosmic ray detector, which primarily enter from the top and traverse downwards, therefore detecting the rays with a set of horizontal wires would maximise the number crossed by a downgoing cosmic ray [144].

The electronics at the far detector are also unique. There are no cold electronics at all in the ICARUS cryostat, the anode plane wire signals are immediately transferred out of

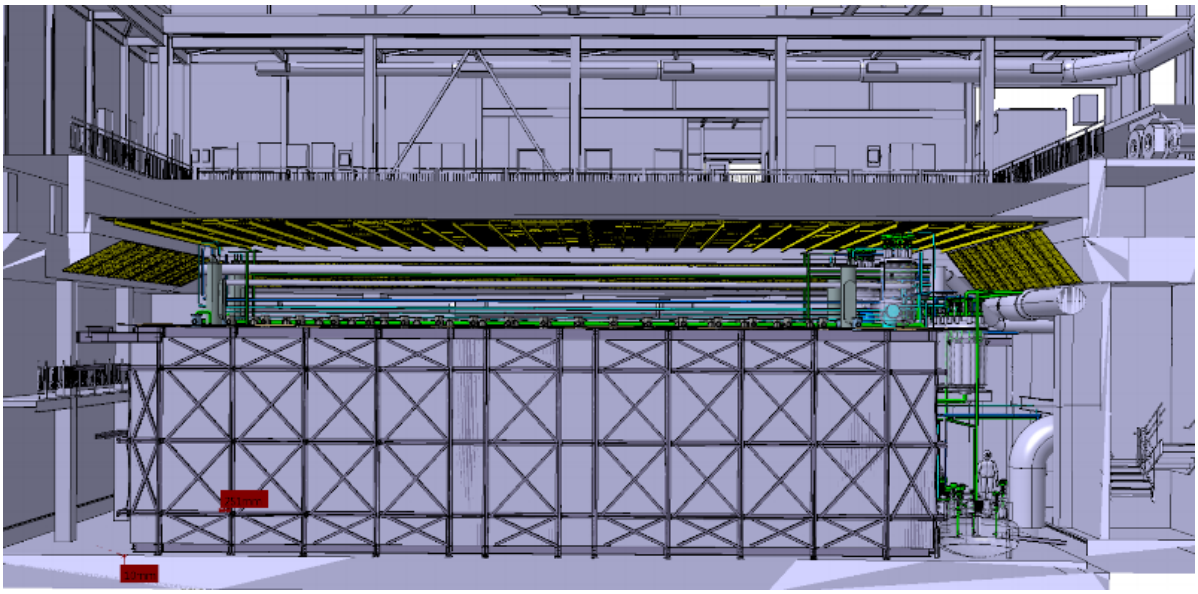

Figure 3.21.: In yellow is the top plane of the ICARUS CRT system, including a subset of inclined planes at the front and back of the detector in the z-plane [145].

the detector [6]. Amplification of the signal is then performed and is crucial in ICARUS in order to maximise the SNR, since the wire signal is not immediately received by the FEM as in SBND and MicroBooNE [6]. The DAQ system in ICARUS was designed and implemented for its exposure to the CNGS beam, long before the development of the MicroBooNE system, and will be updated for its implementation as part of the SBN program.

The CRT system in ICARUS covers the entire detector like in SBND, with only one plane above the top face of the detector. The top plane will be constructed in the same way as in SBND and MicroBooNE with two layers of scintillating strips, each with two optical fibres and readout at one end. In addition there will be a set of inclined modules at either end of the top face of the detector in the z-direction, see Figure 3.21. The CRT planes along the sides and bottom of the detector will be recycled from MINOS and double CHOOZ respectively, the main functional difference is that each scintillating strip of these recycled planes only has a single optical fibre running through it. The bottom plane still only reads out at one end of the strip but the side planes instead read out at both ends [145]. The most significant impact of having different CRT systems across the SBN program is the magnitude of the external background contribution to the oscillation analysis in each detector, the software cosmic ray tagging will need to be independently tuned for each detector and the systematic uncertainty associated with this background must be well understood across the program.

3.4. Physics at the Short Baseline Neutrino program

The primary physics goal of the SBN program is to study neutrino oscillations in the regime of the existing short baseline experimental anomalies and interpret them in the context of sterile neutrino oscillations. In addition to these sterile searches, SBN will be well-equipped to study neutrino interactions on argon given the huge rate of events expected, ∼millions per year. Studies of such interactions enable high-precision cross-section measurements to be made in multiple neutrino-argon interaction channels, paving the way for next-generation liquid argon experiments such as DUNE.

Neutrino physics theory has developed far Beyond the Standard Model (BSM) over the last decade, and SBN will be capable of probing many such exotic hypotheses [7]. The prospects for making measurements of sterile neutrino oscillations, neutrino-argon interaction cross-sections and BSM physics in the SBN program will be discussed here.

3.4.1. The search for sterile neutrinos

The baseline of the SBN program was chosen in order to be maximally sensitive to sterile neutrino oscillations under the (3+1) hypothesis, in all three short baseline neutrino oscillation channels. The probabilities of one such oscillation channel, ν_e appearance, occurring at the baselines and peak energy of the near and far detectors in the SBN program are shown in Figure 3.22. The oscillation probabilities are calculated for two values of the mass splitting and mixing angle consistent with the existing sterile neutrino data limits, $\sin^2 2\theta_{\mu e} = 0.015$ & 0.002 and $\Delta m^2_{41} = 0.3$ eV^2 & 1.5 eV^2 [7].

The far/near ratios of the oscillation probability at each of the two parameter limits implies that SBND will only become sensitive to observing oscillations at values of the mass splitting towards the upper-limit of the sensitivity. Instead, the near detector will primarily constrain the uncertainties in the oscillation analysis. This is possible thanks to the use of the same detector technology in all three detectors, which means a substantial contribution to the reasonably large (10-30% [7]) BNB flux and neutrino-argon interaction cross-sections uncertainties will be correlated across the SBN program, and can therefore be cancelled out in the joint oscillation analyses. The location and energy ranges of MicroBooNE and ICARUS will enable them to measure the oscillated content of the neutrino beam [7].

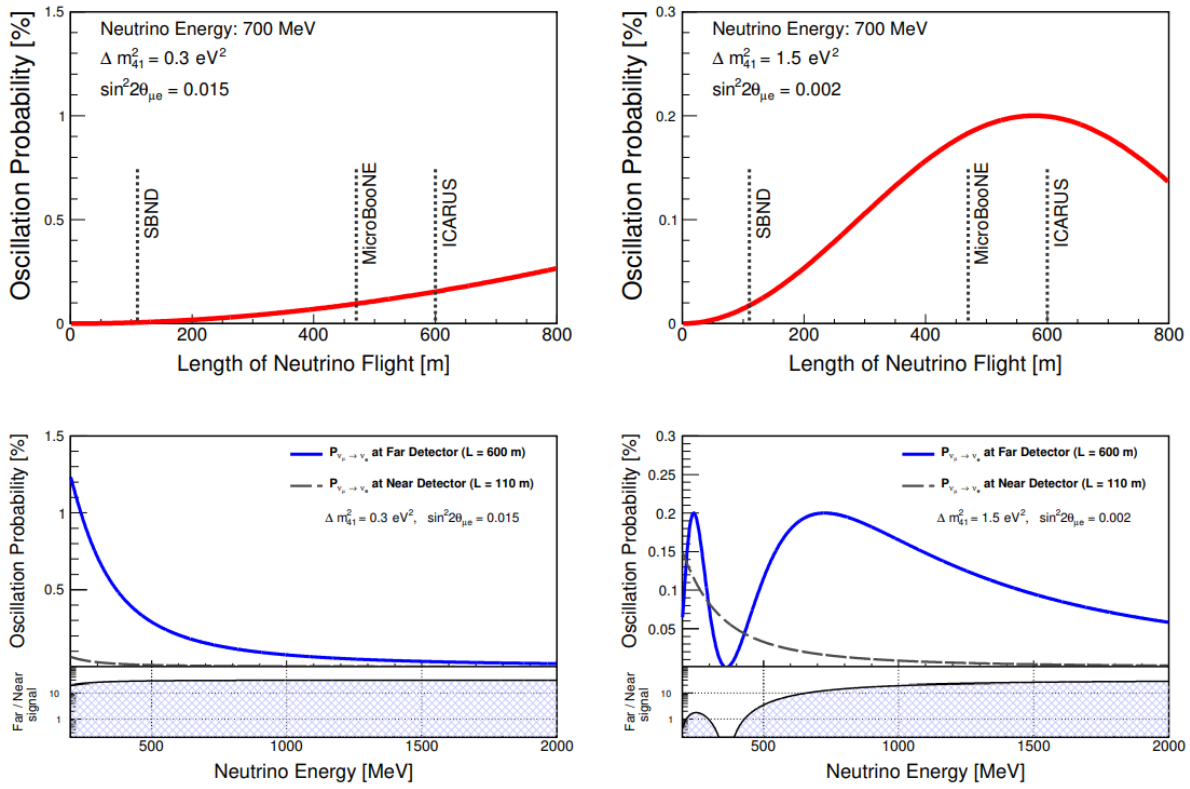

Figure 3.22.: The probability of observing ν_e appearance oscillations at the current global limits in $\sin^2 2\theta_{\mu e} - \Delta m^2_{41}$ parameter space is shown at the near and far detector baselines, 110 m and 600 m, and peak BNB energy, 0.7 GeV. SBN will be sensitive to sterile neutrino oscillations across the entire parameter space. The far/near detector probability ratio is also shown, which highlights the strong discrimination power up to almost the highest values of Δm^2_{41} in the existing limit [7].

One significant issue encountered by MiniBooNE and LSND in their efforts to interpret the anomalies discussed in section 2.4.1.3 was in the mitigation of the topological backgrounds, namely photon-induced electromagnetic showers, when searching for electron neutrino interactions. LArTPC detectors are able to distinguish between electron and photon induced showers, see section 4.12, and therefore this background will be almost entirely removed in all SBN oscillation measurements. The functional capabilities of the LArTPC detector technology along with the reconstruction and background rejection methods will be discussed further in chapter 4.

The status of the SBN sterile neutrino oscillation sensitivities at the time of the SBN proposal [6] are shown in the context of the ν_μ disappearance and ν_e appearance oscillation parameters in Figure 3.23. The contours are constructed with contributions from flux, interaction and uncorrelated detector systematics with an assumed 6.6×10^{20} POT exposure.

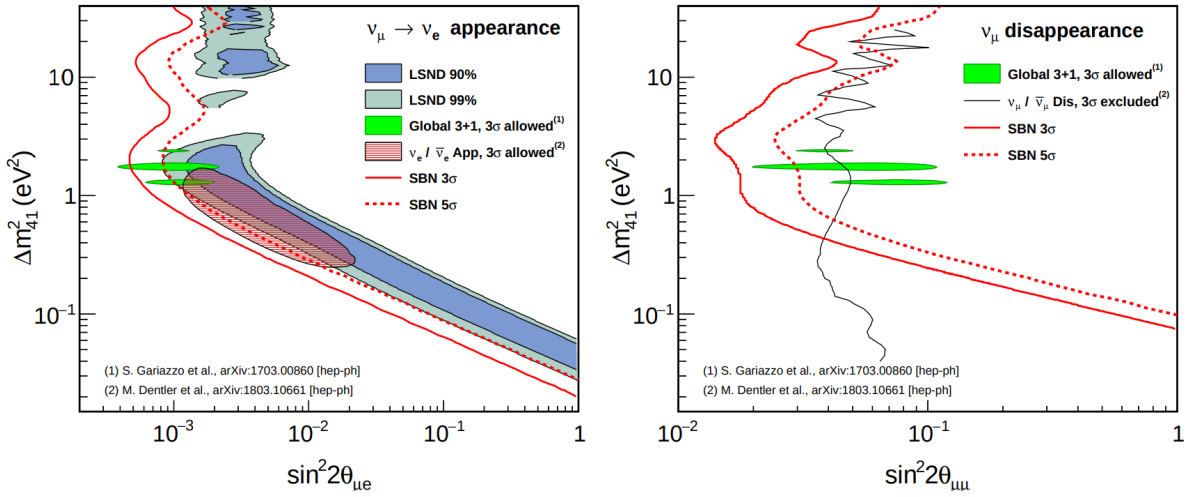

Figure 3.23.: Status of the SBN sterile neutrino oscillation sensitivities as of the SBN proposal in the context of existing data [7]. The ν_e appearance parameter space is shown on the left, with the SBN 3σ (solid red line) and 5σ (dashed red line) exclusion contours compared to the LSND 90 and 99% confidence allowed regions in blue and grey respectively [81]. The red shaded region is the global ν_e appearance allowed data [84]. The right-hand plot shows the ν_μ disappearance parameter space, with the global ν_μ disappearance exclusion region in black [84]. Finally, the green filled regions are the global 3+1 allowed regions [146].

3.4.2. Neutrino interaction cross-section measurements

SBN will be uniquely placed to study the interactions of electron and muon neutrinos with the heavy, argon nucleus. The LArTPC detector technology and statistical significance of the events recorded will enable SBN to produce high-precision cross-section measurements of neutrino-argon scattering in many inclusive and exclusive charged and neutral current topologies. The event rate will be sufficiently large (especially in the near detector) to reduce the statistical uncertainty to below the percent level. The systematic uncertainties will therefore dominate most measurements in SBN [7].

Interaction cross-sections must be well-understood for making neutrino oscillation measurements at the required sensitivity for discovering new physics. This is especially pertinent in experiments involving the complex scattering of neutrinos with heavy-nuclei like argon, since multiple neutrino interactions can result in each observed final state due to nuclear effects and the range of possible neutrino energies from the flux of the beam [147].

As the near detector in the SBN program, SBND will have a baseline of 110m and a flux of neutrinos which is ∼10 times that of the other 2 SBN detectors [6]. The number of events expected during the full run-time (exposure) of the experiment (6.6×10^{20}

Protons on Target, POT) is on the order of 6 million. SBND will therefore be well-suited to making these high-precision cross-section measurements of neutrino interactions with argon. In addition, MicroBooNE has been running since 2015 with statistics still in the tens of thousands, and has therefore already been able to produce a number of precise cross-section measurements in the few-GeV energy range [148] [149].

3.4.3. BSM physics

Over the last few decades, especially since the observation of neutrino oscillations, the possibility for using neutrinos to study more exotic physics has been explored at an ever-growing rate. Many theories now exist which are yet to be probed experimentally, and the LArTPC detector technology coupled with the intense neutrino flux of the BNB means the SBN program has an opportunity to make a number of these exotic physics searches [7]. An exhaustive and detailed list of BSM physics opportunities can be found in this review [7] and includes,

- Large extra dimensions to explain the small size of the active neutrino masses
- The existence of millicharged particles with fractional charge
- Neutrino tridents as a tool for detecting new physics such as dark matter candidates

3.5. Current status of the SBN program

The MicroBooNE detector has been operating since October 2015, it is therefore assumed to contribute double the exposure, 13.2×10^{20} POT, of the near and far detectors to the oscillation analysis. SBND is in the construction phase and at the current rate is expected to begin taking data in 2022. The ICARUS T600 detector was shipped to Fermilab in 2017. The detector was filled in August 2020 and is currently in commissioning to begin taking physics data in October 2021. The near and far detectors are each assumed to contribute 6.6×10^{20} POT to the SBN oscillation analysis, however the final exposures of all three detectors may be larger than the quoted assumptions.

Chapter 4.

Event processing in the SBN program

Monte Carlo, MC, simulations are a critical component in all aspects of neutrino physics experiments. In the design phase, the attainability of the proposed physics can be tested in the context of multiple detector configurations, in order to aid in the optimisation of the physical design of a detector. The physics output of an experiment can then be analysed against its theoretical counterpart through MC simulations of the models. Systematic uncertainties can also be quantified and methods of constraining them can be evaluated [150].

This chapter will first introduce neutrino interactions with matter, before discussing the full procedure for simulating such interactions in LArTPC detectors. In addition, the definition and construction method for the systematic parameter sets used in all SBN analyses will be discussed.

4.1. Neutrino interactions

When neutrinos interact via either the charged or neutral weak currents, they may scatter off the target nucleon(s) via a number of processes. Example schematic and Feynman diagrams for the dominant neutrino scattering processes in the SBN energy regime, around $E_\nu = 1$ GeV, are shown in Figure 4.1. Descriptions of each of the dominant neutrino scattering processes are given in the following sections. The models which are used to define them in neutrino interaction simulations are given in section 4.5.7.

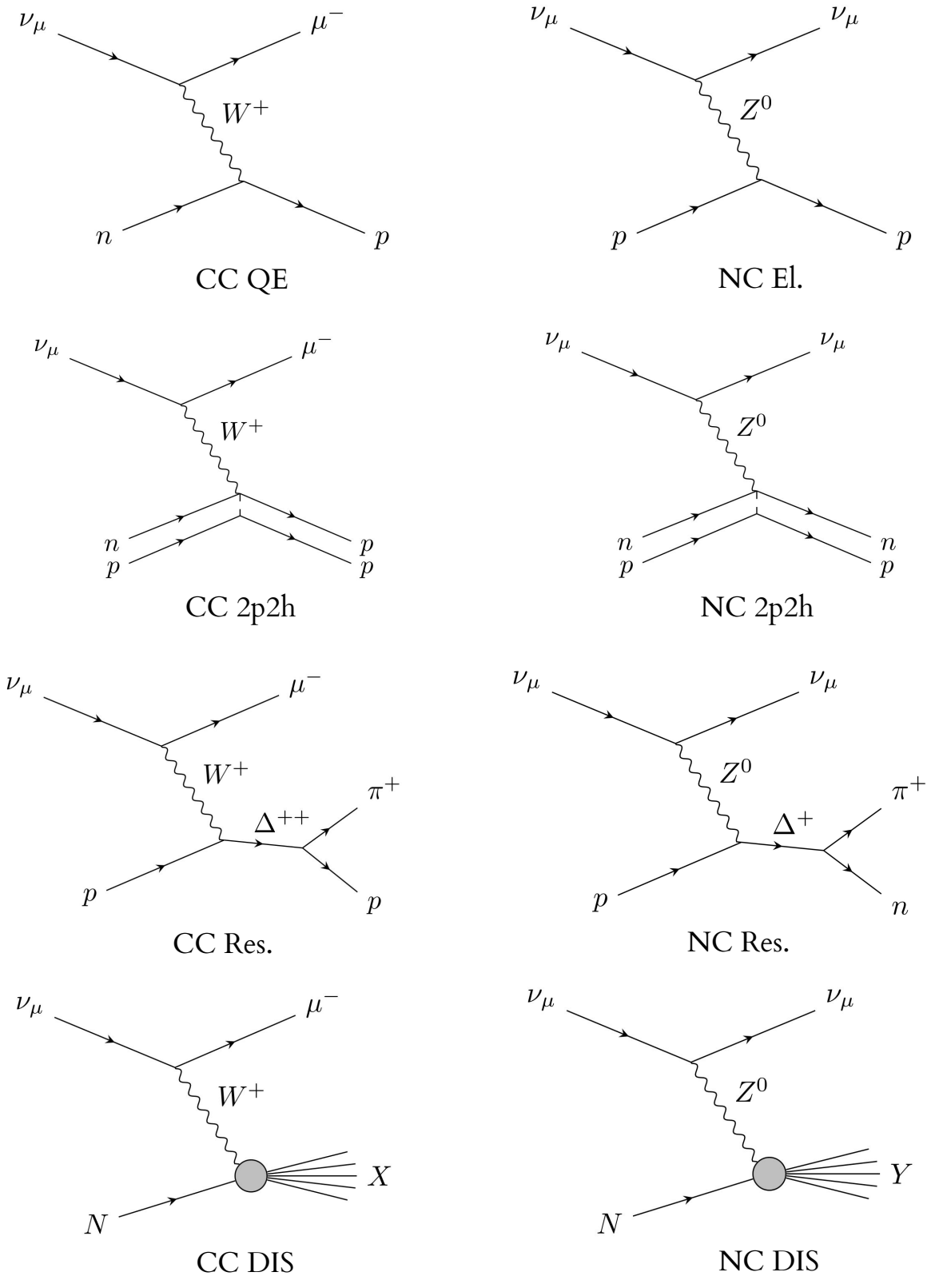

Figure 4.1.: Schematic and Feynman diagrams to demonstrate examples of the dominant neutrino scattering modes in the few-GeV energy range.

4.1.1. Elastic and Quasi-Elastic processes

CC QE is the most simple and abundant scattering process in the few-GeV energy range. The dominant forms of this process occur when a neutrino scatters off a neutron to produce a muon and proton in the final state, or an anti-neutrino scatters off a proton to produce an anti-muon and a neutron in the final state,

$$\nu_\mu + n \longrightarrow \mu^- + p \tag{4.1}$$
$$\bar{\nu}_\mu + p \longrightarrow \mu^+ + n. \tag{4.2}$$

The neutral current elastic scattering (NC El) process involves a neutrino scattering off the nucleon it comes into contact with and the initial products of the reaction remain intact,

$$\nu_\mu + p \longrightarrow \nu_\mu + p. \tag{4.3}$$

4.1.2. Multi-nucleon emission, npnh

The n-particle n-hole (npnh) process is conceptually similar to CC QE, with the added complexity that instead of the neutrino interacting with a single nucleon quasi-elastically in the initial interaction, it interacts with one or more inside the nucleus if they are bound,

$$\nu_\mu + (n + p) \longrightarrow \mu^- + (p + p). \tag{4.4}$$

This process is possible because of the existence of short-range correlations in heavy nuclei, an example of which involves the exchange of a virtual meson between nucleons in a two-body meson exchange current (MEC). Experimental evidence has shown that this can also result in 1p1h final states when one of the bound nucleons is not excited above the Fermi momentum. The 1p1h final state consequently mimics that of true CC QE interactions [151]. Further information on the nuclear effects which impact the neutrino-nucleon scattering models will be discussed in section 4.5.5.

4.1.3. Pion production

The two dominant pion production mechanisms occur through resonant (Res) and coherent (Coh) neutrino scattering. In resonant pion production, when the neutrino interacts with the nucleon, it produces an excited state of a heavy intermediate baryon, for instance Δ^{++}, which quickly decays to another particle, most likely a charged pion, and the relevant nucleon. The resonant particle itself decays too quickly to be visible experimentally, however the decay products can be observed and used to determine its existence. Examples of charged and neutral current resonant scattering include,

$$\nu_\mu + p \xrightarrow{\Delta^{++}} \mu^- + \pi^+ + p \tag{4.5}$$

$$\nu_\mu + p \xrightarrow{\Delta^{+}} \nu_\mu + \pi^+ + n. \tag{4.6}$$

Coherent scattering occurs when the momentum transferred in the interaction is low. In this case, the neutrino interacts with the entire nucleus, rather than the nucleons within it. Many final state particles may be produced following a coherent scattering interaction, including πs, ρ mesons and photons. As a result, coherent scattering contributes to the pion-content of the final state, in which the outgoing pion is generally more forward-going than the one produced in the resonant interaction, due to the increased mass of the interacting body. One example of a charged-current coherent pion-production process is,

$$\nu_\mu + N \longrightarrow \mu^- + \pi^+ + N'. \tag{4.7}$$

4.1.4. Deep inelastic scattering

Rather than interacting with a nucleon or the entire nucleus, in a Deep Inelastic Scattering (DIS) process the neutrino has enough energy to interact with an individual quark constituent of the nucleon it comes into contact with. As a result, the nucleon breaks apart entirely and a shower of hadrons is emitted from the point of interaction in a process called hadronization. This shower can include multiplicities of baryons and mesons and can therefore be an additional source of both single and multiple pion production.

Figure 4.2 shows that DIS is only likely to occur if the neutrino interacts with an energy above at least a few-GeV. Examples of charged and neutral current deep inelastic scattering include,

$$\nu_\mu + N \longrightarrow \mu^- + X \tag{4.8}$$

$$\nu_\mu + N \longrightarrow \nu_\mu + Y, \tag{4.9}$$

where N is the hadronized nucleon and X and Y are the charged and neutral-current-induced hadron showers respectively.

4.2. LArTPC simulation and analysis software

Across all liquid argon experiments, including those in the SBN program, the dedicated software package, LArSoft, is used as a wrapper for the full simulation of neutrino interactions, as well as the analysis of the simulated events. Each detector is defined as a configurable geometry allowing for detector-independent development at every stage of event processing. This also allows for external frameworks to be 'plugged-in' in order to perform part of the simulation in the context of the liquid argon experiment [152].

The first step in the procedure is the neutrino flux simulation. This is modelled using a combination of well-validated theory and data using a GEANT4-based simulation [153] for the BNB, and has been under development by the MiniBooNE collaboration for many years, this will be discussed in section 4.3 followed by a summary of the relevant systematic parameters in section 4.4.

The neutrinos produced in the flux simulation are then propagated to the relevant detector and their interactions are simulated using a number of different models in the GENIE interaction generator [150] [154]. Some models are constructed using entirely theoretical predictions of neutrino interaction cross-sections, while others have been tuned using tens of existing neutrino interaction datasets. Simulating neutrino interactions in LArTPCs and their corresponding systematic parameters will be discussed in section 4.5 and 4.6 respectively.

The particles produced in the interaction are then propagated through the liquid argon using another GEANT4-based simulation [153], this will be discussed in section 4.7.

Upon reaching the anode wire planes of the detector, the charge depositions are read-out as waveforms and converted to a computationally-readable format along with any detector noise. This detector simulation and signal processing will be discussed in section 4.8 along with possible contributions to the detector systematic parameter set in section 4.9.

The 2D `Hits`, discussed in section 3.2.2.2, are fed into the Pandora pattern-recognition software which attempts to reconstruct the final-state particles for use in all physics analyses [155], this will be discussed in section 4.10.

In addition to the reconstruction of neutrino interactions using the charge depositions on the wire planes, each LArTPC in the SBN program has a photon detection system, PDS, which processes the scintillation light produced in the neutrino interaction. Using the PDS in reconstructing and analysing neutrino interaction events will be discussed briefly in section 4.11.1. Similarly, cosmic removal software is used alongside dedicated hardware to mitigate the external backgrounds to neutrino interaction events, this will be discussed briefly in section 4.11.2. Both the PDS and cosmic removal software tools are currently under development in the SBN near and far detectors, therefore neither were utilised in the analyses discussed in this thesis.

Finally, example event displays from various reconstructed ν_μ CC final states in the SBND detector are shown in section 4.12.

4.3. BNB flux simulation

This section will comprise a brief summary of the neutrino flux simulation based on the in-depth description as published by MiniBooNE [120]. The flux simulation begins with the construction of a detailed beamline geometry definition, including the materials encountered by the particles as they traverse the following components of the BNB,

- The final 50 m of the Booster beamline
- The target hall which houses the target, horn and secondary beam collimator
- The 50 m decay pipe,

as discussed physically in section 3.1.

Following the definition of the BNB geometry, the protons produced by the Linac are simulated. Within each bunch, the protons are uncorrelated and can therefore be simu-

lated individually, this is done 1 cm upstream of the Beryllium target. Modelling these interactions in the target geometry is done using a combination of existing GEANT4 models and those tuned to external data to describe the elastic and quasi-elastic scattering interactions respectively.

The secondary particles produced in the proton-Beryllium interactions are configured as a diverging beam. The subsequent propagation of the scattered primary protons and secondary proton-Beryllium interaction products are simulated using GEANT4 throughout each medium encountered along the beamline. This propagation considers the kinematic development of the particles and any potential interactions or decays which may alter the contents of the beam at any given location.

Characterising the beam of neutrinos reaching each detector in the SBN program consequently depends on the cross-section of each proton-Beryllium interaction along with the lifetime, decay modes, branching ratios and kinematic development of the scattered protons and secondary particles. These features therefore dictate the rate and shape of the neutrino flavour profiles shown in Figure 3.4.

4.4. Flux systematic parameters

The flux systematic parameter set is separated into three categories, the hadronic cross-section parameters, the optical flux parameters and the hadronic neutrino production parameters. This section will define the main contributions to each set and is mostly informed by this paper [120], where much more detail can be found.

4.4.1. Hadronic cross-section and optical parameters

The flux parameters involving the interaction cross-section of hadrons in the Beryllium target and Aluminium horn are categorised based on three broad interaction types. The distinction is made between those affecting the total cross-section, σ_{TOT}, the inelastic cross-section, σ_{INEL}, and the quasi-elastic cross-section, σ_{QE}, which is a subset of the inelastic interactions concerning elastic-like collisions similar to those between hadrons and free nucleons.

The split largely stems from the availability of σ_{TOT} and inelastic data sets, along with the omission of a distinct σ_{EL} parameter due to the lack of data in the relevant kinematic

region for interactions within the BNB. The elastic cross-section can instead be inferred from σ_{TOT} and σ_{INEL} by the relation $\sigma_{TOT} = \sigma_{INEL} + \sigma_{EL}$.

The σ_{TOT} cross-section is modelled and compared to n-Be interaction data at similar energies to the BNB. The agreement is sufficient to extend the use of the model to p-Be and $\pi^{\pm}$-Be interactions. The variation between model and data gives the prior systematic uncertainty on the total cross-section.

The global inelastic cross-section data set is much more abundant at the BNB energies, therefore σ_{INEL} for nucleons and pion interactions on both Beryllium and Aluminium can be inferred directly from data, without any need for a comparison with theory. In contrast, the subset of quasi-elastic data is sparse, therefore theoretical models are once again employed to help parametrise the cross-section between nucleons, pions and the target materials.

Variations performed to simulate these parameters take into consideration their relations in the following way:

- While σ_{TOT} is varied, σ_{INEL} is held constant to allow only σ_{EL} to change
- While σ_{INEL} is varied, σ_{EL} is allowed to float within a fixed σ_{TOT}
- The total σ_{INEL} also remains unchanged whilst σ_{QE} is varied, such that only other inelastic processes are allowed to float.

4.4.2. Optical flux parameters

The horn current and skin effect quantify the strength of the magnetic field in the horn and the magnitude of the field's permeation into the surrounding conducting cylinder respectively. Varying the horn current impacts the focussing properties of the horn and therefore the shape of the neutrino flux. The skin effect can induce a variation in the magnitude of the magnetic field following the permeation of the current into the material surrounding the horn.

4.4.3. Hadronic neutrino production flux parameters

Neutrinos observed in the SBN experiments are primarily produced through the decay of hadronic particles exiting the Beryllium target of the BNB. The differential cross-section of each of these particles are parametrised separately through fits to experimental p-Be cross-section data.

This section will serve as a brief summary of the extremely detailed explanation given in [120] and will primarily focus on charged pions since π^+ decay is by far the dominant neutrino production mechanism in the BNB.

1. $\pi^{\pm}$: The Sanford and Wang (SW) parametrisation of the differential cross-section as a function of meson kinematics, p, θ, and incident proton momentum, p_B, is used to describe charged pion production using equation 4.10,

$$\frac{d^2\sigma}{dpd\theta} = c_1 p^{c_2} \left(1 - \frac{p}{p_B - c_9}\right) \exp\left(-c_3 \frac{p^{c_4}}{p_B^{c_5}} - c_6\theta(p - p_B c_7 cos^{c_8}\theta)\right), \tag{4.10}$$

   where $c_{\{1..9\}}$ are determined through fits to the HARP p-Be data at 8.89 GeV/c. It is these 9 correlated parameters which are varied within their uncertainty in the simulation of the charged pion systematic parameters

2. K^+: There is insufficient data for K^+ production following proton-Beryllium interactions at 8.89 GeV/c to apply the SW differential cross-section parametrisation. Instead, Feynman scaling is utilised to translate measurements made at different proton energies to those relevant for SBN

3. K_L^0: The long lifetime and the fact that neutral kaons cannot be focused contribute to the reduced rate of neutrino production from their decay. Forward going data ($< 5°$) from a number of experiments is therefore used in fits to constrain the SW parametrisation

4. K^-: Contrary to the methods of parametrising the other hadronic production mechanisms, a Monte Carlo simulation of p-Be interactions is produced using GEANT4 to determine the K^- differential cross-section. This is once again a method of combating the scarcity of available K^- production data from p-Be interactions at energies relevant to SBN.

4.5. Neutrino interaction simulation

A critical component of making almost any neutrino physics measurement is in the understanding of their interactions with the detector medium. Neutrino experiments have been conducted on both low-Z nuclei in which nucleons are effectively free, and high-Z nuclei in which the nucleons may be bound, each of which require independent modelling, simulation and detector propagation.

The main challenge in experimental neutrino physics stems from the fact that the theory which underpins neutrino interactions on free nucleons falls apart when applied to neutrino interactions with heavy, bound nuclei. This section will outline the current method for modelling neutrino interactions with bound, heavy nuclei.

4.5.1. Neutrino interaction cross-sections

Across all experimental particle physics, event rate measurements are made by characterising and counting the particles we observe following the occurrence of an interaction in the detector material. Certain features of the observables produced in an interaction may be uniquely representative of a particular process. Filtering on these features, for instance by setting an minimum energy or maximum scattering angle threshold on the observable particles, allows an experiment to consciously make measurements of each process separately.

The kinematic filters to apply when searching for each process are defined using the known energy, baseline and material of a detector, along with measurements made by previous experiments to constrain the theoretical nature of the interactions. The probable rate, or cross-section, of a particular interaction occurring can therefore be quantified and predicted using a combination of theoretical modelling and supporting experimental data [156].

The total cross section of a collision defines the overall probability the collision will occur. In an interaction involving a beam of N_{beam} particles traversing an area, A, the total cross-section can be very simply defined as,

$$\sigma_{tot} = \frac{N_{int}}{\Phi \cdot T}, \tag{4.11}$$

where N_{int} is the number of interactions which take place, Φ is the integrated flux of the neutrinos in the detector over a certain exposure, T are the number of target particles and σ_{tot} is therefore measured in units of area.

In an experimental setting, it is often useful to present the cross-section in terms of the distribution of a kinematic variable. This is achieved by instead defining the differential cross-section in the parameter of interest. For example,

$$\frac{d\sigma}{dX} = \frac{N(X)}{\Phi \cdot T}, \tag{4.12}$$

where in this case $N(X)$ is the number of particles scattered as a function of the parameter of interest, X, and integrating over the full phase-space of X gives the total cross-section.

4.5.2. Global neutrino interaction cross-section data

Cross-section measurements have been a primary focus of neutrino physics experiments for decades and comprise a range of measurements from neutrino interactions on free nucleons to those on bound and heavy nuclei. The effort to compile a global dataset of free nucleon cross-sections was kick-started by bubble chamber experiments in the 1970's. A summary of some existing neutrino scattering cross section data broken down into the underlying interaction modes, discussed in section 4.1, is shown in Figure 4.2 [157].

In recent years, an updated understanding neutrino fluxes has driven experiments to revisit these cross-section measurements to refine the results. The global dataset is rapidly and continuously growing and Figure 4.3 includes recent (2019) charged-current neutrino and anti-neutrino scattering data from experiments such as T2K, Minerva, ArgoNEUT and MicroBooNE [123]. Since the data shown in Figure 4.2 was presented in 2012, the global dataset has significantly increased in the few-GeV energy region, however it is clear from Figure 4.3 that there is still room for improvement when it comes to the precision of the measurements made below 10 GeV.

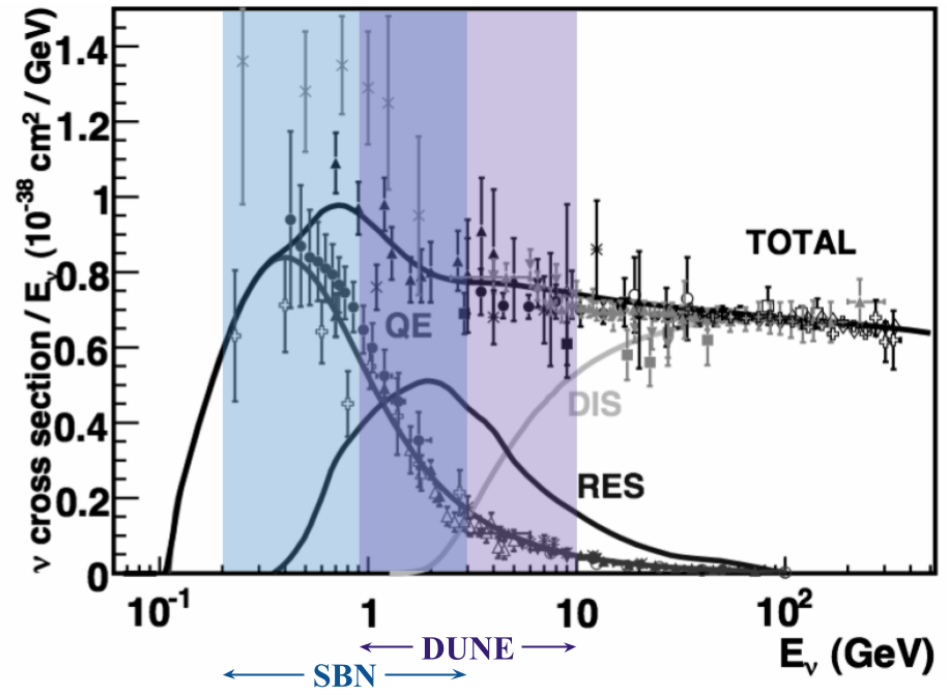

(a) Global charged-current neutrino scattering cross section data.

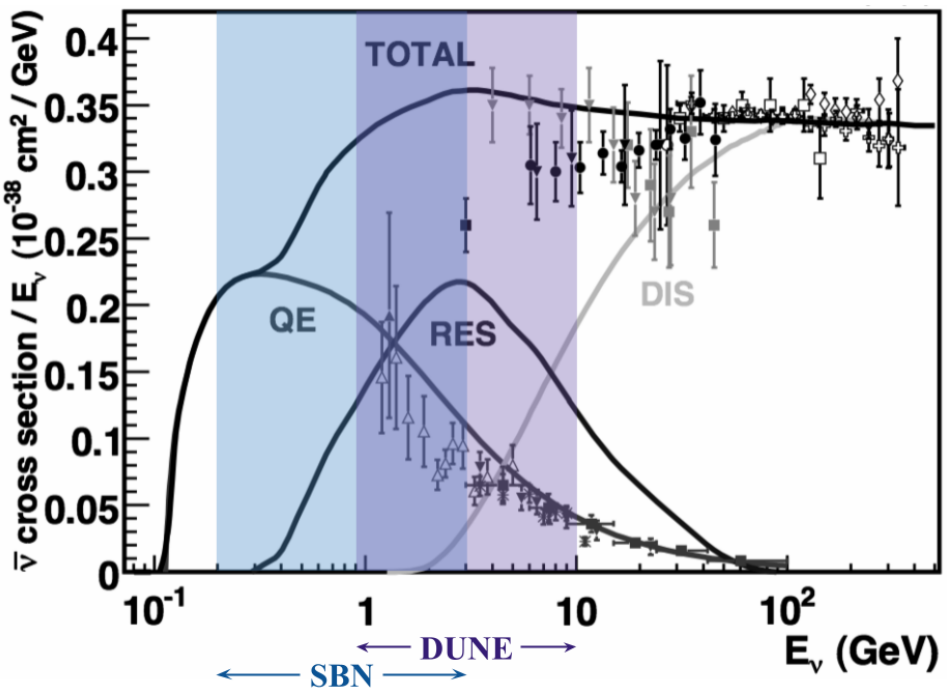

(b) Global charged-current anti-neutrino scattering cross section data.

Figure 4.2.: Existing muon neutrino (a) and anti-neutrino (b) charged-current cross section data and predictions as a function of neutrino energy which includes the region covered by short baseline neutrino experiments. The total cross-section for charged current events is included, as well as a breakdown of interaction-specific data and predictions for QE, RES and DIS interactions [157]. Note the absence of 2p2h (np-nh) data. The regions of interest to SBN and DUNE are highlighted.

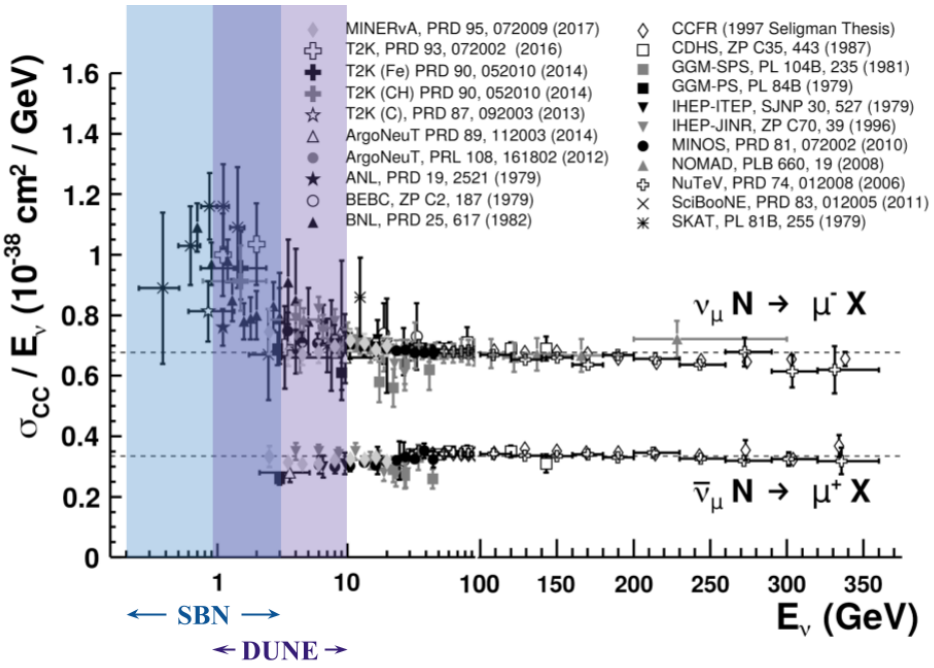

Figure 4.3.: Neutrino and anti-neutrino inclusive charged-current scattering data taken between 1979 and 2019. The neutrino and anti-neutrino data is superimposed and demonstrates the approximate factor of two difference between these cross-sections across almost all energies [123]. The regions of interest for SBN and DUNE are highlighted.

4.5.3. Neutrino event generation

The GENIE interaction generator determines which of the neutrinos present in the flux and entering a given detector's geometry interact, and how that interaction is characterised. This section will outline the basic operating principles of GENIE, along with a breakdown of the models featured in the analyses presented throughout this thesis [150] [154].

GENIE is a multi-purpose tool, primarily built for the Monte Carlo (MC) generation of neutrino interactions with varying nuclear structures spanning energies from 1 MeV to 1 PeV. A tool was recently developed by GENIE which combines existing theoretical models with external neutrino scattering data in global fits to construct model configurations for use in the MC simulation of neutrino events. The tool includes the ability to tune parameters within an existing model, as well as the ability to combine different versions of the individual models within a configuration based on leading theoretical and experimental developments.

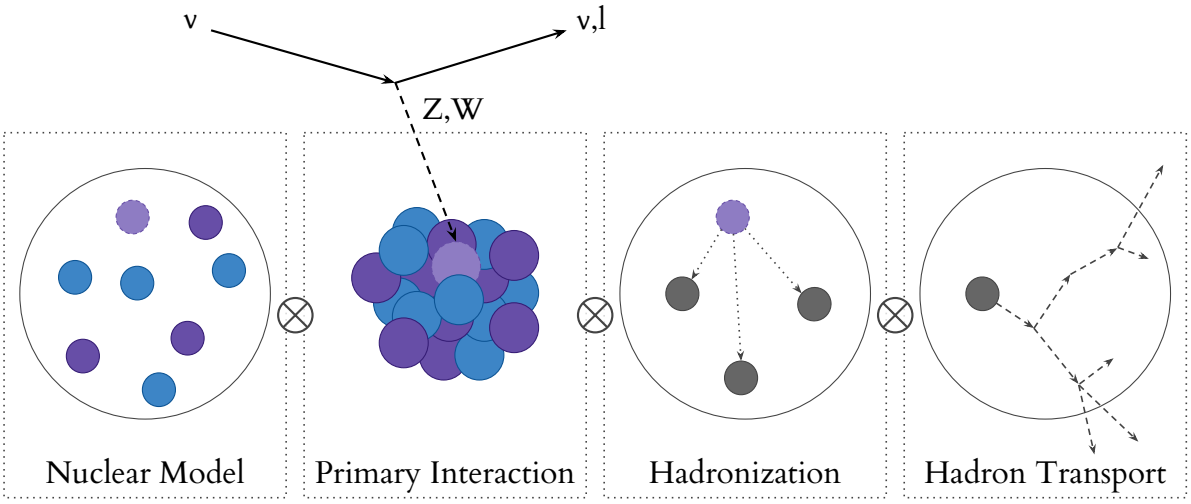

Figure 4.4.: A cartoon depicting one possible formulation of the neutrino interaction simulation layers as they may be implemented in the GENIE neutrino event generator. In this case, the nuclear, interaction, hadronization and hadron transport models are defined separately in the simulation of neutrino interactions. This is not the only possible configuration used by the generator.

Within GENIE, neutrino interactions are simulated using a combination of nuclear physics, cross-section, hadronization and hadron transport models according to how theoretical models define the available phase space. Figure 4.4 depicts one possible example of how these simulation 'layers' may be implemented in the generator as a cartoon. The construction of the relevant model configurations for neutrino interactions at the SBN program are discussed in the following sections.

4.5.4. Model configurations

Neutrino interactions generated using multiple GENIE model configurations contributed to the analyses presented in this thesis. Included are the historical GENIE v2 'Default+MEC'[1] model and from version 3 the configuration which fit best to MicroBooNE neutrino scattering data [158] defined according to the GENIE naming convention, G18_10a_02_11a [150]. Finally, variations of the CC QE+2p2h model components are substituted into the configuration from GENIE v3, including,

[1]Note that MEC and 2p2h may be used interchangeably throughout this explanation, this is simply to reference names as they are/were defined in each situation. However 2p2h is the more-correct definition of the scattering mode itself.

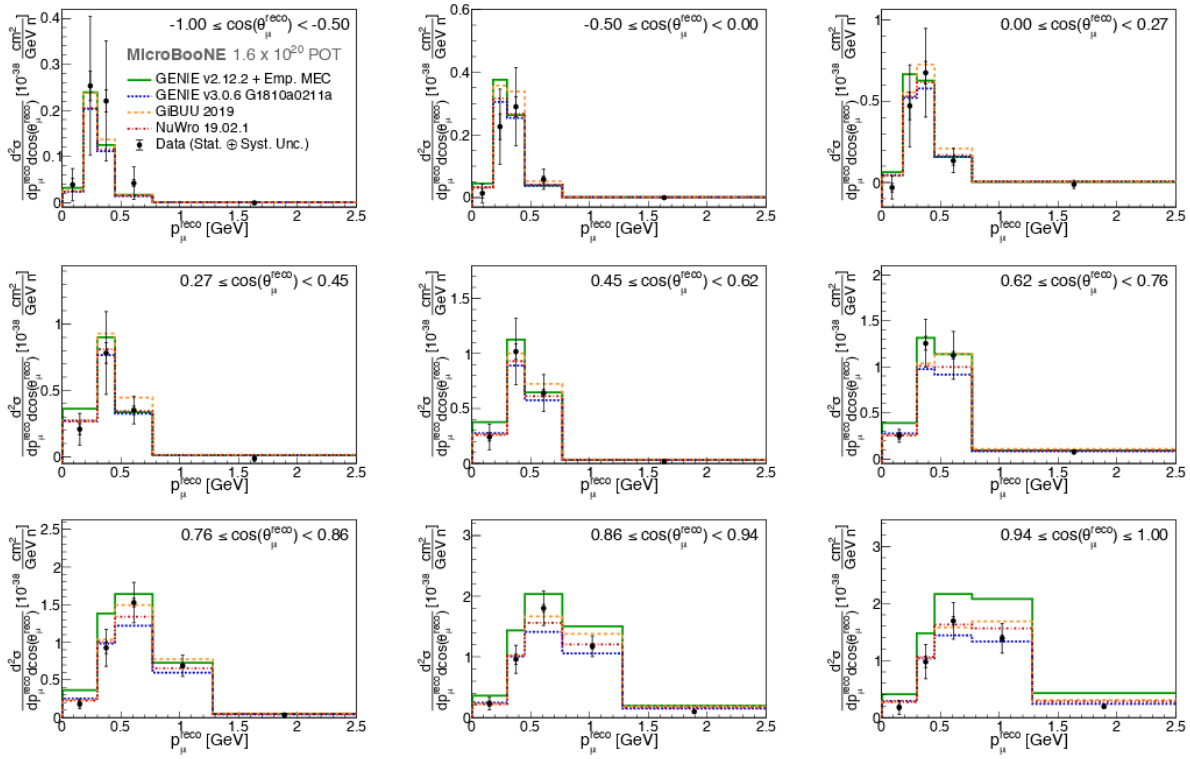

Figure 4.5.: ν_μ CC Inclusive double-differential cross-section MicroBooNE data and multiple model configurations. The data (black dots and error bars) is presented as a function of reconstructed muon momentum in discrete muon scattering angle bins with both statistical and systematic uncertainties. The blue line shows the MicroBooNE-selected new GENIE model whilst the green line shows the historical default+MEC GENIE model [158].

- **Llewellyn Smith + Empirical 2p2h, LS-E**: Default CC QE+2p2h model from GENIE v2 [159].
- **Nieves**: Also known as the 'Valencia' model. The CC QE+2p2h model used in the G18_10a_02_11a configuration [160]
- **SuSAv2**: 'Super-Scaling Approach version 2' [161]
- **Smith-Moniz**: QE(Running M_A), no CC 2p2h [162].

A summary of the contents of these model configurations are shown in Table 4.1 followed by a short description of each element of the table in the following sections. Bold elements of the table highlight components of the configuration which have been switched out from the previous model (when reading from left to right). A comparison of the GENIE v2 Default+MEC and GENIE v3 G18_10a_02_11a model configurations is shown with the MicroBooNE ν_μ CC Inclusive cross-section measurement in Figure 4.5 [158].

	GENIE Model Configuration				
Configuration component	'Default+MEC' v02.12.10	LS-E v03.00.06	G18_10a_02_11a v03.00.06	SuSAv2 v03.02.00	Smith-Moniz v03.02.00
Nuclear	RFG, Bodek-Ritchie [163]	**LFG** [164]	LFG	LFG	LFG
CC QE	Llewellyn Smith [159]	Llewellyn Smith	**Nieves** [160]	**SuSAv2** [161]	**Smith-Moniz** [162]
NC El	Ahrens [165]	Ahrens	Ahrens	Ahrens	Ahrens
CC 2p2h	Empirical [8]	Empirical	**Nieves**	**SuSAv2**	**N/A**
NC 2p2h	Empirical	Empirical	Empirical	Empirical	Empirical
Resonant, π, γ	Rein-Sehgal [166]	**Berger-Sehgal** [167]	Berger-Sehgal	Berger-Sehgal	Berger-Sehgal
Coherent, π	Rein-Sehgal [168]	**Berger-Sehgal** [169]	Berger-Sehgal	Berger-Sehgal	Berger-Sehgal
DIS	Bodek-Yang [170]	Bodek-Yang	Bodek-Yang	Bodek-Yang	Bodek-Yang
Hadronization	AGKY [154]	AGKY	AGKY	AGKY	AGKY
FSI	*hA* [154]	***hA*, 2018**	*hA*, 2018	*hA*, 2018	*hA* 2018

Table 4.1.: A summary of the model configuration components used in the analyses presented in this thesis. The left-most column breaks down the model which may be 'plugged in' to construct the configuration. Included (from left-to-right) are the historical GENIE v2 Default configuration with an empirical form of the 2p2h interaction, the model configuration which best-describes MicroBooNE neutrino scattering data, G18_10a_02_11a [150] [171], with the historical CC QE+2p2h model plugged in, and three variants of this configuration, each substituted with different CC QE+2p2h models. Note that the Smith-Moniz configuration employs the 'Running-M_A' CC QE model and consequently doesn't include a CC 2p2h component. The elements in **bold** indicate models which have been replaced with respect to the configuration to its left.

4.5.5. Nuclear effects

In most experimental contexts, the struck nucleon resides inside a nucleus and therefore cannot be modelled as a free particle. In these cases, especially when the struck nucleus is large, so-called 'nuclear effects' are introduced into the system and must be accounted for when modelling neutrino interactions.

This section will outline the dominant nuclear effects which occur in neutrino interactions with heavy nuclei, along with consequences such as the manifestation of the 2p2h scattering process. A dedicated subsection to the most complicated effect: final state interactions (FSI) will be given in section 4.5.9.

- **Fermi motion**

  In the Fermi gas model of the nucleus, nucleons are subject to the Pauli exclusion principle as they are fermions, or spin-1/2 particles. The Pauli exclusion principle states that a maximum of two fermions with opposite spins may reside in a single energy level within a nucleus. As a result, nucleons may reside in energy levels in which they have $\vec{\mathrm{p}} > 0$ momentum, even at $T = 0K$. This is known as the 'Fermi motion' of the nucleons, where the maximum-occupied energy level in a $T = 0K$ system is called the 'Fermi momentum', p_F, of the nucleus and all possible states are fully-occupied up to the maximum thereby defining the p_F state as the ground state of the nucleus.

- **Pauli blocking**

  Since all possible states are fully-occupied up to the maximum, p_F, in a Fermi gas, the possible states an excited nucleon may occupy following an interaction are limited to those with $p > p_F$. This is known as Pauli blocking, and the impact is to reduce the interaction cross-section [172].

- **Binding energy**

  The mass of a nucleus is always less than the sum of its parts. This 'mass defect' is caused by the requirement that energy must be 'spent' in order to construct the nucleus, whose components are bound by the strong force. Consequently, in order to release a particle from the nucleus, there exists a minimum energy requirement in order to release a particle from a nucleus. This energy is known as the binding energy (BE) and is equivalent to the mass-difference between the nucleus and the sum of its parts [172].

- **Coulomb corrections**

  Neutrino interactions with protons and neutrons behave differently when those nucleons are bound in a heavy nucleus. Since protons are charged, a distortion of its potential due to the Coulomb field of the nucleus results in an decrease in the depth of the proton potential with respect to that of the neutron. This occurs in order to maintain the same Fermi energy level between the proton and neutron potential wells in stable nuclei, therefore there must also be a higher number of neutrons than protons in heavy nuclei [172].

- **Nucleon-nucleon correlations**

  The simplest way of modelling a many-body system like a nucleus is to assume the nucleons are independent of one another. In this formulation, the weak current is constructed from the sum of the individual nucleon currents. Nowadays, this is insufficient due to the precision requirements of neutrino interaction measurements, therefore correlations between the nucleons occur and must be accounted for. In the heavy nuclear system, short range correlations, SRCs, involve the exchange of heavy mesons, such as ρ. Long range correlations, LRCs, instead involve the exchange of pions [172].

  One of the many possible consequences of this formulation is for an interaction to take place on the meson involved in the exchange, known as a two-body current, which is effectively the same as saying the interaction takes place on both of the bound nucleons. If the momentum transfer in such an interaction is sufficient to eject both nucleons from the nucleus, a 2p2h final state is observed. Another possibility is that the momentum transferred to one of the nucleons in the bound-state is not sufficient to excite it above the Fermi momentum. In this case, the 1p1h final state is observed which appears identical to that of a QE interaction, such that it constitutes a background in QE cross-section measurements [151].

4.5.6. Nuclear physics model

The nuclear physics model defines the initial state of the nucleon(s) involved in the neutrino interaction, parametrised by the momentum and binding energy of the struck nucleon(s). The Bodek-Ritchie Relativistic Fermi Gas (RFG) model can be used for all initial nuclear state modelling in GENIE, regardless of the peak neutrino energy or the detector medium of the experiment, as the parametrisation of this model allows

for the relevant kinematics and nuclear structure to be incorporated [163] [173]. The binding energy is assumed to be constant for all nucleons. Additional considerations are introduced depending on the kinematics of the interaction, for instance in the few-GeV energy range it is possible to apply the impulse approximation to the system, wherein the interactions take place on individual nucleons and those cross-sections are combined incoherently [164].

An alternative nuclear physics model used in GENIE is the Local Fermi Gas (LFG) model. The LFG differs from the RFG in its depiction of the Fermi momentum as a function of the nucleon's position in the nucleus rather than a constant allowing for more realistic nucleon momentum definitions [164]. Although the LFG better-characterises the internal behaviour of the nucleus, neither this nor the RFG model alone account for nucleon-nucleon interactions inside the medium. This has been shown in electron scattering data to have an observable impact on the initial distribution of nucleon momenta [174].

When an interaction takes place, nucleon-nucleon interactions such as short range correlations (SRC) can be accounted for by applying suppression factors to the system. For instance, in the Bodek-Ritchie extension to the RFG model, the nucleon produced in an interaction is required to exceed the Fermi momentum in order to be propagated in the simulation. In GENIE, the Fermi momentum, p_F, for protons in the argon nucleus is $p_F = 242$ MeV and $p_F = 259$ MeV for neutrons [150] [164] [173].

4.5.7. Neutrino interaction cross-section models

Neutrino interaction events, examples of which were given in section 4.1, are generated according to the distribution of various differential cross-sections. First, the integrated cross-section and flux from the beam are combined to determine the energy of the neutrino interaction which will take place in a detector. Second, having determined the neutrino kinematics, differential cross-sections for individual processes are then used to determine which interaction took place. The cross-sections for each process are combined in the generator to construct the integrated cross-section model as per,

$$\sigma^{tot} = \sigma^{QEL} \oplus \sigma^{MEC} \oplus \sigma^{RES} \oplus \sigma^{DIS} \oplus \dots \tag{4.13}$$

where σ^X refers to the integrated cross section for the process X [150] [154].

This section will define the differential cross-section models which were used in the construction of σ_{TOT} and simulation of the neutrino interaction processes outlined in section 4.1.

4.5.7.1. Elastic and Quasi-Elastic processes

- **Llewellyn Smith**

  The differential cross-section for the charged-current quasi-elastic process on free nucleons used in all GENIE configurations is defined by the Llewellyn Smith model. Since protons and neutrons are not elementary particles, the differential cross-section depends on form factors [2], which collectively define the weak charge distribution inside a nucleon,

$$\frac{d\sigma}{d|q^2|}\begin{pmatrix}\nu n\to l^- p\\ \bar{\nu}p\to l^+ n\end{pmatrix} = \frac{M^2 G_F^2 \cos^2\theta_c}{8\pi E_\nu^2}\left[A(q^2) \mp B(q^2)\frac{(s-u)}{M^2} + C(q^2)\frac{(s-u)^2}{M^4}\right], \quad (4.14)$$

  in which M is the stuck-nucleon mass, G_F defines the strength of the interaction and is known as the Fermi coupling constant, θ_c is the Cabibbo angle and E_ν the neutrino energy. The Lorentz-invariant Mandelstam variables s, u encode the kinematics of the interaction and in this case, $(s-u) = 4ME_\nu + q^2 - m^2$ where q^2 is the momentum transfer and m is the outgoing lepton mass.

  Finally, $A(q^2), B(q^2)$ and $C(q^2)$ are combinations of a number of form factors including, $F_A, F_V^{1,2}, F_P$ which are all functions of the momentum transfer. The subscript V corresponds to vector form factors, A axial form factors and P a pseudo-scalar form factor. $F_V^{1,2}$, are electromagnetic form factors and have been constrained by electron scattering experiments [175]. F_P is difficult to detect and is therefore defined using a model [159]. The remaining axial form factor, F_A, is usually parametrised as a dipole,

$$F_A(q^2) = g_A\left(1 + \frac{q^2}{M_A}\right), \quad (4.15)$$

$$(4.16)$$

[2] A form factor is simply the Fourier transform of a charge density.

where g_A is the axial coupling constant and M_A is the axial mass, which can only be measured in neutrino scattering experiments [159].

Given the relatively small neutrino-nuclear global dataset and wide range of energies across the experimental neutrino picture, there is some tension in the measurement of M_A. Consequently, current and future neutrino experiments are aiming to constrain M_A, since minimising the uncertainty is critical in precision measurements such as the ones which will be made by SBN [176].

- **Smith-Moniz**

  The approach to modelling QE interactions on heavy nuclei taken by Smith & Moniz is somewhat different to the others studied here. Instead of setting M_A to be a constant with an inherently large uncertainty in the axial form factor, F_A, M_A is allowed to vary as a function of neutrino energy as per,

$$M_A^{Run} = M_A^0 \left(1 + \frac{E_0}{E_\nu}\right). \tag{4.17}$$

  Here, $M_A^0 = 1.006 \pm 0.025$ GeV and the scale factor $E_0 = 0.334^{+0.058}_{-0.054}$ GeV, as measured by NOνA [177], such that $M_A^{Run} \to M_A^0$ when $E_\nu \to \infty$ [162].

- **Ahrens**

  The neutral current elastic scattering model used in all GENIE configurations was written by Ahrens. The axial form factor in this model is defined by,

$$G_A(q^2) = \frac{1}{2} \frac{g_A}{\left(1 + \frac{q^2}{M_A^2}\right)^2} (1 + \eta), \tag{4.18}$$

  where η is a way of parametrising additional isoscalar contributions to the axial form factor in a single parameter and can be calculated by fitting to data [154] [165].

4.5.7.2. Multi-nucleon emission, npnh

- **GENIE Empirical MEC**

  GENIE developed their own MEC model when the need for one was first made clear. This involves three components each modelled independently. First, the Dytman model [8] is used to define the leptonic differential cross-section along with the momentum transfer. This is followed by the hadronic model, which defines the

contributions and kinematics of interacting nucleons, and is the part which becomes tricky in a multinucleon system. In GENIE, a 'nucleon cluster' model was developed which uses the momentum transfer from the leptonic model to define: which nucleons interact in the 'cluster', the kinematics of the cluster, the nuclear recoil kinematics and the outgoing nucleon kinematics. Finally, the hA FSI model [150] is implemented in the same way as for other processes to determine which particles leave the nucleus. This will be discussed in section 4.5.9 [8]. The empirical model is implemented with an intensity proportional to the QE interaction, and enhances the integrated neutrino interaction cross-section.

A schematic diagram of the components of the GENIE 2p2h model is shown in Figure 4.6 [8]. This model is also used in the G18_10a_02_11a configuration for NC multinucleon processes as the Nieves model is only defined for CC interactions.

- **Nieves (a.k.a Valencia) model**

  Rather than defining the 2p2h process separately to QE, expanding the CC QE model with a correction for such exchange currents better-describes interactions between neutrinos and heavier nuclei in general. The same model can then be used to describe neutrinos interacting with any number of nucleons at once, and QE interactions are absorbed into the 1p1h component of the model [160] [178]. The 1p1h+2p2h components of this model are used in the Nieves, G18_10a_02_11a configuration [160].

- **Super-Scaling Approach v2, SuSAv2**

  The SuSAv2 approach to modelling np-nh interactions is somewhat similar to that of the Valencia model, in that they are both based upon the same LFG initial state model, though their implementations involve a number of technical differences which will not all be discussed in detail but can be found here [161] [179].

  The main differences generally involve using fewer approximations than the Valencia model and result in larger energy and momentum phase-space coverage, see Figure 4.7, and a higher predicted rate of np-nh interactions, especially at higher neutrino energies, see Figure 4.8 [179].

  Another major consequence of the differences, which will impact our ability to precisely measure the reconstructed neutrino energy, impacts the relative rate of bound-nn and bound-np contributions to the interaction. Figure 4.9 depicts the shape and rate differences between the np and nn contributions to the 2p2h double-

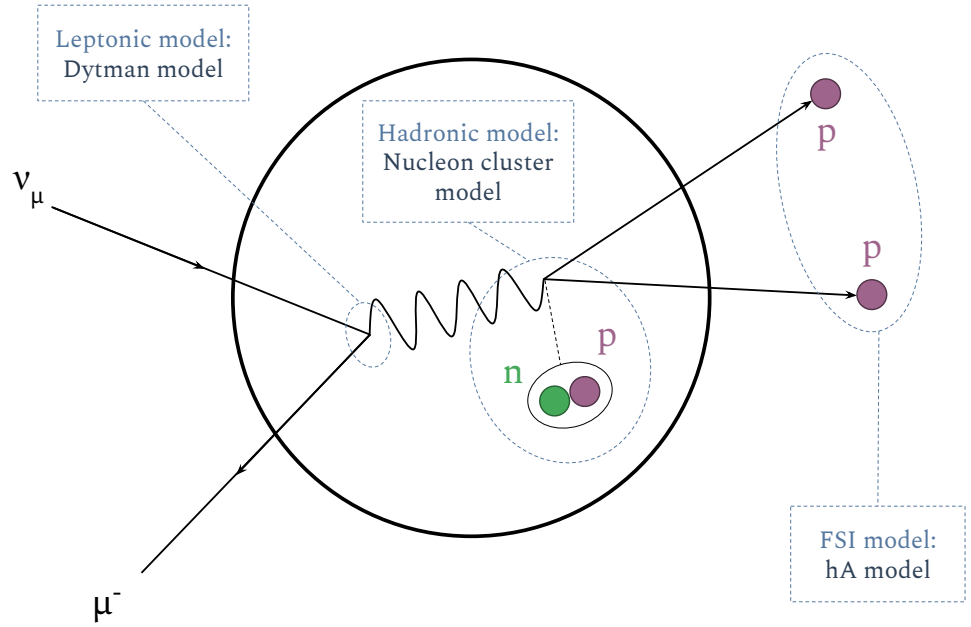

Figure 4.6.: The three components of the GENIE MEC model, including the leptonic model, hadronic model and FSI model [8].

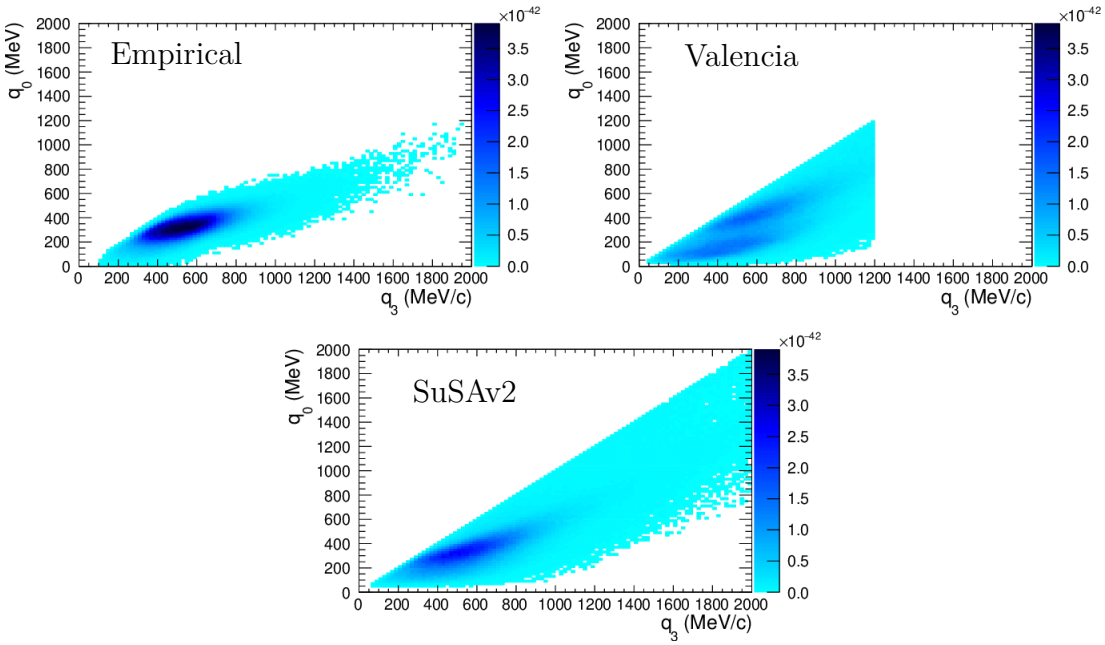

Figure 4.7.: T2K flux-integrated CC 1p1h+2p2h cross-sections on carbon for the three models used to generate events in this analysis. They are shown in units of cm^2 as a function of energy, q_0, and momentum transfer, q_3. From top left to bottom are the empirical model, the Valencia model, in which there is a momentum transfer cut of at 1.2 GeV/c and the SuSAv2 model [179].

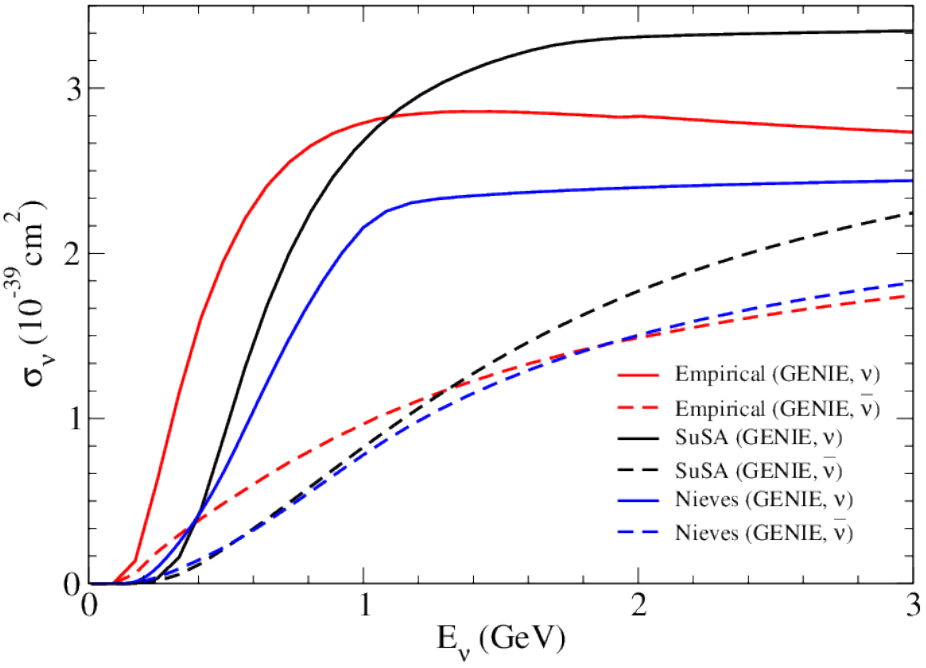

Figure 4.8.: Integrated CC 2p2h cross-sections on carbon for the three models used to generate events in this analysis. Their differences are shown as a function of neutrino energy for neutrinos and anti-neutrinos [179].

differential cross-section for ν_μ-Carbon with respect to muon kinematics, across the three QE+MEC models studied in this analysis [180]. Finally, the SuSAv2 model is able to define both NC multi-nucleon and electron scattering processes, neither of which are currently implemented by the Valencia model.

4.5.7.3. Pion production

- **Rein-Sehgal [166]**

  The simulation of resonant pion production in the historical default GENIE configuration uses the Rein-Sehgal model. The process is separated into two steps: the production and decay of the excited resonance particle.

  18 resonances are modelled in total, assuming no interference between neighbours. Rein & Sehgal implement the Feynman-Kislinger-Ravndal, FKR, harmonic oscillator quark model and extend it to include almost all known resonances [181]. Lepton mass terms are not included in the differential cross-section, however the effect of lepton masses on the phase-space boundaries is taken into account [154].

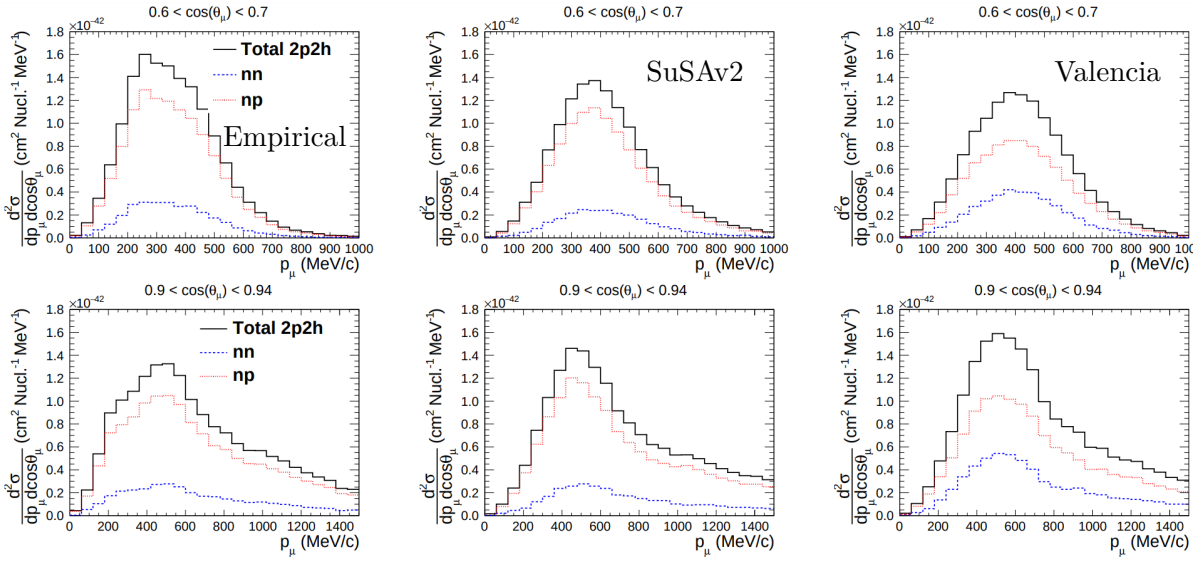

Figure 4.9.: Comparisons of the double-differential CC 2p2h cross-sections for ν_μ-Carbon interactions with respect to muon momentum and scattering angle. The total rates are also shown separated into *nn* (blue-dashed) and *np* (red-dashed) bound nucleon contributions to the initial state interaction. The left-most plots are produced using the GENIE-Empirical model, the middle plots are from SuSAv2 and the right-most plots are produced using the Valencia model [180].

- **Berger-Sehgal [167]**

  In the G18_10a_02_11a GENIE model configuration, an updated version of the resonant pion production model defined by Rein & Sehgal is used, this time written by Berger & Sehgal. This model does incorporate lepton mass terms in the differential cross-section and results in a reduced cross-section in the region of $E_\nu = 1$ GeV.

4.5.8. Hadronization

Simulating hadronization, or fragmentation, involves the modelling of hadronic showers following processes involving interactions on quarks. The cross-section for DIS does not peak until the neutrino energies are much higher than those observed at the peak of the SBN neutrino energy spectrum, see Figure 4.2. That being said, although not a dominant process (<10% of neutrino interactions are generated as DIS in SBND for instance), neutrinos tagged as DIS will be observable in SBN data and will serve primarily as a source of charged and neutral pion production.

Neutrinos undergoing DIS in SBN will predominantly produce secondary hadronic systems with invariant masses below 3 GeV (referred to as low-W). Modelling the process in this region is separated into two parts, the first determines the particle multiplicities present in the hadronic shower and the second defines their kinematics.

The particle content of the fragmented hadronic shower in low-W final states always consists of exactly one nucleon and any number/flavour of pions and kaons possible to satisfy charge and energy conservation. Determining the particle content of the fragmented final state begins with the computation of the average number of charged hadrons present, $\langle n_{ch} \rangle$. This quantity depends on two parameters defined experimentally, a_{ch} and b_{ch}, both of which depend on the initial neutrino flavour, struck nucleon isospin, and the invariant mass of the secondary hadronic system, W,

$$\langle n_{ch} \rangle = a_{ch} + b_{ch} \ln W. \tag{4.19}$$

The average number of charged+neutral particles present is defined to be $\langle n \rangle = 1.5\langle n_{ch} \rangle$, given $\langle n_{\pi^0} \rangle = 0.5\langle n_{ch} \rangle$ [182]. The actual content of the hadronic shower, N, is generated using the relation,

$$\langle n \rangle \cdot P(n) = f\left(\frac{n}{\langle n \rangle}\right), \tag{4.20}$$

where the probability of generating n hadrons, $P(n)$, is absorbed in a scaling function, $f(n/\langle n \rangle)$ which takes the form of a Lévy function and depends on the additional data-driven parameter, c.

Having defined the number of particles present in the shower, the flavour and kinematics of each must be determined. First, the primary baryon is defined with a given mass W which is then allowed to decay to form the hadronic shower. Further information on the GENIE-implementation of the hadronization model can be found here [154].

4.5.9. Hadron Transport

Another experimental complication arises during the passage of final state particles through the nucleus following a neutrino interaction within a heavy nucleus. It is possible

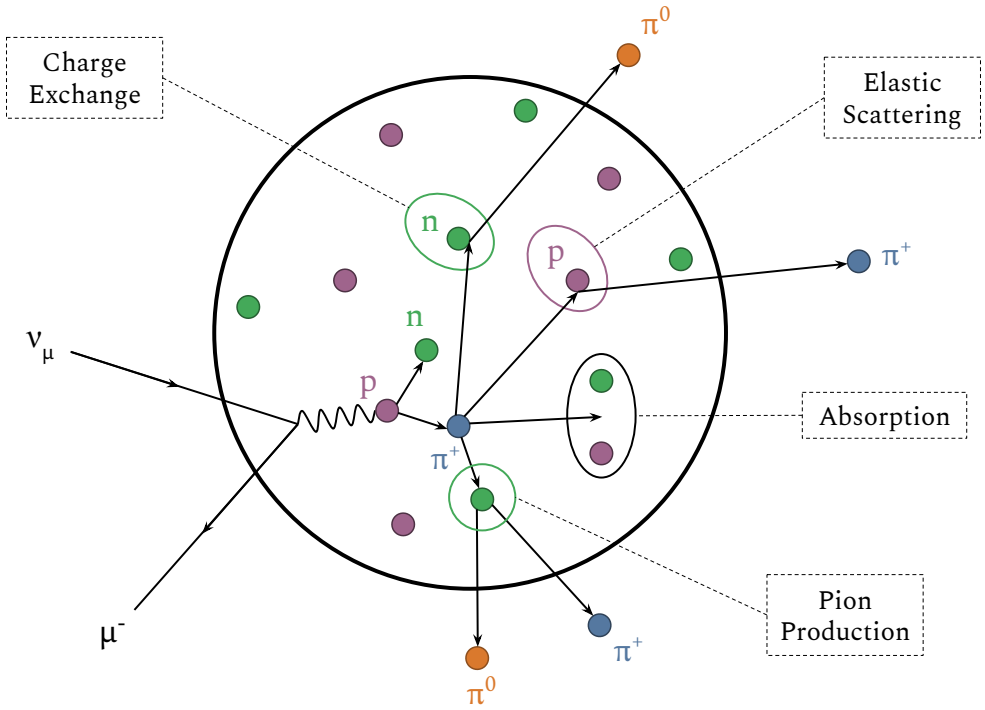

Figure 4.10.: Examples of some possible internuclear final state interaction (FSI) processes which may take place following a neutrino interaction inside a heavy nucleus. Pions may be absorbed or produced after the initial interaction occurred, or additional energy transfers may alter the kinematics of the particles emitted from the nucleus. The observed final state in a detector may therefore not correctly reflect the initial neutrino interaction which took place [183].

for additional processes to occur before the initial neutrino interaction products are able to leave the nucleus, and can consequently alter both the contents and the kinematics of the observed final state in a detector.

Examples of such final state interactions are shown in Figure 4.10. For instance, if a π^+ strikes a neutron, charge may be exchanged such that a proton and a neutral pion are emitted. Another possible process is intranuclear elastic scattering, this involves the transfer of momentum when a pion strikes a nucleon, such that the kinematics of the emitted final state are altered. A pion could be absorbed within the nucleus resulting in no observed pion in the final state at all. Contrastingly, pion production occurs when the initial charged pion strikes a nucleon and the momentum transfer results in the production and emission of an additional, neutral pion [183].

Some experiments, for example those utilising the LArTPC technology, are able to reconstruct and identify many of the final state particles produced following a neutrino

interaction, rather than simply the leading lepton. This provides an opportunity to make exclusive physics measurements and significantly advance our understanding of how neutrinos behave in matter. These experiments are therefore sensitive to FSI modelling.

The result for neutrino experiments with interactions taking place on heavy nuclear targets is that measurements made based on the final states observed in a detector must be modelled by a combination of neutrino interaction cross-sections and final state, intranuclear interactions. For instance, the probability of a QE interaction occurring with only a single proton leaving the nucleus is only 65%. Similarly, the probability of a pion being produced and then absorbed within the nucleus is 20% [154]. Consequently, systematic uncertainties are introduced through the additional modelling parameters and high precision measurements become more difficult to refine.

The hadron transport model implemented in the configurations used in this thesis is the hA model along with an updated version of it, internally developed and implemented by GENIE. The hA model is data-driven, initially written for use by the MINOS experiment whose target material is iron, and works by tracking each hadron produced in the neutrino interaction in 0.05 fm steps through the nucleus, allowing only a single re-interaction per particle.

First, the mean free path of the particle, $\lambda(r, E_h)$, is calculated at each stepped-location within the nucleus, r, from the nucleon density at that position, $\rho(r)$, and the hadron-nucleon cross-section, $\sigma_{hN}(E_h)$, at the energy of the hadron, E_h,

$$\lambda(r, E_h) = \frac{1}{\sigma_{hN}(E_h)\rho(r)}. \tag{4.21}$$

The mean free path is used to determine if the hadron is likely to interact at each position it traverses through the nucleus. If an interaction is deemed to take place, the type and kinematics of the process is once again determined using differential cross-sections. The cross-sections available for the FSI are different to those available to the neutrino itself, and now concern elastic/inelastic scattering, absorption (pions-only), multinucleon knockout (nucleons-only), charge exchange and pion production.

Finally, the 4-vector for each final state product of the intranuclear process is determined from data or from more sophisticated nuclear models. Binding energy and Fermi momentum are taken into account to build the complete picture of the final state topology of the neutrino interaction [150] [154]. The updated hA model used in the G18_10a_02_11a configuration is tuned to additional data.

4.6. Interaction systematic parameters

The method for simulating the neutrino interaction systematic parameters involves variating each parameter within their prior uncertainty using the GENIE ReWeight functionality, which will be briefly summarised in the following section. A complete description of GENIE ReWeight can be found here [154].

4.6.1. GENIE ReWeight

The GENIE ReWeight method begins by assigning a corresponding systematic parameter, x_P, to each physics parameter, P, with standard deviation, $\approx \delta P$. The relation between the tweaked physics parameter, P' and the nominal value with respect to this systematic parameter is given in equation 4.22,

$$P' = P\left(1 + x_P \cdot \frac{\delta P}{P}\right), \tag{4.22}$$

such that if $x_P = \pm 1$, $P' = P \pm \delta P$ and if $x_P = 0$, $P' = P$, i.e. the nominal value. The systematic parameter x_P can be associated to many different forms of physics parameters, from single variables to a complex system such as an entire MC prediction.

4.6.2. Interaction parameters propagated from GENIE

In the case of cross-section modelling uncertainties, the event weight, w_σ^{evt}, associated to a particular variation of a systematic parameter is calculated directly from the resulting neutrino interaction probability variation and is defined as per equation 4.23,

$$w_\sigma^{evt}(x_P) = \left(\frac{d^n\sigma'_\nu}{dK^n}\right) \Big/ \left(\frac{d^n\sigma_\nu}{dK^n}\right), \tag{4.23}$$

where $\frac{d^n\sigma'_\nu}{dK^n}$ and $\frac{d^n\sigma_\nu}{dK^n}$ are the varied and nominal n-dimensional differential cross-sections for the interaction in the n-dimensional kinematic space, K^n , respectively. The event weight, w_σ^{evt} is therefore a function of the systematic parameter, x_P.

For further details on how the event weight functionality is implemented for hadron transport parameters and other direct examples of its application, see [154].

4.6.3. MEC uncertainty

The MEC, or 2p-2h, interaction mode was only added as a permanent component of neutrino event generation in the last decade or so. In addition to the relative novelty of the model, the physics system it encapsulates is incredibly complex. Consequently, the corresponding systematic uncertainty associated to it is less understood than that of the other processes making up the total neutrino interaction cross-section.

Consequently, a well-validated systematic parameter has not yet been propagated from the GENIE event generator for use in the SBN oscillation analysis. Instead, an arbitrary 100% normalisation uncertainty is applied across all energies to account for the missing parameter. The uncertainty is defined to be maximal to encompass the complexity of the 2p-2h process.

4.6.4. Intranuclear hadron transport parameters

Intranuclear re-interactions occur frequently and cause the composition and kinematics of the observed final state to differ from the initial neutrino interaction. They are therefore a major source of systematic uncertainty in any neutrino-nuclear interaction measurement. This section will provide a high level summary of the intranuclear hadron transport model and reweighting scheme, a much more thorough explanation can be found here [154].

The events simulated in the SBN oscillation analysis utilise the internal GENIE INTRANUKE/hA model to propagate neutrino interaction products through the nucleus. This serves as an alternative to a full cascade model, which are much more complex and subsequently don't lend themselves to a reweighting scheme. The GENIE INTRANUKE/hA model instead utilises the total cross-section of each nuclear process for pions and nucleons as a function of energy and is data-driven. The model takes into consideration the fact that hadrons produced in the neutrino interaction will not re-interact with their full cross-section, which is determined from the mean free path, and allows for pion (not nucleon) absorption and production.

The intranuclear systematic uncertainties fall into two categories:

- Uncertainties associated with the total rescattering probability of hadrons produced in the neutrino interaction
- Uncertainties associated with the relative probability of each rescattering mechanism, once the hadron has been determined to reinteract

which are further separated for nucleons and pions.

Variations due to the rescattering probability depend on the mean free path, λ^h, of the hadron, h, and this parameter is modified in the reweighting scheme according to equation 4.24,

$$\lambda^h \to \lambda^{h\prime} = \lambda^h \left(1 + x^h_{mfp} \cdot \frac{\delta\lambda^h}{\lambda^h}\right), \tag{4.24}$$

where $\lambda^{h\prime}$ is the modified mean free path, $\delta\lambda^h$ is it's corresponding uncertainty and x^h_{mfp} is the systematic parameter associated to it.

The weight associated to variations of the re-scattering probability, w^h_{mfp}, depends on the nominal and tweaked survival probabilities of each hadron, P^h_{surv} & $P^{h\prime}_{surv}$,

$$P^{h^{(\prime)}}_{surv} = \int \exp\left(\frac{-r}{\lambda^{h^{(\prime)}}}\right) dr, \tag{4.25}$$

each of which is a function of the corresponding mean free path, $\lambda^{h^{(\prime)}}$, along the hadron's trajectory, r,

$$w^h_{mfp} = \begin{cases} \dfrac{1 - P^{h\prime}_{surv}}{1 - P^h_{surv}}, & h \text{ re-interacts} \\ \\ \dfrac{P^{h\prime}_{surv}}{P^h_{surv}}, & h \text{ escapes.} \end{cases} \tag{4.26}$$

Having determined that a hadron will re-interact, the mode by which this occurs must be defined, m. The mode corresponds to one of the following eventualities,

- Elastic scatter
- Inelastic scatter
- Charge exchange
- Absorption[3]
- Pion production

and the probability of each mode occurring, P_m^h, is calculated using hadron-nucleus cross-section data,

$$P_m^h = \frac{\sigma_m^{hA}}{\sigma_{total}^{hA}}, \tag{4.27}$$

where σ_m^{hA} is the hadron-nucleon (hA) cross-section for the re-scattering mode, m, and σ_{total}^{hA} is the total hadron-nucleon cross-section. The distribution of such probabilities for re-scattered pions, π, and nucleons, N, is shown as a function of the kinetic energy in Figure 4.11.

The determination of the weight associated with the re-scattering mode of the hadron follows the same re-weighting procedure as in the cross-section and mean-free-path cases. First, the cross-section associated to each re-scattering mode is tweaked,

$$\sigma_m^{hA} \to \sigma_m^{hA\prime} = \sigma_m^{hA}\left(1 + x_m^h \cdot \frac{\delta\sigma_m^{hA}}{\sigma_m^{hA}},\right) \tag{4.28}$$

where once again, $\sigma_m^{hA\prime}$ is the tweaked cross-section, $\delta\sigma_m^{hA}$ is the associated uncertainty and x_m^h is the systematic parameter used to represent the tweak. Finally, the weight is defined,

$$w_m^h = \sum_m \delta_{m;m'} \cdot x_m^h \cdot \frac{\delta\sigma_m^{hA}}{\sigma_m^{hA}}, \tag{4.29}$$

where m corresponds to the list of possible re-scattering modes and m' is the actual mode by which the hadron scattered.

[3]Refers to the emission of 2 or more nucleons with no pions in the final state. This can refer to either the absorption of a pion or, if no pion was ever produced, simply multi-nucleon knockout.

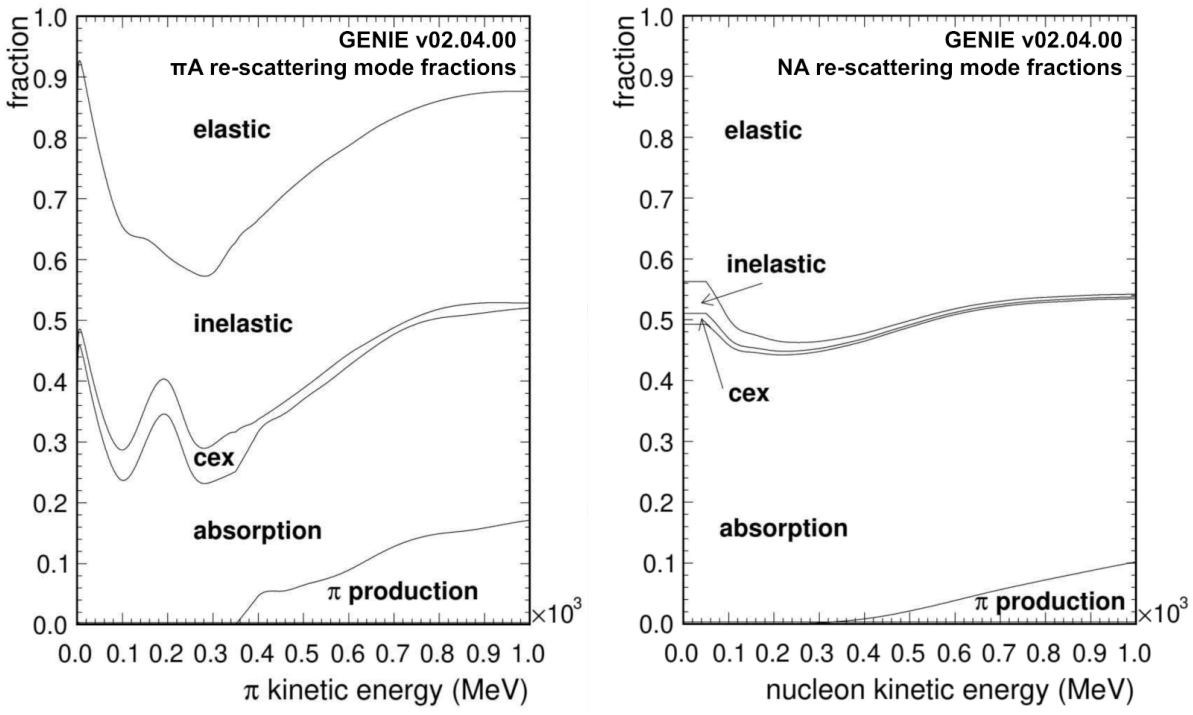

Figure 4.11.: Relative intranuclear re-scattering rates defined in GENIE. On the left is the pion case and on the right is the nucleon case. The sum of all integrated modes for each case should always be 1 [154].

Finally, the total weight applied to a single hadron based on it's probability of interacting combined with, if relevant, the mode by which it is determined to interact is simply,

$$w^h = w^h_{mfp} \cdot w^h_m, \tag{4.30}$$

and this is propagated to the event-level from the single-particle level in the following product,

$$w^{evt}_{HT} = \prod_j w^h_j, \tag{4.31}$$

where j corresponds to all primary hadrons in the event. As is this case for the entire interaction systematic section, more information can be found here [154].

4.7. Particle propagation in liquid argon

Having simulated the neutrino interaction and determined the particles leaving the nucleus along with their kinematics, the next step is to model their transport through the argon itself using a GEANT4-based simulation in LArSoft [153] [152].

First, the particles which successfully left the nucleus following an interaction are propagated through the detector geometry until they either leave it, or they range-out. As they traverse the liquid argon, the drift of the ionisation electrons is simulated and propagated onto the wire planes of the detector. Upon reaching the wire planes, the charge and timing information for every electron is recorded and the true energy of each deposition on each wire is calculated.

The charge, energy and timing information from every electron is combined for each simulated particle as a whole. If the total energy for a single particle is high enough for its type to be visible in the detector, and the particle remained entirely within the detector volume, then the truth-level information about the particle is stored. These truth-level particles are also tagged to be either a `Track` or an electromagnetic `Shower`. Particle hierarchies can then be constructed from each of the simulated particles in order to describe the relationship between all the final state particles produced in the neutrino interaction.

Alongside the simulation of the electron drift, the scintillation light is also propagated to the light detection system in each detector using a GEANT4-based simulation and will briefly be discussed in section 4.11.1.

4.8. Detector simulation and signal processing

In order to convert the information from the TPC wire planes into realistic, fully-reconstructed objects, additional detector-based features must be simulated, for instance the electronics response and noise simulation of the detector. An internal LArSoft package called `DetSim` takes the true charge, energy and timing information from each deposition as input. This timing and charge information is convolved with the induction and collection field shapes to give an ADC count. This is then combined with the detector noise model to produce a list of digitized charge vs timing information for each wire [184]. For real data, the recorded charge and timing information is used to construct the list.

4.9. Detector systematic parameters

Contributions to the detector-based systematic uncertainties in each of the SBN experiments will largely come from the same sources. However, due to the functional uniquities outlined at the end of chapter 3, both the magnitude of the comparable parameters and the content and magnitude of exclusive systematics must be determined separately for each detector. The sources of detector-based uncertainty in the SBN program include,

- **Noise in the TPC**: Defines the signal-to-noise ratio (SNR)
- **Response of the Wires to the Electric Field**: Affects the induced current on a wire from a drifting ionized electron
- **Electronics Response of the TPC**: Affects how precisely the signal on a wire is able to be digitized by the ADC
- **Electron Diffusion**: Uncertainty on the magnitude of longitudinal and transverse electron diffusion
- **Space-Charge**: When argon ions are produced, they are drifted very slowly towards the cathode planes. In the case of large cosmic-ray fluxes, the abundance of such ions may result in regions of positive charge in the detector which can distort the electric field and consequently the drift velocity of the electrons. The space-charge systematic parameter characterises the uncertainty on the magnitude of the space-charge induced due to the huge flux of cosmic rays in surface detectors. The cause and impact of space-charge in LArTPC detectors has been studied carefully by MicroBooNE [185]
- **Electron Lifetime**: Quantifies the electron attenuation and its impact on the induced charge at the wire planes
- **Drift Velocity**: Accuracy of the electron drift velocity prediction
- **Recombination**: At what rate do electrons recombine with argon ions before reaching the wire planes
- **Light Production and Propagation**: How well can we measure the light yield and how accurately can this be used to reconstruct the light produced
- **Argon Purity**: An uncertainty on the amount of impurities such as oxygen which are contaminating the argon, this quantity may change over time.

4.10. Reconstructing events in SBND

Ultimately, the event reconstruction procedures in the SBN program will be consistent across each detector. At present, the implementation is not at the same stage in each detector, therefore the analyses in this thesis will apply the reconstructed method as it stands for SBND to all three detector simulations for consistency. The first stage of the procedure is to reconstruct the `Hit`s, defined in section 3.2.2.2, from the waveforms produced following either the `DetSim` stage of the simulation or by the real charge depositions on the wires in data.

4.10.1. Topological reconstruction

The next reconstruction step is performed by the Pandora pattern-recognition software framework [155] which was first developed for Linear Collider experiments and has since been expanded for use across many LArTPC experiments, including the SBN program and DUNE. The information in this section will form a short summary of the neutrino event reconstruction process from this Pandora-MicroBooNE paper [155].

Since LArTPC detectors have Bubble Chamber imaging capabilities, it is crucial that the reconstruction of neutrino events in such experiments fully extracts the available topological information from those images. This is reasonably straightforward by eye, however the substantial event rates in the SBN program call for the process to be performed in an automated, computational way. Pandora applies a multi-algorithm approach to pattern-recognition with the aim of singling out individual reconstruction tasks and developing targeted algorithms to optimise every aspect of the problem. The pattern-recognition applies a combination of traditional and machine learning techniques in this way.

As input, Pandora takes a list of `Hit`s produced in the initial stage of the reconstruction, for each wire plane of the detector. The x-coordinate is commonly-defined from the `Hit` timing information across the three planes. Within each plane, 2D clusters of `Hit`s which are unambiguously related in a `Track`-like way are defined, and candidate neutrino vertices are located at their start and end points. An example event with all the 3D candidate vertices projected into a single 2D plane are shown in Figure 4.12.

The 2D vertex candidates across the three wire planes are compared and combined to estimate the location of each candidate in 3D. Topological features of the event and

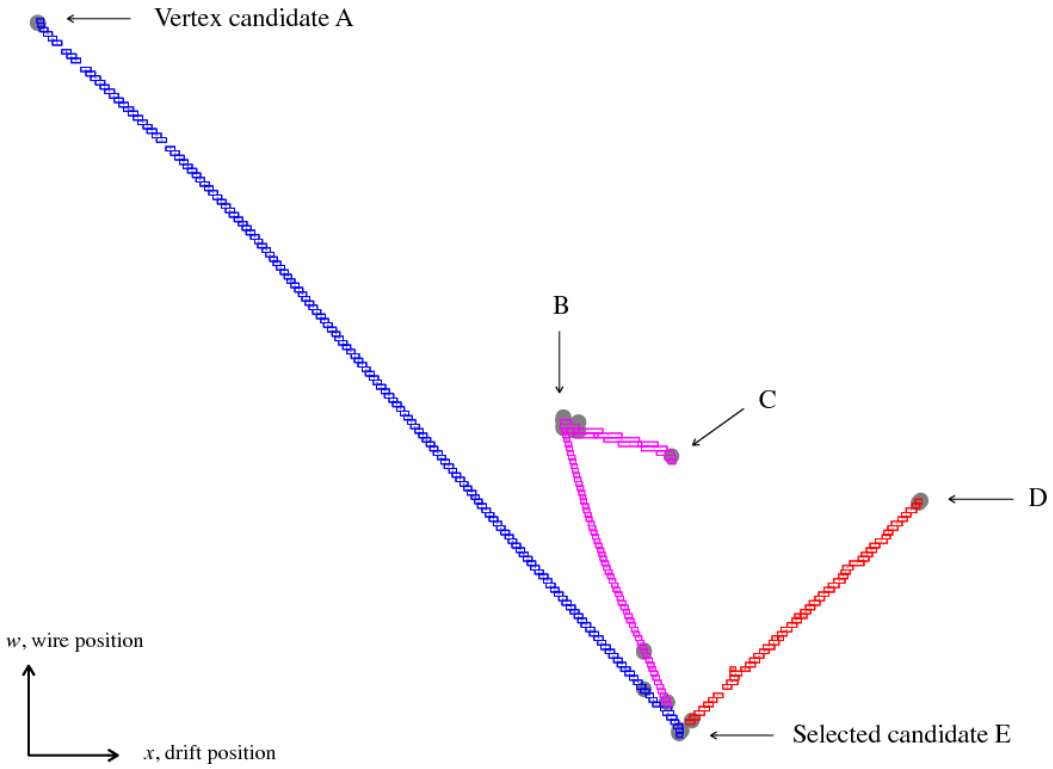

Figure 4.12.: A possible neutrino event projected into a single 2D plane, with all the 3D candidate neutrino vertex locations highlighted. The neutrino vertex which would have been selected by the BDT in the method used by SBND has been highlighted [155].

vertex are then combined in a Boosted Decision Tree (BDT) to determine the location of the best neutrino vertex candidate [186].

Following the identification of the neutrino vertex, any 2D clusters which cross the 3D vertex location are split in two. The outgoing particles from the vertex must then be constructed. First, 3D `Track`-like particles are constructed from the existing 2D clusters by assessing all combinations of clusters across the three planes. Sliding linear fits are used with x-coordinate information to determine if the clusters can be matched and translated into a 3D `Track`-like particle. `Hits` are also translated into 3D with respect to their locations within a constructed 3D particle.

All 2D clusters are then assessed as potential electromagnetic `Shower` candidates, 2D `Showers` are first constructed and any previously-made `Tracks` are allowed to be re-assessed in this way. These 2D `Shower`-like clusters are then translated into 3D using a similar matching method to that of the 3D `Track` construction. Once the 3D `Showers` have been constructed, the remaining clusters are once again passed through the 3D tracking step to account for any now-missing clusters. The constructed 3D particles are

then defined to be `Track`-like, or `Shower`-like. These particles are known as `PFParticle`s when used in the downstream analyses.

Finally, particle hierarchies are defined in order to characterise the event topologically. First, the neutrino `PFParticle` is defined at the location of the previously reconstructed 3D vertex. Any particles deemed to be associated to this vertex are tagged as daughter `PFParticle`s of the neutrino and the one with the most `Hit`s is identified as the leading lepton. The neutrino flavour is defined by whether leading lepton is `Track` (ν_μ) or `Shower` (ν_e)-like. Any remaining particles associated with the end positions of a neutrino daughter are defined to be daughters of that particle, and the process proceeds until all particles in the event have been associated.

4.10.2. Calorimetry

As well as the incredible imaging capabilities, LArTPCs are also built as calorimeters, which means they are able to reconstruct the energy collected on the wire planes of the detector. As a result, the stopping power, or dE/dx of a particle can be measured, which is a critical quantity in physics analyses, particularly in the identification of particle types.

In the SBND approach to neutrino event reconstruction, the distribution of dE/dx for each particle is determined from the charge deposition of the `Hit`s within it on each of the wire planes in the TPC separately. For every hit,

$$\frac{dE}{dx} = \frac{\exp\left(\beta \cdot W_{Ion} \cdot \frac{dQ}{dx}\right) - \alpha}{\beta}, \tag{4.32}$$

where $W_{Ion} = 2.36 \times 10^{-5}$ MeV/e$^-$ is the average energy deposited per electron ionised in the argon, $\alpha = 0.93$ and

$$\beta = \frac{\beta'}{\rho E_{Field}}, \tag{4.33}$$

such that $\beta' = 0.212$ (kV/cm)(g/cm^2)/MeV, $\rho = 1.396$ g/cm^3 is the density of liquid argon and E_{Field} is the electric field strength of the detector. α & β' have been determined by ArgoNeuT [187].

The last remaining quantity to define in equation 4.32 is dQ/dx. This value is measured from the amplitude of each `Hit` in ADC counts divided by the `Track` pitch, which corresponds to the absolute length of the `Track` segment which deposited the charge and is related to the angle of the `Track` to the wires within the plane. The dQ/dx value must then be converted from being per number of ADC counts to per number of electrons, where $\left(\frac{electrons}{ADC}\right) \approx 50$ in the SBND simulation.

Once calculated on all three wire planes, the analyser can determine which plane to read the calorimetry from based on topological information about the particle and any known issues on the planes themselves.

4.11. Additional components of the simulation

Alongside the TPC simulation and reconstruction described so far in this chapter, the photon detection and cosmic ray tagging systems must also be simulated in order to fully exploit the capability of the detectors. A number of external sources of particles will accompany the neutrinos arriving in the TPC volume from the BNB and may contaminate the data sample. Cosmic ray muons will be the dominant external background, followed by interactions occurring in the cryostat of the detector but not in the TPC, known as dirt interactions. If the external backgrounds cause a 'trigger' in one of the detector systems, that event will be recorded in the data [188]. One particular example involves neutrino interactions which occur outside of the fiducial volume (OOFV), if a cosmic ray muon simultaneously enters the detector in coincidence with the beam, it may be the cosmic ray which is incorrectly tagged as the neutrino in these events.

The TPC, CRT and PDS systems will ultimately work together in the removal of non-neutrino backgrounds, such as cosmic rays and OOFV events, to maximise the efficiency of making neutrino physics measurements. At this stage in the lifetime of SBN, neither the CRT nor the PDS simulations have been completed and fully-validated to the same extent as that of the TPC, and therefore were not incorporated into the analyses performed in this thesis. Nevertheless, a brief description of each method is given in this section.

4.11.1. Scintillation light

Scintillation light is a powerful tool in the reconstruction of neutrino interaction events, as it provides the precise timing information needed to determine positioning information about energy depositions in the detector. Furthermore, the timing information from the scintillation light can be used to determine if any depositions were made in conjunction with the neutrino beam, thereby providing a way of removing events with no recorded neutrino interaction. More information on the purpose and functionality of the SBND PDS system was explained in section 3.3.1.3.

In the full simulation of the scintillation light, each photon is produced and propagated to the photon detection system individually using GEANT4. The propagation of the photons within the detector incorporates Rayleigh scattering, wavelength shifting, reflections and absorption. Given the huge flux of photons produced in every interaction, this method is extremely computationally expensive, therefore an alternative will be defined for each detector in the SBN program. A summary of the fast SBND method is as follows [189].

The alternative method, called the fast optical simulation, uses a pre-constructed library of scintillation data, which encompasses all of the aforementioned information about the scintillation photons. The library is constructed by splitting the detector into three dimensional voxels, and simulating the full detector response to hundreds of thousands of photons generated from a point in each voxel, assuming they emerge isotropically. A 'visibility' parameter is then defined which converts the number of photons detected into the number produced.

With each energy deposition, the detector response to the light from that position can therefore be read from the library and converted into the number of photons produced at the deposition point, removing the need for producing and tracking all photons [189]. The analytical method is used currently.

4.11.2. Cosmic ray background removal

Cosmic rays will be one of the dominant background to neutrino interactions in the SBN program, therefore two independent methods of tagging and removing cosmic rays will be implemented in order to maximally mitigate their impact. The first is the hardware-based cosmic ray tagging system itself, the purpose and functionality of which was ex-

plained in section 3.3.1.4. The second is a software-based cosmic ray rejection procedure, which so far has two possible implementations in the SBND detector,

- **Cosmic ray removal with the Pandora pattern-recognition framework**

  The first uses mostly a 'traditional' approach within the Pandora pattern-recognition framework. When switched on, the cosmic ray tagging procedure is applied in conjunction with the reconstruction of neutrino particle hierarchies defined in section 4.10.1.

  In this cosmic ray tagging method, all `Hits` are combined into clusters to determine whether they are `Track` or `Shower`-like, and particle hierarchies are formed as before. Topological features are then used with timing information from the light reconstruction to determine if hierarchies are likely to originate from a neutrino interaction or a cosmic ray [155].

  Candidate neutrino particle hierarchies are first tagged and removed from the list of cosmic ray candidates, and this tagging is defined to maximally preserve neutrino interactions. The remaining particles are then assessed individually, removing the hierarchical structure previously assigned to them.

  Unambiguous cosmic rays are identified if they do not coincide with the beam time, or if both ends of a `Track` traverse the top and bottom planes of the detector respectively. Once all unambiguous cosmic rays have been removed from the candidate neutrino list, remaining `Hits` are grouped into 'slices' and the neutrino reconstruction is applied as per the method in section 4.10.1.

- **Cosmic ray removal with deep neural networks**

  The second uses an image-based deep learning method which has been developed for cosmic ray removal in the SBND detector. The same procedure is not yet available in the MicroBooNE and ICARUS detectors. A brief overview of the SBND approach is as follows and much more information can be found here [188].

  Images are constructed using each wire plane in the TPCs, resulting in a set of 3 2D images in which the number of pixels in each image is proportional to the number of wires in each plane. Training is performed on a dataset containing sets of 3 images in which there are both neutrino and cosmic-induced `Hits`, and images with only cosmic-induced `Hits` with the intention of learning how to identify cosmic and neutrino-induced pixels within the image.

4.12. SBND event displays

This section will show examples of the 2D images visible in the SBND LArTPC along with the contents of the interactions within them. The events were simulated according to the method defined throughout this chapter. Information regarding the true contents of each interaction was obtained at the GEANT4 stage of the simulation, however the events are displayed having undergone the full reconstruction procedure. The `Hits` displayed were recorded on the APA collection planes.

The `Tracks` and `Showers` observable in the event displays were all produced following a charged-current muon neutrino interaction, within the active volume of the detector. The main characteristics of each particle type in a LArTPC is as follows:

- **Muon, μ, Track**: At the momenta observed following BNB neutrino interactions, muons are mostly minimum-ionising particles, MIPs. As a result, a `Track` will always be produced and will generally have low energy depositions along the majority of its trajectory. If the muon is contained and does not re-interact, a Bragg-peak my be observed just before the muon comes to a stop and decays. A 'Michel electron' in the form of a short, low-energy, `Track` may also be observable following the decay-at-rest of the muon [190]. Delta rays may also be visible along the `Track`
- **Charged Pion, $\pi^{\pm}$, Track**: Charged pions often look similar to muons in the TPC and consequently serve as the main background when trying to select charged-current interactions. Charged pions may also undergo further hadronic interactions as they traverse the argon.
- **Neutral Pion, π^0, 2 Showers**: Neutral pions are short-lived and immediately decay to 2 photons after leaving the nucleus with a 99% branching ratio, which subsequently produce electromagnetic `Showers` in the detector. A pair of photons from the neutrino vertex is therefore the dominant π^0 signature
- **Proton, Track**: Protons also produce `Tracks` in the detector, however their substantial mass means that they rarely behave as minimum ionising particles at the momenta available following BNB neutrino interactions. They instead often produce short `Tracks` with relatively large energy depositions along their trajectories
- **Electron, Track or Shower**: If an electron has enough energy, it may cascade into an electromagnetic `Shower`. However if this is not the case, a short `Track` may instead be observable

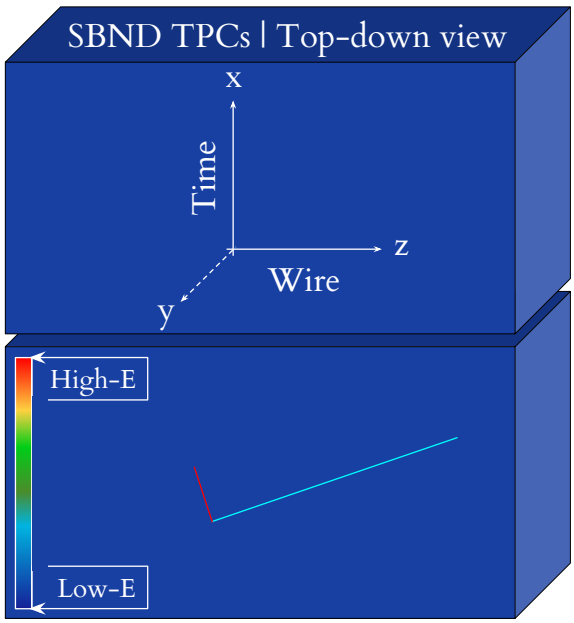

Figure 4.13.: A cartoon depicting the orientation of the following event displays. The time axis corresponds to the reconstructed timing information and in turn defines the x-location of the event. This dimension sets 0 at the mid-point between the two TPCs in SBND. The wire axis resolves `Hits` on each of the vertical wires in the APA collection planes and therefore defines the z-location of the event. This dimension is set to 0 at the front face of the detector. Finally, the cartoon is being observed from the top face of the detector, such that the y-dimension decreases into the page. The y-axis sets 0 at the mid-point of the TPC. This dimension is not depicted in the 2D event displays. The colour scale defining the relative energy, E, depositions is also shown.

- **Photon, Shower**: Visible photons present in the final state of a neutrino interaction predominantly produce electromagnetic `Showers` in the TPC. Photons which are not energetic enough to pair produce may instead undergo Compton scattering, and subsequently produce multiple short and topologically distinct energy depositions in the detector [191].

The resolution of liquid argon detectors allows for the possibility of distinguishing between electron and photon electromagnetic showers. First, the ability to reconstruct the neutrino interaction vertex allows for precise measurements of the start-position of the showers, which is characteristically different between the two particle types. The neutral (and therefore invisible) photon may travel up to 14 cm (known as the conversion or 'radiation' length) before either decaying into an electron-positron pair at the start of the electromagnetic shower, or Compton scattering. The 3 mm resolution of an LArTPC allows for this gap to be clearly distinguished from the electron shower, whose start position is located at the neutrino vertex [192].

A second method is defined for if the vertex reconstruction is not possible (for instance when no other hadronic activity occurs). This instead looks at the beginning of an electromagnetic shower and utilises the fact that a shower produced by an electron begins with a single electron track, whereas a photon shower begins with an electron-positron pair. This method therefore discriminates between ionization depositions consistent with one and two particles [192].

Figure 4.13 is a cartoon depicting the orientation of the event displays with respect to the 3D detector geometry. The time axis corresponds to the reconstructed timing information given by the `Hits`, and in turn defines the x-location of the event. This dimension sets 0 at the mid-point between the two TPCs in SBND. The wire axis resolves `Hits` on each of the vertical wires in the APA collection planes and therefore defines the z-location of the event. This dimension is set to 0 at the front face of the detector. Finally, the event displays are generally being observed from the top face of the detector, such that the y-dimension decreases into the page. In the y-axis, 0 corresponds to the mid-point of the TPC such that this dimension is not depicted in the 2D event displays.

Figure 4.14 depicts a ν_μ CC QE interaction, the most abundant in SBND, with $E_\nu = 1.22$ GeV. The final state consists of 1μ 1p. Both the particles have almost identical momenta, which makes for a reasonably clear comparison of the behaviour of each particle type. The muon re-interacts without producing any further visible particles and therefore does not have a Bragg peak. Before this, the muon travels over 3 m depositing small amounts of energy. A number of delta rays are visible along this trajectory. In the case of the proton, even though the momenta is the same and there is no re-interaction, it travels only 0.6 m with increasing energy depositions along its trajectory. The momentum similarity means that angle between the proton and muon is almost 90° in 3D space and they are approximately ±45° to the neutrino direction respectively. This event is almost perfectly characteristic of how a two-body ν_μ CC QE interaction on a free nucleon would look.

The event display in Figure 4.15 demonstrates one of the more interesting final state topologies relevant to SBND, a ν_μ CC 2p2h interaction, with $E_\nu = 0.54$ GeV and 1μ 2p in the final state. The muon in this case has very low momenta, $p_\mu = 0.193$ GeV/c and is directed down ($p_x < 0$) rather than forwards ($p_x = 0$), only travelling a total of 36.6 cm. Having said that, the muon does come to a stop in this event and demonstrates the characteristic Bragg peak. It then decays-at-rest to a 50 MeV Michel electron, which can be seen as a short `Track` leaving the end of the muon after the short, large energy deposit. The protons are of particular interest in this event, as they are emitted from the neutrino interaction vertex almost perfectly back-to-back, $\cos\theta = -0.98$. They have $p_{p_{1,2}} = 0.63, 0.43$ GeV/c and both deposit increasing amounts of energy along their trajectories. This particular configuration could tell us more about the complex nature of neutrino-nucleus interactions, which has been probed by the ArgoNeuT experiment [193].

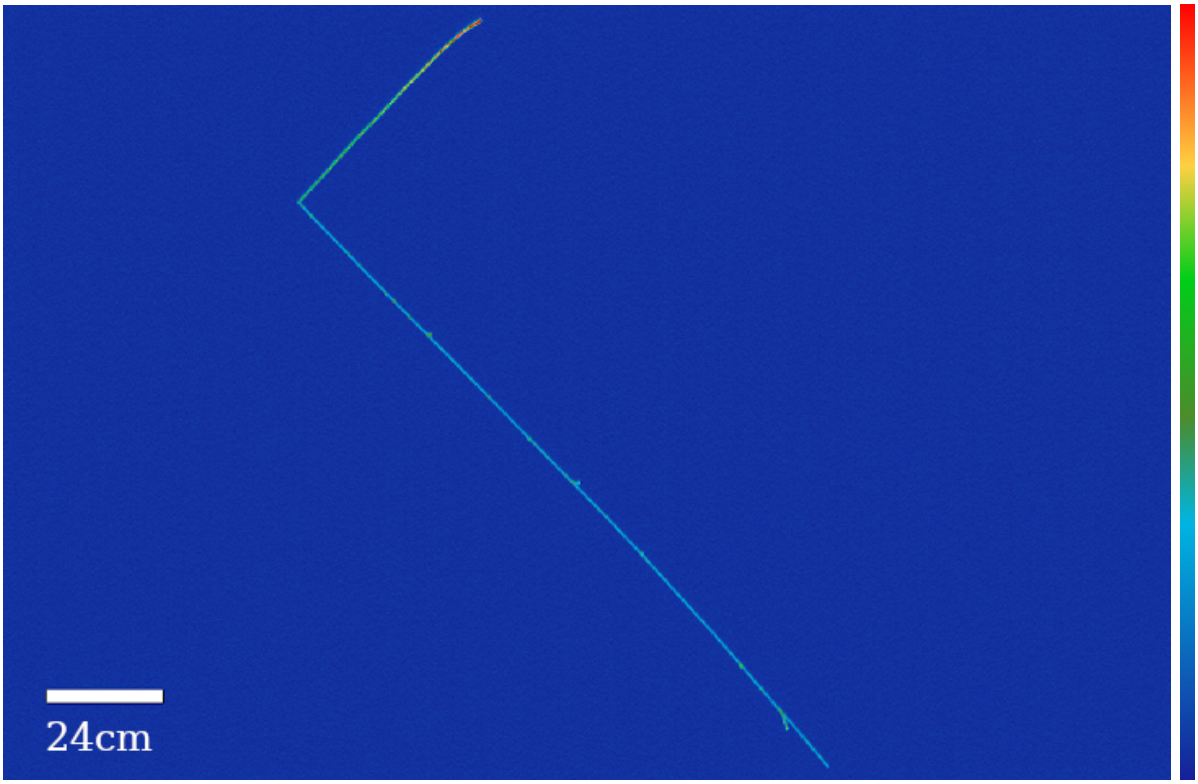

Figure 4.14.: A ν_μ CC QE interaction with 1μ 1p in the final state. The proton and muon momenta are almost identical, such that they emerge at 90° to one another, and at $\approx \pm 45°$ to the neutrino direction respectively.

The final event display demonstrates the clarity of a huge variety of distinguishable information available in the SBND detector. Figure 4.16 shows the particles produced following a ν_μ CC DIS interaction with $E_\nu = 4.36$ GeV. The final state of the primary neutrino interaction consists of 1μ $1\pi^\pm$ $1\pi^0$ $1p$ where $\pi^\pm$ refers to a charged pion with unknown sign.

The `Tracks` and `Showers` visible in the event display are summarised as follows,

- Although the muon had $p_\mu = 1.11$ GeV/c, it re-interacted without producing any visible particles before decaying, such that a Bragg peak cannot be seen. This is the short, most horizontal, `Track` leaving the interaction vertex in the image
- The longest visible `Track` is the charged pion, which had $p_{\pi^\pm} = 1.57$ GeV and traversed the detector with a z-component of almost 1.5 m before re-interacting to produce $1\pi^\pm$ $1\pi^0$. The additional charged pion can be seen as a short red (high-energy) stump at the end of the initial pion `Track`, and the characteristic photon pair also emerges following the immediate decay of the secondary π^0

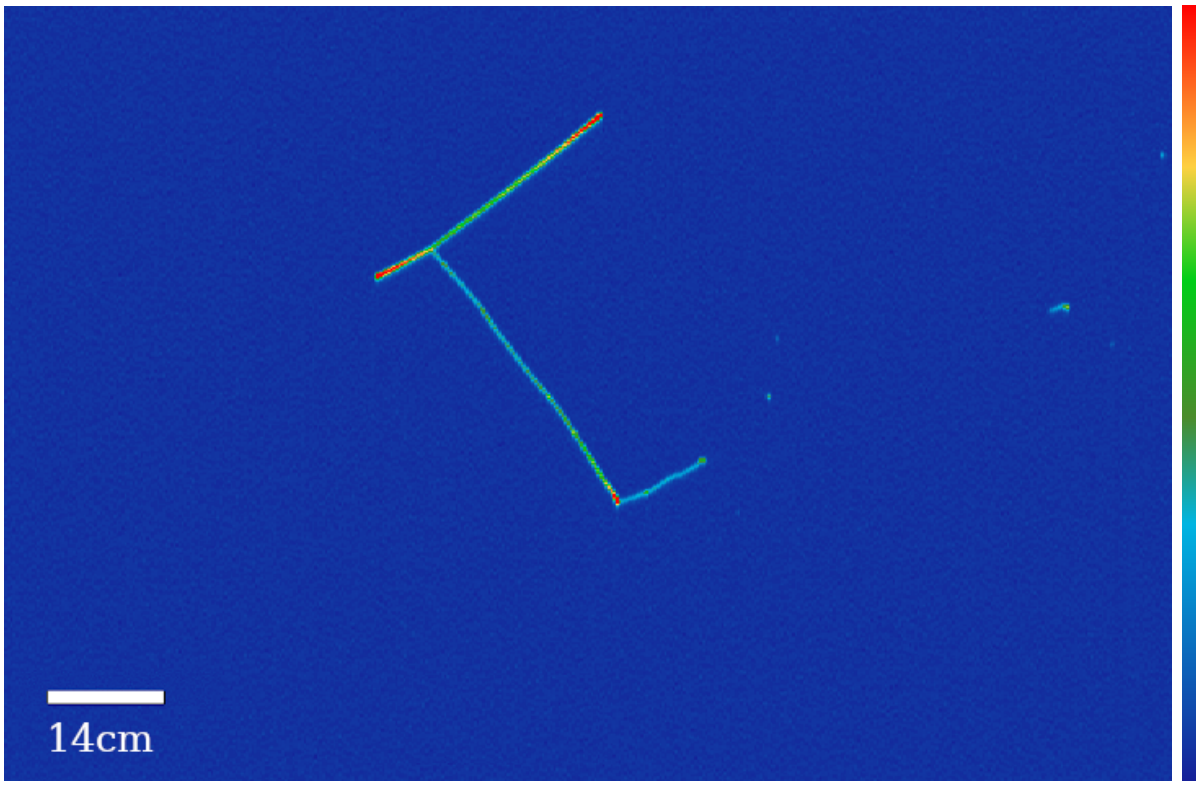

Figure 4.15.: A ν_μ CC 2p2h interaction with 1μ 2p in the final state. The muon is the most downward-going `Track` and decays-at-rest to a Michel electron after depositing a large amount of energy according to the characteristics of a Bragg peak. The protons in this event are emitted almost perfectly back-to-back.

- The π^0 decayed almost immediately into two photons. The corresponding electromagnetic `Showers` produced by both photons can be seen emerging a few cm away from the neutrino vertex
- The proton is also visible, however this quickly re-interacted to produce a secondary visible proton, at a slightly different angle. The secondary proton continuously ionised the argon along its entire trajectory resulting in relatively large energy deposits with every reconstructed `Hit`, the visible `Track` is therefore a strong red in colour.

Since none of the MIPs decayed before re-interacting, there are no visible Bragg peaks in Figure 4.16.

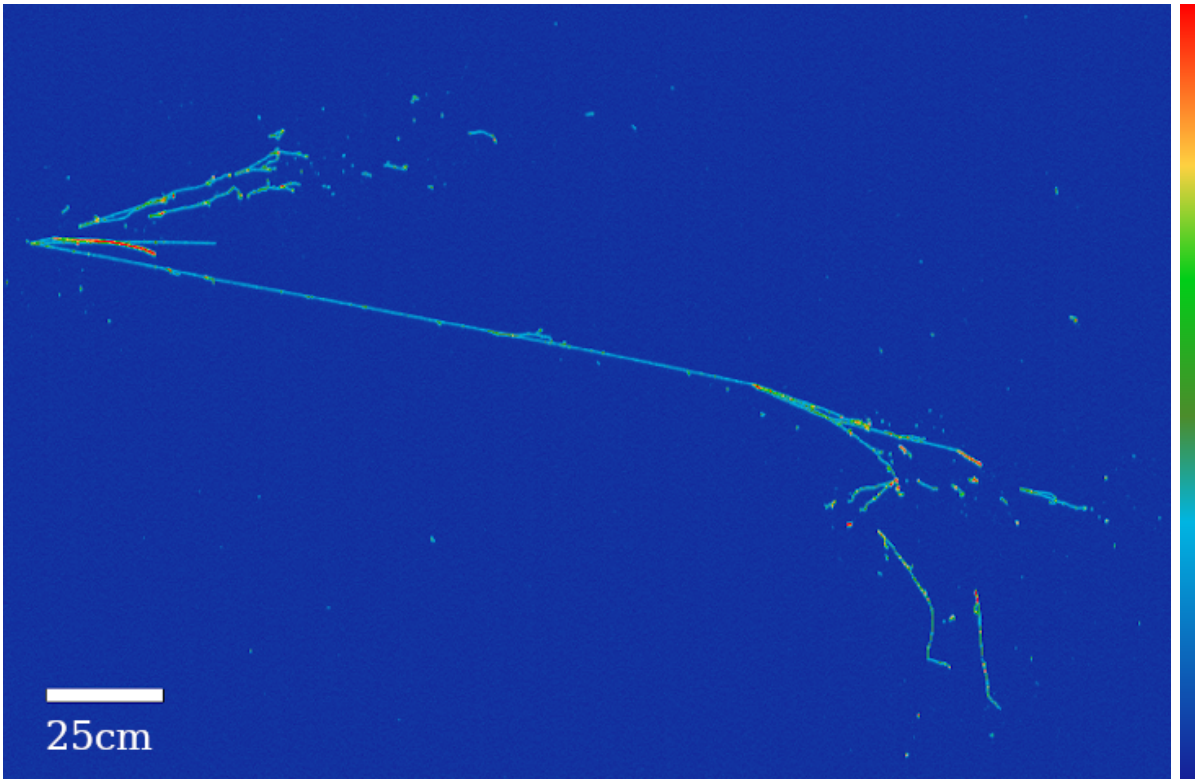

Figure 4.16.: The final state particle content of a ν_μ CC DIS interaction in SBND. The primary interaction products are:
1μ: The short, most-horizontal, `Track` in the image.
$1\pi^{\pm}$: The long `Track` which re-interacts to produce a visible pair of π^0 photon `Showers`.
1 proton which re-interacts to produce another proton: The seemingly-single short red `Track` coming from the neutrino vertex.
$1\pi^0$: A pair of photon `Showers` emerging a few cm from the neutrino interaction vertex.

Chapter 5.

Physics studies of SBND events using multiple model configurations

The SBND experiment will record millions of neutrino interactions per year, due to its size, proximity to the intense neutrino source and fundamental properties of the LArTPC detector technology. We can maximise the information extracted from the detector by looking into exclusive topology contributions to this huge event rate. By determining the rate of each neutrino interaction type in the detector, we are able to predict the physics capabilities of the experiment. For instance, a huge number of events with charged pions in the final state would allow us to make precise measurements of pion kinematic distributions.

In addition, we can repeat all studies with the simulation produced using multiple model configurations. In doing this, we will learn the model-dependent characteristics, such as expected rates, multiplicities and kinematic shapes, of various particle types. This level of detail will enable us to determine which truth-level features impact certain analysis level observations. Studying multiple model configurations in general will likely flag up a number of avenues of interest for further study, for which additional targeted model configurations can be prepared. For instance, one might decide to quantify the impact on observed pion kinematic distributions in changing only the underlying resonant model due to the discovery of a large variation in the pion-based event rate across the configurations.

Multiple model configurations can therefore be used throughout the entire analysis procedure, to first understand what to expect from the analysis and then to decide how best to develop the procedure. This chapter will summarise a number of kinematic studies and comparisons of multiple neutrino interaction model configurations within a sample

of MC-generated charged-current muon neutrino events with no pions in the final state (ν_μ CC 0π). This is the most abundant topology in SBND data, comprising 50% of the entire dataset. The analogous plots from the entire sample of charged-current muon neutrino events (ν_μ CC Inclusive) are presented in appendix A.

The configurations used in the generation of these samples were defined in section 4.5.4, with the breakdown of the model components in each configuration defined in Table 4.1. The studies presented in this chapter will address 4 model configurations generated with GENIE v3 [194] [195], each varying only the CC QE and CC 2p2h components of the G18_10a_02_11a configuration [1]. These 4 models will be pertinent in the analysis of the ν_μ CC 0π final state throughout this thesis.

The MC samples of neutrino interaction events produced for these studies were constructed using the method outlined in sections 4.5 and 4.7. The events are examined entirely at the truth-level, without any consideration of detector effects or reconstruction, in order to determine exactly what the model configurations predict and to serve as a comparison for downstream analyses. Since SBND has been projected to run for at least 3 years, corresponding to 6.6×10^{20} POT, all integrated event rates presented will be normalised to this exposure. The events have all been generated within SBND active volume, with no fiducial border, see section 3.3.1 for details on this geometry definition.

The first studies presented will give an overview of the entire content of the neutrino interaction event rate in SBND. Targeted studies of the ν_μ CC 0π sample content will then be explored. Since the data is defined entirely in truth, there will be no NC or other topological background contributions to the ν_μ CC 0π sample.

5.1. Contributions to the neutrino event rate

The total SBND muon neutrino event rate in each of the 4 model configurations is presented in Table 5.1 as a breakdown of the physical process which took place during the neutrino-argon interaction. Section 4.5.7 gives a description of each scattering mode. The rate is then broken down into various inclusive and exclusive final state topological contributions of muon and electron neutrinos in Table 5.2.

[1] Note, the 2p2h interaction will be sometimes be referred to as 'MEC' throughout this chapter in accordance with the GENIE naming scheme of the interaction model.

Physical Process	Model Configurations (CC QE & CC 2p2h)			
	Nieves	**SuSAv2**	**LS-E**	**SM**
Charged Current				
QE	2,152,939	2,373,600	2,078,485	2,776,187
MEC	483,859	552,181	543,418	0
RES	1,160,763	1,160,763	1,160,763	1,160,763
DIS	220,335	220,335	220,335	220,335
Coherent	6950	6950	6950	6950
Other	2384	2384	2384	2384
Neutral Current				
QE	847,419	847,419	847,419	847,419
MEC	110,119	110,119	110,119	110,119
RES	525,814	525,814	525,814	525,814
DIS	144,808	144,808	144,808	144,808
Coherent	5903	5903	5903	5903
Other	343	343	343	343

Table 5.1.: SBND Event Rates from all neutrino flavours broken down in terms of the neutrino interaction type for 4 model configurations. Note that only the CC QE and CC 2p2h (MEC) models differ between the 4 model configurations.

As well as presenting a general breakdown in terms of absolute particle multiplicities, an additional consideration has been made regarding the proton content of the ν_μ CC 0π final state. Since protons are likely to be the lowest energy particles in a charged-current muon neutrino interaction, the energy reconstruction capability of these particles is of particular interest in SBND.

Two additional rows have therefore been added alongside each CC 0π proton multiplicity contribution, the first counts only protons with kinetic energy above 20 MeV, the goal threshold of SBND which was shown to be possible with excellent vertex reconstruction in ArgoNeuT [193]. The second counting only those with kinetic energy above 50 MeV, which is the current capability demonstrated by the MicroBooNE experiment [196], due to the difficulty in automating the vertex reconstruction in high-statistics samples.

The result of the 20MeV threshold is an increase in the 1,2 and 3 proton rates with respect to that which has no threshold, by decreasing the >3 rate. In the 50MeV case,

only the 1p rate is increased with respect to the no-threshold case and all others go down by incrementally larger amounts.

Table 5.2 highlights that the aforementioned ν_μ CC 0π final state will be the most abundant in SBND data, for instance making up 51.5% of the total $\nu_\mu + \nu_e$ content of the 'Nieves' model configuration. It will also be possible to break down this abundant final state into various proton multiplicities, whilst retaining hundreds of thousands of events. This is an important tool for probing the initial neutrino interaction content of the dataset, for instance the ν_μ CC 0π 2p final state is important for improving our understanding of short range correlations and corresponding bound-nucleon interactions, discussed in section 4.5.5. Events with high pion and proton (n > 2) multiplicities will also help understand the behaviour of hadronic final state interactions and the nuclear model, since the most abundant interactions shown in Table 5.1 (QE, MEC and Res) produce only a single pion and/or a maximum of 2 protons.

In addition to observing high statistics of the most common channels, SBND will be capable of measuring hundreds of events with rare final state topologies, including those containing charged and neutral kaons, charged sigmas and charged lambdas.

Although it is informative to read the contents of each sample in this way, a much more interesting method of presenting the information is through the contributions to various kinematic distributions from initial and final state topologies.

An example can be seen in the true neutrino energy spectra shown in Figure 5.1. These distributions depict the muon and electron neutrino content of the G18_10a_02_11a (Nieves CC QE & CC 2p2h) configuration. The top-left and bottom plots contain the overlaid charged and neutral-current contributions to the muon and electron-neutrino energy spectra respectively. The top-right, stacked, plot breaks the muon-neutrino charged-current component into various final state topological contributions with respect to both proton and pion multiplicities.

Note that no energy thresholds are placed on any particles throughout the kinematic studies, such that we can determine how the continuous range of possible threshold values may impact the various contributions to each distribution. Similarly, all particles are allowed to exit the detector, which will not be the case in real data since we cannot measure the calorimetry of escaping particles. Ultimately, these studies aim to improve our understanding of the neutrino interaction generator output in the context of SBND, rather than realistic capabilities of the detector itself.

Hadronic Final State	Model Configurations (CC QE & CC 2p2h)			
	Nieves	**SuSAv2**	**LS-E**	**SM**
	ν_μ Charged Current			
Inclusive	3,997,680	4,284,429	3,982,337	4,136,515
0π + X	2,916,218	3,205,219	2,913,042	3,059,135
0π 0p	37,046	41,683	37,337	45,316
0π 1p	1,654,344	1,807,774	1,599,552	2,050,570
0π 1p ($>$ 20 MeV)	1,763,812	1,931,406	1,708,194	2,095,631
0π 1p ($>$ 50 MeV)	1,731,683	1,944,339	1,688,232	1,930,148
0π 2p	470,724	539,943	514,509	298,405
0π 2p ($>$ 20 MeV)	498,181	590,309	559,500	341,698
0π 2p ($>$ 50 MeV)	369,006	435,164	426,481	242,523
0π 3p	173,937	188,778	178,265	147,306
0π 3p ($>$ 20 MeV)	194,523	215,391	201,324	163,380
0π 3p ($>$ 50 MeV)	97,679	100,151	93,518	81,316
$0\pi > 3$p	580,166	627,039	583,377	517,536
$0\pi > 3$p ($>$ 20 MeV)	222,931	230,760	212,497	187,098
$0\pi > 3$p ($>$ 50 MeV)	39,659	40,117	34,583	33,721
$1\pi^+$ + X	533,107	531,612	526,606	531,533
$1\pi^-$ + X	35,964	35,586	34,512	35,076
$1\pi^0$ + X	303,781	303,393	299,566	302,162
2π + X	157,081	157,089	157,081	157,081
$\geqslant 3\pi$ + X	51,527	51,527	51,527	51,527
K^+K^- + X	395	395	395	395
$K^0\bar{K}^0$ + X	448	448	448	448
Σ_c^{++} + X	193	193	193	193
Σ_c^{+} + X	96	96	96	96
Λ_c^{+} + X	598	598	598	598
	ν_μ Neutral Current			
Inclusive	1,622,875	1,622,875	1,622,875	1,622,875
0π	1,113,177	1,113,177	1,113,177	1,113,177
$1\pi^\pm$ + X	202,599	202,599	202,599	202,599
$\geqslant 2\pi^\pm$ + X	68,154	68,154	68,154	68,154
	ν_e			
Inclusive	41,084	43,319	41,533	41,639

Table 5.2.: SBND Event Rates broken down in terms of the hadronic final state topology for 4 model configurations. The proton multiplicity contributions are further categorised by kinetic energy, E_k, such that we can get an idea for the event rate with respect to realistic energy thresholds. A threshold of 50 MeV corresponds to the current capabilities of existing LArTPC experiments and 20 MeV is the goal threshold of SBND.

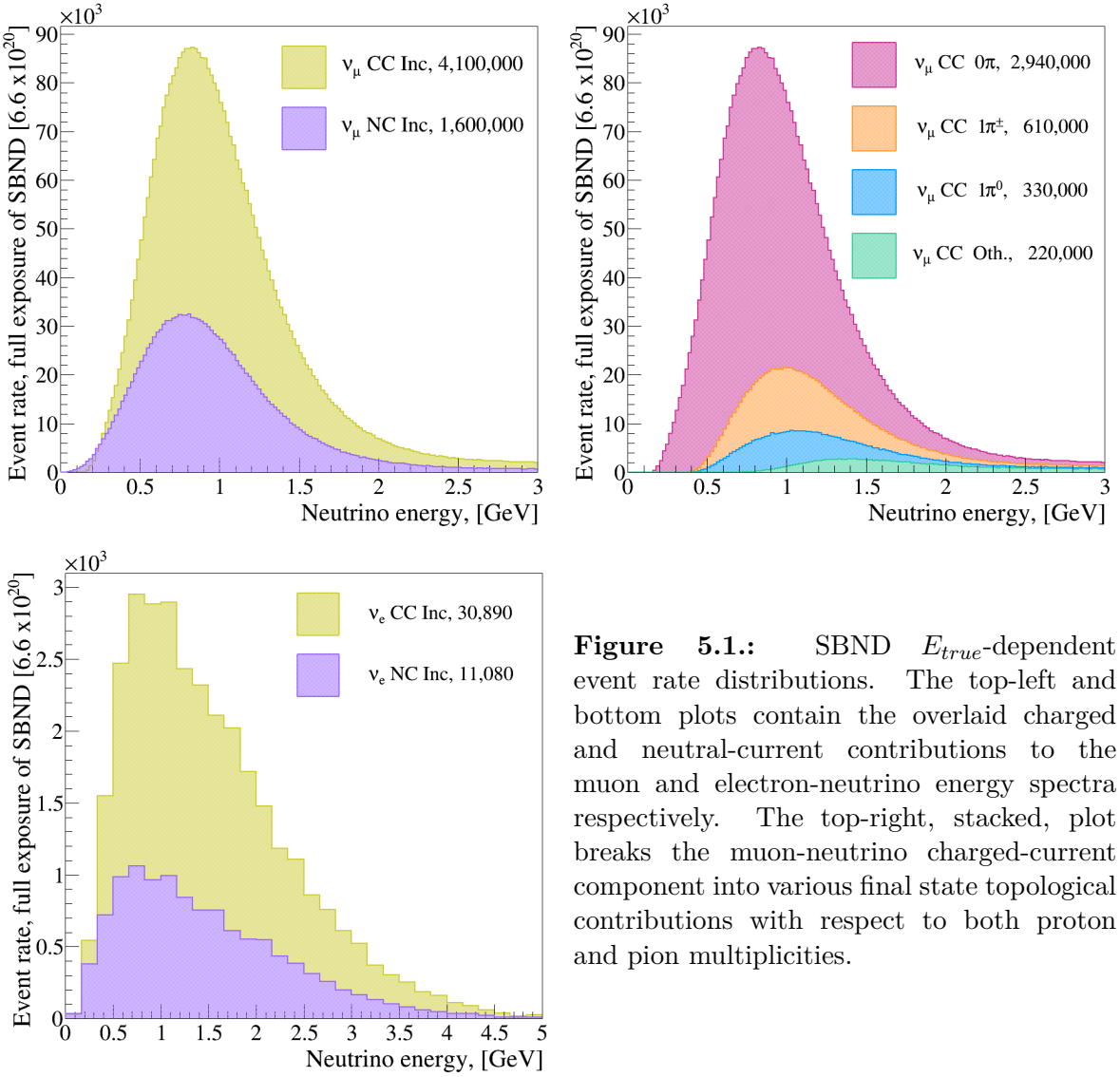

Figure 5.1.: SBND E_{true}-dependent event rate distributions. The top-left and bottom plots contain the overlaid charged and neutral-current contributions to the muon and electron-neutrino energy spectra respectively. The top-right, stacked, plot breaks the muon-neutrino charged-current component into various final state topological contributions with respect to both proton and pion multiplicities.

The kinematic studies presented here will follow a consistent format. Whenever 4 separate histograms are presented in a single figure, they will adhere to this layout:

Llewellyn Smith Empirical (LS-E)	Nieves
Smith Moniz (SM)	SuSAv2

Each variable will first be presented as a set of 4 stacked histograms in either or both of the true initial ν_μ-Ar interaction and final-state topology. A further comparison of the model configurations will then be presented as an overlay of the relevant integrated event-rate. Finally, multiple 1D slices of a 2D distribution will be presented.

5.2. ν_μ CC 0π kinematic studies

5.2.1. Neutrino energy

The true muon-neutrino energy distributions of the ν_μ CC 0π final state are shown in Figure 5.2 as histograms stacked in terms of the neutrino interaction which took place. Note that the Smith Moniz model configuration does not contain 2p2h, see section 4.5 for details. Instead the rate of QE interactions is much higher, such that the integrated event rate does not differ largely from that of the other configurations.

The LS-E configuration has the largest contribution from lower-energy neutrinos undergoing the 2p2h (MEC) interaction. In contrast SuSAv2 has a noticeably lower contribution from low-energy neutrinos undergoing 2p2h, although it is difficult to determine if this is due to a larger QE interaction rate for low-energy neutrinos.

In order to better-assess the overall differences between the muon-neutrino energy-dependent event rates in each configuration, the area-normalised integrated rates are plotted as an overlay in Figure 5.3. This overlay confirms that the LS-E QE+2p2h rate at low energies is lower than Nieves and SuSAv2, but it is matched if not slightly superseded by the QE-only low-energy rate in Smith Moniz. The Nieves model configuration has the largest value of neutrino energy at the peak, with the largest difference in peak E_ν-values of 6.7%. The spread of standard deviations is 5.3% of the average value.

5.2.2. Proton multiplicity and momentum

Since neutrons are neutral particles and do no produce electromagnetic showers as they traverse the liquid argon, they are not directly observable in an LArTPC detector. Protons are therefore the dominant, directly-observable, hadron in the final state of a CC 0π sample, and varying numbers of them may be emitted from the nucleus following the ν_μ-Ar interaction. The proton multiplicity is therefore a parameter of interest in this final state topology, and Figure 5.4 breaks down these multiplicities into the initial ν_μ-Ar interactions which produced them.

These plots confirm the increased rate of the QE contribution to the 1p final state in the Smith Moniz configuration, along with the substantially larger contribution from the 1p final state to the entire sample. It is difficult to distinguish differences between

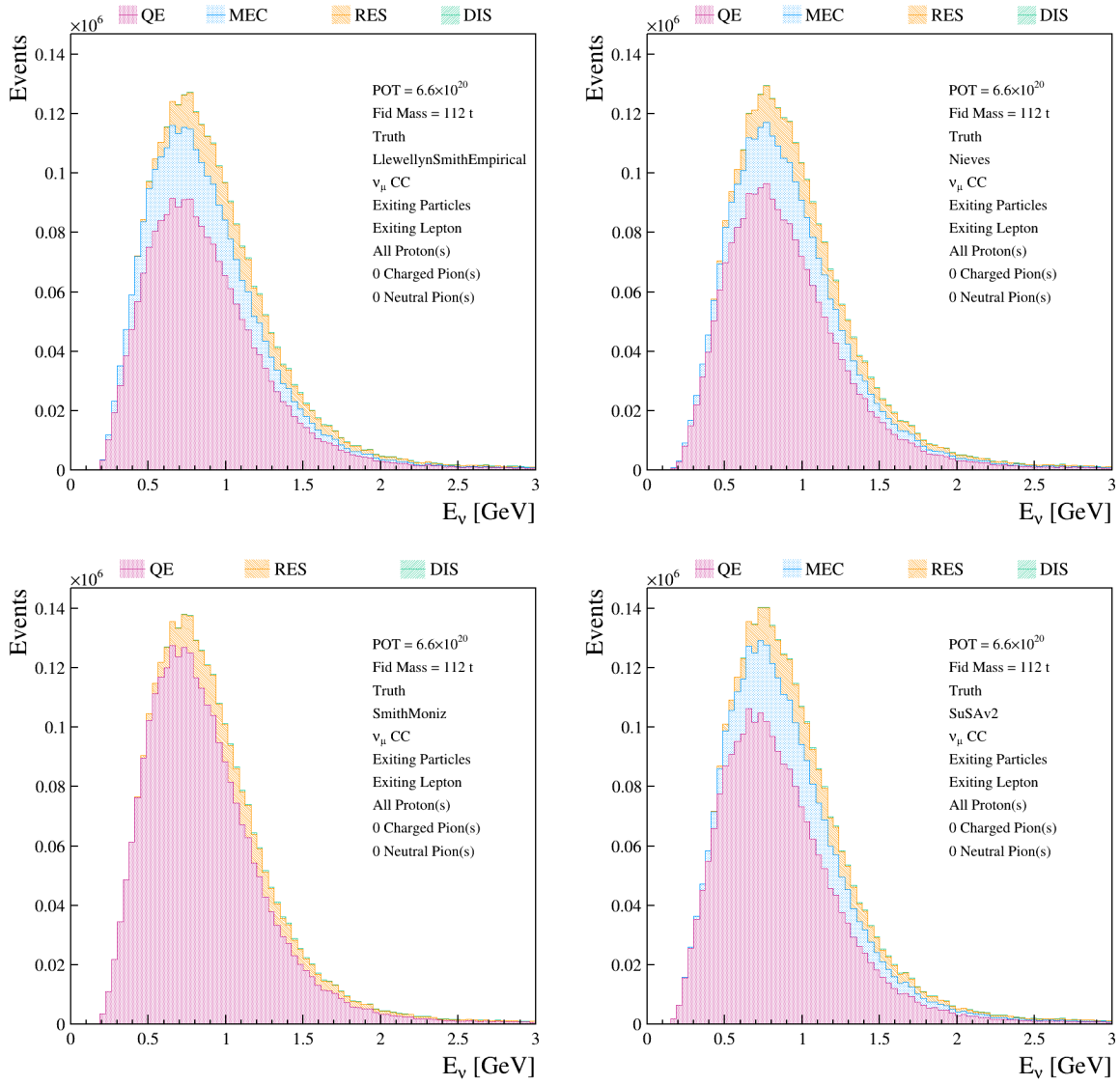

Figure 5.2.: SBND E_{true}-dependent CC 0π event rate distributions for the 4 GENIE model configurations based on G18_10a_02_11a. From top-left to bottom-right are Llewellyn Smith-Empirical, Nieves, Smith-Moniz, SuSAv2. All distributions are stacked with a breakdown of the true interaction type which took place between a muon neutrino and the argon.

the other model configurations through this study, since the RES and DIS contributions are identical by construction.

It is not until you look at the shape comparisons of the proton multiplicities between models in Figure 5.5 that you notice the comparability in the relative rates of all multiplicities in the Nieves and SuSAv2 configurations. This is likely due to the similarities in the fundamental definition of the two QE+2p2h models. As expected, Smith Moniz boasts the largest 1p rate with consistently lower rates at all other multiplicities. LS-E

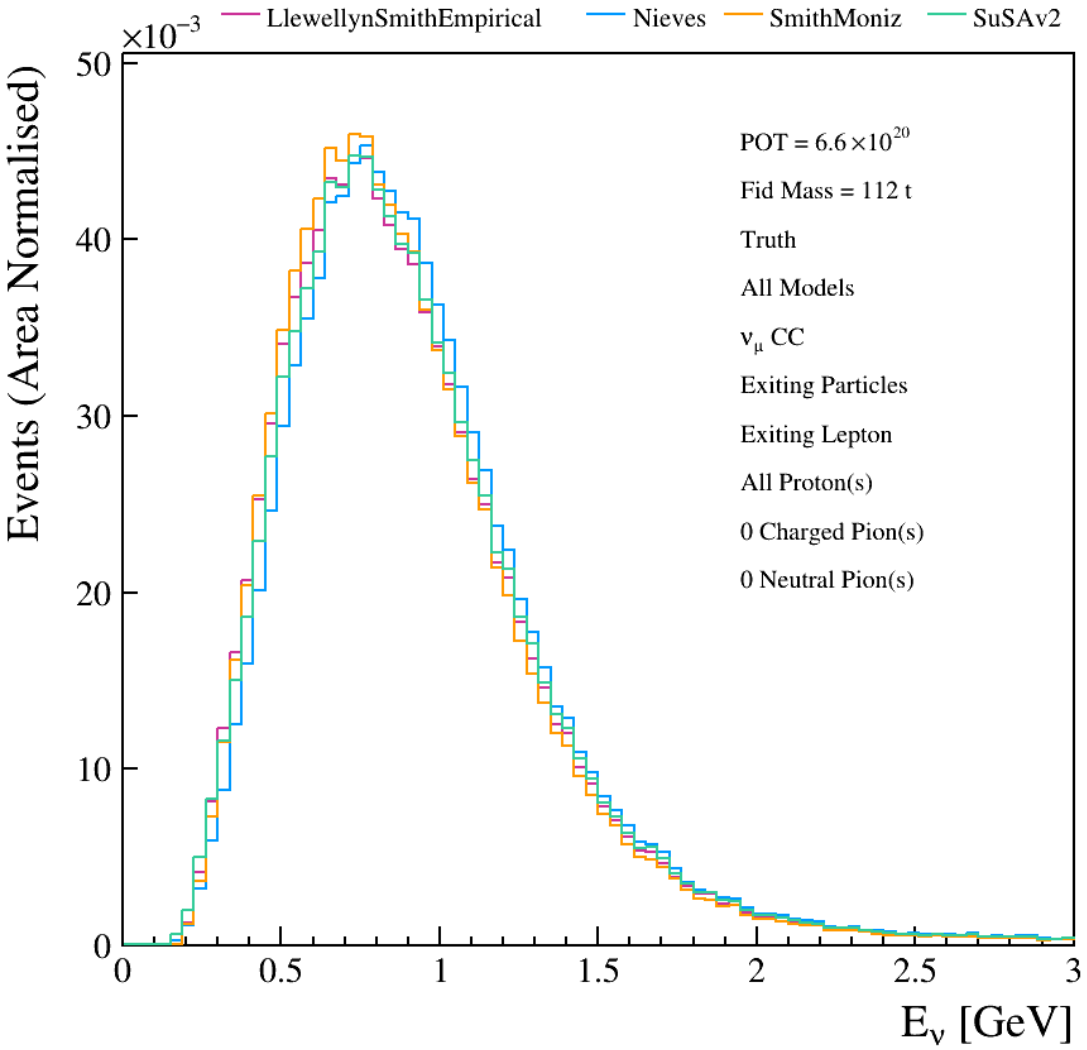

Figure 5.3.: SBND E_{true}-dependent CC 0π event rate distributions for the 4 GENIE model configurations based on G18_10a_02_11a. The integrated event rates for all 4 model configurations are overlaid and normalised to their respective event rates such that shape differences can be determined.

has the highest relative rate of 2p and lowest of 1p, with higher multiplicities remaining consistent with Nieves and SuSAv2.

Knowing the importance of carefully reconstructing protons in this final state, we can also look into an additional parameter, the leading proton momentum, p_p. Figure 5.6 does exactly this by presenting them in the usual way, with stacked histograms broken down by interaction type. These distributions are much less regular than those of p_μ and E_ν, and we can therefore learn a little more about model-based characteristics from this parameter.

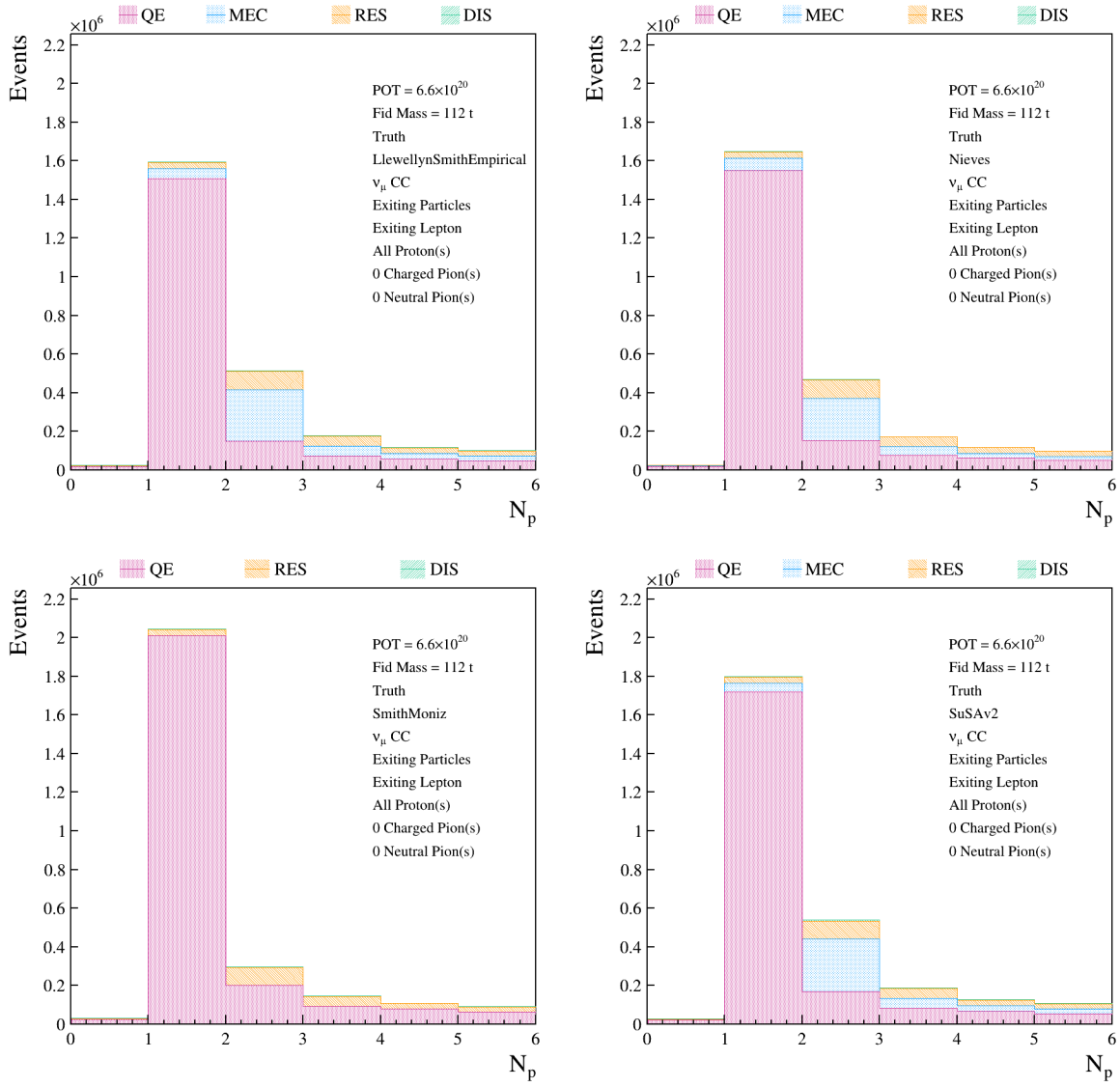

Figure 5.4.: SBND N_p-dependent CC 0π event rate distributions for the 4 GENIE model configurations based on G18_10a_02_11a. From top-left to bottom-right are Llewellyn Smith-Empirical, Nieves, Smith-Moniz, SuSAv2. All distributions are stacked with a breakdown of the true interaction type which took place between a muon neutrino and the argon.

Firstly, across all the model configurations there is a second bump in the momentum at around 0.6 GeV. The interaction breakdown shows that this is caused by a general increase in leading proton momentum following resonant and 2p2h interactions. As a result, this secondary bump is noticeably lower in the Smith Moniz configuration, even when only comparing them side-by-side. The Nieves configuration also has a smaller contribution to this second bump from 2p2h interactions than the LS-E and SuSAv2 models. The general QE shape is substantially different in general across all the models.

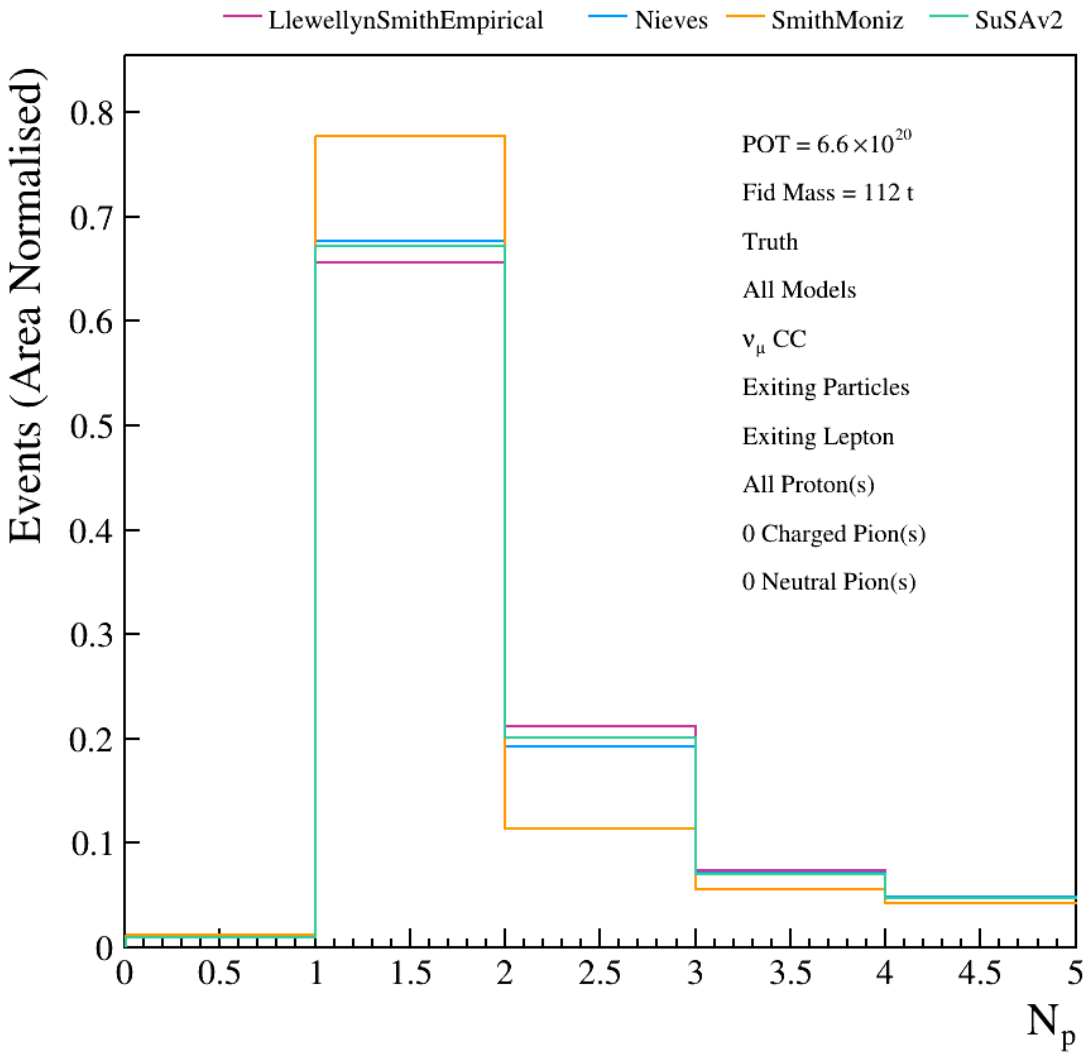

Figure 5.5.: SBND N_p-dependent CC 0π event rate distributions for the 4 GENIE model configurations based on G18_10a_02_11a. The integrated event rates for all 4 model configurations are overlaid and normalised to their respective event rates such that shape differences can be determined.

The next study involves the overlay of all model configurations for the p_p parameter in Figure 5.7. The grey and black dashed lines included in this plot are the ArgoNeuT and MicroBooNE energy thresholds respectively, which were accounted for in Table 5.2. Previously these thresholds were defined in terms of the proton E_k, but for the purposes of this study they have been translated into momentum thresholds via equation 5.1,

$$p = \sqrt{(E_k + M)^2 - M^2}, \tag{5.1}$$

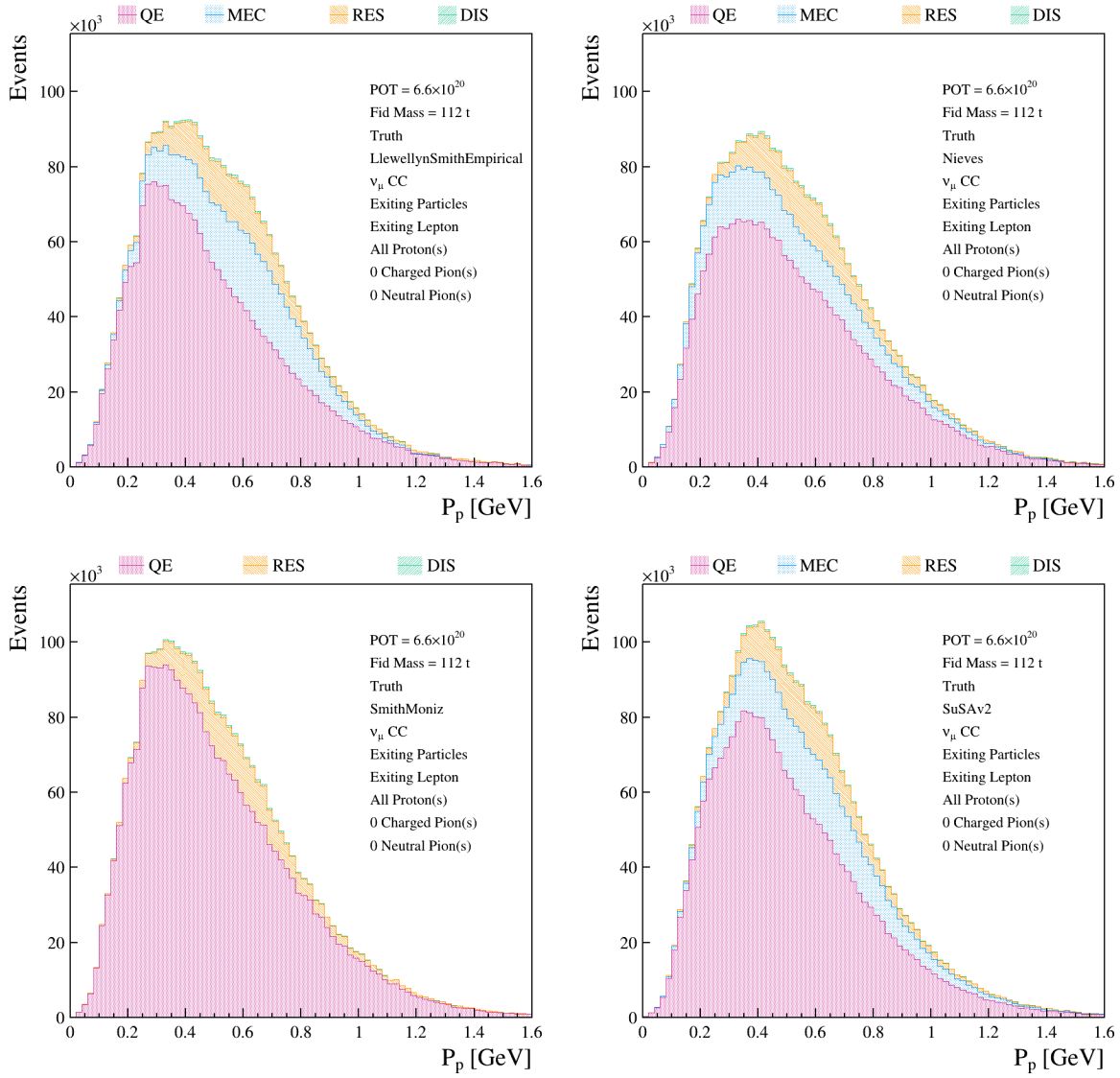

Figure 5.6.: SBND p_p-dependent CC 0π event rate distributions for the 4 GENIE model configurations based on G18_10a_02_11a. From top-left to bottom-right are Llewellyn Smith-Empirical, Nieves, Smith-Moniz, SuSAv2. All distributions are stacked with a breakdown of the true interaction type which took place between a muon neutrino and the argon.

where, $M = M_p = 0.938$ GeV. Therefore $E_k = 20, 50$ MeV correspond to $p \approx 200, 300$ MeV respectively.

One significant feature of this comparison is in the model-dependence of the consequence of setting each proton momentum threshold. If we are able to resolve protons down to $p_p = 200$ MeV, then the number of protons we lose are reasonably model-independent. However, if we are only able to resolve protons down to $p_p = 300$ MeV, then a significant model-dependence is introduced in the number of protons we lose. The observed

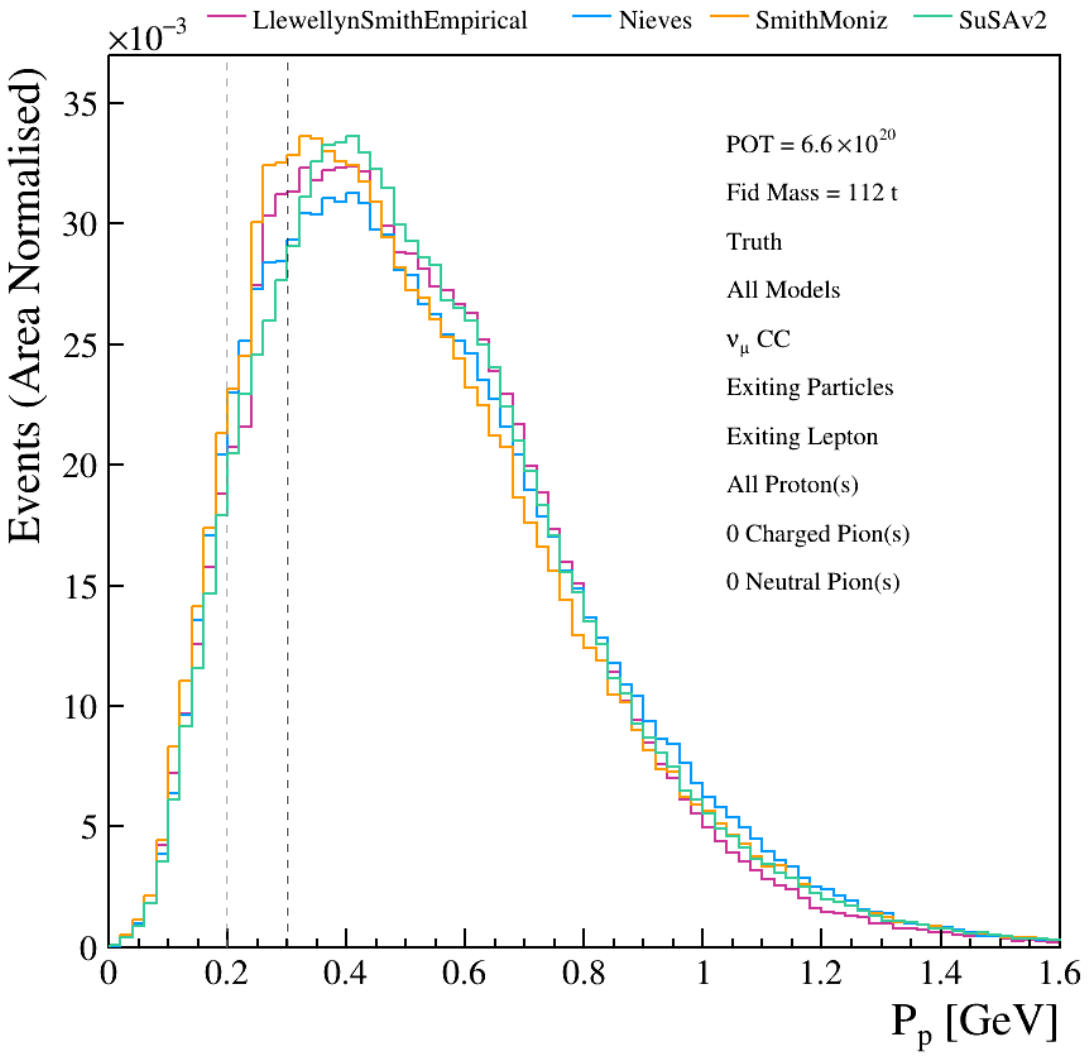

Figure 5.7.: SBND p_p-dependent CC 0π event rate distributions for the 4 GENIE model configurations based on G18_10a_02_11a. The integrated event rates for all 4 model configurations are overlaid and normalised to their respective event rates such that shape differences can be determined. The grey (left) and black (right) dashed lines correspond to the ArgoNeuT and MicroBooNE momentum thresholds respectively.

model-dependence is a strong motivator for pushing the momentum threshold down, to maximise the possibility of determining which model agrees best with the measured data.

Finally, the reduced size of the second bump in the Smith Moniz sample is clear in this overlay.

5.2.3. Muon kinematics

Having studied the kinematics of the neutrino and the multiplicities of the final state protons, we now turn to examining the kinematics of the muon produced following a charged-current interaction with no pions in the final state. The two parameters of interest are the momentum of the muon, p_μ, and the angle of its trajectory with respect to the neutrino beam direction, θ_μ.

The ν_μ-Ar interaction breakdown of the muon momentum distributions are given in Figure 5.8. One noticeable feature is the larger 2p2h contribution to events with $p_\mu < 0.3$ GeV in the LS-E sample than in the rest of the models containing 2p2h.

There is slightly more to see in the integrated overlay of the muon momentum in Figure 5.9. Firstly, the observation in Figure 5.8 that there appeared to be a larger low-momentum contribution from 2p2h in LS-E seems to have amounted to an overall reduction in the muon momentum peak. In addition, although we have previously noticed general differences in the Smith Moniz distributions due to the lack of 2p2h, it also seems to have resulted in a generally narrower muon momentum peak.

The final observable studied is the scattering angle of the muon. Figure 5.10 contains the distributions from each model broken down into initial interactions. In general, there are mostly forward-going muons in every configuration ($\cos\theta_\mu \rightarrow 1$), which is to be expected from the primary interaction product. It is difficult to pick-out any interaction-dependent differences when the distributions are side-by-side in this parameter, over and above what has been deduced in previous studies.

It is more informative to move directly to the integrated, area-normalised overlay to compare the muon scattering angle across the models. Figure 5.11 shows that the Smith Moniz configuration produces the lowest rate of forward going muons, whilst LS-E and SuSAv2 produce the highest rates in almost equal measures. Looking back at Figure 5.10 we can actually see that the 2p2h interaction does produce mostly forward-going muons. Given that LS-E has the highest relative rate of 2p2h interactions, whilst SuSAv2 has the highest rate of QE+2p2h, these findings are consistent.

The high statistics available in SBND will consequently allow us to probe the low-momentum transfer ($\cos\theta_\mu \rightarrow 1$) region of neutrino interactions on argon, where data-MC discrepancies have been recorded, for instance by MicroBooNE [197] and T2K [198]. It will be useful to utilise the abundance of different proton multiplicities (in particular 0p and 1p) for these studies, in order to maximise the contribution from true CC QE

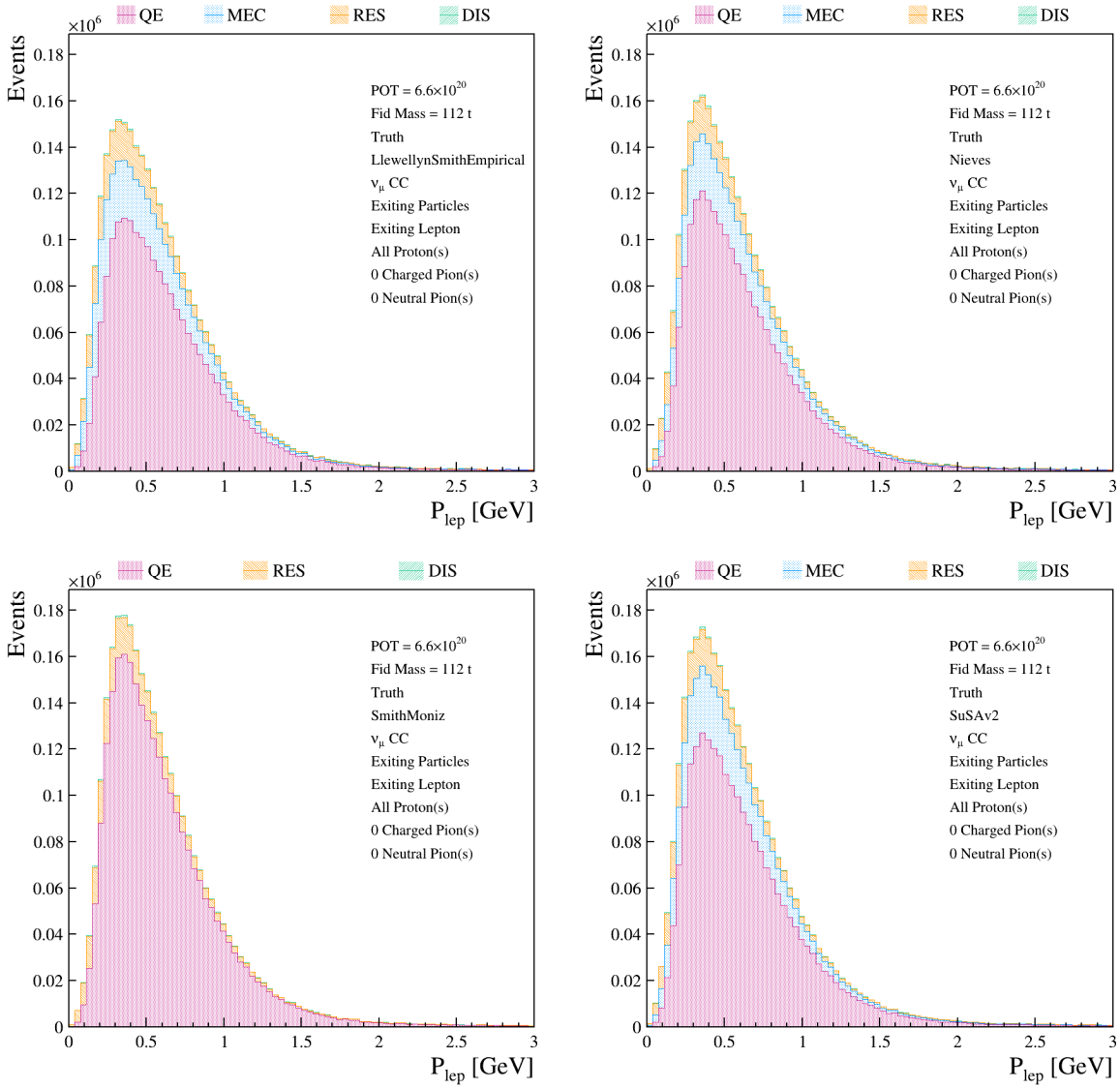

Figure 5.8.: SBND p_μ-dependent CC 0π event rate distributions for the 4 GENIE model configurations based on G18_10a_02_11a. From top-left to bottom-right are Llewellyn Smith-Empirical, Nieves, Smith-Moniz, SuSAv2. All distributions are stacked with a breakdown of the true interaction type which took place between a muon neutrino and the argon.

interactions and therefore optimise the momentum transfer calculation and neutrino energy reconstruction. The clear model-dependence of the low momentum-transfer region in the SBND MC samples could provide an insight into the source of this discrepancy.

One final way to present these kinematics is to take $\cos\theta_\mu$ slices of the 2D $p_\mu - \cos\theta_\mu$ distribution, in order to determine the angular contributions to the momentum distributions. Figure 5.12 therefore presents 9 such $\cos\theta_\mu$ slices, with the p_μ overlay distributions area-normalised for observing shape differences as per the other overlay plots.

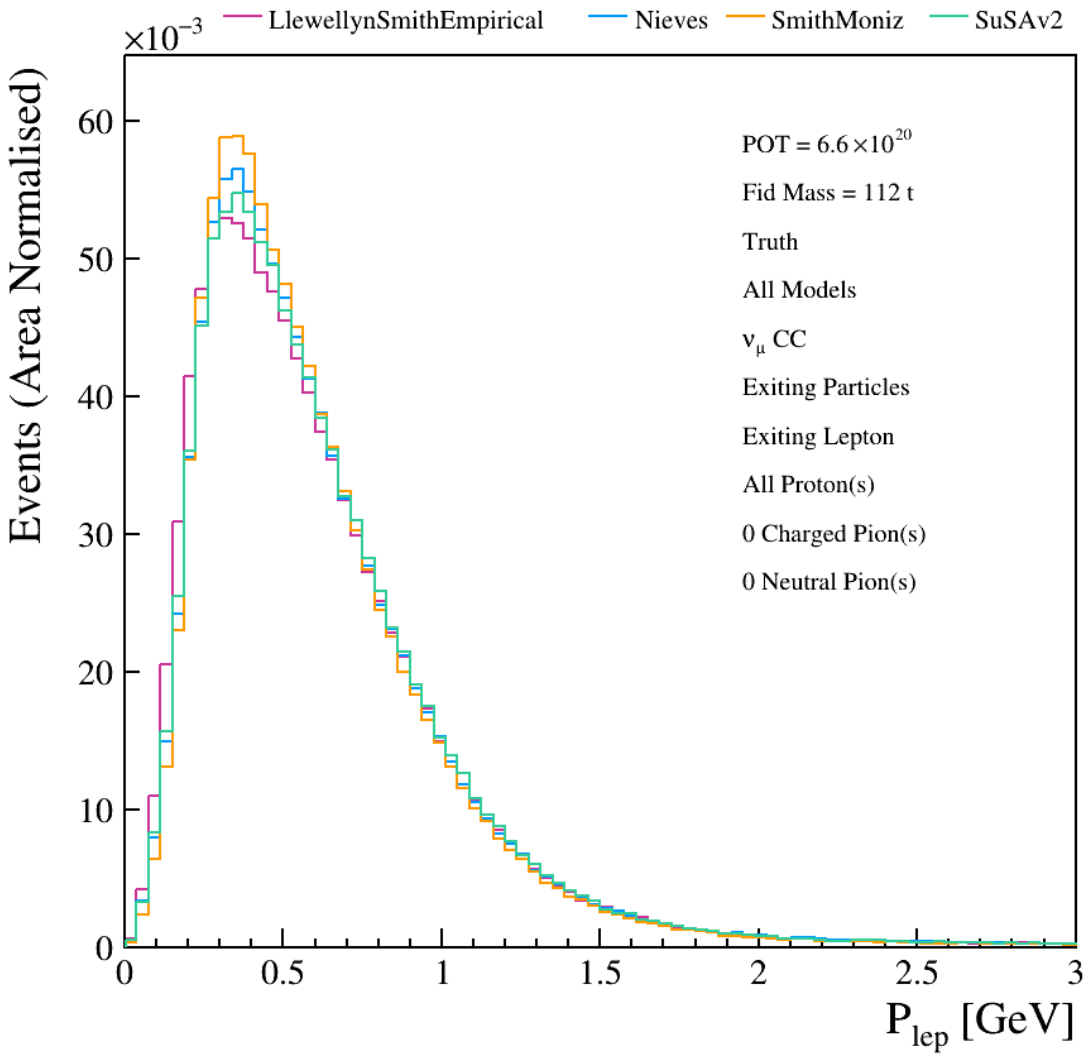

Figure 5.9.: SBND p_μ-dependent event rate distributions for the 4 GENIE model configurations based on G18_10a_02_11a. The integrated event rates for all 4 model configurations are overlaid and normalised to their respective event rates such that shape differences can be determined.

The most substantial differences appear in the higher scattering angle ($\cos\theta_\mu < 0.6$) slices, wherein it is once again clear that the LS-E model has the lowest muon momentum peak, however this is no longer distinct for μ angles above $\cos\theta_\mu > 0.6$. It is also interesting to see that there is no region of muon momentum which is responsible for the reduced rate of forward-going muons in the Smith Moniz model configuration.

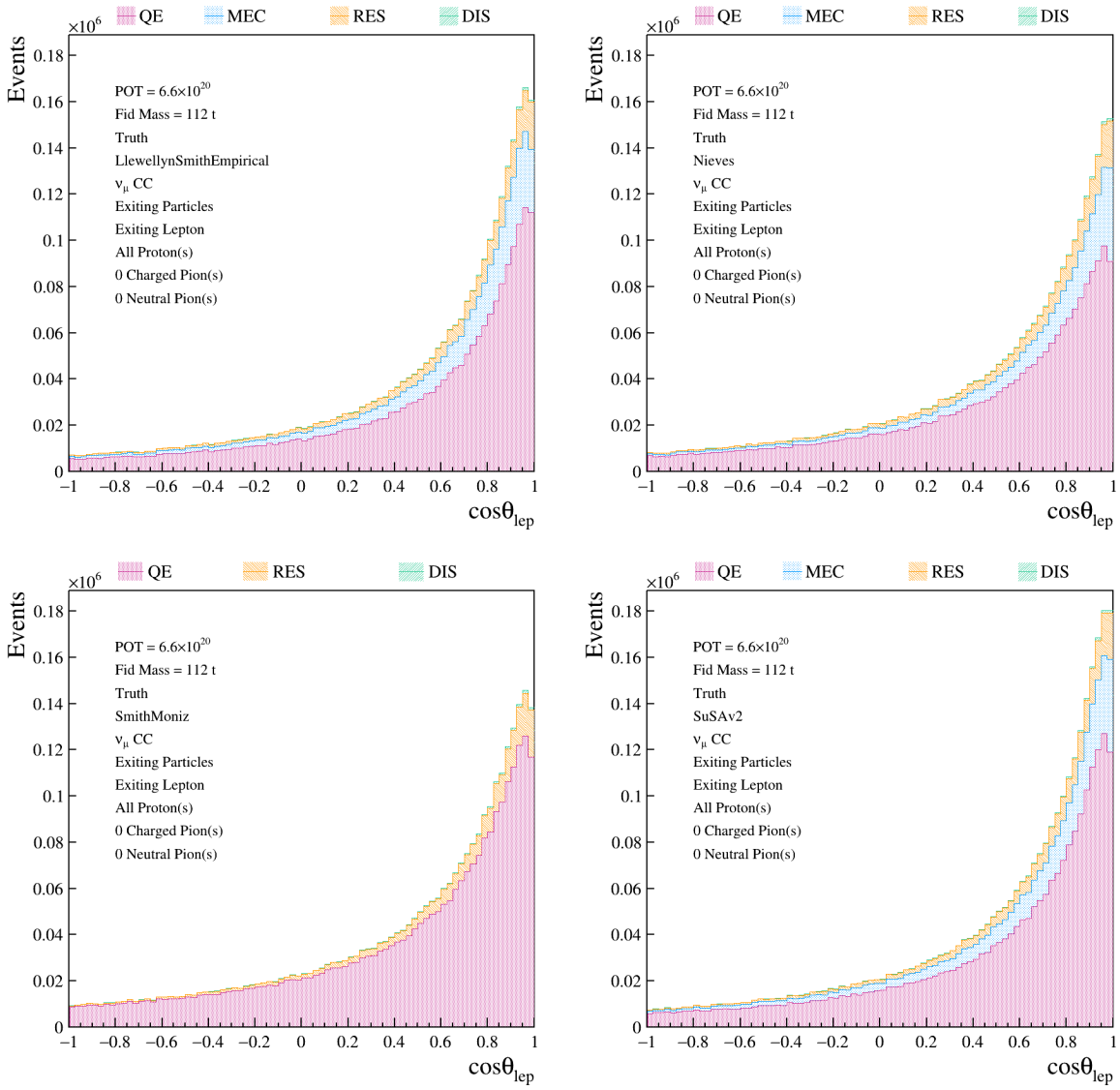

Figure 5.10.: SBND $\cos\theta_\mu$-dependent CC 0π event rate distributions for the 4 GENIE model configurations based on G18_10a_02_11a. From top-left to bottom-right are Llewellyn Smith-Empirical, Nieves, Smith-Moniz, SuSAv2. All distributions are stacked with a breakdown of the true interaction type which took place between a muon neutrino and the argon.

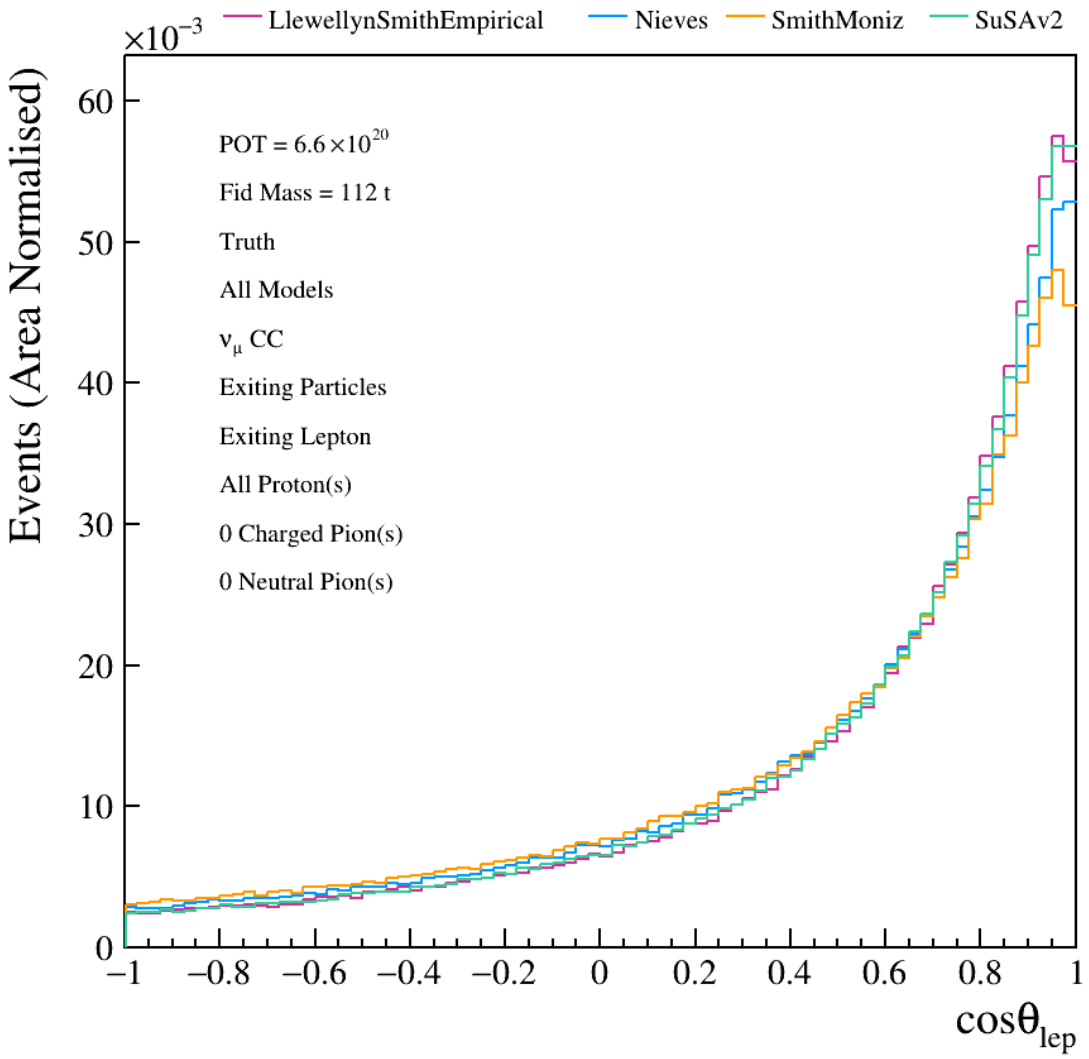

Figure 5.11.: SBND $\cos\theta_\mu$-dependent CC 0π event rate distributions for the 4 GENIE model configurations based on G18_10a_02_11a. The integrated event rates for all 4 model configurations are overlaid and normalised to their respective event rates such that shape differences can be determined.

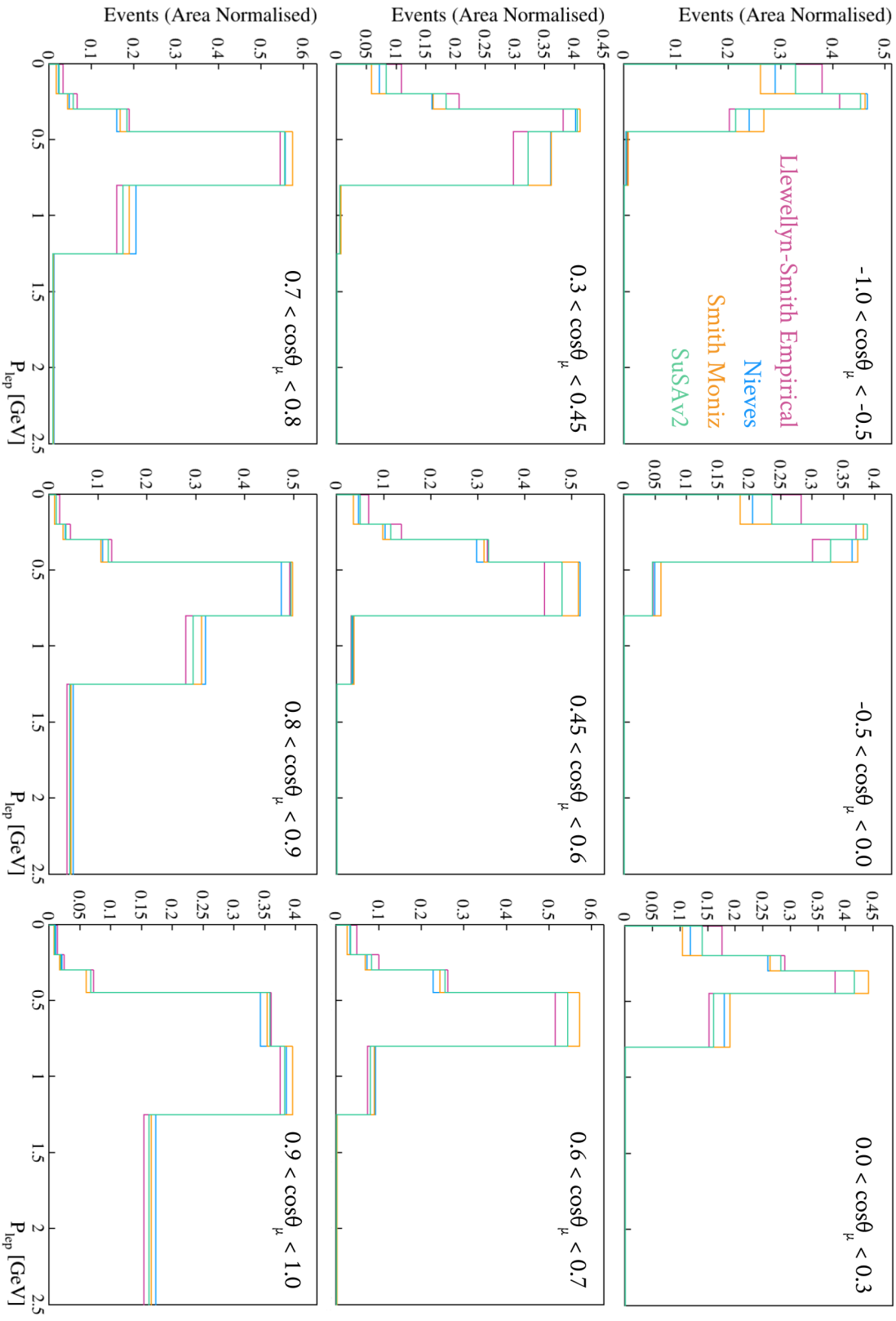

Figure 5.12.: SBND $\cos\theta_\mu$ slices of the p_μ-dependent CC 0π event rate distributions for the 4 GENIE model configurations based on G18_10a_02_11a. The integrated event rates for all 4 model configurations are overlaid and normalised to their respective event rates such that shape differences can be determined.

5.3. Concluding the physics studies

The results presented in this chapter provide us with an interesting and exhaustive summary of the contents and kinematic characteristics of multiple GENIE model configurations. By constructing direct comparisons between the initial interaction contributions to the ν_μ CC 0π event rate in terms of various kinematic parameters, we can identify the consequences of the nuclear effects discussed in section 4.5.5 in a number of ways. Similarly, by holding the FSI model constant across the model configurations, we are solely interpreting the cross-section model-dependence of these effects.

One observed consequence of changing between definitions of the QE+2p2h models in each configuration, is the starkly different final-state proton multiplicities. This could be driven by either the variation in the configurations at the cross-section level, or by variations in the down-stream nuclear effects caused by the kinematic differences between the models. This is a prime example of complexities involved in the heavy-nuclear modelling procedure. In addition, the model-dependence of the muon scattering angle could provide a new insight into existing low momentum-transfer MC-data discrepancies, in particular through the assessment of different final state proton multiplicities.

When analysing physics results in SBN and SBND, it will be useful to refer back to these studies for understanding intricacies of their model-dependence. For instance, if a systematic uncertainty which is only expected to modify pion-production interactions modifies events in a seemingly-pure CC 0π sample, we know that it is due to the non-negligible rate of pion absorption during FSI.

We can use these studies to determine areas of the simulation and analysis chain in which improvements must be a priority. For instance, there exists a model-dependence in the location of the proton momentum threshold, which substantiates the need for optimising our proton momentum reconstruction beyond what is currently possible in MicroBooNE.

SBND will be capable of measuring neutrino interaction cross-sections with unprecedented precision, in the energy range concerned with numerous physical processes. Making these measurements in exclusive topologies and across multiple kinematic phase-spaces will be possible without limiting their statistical sensitivity. As such, our theoretical understanding and modelling of neutrino interaction phenomenology will be constrained considerably with respect to existing data. Similarly, the interaction systematic uncertainties can be constrained through these targeted, topological measurements.

Chapter 6.

SBN sterile oscillation analysis inputs and fitting procedure

The general oscillation analysis procedure involves a simultaneous fit of systematic and oscillation parameters to kinematic distributions of topological event samples from all SBN detectors, providing an indirect extrapolation from the near to the far detectors. The method is summarised graphically in Figure 6.1.

Event rate predictions are constructed in each sample, beam and detector defined in the analysis. A physics hypothesis may then be combined with any prior systematics and both are applied to the event rate predictions. These predictions and the corresponding observations from any number of detectors and samples can then be combined in a binned-likelihood fitting procedure, from which the sensitivity to the physics hypothesis can be determined at a given confidence level. Every aspect of this method will be discussed in detail throughout this chapter.

The first step in the analysis procedure is to construct Monte Carlo templates of the event rate predictions in a given kinematic parameter space, and will be defined in section 6.1. The (3+1) sterile neutrino oscillation hypothesis will be defined in section 6.2, along with the aforementioned binned-likelihood fitting method used to perform the sensitivity studies.

The ν_μ disappearance oscillation analyses presented in chapters 7 and 8 will primarily use samples of events constructed with the methods described in section 6.3. SBN-specific analysis choices will be discussed in section 6.4. Analysis-specific methods, such as the sensitivity calculation procedure, will be discussed in the relevant chapters.

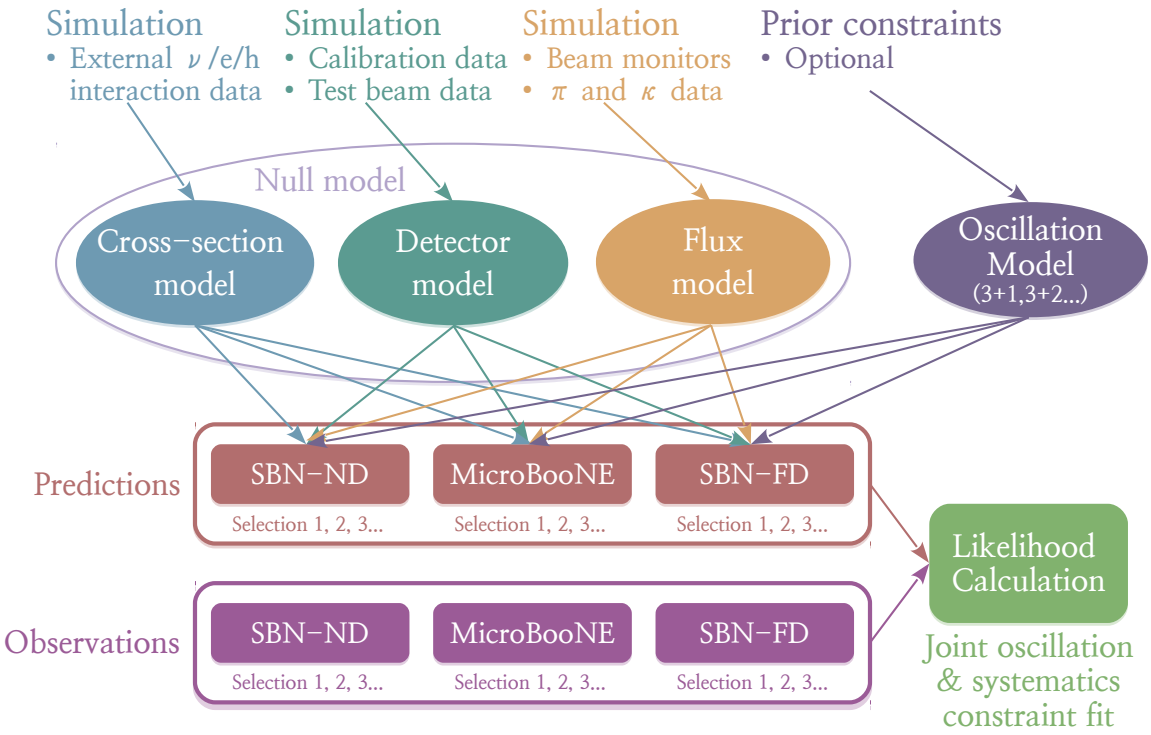

Figure 6.1.: General overview of the 3-detector joint oscillation analysis procedure.

The systematic uncertainties on the predictions must be parametrised such that they can be processed by the fitting framework. This is made complex when fitting a binned-likelihood, as some granularity in the data is lost if the observable kinematic binning definition is coarse with respect to variations of the systematic parameters. A huge amount of work has been done to mitigate this issue, and will be explained in section 6.5.

6.1. MC templates of neutrino event rate predictons

The main inputs to the oscillation sensitivity calculation are the predicted (Monte Carlo) neutrino interaction event rates, which may be parametrised in many ways. For instance, the predictions can be defined for any combination of,

- Beam configurations, b
- Detectors, d
- Observed final state topologies, s,

in terms of the desired observable kinematic parameters in a reconstructed parameter bin, r. The Monte Carlo prediction will be constructed with both true and reconstructed quantities, as an ($N_R \times N_T$) matrix, where N_R is the total number of reconstructed bins and N_T is the total number of true bins in the parameter space.

For instance, one may choose to construct the prediction in the SBND detector, using the FHC BNB configuration, for the CC 0π final state topology in terms of the reconstructed neutrino energy, E_r. These dependencies are summarised for the event rate predictions in Monte Carlo Templates (MCT's),

$$T = T_{b;d;s;m}(r, t), \tag{6.1}$$

an ($N_R \times N_T$) matrix which maps between the event rate in true and reconstructed kinematic parameter space such that t is a bin in the true kinematic parameter space and m is the true interaction mode which took place in each event.

The definition of T can then be used to construct Monte Carlo predictions of the observable event rate, $n^{pred}_{b;d;s}(r; \vec{\theta}; \vec{f})$ for all of the pre-defined dependencies. The event rate prediction may also encapsulate physics effects (for instance the oscillation hypothesis) and/or systematic variations, through the incorporation of the relevant set of physics, $\vec{\theta}$ and systematic[1], $\vec{f}$ parameters,

$$n^{pred}_{b;d;s}(r; \vec{\theta}; \vec{f}) = \sum_m \sum_t P_{b;d;m}(t; \vec{\theta}) \cdot R_{b;d;s;m}(r, t; \vec{f}) \cdot T_{b;d;s;m}(r, t) \cdot N^{MC}, \tag{6.2}$$

where $P_{b;d;m}(t; \vec{\theta})$ parametrises the impact of a physics effect on the event rate for a given true kinematic bin, $R_{b;d;s;m}(r, t; \vec{f})$ defines the response of the event rate to variations of each systematic parameter in true-reconstructed parameter space and $N^{MC} = \mathrm{POT}^{data}_{b;d}/\mathrm{POT}^{MC}_{b;d}$ is the normalisation by which to scale the event rate, to account for the POT which was used to construct the sample of neutrino events with respect to the nominal POT in the analysis. The SBN-specific components of equation 6.2 followed by the fitting method they are applied to are discussed throughout the rest of this chapter.

[1]Systematic parameters are also referred to as nuisance parameters and these may be used interchangeably from hereon.

6.2. Fitting procedure

6.2.1. Sterile neutrino oscillation hypothesis

Chapter 7 will present an analysis of the SBN sensitivity to the (3+1) sterile oscillation model through the observation of ν_μ disappearance in SBN. The physics hypothesis used in the construction of the MCT's for this analysis will be discussed here.

Given that existing results suggest $\Delta m^2_{41} \gg \Delta m^2_{sol,atm}$ in the (3+1) sterile neutrino hypothesis, the effective two-flavour oscillation probability can be employed. This probability is parametrised by Δm^2_{41} and $\sin^2 2\theta_{\mu\mu}$ for ν_μ disappearance searches, as per equation 2.40. SBN will be sensitive to the same region of parameter space previously explored by MiniBooNE and MINOS/MINOS+ and shown in Figure 2.13, where $10^{-2} < \Delta m^2_{41}$ eV^2 and $10^{-3} < \sin^2 2\theta_{\mu\mu} < 1$. SBN will aim to push below the existing $\sin^2 2\theta_{\mu\mu}$ limit.

Due to the short baseline of the SBN experiment, along with the validity of the approximation that $\Delta m^2_{41} \gg \Delta m^2_{sol,atm}$, $\Delta m^2_{sol} = \Delta m^2_{atm} = 0$, SBN is completely insensitive to active neutrino oscillations. The active neutrino oscillation hypothesis is therefore not applied alongside the sterile hypothesis in the SBN (3+1) sensitivity analyses and $\sin^2 2\theta_{\mu\mu}$ is the relevant mixing parameter in the two-flavour approximation.

The fits presented in chapter 8 are an assessment of only the systematic contributions to the SBN ν_μ disappearance analysis. In this case, the MC templates will therefore be constructed assuming a null sterile neutrino physics hypothesis, such that $P_{b;d;s;m}(t, \vec{\theta}) = 1$.

6.2.2. Binned-likelihood ratio

SBN oscillation analyses are performed by making comparisons between MC predictions and real or fake sets of data using the approach outlined in this section. First, for each of the predefined d, b, s in the reconstructed kinematic parameter space, the MC predictions, $n^{pred}_{b;d;s}(r; \vec{\theta}; \vec{f})$, are constructed using equation 6.2 and the real or fake data, $n^{data}_{b;d;s}(r)$, is measured or defined. The binned-likelihood method is used for comparing between the two event rates through the minimisation of,

$$\chi^2 = -2 \ln \mathscr{L}(\vec{\theta}; \vec{f}) = -2 \ln \mathscr{L}_0(\vec{\theta}; \vec{f}) - 2 \ln \mathscr{L}_{phys}(\vec{\theta}; \vec{f}) - 2 \ln \mathscr{L}_{syst}(\vec{f}), \tag{6.3}$$

where,

$$\chi^2_0 = -2\ln\mathscr{L}_0(\vec{\theta};\vec{f}) = 2\sum_{b,d,s,r}\left(n^{data}_{b;d;s}(r)\cdot\ln\frac{n^{data}_{b;d;s}(r)}{n^{pred}_{b;d;s}(r;\vec{\theta};\vec{f})} + (n^{pred}_{b;d;s}(r;\vec{\theta};\vec{f}) - n^{data}_{b;d;s}(r))\right), \tag{6.4}$$

is the contribution to the likelihood ratio from SBN data. In addition,

$$\chi^2_{phys} = -2\ln\mathscr{L}_{phys}(\vec{f}) = 0, \tag{6.5}$$

is the physics penalty term based on prior constraints on new physics parameters and is not implemented in the SBN-only analyses.

The systematic parameters are eliminated by profiling in the fits, through the inclusion of a penalty term in the definition of χ^2 to account for prior constraints and correlations of systematic parameters. This penalty term takes the form,

$$\chi^2_{syst} = -2\ln\mathscr{L}_{syst}(\vec{f}) = (\vec{f}-\vec{f}_0)^T\cdot\mathbf{V^{-1}}\cdot(\vec{f}-\vec{f}_0), \tag{6.6}$$

where $\vec{f}_0$ is the set of nominal systematic parameter values, $\vec{f}$ is the set of systematic parameter values currently set by the fit and $\mathbf{V}$ is the covariance matrix containing their uncertainties.

This contribution is essentially a systematic penalty which is intended to penalise the fit increasingly with larger systematic pulls.

When the (3+1) sterile neutrino oscillation hypothesis is implemented, the mixing parameters which are not held constant under the ν_μ disappearance hypothesis are allowed to float in the fits between their physical parameter limits, $0 < \sin^2 2\theta < 1$. Initially, they are set to the current global best-fit values shown in Table 6.1.

In all fits, the relevant set of systematic parameters are initially set to their nominal value, and are allowed to float between $-5\sigma_f < f < 5\sigma_f$, where σ_f is the prior uncertainty on the parameter f. The aforementioned penalty is applied as an incentive to minimise the magnitude of any single pull.

The advantage of the likelihood ratio method is that in the large-sample limit, when there are many events in every fitted bin, the quantity $-2\ln\mathscr{L}(\vec{\theta};\vec{f})$ has a χ^2 distribution and

Parameter	Global Best Fit
$\lvert U_{e4}\rvert$	0.116
$\lvert U_{\mu 4}\rvert$	0.135
$\sin^2 2\theta_{\mu\mu}$	0.0716
$\sin^2 2\theta_{\mu e}$	0.000981
$\sin^2 2\theta_{ee}$	0.0531
Δm^2_{41}	1.32

Table 6.1.: Global best fit sterile neutrino oscillation parameters [28]

it can therefore be used as a goodness-of-fit test. The MIGRAD minimisation method is used to execute the fits, along with the HESSE (Hessian) error determination, and are both implemented inside MINUIT [199].

6.3. Constructing the physics sample

Presently, the reconstruction in both SBND and ICARUS is under active development, such that a completely validated production is not yet available in either detector. The primary sample used in this analysis is therefore a truth-based sample, with simple modifications applied to emulate shape and rate differences which might be expected in fully-reconstructed events. The sample of neutrino scattering events used in the main analyses in this thesis is constructed in the following way,

1. Generate $\mathcal{O}(10^6)$ ν_μ GENIE neutrino scattering events in the active volume of each detector
2. Propagate the final state particles through GEANT4 in each detector
3. Apply a combination of threshold cuts and smearing to the propagated particles, to emulate a 'reconstructed' sample
4. Select only the charged-current neutrino interaction events from the 'reconstructed' sample
5. Define the 'reconstructed' neutrino energy in each selected event.

Steps 1 and 2 are discussed in sections 4.5 and 4.7 respectively. Steps 3-through-5 will be discussed here.

6.3.1. SBN geometries

The SBN volume definitions are given in Table 6.2, and refer to the active and fiducial volumes of each detector. An active volume is a geometry definition which contains all the liquid argon, and extends to the outer walls of each detector. The fiducial volumes are smaller geometries, entirely contained within one of the active volumes in a detector. A fiducial volume is used to minimise the number of tracks and showers which leave the active volume following a neutrino interaction, such that the number of particles it is possible to reconstruct is maximised in the event. A fiducial volume also provides shielding from external activity in the detector volume.

SBND has a single active volume with two fiducial volumes separated by the CPA. MicroBooNE has a single active volume with a single fiducial volume contained within it. In the case of ICARUS, there are two separate cryostats, each with two TPC's, therefore the ICARUS detector comprises 2 active and 4 fiducial volumes.

6.3.2. Truth-based event selection

The pseudo-reconstruction method employed in this analysis is based on the studies performed at time of the SBN proposal [6] in which fake reconstruction and a ν_μ CC event selection are applied simultaneously. The main reason for utilising this approach is that when the new SBN fitting frameworks were developing their analysis procedure, the SBN proposal served as a reference for validation. Having now completed this analysis validation, some features of the proposal-era method have been necessarily updated to account for fundamental modifications to the SBN program.

Given that this entire procedure is a placeholder for when fully-reconstructed samples become available, additional development of the finer details, such as the magnitude of the kinematic thresholds, has not been conducted since the SBN proposal was written. The combined pseudo-reconstruction and selection is described below, followed by a summary of the quantitative, detector-specific definitions.

The first step is to reconstruct and identify muon-neutrino-like interactions from the sample, which involves finding the primary track in every event as follows,

Volume	X [cm]		Y [cm]		Z [cm]	
	Active	Fiducial	Active	Fiducial	Active	Fiducial
SBND TPC1	-199.15, 199.15	-190.0, 5.6	-200.0, 200.0	-185.0, 185.0	0.0, 500.0	15.0, 415.0
SBND TPC2		10.9, 190.9		-185.0, 185.0		15.0, 415.0
MicroBooNE	-1.6, 254.8	13.5, 239.8	-115.5, 117.5	-100.5, 102.5	0.1, 1036.9	15.1, 956.9
ICARUS TPC1	-364.5, -67.9	-356.2, -224.5	-177.4, 143.4	-158.4, 128.4	-910.0, 880.0	-895.0, 800.0
ICARUS TPC2		-207.9, -76.2		-158.4, 128.4		-895.0, 800.0
ICARUS TPC3	67.94, 364.5	76.2, 207.9	-177.4, 143.4	-158.4, 128.4	-910.0, 880.0	-895.0, 800.0
ICARUS TPC4		224.5, 356.2		-158.4, 128.4		-895.0, 800.0

Table 6.2.: The active and fiducial volume definitions used throughout the analyses for SBND, MicroBooNE and ICARUS.

1. Generate events as per steps 1 & 2 above
2. Remove any events whose true interaction vertex is not located in the fiducial volume
3. Remove any events which do not produce a muon or a charged pion track. Events in which muons are produced are the CC signal events, whilst events with no muon but instead have a leading pion are candidate NC background events
4. Remove events in which the primary track,
   a) Has a true kinetic energy, $E_k < 21$ MeV

b) Is entirely contained in the detector but their full trajectory length, $L_c < 50$ cm. This removes any NC backgrounds which aren't likely to be mis-identified in data from the sample

c) Exits the detector but their full trajectory length, $L_e < 100$ cm. This accounts for the ability to reconstruct escaping tracks

5. Assume an 80% reconstruction efficiency by removing 20% of all true signal events. This accounts for the estimated rate of neutrino interaction contamination in the external background removal, along with all other unaccounted-for losses.

Having selected the event, more pseudo-reconstruction can be performed on the remaining tracks in the sample for the purpose of calculating the 'reconstructed' neutrino energy and defining the 'reconstructed' content of the events for exclusive sample definitions. The resulting neutrino-induced sample contamination of the pseudo-selected ν_μ CC Inclusive event rate is 2%.

6.3.3. Reconstructed sample and energy definitions

First, any tracks with true $E_k < 21$ MeV are removed from the event. The true kinetic energy of any remaining tracks are then smeared by selecting a value from a Gaussian with $\mu = E_{k,true}$ and $\sigma = \alpha E_{k,true}$, where,

$$\alpha = \begin{cases} 0.05 & \text{Non-primary tracks} \\ 0.02 & \text{Contained, primary track,} \end{cases} \tag{6.7}$$

where 'primary' tracks refer to the leading lepton (in this case the muon) and 'non-primary' tracks refer to everything else in the final state.

In the case of escaping primary tracks, the amount by which to smear the kinetic energy is defined as a function of track length to emulate Multiple Coulomb Scattering (MCS),

$$\alpha = -A \ln(BL), \tag{6.8}$$

where $A = 0.102$ and $B = 0.0006121$ cm^{-1}. The functional form of equation 6.8 and values of A and B are shown in Figure 6.2 and were defined following a study conducted by the ICARUS experiment [200].

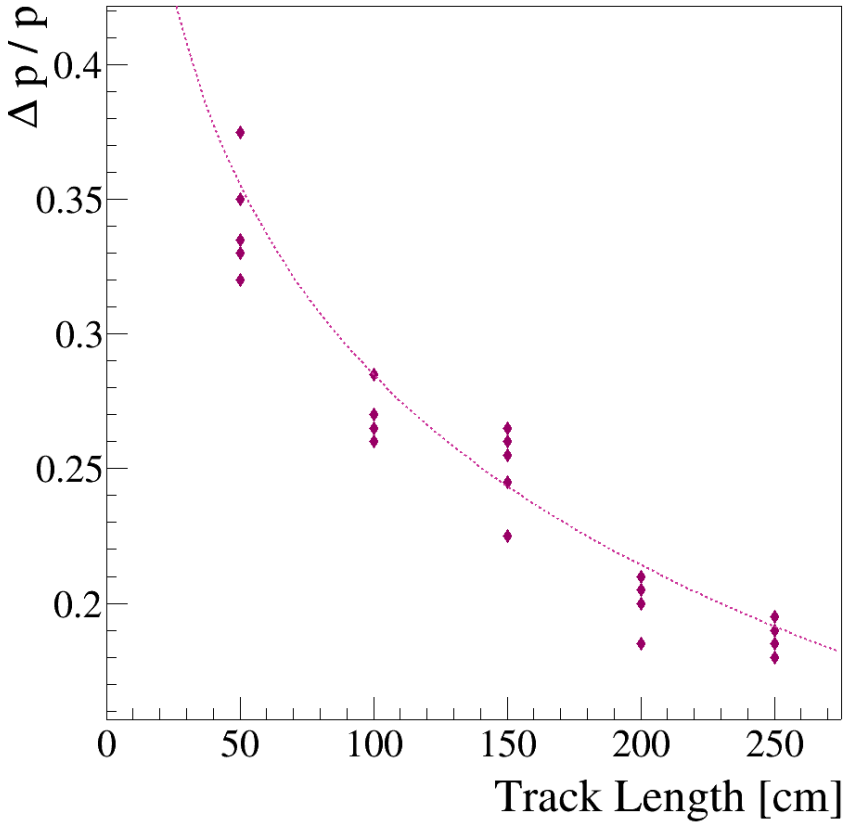

Figure 6.2.: The momentum resolution of reconstructed muons as a function of track length, plotted from data in [200]. The functional form of the line-of-best-fit follows equation 6.8 with $A = 0.102$ and $B = 0.0006121$ cm^{-1}.

No smearing of shower-like particles is performed in the construction of the charged-current inclusive sample. The 'reconstructed' neutrino energy is then simply calculated by,

$$E_\nu = \sum_{n=0}^{N_t} E^n_{smeared}, \tag{6.9}$$

where N_t is the number of tracks above the true kinetic energy threshold and $E^n_{smeared}$ is the smeared total energy of each track.

An exclusive topology can then be selected by counting the remaining 'reconstructed' particles in each event. For instance, a ν_μ CC 0π N_p topology would ensure that the number of $N_{\pi^{\pm,0}} = 0$ without regard for the proton content, N_p, of the final state.

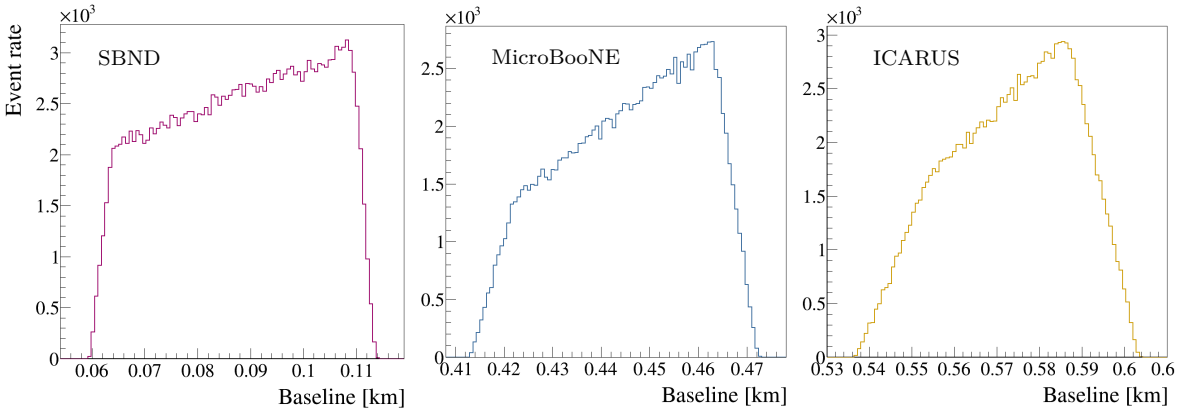

Figure 6.3.: Baseline distributions at each of the SBN detectors

6.4. SBN analysis choices

6.4.1. Baseline approximation

In SBN sterile oscillation searches, the d component of equation 6.2 effectively defines the baseline input to the oscillation probability. Initially, the baselines used at each of the SBN detectors were defined as the single, average value at each location,

- SBND, 87.6m
- MicroBooNE, 446m
- ICARUS, 574m,

such that the probability was calculated once in each of the true energy bins defined in Table 6.5. The true shapes of the baseline distribution in each detector, from which the averages are calculated, are shown in Figure 6.3.

Looking instead at the energy dependence of the baseline in each detector raises a concern about the validity of using such a simple approximation. Figure 6.4 shows that in all three SBN detectors, the baselines distributions are not constant as a function of energy, which is a critical requirement for the approximation to hold.

Having determined that simply using the average value at each detector is not sufficient to describe the baseline, a simple validation procedure was defined. The SBND oscillation probability distribution was constructed as a function of true neutrino energy at a single point in the ν_μ disappearance parameter space, $\sin^2 2\theta_{\mu\mu} = 0.01$, $\Delta m^2_{41} = 50$ eV^2.

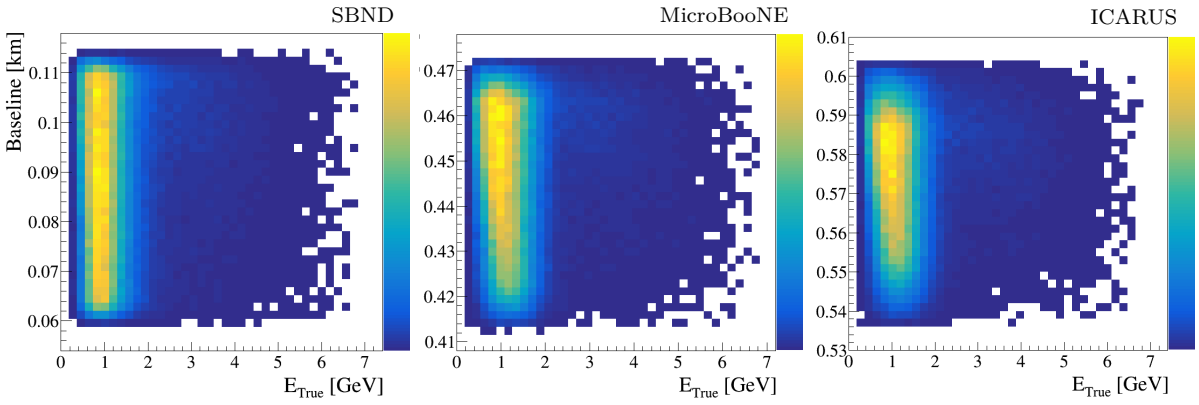

Figure 6.4.: Energy vs baseline distributions in each of the SBN detectors.

The distribution was first constructed using the true value of L/E in every event, before being compared against the calculation with L_{avg}/E. A number of iterative improvements to the baseline definition were implemented in attempts to improve the parametrisation without drastically increasing the computational expense, after each iteration the oscillation probability was calculated and compared against the previous methods and ultimately, truth.

The first iteration involved defining the baseline in splines at 4 points in energy space, in the hopes it would better-represent the true behaviour. This was quickly superseded by the construction of many such splines at many points in energy space. Each incrementally improved the agreement with truth, whilst increasing the computational cost. Ultimately, it was determined that using the true baseline in every event was the only sufficient option for performing physics studies at the precision required in SBN. The oscillation probabilities at the aforementioned point in ν_μ disappearance parameter space for each of the baseline definition iterations are shown in Figure 6.5.

6.4.2. Reaction modes and beam configuration

The reaction modes, m, in the oscillation analysis define the topology of the neutrino interaction within the nucleus, before any FSI take place. Contributions from each reaction mode to the event rate predictions directly depend on the model used as input to the physics simulation. The beam configuration, b, defines the primary neutrino content of the beam and is set to FHC in all SBN analyses, since the BNB currently only runs in neutrino mode.

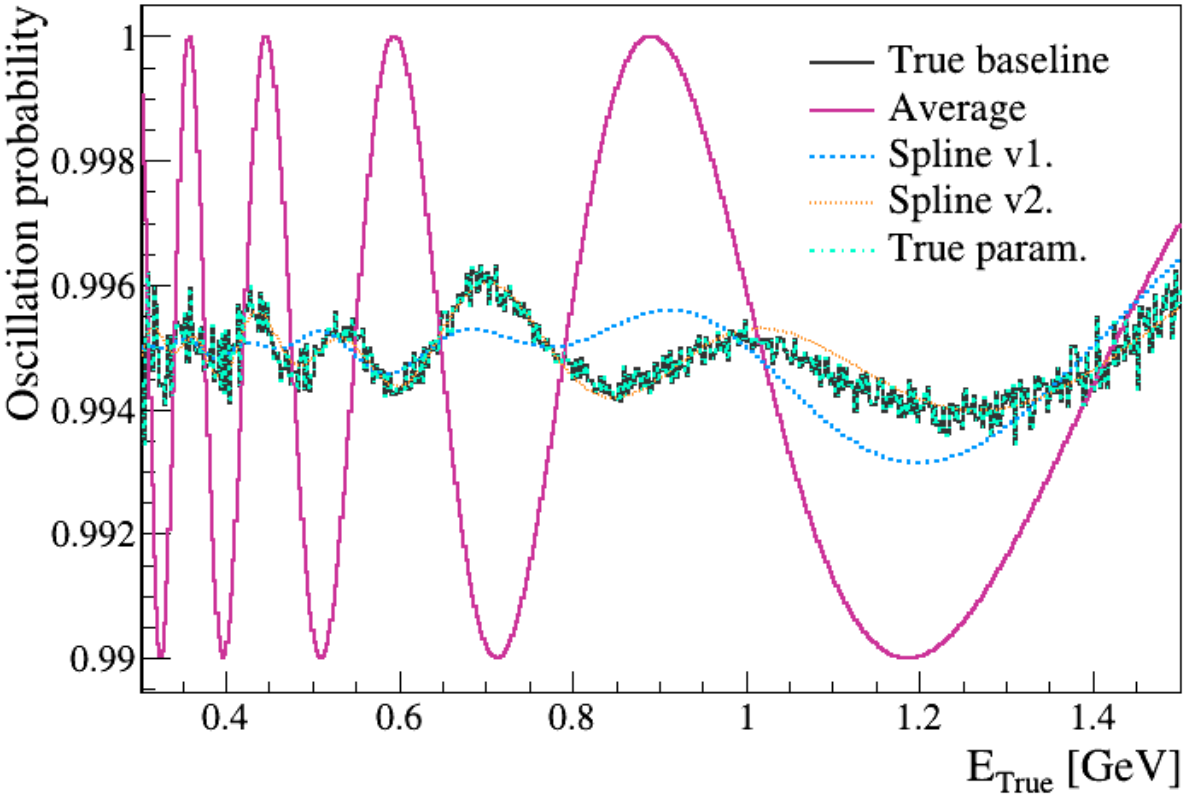

Figure 6.5.: SBN ν_μ disappearance oscillation probability in the (3+1) sterile neutrino framework at $\sin^2 2\theta_{\mu\mu} = 0.01$ & $\Delta m^2_{41} = 50$ eV^2 for each of the methods of parametrising the baseline in SBND.

The list of reaction modes used in the SBN oscillation analysis comes in two forms, fine and coarse. The fine list consists of all possible neutrino interaction modes, categorised by neutrino flavour and current, and is used in the construction of the systematic response functions and MC templates. The coarse list is defined separately for every analysis based on specific features, such as energy and topology of the sample, to absorb the dominant signal interaction modes along with an informative set of background modes. The coarse list is more often used in the presentation of results, and ensures the maximum amount of information is demonstrated concisely. The fine list of reaction modes is given for each neutrino flavour in Table 6.3. The coarse list of reaction modes for the SBN ν_μ CC oscillation analysis is given in Table 6.4.

Note that intranuclear pion production reaction modes, such as resonant interactions and DIS, are combined to form the pion multiplicity modes. This is clearer for studies of final state pion multiplicities in neutrino interactions on heavy nuclei, in which hadron transport plays such a huge part.

ν_μ, $\bar{\nu}_\mu$	ν_e, $\bar{\nu}_e$
CC QE	CC QE
NC Elastic	NC Elastic
CC, NC 2p2h	CC, NC 2p2h
CC, NC $1\pi^\pm$	CC, NC $1\pi^\pm$
CC, NC $1\pi^0$	CC, NC $1\pi^0$
CC, NC $2\pi^\pm$	CC, NC $2\pi^\pm$
CC, NC $2\pi^0$	CC, NC $2\pi^0$
CC, NC $\pi^\pm\pi^0$	CC, NC $\pi^\pm\pi^0$
CC, NC Coh	CC, NC Coh
CC, NC Elastic Scattering	CC+NC Elastic Scattering
NC 1γ	NC 1γ
CC, NC Other	CC, NC Other
Cosmic & Dirt	

Table 6.3.: The extensive list of reaction modes used in the construction of MC templates and systematic response functions in the SBN analysis procedure. These modes correspond to the primary topology of the neutrino interaction, before any FSI take place. Note that many such modes will have negligible contributions from events in the SBN ν_μ CC disappearance analysis, but are still included for validation and completeness purposes. The cosmic and dirt modes represent external backgrounds though are not yet generated as part of the sample.

6.4.3. Samples

The samples used in the SBN oscillation analyses are the ν_μ CC Inclusive, ν_μ CC 0π and ν_μ CC 'Other' final state topologies.

These samples are used in two configurations of the analysis. The first set of fits use the single, ν_μ CC Inclusive sample and the second uses semi-exclusive joint fits of the inclusive sample split into ν_μ CC 0π and ν_μ CC 'Other' final state topologies. It is important to note that the sum-total of the number of events across the two semi-exclusive samples equals that of the inclusive sample.

Reaction modes
Signal
ν_μ CC QE
ν_μ CC 2p2h
ν_μ CC 1π
ν_μ CC 2π
ν_μ CC $>2\pi$
Background
$\bar{\nu}_\mu$ CC
ν_e & $\bar{\nu}_e$ CC
NC 0π
NC Other
Cosmic
Dirt

Table 6.4.: The signal and background reaction modes used in the SBN ν_μ CC disappearance analysis. Note, the external background contributions, *Cosmic* and *Dirt*, are not yet generated as part of the ν_μ CC sample.

6.4.4. Kinematic binning

The SBND neutrino energy distributions shown in Figure 6.6 are taken into consideration when defining the true and reconstructed binning schemes for the ν_μ disappearance oscillation analysis in SBN. The shape of the true and reconstructed energy distributions helps make a number of decisions. First, since the location of the neutrino energy peaks remains consistent between underlying models, the same binning scheme can be used in all iterations of the analysis. Second, the general location and widths of the distributions guides the specification of the variable bin widths across the true and reconstructed space. Although not shown in Figure 6.6, the peak locations and widths are also consistent between SBND, MicroBooNE and ICARUS. The same binning schemes are therefore used across all 3 detectors within the analysis and are defined in Table 6.5.

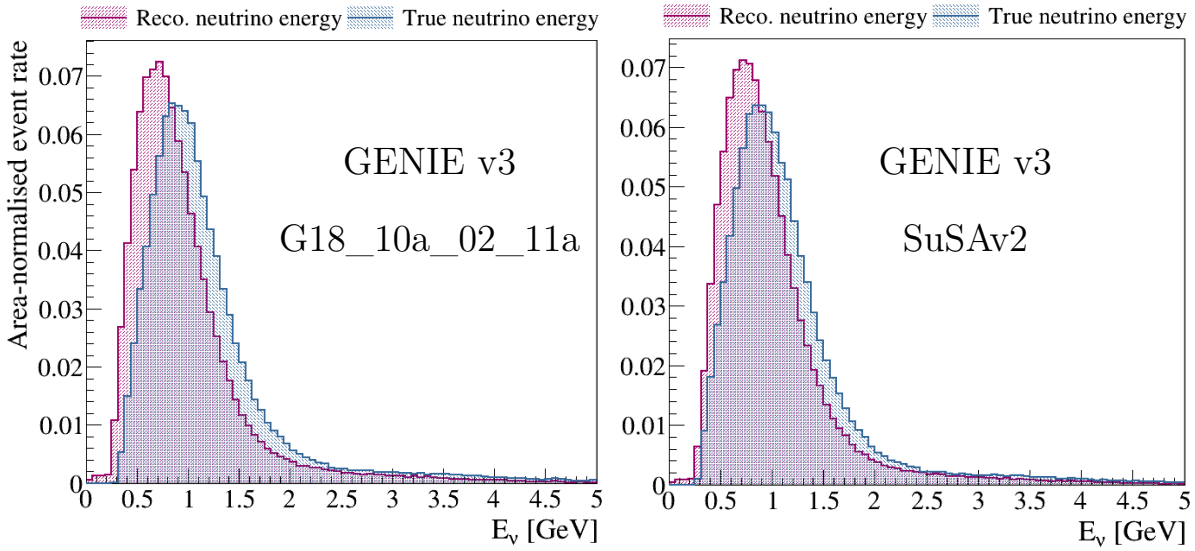

Figure 6.6.: Shapes of the true and reconstructed neutrino energy distributions following the truth-level ν_μ CC Inclusive event selection in SBND. These energy distributions are considered when defining the ν_μ disappearance oscillation analysis true and reconstructed neutrino energy binning schemes. Two of the model configurations discussed in this thesis are shown, G18_10a_02_11a and SuSAv2 from GENIE v3.

E_{Reco}		E_{True}	
Range [GeV]	Width [GeV]	Range [GeV]	Width [GeV]
0.0-0.2	0.2	0.0-0.3	0.3
0.2-0.4	0.1	0.3-0.6	0.1
0.4-1.0	0.05	0.6-1.2	0.05
1.0-1.5	0.25	1.2-1.5	0.3
1.5-3.0	0.5	1.5-3.0	0.5
3.0-10.0	7.0	3.0-5.0	2.0
-	-	5.0-10.0	5.0

Table 6.5.: The true and reconstructed binning scheme used in the construction of MC templates in the SBN ν_μ disappearance analysis. Different binning schemes are used in reconstructed and true space as they are each defined according to the shape and rate of the uniformly-binned reconstructed and true neutrino energy distributions, shown in Figure 6.6.

6.5. Systematic parameter definitions

The systematic inputs to the oscillation analysis together define $R_{b;d;s;m}(r, t; \vec{f})$ in equation 6.2. This section will define and validate how the flux, interaction and detector systematic parameter sets are parametrised in the oscillation analysis.

The flux and interaction systematic uncertainties are separated into two categories by construction. The first are known as 'unisims' in which the prior uncertainty on each parameter is either defined by,

(a) Determining the magnitude of a single, 1σ variation of the parameter

(b) By generating two samples with the parameter switched on in the first and off in the second, and setting the observed rate difference to be the 1σ variation

(c) By generating multiple samples with different underlying models of the parameter and assuming a Gaussian variation of the models, such that the standard deviation corresponds to a 1σ variation of the parameter.

Treating every parameter independently, the magnitude of the prior 1σ uncertainty can then be used as an input to a generation of many MC universes, to determine the effect of varying the parameter with respect to its prior uncertainty on the content and kinematics of neutrino interactions observed in the detector. All unisim parameters must consequently be entirely uncorrelated. The second category contains 'multisim' parameters, in which each universe is constructed following the variation of multiple, correlated parameters within their prior 1σ uncertainties.

Every flux and interaction systematic parameter is represented in the analysis samples by a set of weights, with one weight taken from each of the aforementioned MC universes. In the case of unisim parameters, every weight corresponds to a single n σ variation of the parameter. Whereas for the multisim parameters, every weight corresponds to a unique throw of all correlated parameters used in the construction of the multisim universes.

In order to proceed with the analysis, the weights must be converted into a format which can be processed by the fitter. In the case of unisim parameters, a set of 1D responses[2] are constructed at each point in the 2D true and reconstructed neutrino energy parameter

[2]Systematic parameter response functions are also known as 'splines'. The two will be referred to interchangeably throughout the setup and discussion of the analysis.

space (E_{True}, E_{Reco}) for every neutrino interaction mode listed in section 6.1. The knots, $\mathscr{R}_{m;t,r}(k)$, of the spline are defined as follows,

$$\mathscr{R}_{m;t,r}(k) = \frac{N^{v}_{m;t,r}(k)}{N^{n}_{m;t,r}},\ k \in \{0, \pm 0.5, \pm 1, \pm 1.5, \pm 2, \pm 2.5, \pm 3\}, \tag{6.10}$$

for reaction mode, m, in the (E_{True}, E_{Reco}) bins, t, r. Each of the 13 knots in the response function are defined as the ratio of the $k\sigma$-varied event rate, $N^{v}_{m;t,r}(k)$, to the nominal event rate, $N^{n}_{m;t,r}$ in the corresponding mode and bin.

In the case of the multisim parameters it is not trivial to construct response functions to represent them. This is due to the fact that $n > 1$ correlated parameters are used to construct each event weight such that a single knot does not represent a single variation, and it is not possible to efficiently process high-dimensionality ($\mathcal{O}(10)$) splines. Instead, a covariance matrix is constructed in E_{True} parameter space to define how the multisim systematic variations behave as a function of energy.

The covariance matrix, $\mathbf{C_{ij}}$, is constructed by computing the event rates in each of the U universes and finding,

$$\mathbf{C_{ij}} = \frac{1}{U}\sum_{u=1}^{U}(N^{u}_{i} - N^{cv}_{i})(N^{u}_{j} - N^{cv}_{j}), \tag{6.11}$$

where $N^{u}_{i,j}$ is the event rate in universe u in bin i or j and $N^{cv}_{i,j}$ is the central value, or nominal, event rate in bin i or j.

Frequently throughout the introduction to the analysis procedure as well as within the analysis itself, the neutrino event rate spectra will be shown as a function of the reconstructed neutrino energy with a representative $\pm 1\sigma$ error envelope. These envelopes are produced by constructing 1000 toy MC samples with the specified set of systematic parameters randomised and taking the $\pm 1\sigma$ spread of the 1000 toys with all correlations considered.

6.5.1. Flux systematic parameters

The unisim flux systematic parameters are those associated with hadronic (p, n & $\pi^{\pm}$) interaction cross-sections in the Beryllium target and Aluminium horn, along with optical, beam-focusing parameters. The multisim parameters comprise the differential cross-section associated with the production of π^{+}, π^{-}, K^{+}, K^{-} & K^{0}, in inelastic proton-Beryllium interactions. The subsequent decay of each of these hadrons are the primary neutrino production mechanisms which were discussed in section 4.4.1.

The complete list of flux systematic parameters along with the prior 1σ uncertainties used in the construction of the systematic universe variations are given in Tables 6.6, 6.7 and 6.8. These are associated with the optical unisim parameters, hadronic unisim parameters and multisim parameters respectively. A brief discussion of the unisim and multisim parameters were given in section 4.4.

6.5.2. Parametrising the flux systematics

The left-hand plot in Figure 6.7 demonstrates the 1σ uncertainty envelopes introduced by the flux unisim parameter set with respect to the ν_{μ} CC Inclusive sample of events in SBND. The systematic variations are applied in two ways: first, with the uncertainties taken directly from the universe input files and second, with the uncertainties calculated from the systematic parameter response functions.

The right-hand plot in Figure 6.7 serves as a validation of the systematic parametrisation. The validation involves a double ratio, which is constructed by first taking the ratio of the event rate from the 1σ variation of all flux parameters to the nominal event rate, and then calculating a second ratio, between the spline-based parametrisation and the variations taken from the input universes. A flat line at 1 would indicate perfect agreement between the input variations and the spline-based variations. Although this is not quite the case, the discrepancies are well below 1% across the entire energy range.

In summary, the response functions defined to represent the flux unisim parameters in all SBN oscillation analyses serve as an excellent approximation of the input systematic variations. Appendix B.1 includes examples of the splines themselves along with the plots produced to validate them individually. These studies have been repeated for all input samples, s, and detectors, d, and a comparable level of agreement is observed in all cases. Each of the flux spline parameters are applied to all reaction modes.

Parameter	Description	Uncertainty	
		Be	Al
$f_{\sigma^N_{INEL}}$	Secondary nucleon interactions in the target (Be) and horn (Al), inelastic cross-section	±5%	±10%
$f_{\sigma^N_{QE}}$	Secondary nucleon interactions in the target (Be) and horn (Al), quasi-elastic cross-section	±20%	±45%
$f_{\sigma^N_{TOT}}$	Secondary nucleon interactions in the target (Be) and horn (Al), total cross-section	±15%	±25%
$f_{\sigma^\pi_{INEL}}$	Secondary pion interactions in the target (Be) and horn (Al), inelastic cross-section	±10%	±20%
$f_{\sigma^\pi_{QE}}$	Secondary pion interactions in the target (Be) and horn (Al), quasi-elastic cross-section	±11.2%	±25.9%
$f_{\sigma^\pi_{TOT}}$	Secondary pion interactions in the target (Be) and horn (Al), total cross-section	±11.9%	±28.7%

Table 6.6.: Hadronic secondary interaction flux unisim systematic uncertainties, the cross-sections are treated separately for Aluminium and Beryllium [6].

Parameter	Description	Uncertainty
$f_{SkinEffect}$	Depth that the current penetrates the horn conductor	$< 18\%$
$f_{HornCurrent}$	Current running in the horn conductor	±0.6%

Table 6.7.: Optical, beam focusing flux unisim systematic uncertainties [120].

Parameter	Description	Uncertainty			
		ν_μ	$\bar{\nu}_\mu$	ν_e	$\bar{\nu}_e$
f_{π^+}	ν production mechanism: π^+	±11.7%	±1.0%	±10.7%	±0.03%
f_{π^-}	ν production mechanism: π^-	±0.0%	±11.6%	±0.0%	±3.0%
f_{K^+}	ν production mechanism: K^+	±0.2%	±0.1%	±2.0%	±0.1%
f_{K^-}	ν production mechanism: K^-	±0.0%	±0.4%	±0.0%	±3.0%
f_{K^0}	ν production mechanism: K^0	±0.0%	±0.3%	±2.3%	±21.4%

Table 6.8.: Hadron production flux multisim systematic uncertainties [201].

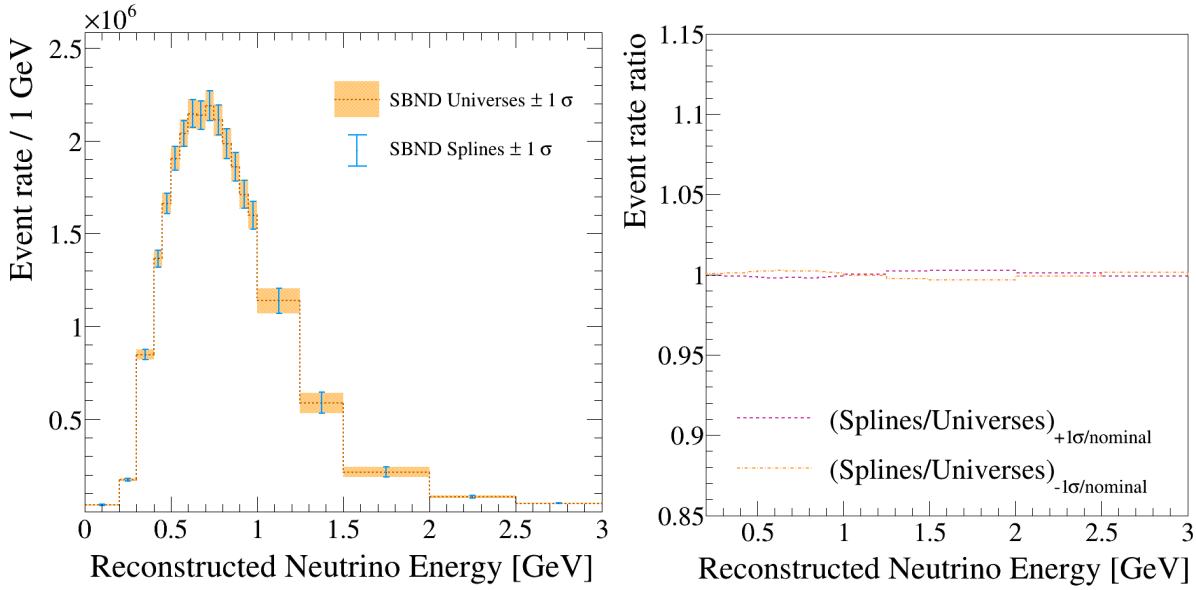

Figure 6.7.: On the left is the SBND ν_μ CC Inclusive event rate plotted with the 1σ SBN uncorrelated flux parameter uncertainty envelope constructed in two ways. The blue band takes the 1σ variation directly from the input universes, and the orange band constructs the 1σ variation from the response functions. On the right is a more quantitative assessment of this comparison, the $\pm 1\sigma$/nominal event rate in each energy bin is calculated in the universe and spline-based uncertainty definitions which is in turn taken as a ratio, pink line.

The multisim flux parameters are defined in a covariance matrix parametrised in E_{True} bins as per equation 6.11. The covariance matrix elements are also separated into neutrino flavour with an appropriate binning defined based on their relative rates. These bin edges are given in Table 6.9 and closely follow the E_{True} scheme laid out in Table 6.5 for muon neutrinos. Figure 6.8 shows the true and covariance-defined 1σ variation envelopes as well as the double ratio which more-quantitatively assesses the performance. The covariance matrix approach is naturally less precise than the response function approach, however the disagreement still does not exceed 1%.

ν_μ		$\bar{\nu}_\mu$	ν_e	$\bar{\nu}_e$
Range [GeV]	Width [GeV]	Bin edges [GeV]		
0.3-0.6	0.1	0.0	0.0	0.0
0.6-1.2	0.05	0.7	0.5	2.5
1.2-1.5	0.3	1.0	0.7	10.0
1.5-3.0	0.5	1.5	0.8	-
3.0-10.0	7.0	2.5	1.5	-
	-	10.0	2.5	-
	-	-	10.0	-

Table 6.9.: The binning defintions in each neutrino flavour which are used in the construction of the flux multisim covariance matrix.

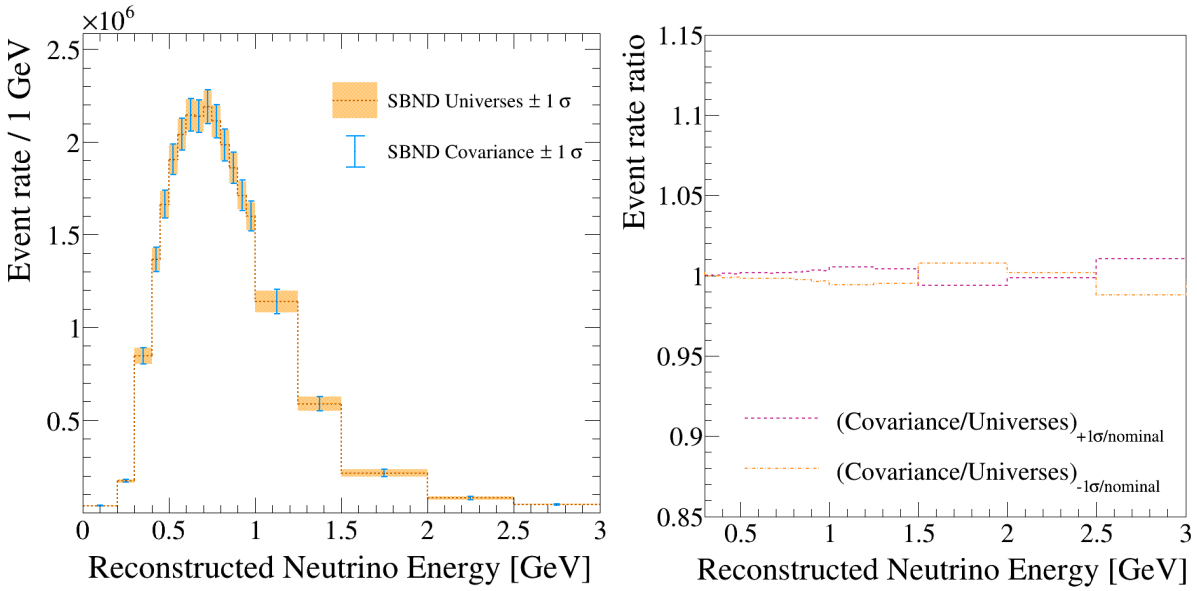

Figure 6.8.: On the left is the SBND ν_μ CC Inclusive event rate plotted with the 1σ SBN correlated flux parameter uncertainty envelope constructed in two ways. The blue band takes the 1σ variation directly from the input universes, and the orange band constructs the 1σ variation from the covariance matrix. On the right is a more quantitative assessment of this comparison, the $\pm1\sigma$/nominal event rate in each energy bin is calculated in the universe and covariance-based uncertainty definitions which is in turn taken as a ratio, pink line.

6.5.3. Interaction systematic parameters

All interaction systematic uncertainties considered in the SBN oscillation analyses concern the GENIE stage of the simulation. There are currently no uncertainties implemented for the subsequent interactions of final state particles as they are propagated by GEANT4 through the liquid argon, following their emission from the argon nucleus. A complete list of the interaction parameters considered in the SBN oscillation analyses along with the prior uncertainties used in the construction of the universe variations are given in Tables 6.10, 6.11 and 6.12.

The GENIE neutrino interaction systematic parameters are all unisims, and every parameter is varied independently in the construction of many MC universes. The full interaction parameter set can be separated into two categories, the first are cross-section modelling parameters, encompassing those related to the parametrisations of the numerous neutrino-argon interaction cross-section models. The second are hadron transport parameters, covering those related to the modelling of intra-nuclear propagation of hadrons. The cross-section modelling parameters have been further-subdivided into those which were available at the time of the SBN proposal publication [6] and those which have been added as an update to the analysis procedure. Note that no FSI parameters were used in the SBN proposal-era of the analysis.

6.5.4. Parametrising the interaction systematics

All interaction systematics are unisims and can therefore be parametrised by the response functions constructed using equation 6.10. The interaction parameters are separated into those which were applied at the time of the proposal, and those which have been added since. The 'proposal'-'modern' split will persist through the analysis, to maintain the ability to validate the analysis against that which was performed for the SBN proposal.

The two interaction parameter sets are validated using the same procedure as that of the flux, the results of which are given for the proposal parameter set in Figure 6.9 and the modern parameter set in Figure 6.10. Example interaction splines along with their individual validation are given in appendix B.2. Although there are 20 and 22 proposal and modern parameters respectively, compared with the 8 from the flux, the agreement between the input and parametrised SBN proposal-era systematic uncertainties is extremely precise.

Parameter	Description	$\delta P/P$
$f_{M_A^{CCQE}}$	Axial mass for CC quasi-elastic	-15% +25%
$f_{M_A^{CCRes}}$	Axial mass for CC resonance neutrino production	±20%
$f_{M_A^{NCRes}}$	Axial mass for NC resonance neutrino production	±20%
f_{NC}	Additional error on NC/CC ratio	±25%
$f_{nR_{\nu n}^{CC1\pi}}$	Non-resonance bkg normalisation in νn CC1π reactions	±50%
$f_{nR_{\nu p}^{CC1\pi}}$	Non-resonance bkg normalisation in νp CC1π reactions	±50%
$f_{nR_{\nu n}^{CC2\pi}}$	Non-resonance bkg normalisation in νn CC2π reactions	±50%
$f_{nR_{\nu p}^{CC2\pi}}$	Non-resonance bkg normalisation in νp CC2π reactions	±50%
$f_{nR_{\bar{\nu} n}^{CC1\pi}}$	Non-resonance bkg normalisation in $\bar{\nu} n$ CC1π reactions	±50%
$f_{nR_{\bar{\nu} p}^{CC1\pi}}$	Non-resonance bkg normalisation in $\bar{\nu} p$ CC1π reactions	±50%
$f_{nR_{\bar{\nu} n}^{CC2\pi}}$	Non-resonance bkg normalisation in $\bar{\nu} n$ CC2π reactions	±50%
$f_{nR_{\bar{\nu} p}^{CC2\pi}}$	Non-resonance bkg normalisation in $\bar{\nu} p$ CC2π reactions	±50%
$f_{nR_{\nu n}^{NC1\pi}}$	Non-resonance bkg normalisation in νn NC1π reactions	±50%
$f_{nR_{\nu p}^{NC1\pi}}$	Non-resonance bkg normalisation in νp NC1π reactions	±50%
$f_{nR_{\nu n}^{NC2\pi}}$	Non-resonance bkg normalisation in νn NC2π reactions	±50%
$f_{nR_{\nu p}^{NC2\pi}}$	Non-resonance bkg normalisation in νp NC2π reactions	±50%
$f_{nR_{\bar{\nu} n}^{NC1\pi}}$	Non-resonance bkg normalisation in $\bar{\nu} n$ NC1π reactions	±50%
$f_{nR_{\bar{\nu} p}^{NC1\pi}}$	Non-resonance bkg normalisation in $\bar{\nu} p$ NC1π reactions	±50%
$f_{nR_{\bar{\nu} n}^{NC2\pi}}$	Non-resonance bkg normalisation in $\bar{\nu} n$ NC2π reactions	±50%
$f_{nR_{\bar{\nu} p}^{NC2\pi}}$	Non-resonance bkg normalisation in $\bar{\nu} p$ NC2π reactions	±50%

Table 6.10.: SBN proposal-era neutrino interaction cross-section systematic parameters considered in GENIE [154].

The modern-era systematic agreement between the universe input and parametrised approach is a little less precise. This is predominantly due to the parameters in the set which only impact reaction modes that occur relatively infrequently in the SBN analysis, such that the rate of events used to construct the splines is low. That being said, only 2 reconstructed neutrino energy bins have a magnitude of the disagreement exceeding 1% of the event rate in that bin. Finally, a full list of the interaction modes which are affected by each of the proposal and modern interaction parameters is given in Table 6.14 and 6.15 respectively.

Parameter	Description	$\delta P/P$
$f_{M_A^{NCEl}}$	Axial mass for NC elastic	±25%
$f_{\eta^{NCEl}}$	Strange axial form factor for NC elastic	±30%
f_{2p2h}	Normalisation uncertainty for 2p2h interactions	±100%
$f_{M_V^{CCRes}}$	Vector mass for CC resonance neutrino production	±10%
$f_{M_V^{NCRes}}$	Vector mass for NC resonance neutrino production	±10%
$f_{A_{HT}}$	Higher-twist parameter A for NC and CC DIS events	±25%
$f_{B_{HT}}$	Higher-twist parameter B for NC and CC DIS events	±25%
$f_{C_{v1u}}$	Valence p.d.f. correction factor C_{v1u} for DIS events	±30%
$f_{C_{v2u}}$	Valence p.d.f. correction factor C_{v2u} for DIS events	±40%
$f_{M_A^{Coh}}$	Axial mass for NC and CC coherent pion production	±50%
$f_{R_0^{Coh}}$	Nuclear size parameter controlling π absorption	±20%
$f_{\Delta\to N\gamma}$	Branching ratio for Δ radiative decay	±50%

Table 6.11.: The additional neutrino interaction cross-section systematic parameters considered in GENIE [154] with respect to those available in the SBN proposal analysis. Note the 2p2h parameter is not propagated from the event generator.

Parameter	Description	$\delta P/P$
f_{λ_π}	Intranuclear mean free path for pions	±20%
$f_{R_\pi^{CEx}}$	Intranuclear charge exchange rescattering fraction for pions	±50%
$f_{R_\pi^{Inel}}$	Intranuclear inelastic rescattering fraction for pions	±40%
$f_{R_\pi^{\pi}}$	Intranuclear pion-production rescattering fraction for pions	±20%
$f_{R_\pi^{Abs}}$	Intranuclear absorption fraction for pions	±20%
f_{λ_N}	Intranuclear mean free path for nucleons	±20%
$f_{R_N^{CEx}}$	Intranuclear charge exchange rescattering fraction for nucleons	±50%
$f_{R_N^{Inel}}$	Intranuclear inelastic rescattering fraction for nucleons	±40%
$f_{R_N^{\pi}}$	Intranuclear pion-production rescattering fraction for nucleons	±20%
$f_{R_N^{Abs}}$	Intranuclear absorption fraction for nucleons	±20%

Table 6.12.: Intranuclear hadron transport (FSI) systematic parameters [154].

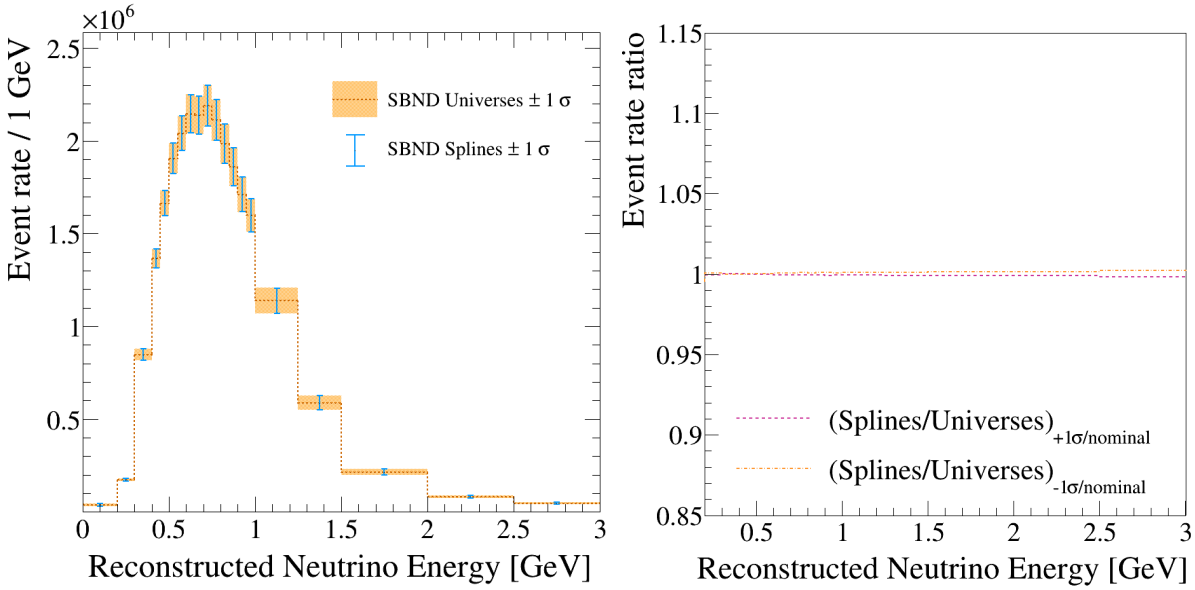

Figure 6.9.: On the left is the SBND ν_μ CC Inclusive event rate plotted with the 1σ SBN proposal-era interaction systematic uncertainty envelope constructed in two ways. The blue band takes the 1σ variation directly from the input universes, and the orange band constructs the 1σ variation from the response functions. On the right is a more quantitative assessment of this comparison, the $\pm1\sigma$/nominal event rate in each energy bin is calculated in the universe and spline-based uncertainty definitions which is in turn taken as a ratio, pink line.

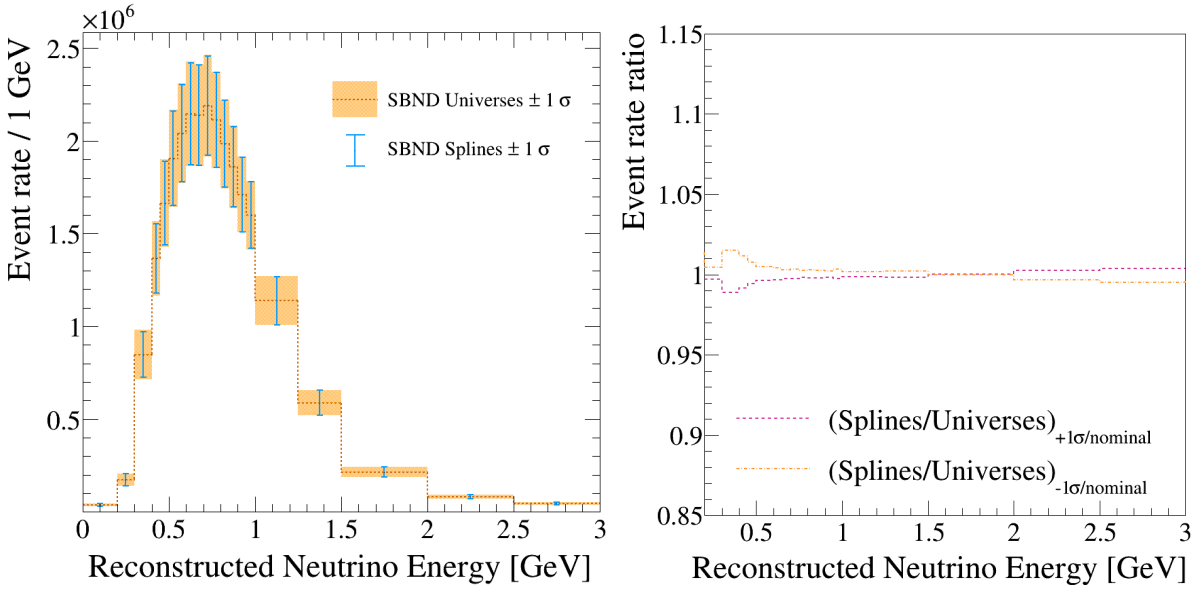

Figure 6.10.: On the left is the SBND ν_μ CC Inclusive event rate plotted with the 1σ modern-era interaction systematic uncertainty envelope constructed in two ways. The blue band takes the 1σ variation directly from the input universes, and the orange band constructs the 1σ variation from the response functions. On the right is a more quantitative assessment of this comparison, the $\pm1\sigma$/nominal event rate in each energy bin is calculated in the universe and spline-based uncertainty definitions which is in turn taken as a ratio, pink line.

6.5.5. Detector systematic parameters

Detector systematics in the near and far detectors of the SBN program have not yet been propagated through the analysis chain. The main reason for this is that to constrain many of the parameters, measurements must be made in an operational detector through the calibration of various components. At the time of performing this analysis, neither SBND or ICARUS had performed and validated any such measurements. In order for consistency across the 3-detectors in joint fits, the well-validated MicroBooNE detector systematics have not yet been included either. Instead, we can use the wealth of experience provided by MicroBooNE to estimate the magnitude of the detector systematics as a whole, and apply them in this way to all three detectors in the analysis.

In addition to the pseudo-detector systematics, further considerations have been made to encompass the analysis choices outlined in this chapter. Assessing the impact of these parameters on the sensitivity of SBN to sterile neutrino oscillations will be used to determine performance requirements of the SBN reconstruction. These parameters are defined as follows:

- **Energy-scale**: Quantifies the uncertainty due to the migration of events between reconstructed energy bins.
- **Sample-migration**: Quantifies the uncertainty on the purity of a selection procedure applied to a sample of pseudo-reconstructed events.

Even as a placeholder, the pseudo detector systematics can give a more realistic idea of the achievable sensitivity to new physics that the SBN program has. For the analyses presented in this thesis, the placeholder detector systematic parameters are defined broadly, as in Table 6.13. These intend to encapsulate the total effect on the signal and dominant background contributions to each sample.

6.5.6. Parametrising the detector systematics

The temporary detector systematic parametrisation laid out above was used in the construction of a covariance matrix, in which a 5% correlated and 0.5% uncorrelated uncertainty is applied to the binning scheme defined in Table 6.13. These values were chosen to be realistic, whilst minimising the reduction in sensitivity to observing new physics, thereby serving as a goal for the development of the real detector systematics.

Parameter	Detector	Sample	Modes	E_{Reco} bin edges
$f_0 - f_7$	SBND	ν_μ CC	ν_μ CC	{0.0, 0.2, 0.4, 0.6, 0.8, 1.0, 1.5, 2.0, ∞}
$f_8 - f_{11}$	SBND	ν_μ CC	NC	{0.0, 0.2, 0.4, 0.6, 0.8, 1.0, ∞}
f_{14}	SBND	ν_μ CC	Dirt	{0.0, ∞}
f_{15}	SBND	ν_μ CC	Cosmic	{0.0, ∞}
$f_{16} - f_{32}$	μBooNE	As above		
$f_{33} - f_{49}$	ICARUS	As above		
f_{EScale}	All	All	All	E_{Reco} binning scheme, Table 6.5
$f_{Migration}$	All	ν_μ CC Exc.	All	(E_{Reco}, E_{True}) binning scheme, Table 6.5

Table 6.13.: A temporary detector systematic scheme for use across all three SBN experiments in the current ν_μ-disappearance oscillation analysis. This set will gradually evolve to include calibration data and external considerations.

The energy-scale systematic has been defined to represent the uncertainty due to events which may migrate between the reconstructed neutrino energy bins defined in the analysis. The form of many systematic parameters depend on the way in which the neutrino energy is binned, therefore this parameter is applied to account for any variations in the analysis resulting from alterations to the binning scheme. The magnitude of this parameter may remain small if the binning scheme is robust to small changes.

The energy-scale uncertainty is constructed by scaling every bin edge by the magnitude of the uncertainty and, assuming a flat distribution of events within each bin, re-defining the E_{Reco} distribution, such that any events which lie close to a bin edge may end up in a neighbouring bin. Figure 6.11 shows the shape and size of the 1σ energy-scale uncertainty for bins scaled by 1%, 2% and 5%. The energy-scale is applied after all other systematic and physics parameters when constructing the reconstructed neutrino energy distributions.

The final detector systematic considered in the analysis involves the migration of true events between selected sample definitions. In the case where the ν_μ CC Inclusive sample is separated into semi-exclusive components based on reconstructed parameters, a certain magnitude of sample migration will always occur. To account for this, response functions were constructed using a method similar to the one defined for the flux and interaction unisim systematic parameters with an additional consideration of the correlations between the migration in each sample.

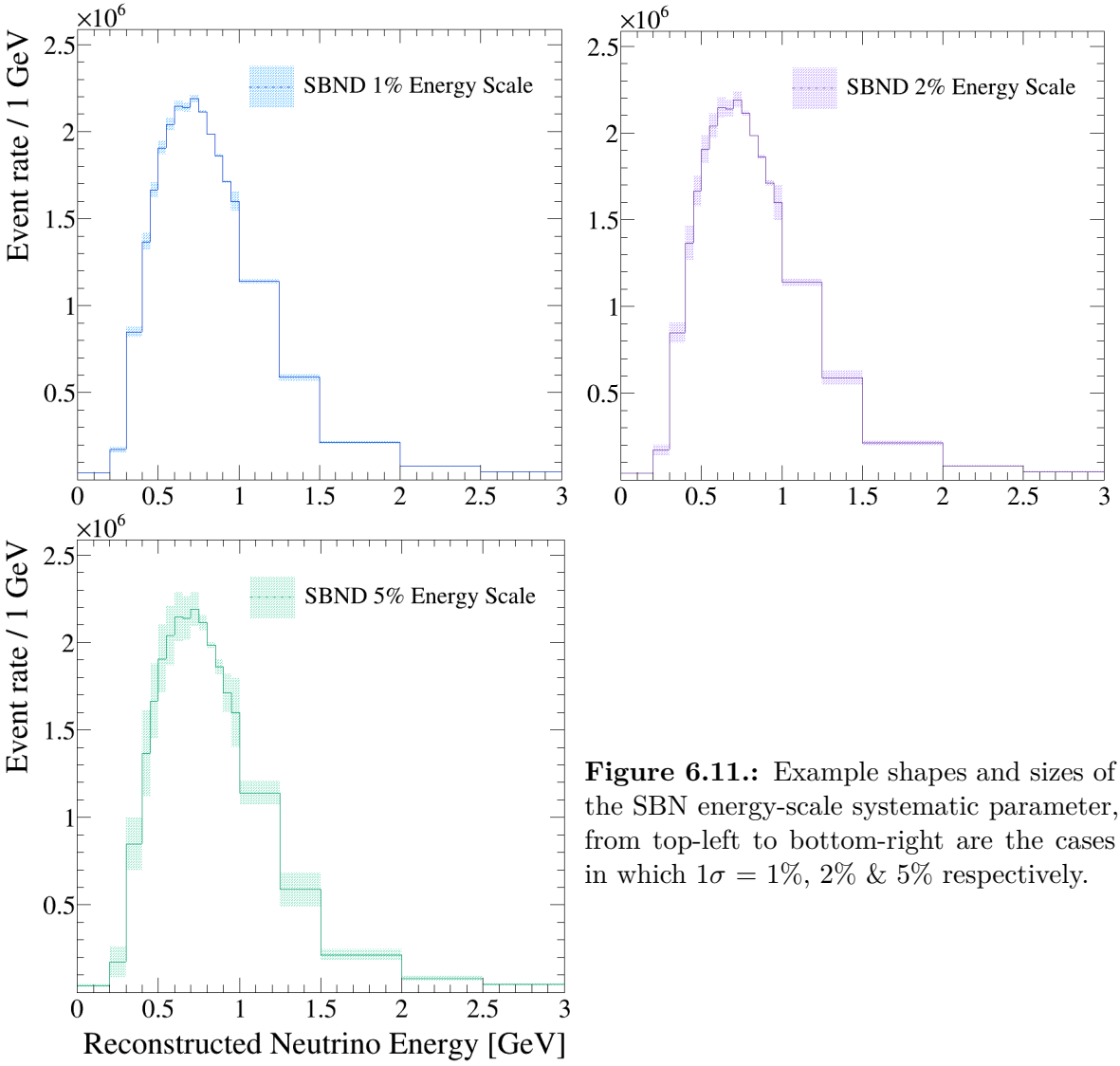

Figure 6.11.: Example shapes and sizes of the SBN energy-scale systematic parameter, from top-left to bottom-right are the cases in which 1σ = 1%, 2% & 5% respectively.

In the existing definition of the pseudo-reconstructed sample, the contamination is uni-directional: There only exists sample migration from true ν_μ CC Other events into the 'reconstructed' ν_μ CC 0π sample. A single parameter was therefore defined to quantify this uni-directional contamination along with the anti-correlation of its impact between the two samples. The definition of the knots with the splines for each sample are,

$$\mathscr{S}_{m;t,r}(k) = \begin{cases} 1 + \dfrac{w \cdot k \cdot M^{\text{CCOther}\to\text{CC0}\pi}_{t,r}}{N^{R}_{s,m;t,r}}, & s = \text{CC0}\pi \\ \\ 1 - \dfrac{w \cdot k \cdot M^{\text{CCOther}\to\text{CC0}\pi}_{t,r}}{N^{R}_{s,m;t,r}}, & s = \text{CCOther}, \end{cases} \qquad k \in \{0, \pm1, \pm2, \pm3\}, \quad (6.12)$$

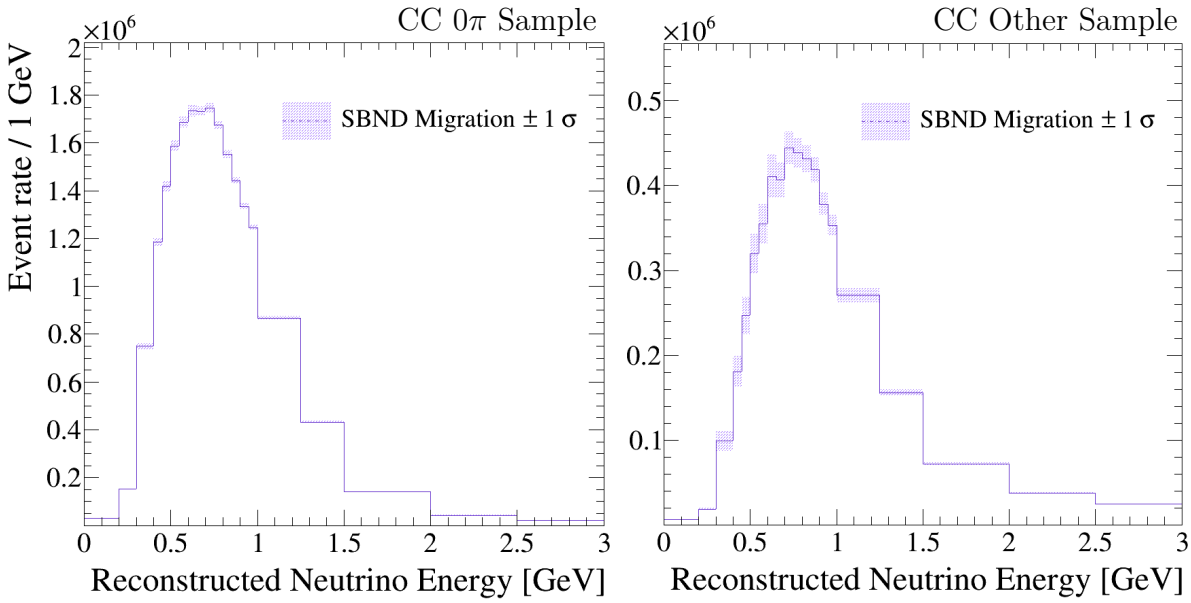

Figure 6.12.: The $\pm 1\sigma$ sample migration uncertainty envelopes when the systematic parameter is applied to the CC 0π sample (left) and CC Other sample (right).

and the values, $\mathscr{S}_{m;t,r}(k)$, are once again defined for the reaction mode m, the E_{True}, E_{Reco} bin, t, r, for each of the $k\sigma$-points such that $\mathscr{S}_{m;t,r}(0) = 1$. The quantity $M_{t,r}^{\text{CCOther}\to\text{CC0}\pi}$ defines the number of true CC Other events which have migrated into the reconstructed CC 0π events in the bin t, r.

The magnitude of the 1σ variation in a given mode and bin depends on w, which is defined as the fractional change in migration when varying the kinetic energy threshold for reconstructing tracks. In order to calculate the magnitude of w, the value of $M_{t,r}^{\text{CCOther}\to\text{CC0}\pi}$ was first determined in the MC sample using the nominal reconstruction and selection definition described in section 6.3.2, in which the track reconstruction kinetic energy threshold is set to the best-value determined by ArgoNeuT, $E_k = 21$ MeV [202]. $M_{t,r}^{\text{CCOther}\to\text{CC0}\pi}$ was then re-determined using the track kinetic energy threshold set by MicroBooNE, $E_k = 47$ MeV [196], resulting in a fractional migration difference between the two cases of $w = 0.246$.

Figure 6.12 demonstrates the size of the $\pm 1\sigma$ sample migration uncertainty when applied to the CC 0π and CC Other samples. The integrated migration uncertainty on the CC 0π and CC Other samples are $f_{Migration}^{CC0\pi} = 1.2\%$ and $f_{Migration}^{CC0\pi} = 4.1\%$ respectively. The method and results of validating this parameter are given in appendix B.3.

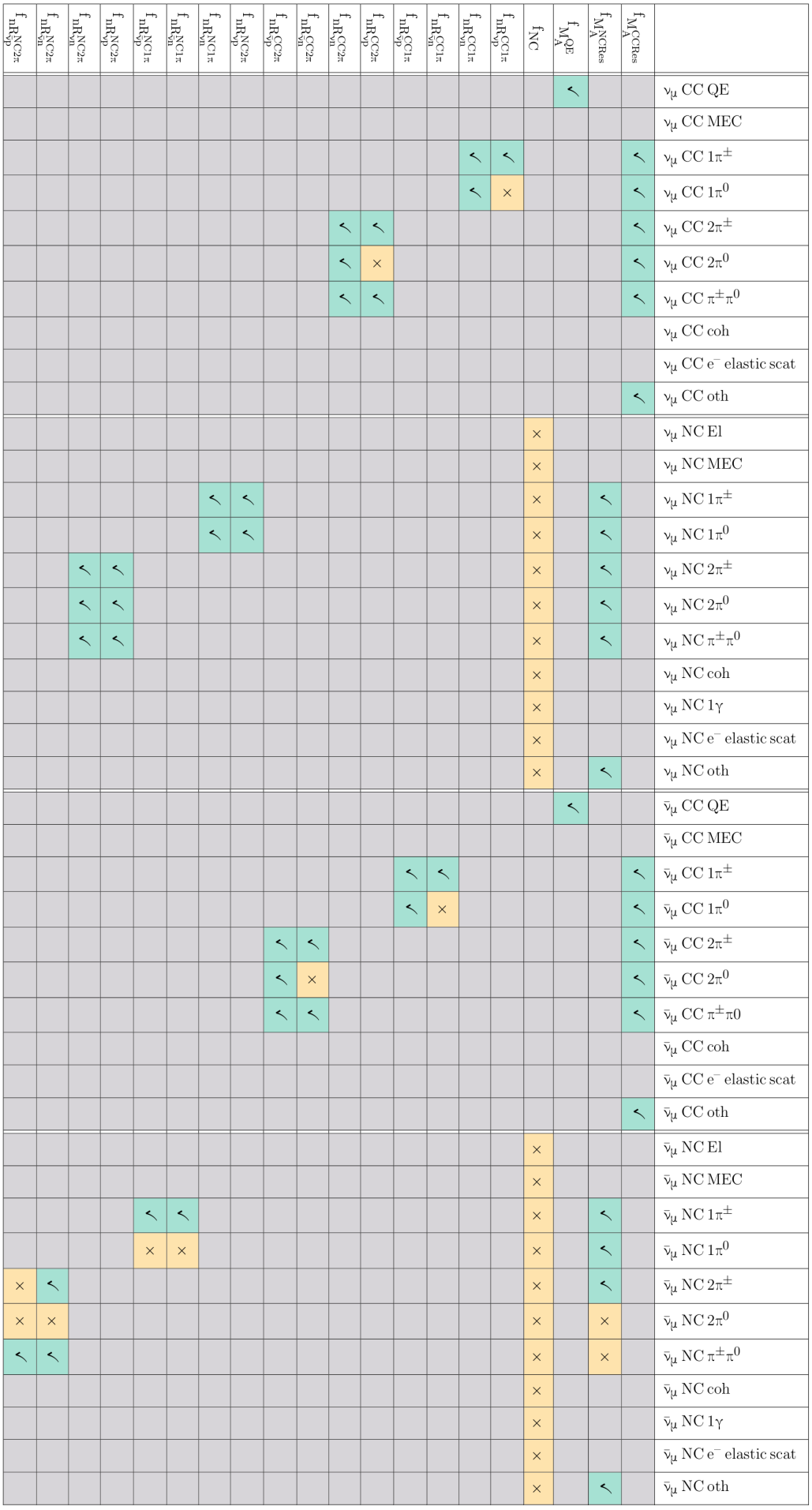

Table 6.14.: A list of interaction modes impacted by the proposal interaction spline parameters. A green tick indicates that the mode should have been affected, and was. An orange cross indicates that the mode could have been affected, but there were too few events in the relevant mode and binning scheme to pass the spline-construction threshold.

f_{2p2h}	f_{γ}^{NCEl}	$f_{M_A^{NCEl}}$	$f_{R_0^{COH}}$	$f_{M_A^{COH}}$	$f_{M_V^{NCRes}}$	$f_{M_V^{CCRes}}$	$f_{\Delta\to N\gamma}$	$f_{R_\pi^{\bar{\pi}}}$	f_{λ_π}	$f_{R_\pi^{Inel}}$	$f_{R_\pi^{CEx}}$	$f_{R_\pi^{Abs}}$	$f_{R_N^{\bar{\pi}}}$	f_{λ_N}	$f_{R_N^{Inel}}$	$f_{R_N^{CEx}}$	$f_{R_N^{Abs}}$	$f_{C_{V2n}}$	$f_{C_{V1u}}$	$f_{B_{HT}}$	$f_{A_{HT}}$	
													✓	✓	✓	✓	✓					ν_μ CC QE
✓													✓	✓	✓	✓	✓					ν_μ CC MEC
						✓	✓	✓	✓	✓	✓	✓	✓	✓	✓	✓	✓	✓	✓	✓	✓	ν_μ CC $1\pi^\pm$
						✓	✓	✓	✓	✓	✓	✓	✓	✓	✓	✓	✓	✓	✓	✓	✓	ν_μ CC $1\pi^0$
						✓	✓	✓	✓	✓	✓	✓	✓	✓	✓	✓	✓	✓	✓	✓	✓	ν_μ CC $2\pi^\pm$
						✓	✓	✓	✓	✓	✓	✓	✓	✓	✓	✓	✓	✓	✓	✓	✓	ν_μ CC $2\pi^0$
						✓	✓	✓	✓	✓	✓	✓	✓	✓	✓	✓	✓	✓	✓	✓	✓	ν_μ CC $\pi^\pm\pi^0$
			×	×																		ν_μ CC coh
																						ν_μ CC e^- elastic scat
						✓	✓	✓	✓	✓	✓	✓	✓	✓	✓	✓	✓	✓	✓	✓	✓	ν_μ CC oth
	✓	✓											×	✓	×	×	×					ν_μ NC El
✓													×	×	×	×	×					ν_μ NC MEC
					✓		✓	✓	✓	✓	✓	✓	✓	✓	✓	✓	✓	✓	✓	✓	✓	ν_μ NC $1\pi^\pm$
					✓		✓	✓	✓	✓	✓	✓	✓	✓	✓	✓	✓	✓	✓	✓	✓	ν_μ NC $1\pi^0$
					✓		✓	✓	✓	✓	✓	✓	✓	✓	✓	✓	✓	✓	✓	✓	✓	ν_μ NC $2\pi^\pm$
					✓		✓	✓	✓	✓	✓	✓	✓	✓	✓	✓	✓	✓	✓	✓	✓	ν_μ NC $2\pi^0$
					✓		✓	✓	✓	✓	✓	✓	✓	✓	✓	✓	✓	✓	✓	✓	✓	ν_μ NC $\pi^\pm\pi^0$
			×	×																		ν_μ NC coh
																						ν_μ NC 1γ
																						ν_μ NC e^- elastic scat
					✓		✓	✓	✓	✓	✓	✓	✓	✓	✓	✓	✓	✓	✓	✓	✓	ν_μ NC oth
													✓	✓	✓	✓	✓					$\bar{\nu}_\mu$ CC QE
✓													✓	✓	✓	✓	✓					$\bar{\nu}_\mu$ CC MEC
						✓	✓	✓	✓	✓	✓	✓	✓	✓	✓	✓	✓	×	×	×	×	$\bar{\nu}_\mu$ CC $1\pi^\pm$
						✓	✓	✓	✓	✓	✓	✓	✓	✓	✓	✓	✓	✓	✓	✓	✓	$\bar{\nu}_\mu$ CC $1\pi^0$
						✓	✓	✓	✓	✓	✓	✓	✓	✓	✓	✓	✓	×	×	×	×	$\bar{\nu}_\mu$ CC $2\pi^\pm$
						✓	✓	✓	✓	✓	✓	✓	✓	✓	✓	✓	✓	×	×	×	×	$\bar{\nu}_\mu$ CC $2\pi^0$
						✓	✓	✓	✓	✓	✓	✓	✓	✓	✓	✓	✓	✓	✓	✓	✓	$\bar{\nu}_\mu$ CC $\pi^\pm\pi0$
			×	×																		$\bar{\nu}_\mu$ CC coh
																						$\bar{\nu}_\mu$ CC e^- elastic scat
						✓	×	✓	✓	✓	✓	✓	✓	✓	✓	✓	✓	×	×	×	×	$\bar{\nu}_\mu$ CC oth
	×	×											×	×	×	×	×					$\bar{\nu}_\mu$ NC El
✓													×	×	×	×	×					$\bar{\nu}_\mu$ NC MEC
					✓		✓	×	✓	✓	✓	✓	×	✓	✓	✓	✓	×	×	×	×	$\bar{\nu}_\mu$ NC $1\pi^\pm$
					✓		✓	✓	✓	✓	✓	✓	✓	✓	✓	✓	✓	×	×	×	×	$\bar{\nu}_\mu$ NC $1\pi^0$
					✓		✓	×	✓	×	×	×	✓	✓	✓	✓	✓	×	×	×	×	$\bar{\nu}_\mu$ NC $2\pi^\pm$
					×		×	×	×	×	×	×	×	×	×	×	×	×	×	×	×	$\bar{\nu}_\mu$ NC $2\pi^0$
					×		×	×	✓	✓	✓	✓	×	×	×	×	×	×	×	✓	✓	$\bar{\nu}_\mu$ NC $\pi^\pm\pi^0$
			×	×																		$\bar{\nu}_\mu$ NC coh
																						$\bar{\nu}_\mu$ NC 1γ
																						$\bar{\nu}_\mu$ NC e^- elastic scat
					✓		×	×	×	×	×	×	×	×	×	×	×	×	×	×	×	$\bar{\nu}_\mu$ NC oth

Table 6.15.: A list of interaction modes impacted by the modern interaction spline parameters. A green tick indicates that the mode should have been affected, and was. An orange cross indicates that the mode could have been affected, but there were too few events in the relevant mode and binning scheme to pass the spline-construction threshold.

Chapter 7.

ν_μ disappearance in the search for sterile neutrinos at SBN

The SBN proposal presented an analysis of the sensitivity of SBN to detecting oscillations under the (3+1) sterile neutrino hypothesis through ν_μ disappearance and ν_e appearance measurements [6]. This chapter will present an updated ν_μ disappearance analysis under the (3+1) sterile neutrino hypothesis.

The MC sample of neutrino events and set of systematic parameters available at the time of the SBN proposal have since been superseded. A full list of updates to the samples and systematic parameter inputs with respect to those used in the SBN proposal sensitivity studies are as follows,

- The default neutrino interaction model configuration has been updated from GENIE v2, Default, to GENIE v3, G18_10a_02_11a. The latter of which has been validated in the context of neutrino interactions on argon by the MicroBooNE experiment. The individual model contributions to both configurations are defined in Table 4.1
- The 2p2h interaction was not included in the GENIE v2 model configuration, and has since been shown to contribute approximately 10% of the total CC SBND event rate, see Table 5.1
- The baseline of SBND has moved from 100m to 110m. The magnitude of the flux arriving at the front face of the detector is inversely proportional to the distance of the detector to the neutrino source, $\Phi \propto 1/r^2$, therefore the expected SBND event rate has decreased by a factor of approximately $(100/110)^2 = 0.826$

- The SBND TPC-sensitive volume has been been increased, from 4 x 4 x 3.65 = 58.4m^3 to 4 x 4 x 5 = 80m^3
- The systematic parameters incorporated into the SBN proposal sensitivity included all flux parameters defined in section 6.5.1 along with the interaction systematic parameters listed in Table 6.10. The additional interaction systematic parameters included in the updated analysis are listed in Tables 6.11 and 6.12
- Finally, the set of pseudo-detector systematics has only recently been constructed, therefore these were not included at the time of the SBN proposal.

The pseudo-reconstruction performed at the time of the proposal, discussed in section 6.3, will be applied to all samples used to perform the sensitivity studies in this chapter.

This chapter will first discuss the method for determining the sensitivity of SBN to observing neutrino oscillations under the (3+1) sterile hypothesis in section 7.1. Confidence regions are constructed using the method outlined in section 7.1.1 following fits of the E_{Reco} spectra from all three detectors to the ν_μ disappearance parameters in the phase-space defined in section 6.2.1. The sensitivity analysis will then be presented in the context of both inclusive and semi-exclusive joint fits in sections 7.2, 7.3 and 7.4.

7.1. Sensitivity determination

The sensitivity of SBN to the ν_μ disappearance sterile neutrino oscillation parameters can be defined in two ways. The first is known as an 'exclusion' sensitivity, and corresponds to the region of parameter space in which the hypothesis of no oscillations (the 'null' hypothesis) can be excluded with a given confidence. The second is known as an 'allowed' sensitivity, and corresponds to the region of parameter space that is allowed with a given confidence from the analysis of samples with an injected oscillation signal.

Both methods utilise an 'Asimov' dataset, which serves as the representative sample in which all quantities are set to their nominal values [203]. When determining the exclusion sensitivity, the Asmiov dataset corresponds to the nominal MC sample with all systematics set to their prior values, and $\sin^2 2\theta_{\mu\mu}$ and Δm^2_{41} are set to 0 as per the null oscillation hypothesis. For the allowed region, the nominal sample is once again constructed, but this time the oscillation parameters are set to the values of the injected signal. The method for constructing both forms of the sensitivity is as follows,

- Separate the phase space into a 40x40-point grid, logarithmically-spaced. The choice to use 40 points in each dimension is driven only by the amount of processing required to perform the fits
- At each grid point in the parameter space, a fit is performed between the relevant Asimov dataset and the MC template constructed with the ν_μ disappearance parameters set to the value at the current grid point
- If a set of systematic parameters has been included in the fit, they are allowed to float between their $\pm 5\sigma$ limits whilst the profiling and minimisation procedures defined in section 6.2 are performed
- The value of χ^2 is extracted from every fit in the parameter space to form a 2D surface in a 3D volume, from which confidence regions can be extracted.

7.1.1. Constructing confidence regions

The high statistical significance of the SBN datasets allows for the results in this thesis to be presented entirely at the 5σ confidence level, though it is also commonplace to present results at the 68%, 90% and 3σ confidence levels. The constant-$\Delta\chi^2$ method is employed to construct the SBN sensitivity curves at the chosen confidence level, in which lines of constant-$\chi^2_{critical}$ are drawn in the 2D parameter space. The regions of parameter space in which $\chi^2 > \chi^2_{critical}$ are those which are sensitive to discriminating a real physics (or null) result from a systematic discrepancy.

Values of $\chi^2_{critical}$ are defined separately for the exclusion and allowed sensitivity definitions. The χ^2 surface across the 2-dimensional exclusion parameter space is constructed by performing a raster scan at each Δm^2_{41} point to define a 1-dimensional limit, therefore 1 degree-of-freedom is used to define the value of $\chi^2_{critical}$ at each confidence level. The raster-scanning method is not employed in the construction of the allowed distributions, and instead 2-dimensional limits are determined, therefore 2 degrees-of-freedom are used in the definition of each $\chi^2_{critical}$ value. Table 7.1 lists the relevant values of $\chi^2_{critical}$ for a range of confidence levels.

Contour type	Confidence Level			
	68%	90%	3σ	5σ
Exclusion limits	0.23	1.64	7.74	23.66
Allowed regions	2.30	4.61	11.83	28.74

Table 7.1.: Values of $\chi^2_{critical}$ at various confidence levels defined in the construction of exclusion limit and allowed region sensitivity contours.

7.2. SBN exclusion-region sensitivity studies

The studies presented in this section were performed in order to fully understand the impact of each component of the SBN oscillation analysis procedure in the sensitivity of the experiment to observing oscillations under the (3+1) sterile neutrino hypothesis. Contributions to the sensitivity from each SBN detector, various model configurations and sets of systematic parameters will be explored.

Each contour will depict the region of $\sin^2 2\theta_{\mu\mu}$, Δm^2_{41} parameter space in which the null hypothesis (no oscillations) can be excluded with 5σ confidence, unless otherwise stated. All fits are performed with the ν_μ CC Inclusive samples of pseudo-reconstructed events, generated using the GENIE v3 G18_10a Valencia 1p1h+2p2h model, unless otherwise stated.

7.2.1. Sample contributions

The reconstructed neutrino energy spectra which are the inputs to the oscillation sensitivity fits are presented for each of the three SBN detectors in the ν_μ CC Inclusive samples in Figure 7.1 and for the semi-exclusive ν_μ CC 0π and ν_μ CC Other samples in Figure 7.2. The spectra are broken down into the pre-FSI neutrino interaction modes, in order to demonstrate the signal and background contributions to the samples. Figure 7.3 shows the integrated event rate spectra in each of the three detectors and two sample topologies with 1σ error envelopes corresponding from the uncertainty contributions from the full set of interaction, flux and pseudo-detector systematic parameters. The integrated event rates in each sample and detector are given in Table 7.2 alongside the 1σ statistical and systematic uncertainties. All events are contained within the fiducial volume, following the method outlined in section 6.3.2.

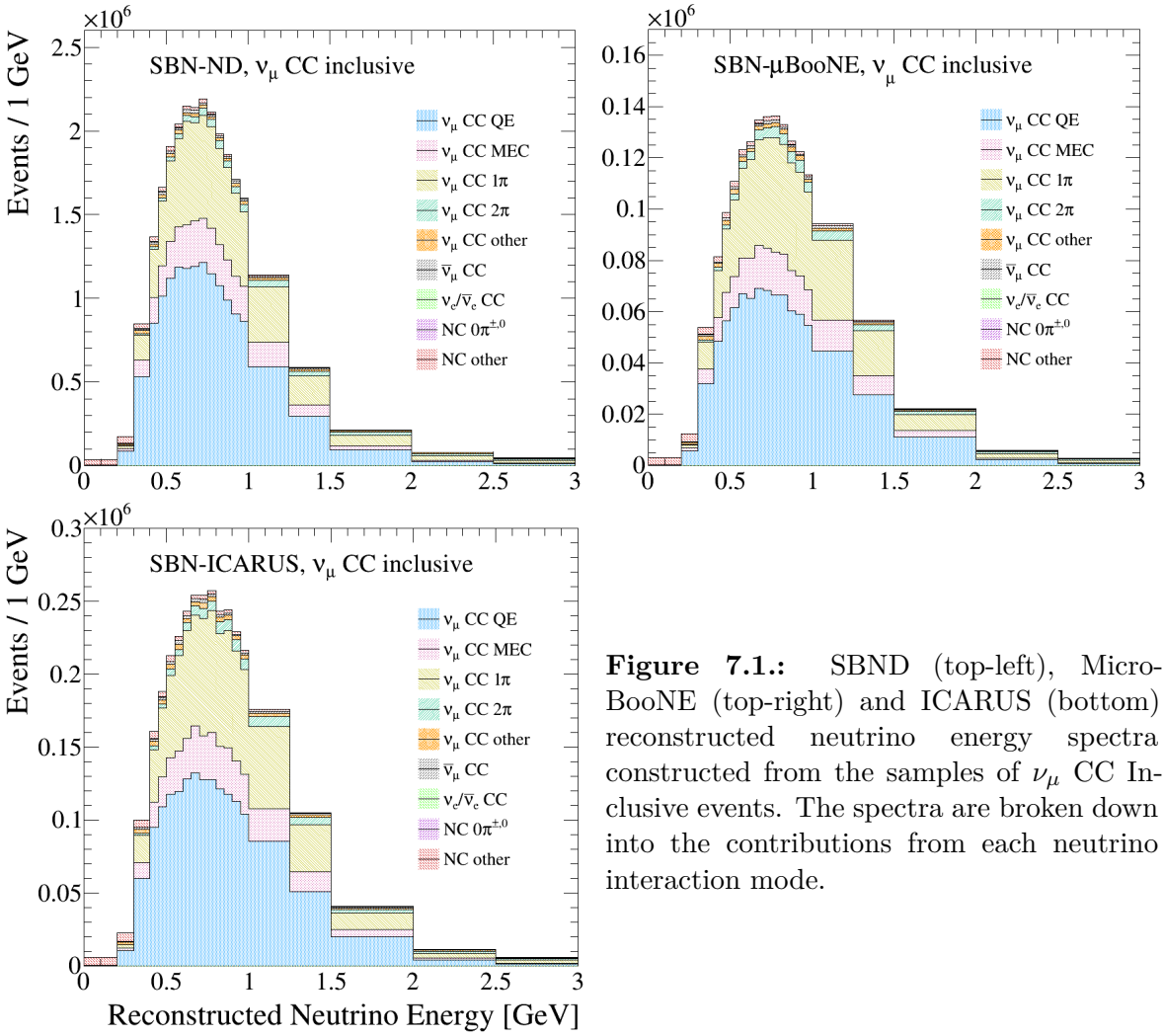

Figure 7.1.: SBND (top-left), MicroBooNE (top-right) and ICARUS (bottom) reconstructed neutrino energy spectra constructed from the samples of ν_μ CC Inclusive events. The spectra are broken down into the contributions from each neutrino interaction mode.

Detector	ν_μ CC Inclusive			ν_μ CC 0π		
	Rate	Stat. %	Syst. %	Rate	Stat. %	Syst. %
SBND	1,885,340	0.07	21.49	1,457,880	0.08	22.36
MicroBooNE	135,400	0.27	20.32	100,100	0.32	22.85
ICARUS	254,200	0.20	20.83	187,240	0.23	22.27

Table 7.2.: SBN event rates as inputs to the sensitivity study following the pseudo-selection of ν_μ CC Inclusive and ν_μ CC 0π events scaled to the full 6.6×10^{20} POT in SBND and ICARUS and 13.2×10^{20} POT in MicroBooNE. Statistical and systematic uncertainties are quoted separately for each sample as a percentage of the full event rate. All events are contained within the fiducial volume, following the method defined in section 6.3.2.

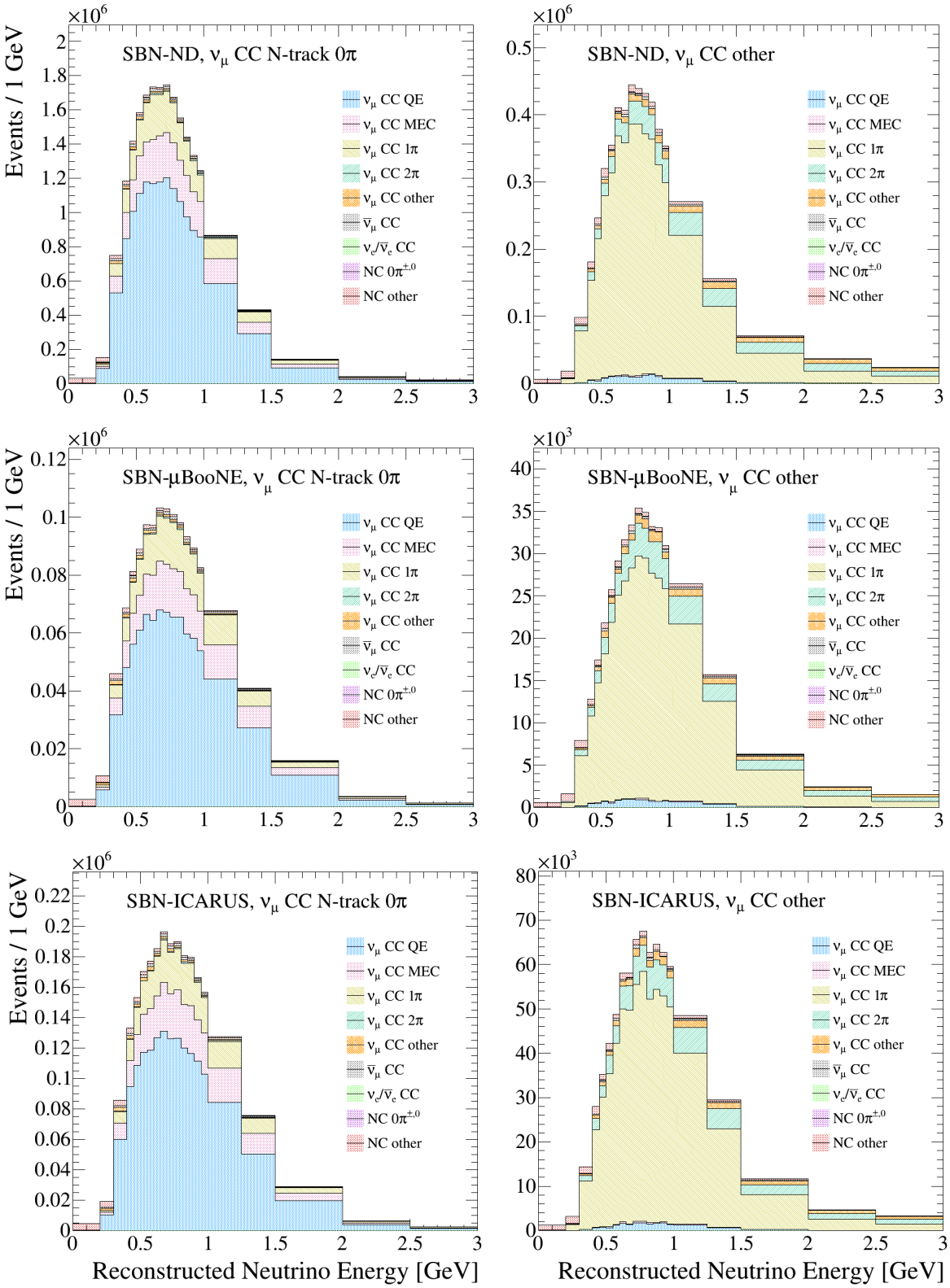

Figure 7.2.: SBND (top), MicroBooNE (middle) and ICARUS (bottom) reconstructed neutrino energy spectra with of ν_μ CC 0π (left) and ν_μ CC Other (right) events. The spectra are broken down into the contributions from each neutrino interaction mode.

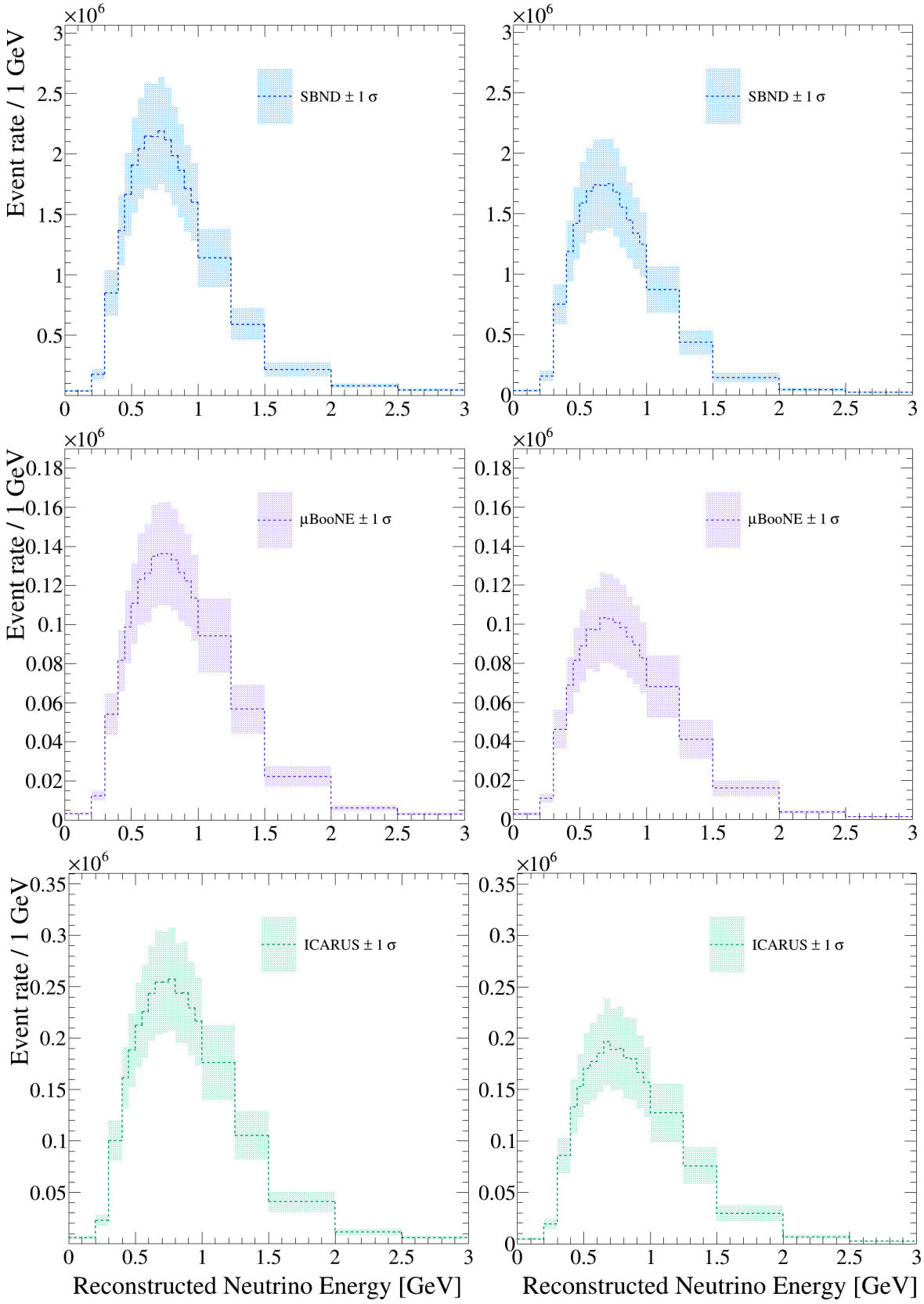

Figure 7.3.: SBND (top), MicroBooNE (middle) and ICARUS (bottom) reconstructed neutrino energy spectra with of ν_μ CC Inclusive (left) and ν_μ CC 0π (right) events and the 1σ systematic uncertainty envelopes from all interaction, flux and pseudo-detector parameters.

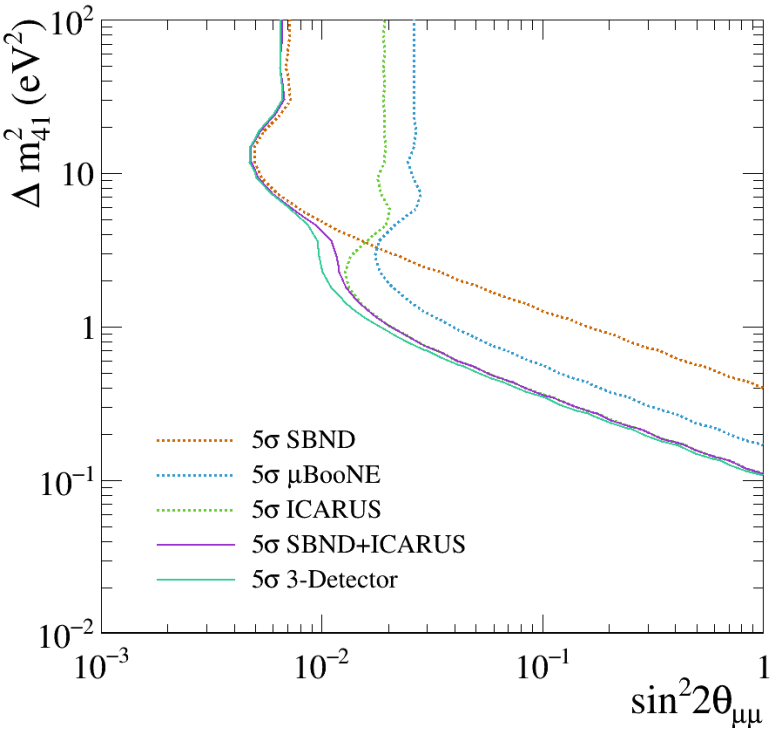

Figure 7.4.: Contributions to the SBN sterile oscillation sensitivity from each detector and combinations of detectors in the SBN program. SBND is most sensitive to the region $\Delta m^2_{41} > 4$ eV^2, MicroBooNE is sensitive between $1 < \Delta m^2_{41} < 4$ eV^2 and ICARUS is most sensitive below $\Delta m^2_{41} < 1$ eV^2. No systematic parameters are considered in the fits.

7.2.2. Impact of the three SBN detectors

The statistical contributions to the sterile oscillation sensitivity from each SBN detector is shown in Figure 7.4. Combining the near and far detectors in the fits shows a substantial improvement to the sensitivity compared to their individual contributions. Adding in the MicroBooNE detector improves the sensitivity further still, across most of the parameter space.

Figure 7.4 highlights the locations in which each detector is most sensitive. The short baseline of SBND lends itself to the region in which $\Delta m^2_{41} > 4$ eV^2, MicroBooNE improves the sensitivity between $1 < \Delta m^2_{41} < 4$ eV^2 and ICARUS, the far detector, is most sensitive below $\Delta m^2_{41} < 1$ eV^2. No systematic parameters are considered in the fits.

7.2.3. Impact of multiple theoretical models

The SBN sterile oscillation sensitivity in this study was calculated following joint SBND and ICARUS fits using each of the model configurations defined in section 4.5.4, which will be explored by the mock data analysis in chapter 8. Since the systematic parameters were defined and validated in chapter 6 for a single model configuration, only statistical exclusion contours were constructed in this comparison.

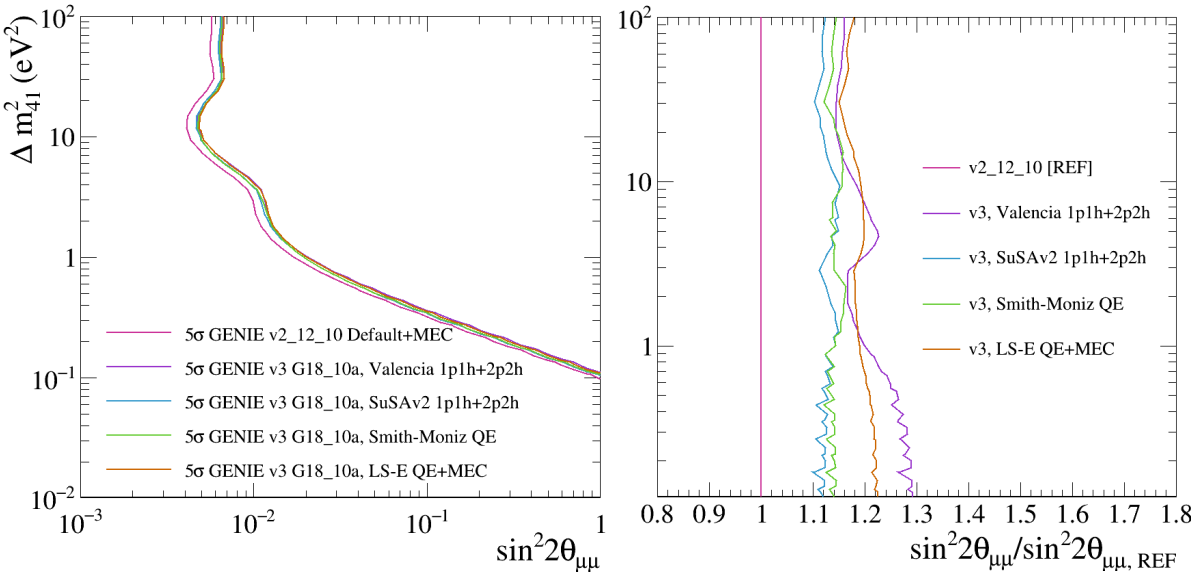

Figure 7.5.: Variations to the SBND+ICARUS statistics-only sensitivity when changing the theoretical model used in the construction of the sample. The left plot shows the region of oscillation parameter space each model is sensitive to. The right plot shows the relative location of the 5σ contour in $\sin^2 2\theta_{\mu\mu}$ space for each model, with respect to the GENIE v2_12_10 Default+MEC model. The fractional contours are shown across the active Δm^2_{41} phase space.

The plots in Figure 7.5 therefore demonstrate the impact of the shape and rate variations between the energy distributions of the samples on the oscillation sensitivity. The left-hand plot shows that the most substantial variation is between GENIE v2 and all model configurations from GENIE v3, due to the almost 25% reduction in the event rates in each case. The similarities between the GENIE v3 configurations arise because the only the QE+2p2h models are altered.

The right-hand plot in Figure 7.5 provides slightly more information about the relative sensitivities. Across the Δm^2_{41} parameter space, the ratio of $\sin^2 2\theta_{\mu\mu}$ between each model configuration and GENIE v2_12_10 Default+MEC model is shown. A higher fraction corresponds to a larger value of $\sin^2 2\theta_{\mu\mu}$ at the point where the contour is drawn, and therefore to a reduction in the sensitivity.

Although there are statistical fluctuations in the region of the contour in which ICARUS is most-sensitive, it is clear that the largest model variations occur in this low-Δm^2_{41} range. In addition, when considering the region above $\Delta m^2_{41} > 8$ eV^2, the GENIE v3 LS-E QE+MEC model appears to have the least sensitivity to the sterile oscillations, however when $\Delta m^2_{41} < 1$ eV^2, it is the Valencia 1p1h+2p2h model which is the least sensitive. This demonstrates the model-dependence of the L/E distribution.

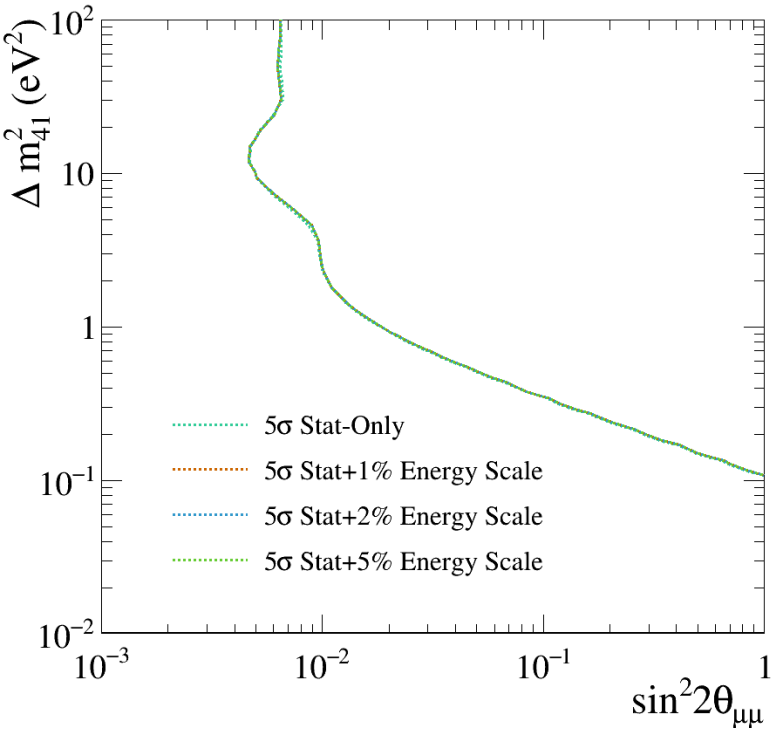

Figure 7.6.: The ν_μ disappearance exclusion sensitivity when including three magnitudes of the energy scale systematic parameter, 1% (orange), 2% (blue) and 5% (green) alongside the statistics-only sensitivity.

7.2.4. Impact of systematic groups

Having assessed the sensitivity of SBN to observing sterile neutrino oscillations through various statistical-only fits, studies of how this sensitivity changes with the inclusion of systematics were then performed. The first systematic assessment involves the energy scale parameter, defined in 6.5.5. The 1, 2 and 5% envelopes applied to the ν_μ CC Inclusive event rate were shown in Figure 6.11, and the negligible impact of each of these magnitudes on the ν_μ disappearance sensitivity is shown in Figure 7.6. The binning scheme chosen is therefore robust to changes in the size of this parameter.

The systematic parameter sets defined and quantified in chapters 4 and 6 respectively were added to the fits individually. The left plot in Figure 7.7 shows the exclusion contours for each of the proposal interaction, proposal+modern interaction, flux and pseudo-detector systematics with respect to the statistical-only sensitivity. The impact in the region where $\Delta m^2_{41} > 1$ eV^2 is immediately apparent, and is exacerbated in the right-hand ratio plot.

The flux systematics conduce the largest reduction in sensitivity in this region, however these parameters have been thoroughly validated by both the MiniBooNE and MicroBooNE experiments, and are unlikely to be constrained much further. The pseudo-detector systematics appear to contribute the second largest reduction in the sensitivity,

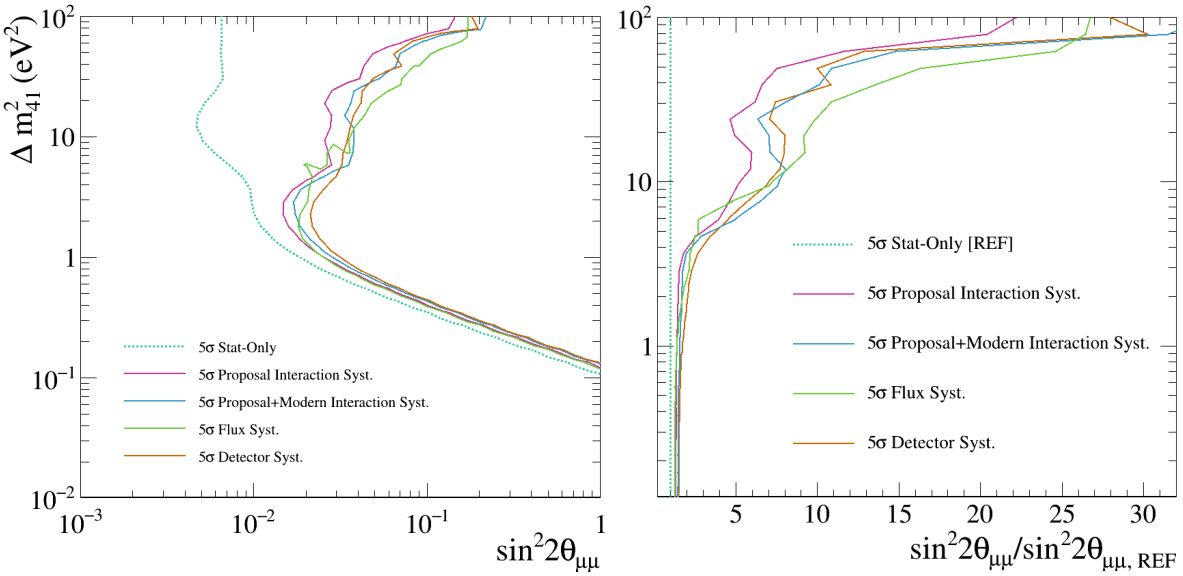

Figure 7.7.: The left plot shows the reduction in sensitivity from the stat-only contour when including each set of systematic parameters in the fits. The right plot shows the relative location of each systematic contour in $\sin^2 2\theta_{\mu\mu}$ space, with respect to the statistical-only case, for the active region of Δm^2_{41} phase space.

and in direct contrast with the flux parameters, have not yet been fully defined or validated in all 3 detectors. Once these parameters have been developed, iterations of this and the mock data study can be conducted in order to understand and attempt to minimise the real-life effect of the detector systematics.

Finally, the proposal interaction systematic parameters contribute the smallest reduction to the sensitivity whilst the full interaction parameter set has a comparable effect to the detector systematics. Some of these parameters are still being constrained and therefore may have their impact reduced. Ultimately, the overall interaction systematic contribution is model-dependent, the impact of which cannot be tested here.

7.2.5. Impact of the sample definitions

The analyses presented so far have shown the impact of the SBN detectors and various systematic sets on fits involving the ν_μ CC Inclusive sample. The following study will show the impact of switching to joint fits involving the ν_μ CC Inclusive sample separated into ν_μ CC 0π and ν_μ CC Other semi-exclusive samples.

In this demonstration, only the flux and interaction systematics are included as they constitute the most well-validated parameter sets. In addition, the semi-exclusive joint

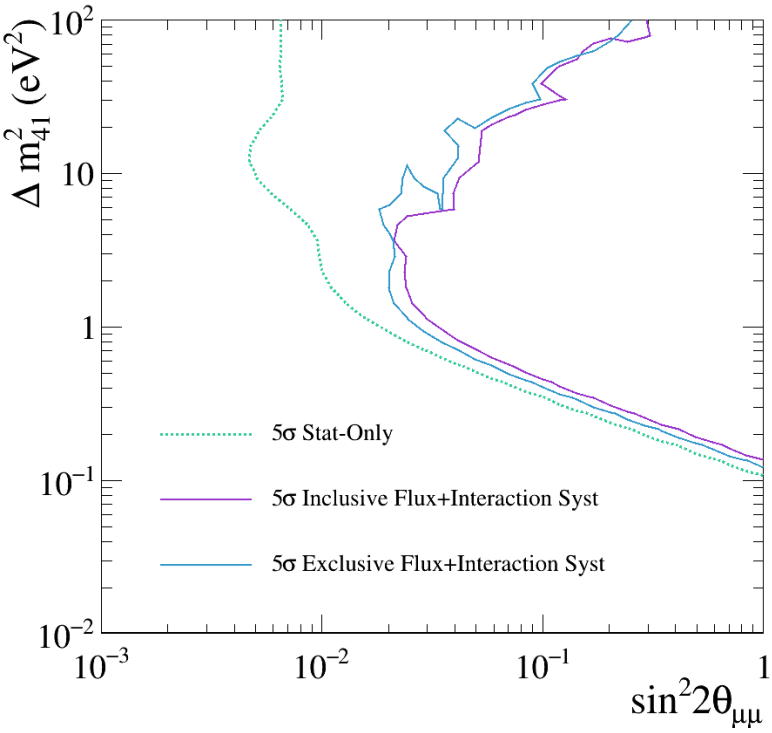

Figure 7.8.: ν_μ disappearance exclusion sensitivity comparison between fitting single samples in each detector and fitting joint, semi-exclusive samples in which the ν_μ CC Inclusive event rate is separated into ν_μ CC 0π and ν_μ CC Other events. The systematic parameters included in the fits are the full flux and interaction sets, with an additional parameter included in the semi-exclusive fits to account for migration between the samples. The statistical-only sensitivity is included for reference.

fits also include the sample migration systematic, defined in section 6.5.5, to account for possible contamination due to particle misidentification.

Figure 7.8 shows the ν_μ disappearance exclusion sensitivity constructed from fits performed using the two different sample definitions, and includes the statistical-only sensitivity for reference. The improvement when switching from fitting the single, inclusive sample to fitting the joint, semi-exclusive samples is substantial across the entire Δm^2_{41} parameter space, regardless of the inclusion of an additional systematic parameter. Joint fits of the semi-exclusive samples will be implemented in the rest of the SBN sterile oscillation analysis.

7.2.6. Full systematic sensitivity studies

Figure 7.9 shows the final comparisons made in the SBN exclusion sensitivity studies. The pseudo-detector systematics are added to the fully-validated flux and interaction parameter sets in the updated sensitivity. The result is a reduction in sensitivity across the entire Δm^2_{41} parameter space. Since the parameters have not yet been finalised, it will be possible to minimise their impact through careful treatment during calibrations of the near and far detectors.

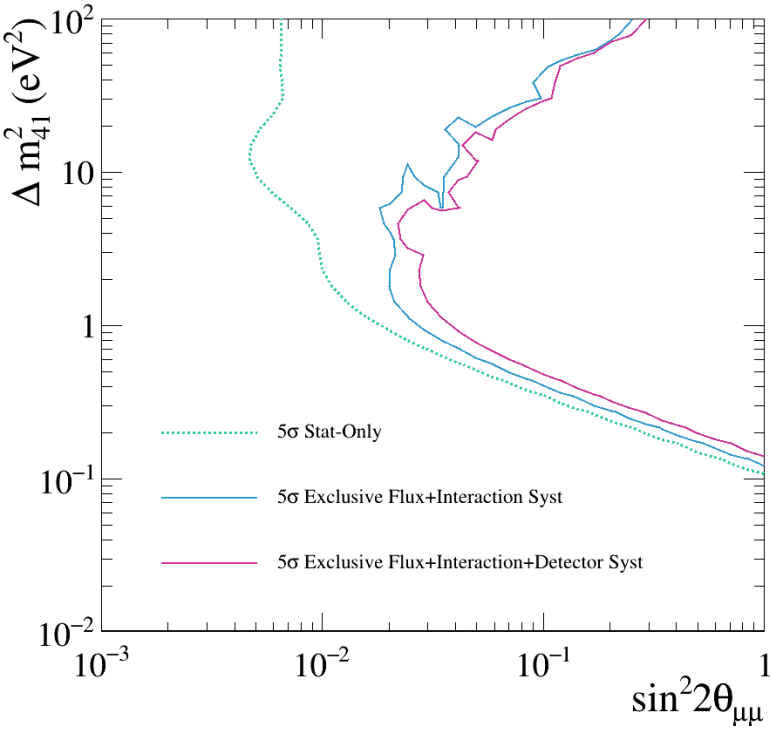

Figure 7.9.: ν_μ disappearance exclusion sensitivity comparison between the well-validated flux and interaction systematic parameter set (blue) and the addition of pseudo-detector systematics (pink). The statistical-only sensitivity is included for reference.

7.3. SBN allowed-region sensitivity studies

This section will present allowed-region (3+1) sterile neutrino oscillation sensitivities following joint semi-exclusive three-detector SBN fits with all systematic parameters. Each contour will depict the region of $\sin^2 2\theta_{\mu\mu}$, Δm^2_{41} parameter space in which the SBN experiment is sensitive to an injected hypothesis at the 5σ confidence level. The injection point corresponds to the global best fit values, $\sin^2 2\theta_{\mu\mu} = 0.07$ and $\Delta m^2_{41} = 1.32$ [28]. All fits are performed with the ν_μ CC 0π and ν_μ CC Other samples of pseudo-reconstructed events, generated using the GENIE v3 G18_10a Valencia 1p1h+2p2h model.

Figure 7.10 shows the statistical-only allowed region along with the impact of incrementally adding systematic sets. The first set includes all of the fully-validated flux and interaction systematic parameters, and results in a decrease in sensitivity from the statistical-only case in all directions. The pseudo-detector systematics are then added and the sensitivity is further reduced across the entire parameter space.

7.4. Global sensitivity studies

Finally, the SBN sensitivity to ν_μ disappearance under the (3+1) sterile neutrino hypothesis is compared to the existing global data. The SBN contours involved in this comparison were constructed with the three-detector semi-exclusive joints fits, and include all systematic parameters. Figure 7.11 demonstrates how the 5σ SBN exclusion confidence limits compare with MiniBooNE and MINOS/MINOS+ data at the 90% confidence level [204] [117] as well as eight years of IceCube data at the 90 and 99% confidence levels [111]. In IceCube, $\theta_{\mu\mu}$ depends on both θ_{24} and θ_{34}, however in this particular dataset the assumption $\theta_{34} = 0$ from [111] allows for the approximation $\theta_{24} = \theta_{\mu\mu}$.

The SBN sensitivity is comparable to that of MINOS/MINOS+ in the region $\Delta m^2_{41} > 1\text{eV}^2$, and supersedes the MiniBooNE sensitivity across the entire parameter space. The IceCube 99% exclusion limit is strong for $\Delta m^2_{41} < 1$ eV^2 and reduces as the mass splitting increases, in the opposite way to the SBN sensitivity. The IceCube 90% closed contour does not quite overlap with the global best-fit point in the 5σ SBN allowed region.

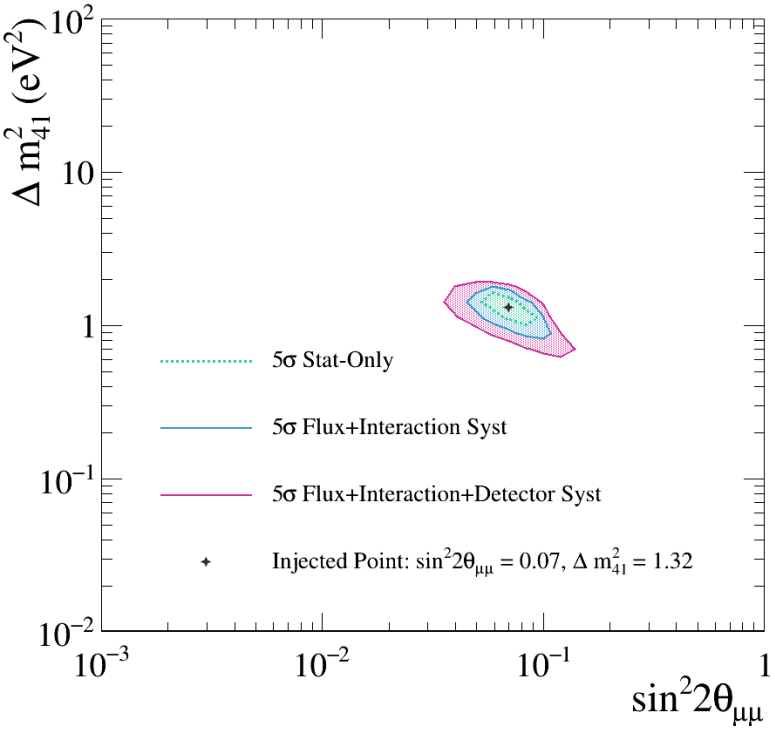

Figure 7.10.: SBN allowed region contours following the three-detector semi-exclusive joint fits of ν_μ CC 0π and ν_μ CC Other samples. The global best fit injected point $\Delta m^2_{41} = 1.32$, $\sin^2 2\theta_{\mu\mu} = 0.07$, is surrounded by the statistical-only contour in green. The flux and interaction systematic parameters are added to the fits in blue. The current set of detector systematic parameters is added and shown in pink.

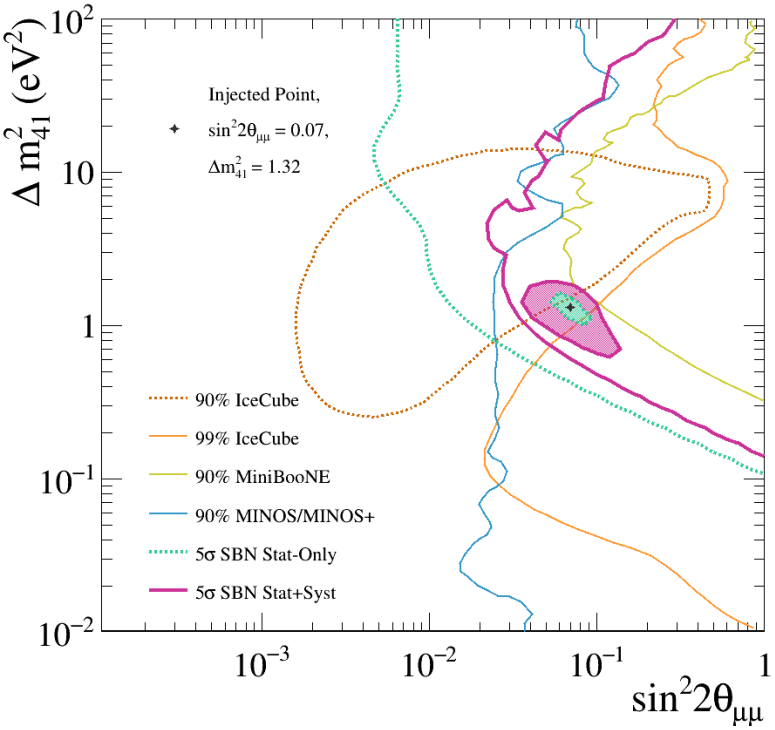

Figure 7.11.: The SBN exclusion and allowed-region sensitivities to ν_μ disappearance under the (3+1) sterile neutrino hypothesis. All interaction, flux and detector systematic parameters are included in the three-detector semi-exclusive joint fits. Also added to the plot are the contours produced with MiniBooNE data (yellow) [204], MINOS/MINOS+ data (blue) [117] and two confidence intervals from eight years of IceCube data (orange solid and dashed) [111]. The confidence levels are specified for each contour in the legend.

7.5. Concluding the SBN sensitivity studies

The complexity of the SBN experimental program requires careful treatment of systematic parameters. It is therefore extremely informative to study the contributions to this sensitivity from each input to, and format of, the analysis. Areas for improvement can then be targeted and constrained, and areas of strength can be identified and pursued.

Firstly, although SBND and ICARUS have the largest impact on the sensitivity across the entire $\sin^2 2\theta_{\mu\mu}$, Δm^2_{41} parameter space, every detector in the SBN program contributes to the ν_μ disappearance sensitivity in a distinct region. The statistical-only model dependence of the sensitivity is non-negligible, and would likely increase substantially with the inclusion of dedicated systematic parameters. If this is the case, each systematic parameter set must be capable of accurately accounting for every model-dependent feature of a sample.

Incorporating systematics into the analysis results in a substantial reduction in sensitivity, especially in the region where SBND is most sensitive, $\Delta m^2_{41} > 1\text{eV}^2$. This is due to the aforementioned role of the near detector in constraining the systematic parameters in the fits, and emphasises the importance performing studies like the mock data analysis. Furthermore, since the flux and interaction systematics are already well-constrained, they are unlikely to be substantially reduced in future. In contrast, the detector parameters currently implemented are placeholders, and the possible degradation to the sensitivity should be carefully considered as they are developed.

One significant improvement to the sensitivity can be made when fitting joint, semi-exclusive, ν_μ CC 0π and ν_μ CC Other samples instead of single, inclusive samples. This is due to the topological dependence of the interaction systematic parameters, which results in certain systematic parameter tweaks having a polarising effect on each of the exclusive samples. This result indicates that separation of the ν_μ CC Other sample into higher pion multiples, as well as the separation of the ν_μ CC 0π sample into proton-multiplicities (with significant statistics) will likely see additional improvements to the sensitivity whilst harnessing the full capabilities of the substantial SBN event rates.

Finally, the current status of the SBN sensitivity is comparable to that of MINOS/MINOS+ in the region $\Delta m^2_{41} > 1\text{eV}^2$ and supersedes the MiniBooNE sensitivity across the entire parameter space. The 99% C.L. IceCube sensitivity is strong in the region $\Delta m^2_{41} < 1\text{eV}^2$ but reduces with increasing Δm^2_{41} as SBN becomes more sensitive. The overall parameter space coverage will improve with updated systematic constraints.

Chapter 8.

Mock data analysis

In high-statistics datasets, such as those in the SBN program, problems may arise if the theoretical model used in the construction of the Monte Carlo samples for the experiment is not sufficiently predictive. For instance, a poor fit result (large χ^2) may be accompanied by tightly constrained systematic parameters, since small deviations from the best-fit point will cause substantial increases to the goodness-of-fit, χ^2, value. Consequently, the uncertainties assigned to the systematic parameters by the fit are incapable of characterising the fit result on their own. The intrinsic inability of the model to describe the data may instead result in large biases postfit, which are not accurately quantifiable through the assigned systematic variances.

If this is the case, when the oscillation analysis procedure is applied to data it is possible that either real oscillation signals may be incorrectly characterised as a systematic fluctuation, or instead that a systematic fluctuation is incorrectly identified as a real oscillation signal. A procedure for assessing and mitigating this issue has been developed in the VALOR fitting framework for the SBN oscillation physics program.

The GENIE model configuration used in the simulation of the SBN MC event samples for the oscillation analyses, G18_10a_02_11a, has been chosen based on a number of studies made by SBN and MicroBooNE which indicated that it best represents how neutrinos interact in LArTPC detectors. It is already known that this model configuration is imperfect, and that in time, we may come to learn of a better representation from new theories and experimental data studies. This further emphasises the importance of understanding the systematic discrepancies for the purpose of accurately extracting real physics results from any systematic variations with appropriately-allocated systematic uncertainties, regardless of the MC-data agreement.

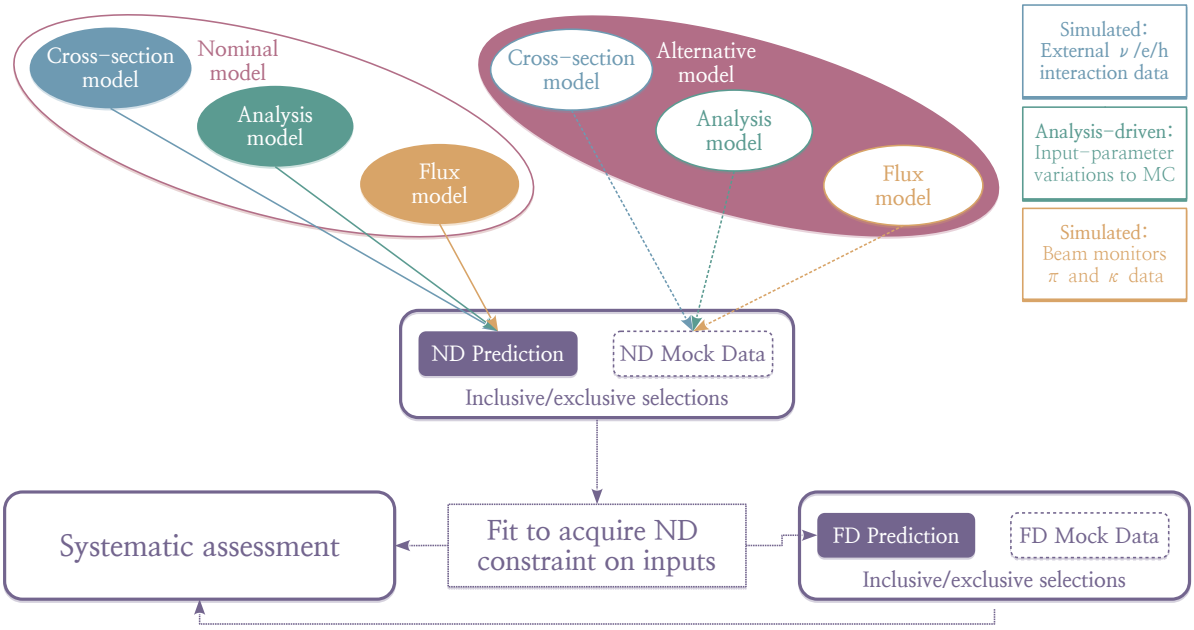

Figure 8.1.: Overview of the mock data analysis procedure involving ND fits and extrapolation to the far detector for assessment.

8.1. Overview of the mock data analysis procedure

In the SBN mock data analysis, near-detector-only fits are performed between the nominal MC sample of neutrino events and 'mock data'. The general analysis procedure is demonstrated graphically in Figure 8.1 and an in-depth explanation will be given throughout the rest of this section.

The SBN 'mock data' samples are constructed from both fundamentally different MC inputs and by altering the magnitude of some parameters in the nominal MC sample. Each mock data sample is constructed in the same way for both the near and far detectors in the analysis. The mock data is designed to encompass possible systematic variations from the MC which may be present in real data. All samples of events used throughout this chapter will be scaled to the nominal SBND and ICARUS exposures, 6.6×10^{20} POT.

SBND-only fits are employed in the mock data analysis, as the near detector should be capable of placing accurate constraints on the input systematic parameters which are correlated between the detectors. This is true because the proximity to the neutrino source means it has the lowest sensitivity to observing both active and sterile neutrino oscillations. Consequently, the cross-section, flux and detector models alone should

characterise the behaviour of the high rate of neutrinos interacting in the active volume in most of the sterile parameter space.

In these fits, every systematic input parameter is allowed to float within limits dependent on the prior uncertainties, and the goodness-of-fit parameter is minimised as per the procedure outlined in section 6.2. These limits are set to $\pm 5\sigma$ for every parameter.

The mock data analysis has explicitly been employed to assess the capability of the analysis procedure of detecting systematic variations according to the input systematic uncertainties, therefore all sterile oscillation physics parameters were set to 0 in the fitting procedure.

In addition, sources of the systematic variations in the mock data are, at present, exclusively driven by the cross-section model. Since the detector model and corresponding systematic parameter set are actively under development across the SBN program and have not yet been finalised, they may not be able to provide a robust indication of any issues in the analysis procedure at this time. The pseudo-detector systematic parameter set has therefore not been incorporated into the current iteration of this analysis.

Following the near detector fit, the mock data analysis is performed in two stages:

1. First, every systematic parameter pull and corresponding uncertainty assignment are assessed, in order to check if the existing systematic parameter set and analysis procedure is capable of describing the various types of data which may be observed. If systematic parameters and/or the analysis procedure itself are not well defined, it may be possible for multiple combinations of systematic parameter tweaks to describe a given set of data with the same accuracy.

2. The second stage is extremely important in the Monte Carlo analysis, as no cross-check will be possible with real data. This stage involves taking advantage of the role of the near detector in constraining the input systematic parameters in the analysis, by applying the postfit parameter pulls and uncertainty assignments to the far detector MC sample. If the near detector constraints were well-defined with sensible error assignments, the mock data at the far detector should agree with the extrapolated MC far detector sample to within these uncertainties.

   Ultimately, the near-far detector extrapolation should consistently describe the unoscillated content of the far detector data, regardless of the differences between the model and data involved in the fits.

8.1.1. MC samples at the near and far detector

The MC samples used in the near detector fits and far detector predictions remain the same throughout the entire analysis. The samples are constructed using the Valencia model configuration in GENIE v3 as per the methods described in sections 4.5 and 4.7. These MC events are then propagated through the pseudo-selection procedure defined in section 6.3.

Figure 8.2 contains the pseudo-reconstructed and selected event rates as a function of reconstructed neutrino energy at the near detector. Each distribution of events is presented as a stacked histogram, broken down into the initial interactions which took place. This is shown for three sample definitions, ν_μ CC Inclusive, ν_μ CC 0π and ν_μ CC Other. Figure 8.3 contains the analogous distributions at the far detector.

Two formats of the fitting procedure will be run throughout this analysis, the first will use a single near detector fit of ν_μ CC Inclusive data, and the second will separate out this near detector sample into ν_μ CC 0π and ν_μ CC Other components to perform a joint fit of the semi-exclusive samples.

The motivation for separating out the sample into semi-exclusive channels is to give the fit a better chance at assessing these model-dependencies through the systematic pulls. For instance, if the model used to construct the mock data contains 50% more 2p2h events than the MC sample, Figure 8.2 demonstrates that this will result almost entirely in an increase of ν_μ CC 0π events. When the fit then assess the variation of systematic parameters which impact the 2p2h rate, this topological dependence would likely be more distinct and therefore easier to get right when the samples have been separated. The sensitivity study presented in section 7.2.5 also demonstrated an improvement when switching to the semi-exclusive analysis.

8.2. Validating the analysis procedure

Before performing the full mock data analysis, in which all systematic parameters are allowed to float in the fits, it is useful to determine the expected performances of the analysis procedure. To this end, a subset of the full cross-section and flux systematic parameter list were chosen, based broadly on the magnitude of their impact whilst maintaining a reasonable level of diversity in the source of the uncertainties and the range of impacted reaction modes in the set. This list is given in Table 8.1.

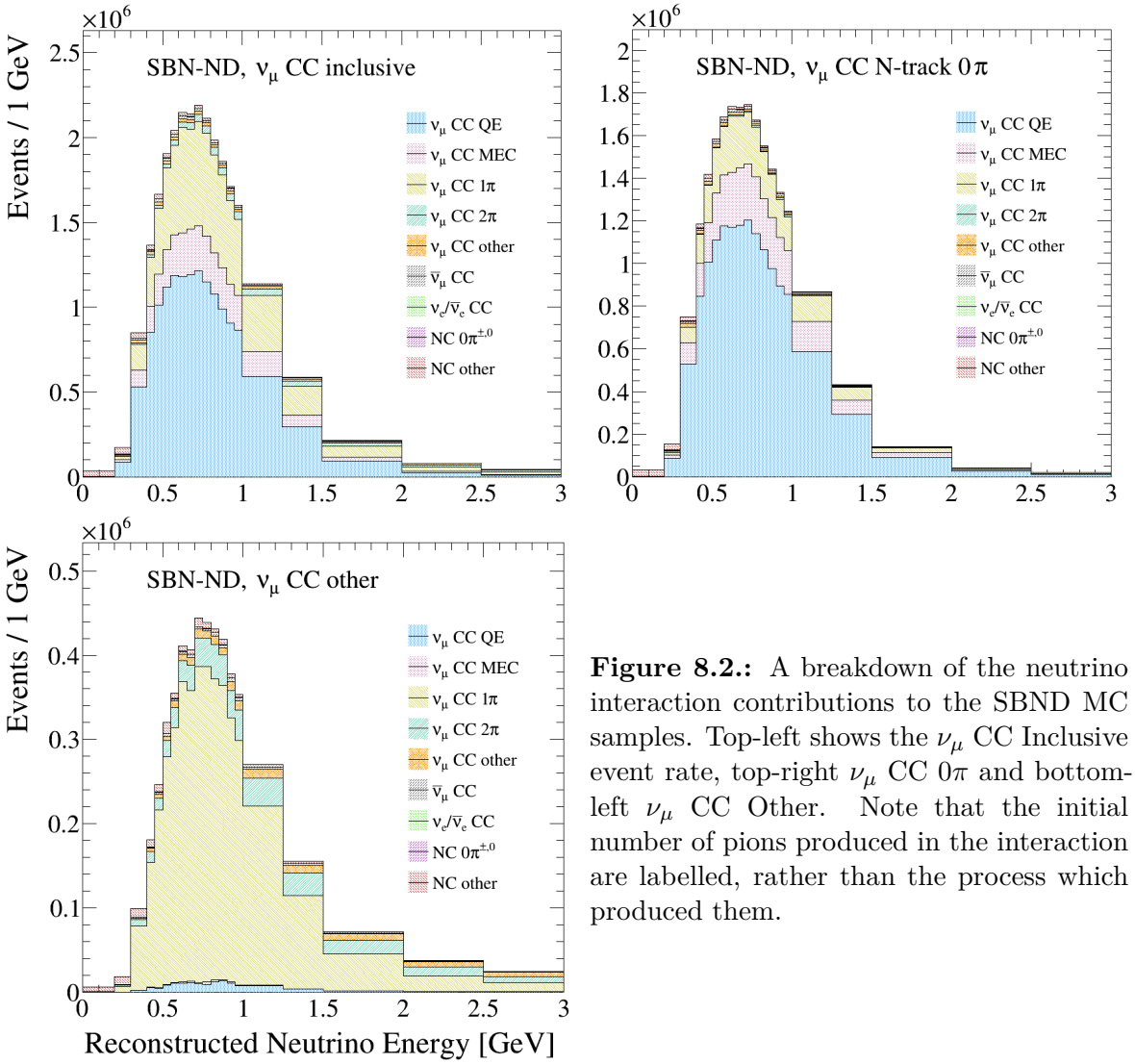

Figure 8.2.: A breakdown of the neutrino interaction contributions to the SBND MC samples. Top-left shows the ν_μ CC Inclusive event rate, top-right ν_μ CC 0π and bottom-left ν_μ CC Other. Note that the initial number of pions produced in the interaction are labelled, rather than the process which produced them.

The validation method is conducted as follows:

1. Tweak each of the aforementioned systematic parameters by a random amount, between the limits $\pm 5\sigma$
2. Define a toy MC dataset as the nominal MC sample with the tweaked systematic parameter values applied
3. Fit the nominal, un-oscillated CC Inclusive MC sample to this toy MC
4. Fit the nominal, un-oscillated CC Semi-exclusive MC samples to this toy MC
5. Repeat $N_{i,e} = 10,000$ times; i =inclusive, e =exclusive.

Following the $N_{i,e}$ fits, two main analysis components can be assessed simultaneously,

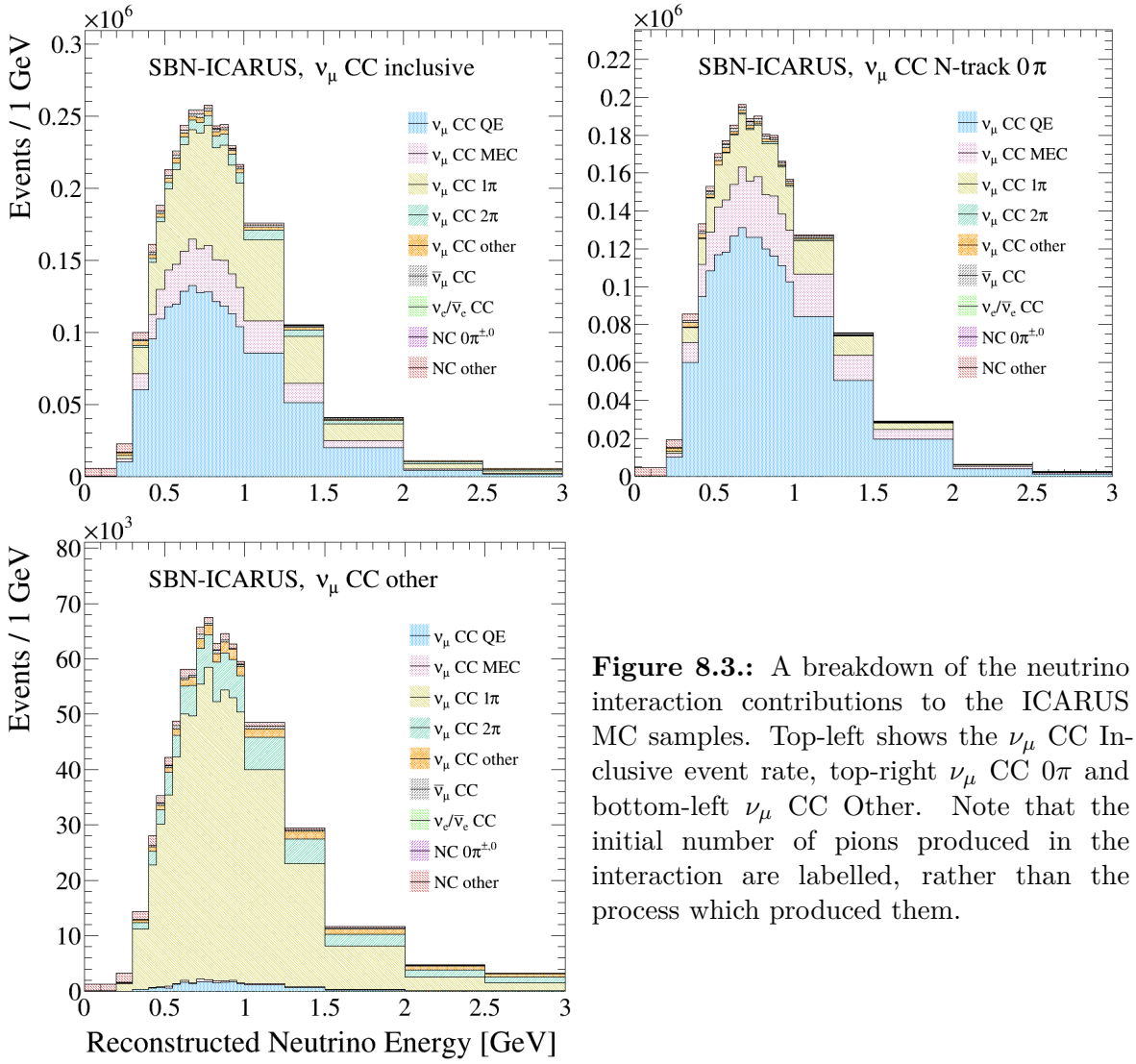

Figure 8.3.: A breakdown of the neutrino interaction contributions to the ICARUS MC samples. Top-left shows the ν_μ CC Inclusive event rate, top-right ν_μ CC 0π and bottom-left ν_μ CC Other. Note that the initial number of pions produced in the interaction are labelled, rather than the process which produced them.

- Whether the analysis procedure is capable of correctly determining the tweaks applied to a small number of systematic parameters in the MC sample by assigning appropriate parameter pulls and corresponding uncertainties
- Whether the semi-exclusive fits perform better than the inclusive fits when searching for these systematic parameter tweaks.

Figure 8.4 shows each of the true parameter tweaks in the first toy MC dataset, along with the postfit pull and corresponding uncertainty following both the inclusive and exclusive fits of that dataset. The inclusive fit correctly[1] finds the true pull to within

[1] 'Correct' corresponds to a pull±uncertainty assigment which overlaps with the true parameter value.

Parameter	Description	$\delta P/P$
	Interaction parameters	
$f_{M_A^{CCQE}}$	Axial mass for CC quasi-elastic	-15% +25%
$f_{M_A^{CCRes}}$	Axial mass for CC resonance neutrino production	±20%
$f_{nR_{\nu n}^{CC1\pi}}$	Non-resonance bkg normalisation in νn CC 1π reactions	±50%
$f_{nR_{\nu p}^{NC2\pi}}$	Non-resonance bkg normalisation in νp NC 2π reactions	±50%
$f_{M_V^{NCRes}}$	Vector mass for NC resonance neutrino production	±10%
$f_{B_{HT}}$	Higher-twist parameter B for NC and CC DIS events	±25%
$f_{R_\pi^{Abs}}$	Intranuclear absorption fraction for pions	±20%
$f_{R_N^{Inel}}$	Intranuclear inelastic re-scattering fraction for nucleons	±40%
	Flux parameters	
$f_{\sigma_{QE}^N}$	Secondary nucleon interactions in the target (Be) and horn (Al), quasi-elastic cross-section	±20% (Be) ±45% (Al)
$f_{SkinEffect}$	Depth that the current penetrates the horn conductor	$< 18\%$

Table 8.1.: The subset of systematic parameters involved in the analysis validation procedure. Included are 8 interaction parameters: 4 proposal-based, 2 modern and 2 FSI. There are 2 flux parameters: 1 optical and 1 cross-section.

the assigned postfit uncertainty in 6 of the 10 parameters, whilst the exclusive fit is able to find the true pull to within the postfit uncertainty in all 10 parameters.

Although this single example does demonstrate the significant improvement possible when switching from inclusive to exclusive fits, it is of course more informative to look at the result of all the fits. Table 8.2 summarises numerically the total number of fits in which the true pull was found to within the assigned uncertainty for each of the parameters in both the inclusive and exclusive analysis variants. In summary,

- The number of correct pulls never goes down when switching from inclusive to exclusive fits
- The inclusive fits get the pull correct over 90% of the time in 3 of the 10 parameters. The exclusive fits get the pull correct over 90% of the time in 6 of the 10 parameters
- The inclusive fits get the pull correct $< 80\%$ of the time in half of the parameters. The exclusive fits get the pull correct $< 80\%$ of the time in none of the parameters

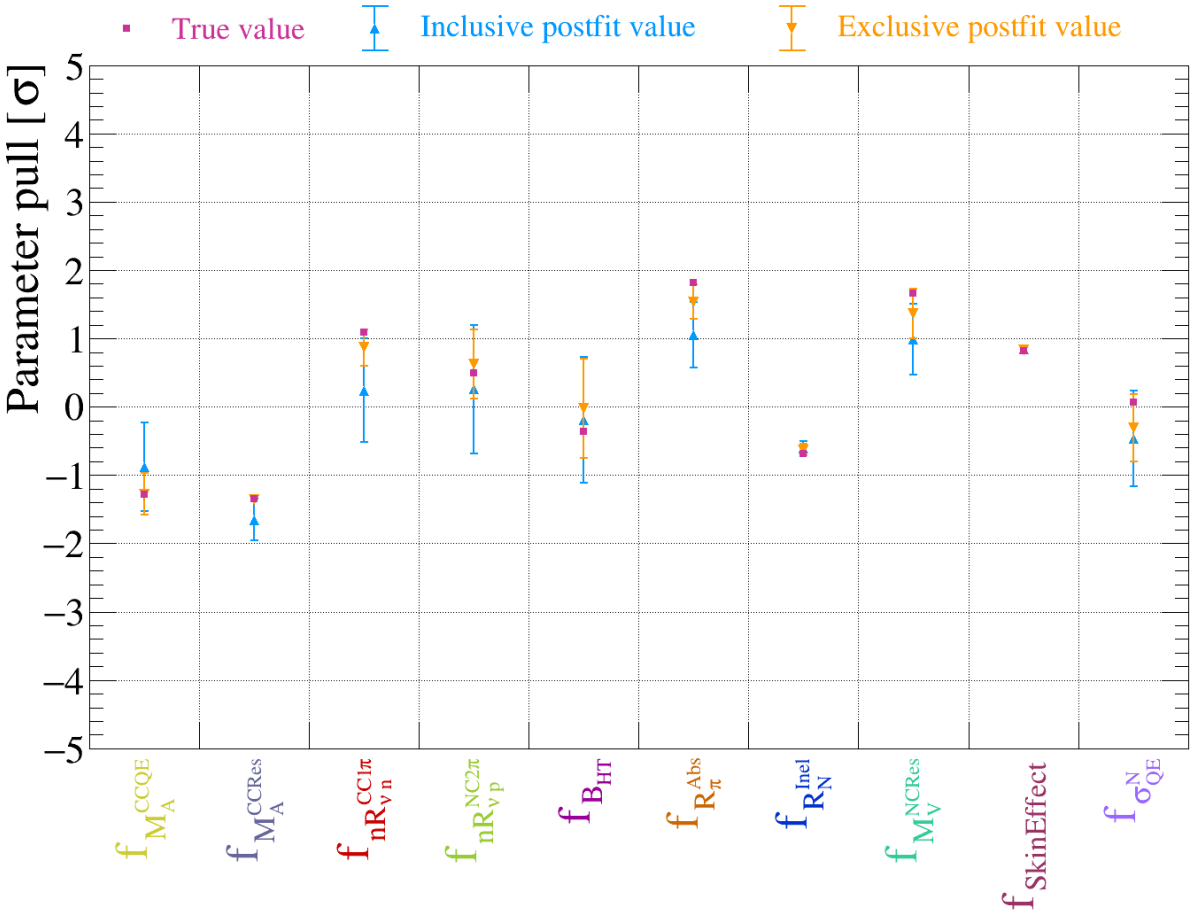

Figure 8.4.: Systematic parameter pull comparisons between the true and postfit values. The true pull is shown in pink, the postfit values and assigned uncertainties are in blue following the inclusive fit and orange for the exclusive fit.

- When assessing all the parameters together, the inclusive fits find the pull 82% of the time and the exclusive fits find the pull 90% of the time.

A further metric which can be constructed to assess the performance of the fits is a simple resolution definition, $\text{Pull}_{\text{Bestfit}} - \text{Pull}_{\text{True}}$ in units of the prefit uncertainty, σ_{Prefit}, such that a value of 0 would indicate that the fit correctly found the true parameter pull. This metric does not take into consideration the assigned postfit uncertainty on the pull. Figure 8.5 and 8.6 demonstrate this parameter for each of the systematic parameter pulls individually.

In every single case, the resolution improves when moving from inclusive to exclusive fits. This is especially clear in the interaction cross-section systematic parameters, since the exclusive sample definitions are able to distinguish the topological differences in the behaviour of the tweaks. Although the FSI parameters impact almost all of the

Parameter	Inclusive	Exclusive
$f_{SkinEffect}$	9523	9734
$f_{M_A^{CCRes}}$	9150	9213
$f_{R_N^{Inel}}$	9030	9423
$f_{nR_{\nu n}^{CC1\pi}}$	8504	9401
$f_{R_\pi^{Abs}}$	8548	8911
$f_{M_V^{NCRes}}$	7831	9165
$f_{M_A^{CCQE}}$	7810	8479
$f_{\sigma_{QE}^N}$	7337	8373
$f_{B_{HT}}$	7025	8386
$f_{nR_{\nu p}^{NC2\pi}}$	6947	9349
Total	81,615	90,434

Table 8.2.: The number of inclusive (left) and exclusive (right) fits which correctly found the true parameter pull to within the assigned postfit uncertainty. The list is ordered from most to least in the context of the inclusive fits.

interaction modes and are therefore less topology-dependent, there is still a noticable improvement when switching the fitting method. On the other hand, although the exclusive samples include the 0π final state, the $f_{M_A^{CCQE}}$ parameter does not observe the best improvement when switching to the joint fits.

The entire parameter set is shown together in Figure 8.7. Since a delta-peak at 0 would indicate that the fits found the true pulls correctly every single time, the reduction in standard deviation of the distributions by 50% when moving from inclusive to exclusive fits quantifies the magnitude of this improvement.

The final metric analysed following the inclusive and exclusive fits was the goodness-of-fit statistic per degrees of freedom, of which there were 10. This has been plotted following all inclusive and exclusive fits in Figure 8.8. Given that a value of 1 would indicate a perfect assignment of the postfit uncertainty, the shift of the mean of the distribution from 0.66 in the inclusive fits to 0.85 in the exclusive fits demonstrates the improved postfit uncertainty assignments in the exclusive fits.

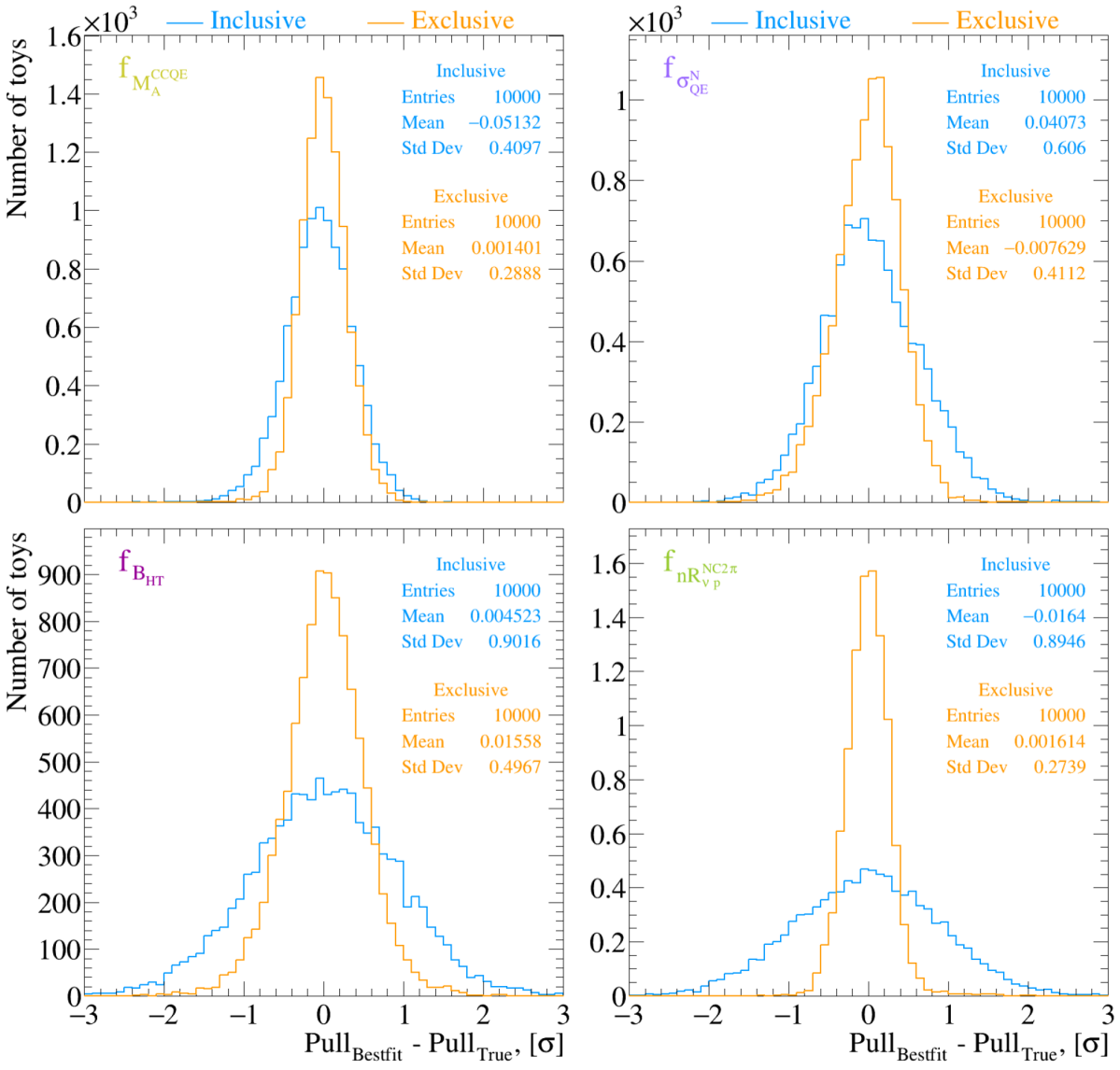

Figure 8.5.: An overlay of the inclusive (blue) and exclusive (orange) fit resolutions, $\text{Pull}_{\text{Bestfit}} - \text{Pull}_{\text{True}}$ in units of σ_{Prefit} for the remaining 4 parameters.

In summary, switching from inclusive to joint exclusive samples should substantially improve the performance of the fits. This is true for both the ability of the fit to find any explicit parameter pulls as well as in the assignment of the uncertainty on the pull. When developing this into the full mock data analysis, there will no longer be explicit parameter tweaks to find, and instead fundamental differences between samples must be characterised by the set of systematic parameter knobs and their prior uncertainty. A well-defined analysis procedure should be capabable of using a well-defined set of systematic knobs to characterise the complex mock data-MC differences.

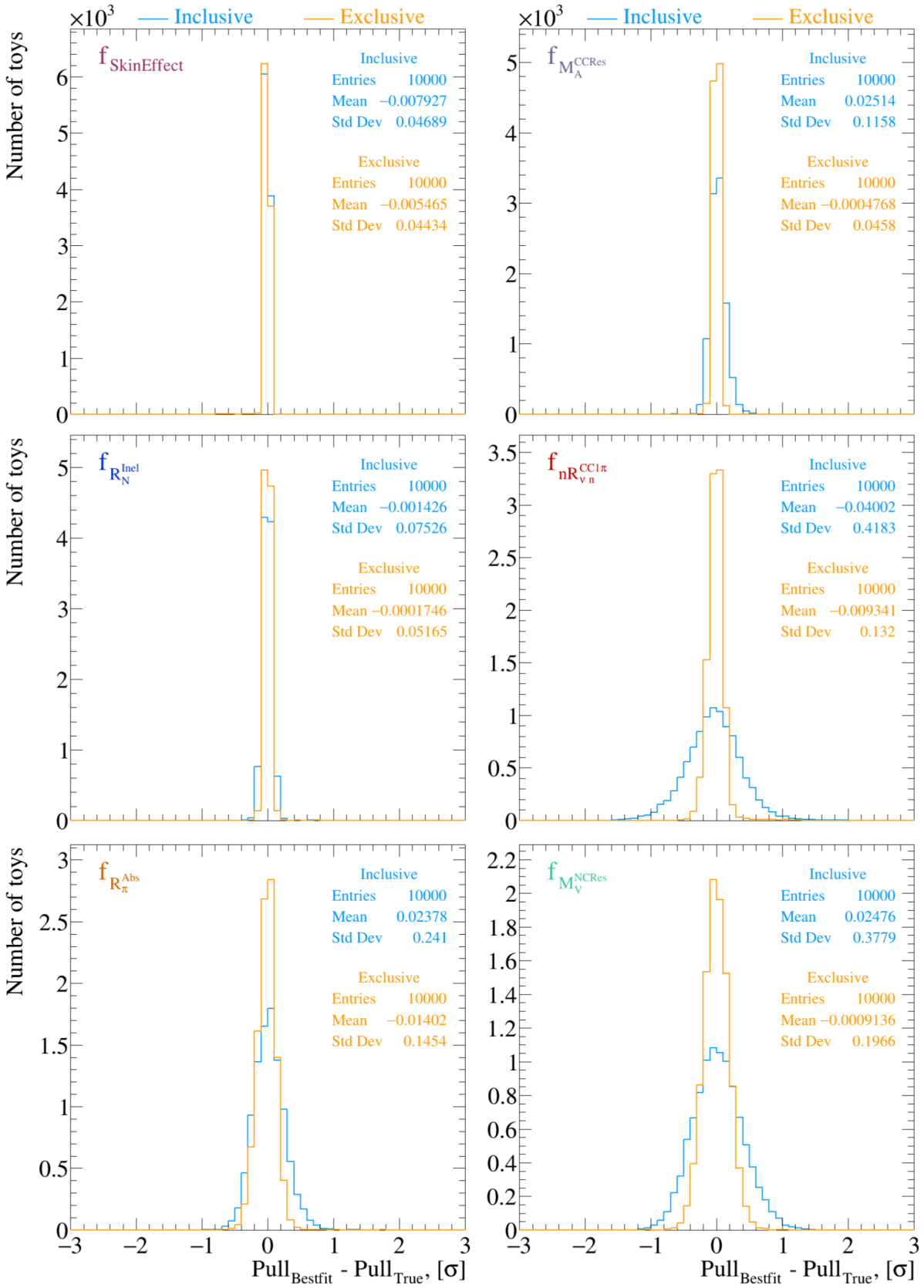

Figure 8.6.: An overlay of the inclusive (blue) and exclusive (orange) fit resolutions, $\text{Pull}_{\text{Bestfit}} - \text{Pull}_{\text{True}}$ in units of σ_{Prefit} for 6 of the 10 parameters.

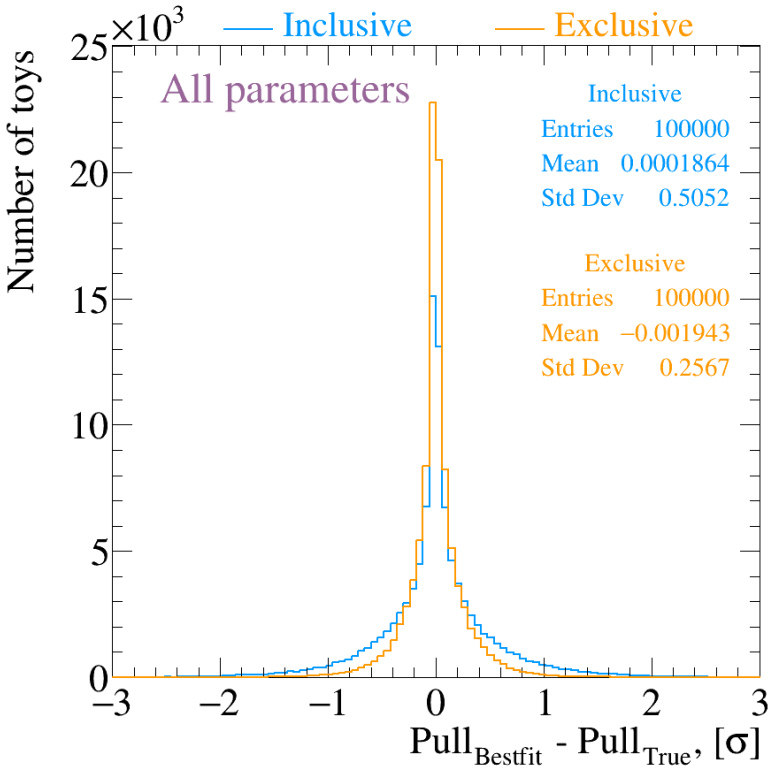

Figure 8.7.: An overlay of the inclusive (blue) and exclusive (orange) fit resolutions, $\text{Pull}_{\text{Bestfit}} - \text{Pull}_{\text{True}}$ in units of σ_{Prefit} for all parameters in all fits.

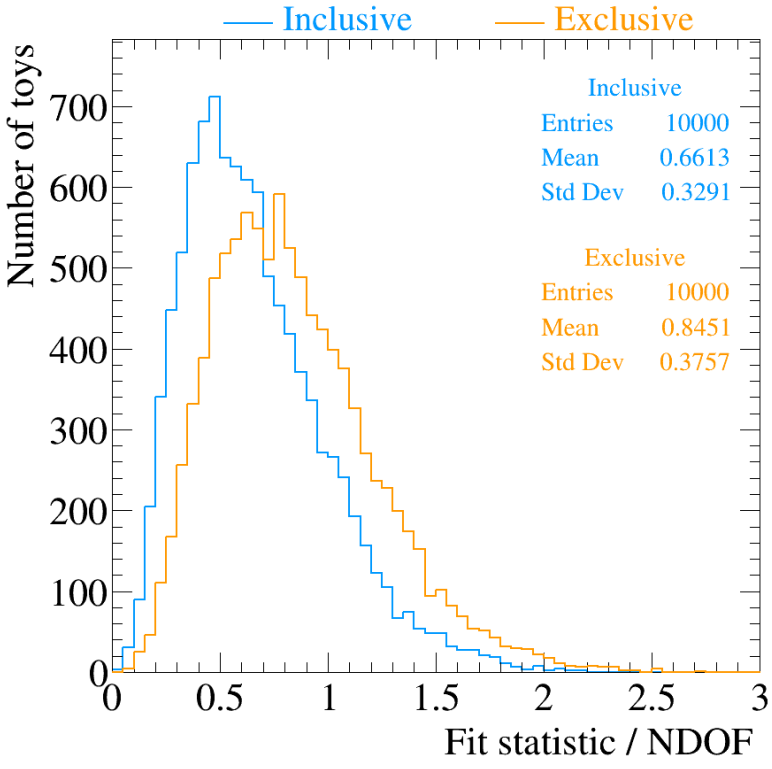

Figure 8.8.: Comparing the goodness-of-fit statistic per 10 degress of freedom following the inclusive (blue) and exclusive (orange) fits. A value of 1 would indicate the errors were assigned perfectly by the fit.

8.3. First iteration of the mock data analysis

The first mock data sample analysed was constructed using the GENIE v2 Default+MEC model configuration. A breakdown of the post-selection interaction contributions to the reconstructed neutrino energy event rate spectra for each of the three sample definitions is shown at the near detector in Figure 8.9 and the far detector in Figure 8.10. A numerical summary of the near detector event rates in each of the three samples for both the nominal MC and current mock dataset is given in Table 8.3. The rates are calculated following the selection procedure. The full set of interaction and flux systematic parameters were included in the fits.

8.3.1. Inclusive analysis

The systematic parameter pulls and the corresponding uncertainties assigned by the inclusive near detector fit are shown in Figure 8.11. Since the difference between the mock data and MC sample cannot be characterised by specific alterations of the systematic parameters, an interpretive approach to analysing the output must be taken.

The issue which is immediately apparent in the systematic pulls is that the flux parameters have been tweaked and have had extremely small uncertainties assigned to them. This is likely due to the overall difference in event rate between the MC and mock data samples, however there are no differences in the flux between the two samples. One tweak the fit does appear to correctly allocate is an increase of the parameter controlling the 2p2h event rate by approximately 100%. According to Table 8.3 this would bring the total number of 2p2h events to almost 500,000, which is around the rate present in the mock data.

It is extremely difficult to assess the rest of the interaction parameter pulls, as tweaks of many different systematic knobs will impact the event rate of a single initial state in a unique way. An alternate method of assessing the fit results is to look at the impact on the near detector reconstructed neutrino energy spectra. This is shown in Figure 8.12 as a comparison between the mock data spectra, the prefit spectra $\pm 1\sigma$ and the postfit spectra $\pm 1\sigma$. This assessment shows that there is good, but not perfect, agreement between the postfit and mock data spectra, and in a number of bins the postfit uncertainty appears to have been underestimated.

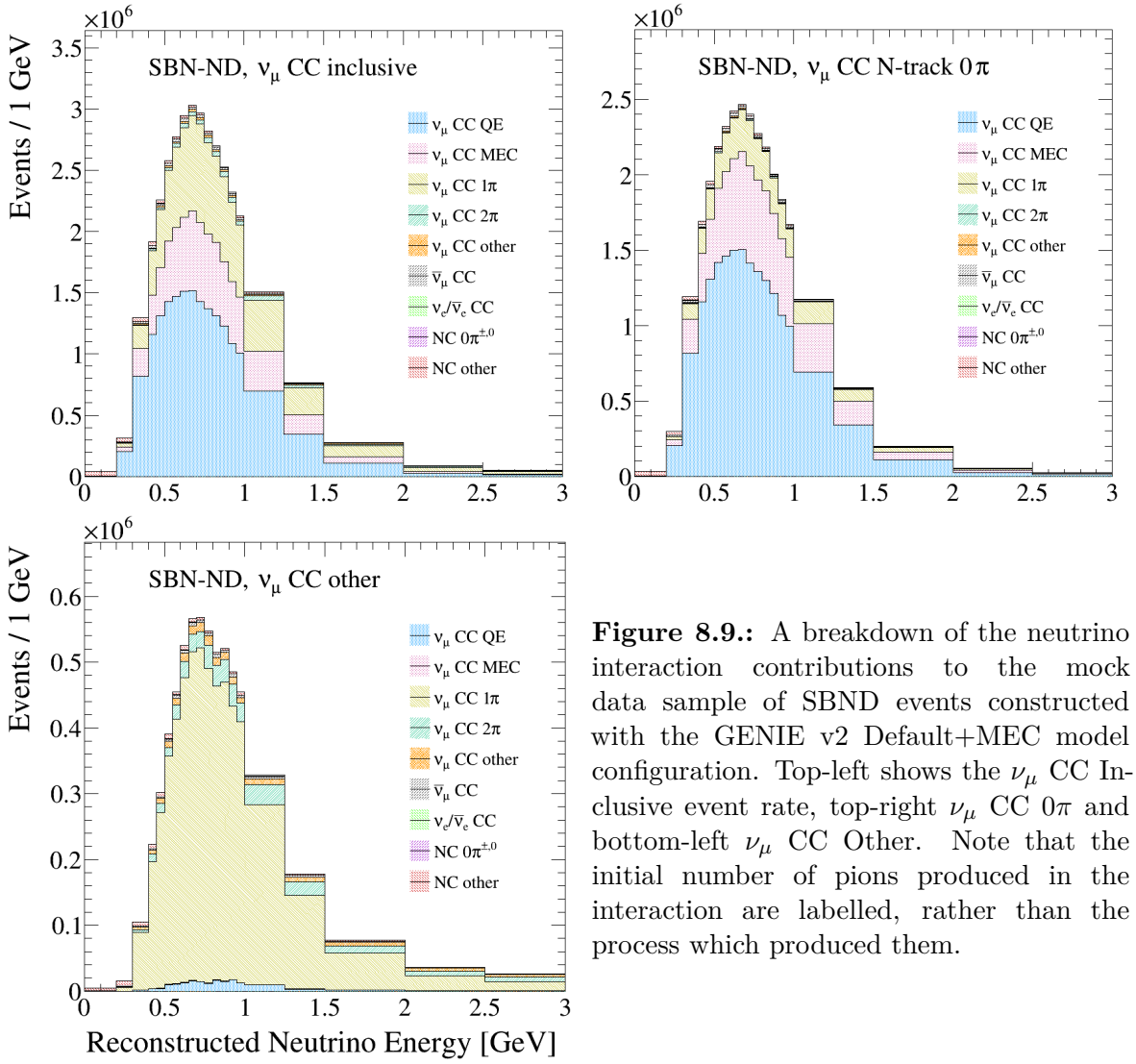

Figure 8.9.: A breakdown of the neutrino interaction contributions to the mock data sample of SBND events constructed with the GENIE v2 Default+MEC model configuration. Top-left shows the ν_μ CC Inclusive event rate, top-right ν_μ CC 0π and bottom-left ν_μ CC Other. Note that the initial number of pions produced in the interaction are labelled, rather than the process which produced them.

Rather than analysing every systematic parameter pull individually from Figure 8.11, one can make a general assessment of the systematic parameter tweaks by observing how their values and uncertainties modify the MC sample at the far detector with respect to the mock data at the far detector. To that end, the mock data, prefit and postfit reconstructed neutrino energy spectra are shown as an overlay in Figure 8.13.

Two things are immediately clear when analysing the far detector spectra,

1. The parameter pulls determined by the fit are insufficient for characterising the mock data, as the integrated postfit event rate has been overestimated by 3.4% of the integrated mock data event rate. This is a direct indication that the current form of the analysis procedure is not capable of correctly-interpreting variations to theoretical model through systematic parameter tweaks.

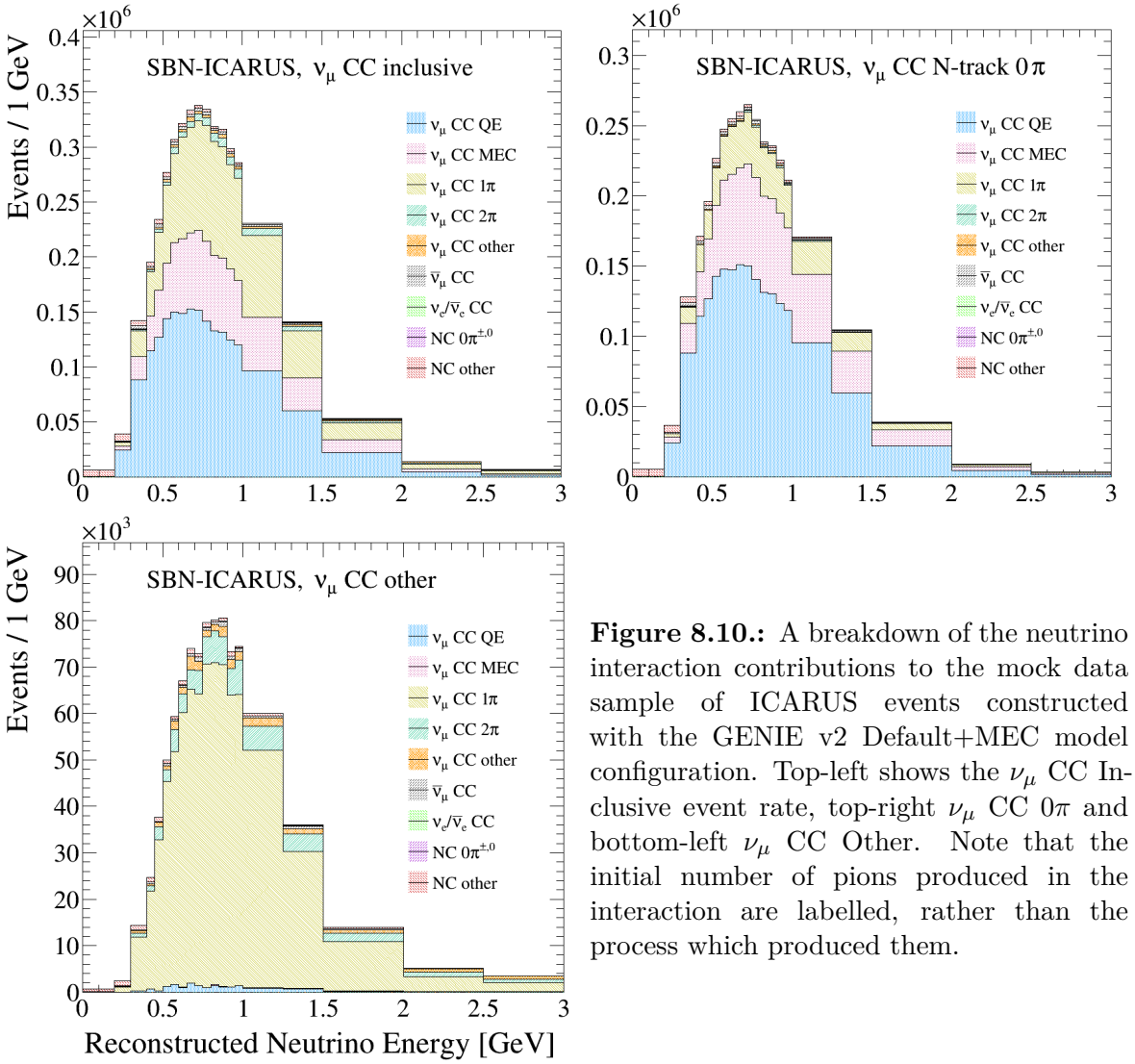

Figure 8.10.: A breakdown of the neutrino interaction contributions to the mock data sample of ICARUS events constructed with the GENIE v2 Default+MEC model configuration. Top-left shows the ν_μ CC Inclusive event rate, top-right ν_μ CC 0π and bottom-left ν_μ CC Other. Note that the initial number of pions produced in the interaction are labelled, rather than the process which produced them.

2. The uncertainties assigned to the postfit parameter values are significantly smaller than this difference, as the same event rate difference can be quantified as 6.6 times the size of the statistical + assigned systematic postfit uncertainty, σ_{Postfit}.

The result of the near detector inclusive fit makes it clear that the current analysis method is not capable of extracting the correct information from the mock data fits. In real data, this discrepancy could be incorrectly interpreted as an oscillation signal as there is no way of disentangling systematic from physics effects. It is therefore critical that the systematic parameter definitions, prior uncertainty assignments and the oscillation analysis procedure are carefully analysed and improved in order to eliminate the possibility of finding a false oscillation signal, this is attempted in the following sections.

Contribution	ν_μ CC Inc.		ν_μ CC 0π		ν_μ CC Oth.	
	Rate	% total	Rate	% total	Rate	% total
Monte Carlo sample, GENIE v3 G18_10a_02_11a						
Total	1,885,300	100	1,457,900	100	427,500	100
ν_μ CC QE	994,800	52.8	984,900	67.6	9900	2.3
ν_μ CC 2p2h	223,300	11.8	221,800	15.2	1400	0.3
ν_μ CC $1\pi^{\pm,0}$	518,500	27.5	198,000	13.6	320,400	75.0
ν_μ CC $2\pi^{\pm,0}$	64,900	3.4	7700	0.5	57,100	13.4
ν_μ CC Other	37,000	2.0	13,300	0.9	23,700	5.5
Other	46,800	2.5	32,200	2.2	15,000	3.5
Mock data sample, GENIE v2 Default+MEC						
Total	2,534,500	100	2,025,500	100	509,000	100
ν_μ CC QE	1,239,500	48.9	1,227,800	60.6	11,700	2.3
ν_μ CC 2p2h	506,000	20.0	505,000	24.9	900	0.2
ν_μ CC $1\pi^{\pm,0}$	656,600	25.9	241,100	11.9	415,500	81.6
ν_μ CC $2\pi^{\pm,0}$	52,900	2.1	7600	0.3	45,300	8.9
ν_μ CC Other	28,700	1.1	5600	0.2	23,100	4.5
Other	50,800	2.0	43,400	2.1	12,500	2.5

Table 8.3.: Initial state contributions to the mock data and MC event rates in SBND along with the relative fraction of the contribution to the total rate of the sample. Note that the initial number of pions produced in the interaction are labelled, rather than the process which produced them.

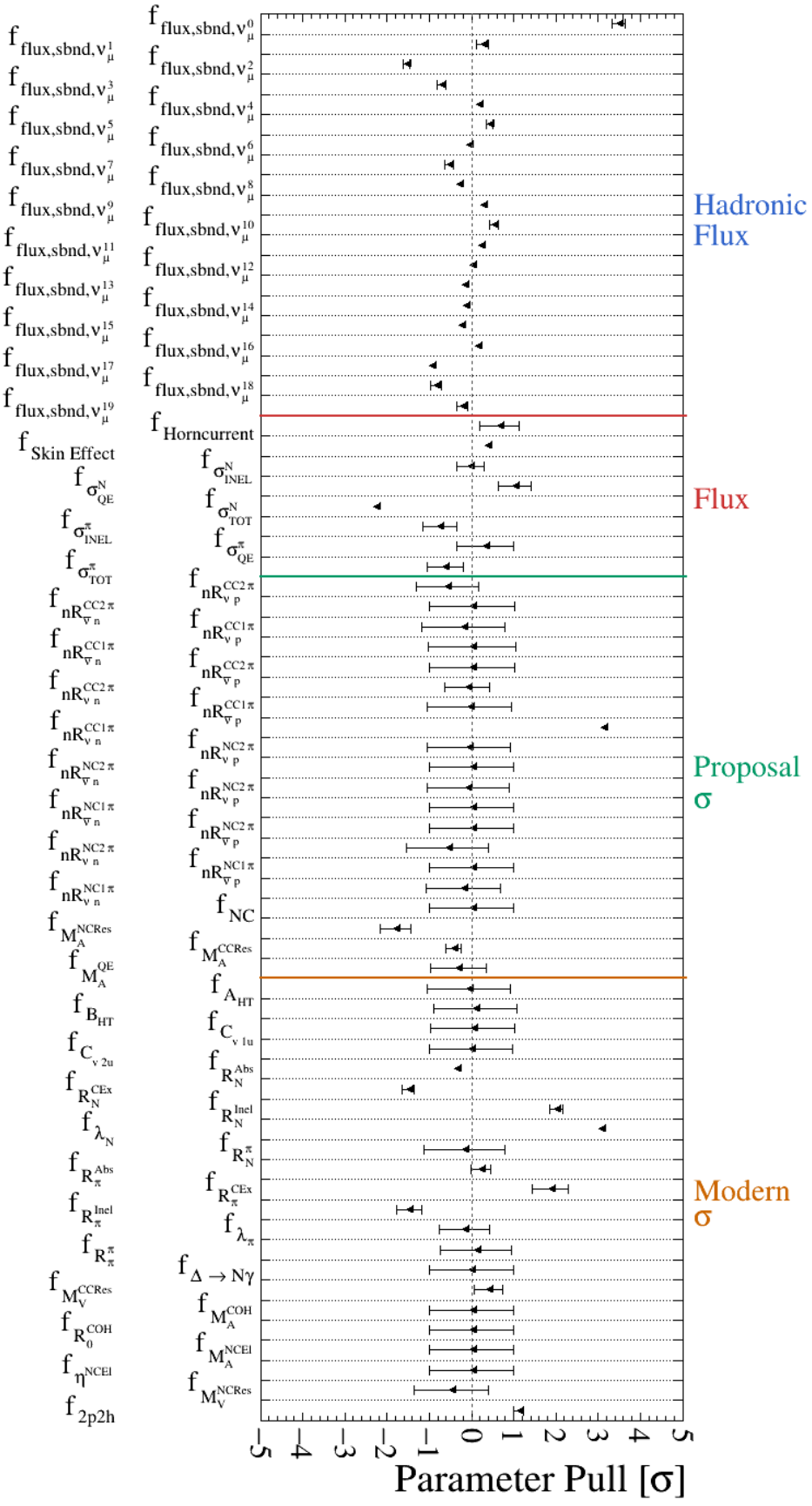

Figure 8.11.: The parameter pulls and corresponding uncertainties assigned when fitting the inclusive MC sample to the inclusive GENIE v2, Default+MEC mock dataset.

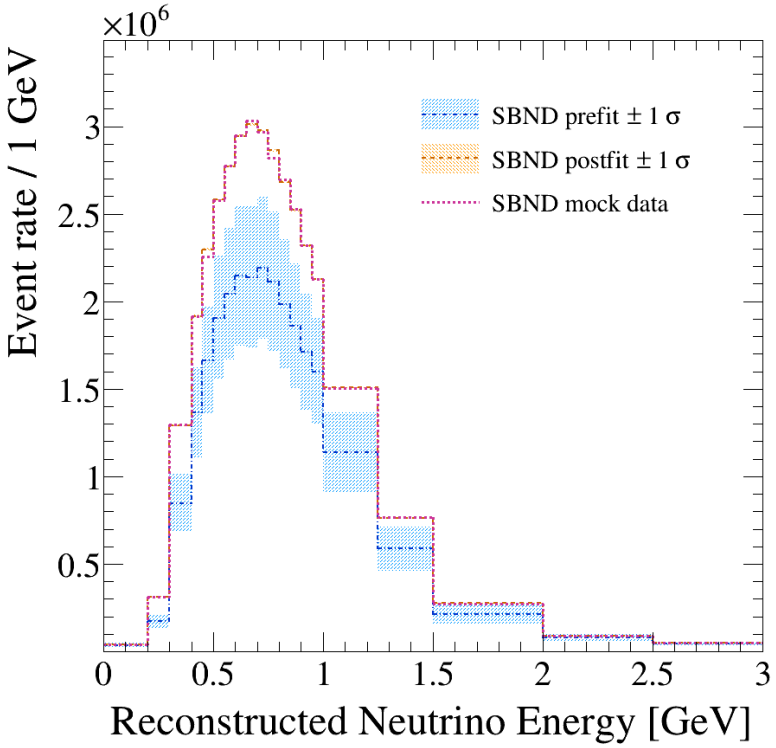

Figure 8.12.: The near detector mock data reconstructed neutrino energy spectra is shown in pink. The prefit MC spectra along with the $\pm 1\sigma$ error envelope is shown in blue and the analogous distribution is shown in orange following the inclusive fit.

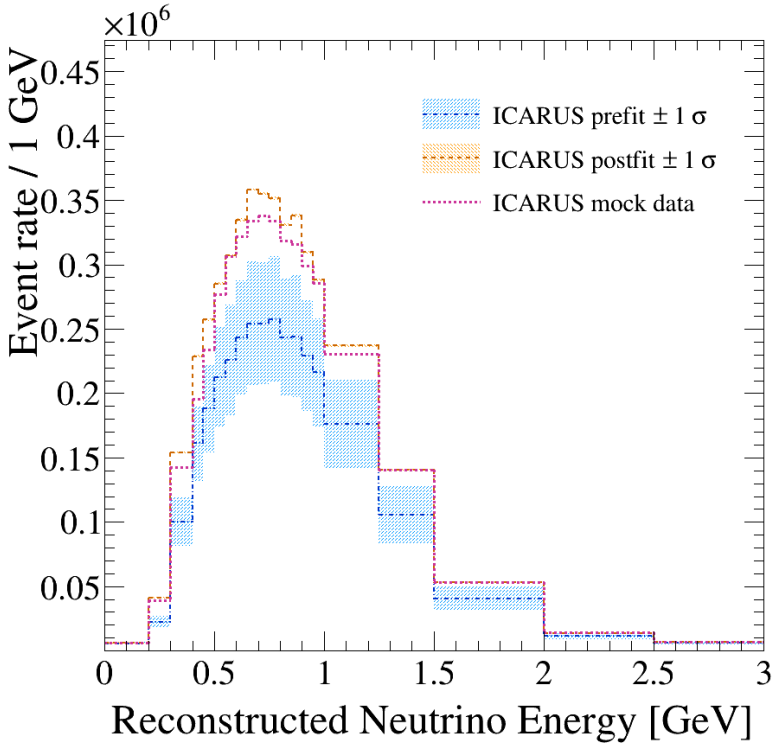

Figure 8.13.: The far detector mock data reconstructed neutrino energy spectra is shown in pink. The prefit MC spectra along with the $\pm 1\sigma$ error envelope is shown in blue and the analogous distribution is shown in orange following the inclusive fit.

8.3.2. Exclusive analysis

In order for the analysis procedure to have a better handle on the systematic differences between the mock data and MC samples, a joint, near detector-only fit of the ν_μ CC Inclusive sample separated into ν_μ CC 0π and ν_μ CC Other events is instead performed. The ν_μ CC 0π topology was chosen as it the dominant channel in the SBN datasets. ν_μ CC Other was not further-subdivided at this stage of the analysis, in order to minimise the corresponding systematic contributions to the analysis when switching to semi-exclusive fits and maximise the statistics in each of the semi-exclusive samples. The same mock data analysis procedure was followed as in the inclusive case, by first studying the systematic parameter pulls and corresponding uncertainties assigned by the exclusive fit.

The systematic parameter pull plot for this iteration of the analysis is given in Figure 8.14. In this case, more of both the flux and interaction parameters have been pulled from the nominal values. This is reflected in the systematic penalty assigned to the exclusive fit statistic, $\chi^2_{syst,exc} = 215$, up from $\chi^2_{syst,inc} = 135$ in the inclusive fit, both of which have 149 degrees-of-freedom. More specifically, the hadronic flux parameters have once again been pulled incorrectly, however the uncertainties assigned to those pulls are distinctly more suitable than in the inclusive case. The remaining flux parameters have been tweaked much further than in the inclusive fits, although the uncertainty assignment is once again more substantial in the exclusive fits. In contrast to the correctly-defined increased pull in the inclusive fits, the 2p2h systematic has this time been reduced by a very small amount.

Aside from comparing small differences with the inclusive parameter pulls, it is still extremely difficult to learn much from this plot. Looking instead at the near and far detector spectra in Figures 8.15 and 8.16, the postfit spectra and uncertainties can be assessed once more. What is immediately clear, even in the near detector overlay, is that the postfit uncertainty assignment has improved significantly in the exclusive fits. When the extrapolation to the far detector is then performed, this becomes even more apparent. The integrated event rate difference between the far detector postfit and mock data rates has only been slightly reduced, to 2.9%. However, the improvement is quantified when this event rate difference is expressed with respect to the stat+syst postfit uncertainty assignment: 2.0 σ_{Postfit}, down from 6.6 σ_{Postfit} from the inclusive fit.

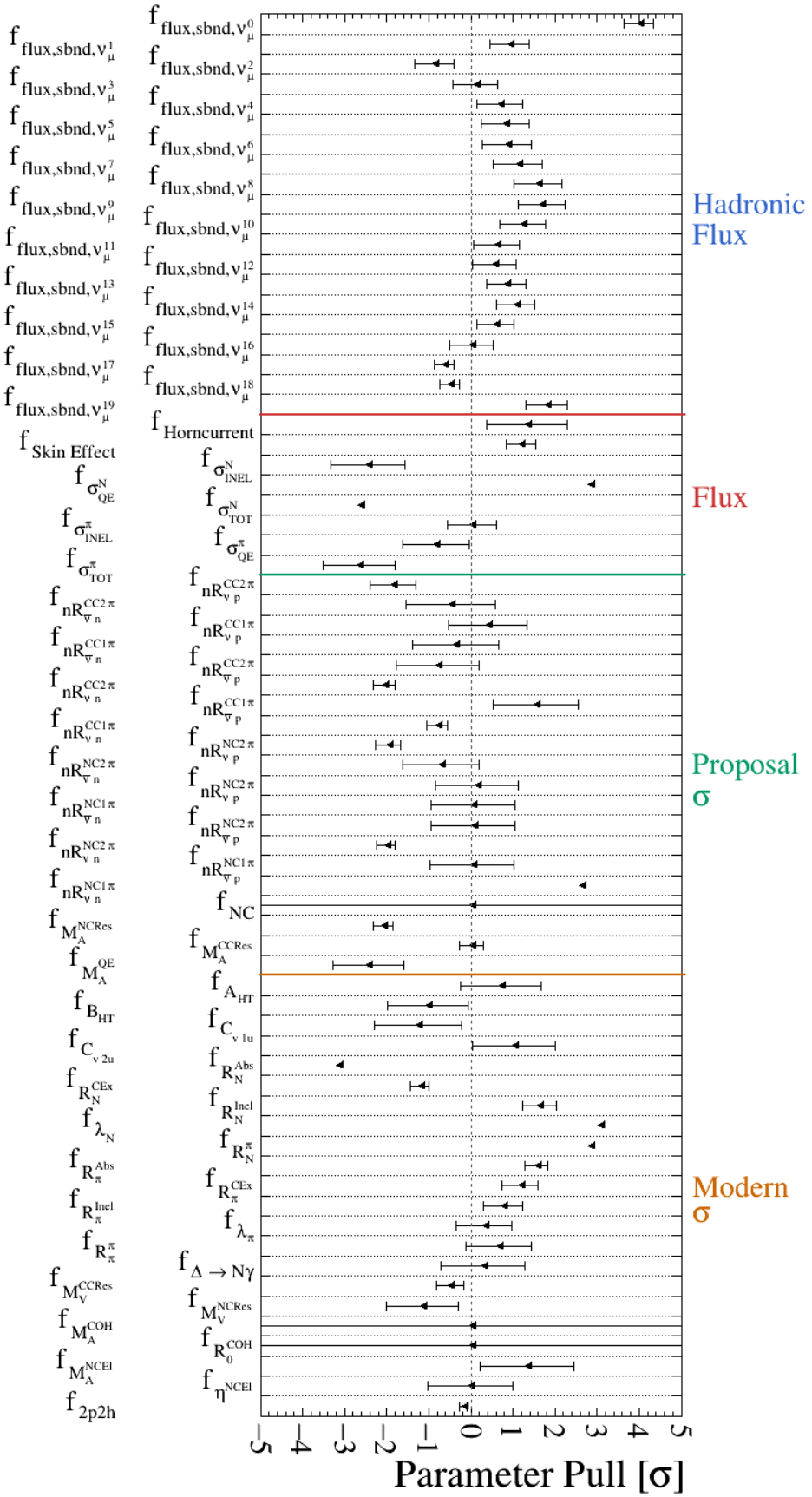

Figure 8.14.: The parameter pulls and corresponding uncertainties assigned when fitting the exclusive MC samples to the exclusive GENIE v2, Default+MEC mock dataset.

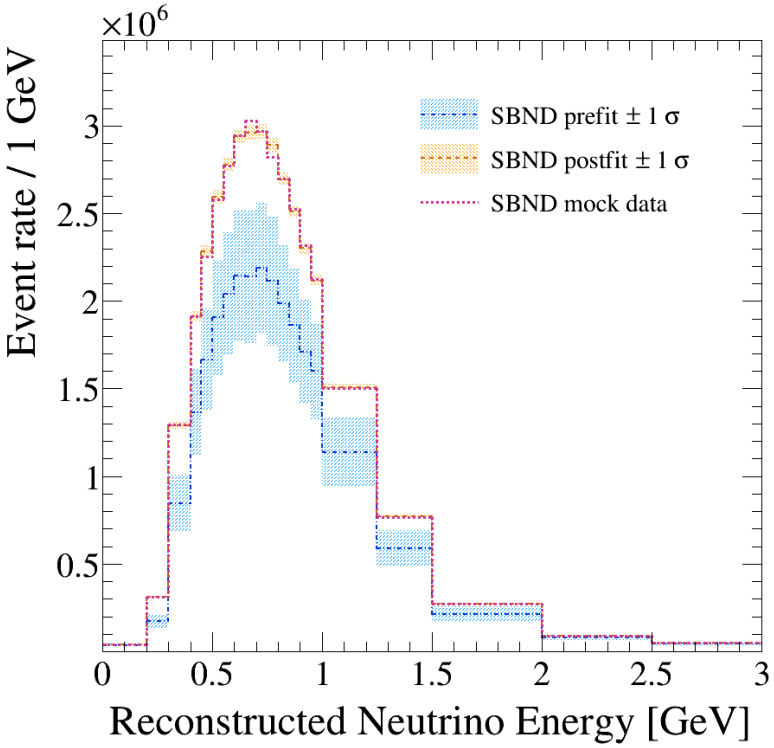

Figure 8.15.: The near detector mock data reconstructed neutrino energy spectra is shown in pink. The prefit MC spectra along with the $\pm 1\sigma$ error envelope is shown in blue and the analogous distribution is shown in orange following the exclusive fit.

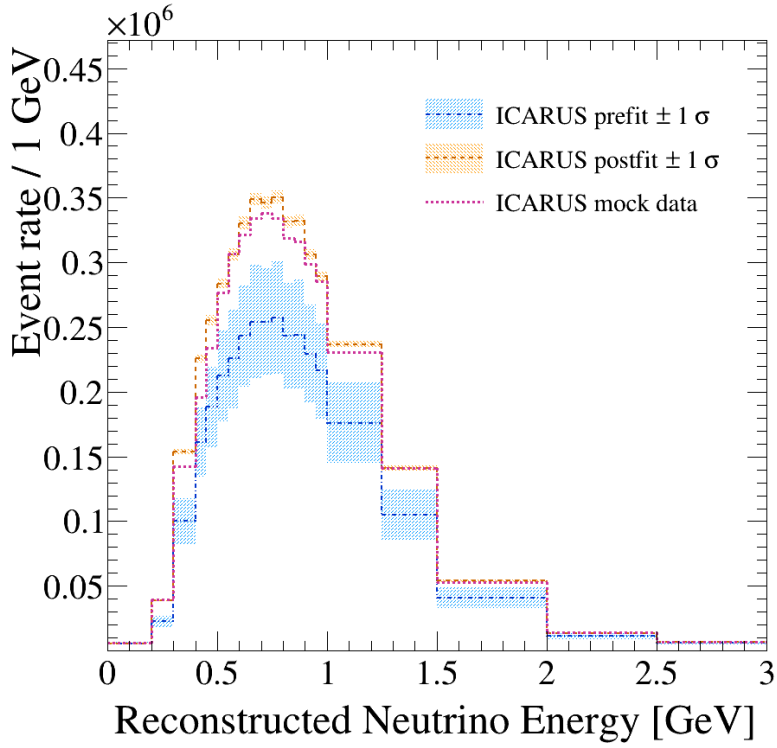

Figure 8.16.: The far detector mock data reconstructed neutrino energy spectra is shown in pink. The prefit MC spectra along with the $\pm 1\sigma$ error envelope is shown in blue and the analogous distribution is shown in orange following the exclusive fit.

8.3.3. Updated inclusive and exclusive analysis

The first iteration of the mock data analysis confirmed that updating the procedure to fit exclusive samples rather than inclusive samples provided a quantifiable improvement. However, it is important to note that no additional systematic parameters were defined to account for any aspect of either version of the analysis procedure. The second round of mock data fits were performed to assess how the incorporation of such additional systematics would impact the fits in general, and more critically in the improvement we initially saw in the switch to running exclusive fits. To this end, two parameters have been added to the list of free parameters in the fit,

- The sample migration systematic, which is only applicable in the exclusive fits
- A 1% energy scale systematic, which is applied to all fits to account for uncertainties in the reconstructed neutrino energy spectra due to the chosen binning scheme

The remaining complex systematic parameter pull plots will be given in appendix C and interpreted in the text. Although the additional systematic parameters have hardly been pulled at all, the incorrectly-pulled flux parameters appear to have had smaller errors assigned to them in this iteration of the inclusive fit. There is little more that can be inferred from the parameter pull plot, aside from the fact that even a negligible pull of the new parameter has resulted in a noticeable change in the way the rest of the parameters have been pulled. The near and far detector reconstructed neutrino energy spectra overlays are given in Figures 8.17 and 8.18 following the updated inclusive fit. The spectra overlays tell largely the same story as in the first iteration of the fits, in that the total uncertainty assigned across all parameters is incapable of accounting for the similarly large overestimate of the postfit event rate when extrapolating the fit results to the far detector.

The near and far detector reconstructed neutrino energy spectra overlays are shown in Figures 8.19 and 8.20 following the updated exclusive fit. In this iteration, the analysis-driven systematic parameters have both been pulled upwards by $> 0.5\sigma$. In addition, the hadronic flux parameter uncertainties have been reduced with respect to those assigned in the first exclusive fit. The significance of the new parameters once again becomes clear when analysing the postfit spectra. The total postfit stat+syst uncertainty assignment has been reduced significantly to 0.7%, from 1.4% in the first exclusive fit. As a result, the disagreement at the far detector with respect to the uncertainty has increased, from 2.0 σ_{Postfit} in the first exclusive fit to 4.6 σ_{Postfit} in the second exclusive fit.

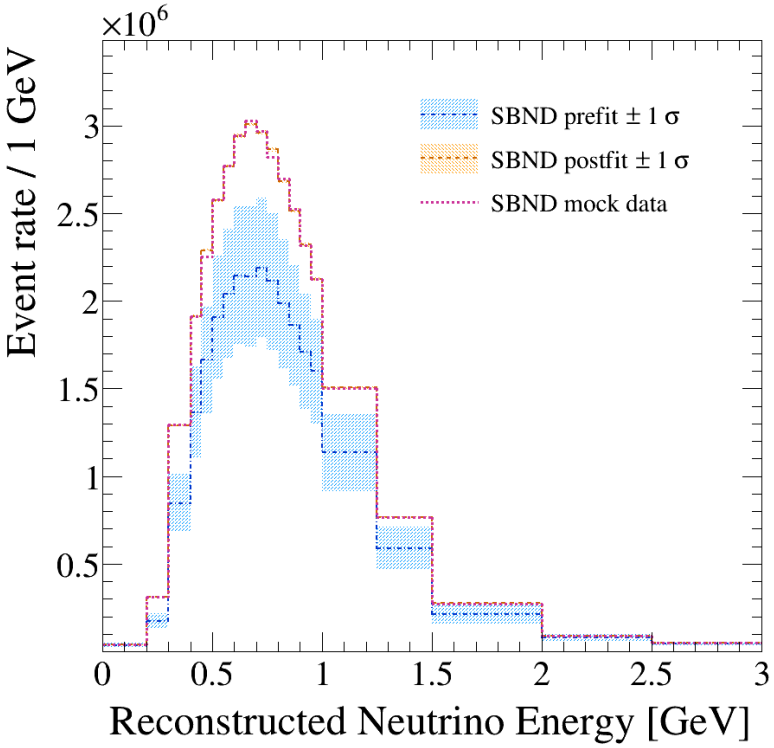

Figure 8.17.: The near detector mock data reconstructed neutrino energy spectra is shown in pink. The prefit MC spectra along with the $\pm 1\sigma$ error envelope is shown in blue and the analogous distribution is shown in orange following the inclusive fit with additional, analysis-driven systematic parameters.

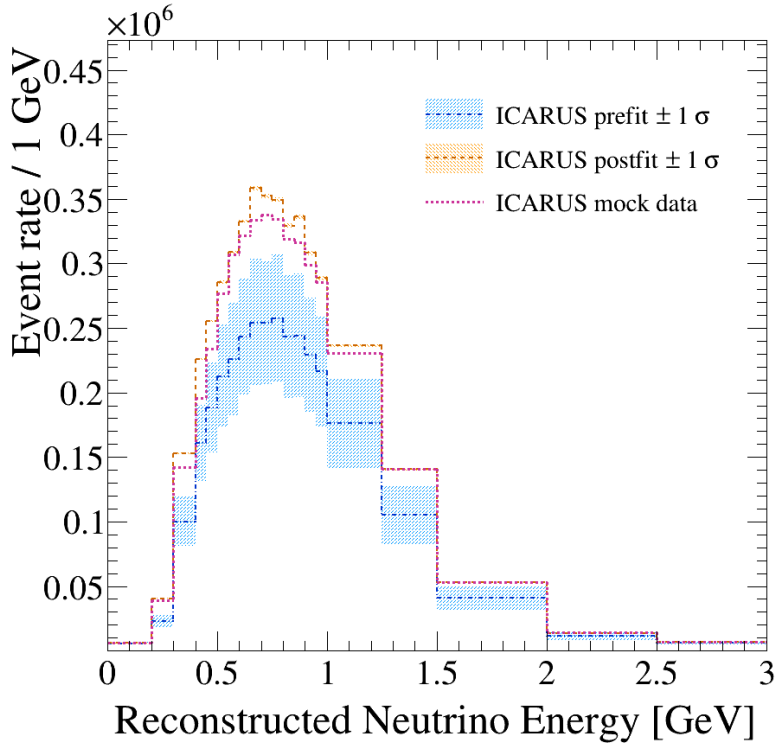

Figure 8.18.: The far detector mock data reconstructed neutrino energy spectra is shown in pink. The prefit MC spectra along with the $\pm 1\sigma$ error envelope is shown in blue and the analogous distribution is shown in orange following the inclusive fit with additional, analysis-driven systematic parameters.

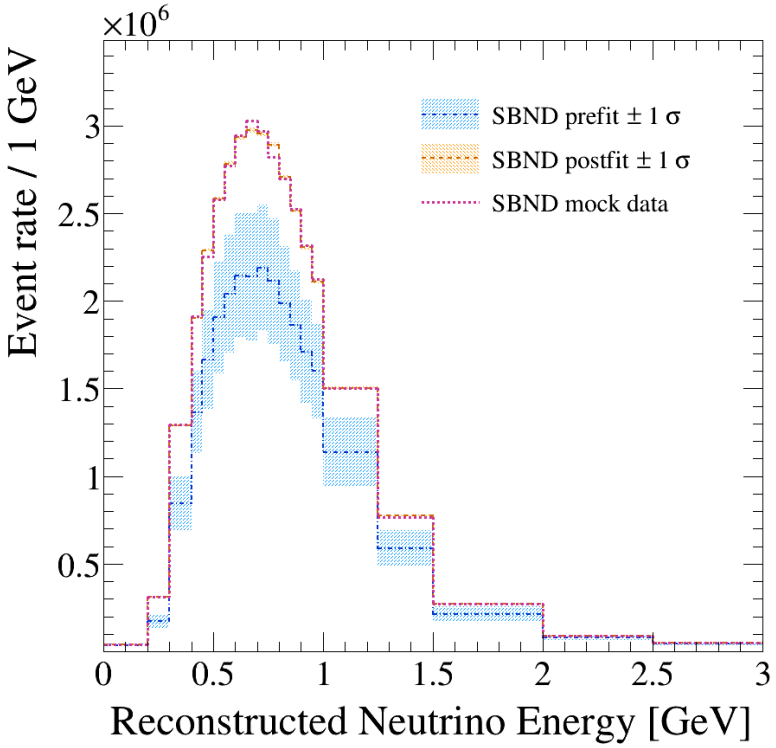

Figure 8.19.: The near detector mock data reconstructed neutrino energy spectra is shown in pink. The prefit MC spectra along with the $\pm 1\sigma$ error envelope is shown in blue and the analogous distribution is shown in orange following the exclusive fit with additional, analysis-driven systematic parameters.

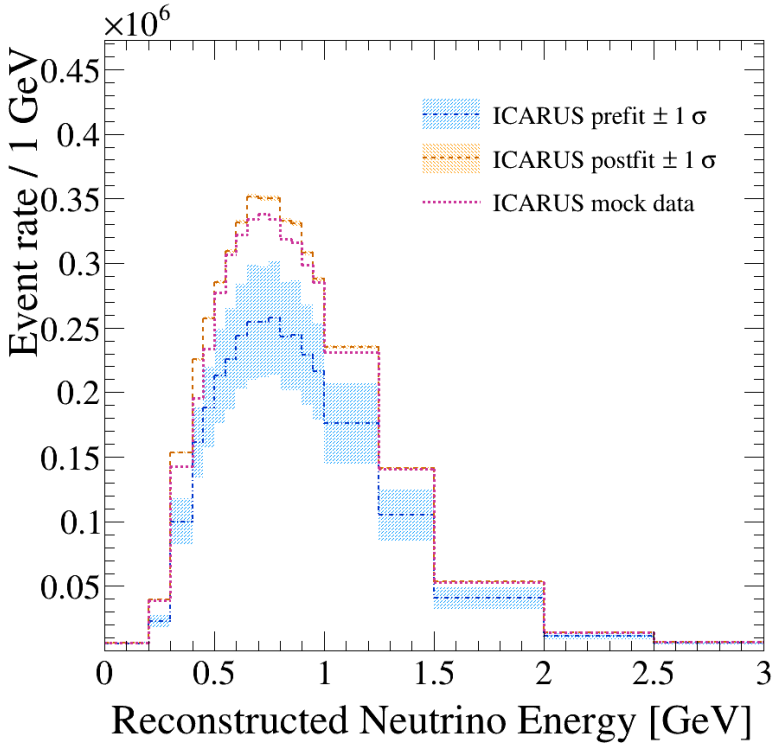

Figure 8.20.: The far detector mock data reconstructed neutrino energy spectra is shown in pink. The prefit MC spectra along with the $\pm 1\sigma$ error envelope is shown in blue and the analogous distribution is shown in orange following the exclusive fit with additional, analysis-driven systematic parameters.

Analysis	Fit statistic contributions			$\frac{\sigma_{\text{Postfit}}}{N_{\text{Postfit}}}$	$\frac{\Delta N}{N_{\text{Mockdata}}}$	$\frac{\Delta N_{\text{Pre}}}{N_{\text{Mockdata}}}$	$\frac{\Delta N}{\sigma_{\text{Postfit}}}$
	χ^2	χ^2_{syst}	NDOF				
Iteration 1							
Inclusive	223	135	149	0.50%	3.43%	23.73%	6.61
Exclusive	830	215	149	1.41%	2.90%	23.73%	2.00
Iteration 2: Including analysis-driven systematics							
Inclusive	218	133	150	0.60%	3.16%	23.73%	5.07
Exclusive	785	219	151	0.65%	3.07%	23.73%	4.58

Table 8.4.: A numerical summary of the first round of mock data fits. ΔN and ΔN_{Pre} are the integrated far detector rate difference between the mock data spectra and the postfit and prefit spectra respectively. σ_{Postfit} is the postfit stat+syst uncertainty. χ^2 is the total fit statistic and χ^2_{syst} is the contribution to it from the systematic penalty.

8.3.4. Summary of the first mock data fit results

A numerical summary of the first 4 fits in the mock data analysis is given in Table 8.4. This includes all numbers assessed throughout the analysis, as well as the fit statistic and systematic penalty assigned in each of the near-detector fits.

The exclusive fit statistic is significantly larger than the inclusive fit statistic in both iterations of the analysis, and all analyses have comparable degrees-of-freedom. This indicates that the exclusive near-detector fit result is able to better-describe the performance of the fit following the assignment of a particular set of systematic parameters and uncertainties during the minimisation procedure, before even the far detector extrapolation has been assessed. In other words, the inclusive fit is more-likely to determine that an incorrect set of assigned systematics and their uncertainties are sufficient for describing the data, due to obtaining a good fit statistic for that set.

Switching to the exclusive fits has the potential to improve the performance of the SBN oscillation analysis, as indicated by the results of the first iteration. However, the second iteration of the analysis highlights the requirement for a tight constraint to be placed on the sample migration systematic parameter if this improvement is to be achieved. This constraint may be met by optimising the efficiency and purity of the SBN event selection procedure when it is implemented in future analyses and data.

8.4. Targeted mock data samples

The first iteration of the mock data analysis highlighted the complexity involved in assessing the results of such a study. This stems largely from the substantial differences in every component of the cross-section models used to construct the mock data and MC samples. In future versions of the SBN analyses, fits will be performed with many exclusive samples, intended to be capable of disentangling effects from as many components of the cross-section model differences as possible.

In order to simplify the problem of correctly-quantifying all possible systematic effects between the mock data and MC samples with only two exclusive channels, additional mock data was constructed for the next iteration of the analysis. Given the expectation that the ν_μ CC 0π final state should be most-sensitive to variations of the neutrino interaction models which produce no pions, mock data with only variations of the CC QE and CC 2p2h models in the cross-section configuration were defined.

Two methods of constructing the targeted mock data were employed, the first was to change the fundamental CC QE+CC 2p2h models used in the GENIE G18_10a_02_11a (Valencia) configuration, as described in section 4.5, where Table 4.1 gives the full list of models included in each sample configuration. Kinematic comparisons of these model configurations with the nominal MC were demonstrated in chapter 5 in the context of the true ν_μ CC 0π components of the full event rate. The second method of constructing the mock data was to vary singular features of the nominal MC, including the size of the binding energy and the 2p2h event rate.

The list of inter and intra-model-variation samples used throughout the mock data analysis is given along with the total inclusive and semi-exclusive event rates in Table 8.5. A brief summary of the model-specific variations to the Valencia configuration is as follows,

- SuSAv2 CC QE+CC 2p2h model
- Smith-Moniz CC QE model (no 2p2h)
- Llewellyn Smith-Empirical (LS-E) CC QE+CC 2p2h model
- CC QE+CC 2p2h binding energy increased (and decreased) by 50%
- CC 2p2h event rate increased (and decreased) by 50%.

Sample	ν_μ CC Inc.	ν_μ CC 0π	ν_μ CC Oth
Valencia (MC)	1,885,300	1,457,900	427,500
SuSAv2	2,011,900	1,601,700	410,200
Smith-Moniz	1,946,600	1,535,200	411,400
Llewellyn Smith-Empirical	1,845,900	1,438,800	407,100
+50% Binding Energy	1,781,100	1,369,900	411,200
-50% Binding Energy	1,899,300	1,485,900	413,400
+50% CC 2p2h Rate	1,998,300	1,570,100	428,200
-50% CC 2p2h Rate	1,772,500	1,345,700	426,800

Table 8.5.: SBND event rates for each of the mock data samples. The total for each topological sample definition is presented, ν_μ CC Inclusive, ν_μ CC 0π, ν_μ CC Other. The Valencia (MC) sample is included for ease of reference.

To provide an overview of the mock data sample contents after undergoing the pseudo-reconstruction and selection, the CC Inclusive reconstructed neutrino energy event rate spectra is shown for the near detector in the SuSAv2, Smith-Moniz and Llewellyn Smith-Empirical mock data samples, along with the nominal MC for reference, in Figure 8.21. The spectra are then shown for the binding energy and CC 2p2h rate variations in Figure 8.22.

A more exhaustive breakdown of the inter-model-variation sample components can be found in Tables 5.1 and 5.2. A similar breakdown for the samples constructed with binding energy variations is given in Tables 8.6 and 8.7. The same event rate breakdown has not been included for the samples constructed with $\pm 50\%$ CC 2p2h events as this is implemented at the pseudo-reconstruction stage of the production, resulting in no additional variations to any other components of the MC sample.

What is interesting about the binding energy variations is that an increase and decrease of 50% do not produce equal and opposite event rate variations. For instance, increasing the binding energy results in an 8.5% CC QE event rate reduction, however decreasing the binding energy by the same amount only results in a 1.4% increase in the CC QE event rate. What's more, the CC 2p2h event rate goes down in both cases, albeit by different amounts: a 0.5% decrease occurs when the binding energy is reduced and a 0.8% decrease occurs when the binding energy is increased.

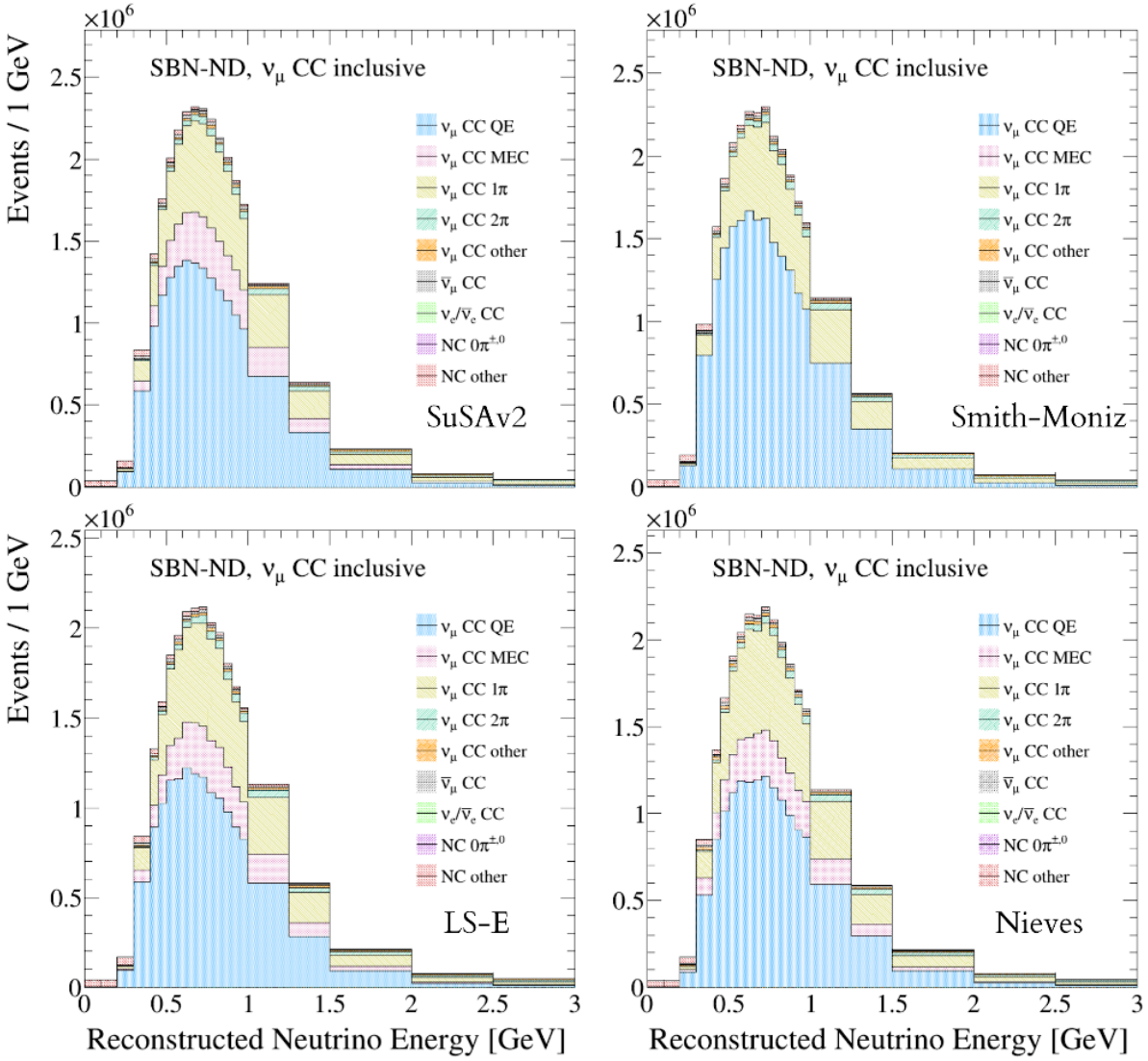

Figure 8.21.: Reconstructed neutrino energy spectra for the full CC Inclusive sample in each of the three mock data samples constructed with different CC QE+CC 2p2h models. SuSAv2 (top-left), Smith-Moniz (top-right), Llewellyn Smith-Empirical (bottom-left). The Valencia (Nieves) configuration, which is the default MC CC QE+CC 2p2h model, is included for reference (bottom-right).

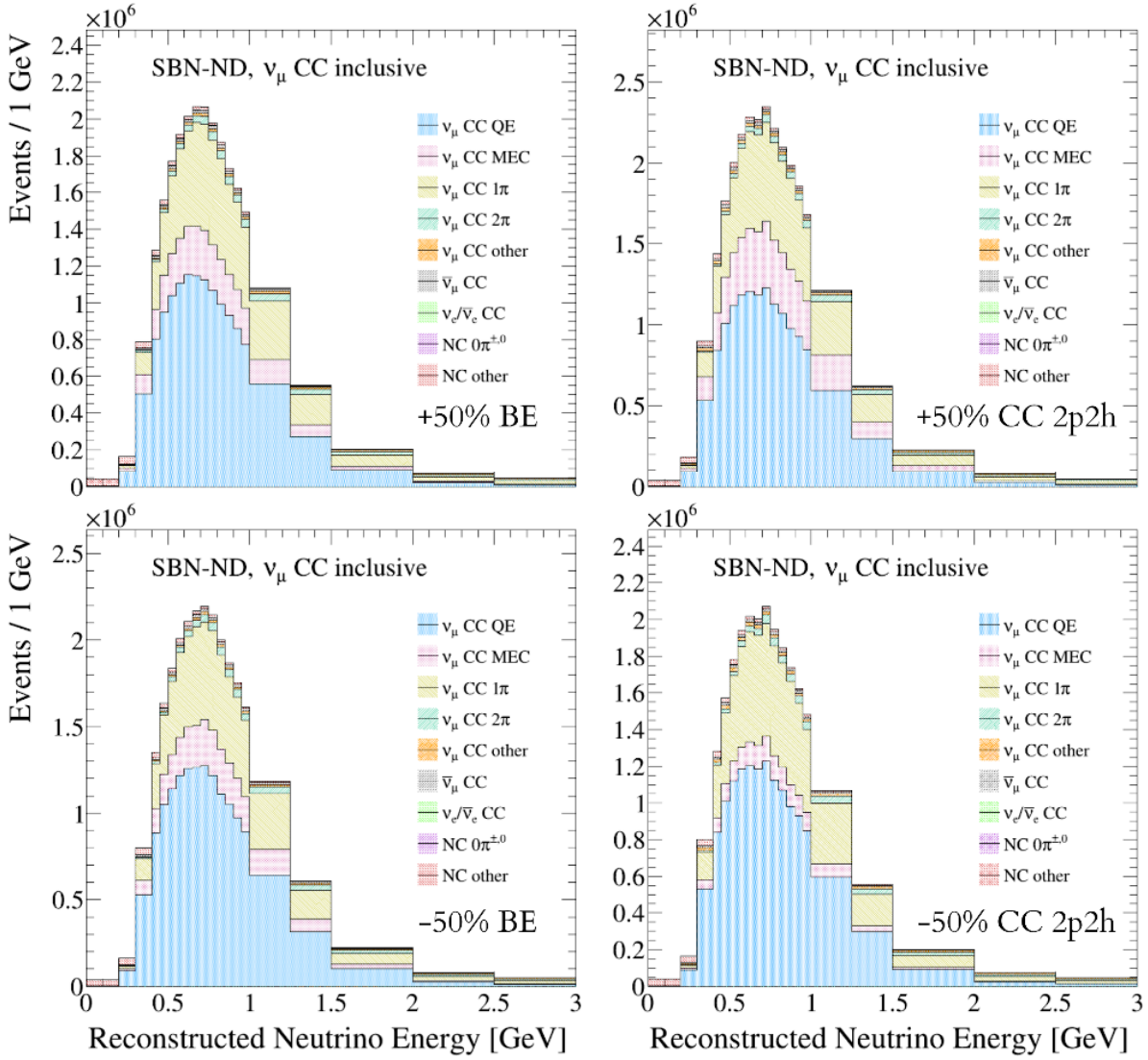

Figure 8.22.: Reconstructed neutrino energy spectra for the full CC Inclusive sample in each of the four mock data samples constructed with variations to the nominal CC QE+CC 2p2h models. +50% CC QE+CC 2p2h binding energy (top-left), +50% CC 2p2h (top-right), -50% CC QE+CC 2p2h binding energy (bottom-left) and -50% CC 2p2h (bottom-right).

Hadronic Final State	Model Configurations (CC QE & CC 2p2h)		
	+50% BE	**Nieves**	**-50% BE**
	ν_μ Charged Current		
Inclusive	3,812,187	3,998,460	4,026,838
0π + X	2,734,403	2,916,787	2,944,153
0π 0p	34,246	37,053	37,969
0π 1p	1,526,311	1,654,666	1,676,955
0π 1p ($>$ 20 MeV)	1,639,171	1,764,156	1,780,866
0π 1p ($>$ 50 MeV)	1,607,159	1,732,021	1,753,738
0π 2p	453,525	470,816	473,315
0π 2p ($>$ 20 MeV)	473,007	498,278	507,729
0π 2p ($>$ 50 MeV)	351,171	369,078	381,590
0π 3p	167,750	173,971	172,290
0π 3p ($>$ 20 MeV)	184,169	194,561	196,057
0π 3p ($>$ 50 MeV)	92,885	97,698	98,772
$0\pi > 3$p	552,570	580,279	583,623
$0\pi > 3$p ($>$ 20 MeV)	210,778	222,974	229,116
$0\pi > 3$p ($>$ 50 MeV)	37,608	39,667	41,550
$1\pi^+$ + X	531,029	533,211	534,259
$1\pi^-$ + X	35,443	35,971	35,778
$1\pi^0$ + X	302,661	303,840	303,998
2π + X	157,111	157,111	157,111
$\geqslant 3\pi$ + X	51,537	51,537	51,537
K^+K^- + X	395	395	395
$K^0\bar{K}^0$ + X	448	448	448
Σ_c^{++} + X	193	193	193
Σ_c^{+} + X	96	96	96
Λ_c^{+} + X	598	598	598
	ν_μ Neutral Current		
Inclusive	1,623,191	1,623,191	1,623,191
0π	1,113,394	1,113,394	1,113,394
$1\pi^\pm$ + X	202,639	202,639	202,639
$\geqslant 2\pi^\pm$ + X	68,168	68,168	68,168
	ν_e		
Inclusive	40,987	41,092	41,154

Table 8.6.: SBND Event Rates broken down in terms of the hadronic final state topology for the nominal MC model configuration with ±50% binding energy applied to CC QE+CC 2p2h events. The proton multiplicity contributions are further categorised by kinetic energy, E_k, such that we can get an idea for the event rate with respect to realistic energy thresholds. A threshold of 50 MeV corresponds to the current capabilities of existing LArTPC experiments and 20 MeV is the goal threshold of SBND.

Physical Process	Model Configurations (CC QE & CC 2p2h)		
	+50% BE	**Nieves**	**-50% BE**
Charged Current			
QE	1,970,896	2,153,358	2,184,112
MEC	480,037	483,953	481,639
RES	1,160,990	1,160,990	1,160,990
DIS	220,378	220,378	220,378
Coherent	6951	6951	6951
Other	2384	2384	2384
Neutral Current			
QE	847,584	847,584	847,584
MEC	110,140	110,140	110,140
RES	525,917	525,917	525,917
DIS	144,836	144,836	144,836
Coherent	5904	5904	5904
Other	343	343	343

Table 8.7.: SBND Event Rates broken down in terms of the physical process which took place for the nominal MC model configuration with ±50% binding energy applied to CC QE+CC 2p2h events.

8.5. Targeted mock data analyses

Having defined and constructed the additional samples, the mock data analysis procedure was performed in exactly the same way as in the first iteration of the analysis. All fits will use the exclusive samples and the set of parameters allowed to float will be all flux, interaction and analysis-driven systematics.

The only two systematic parameters which directly impact the two neutrino interaction modes modified in the mock data samples are $f_{M_A^{QE}}$ and f_{2p2h}. Additional parameters which will be indirectly affected are those which modify the FSI model, since a variation in the initial neutrino interaction products will be propagated into corresponding changes to the rates of various FSI processes.

First, the analyses involving the inter-model-variations were studied in section 8.5.1, followed by the intra-model variations in section 8.5.2. An interpretation of the complex parameter pull plots following each iteration of the targeted mock data analysis will be summarised in this section, and the plots are included in appendix C.

8.5.1. Inter-model CC QE+CC 2p2h variations.

SuSAv2

The pulls following the SuSAv2 fit are shown in Figure C.3. In this sample, both the CC QE and CC 2p2h event rates are higher than the MC, however f_{2p2h} was increased but $f_{M_A^{QE}}$ was decreased in the fit. In addition, the pion-based FSI parameters were reduced whilst the nucleon-based FSI parameters were increased, which is likely to account for the increase and decrease in ν_μ CC 0π and ν_μ CC 1π final states respectively.

Furthermore, the agreement between the postfit and mock data reconstructed neutrino energy spectra has improved at both the near and far detectors and are shown in Figure 8.23 and 8.24 respectively. The fractional integrated far detector event rate difference between the mock data and postfit spectra is only 1.6%. This indicates that reducing the complexity of the mock data and MC samples has given the fit a better handle on how to interpret the data. The assigned uncertainties are still too small to cover the far detector discrepancy, however there is only a single bin at the near detector in which the postfit spectra does not agree with the mock data to within the assigned uncertainty. The far detector mock data rate is this time 3.7 σ_{Postfit} away from the postfit rate.

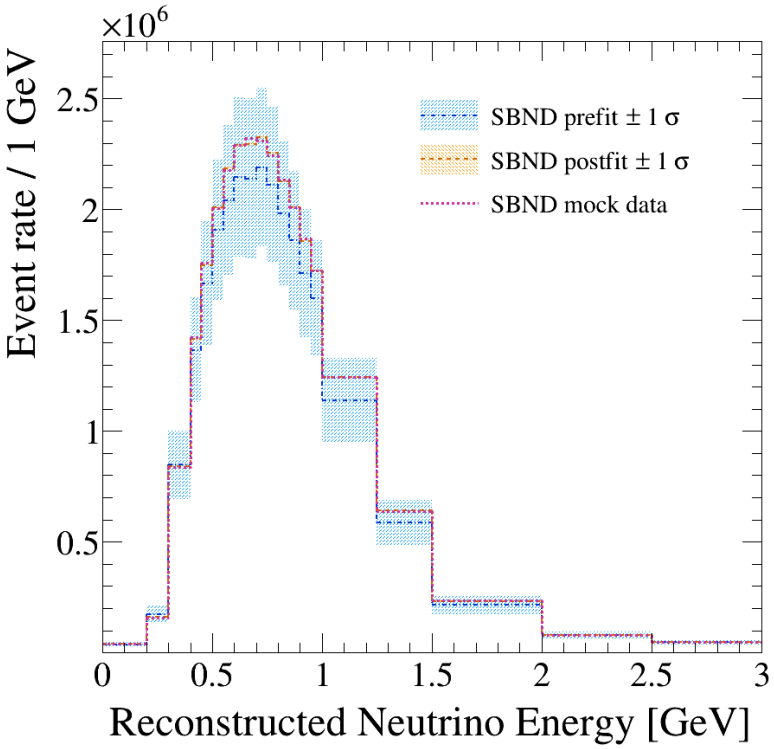

Figure 8.23.: The near detector GENIE v3 SuSAv2 mock data reconstructed neutrino energy spectra is shown in pink. The prefit MC spectra along with the $\pm 1\sigma$ error envelope is shown in blue and the analogous distribution is shown in orange following the exclusive fit.

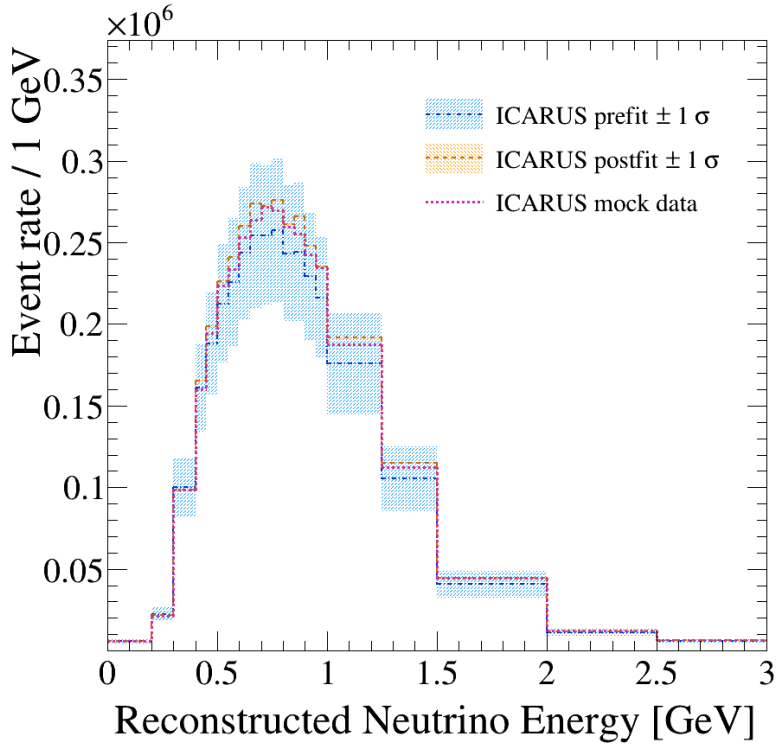

Figure 8.24.: The far detector GENIE v3 SuSAv2 mock data reconstructed neutrino energy spectra is shown in pink. The prefit MC spectra along with the $\pm 1\sigma$ error envelope is shown in blue and the analogous distribution is shown in orange following the exclusive fit.

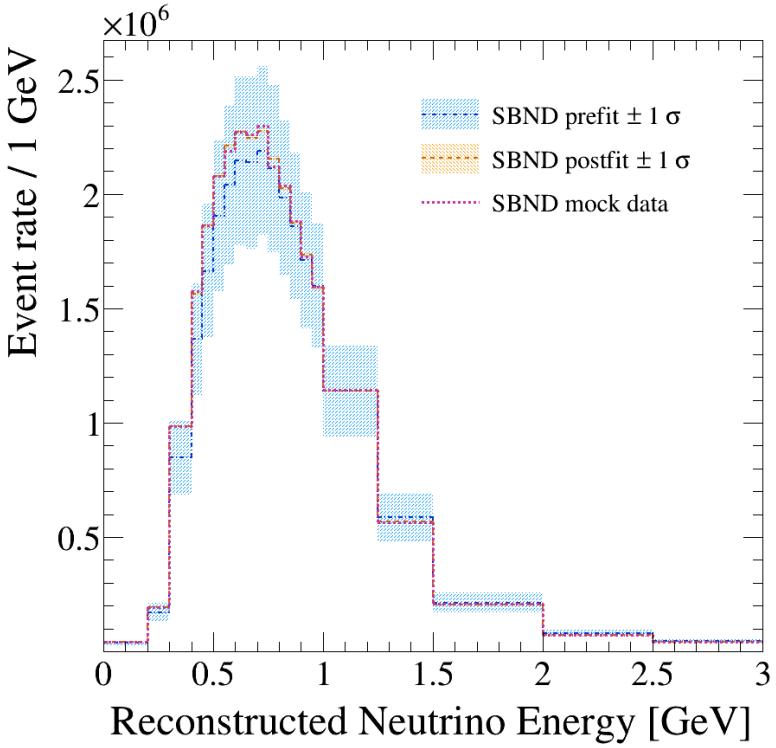

Figure 8.25.: The near detector GENIE v3 Smith-Moniz mock data reconstructed neutrino energy spectra is shown in pink. The prefit MC spectra along with the $\pm 1\sigma$ error envelope is shown in blue and the analogous distribution is shown in orange following the exclusive fit.

Smith-Moniz

A summary of the systematic parameter tweaks which were assigned by the fit is as follows, the pulls themselves are shown in Figure C.4. In this sample, the CC QE event rate is increased to account for the complete removal of the CC 2p2h events. Once again, the f_{2p2h} parameter was tweaked in the correct direction, with almost a 1σ (100%) reduction. The $f_{M_A^{QE}}$ parameter was this time not tweaked very far, however the uncertainty assignment to this pull was large.

The reconstructed neutrino energy spectra are shown for the near and far detectors in Figure 8.25 and 8.26 respectively. The spectral differences are also complex in this case, as the shape changes between the two samples much more significantly than in any of the other mock data. This fit seems to be attributing these shape differences to the analysis-driven systematic components, through a large increase in the sample migration parameter, f_{CCOther} along with a small decrease in the energy scale parameter, $f_{\mathrm{E;r}}$. The consequences are once again reflected in the poor agreement at the far detector. The fractional integrated event rate difference between the postfit spectra and the mock data is this time 2.8%. In terms of the postfit uncertainty, the postfit event rate is 4.1 $\sigma_{\mathrm{Postfit}}$ away from the mock data rate.

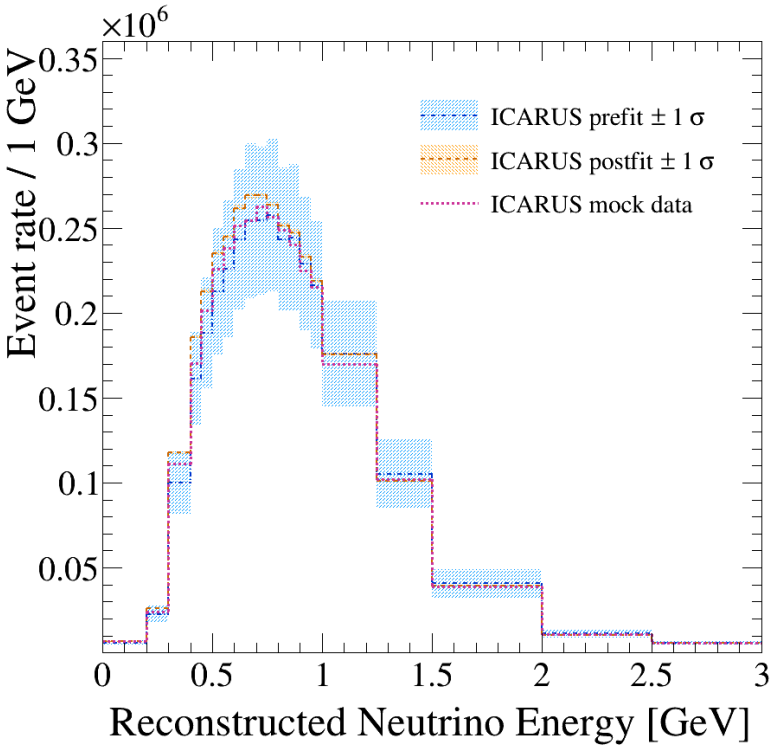

Figure 8.26.: The far detector GENIE v3 Smith-Moniz mock data reconstructed neutrino energy spectra is shown in pink. The prefit MC spectra along with the $\pm 1\sigma$ error envelope is shown in blue and the analogous distribution is shown in orange following the exclusive fit.

Llewellyn Smith-Empirical

A summary of the systematic parameter tweaks which were assigned by the fit is as follows, the pulls themselves are shown in Figure C.5. This time the fit does not tweak the analysis-driven systematic parameters at all. In this mock data sample, the CC QE event rate goes down and the CC 2p2h event rate goes up. The $f_{M_A^{QE}}$ and f_{2p2h} parameters are correctly pulled down and up, respectively. The integrated event rates are very similar between the mock data and MC samples in this case, however many of the interaction and flux parameters are still pulled by the fit.

The next assessment is once again of the near and far detector reconstructed neutrino energy spectra, shown in Figures 8.27 and 8.28 respectively. This time, the near detector agreement is at a similar, if not slightly worse standard to the previous fits, however the far detector agreement is much better, with a 1.5% fractional difference between the integrated event rates. The postfit uncertainties have once again been underestimated, even when assessing the result at the near detector, though the difference at the far detector amounts to only 1.9 σ_{Postfit}.

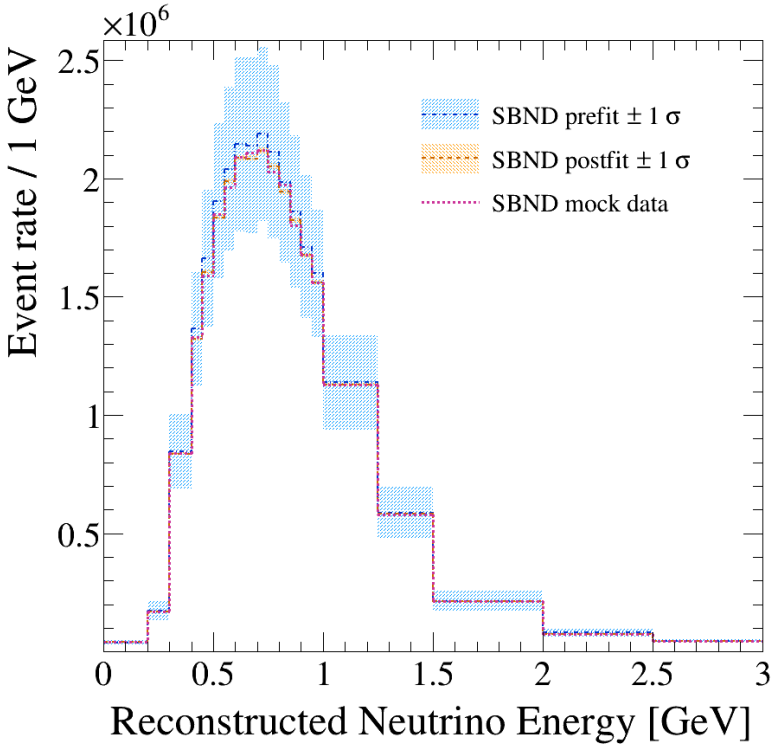

Figure 8.27.: The near detector GENIE v3 Llewellyn Smith-Empirical mock data reconstructed neutrino energy spectra is shown in pink. The prefit MC spectra along with the $\pm 1\sigma$ error envelope is shown in blue and the analogous distribution is shown in orange following the exclusive fit.

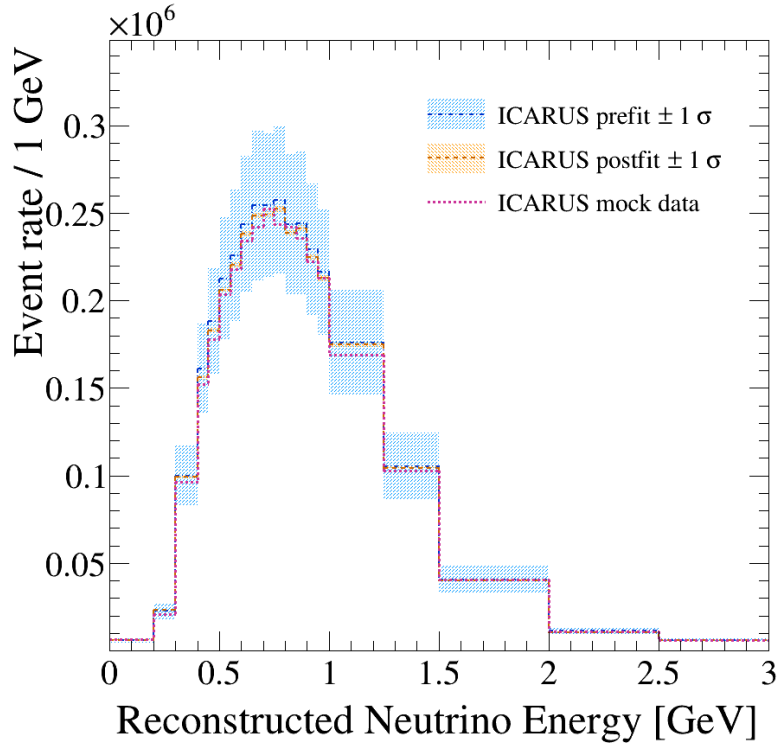

Figure 8.28.: The far detector GENIE v3 Llewellyn Smith-Empirical mock data reconstructed neutrino energy spectra is shown in pink. The prefit MC spectra along with the $\pm 1\sigma$ error envelope is shown in blue and the analogous distribution is shown in orange following the exclusive fit.

8.5.2. Intra-model CC QE+CC 2p2h variations.

Binding energy

To reduce the complexity of the problem further still, the mock data samples were constructed with variations to singular components of the MC cross-section model. The first set of variations involved the changing the binding energy by ±50% in the case of only CC QE and CC 2p2h neutrino interactions, for consistency with the previous studies.

A summary of the systematic parameter tweaks which were assigned by the fit is as follows, the pulls themselves are shown in Figure C.6 for the +50% variation and Figure C.7 for the -50% variation. From the information given in Table 8.7, the f_{2p2h} and $f_{M_A^{QE}}$ parameters should both be tweaked down in the +50% fit. In reality, f_{2p2h} is slightly increased and $f_{M_A^{QE}}$ is substantially ($> 1\sigma_{\text{Prefit}}$) reduced. In the -50% fit, the expectation would be for f_{2p2h} to be decreased and $f_{M_A^{QE}}$ to be increased very slightly. In this case, both parameters are slightly reduced.

It in interesting to compare the results of the ±50% variations side-by-side, therefore Figure 8.29 presents a comparison of the near detector reconstructed neutrino energy spectra for the two cases and Figure 8.30 the far detector comparison.

In both cases, the near detector performance largely follows the same story as the rest of the fits, there is good agreement in general but a handful of bins still do not agree to within the assigned uncertainty. At the far detector, the agreement appears to have improved significantly, especially in the +50% BE case whose postfit integrated event rate is only 0.24% away from the mock data. In the -50% case, the MC integrated event rate difference with the mock data actually gets worse after the fit, beginning with a 0.28% difference and ending up with a 2.19% difference.

2p2h

The final mock data studies which will be presented in this chapter involve simply increasing and decreasing the reconstructed CC 2p2h event rate by ±50%. A summary of the systematic parameter tweaks which were assigned by the fit is as follows, the pulls themselves are shown in Figure C.8 for the +50% variation and Figure C.9 for the -50% variation.

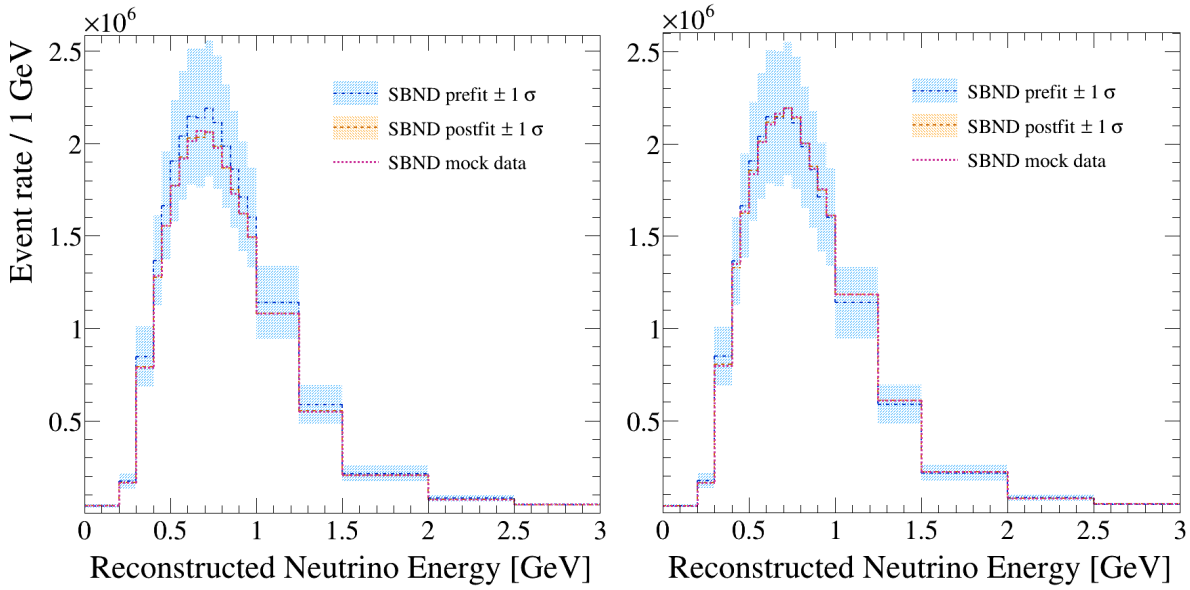

Figure 8.29.: The near detector reconstructed neutrino energy spectra for the GENIE v3 G18_10a_02_11a, ±50% binding energy, mock data is shown in pink. The prefit MC spectra along with the $\pm 1\sigma$ error envelope is shown in blue and the analogous distribution is shown in orange following the exclusive fit. On the left is the +50% BE case and on the right is the -50% BE case.

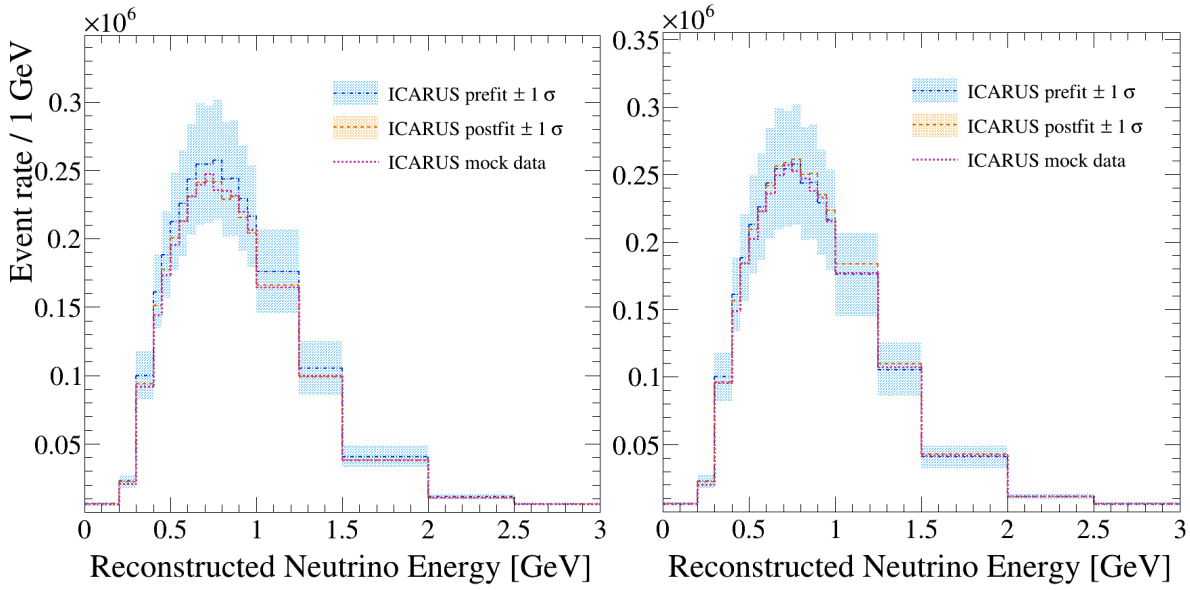

Figure 8.30.: The far detector reconstructed neutrino energy spectra for the GENIE v3 G18_10a_02_11a, ±50% binding energy, mock data is shown in pink. The prefit MC spectra along with the $\pm 1\sigma$ error envelope is shown in blue and the analogous distribution is shown in orange following the exclusive fit. On the left is the +50% BE case and on the right is the -50% BE case.

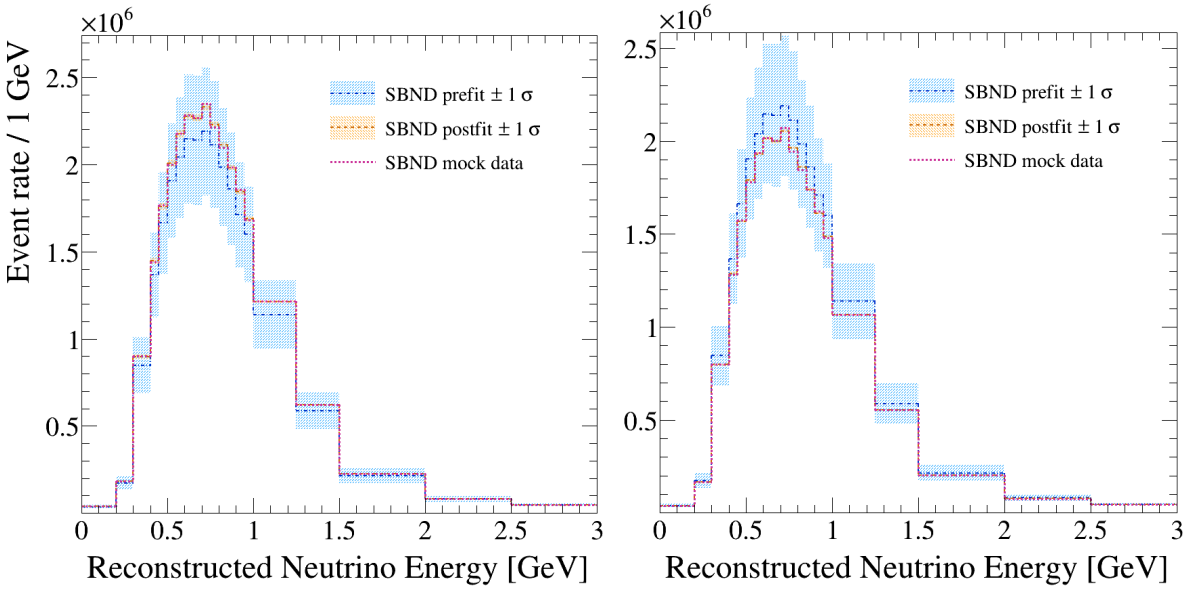

Figure 8.31.: The near detector reconstructed neutrino energy spectra for the GENIE v3 G18_10a_02_11a, ±50% 2p2h, mock data is shown in pink. The prefit MC spectra along with the $\pm 1\sigma$ error envelope is shown in blue and the analogous distribution is shown in orange following the exclusive fit. On the left is the +50% 2p2h case and on the right is the -50% 2p2h case.

Unfortunately, even though the only difference between the MC and mock data set is a 50% increase in the CC 2p2h event rate: The fit pulls down the f_{2p2h} parameter and tweaks many of the others incorrectly. The fit with the -50% CC 2p2h mock data does decrease the f_{2p2h} parameter, however the tweak is to reduce the 2p2h rate by 100% ($1\sigma_{\text{Prefit}}$) and once again many others are incorrectly pulled, presumably to compensate for the overshoot. Of all the interaction systematics, the group of FSI parameters which affect the nucleon propagation have been tweaked significantly by both sample fits. This is an understandable mis-interpretation of the multi-nucleon knockout variation. The spectra are once more shown side-by-side in Figure 8.31 at the near detector and at the far detector in Figure 8.32.

Although the parameter pulls in this case can be clearly assessed as being largely incorrect, the fit performance at the specra-level is very good. At the near detector in both the ±50% samples the mock data and postfit spectra agree to within the assigned uncertainty in every bin. Similarly at the far detector, there are only 2 or 3 bins in which the postfit and mock data spectra don't agree to within the postfit uncertainty in both samples. The fractional far detector event rate differences between the postfit integrated spectra and the mock data for the +50% and -50% variation samples are 1.22% and 1.33% respectively. Both differences are below $2\sigma_{\text{Posfit}}$.

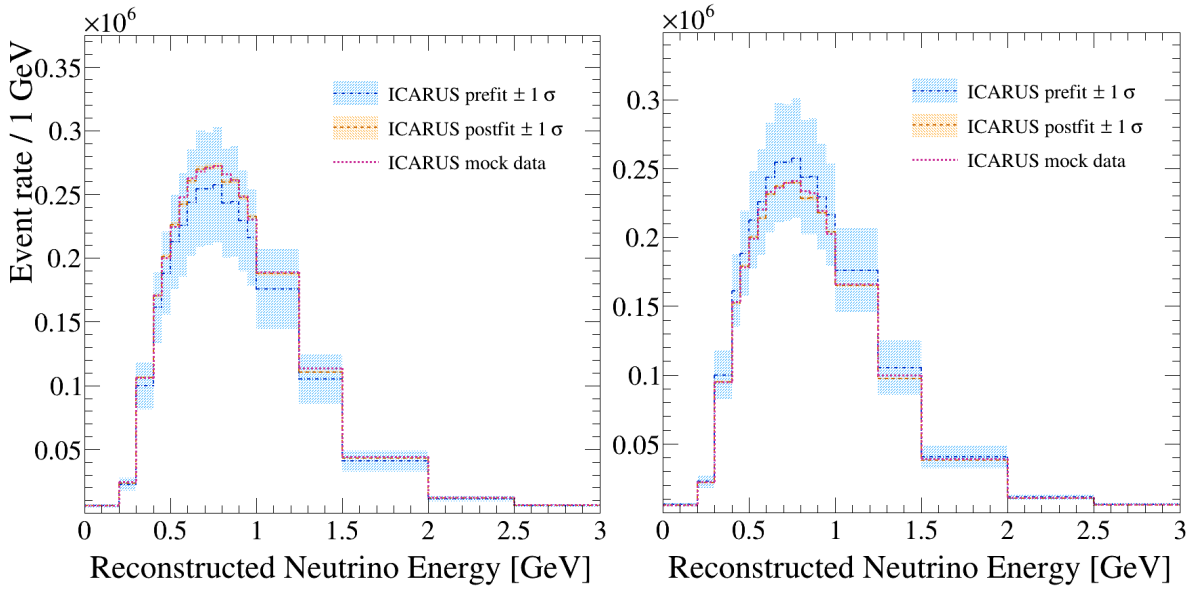

Figure 8.32.: The far detector reconstructed neutrino energy spectra for the GENIE v3 G18_10a_02_11a, ±50% 2p2h, mock data is shown in pink. The prefit MC spectra along with the $\pm 1\sigma$ error envelope is shown in blue and the analogous distribution is shown in orange following the exclusive fit. On the left is the +50% 2p2h case and on the right is the -50% 2p2h case.

8.5.3. Summary of the targeted mock data fit results

A numerical summary of the exclusive fits with analysis-driven systematics is given in Table 8.8. The mock data analysis has made clear the complex relationship between the systematic parameters. Although they may not be correlated, singular variations to the interaction model can be well-represented by multiple sets of systematic variations. For instance, when only the CC 2p2h rate was modified, the fit did not necessarily even pull the f_{2p2h} parameter in the right direction, however the postfit-mock data agreement was better than in almost all the other fits. At the same time, the postfit uncertainties were also better-defined than in the other fits. In addition, the fit-statistic is also defined to be on the order of the number of free parameters in the 2p2h tweaked-samples. This suggests that even when the parameter pulls are incorrect, there is a combination of other pulls which represent the variation extremely well.

What is also clear from the studies on targeted mock data samples, is that when the exclusive fit is between the MC and mock data whose variations align with the sample definitions, the performance is generally improved in every metric. This implies that when exclusive fits are performed using a more granular breakdown of the topologies, the fit will improve even in the complex case of the first mock dataset.

Mock Data	Fit statistic contributions			$\frac{\sigma_{\text{Postfit}}}{N_{\text{Postfit}}}$	$\frac{\Delta N}{N_{\text{Mockdata}}}$	$\frac{\Delta N_{\text{Pre}}}{N_{\text{Mockdata}}}$	$\frac{\Delta N}{\sigma_{\text{Postfit}}}$
	χ^2	χ^2_{syst}	NDOF				
Exclusive	785	219	151	0.65%	3.07%	23.73%	4.58
SuSAv2	199	95	151	0.44%	1.63%	5.21%	3.68
Smith-Moniz	384	159	151	0.68%	2.84%	0.28%	4.06
LS-E	331	92	151	0.77%	1.45%	3.08%	1.86
+50% BE	283	88	151	0.36%	0.24%	6.01%	0.68
-50% BE	291	80	151	0.32%	2.19%	0.28%	6.80
+50% CC 2p2h	176	41	151	0.88%	1.22%	7.00%	1.41
-50% CC 2p2h	172	37	151	0.68%	1.33%	4.91%	1.97

Table 8.8.: A numerical summary of the exclusive mock data fits with the analysis-driven systematic parameters. ΔN and ΔN_{Pre} are the integrated far detector rate difference between the mock data spectra and the postfit and prefit spectra respectively. σ_{Postfit} is the postfit stat+syst uncertainty. χ^2 is the total fit statistic and χ^2_{syst} is the contribution to it from the systematic penalty.

Finally, although some improvements were seen when developing the analysis procedure to use exclusive fits, further development is clearly necessary. Propagating the exclusive fits to include a finer breakdown of the ν_μ CC Inclusive samples will likely see immediate improvements, even in the dedicated CC QE+CC 2p2h mock data samples. Another update would be to define the spectra in higher-dimensions of observable parameters, such as the muon kinematics. This would immediately remove the uncertainty due to the reconstructed energy resolution capabilities, therefore constraining the detector systematic associated with it. As was demonstrated in the comparison between including the analysis-driven systematics and omitting them, such constraints will make a substantial difference to the fit performance.

In addition, the physics studies presented in chapter 5 demonstrated that the muon kinematic distributions had more-substantial shape and rate differences between model configurations than the reconstructed neutrino energy distributions. This indicates that updating the analysis procedure to fit two-dimensional spectra in the two muon kinematic parameters will give the fit greater model-discrimination power and possibly reduce the postfit-mock data far detector bias.

8.6. Parametrising the far detector discrepancy

Ultimately, the role of the near detector in the SBN oscillation analysis is to constrain the systematic parameters. In doing so, any measurements made at the far detector which contain interesting physics results can be extracted with maximum confidence.

The discrepancies observed between the far detector prediction and mock data following the extensive mock data fits indicate that the analysis procedure is insufficient to accurately constrain the systematics. In order to account for this in the oscillation analyses, the observed discrepancy can be quantified in a single systematic parameter, known as the 'bias'. This parameter can then be constrained through improvements to the analysis inputs and procedure.

The bias parameter is defined as a covariance matrix in the same E_{Reco} binning scheme as the fits are performed, specified in Table 6.5. The covariance matrix, B_{ij}, is constructed by calculating the maximum discrepancy as a fraction of the mock data rate in each far detector reconstructed neutrino energy bin across a set of, M, mock data fit results,

$$\mathbf{B_{ij}} = \max_{\{m,p\in M\}} \left(\frac{(N_i^p - N_i^m)}{N_i^m} \right) \cdot \max_{\{m,p\in M\}} \left(\frac{(N_j^p - N_j^m)}{N_j^m} \right), \tag{8.1}$$

where $N_{i,j}^m$ is the mock data event rate in dataset m and bin i or j. $N_{i,j}^p$ is the postfit event rate following the fit p to mock data set m in bin i or j.

The maximum discrepancy is used to ensure that the systematic is over-estimated rather than underestimated when many fits have been incorporated. Combining the results of many similarly-defined fits will reduce the model-dependence of the parameter definition.

This systematic was first calculated following only the inclusive fit of the GENIE v2 Default+MEC mock data with all analysis-driven systematics included. The 1σ variation of this parameter is shown in Figure 8.33 as an envelope over the postfit reconstructed neutrino energy spectra and overlaid with the inclusive mock data. This comparison demonstrates that the systematic is well defined as it covers the entire discrepancy in every bin. The integrated 1σ discrepancy systematic as a fraction of the far detector nominal MC event rate is 4.94%.

Having updated the analysis procedure to fit exclusive samples instead, the discrepancy was calculated again following only the exclusive fit with the GENIE v2 Default+MEC

mock data. For comparison purposes, the 1σ overlay of this definition of the systematic is once again applied to the inclusive postfit spectra and compared to the same mock data in Figure 8.34. This application allows for a direct comparison between the parameter defined following the inclusive fit. Many bins appear to have almost the same discrepancy as the inclusive result, both larger and smaller discrepancies are also evident around the peak. The integrated discrepancy as a fraction of the nominal far detector event rate following the exclusive fit is reduced to 4.41%.

Finally, the discrepancy systematic was calculated once more from all of the 7 mock data fits defined as targeted analyses of the exclusive ν_μ CC 0π, ν_μ CC Other joint fits. The 1σ envelope constructed from this definition of the parameter is shown once more on the GENIE v2 Default+MEC postfit spectra with the corresponding mock data in Figure 8.35, for ease of comparison with the previous two definitions of the systematic.

Whilst many more bins have a smaller discrepancy than in both the single GENIE v2 Default+MEC inclusive and exclusive cases, there appears to be an increase in the number of bins with a larger discrepancy too. Including 7 results in the parameter definition causes the integrated discrepancy to increase with respect to both the singular inclusive and exclusive discrepancy definitions, to 5.49%. This final, model-independent, definition of the discrepancy parameter will be propagated to the analysis presented in the next section.

8.6.1. Updated sensitivity study

In Figures 8.36 and 8.37, the far detector bias parameter is added to the flux, interaction and detector systematics in the construction of the exclusion and allowed-region sensitivity contours respectively. In the exclusion sensitivity, the impact of adding in the contribution from the far detector bias parameter is comparable to that of the pseudo-detector systematics in the $\Delta m^2_{41} < 1\text{eV}^2$ region of the phase space, where the far detector is most sensitive. There is also a small reduction in the sensitivity at higher values of Δm^2_{41}. In the allowed-region, the reduction in sensitivity predominantly impacts $\sin^2 2\theta_{\mu\mu}$ and as expected from the exclusion case, has a smaller impact than adding the detector systematics. The non-negligible reduction in sensitivity of SBN to observing sterile neutrino oscillations due to the bias parameter is a direct quantification of the model-dependence of the analysis. Constraining the magnitude of this bias, through improvements to the oscillation analysis procedure, will restore the sensitivity and mitigate the effect.

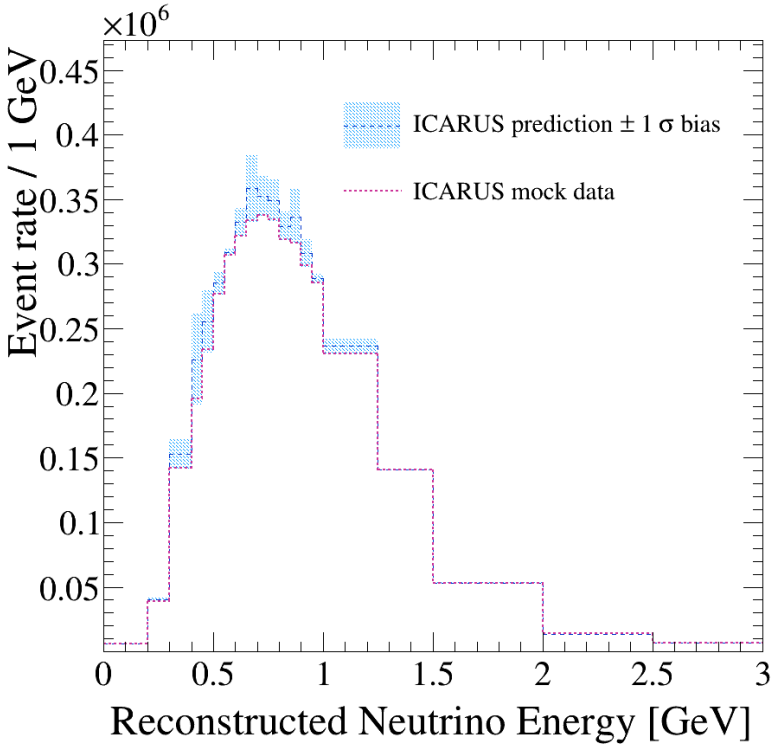

Figure 8.33.: The 1σ discrepancy systematic calculated from the difference between the GENIE v2 Default+MEC mock data and the inclusive postfit spectra. The envelope is applied to the inclusive postfit spectra and the mock data spectra is included for comparison.

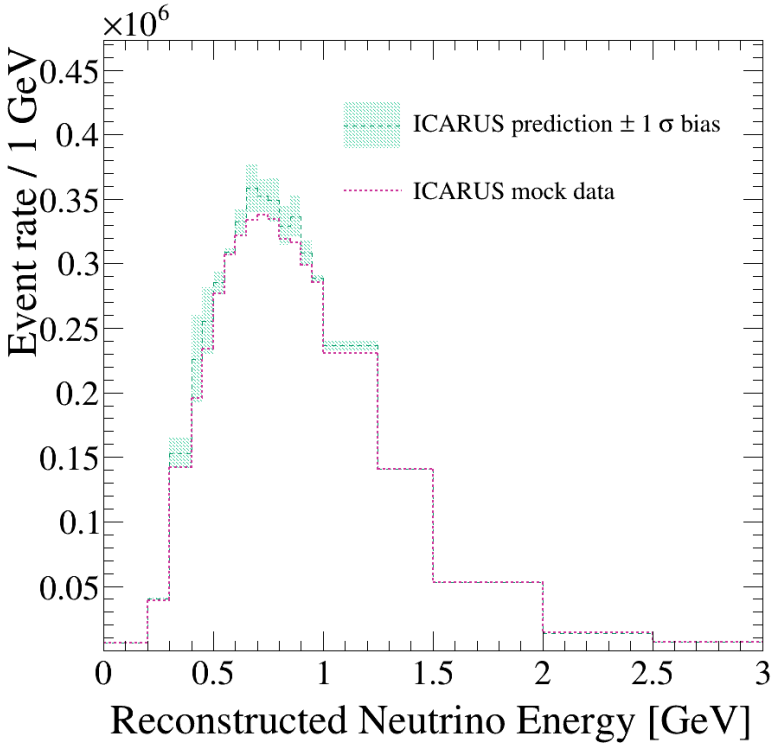

Figure 8.34.: The 1σ discrepancy systematic calculated from the difference between the GENIE v2 Default+MEC mock data and the exclusive postfit spectra. The envelope is applied to the inclusive postfit spectra such that a direct comparison can be made to the envelope and discrepancy observed following the inclusive fit. The mock data spectra is once again included for comparison.

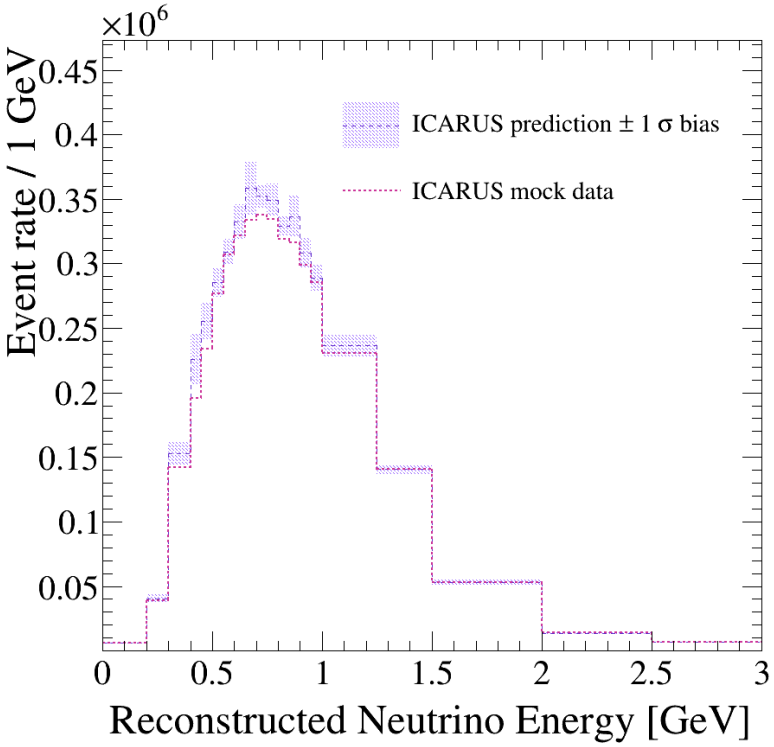

Figure 8.35.: The 1σ discrepancy systematic calculated from the difference between all of the targeted mock data and corresponding postfit spectra. The envelope is applied to the inclusive GENIE v2 Default+MEC postfit spectra such that a direct comparison can be made to the envelope and discrepancy observed following the inclusive and exclusive GENIE v2 fits. The same mock data spectra is once again included for this comparison.

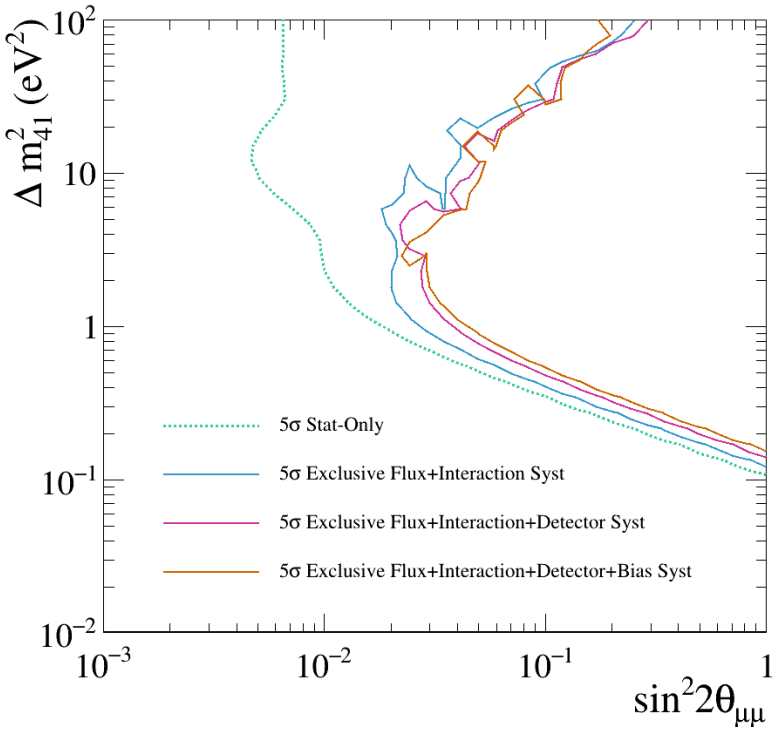

Figure 8.36.: ν_μ disappearance exclusion sensitivity comparison between the well-validated flux and interaction systematic parameter set (blue), the addition of pseudo-detector systematics (pink) and the addition of the far detector bias parameter (orange). The statistical-only sensitivity is included for reference.

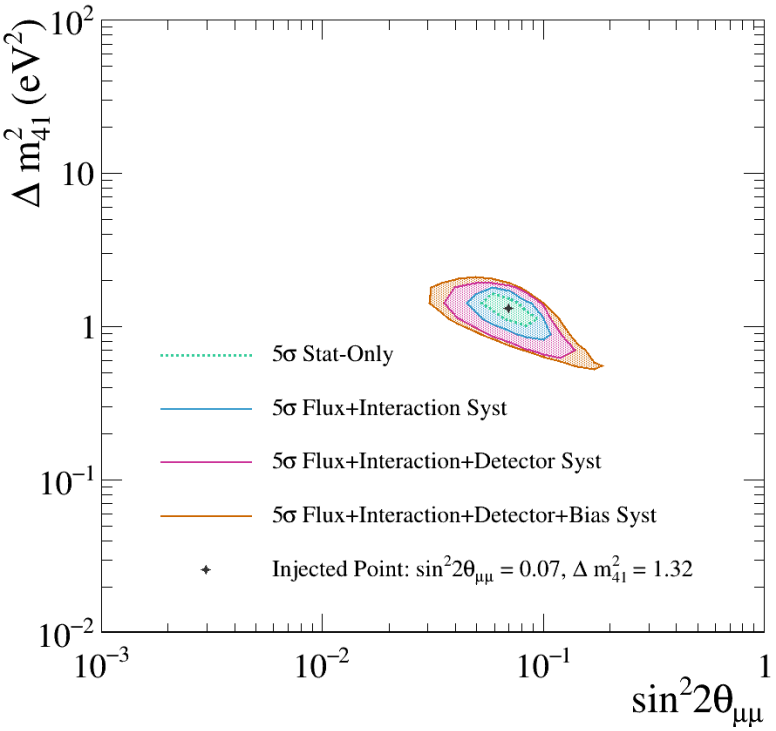

Figure 8.37.: SBN allowed region contours following the three-detector semi-exclusive joint fits of ν_μ CC 0π and ν_μ CC Other samples. The statistical-only contour is shown in green. The flux and interaction systematic parameters are added to the fits in blue. The current set of detector systematic parameters is added and shown in pink. Finally, the far detector bias parameter is added to the flux, interaction and detector systematics in orange.

Chapter 9.

Topological selection of the ν_μ CC 0π final state in SBND

Throughout the analyses discussed in chapters 7 and 8, truth level neutrino events were passed through a pseudo-reconstruction and selection procedure to emulate what we may observe in SBN data. The next iteration of the SBN sensitivity analysis will instead utilise samples of fully-reconstructed neutrino interaction events with a dedicated selection procedure. This chapter will discuss one such topological selection method, constructed in preparation for the next-generation of analyses.

Ultimately, the reconstruction procedure will have to disentangle true neutrino interactions in the fiducial volume from external backgrounds such as cosmic ray and dirt muons. An active effort to develop both the software and hardware external background reconstruction and removal procedures is underway in both the near and far detectors of the SBN program. Novel techniques will be combined with pre-existing tools developed by the MicroBooNE experiment in order to define a particle identification procedure tuned explicitly to the SBND detector geometry and technology.

Following the selection of candidate neutrino interaction events in each of the detectors, the topology of the event can be determined using geometric and calorimetric information. This chapter will outline one such particle identification (PID) method developed with the goal of selecting ν_μ CC 0π events from a sample of ν events. Perfect external background rejection will be assumed, since external background removal procedures are currently under development in SBND. The method will therefore determine ceiling performance metrics of the topological selection procedure using the current reconstruction procedure. Realistic goals can then be set for the final, full neutrino selection procedure.

9.1. Selection inputs

The goal of the selection procedure is to identify the most abundant final state topology following neutrino interactions in SBND, ν_μ CC 0π. This topology consists of a single muon, any number of protons and no charged or neutral pions. The particles which are being identified are characterised as daughters of the neutrino by the reconstruction software, as described in section 4.10.1. There will be no attempt to identify particles which are produced following the re-interaction or decay of the neutrino daughters. This may change in future developments of the selection procedure for the purpose of distinguishing between muons and pions.

As described in section 4.12, muons and protons both produce `Track`-like objects in the detector. Consequently, any event in which an electromagnetic `Shower`-like object is found to have been emitted from the neutrino interaction vertex can be identified as a background to the ν_μ CC 0π signal. Similarly, an electron selection procedure was not developed, as the only electrons which are allowed to be present in the topology definition would be produced in the re-interaction or decay of the neutrino daughters. Events in which more than 1 muon are present in the final state, for instance though the production and decay of a short-lived charm quark [205], makeup 1% of the SBND event rate and will be rejected by requiring there is only a single muon-like `Track` in the final state. Finally, events in which Kaons are produced makeup 0.02% of the SBND sample, see Table 5.2, therefore a targeted effort to identify and remove these backgrounds was not prioritised. On the other hand, the dominant background to ν_μ CC 0π events will contain pions, which is why a pion-tagging procedure was included in the method.

9.1.1. MC sample

The sample of SBND neutrino events used in the development of the topological selection was constructed with the GENIE v2 Default+MEC model and propagated through the entire SBND simulation chain as described in chapter 4. The sample is limited to containing a single neutrino interaction, thus assuming no pile-up occurs. In real data, this assumption would not hold at the near detector, where there is a 3.36% probability of observing more than 1 neutrino in the detector at a time, however for the purpose of training the selection procedure, the no pile-up definition was implemented. All events are produced with an interaction vertex contained within the fiducial volume of the detector and are scaled to the nominal exposure of the detector, 6.6×10^{20} POT.

9.1.2. Kinematic parameter definitions

A combination of geometric and calorimetric features of each neutrino interaction event will be utilised in an effort to identify muon, pion and proton `Tracks` in the SBND ν_μ CC 0π selection procedure. Metrics for quantitatively assessing the performance of the selection procedure are defined alongside the geometric and calorimetric particle identification features as follows:

- **Particle reconstructability**

  A true particle is considered 'reconstructable' if it contains more than 5 `Hits`, which were defined in section 4.10. A similar, though more conservative, requirement is set by the pattern recognition software validation procedure. The 5-`Hit` threshold is set in this context to ensure calorimetry can be properly reconstructed, particularly in the χ^2 parameter definitions, see below [206]. Furthermore, a true proton `Track` is considered 'reconstructable' if the kinetic energy is greater than 21 MeV, a threshold shown to be achievable in liquid argon by the ArgoNeuT experiment [193]. This requirement is applied to both and numerator and the denominator of the efficiency definition, which will be discussed later in the chapter.

- **Reconstructed neutrino vertex**

  The reconstructed 3D location in the detector of the neutrino interaction vertex, given by the pattern recognition as per the method outlined in section 4.10.1.

- **Track/Shower identification**

  Following the method implemented by the pattern recognition in section 4.10.1, each reconstructed particle is defined as a `Track` or an electromagnetic `Shower`.

- **Track Length**

  The sum of the Euclidean distances between trajectory points along a `Track`. Each trajectory point is reconstructed as a 3D position from a `Hit` recorded on the wire planes of the detector.

- **Fractional `Track` length difference, $\Delta L/L$**

  In an event with 2 or more reconstructed `Tracks`, the length difference between the two longest is found as a fraction of the longest `Track` length.

- **χ^2**

  A powerful parameter defined to utilise calorimetric information to identify whether a `Track` is a likely to be a proton or instead exhibits MIP-like behaviour. This method is particularly effective thanks to the technological capabilities of LArTPC detectors.

  If a `Track` stops in the detector before interacting inelastically, it will produce a characteristic 'Bragg peak', in which a large amount of energy is deposited in the detector by the final segment of the `Track`. The amount of energy deposited per unit length, dE/dx, will vary according to how far along the `Track` you are looking, and the mass of the particle which produced it. Looking at the distribution of dE/dx with respect to the length of `Track` which remains, or residual range, is therefore a useful device for the distinction between particle types.

  Muons and pions cannot be separated using this method, since they have similar masses and consequently both often behave like MIPs. In contrast, protons have the potential to be distinguished from MIP-like particles with extreme clarity, since kaon `Tracks` longer than the minimum tracking length (6mm) are very rarely produced at the energies observed by SBN [196].

  ArgoNeuT defined the χ^2_h parameter to quantify the agreement between the dE/dx vs. residual range for the distribution of `Hits` produced by a reconstructed `Track` and the theoretical distribution for each particle hypothesis, h. To do this, the average value of $dE/dx_{\text{theory},h}$ under each hypothesis in 0.08cm residual range bins is calculated.

  Figure 9.1 gives an example of this method from the ArgoNeuT experiment, in which values of dE/dx_{measured} from the `Hits` of a reconstructed `Track` are overlaid with the theoretical, averaged distributions. The agreement between the reconstructed distribution and each of the true particle hypotheses which commonly includes protons, kaons, muons and pions, is defined as χ^2_h and calculated like so,

$$\chi^2_h = \sum_{\texttt{Hits}} \left(\frac{(dE/dx_{\text{measured}} - dE/dx_{\text{theory},h})}{\sigma_{dE/dx}} \right)^2 \Big/ \, N_{d.o.f}, \tag{9.1}$$

  where $N_{d.o.f}$ is the number of degrees of freedom and corresponds to the number of collection plane `Hits` recorded. $\sigma_{dE/dx}$ is the estimated resolution of dE/dx per `Hit` defined in studies performed by ArgoNeuT and is on the order of 4% [206] [207].

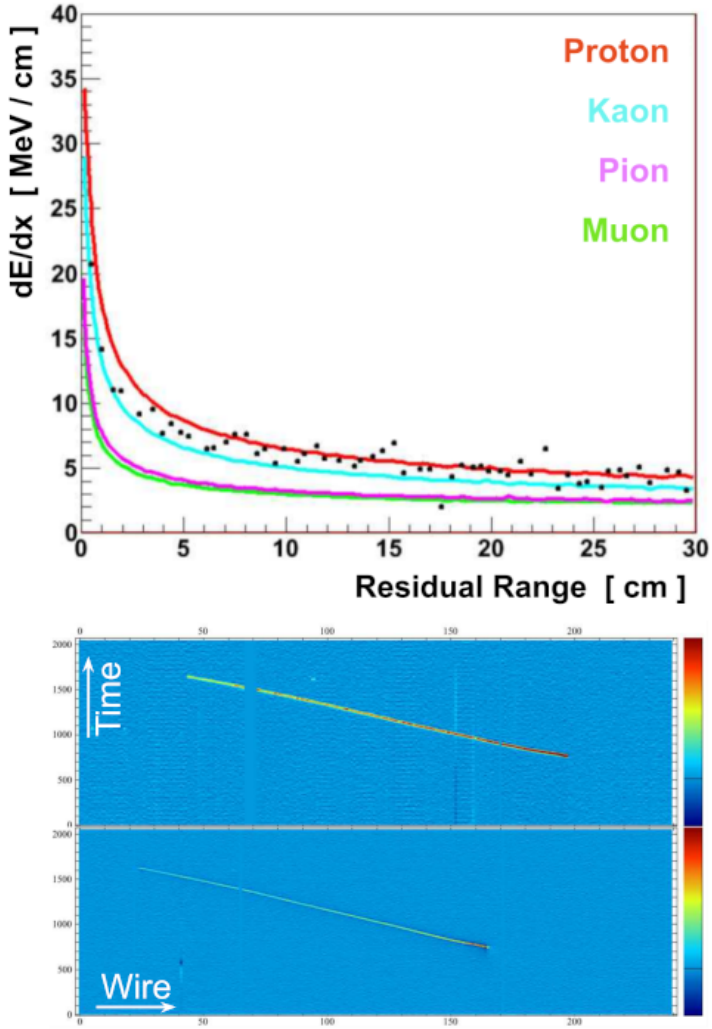

Figure 9.1.: Averaged theoretical dE/dx vs. residual range distributions are presented at the top, with an overlay of the dE/dx_{measured} vs residual range values from the `Hits` produced by the `Track` in the event display at the bottom. In this case, the `Track` fits well to the proton hypothesis. Figure adapted from [128].

χ^2_h is calculated for all but the two `Hits` at each end of a `Track`, to account for ambiguities in determining the location of the first and last `Hit` when they are located between two wires, as well for minimising the accumulation of overlapping energy depositions near the neutrino interaction vertex. This detail contributes to the aforementioned minimum `Hit` requirement for a `Track` to be defined 'reconstructable' [206].

In the application to SBN, the χ^2_h parameters are defined by constructing the dE/dx vs. residual range distribution from `Hits` acquired on the collection plane of each detector and comparing them to the theoretical distributions of the relevant particle hypothesis.

9.2. Selection procedure

The selection of ν_μ CC 0π events was performed in two stages, such that the procedure remains adaptable for the addition of external backgrounds and pile-up in future. First, ν_μ CC events are selected from the ν sample using a muon-finding procedure. This step can be developed continuously as the input sample increases in complexity. Second, the contents of the ν_μ CC events are characterised topologically with the aim of identifying those with no reconstructed pions in the final state.

9.2.1. ν_μ CC inclusive selection

The ν_μ CC Inclusive stage of the selection follows the steps outlined in Figure 9.2 and is explained as follows. This method is defined to maximise the efficiency rather than the purity of the ν_μ CC inclusive selection, more scrutinous checks will be performed at the PID stage of the selection. The overall goal is to remove ν_μ NC and ν_e events from the sample, leaving behind only those with a muon in the final state.

The following initial criteria must be passed in order for a particle to be deemed 'reconstructable' in the denominator of the efficiency as defined in section 9.1.2,

1. The reconstructed neutrino vertex must be contained within the fiducial volume of the detector. This is defined to maximise the number of events in which all particles are contained in the detector. In future iterations of the analysis, this will also serve as a method of rejecting cosmic rays, which are characteristically produced outside of the detector volume

2. Since we are primarily interested in charged current events, there must exist at least 1 reconstructable `Track` in the event

3. Only a single `Track` may leave the detector, all other `Tracks` and `Showers` must be entirely contained within the active volume of the detector. This is to ensure the geometry and calorimetry of every particle can be fully reconstructed, since only the momentum of muons can be reconstructed if they leave the active volume of the detector.

Having passed the initial criteria, the `Tracks` in the event are then propagated through the following checks to determine if one of them is likely to be a muon. Each plot was used to determine an appropriate cut value by-eye.

1. If a single `Track` does leave the detector whose length is less than 1m, discard the event. If it is longer than 1m, tag the candidate ν_μ CC Inclusive event. This criterion is allowed because the momentum of long, escaping muons can be determined using MCS such that the calorimetry lost will not impact the muon reconstruction

2. If all `Tracks` are contained, but the longest is shorter than 10cm, discard the event. This value was determined to maximally remove proton-only events by comparing the `Track` lengths for true muons, protons and pions shown for SBND in Figure 9.3

3. The `Tracks` in any remaining events must pass a number of checks in order to determine if there is a muon,

    a) If there is greater than 1 `Track`, calculate the difference between the longest two as a fraction of the longest track length. If this exceeds 0.7, as shown in Figure 9.4, the longest `Track` is most likely to be a muon and the candidate ν_μ CC Inclusive event is tagged

    b) The events which remain either did not pass the fractional `Track` cut, or there is only a single `Track`. Of these, candidate ν_μ CC Inclusive events are selected if at least 1 `Track` passes one of the following cuts,

        - If the length of the longest track exceeds 50cm as per Figure 9.5, or,
        - If the fraction, $\chi^2_\mu/\chi^2_{\text{proton}} < 0.08$ as per Figure 9.6, or,
        - If $\chi^2_{\text{proton}} > 65$ and $\chi^2_\mu < 19$ as per Figure 9.7.

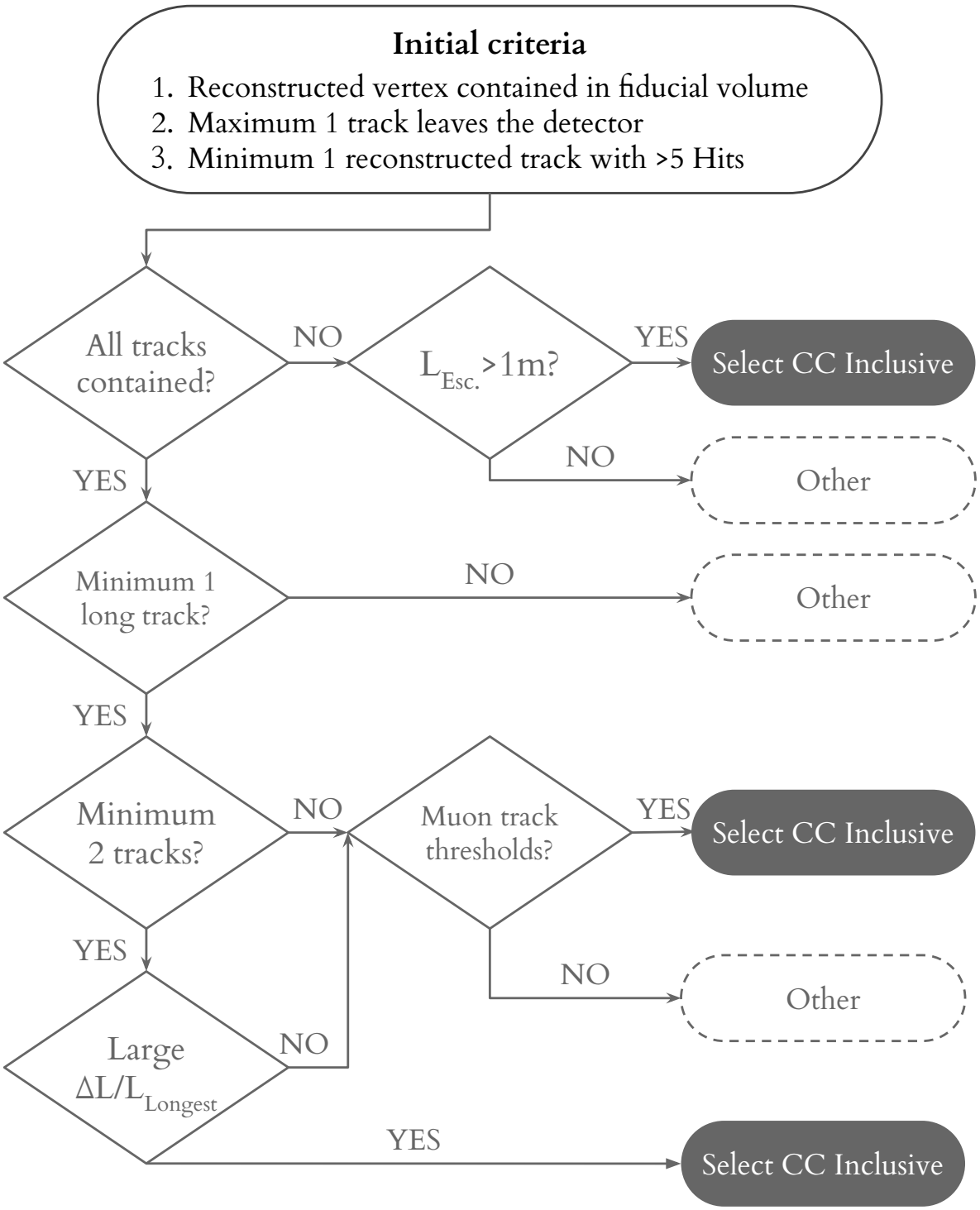

Figure 9.2.: A flowchart depicting the ν_μ CC Inclusive selection procedure. Every element of the flow chart is defined in the main body of the text.

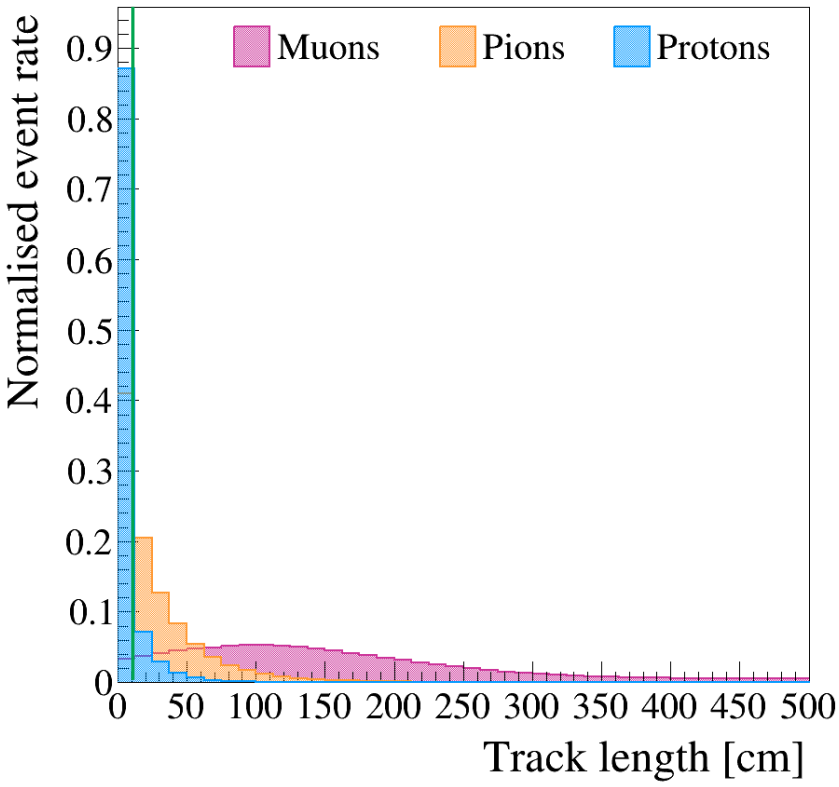

Figure 9.3.: ν_μ CC Inclusive pre-selection, track lengths for muons protons and pions in SBND. The green line indicates the cut location defined to maximise the removal of events with only protons in them.

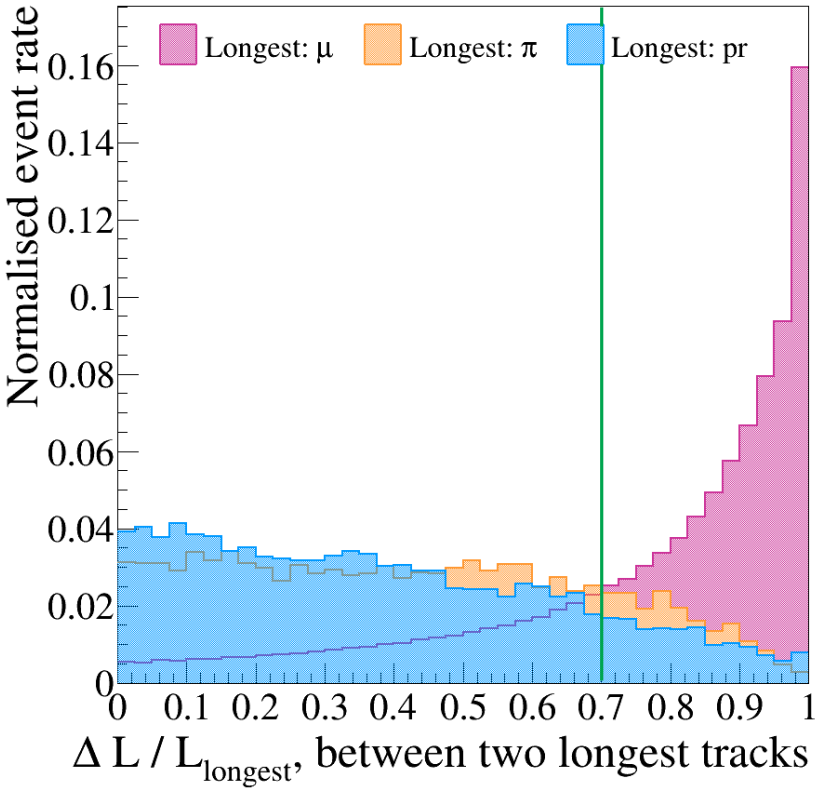

Figure 9.4.: ν_μ CC Inclusive pre-selection, fractional difference between the two longest tracks lengths in events with >1 reconstructable `Track` for muons protons and pions in SBND. The green line indicates the cut location defined to maximise the removal of events with a leading proton or pion.

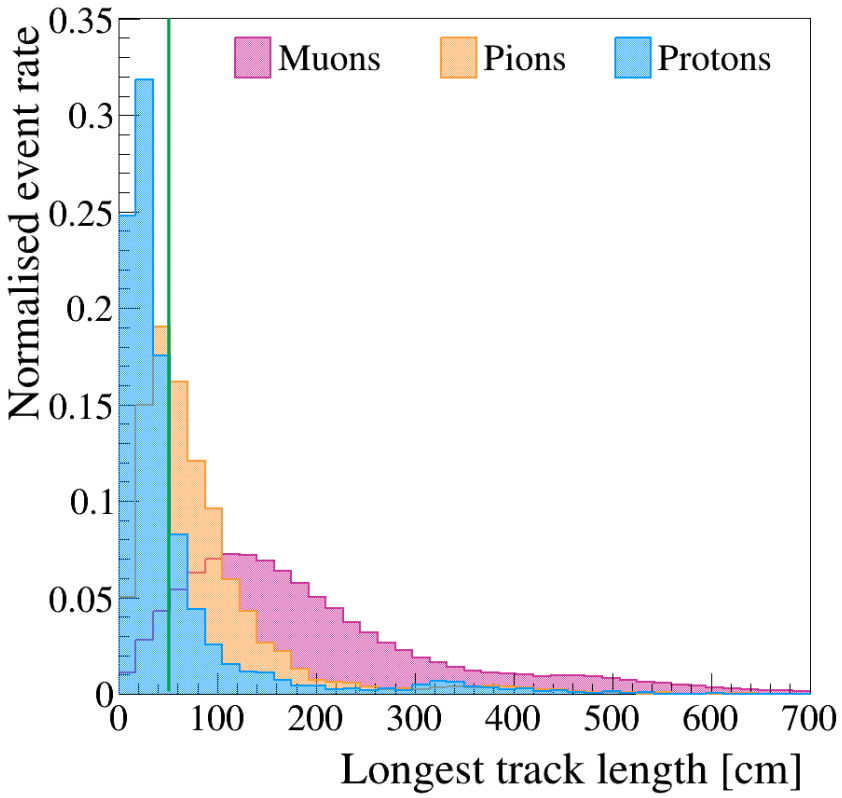

Figure 9.5.: ν_μ CC Inclusive pre-selection, longest track lengths for muons protons and pions in SBND. The green line indicates the cut location defined to maximise the removal of events in which the longest `Track` is a proton.

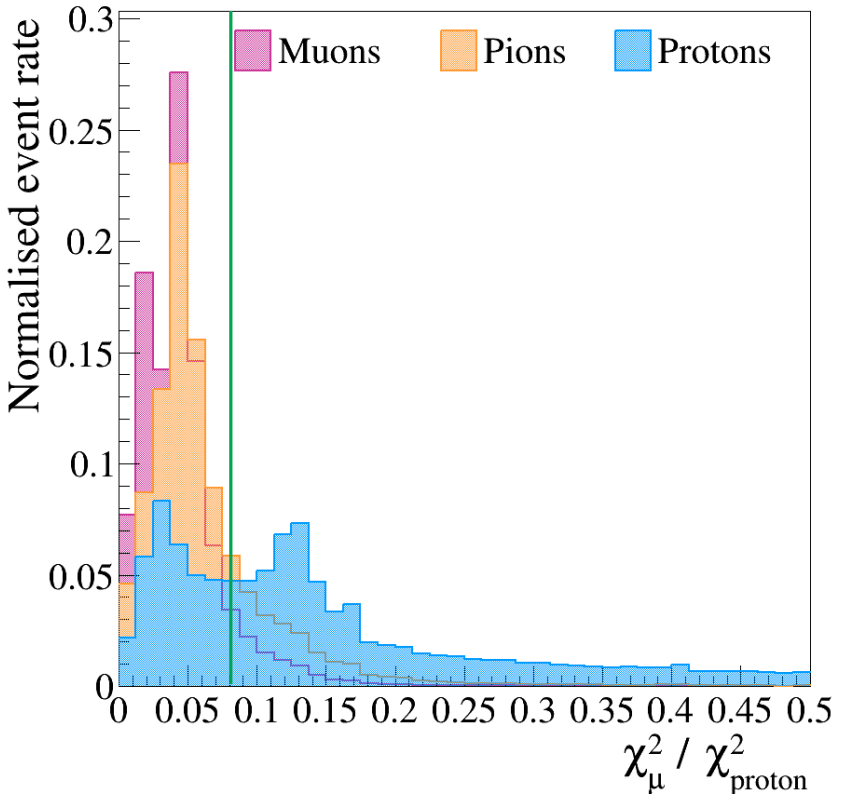

Figure 9.6.: ν_μ CC Inclusive pre-selection, $\chi^2_\mu/\chi^2_{\text{proton}}$ for muons protons and pions in SBND. The green line indicates the cut location defined to maximise the removal of events in which the longest `Track` is a proton.

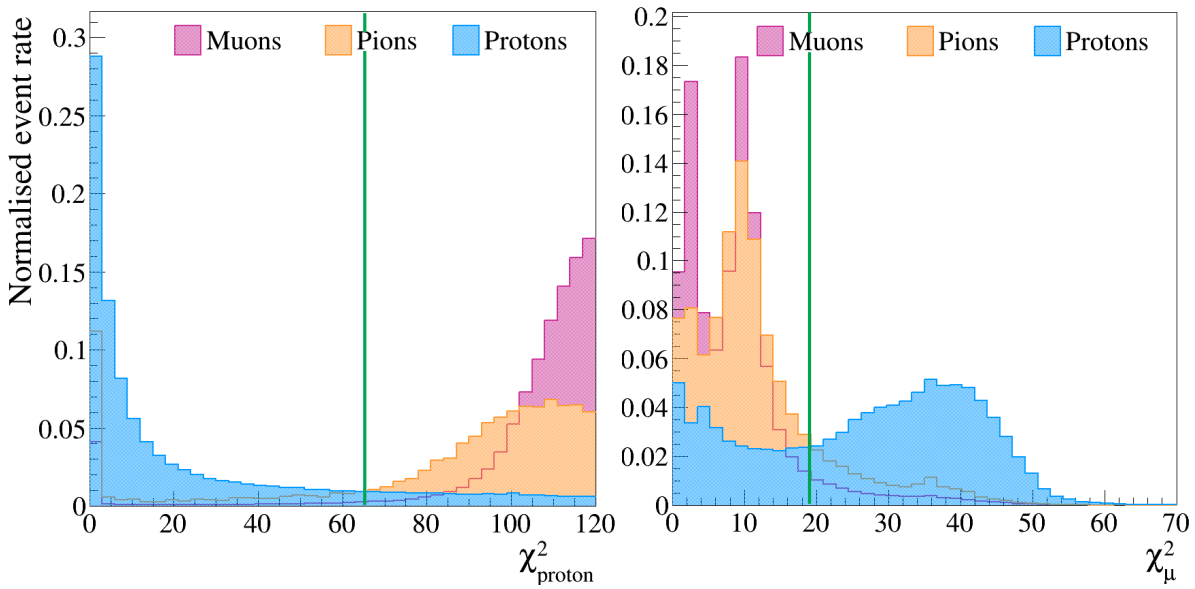

Figure 9.7.: ν_μ CC Inclusive pre-selection, χ^2_{proton} (left) and χ^2_μ (right) for muons protons and pions in SBND. The green lines indicates the cut location defined to maximise the removal of events in which the longest `Track` is a proton.

9.2.2. Particle identification

The PID stage of the selection was defined for the purpose of selecting ν_μ CC 0π events, through a `Track`-based particle identification method which follows the steps outlined in Figure 9.8 and is applied to the pre-selected sample of ν_μ CC Inclusive events. The first part of the particle identification procedure compiles a list of muon candidate particles in an event, and categorises the remaining particles according to whether they are more likely to be a proton or a pion. The method is applied as follows with corresponding plots given in appendix D,

1. If the event has a single escaping `Track` which passes the thresholds set by the CC Inclusive pre-selection, tag the escaping `Track` as the muon

2. In the case where all `Tracks` are contained, or the muon has already been tagged, clear protons are distinguished with respect to muons by selecting those with either $\chi^2_{\text{proton}} < 87$ or length < 10cm. These values were determined by reproducing the χ^2_{proton} and `Track` length distributions for all events passing the ν_μ CC Inclusive selection and once again defining a cut value such that all clear protons are tagged. Muon-candidate contamination is minimised to account for events in which the muon has not yet been tagged. Pions are not being considered at this stage

3. If a muon has not yet been selected, `Tracks` which did not pass either of the proton criteria in the previous cut are then assessed as potentially being the muon. Any track will be tagged as a muon candidate if it passes at least one of the following criteria,

   - $\chi^2_{\text{proton}} > 87$
   - The longest `Track` exceeds 1m
   - $\Delta L/L_{\text{longest}} > 0.7$

4. The remaining `Tracks` are determined to be more likely to be a pion or a proton by tagging pions if $\chi^2_\pi > \chi^2_{\text{proton}}$ and vice versa. This more-often-than-not will return a pion due to the general differences between the distributions in Figure 9.7, however this in not a problem because of the dedicated proton-finding methods which have already been implemented.

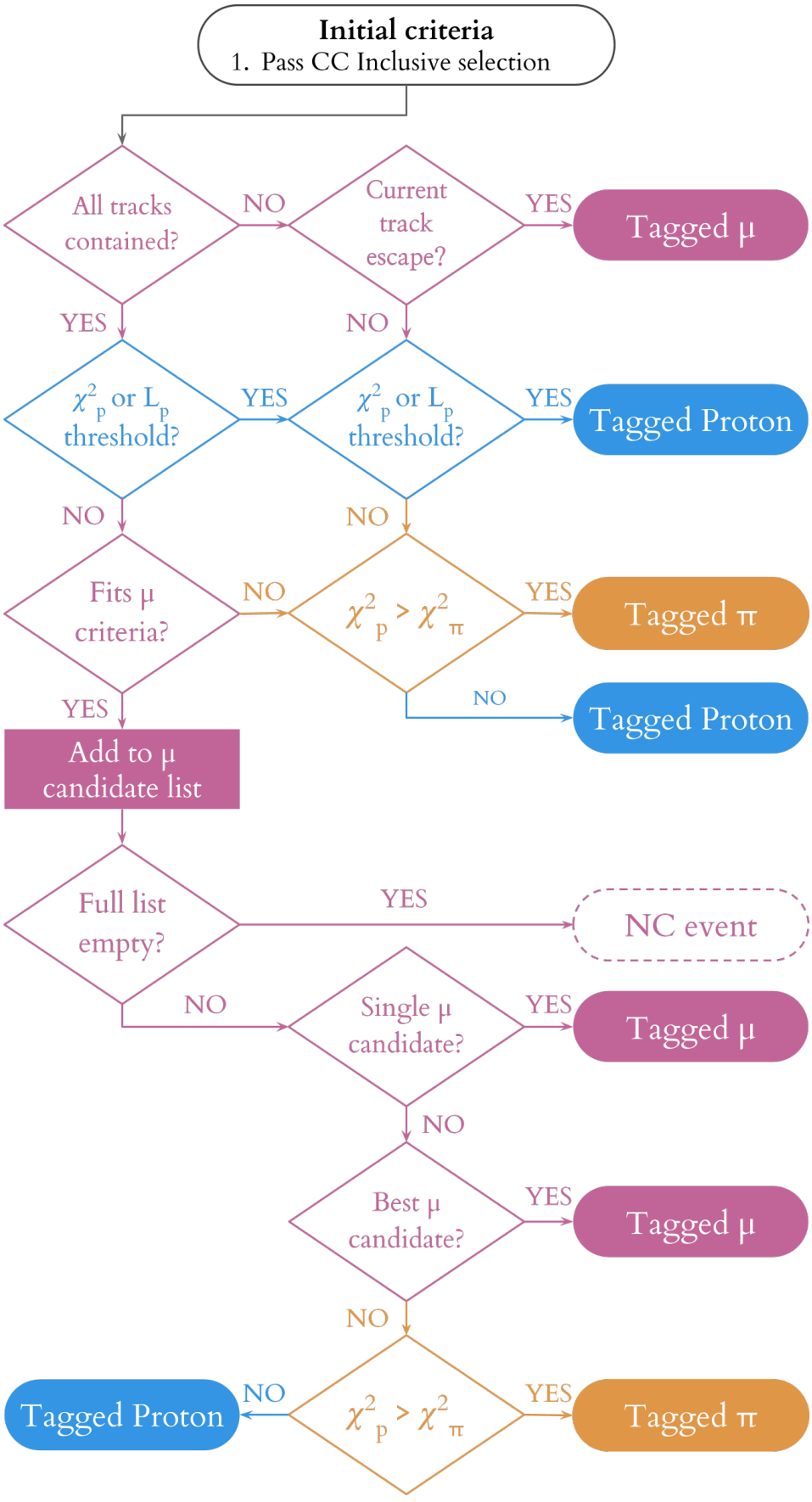

Figure 9.8.: A flowchart depicting the `Track`-based particle identification procedure, developed for the purpose of selecting ν_μ CC 0π events from the pre-selected ν_μ CC Inclusive sample. Every element of the flow chart is defined in the main body of the text.

True topology → ↓ Cut applied	ν_μ CC	ν_μ NC	$\nu, \bar{\nu}$ Other	ν_μ CC Purity
Total	5,918,559	1,694,408	131,149	76.43 %
True fiducial	3,392,049	703,818	67,780	81.47 %
Reco fiducial	3,318,926	666,638	65,858	81.92 %
Max. 1 escapes	3,229,717	663,523	64,970	81.60 %
Min. 1 track	3,197,603	584,999	57,473	83.27 %

Table 9.1.: Contents of the SBND sample following each of the initial criteria, prior to undergoing the ν_μ CC Inclusive pre-selection procedure. The sample has been scaled to the full exposure of SBND, 6.6×10^{20} POT.

Following the compilation of a muon candidate list, the rest of the PID method is implemented as follows,

1. If the muon candidate list is empty, discard the event
2. If there is a single muon candidate, tag the muon
3. The muon is chosen from multiple candidates as follows,
    - If the longest `Track` is on the list, tag it as the muon
    - Otherwise, find the `Track` with the smallest χ^2_μ value
4. Of the remaining `Tracks`, tag pions if $\chi^2_\pi > \chi^2_{\text{proton}}$ and vice versa.

At this stage, all `Tracks` have been identified as either a muon, proton or pion. Events in which there are no showers and no reconstructed pions are deemed to pass the ν_μ CC 0π selection. The corresponding plots showing the locations of each cut value are given in appendix D.

9.3. Selection performance

The number of events in the SBND sample passing each of the initial criteria is given in Table 9.1. All event rates have been scaled to the full exposure of SBND, 6.6×10^{20} POT, and are contained within the fiducial volume of the LArTPC.

The purity, $\rho_{t,s}$, of selecting events of type, t, at stage, s, is defined as the fraction of events which were correctly selected as type t, $N_{t,s}^{\text{Selected, True}}$, with respect to the total number of selected events of type t at that stage, $N_{t,s}^{\text{Selected}}$,

$$\rho_{t,s} = \frac{N_{t,s}^{\text{Selected, True}}}{N_{t,s}^{\text{Selected}}}. \tag{9.2}$$

The total number of true ν_μ CC Inclusive events used in all efficiencies will be the final ν_μ CC event rate passing the initial criteria presented in Table 9.1, 3,197,603.

9.3.1. ν_μ CC Inclusive pre-selection

The cumulative efficiency at each stage of the ν_μ CC Inclusive pre-selection is presented in terms of the true neutrino energy in Figure 9.9, in terms of the true muon momentum in Figure 9.10 and finally in terms of the cosine of the true angle of the muon track with respect to the neutrino beam direction in Figure 9.11.

The efficiency, $\epsilon_{t,s}$, at each stage, s, is defined as the fraction of selected events which were truly of type t, $N_{t,s}^{\text{Selected, True}}$, with respect to the total number of true events of type t, $N_{t,s}^{\text{True}}$,

$$\epsilon_{t,s} = \frac{N_{t,s}^{\text{Selected, True}}}{N_{t,s}^{\text{True}}}. \tag{9.3}$$

The main loss of efficiency arises when the muon has either very low momentum, $p_\mu < 200$ MeV, or when the scattering angle is close to the vertical, $\cos\theta_\mu \approx 0$, such that the `Hits` may cover only a small number of collection plane wires. In this case, both the calorimetry and the geometry of the `Track` is much harder to reconstruct. This angular-dependence could be resolved when utilising all three wire planes to interpret the calorimetry.

True topology → ↓ Cut applied	ν_μ CC	ν_μ NC	$\nu, \bar{\nu}$ Other	ν_μ CC Pur.	ν_μ CC Eff.
Total	3,197,603	584,999	57,473	83.27 ± 0.07 %	100.00 ± 0.00 %
One escapes	240,244	1222	2416	98.51 ± 0.09 %	7.51 ± 0.06 %
+ $\Delta L/L_{\text{longest}}$	1,695,238	88,568	16,581	94.16 ± 0.07 %	53.02 ± 0.11 %
+ χ^2 & length	3,078,841	236,008	40,615	91.76 ± 0.06 %	96.29 ± 0.04 %

Table 9.2.: Contents of the SBND sample following each cut applied in the ν_μ CC Inclusive pre-selection procedure. The sample has been scaled to the full exposure of SBND, 6.6×10^{20} POT and the statistical uncertainty is given alongside the efficiency and purity.

A summary of the integrated event rates at each stage is given in Table 9.2. Where the purity is once again defined by equation 9.2 and the efficiency is defined by equation 9.3. In the first stage, the efficiency of the selection is calculated for events in which exactly one `Track` above the minimum required length leaves the detector. Second, events are added in which there are two or more `Tracks` and the longest two have a large enough fractional length difference. Finally, of the remaining events, those with at least one muon candidate based on the geometry and calorimetry of the `Tracks` are added. The final efficiency and purity following the ν_μ CC pre-selection both exceed 90%, which is extremely high and is an excellent starting point for the particle identification and exclusive selection procedure.

9.3.2. Particle identification

For the purpose of assessing the performance of the particle identification, the efficiency and purity are defined as follows,

$$\epsilon_p = \frac{N_p^{\text{Selected,True,R}}}{N_p^{\text{True}}} \tag{9.4}$$

$$\rho_p = \frac{N_p^{\text{Selected,True,R}}}{N_p^{\text{Selected,R}}}, \tag{9.5}$$

where p is the particle type under assessment, $N_p^{Selected,True,R}$ is the number of correctly-selected particles of type p ensuring each reconstructed particle has exactly one cor-

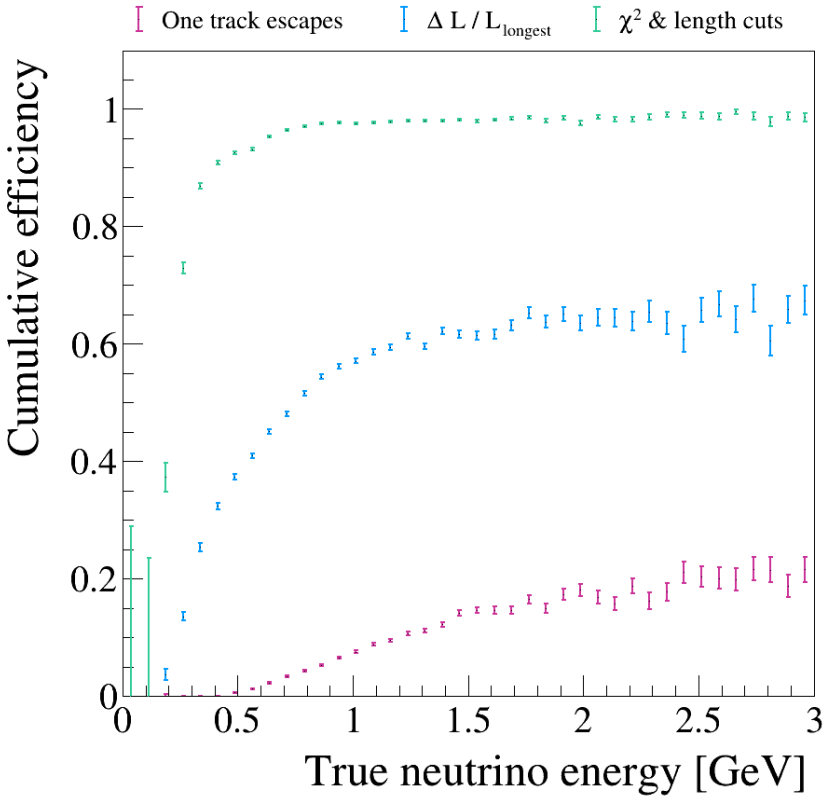

Figure 9.9.: The cumulative efficiency of the ν_μ CC Inclusive pre-selection at each of the selection stages in terms of the true neutrino energy, E_ν. Statistical uncertainties are included.

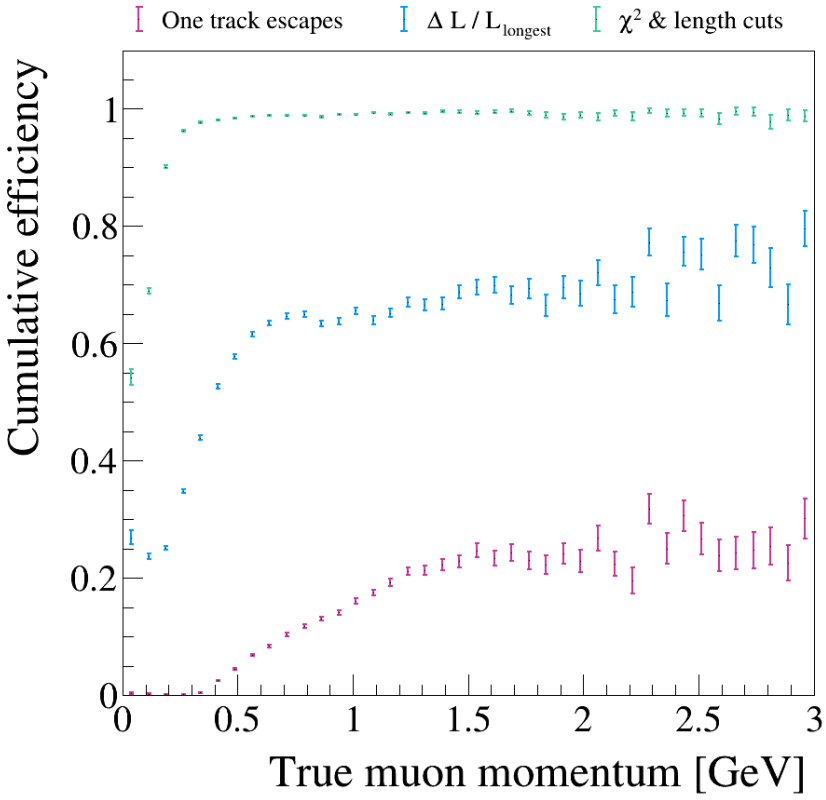

Figure 9.10.: The cumulative efficiency of the ν_μ CC Inclusive pre-selection at each of the selection stages in terms of the true muon momentum, p_μ. Statistical uncertainties are included.

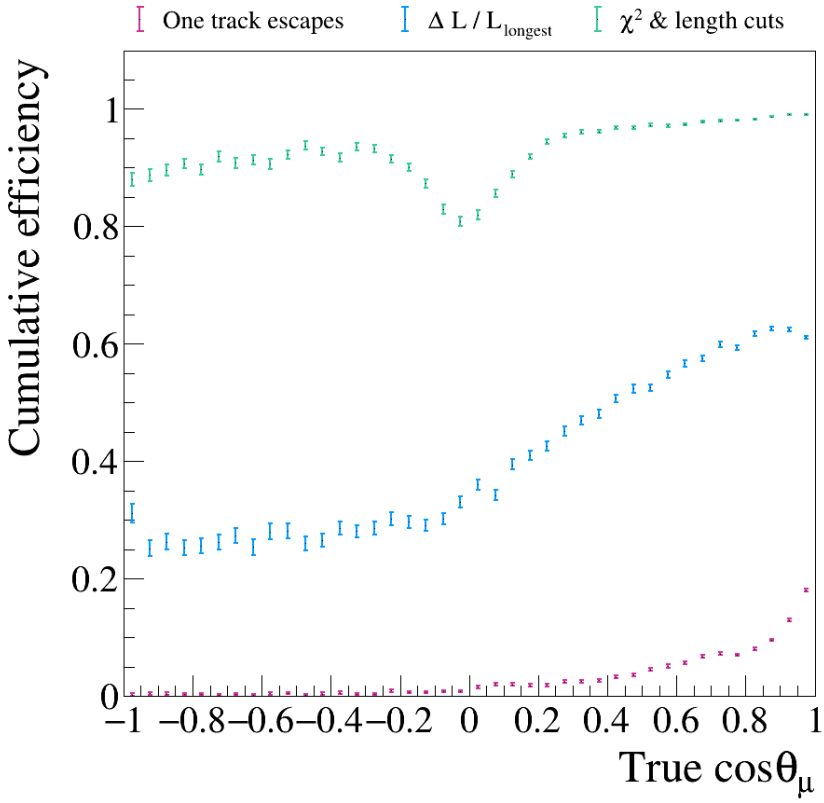

Figure 9.11.: The cumulative efficiency of the ν_μ CC Inclusive pre-selection at each of the selection stages in terms of the true cosine of the muon scattering angle with respect to the incoming neutrino direction, $\cos\theta_\mu$. Statistical uncertainties are included.

responding true particle, R. This mitigates double counting in the numerator of the efficiency and only assess the purity of reconstructed particles from which it is possible to determine the true counterpart. The purity therefore defines the performance of the particle identification method, whilst the efficiency accounts for all possible losses. A summary of the muon, pion and proton identification performance following the ν_μ CC Inclusive pre-selection is given in Table 9.3. The purity of the proton selection is extremely good, which reflects the targeted development of the particle identification procedure to selecting protons. Similarly, the pion selection performs poorly as there was no focussed effort to tag pions.

Since the selection efficiency is determined with respect to the rate following the ν_μ CC Inclusive pre-selection, and therefore characterises the performance of only the particle identification, it should be possible to achieve a 100% muon-selection efficiency using this metric. The loss of efficiency mostly occurs when the muon is travelling vertically, and therefore parallel to the collection plane wires in the detector. This impedes the reconstruction of the `Hits` and consequently the energy of the muon on the collection plane as many `Hits` may be collected on a single wire such that it is difficult to disentangle them. This will be discussed in the context of the topological selection in section 9.3.3.

Reco → ↓ True	μ^-	$\pi^\pm$	Proton
μ^-	196,145	9248	8574
$\pi^\pm$	11,712	19,392	8014
Proton	4757	11,868	167,657
Other	1837	165	336
Efficiency	88.58 ± 0.07 %	32.90 ± 0.20 %	51.92 ± 0.09 %
Purity	91.46 ± 0.06 %	47.68 ± 0.25 %	90.83 ± 0.07 %

Table 9.3.: A breakdown of the particle identification performance in terms of the muon, pion and proton tagging. The particle rates have not been scaled to the full POT of SBND.

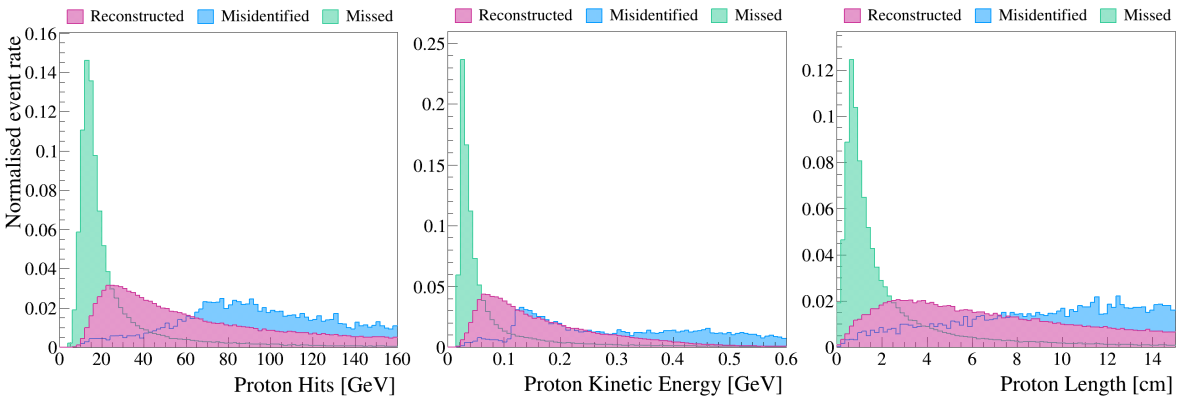

Figure 9.12.: The shapes of the distribution of `Hits` (left), kinetic energy (centre) and length (right) of the true reconstructable proton `Tracks` in terms of whether they were correctly reconstructed, incorrectly reconstructed or entirely missed in the particle identification.

The inefficiency of selecting protons stems from the frequency with which they have too-few `Hits` to be well-reconstructed, even above the reconstructability limit. This behaviour is shown in terms of the number of `Hits` in each proton, the true kinetic energy of the proton and the true length of the proton in Figure 9.12. The misidentified protons generally have more `Hits` than those which are correctly reconstructed. The missed protons generally have a very low number of `Hits`. The low-`Hit` protons are likely to be poorly reconstructed when the reconstructed neutrino interaction vertex is incorrectly located. In this case, the few `Hits` from a single proton may be assigned to multiple particles such that the calorimetry is poorly defined and the χ^2_{proton} is not comparable with expectation.

9.3.3. ν_μ CC 0π sample selection

Having defined and identified all particles from the `Tracks` in the ν_μ CC Inclusive-selected sample, it is possible to further separate the sample into exclusive channels. The performance of a ν_μ CC 0π selection as well as the final topological ν_μ CC Inclusive selection following the PID procedure is given in Table 9.4 in terms of the breakdown of contributing true final states. The efficiencies are demonstrated as a function of the true neutrino energy in Figure 9.13, the true muon momentum in Figure 9.14 and the true muon scattering angle, $\cos\theta_\mu$ in Figure 9.15. The purity and efficiency definitions follow those defined in equations 9.2 and 9.3 respectively.

The purity of the ν_μ CC selection increases by 2% from the pre-selection performance, at the cost of a 2% decrease in the efficiency from the pre-selection performance. Both quantities lie close to 95% and are therefore comparable to the 95% muon selection purity reported by MicroBooNE [149]. The exclusive ν_μ CC 0π selection performance is also very high, with both an efficiency and purity of almost 85%. This performance is almost 10% higher than the 76% purity reported by MicroBooNE in their ν_μ CC 0π selection with no cosmic backgrounds [196].

As verified by Tables 9.3 and 9.4, the largest contamination in the ν_μ CC 0π-selected sample comes from mis-identified charged pions. When true ν_μ CC 1π events are incorrectly selected, the pion has been incorrectly tagged as a proton. When true ν_μ NC 1π events are incorrectly selected, the pion has been incorrectly tagged as a muon. Another dominant background occurs when incorrectly selecting true ν_μ NC 0π events, in which a proton has been misidentified as the muon instead. One additional type of background involves a ν_e event being tagged as a ν_μ event. In ν_e CC events, this is likely caused by the electron appearing track-like and being tagged most-probably as a proton.

Figures 9.13, 9.14 and 9.15 also indicate where the muon selection efficiency is lost. The dip region in Figure 9.15 occurs when the muon travels along the vertical and consequently the `Hits` reach very few collection-plane wires, making their reconstruction and the extrapolation to the geometry of the `Track` more difficult. Consequently, the dE/dx distribution cannot be well-defined, such that the comparison with the theoretical distributions results in a χ^2 value which does not represent the true particle type.

Reco → ↓ True	CC Inc.	CC 0π
CC 0π	2,405,448	2,157,036
CC $1\pi^\pm$	565,477	233,694
CC Oth.	45,128	9870
NC 0π	59,700	52,713
NC $1\pi^\pm$	84,230	68,624
NC Oth.	13,524	6696
ν_e, $\bar{\nu}_e$	8996	6929
$\bar{\nu}_\mu$	26,931	22,098
Efficiency	94.32 ± 0.05 %	84.49 ± 0.09 %
Purity	93.97 ± 0.05 %	84.34 ± 0.09 %

Table 9.4.: A breakdown of the SBND ν_μ CC Inclusive and ν_μ CC 0π selected samples in terms of the contributing true final state topologies. The sample has been scaled to 6.6×10^{20} POT and the statistical uncertainty is given alongside the efficiency and purity.

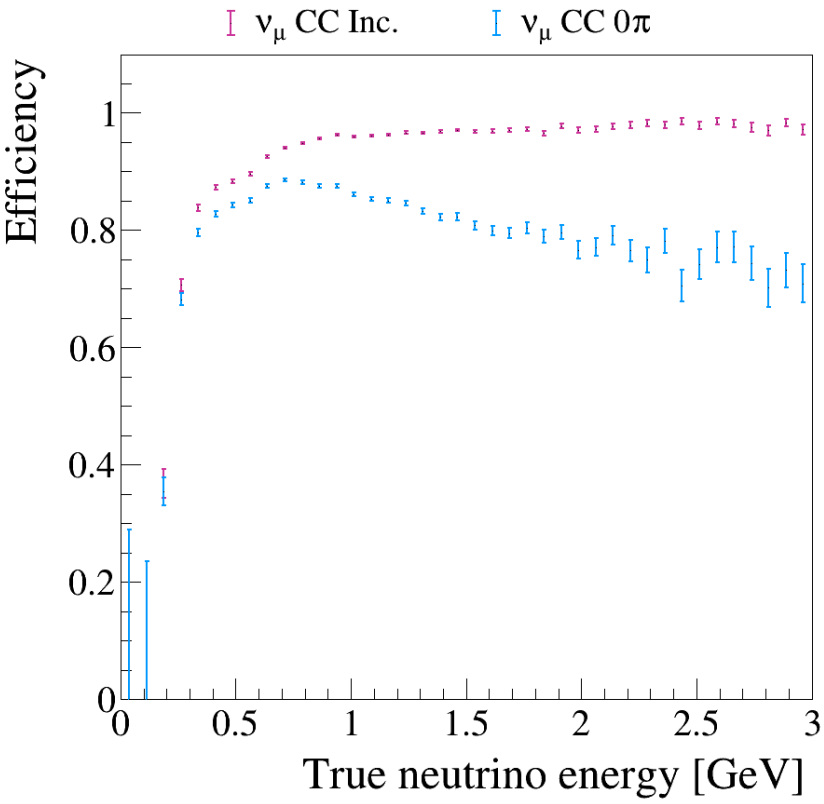

Figure 9.13.: The efficiency of the ν_μ CC Inclusive and ν_μ CC 0π selections in terms of the true neutrino energy, E_ν. Statistical uncertainties are included.

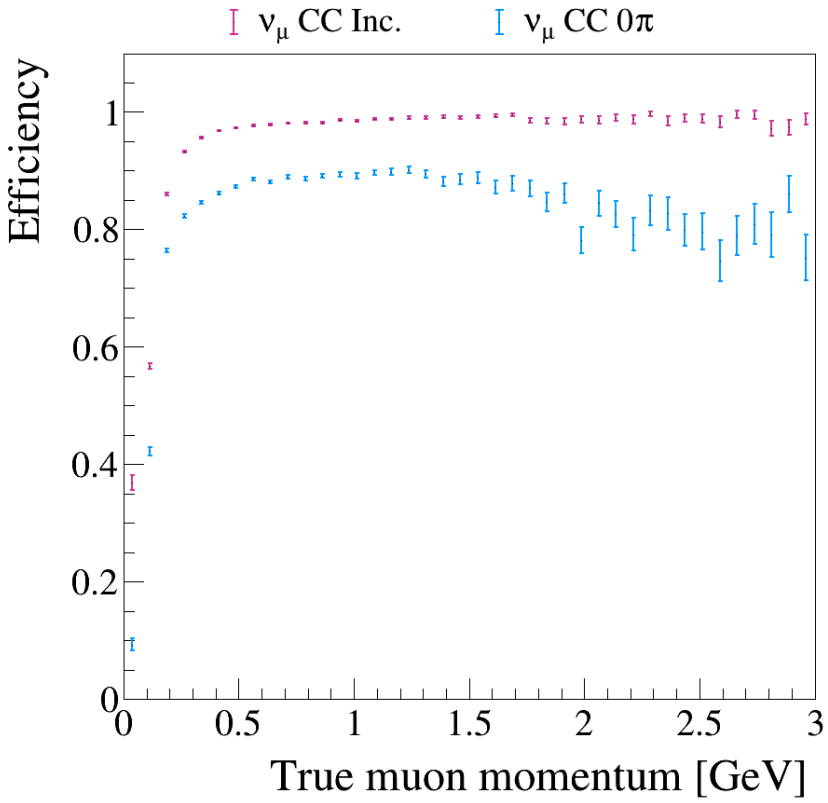

Figure 9.14.: The efficiency of the ν_μ CC Inclusive and ν_μ CC 0π selections in terms of the true muon momentum, p_μ. Statistical uncertainties are included.

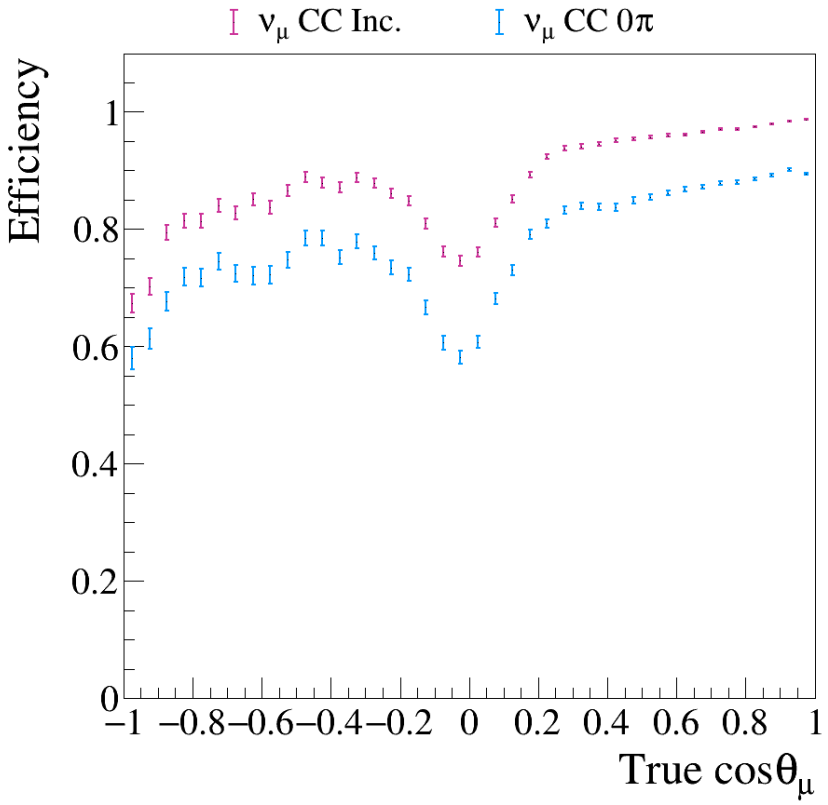

Figure 9.15.: The efficiency of the ν_μ CC Inclusive and ν_μ CC 0π selections in terms of the true cosine of the muon scattering angle with respect to the incoming neutrino direction, $\cos\theta_\mu$. Statistical uncertainties are included.

9.4. Towards a reconstructed sensitivity analysis

Following the implementation of the event selection procedure in the near detector, it is possible to determine the sensitivity to sterile neutrino oscillations using a fully-reconstructed sample of SBND events. In order for comparisons to be made with the sensitivities conducted using MC samples, an additional 80% efficiency was applied to all events in the selected samples to account for the estimated loss due to incorrect external background removal and any other non-topological losses. This value was chosen to exactly match that which was implemented in the pseudo-reconstruction procedure outlined in section 6.3.2.

The event rates from each of the ν_μ CC Inclusive and ν_μ CC 0π-selected samples are given in Table 9.5. The SBND ν_μ CC Inclusive event rate is higher in the reconstructed sample than that of the MC, which occurs because of the higher contamination from neutrino-induced backgrounds in the reconstructed sample (6%) than the MC sample (2%).

9.4.1. Reconstructed neutrino energy

Calorimetry will be one of the best ways of calculating the reconstructed neutrino energy in data, due to the exceptional capabilities of the LArTPC detector technology. Currently, the reconstruction has not yet been fully-validated, therefore the calorimetry in SBND is still in the early stages of development. For the time being, an alternative method for calculating the reconstructed neutrino energy is employed, which primarily utilises the reconstructed momentum of the final state particles. The intention is to represent the calorimetric method as closely as possible, therefore the energy is defined as,

$$E_\nu = \sum_{j=0}^{N_p} M^j + \sum_{i=0}^{N_r} E_k^i, \tag{9.6}$$

where N_p corresponds to the number of reconstructed particles in the final state which were produced in the interaction and M^j is the mass of particle j. N_r is the total number of reconstructed particles in the event and E_k^i is the kinetic energy of particle i, calculated from the momentum as per,

Sample	ν_μ CC Inclusive	ν_μ CC 0π
MC, GENIE v2	2,546,800	-
Reco. GENIE v2	2,567,500	2,046,100

Table 9.5.: SBND event rates as inputs to the reconstructed sensitivity study. The rates are given following the ν_μ CC Inclusive selection in each of the reconstructed and two MC samples. The rates are given following the ν_μ CC 0π-selection in only the reconstructed samples, since at the time of running the GENIE v2 MC production, the exclusive contributions to the MC event rate were not available. All event rates are scaled to 6.6×10^{20} POT.

$$E_k = \sqrt{\vec{p}^2 + M^2} - M. \tag{9.7}$$

The momentum is determined in one of three ways, according to the characteristics of the particle in question,

1. If a particle that has been reconstructed as a muon is longer than 1m, its momentum is calculated using MCS using a method developed by MicroBooNE [208].
2. If a reconstructed muon is between 50 and 100cm long, the momentum is determined from the range of the particle. Similarly, if the length of a tagged proton is greater than 50cm, its momentum can also be determined by range [209] [210].
3. Finally, if none of the above criteria have been met, the particle's momentum is calculated using calorimetry information.

The main limitation of this method is that the kinetic energy depends on the type of particle which has been selected. When particles are misidentified in the selection, a contamination factor related to the mass of the identified particle is included.

The SBND reconstructed neutrino energy spectra are given in Figures 9.16, for each of the ν_μ CC Inclusive and ν_μ CC 0π-selected samples. The spectra are shown with the true neutrino interaction mode contributions. A comparison between the ν_μ CC Inclusive spectra plotted in terms of the E_{Reco} and E_{True} definitions is shown as an area-normalised overlay in the left-hand plot of Figure 9.17 for the purpose of assessing the shape differences. The difference, $E_{Reco} - E_{True}$, is shown in the right-hand plot of Figure 9.17. This indicates that the reconstructed neutrino energy definition is under-estimated with respect to the true values, which is likely to be predominantly due to the visible energy

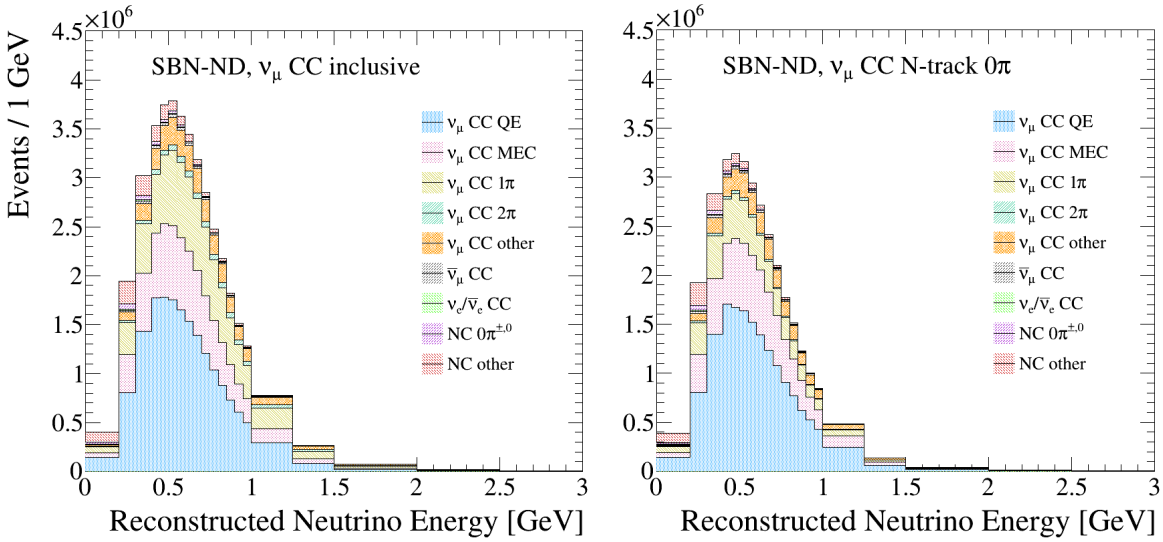

Figure 9.16.: SBND reconstructed neutrino energy spectra following the topological selection of ν_μ CC Inclusive (left) and ν_μ CC 0π (right) events. The spectra are broken down into the contributions from each neutrino interaction mode.

missed in the calorimetric method of calculating E_{Reco}. This missed energy will comprise both `Hits` which have not been reconstructed, as well as from final state primary, neutral particles which do not leave energy depositions in the detector, such as neutrons.

Figure 9.19 shows how this under-estimation is distributed with respect to the true neutrino energy, and shows that the majority of the discrepancy occurs at energies around the BNB peak, $E_{True} = 0.7$ GeV. The magnitude of this discrepancy increases, albeit with only a few events per bin, towards the high-energy tail of the true neutrino energy distribution.

In addition, it is useful to compare the reconstructed spectra with the pseudo-reconstructed spectra using the same model configuration, which was shown in Figure 8.9. This highlights that the reconstructed peak is also lower than pseudo-reconstructed peak, which is shown to match more-closely with the corresponding true energy spectra in Figure 9.18. The consequences of this distinction will become apparent in the sensitivity studies.

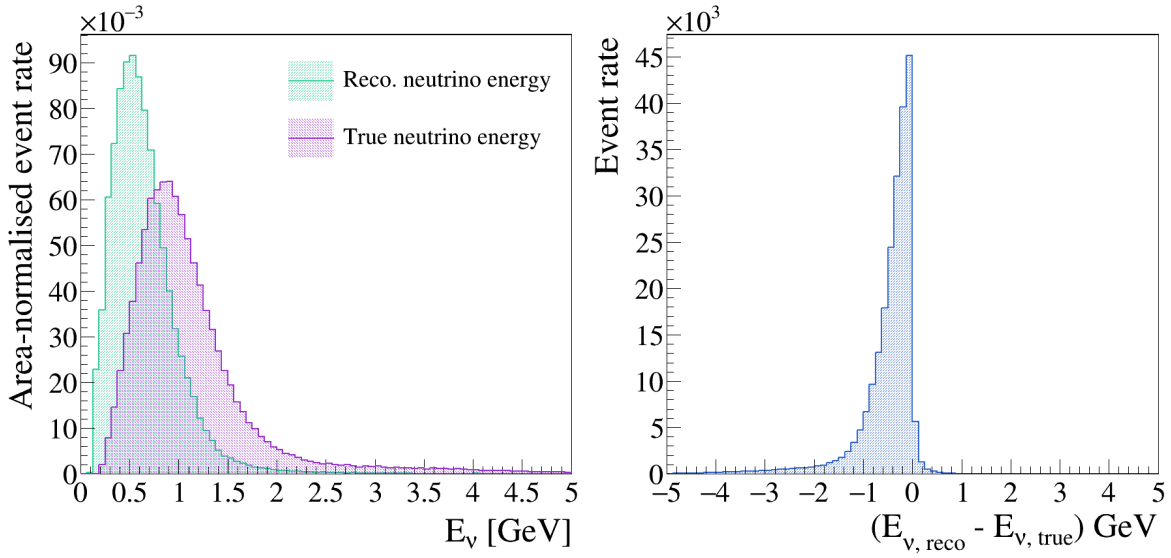

Figure 9.17.: Comparisons between the SBND true and reconstructed neutrino energy spectra following the topological selection of ν_μ CC Inclusive events. The left-hand plot is an area-normalised overlay of the two distributions, the right-hand plot takes the difference between them.

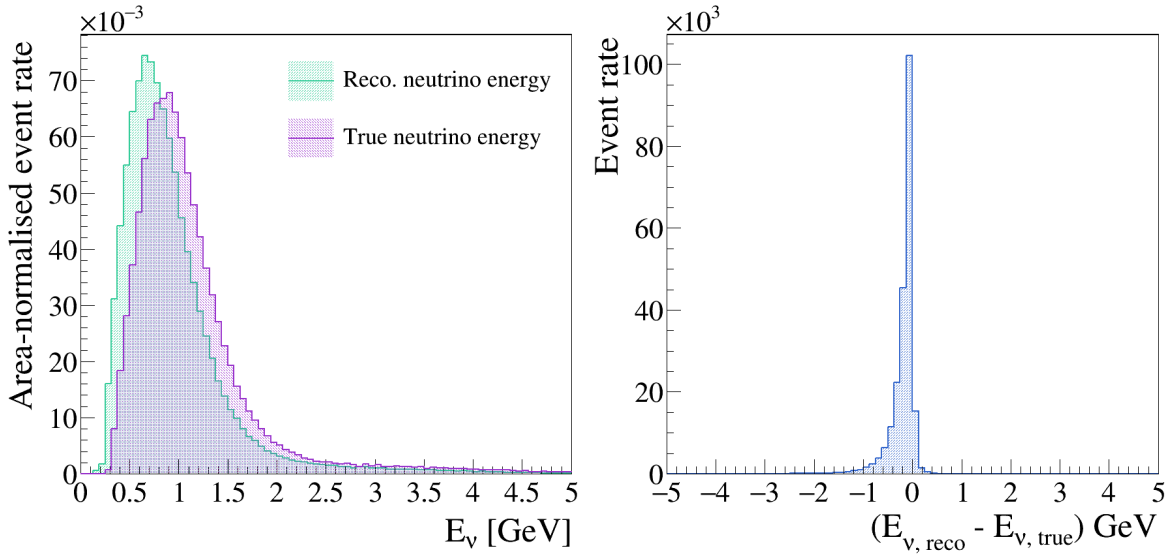

Figure 9.18.: Comparisons between the SBND true and pseudo-reconstructed ν_μ CC Inclusive neutrino events. The left-hand plot is an area-normalised overlay of the two distributions, the right-hand plot takes the difference between them.

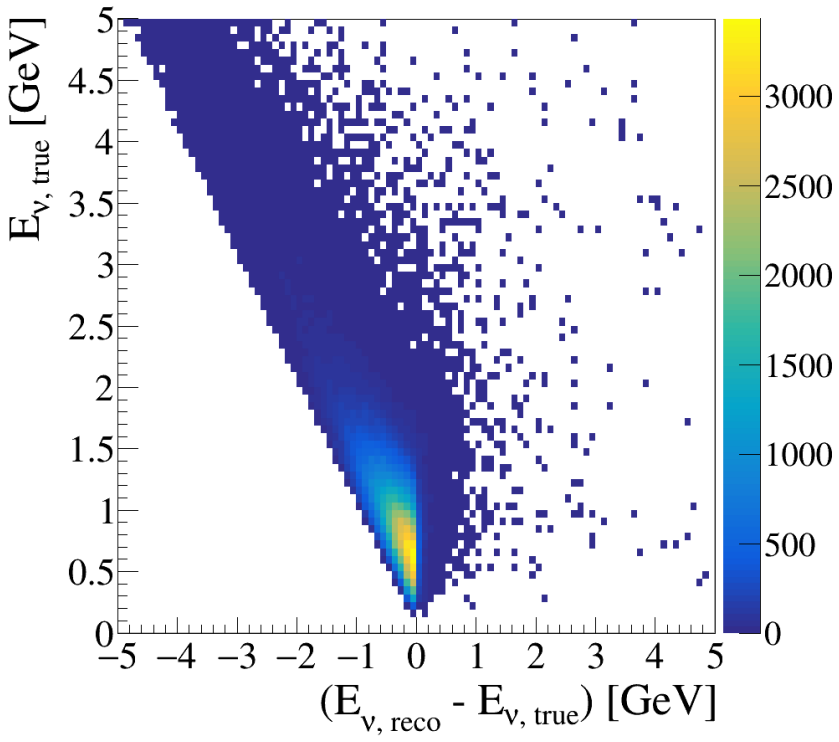

Figure 9.19.: Comparisons between the SBND true and reconstructed neutrino energy spectra following the topological selection of ν_μ CC Inclusive events. The difference between the true and reconstructed neutrino energy distributions is plotted against the true neutrino energy distribution.

9.4.2. Statistical exclusion region sensitivity study

The sterile neutrino oscillation sensitivity study conducted with the reconstructed samples involved the statistical-only contributions from the near detector. Since the GENIE model used to construct the reconstructed sample was v2_12_10, the MC-based sensitivities constructed from the GENIE v2_12_10 are included in the studies for comparison.

The left-hand plot in Figure 9.20 is an overlay of the statistical-only exclusion sensitivities constructed with the reconstructed and MC samples. The size and shape of the differences between the reconstructed and MC curves is clarified in the right-hand plot of Figure 9.20, which shows the ratio $\sin^2 2\theta_{\mu\mu,MC}/\sin^2 2\theta_{\mu\mu,Reco}$. This distribution indicates that in the region $\Delta m^2_{41} < 1$ eV^2 the sensitivity is higher when using reconstructed events ($\sin^2 2\theta_{\mu\mu,MC}/\sin^2 2\theta_{\mu\mu,Reco} > 1$) and lower when $\Delta m^2_{41} > 1$ eV^2. This is caused by fact that the peak of the SBND reconstructed neutrino energy distribution is lower in the reconstructed sample, such that the sensitivity at lower values of Δm^2_{41} is increased with respect to the MC version as per equation 2.30.

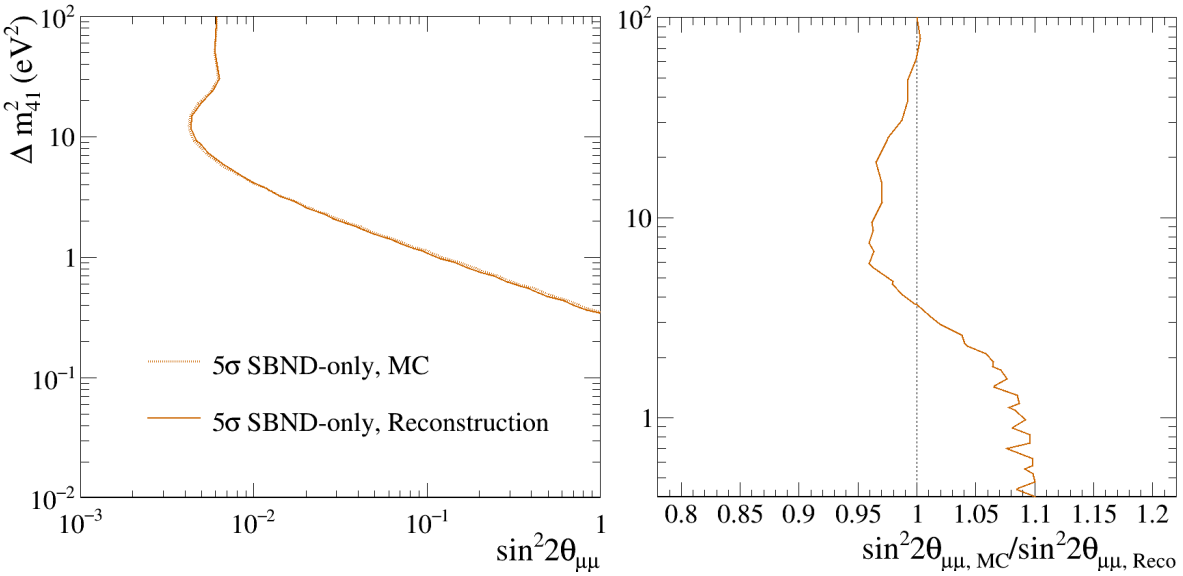

Figure 9.20.: The SBND-only sterile oscillation sensitivity. Included in the left-hand plot is the ν_μ-disappearance sensitivity produced with the reconstructed sample of ν_μ CC Inclusive events, along with the MC sample of events generated with GENIE version 2 for comparison. The right-hand plot shows the ratio of $\sin^2 2\theta_{\mu\mu,MC}/\sin^2 2\theta_{\mu\mu,Reco}$ across the active Δm^2_{41} parameter space with a reference line at 1. No systematic parameters are considered in the fits.

9.5. Concluding the topological selection

The selection procedure was able to tag ν_μ CC 0π events with an 84.5% efficiency and 84.3% purity, an improvement on the MicroBooNE-measured ν_μ CC 0π purity of 76% (excluding cosmics) [196]. The selection procedure was also capable of tagging ν_μ CC Inclusive events with a 94.3% efficiency and 94.0% purity, which is comparable to the 95% muon selection purity reported by MicroBooNE [149].

There are two major considerations which must be made when assessing the performance of this selection procedure. The first is the exclusion of the cosmic ray and out-of-fiducial-volume background contamination of the neutrino sample. Although the location of the SBND detector on the surface of the earth mean that the rate of cosmic rays in particular will be on the order of 3 per neutrino interaction, a huge effort is being undertaken in order to mitigate their effect. The result of such contamination will be to reduce the overall neutrino selection efficiency.

Second, the reconstruction is currently under active development and will likely see substantial improvements to many aspects before this selection procedure will be applied to data. For instance, updates to the vertex-finding in the pattern recognition will likely

improve the reconstruction and identification of short proton tracks. In addition, only the collection wire plane was used in the calorimetric reconstruction and resulted in direction-dependent track identification. Including all three planes would mitigate this dependence, whilst also improving the overall energy reconstruction.

Targeted muon-pion separation would help reduce the largest topological background in the muon tagging procedure. In summary, the addition of external backgrounds will ultimately reduce the ν_μ CC 0π selection performance, whilst improvements to the reconstruction will improve the current performance.

Finally, the SBND-only sterile neutrino oscillation sensitivity using this reconstructed sample of events was comparable to the pseudo-reconstruction version. This demonstrates that the performance of the existing reconstruction combined with this topological selection procedure is capable of matching the estimated best-case scenario.

One improvement to this oscillation analysis, on top of the general reconstruction-based improvements, would be to parametrise the samples in terms of directly measurable parameters, instead of the reconstructed neutrino energy. The main limitation of using E_{Reco} was demonstrated in the comparison between E_{True} and E_{Reco} distributions, in which the method of calculating of E_{Reco} resulted in a substantial reduction in the neutrino energy peak. Developing and improving the neutrino energy reconstruction will have a substantial impact on the sensitivity and will therefore also be one of the main development areas for future iterations of the analysis.

Chapter 10.

Conclusions

This thesis presented three analyses within SBND and the SBN program. These experiments will be capable of making cross-section, sterile oscillation and beyond the standard model physics measurements. All analyses were performed on MC samples normalised to 6.6×10^{20} POT in each of the SBND and ICARUS detectors, and 1.32×10^{21} POT in the MicroBooNE detector. Prior to the first analysis, the GENIE event generator was used to construct multiple samples of neutrino interaction events in the SBND detector, from different theoretical and empirical model configurations. SBND will record >1 million neutrino interactions per year, with around 50% of the sample made up by the ν_μ CC 0π final state. The truth-level content and kinematics of the ν_μ CC 0π topology were studied, in order to form the groundwork for downstream analyses.

The first analysis determined the sensitivity of SBN to measuring the ν_μ disappearance parameters in the context of sterile neutrino oscillations under the (3+1) hypothesis, $\sin^2 2\theta_{\mu\mu}$ and Δm^2_{41}. This study was performed as an update to the work presented in the SBN proposal, with careful treatment and assessment of each input to the analysis. In particular, semi-exclusive joint fits of the ν_μ CC 0π and ν_μ CC Other samples were implemented in place of the single, ν_μ CC Inclusive, fits.

The results of the sensitivity analysis determined that the SBN exclusion sensitivity at the 5σ confidence level will supersede the measurements made by MiniBooNE across the entire $\sin^2 2\theta_{\mu\mu}, \Delta m^2_{41}$ parameter space. In addition, the SBN sensitivity at the 5σ confidence level in the region $\Delta m^2_{41} > 1$ eV^2 will be comparable that which was measured by MINOS/MINOS+ at the 90% confidence level and will be more sensitive than IceCube at the 99% confidence level, whose data is mostly sensitive to the ν_μ-disappearance parameters below $\Delta m^2_{41} = 1$ eV^2.

The second analysis took into consideration the systematically-limited SBN datasets, which mean that the physics capabilities of the experiment depend entirely on the definition and magnitude of the prior systematic parameters and uncertainties. The ability of the current oscillation analysis procedure to disentangle systematic effects from real physics was assessed through near detector semi-exclusive joint fits of the ν_μ CC 0π and ν_μ CC Other samples in a mock data analysis. These fits were performed between MC and mock data samples constructed with the previously-studied model configurations.

The results of the mock data analysis indicated that the current implementation of the oscillation analysis procedure is insufficient for accurately assigning systematic parameter pulls and well-constrained uncertainties. This performance was quantified as the magnitude of the discrepancy between the mock data and postfit spectra at the far detector, having been extrapolated following the near detector fits. Combining the results of all the mock data fits, the maximal integrated event rate difference at the far detector was calculated to be 5.49% of the far detector event rate. This value will be constrained as the analysis procedure is developed.

Finally, a topological selection procedure was defined in SBND, which was capable of selecting the ν_μ CC 0π final state from a sample of neutrinos with an 84.5% efficiency and 84.3% purity and the ν_μ CC Inclusive final state with a 94.3% efficiency and 94.0% purity, only slightly lower than the best-case purity used in the pseudo-selection, 98%, which only took into consideration NC contamination due to pion mis-identification. The ν_μ disappearance sterile neutrino oscillation analysis was then performed on these samples of reconstructed events, which resulted in a consistent sensitivity across the entire parameter space with respect to the pseudo-reconstruction version of the study. Dedicated improvements to the SBN reconstruction tools will further improve this sensitivity, above and beyond the MC-based expectation.

In summary, the abundance of the ν_μ CC 0π final state in the SBN detectors and mm-scale resolving capabilities of the LArTPC technology effectuates the near detector to place tight systematic constraints in the oscillation analysis. SBN will consequently be capable of measuring the ν_μ disappearance sterile neutrino oscillation parameters with unprecedented precision. The oscillation analysis procedure will ultimately be extended to perform joint fits of ν_μ disappearance, ν_e disappearance and ν_e appearance channels, as well as higher-order semi-exclusive samples. These updates will further improve the SBN oscillation sensitivity as the individual channels will provide a unique handle on a subset of the systematic parameters.

Appendix A.

Physics studies of ν_μ CC Inclusive SBND events

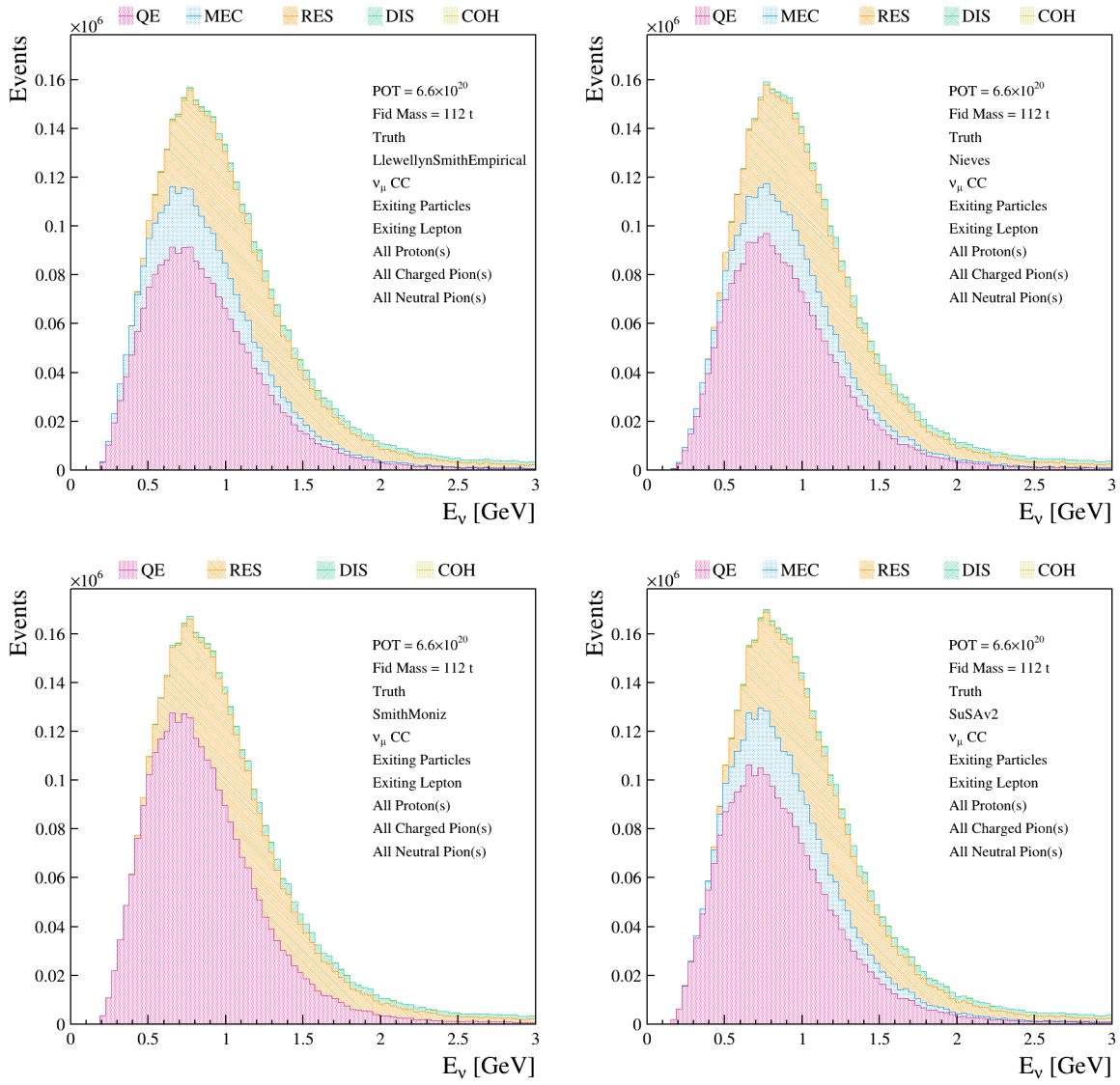

Figure A.1.: SBND E_{true}-dependent CC Inclusive event rate distributions for the 4 GENIE model configurations based on G18_10a_02_11a. From top-left to bottom-right are Llewellyn Smith-Empirical, Nieves, Smith-Moniz, SuSAv2. All distributions are stacked with a breakdown of the true interaction type which took place between a muon neutrino and the argon.

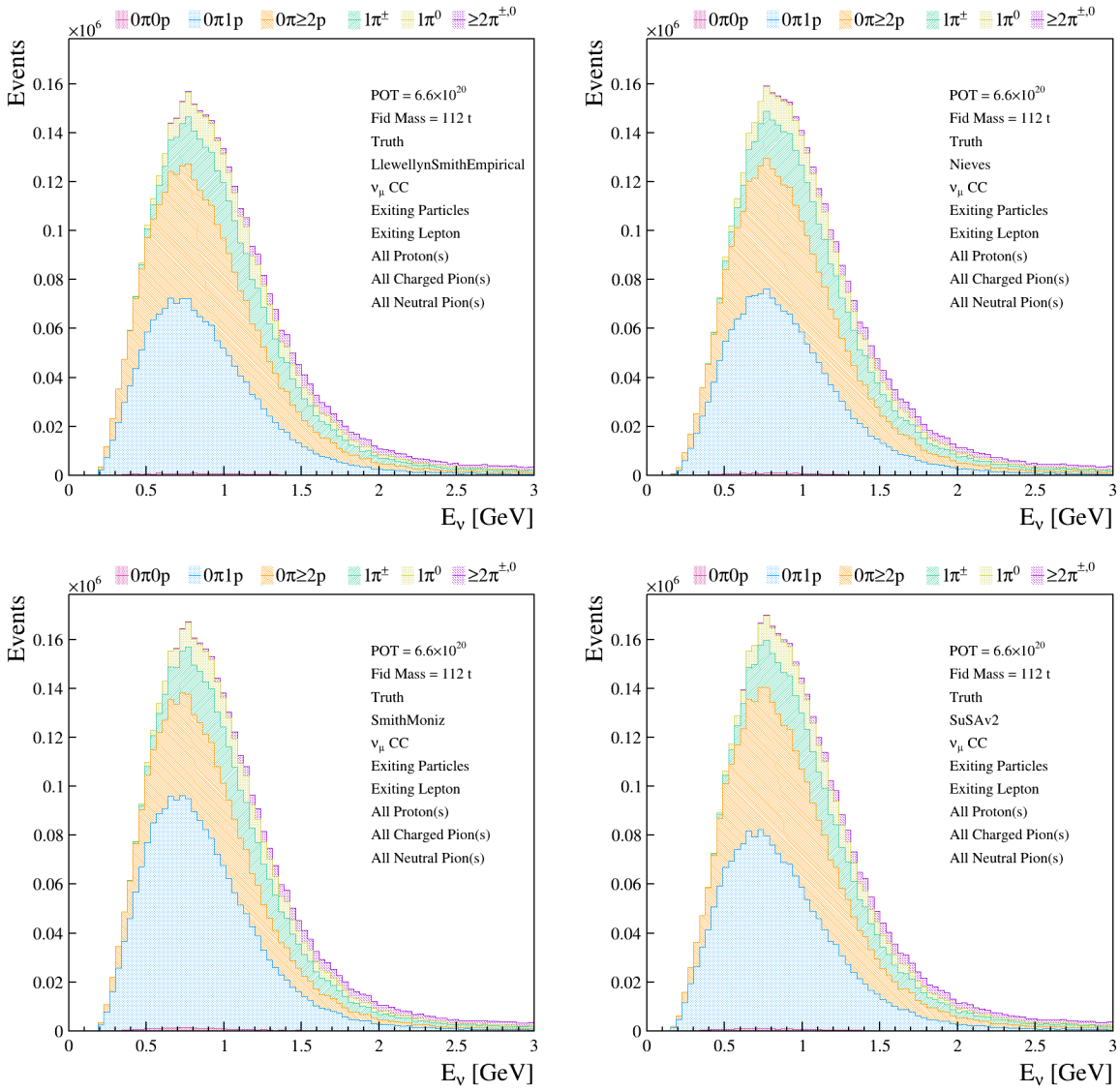

Figure A.2.: SBND E_{true}-dependent CC Inclusive event rate distributions for the 4 GENIE model configurations based on G18_10a_02_11a. From top-left to bottom-right are Llewellyn Smith-Empirical, Nieves, Smith-Moniz, SuSAv2. All distributions are stacked with a breakdown of the true final state topology which emerged following the ν_μ-Ar interaction.

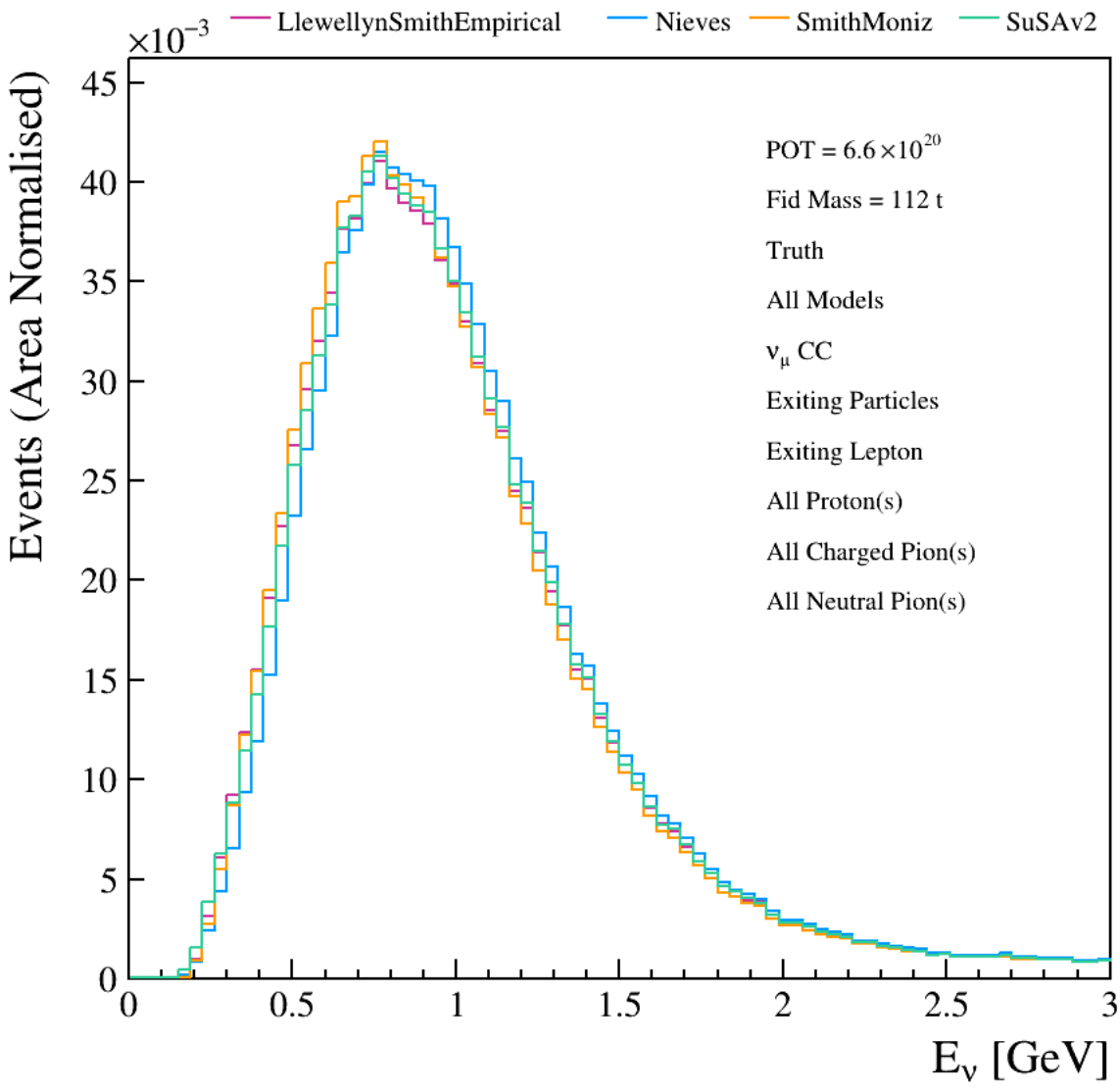

Figure A.3.: SBND E_{true}-dependent CC Inclusive event rate distributions for the 4 GENIE model configurations based on G18_10a_02_11a. The integrated event rates for all 4 model configurations are overlaid and normalised to their respective event rates such that shape differences can be determined.

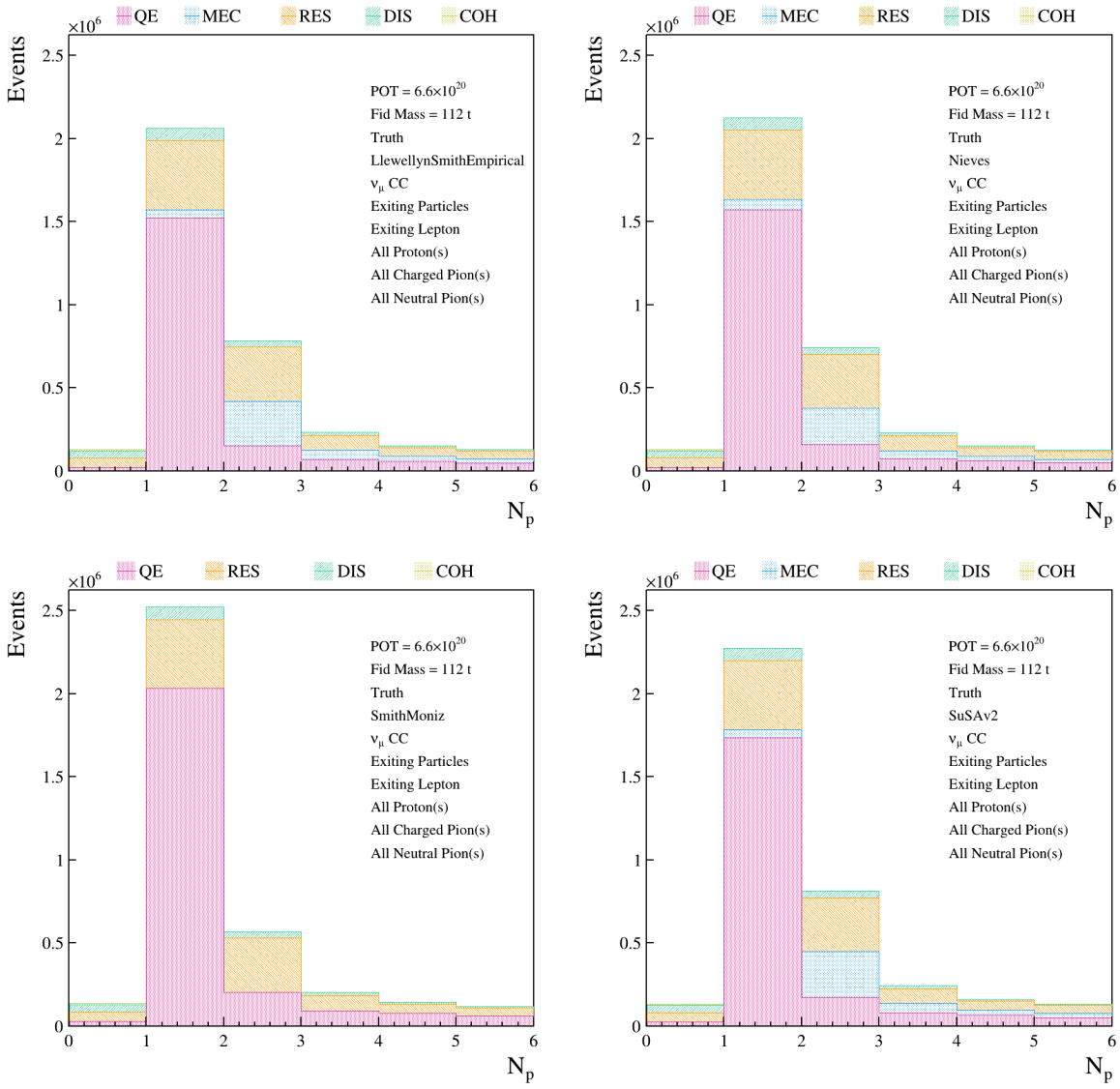

Figure A.4.: SBND N_p-dependent CC Inclusive event rate distributions for the 4 GENIE model configurations based on G18_10a_02_11a. From top-left to bottom-right are Llewellyn Smith-Empirical, Nieves, Smith-Moniz, SuSAv2. All distributions are stacked with a breakdown of the true interaction type which took place between a muon neutrino and the argon.

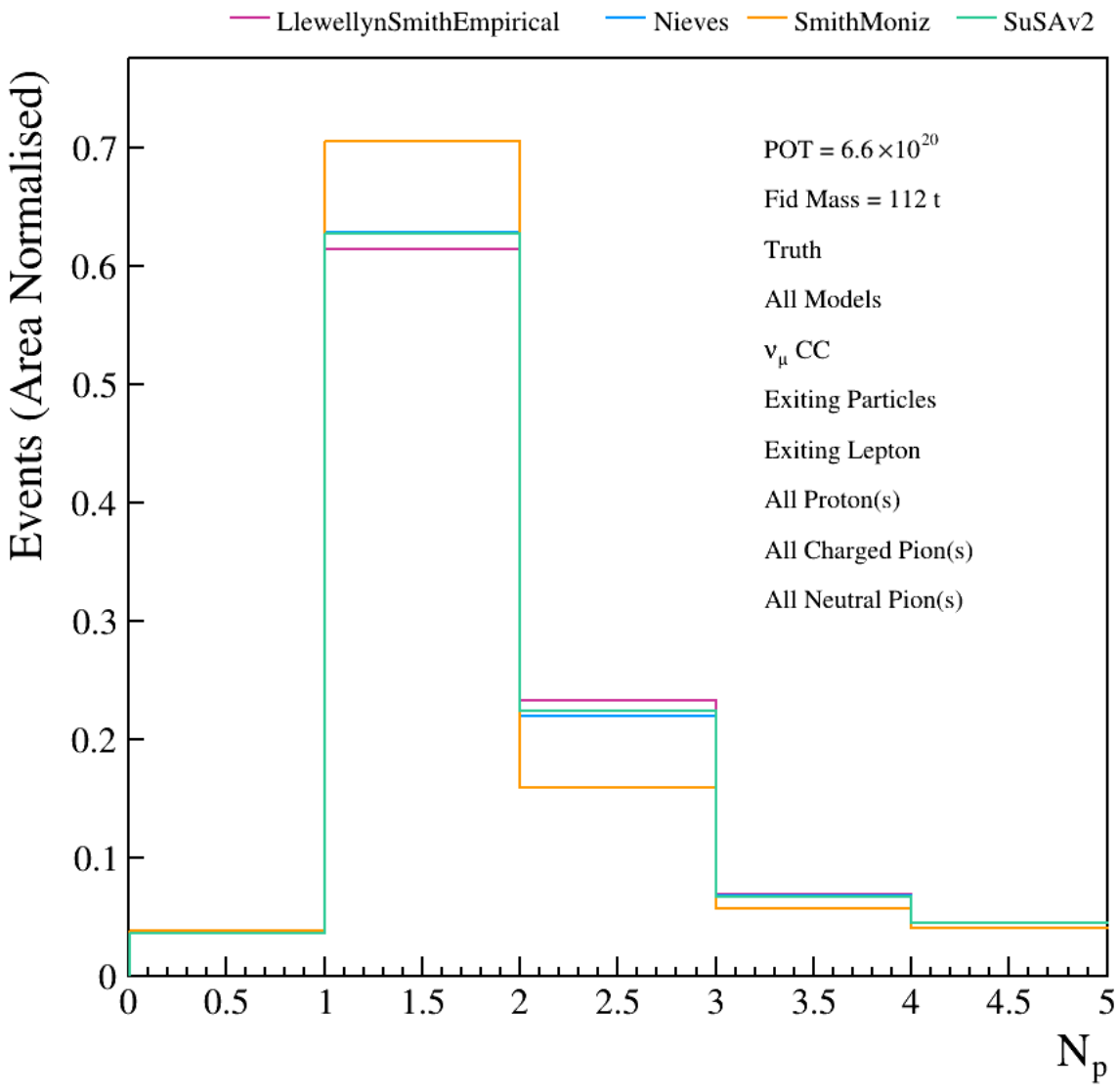

Figure A.5.: SBND N_p-dependent CC Inclusive event rate distributions for the 4 GENIE model configurations based on G18_10a_02_11a. The integrated event rates for all 4 model configurations are overlaid and normalised to their respective event rates such that shape differences can be determined.

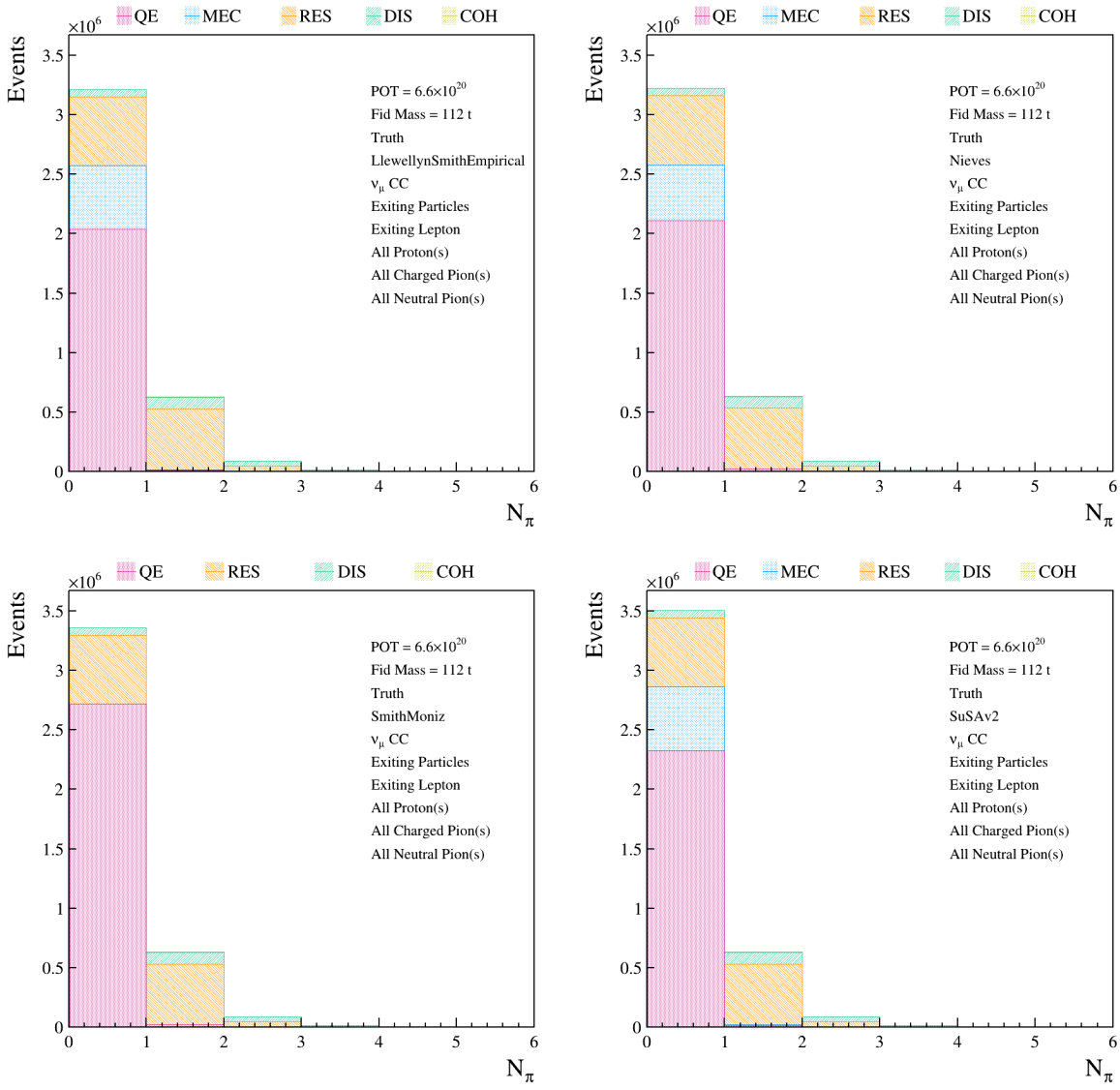

Figure A.6.: SBND $N_{\pi^\pm}$-dependent CC Inclusive event rate distributions for the 4 GENIE model configurations based on G18_10a_02_11a. From top-left to bottom-right are Llewellyn Smith-Empirical, Nieves, Smith-Moniz, SuSAv2. All distributions are stacked with a breakdown of the true interaction type which took place between a muon neutrino and the argon.

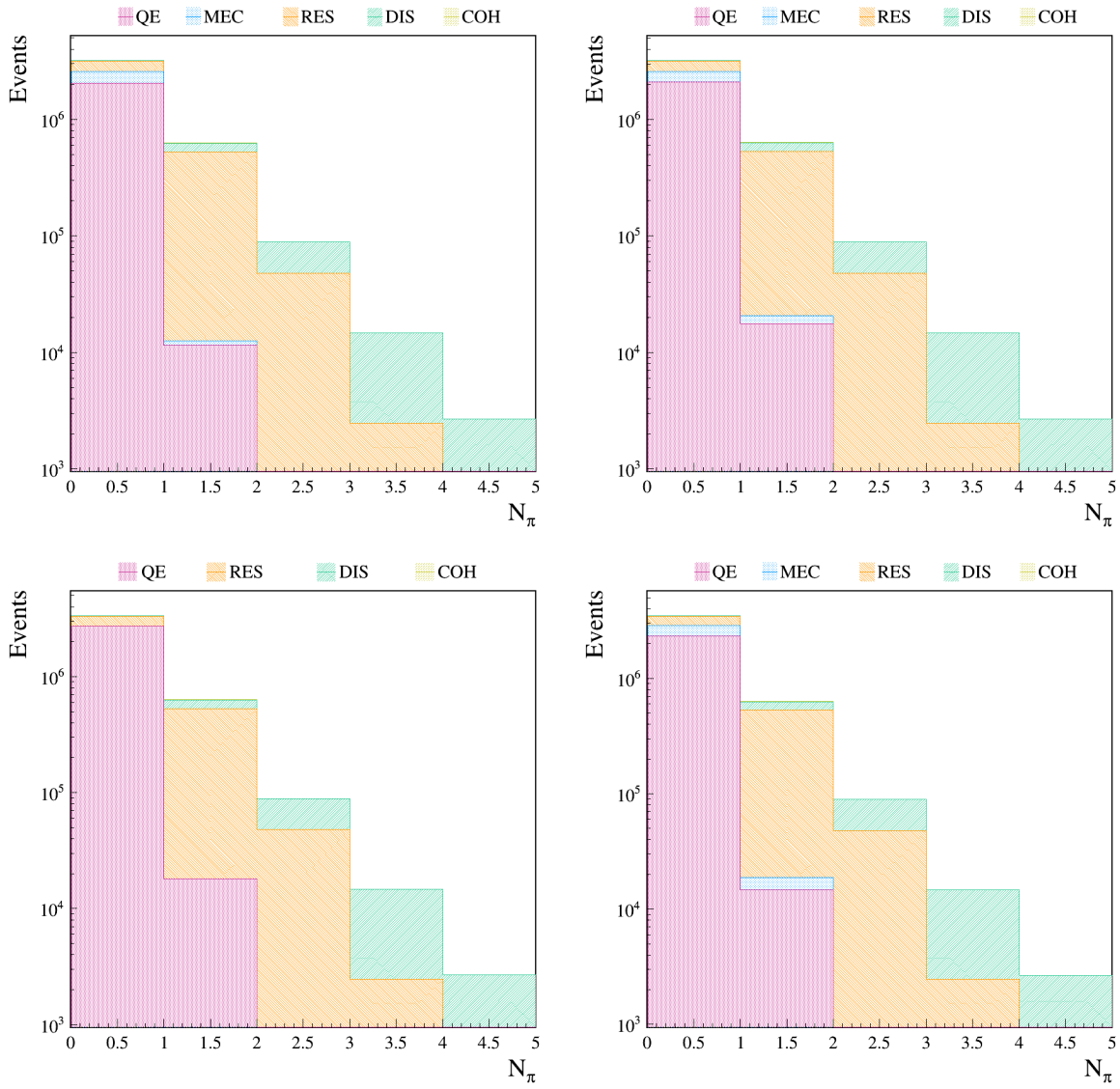

Figure A.7.: SBND $N_{\pi^\pm}$-dependent CC Inclusive event rate distributions for the 4 GENIE model configurations based on G18_10a_02_11a. From top-left to bottom-right are Llewellyn Smith-Empirical, Nieves, Smith-Moniz, SuSAv2. All distributions are stacked with a breakdown of the true interaction type which took place between a muon neutrino and the argon. The Y-axis has this time been set to a log scale

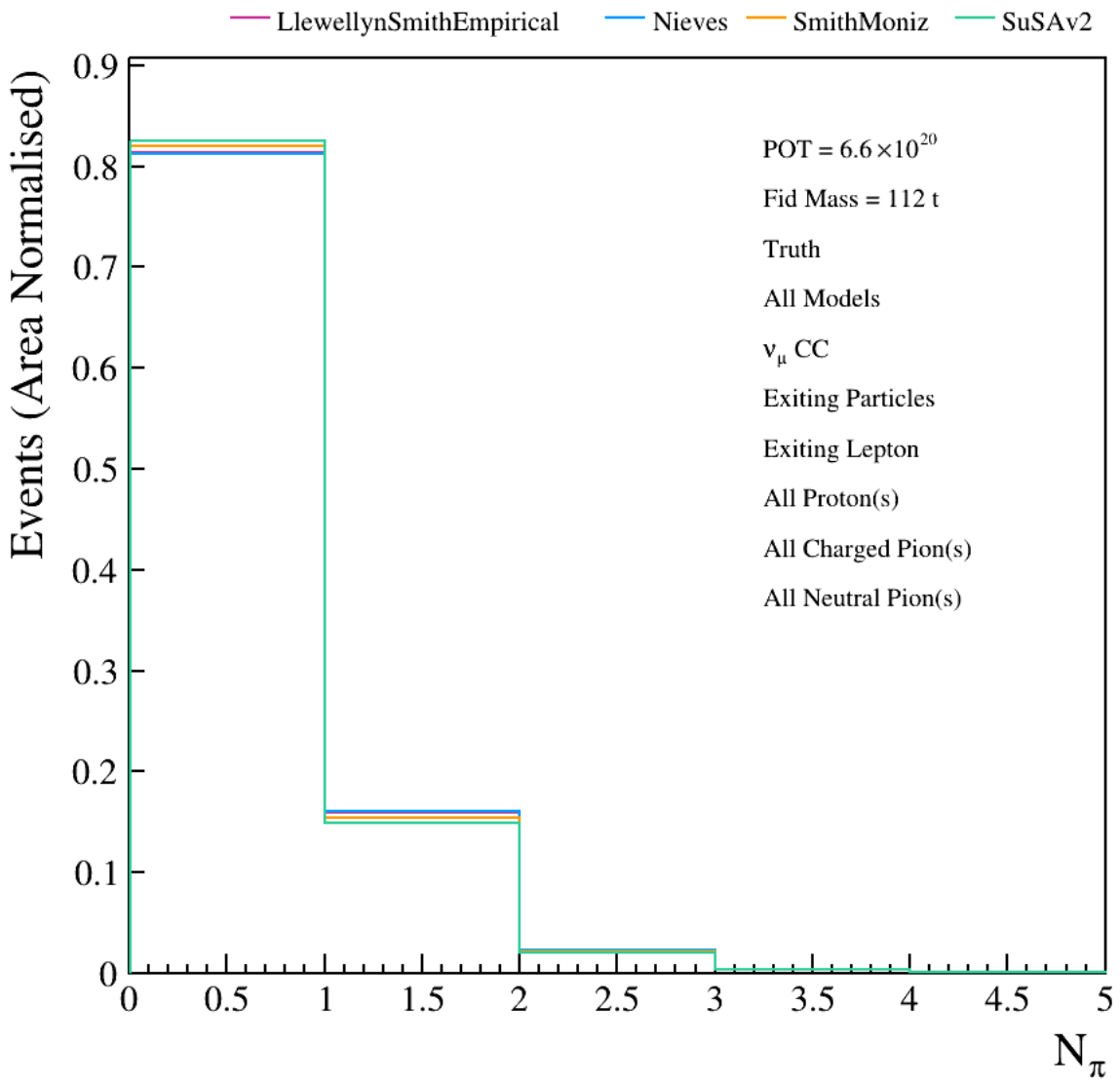

Figure A.8.: SBND $N_{\pi^\pm}$-dependent CC Inclusive event rate distributions for the 4 GENIE model configurations based on G18_10a_02_11a. The integrated event rates for all 4 model configurations are overlaid and normalised to their respective event rates such that shape differences can be determined.

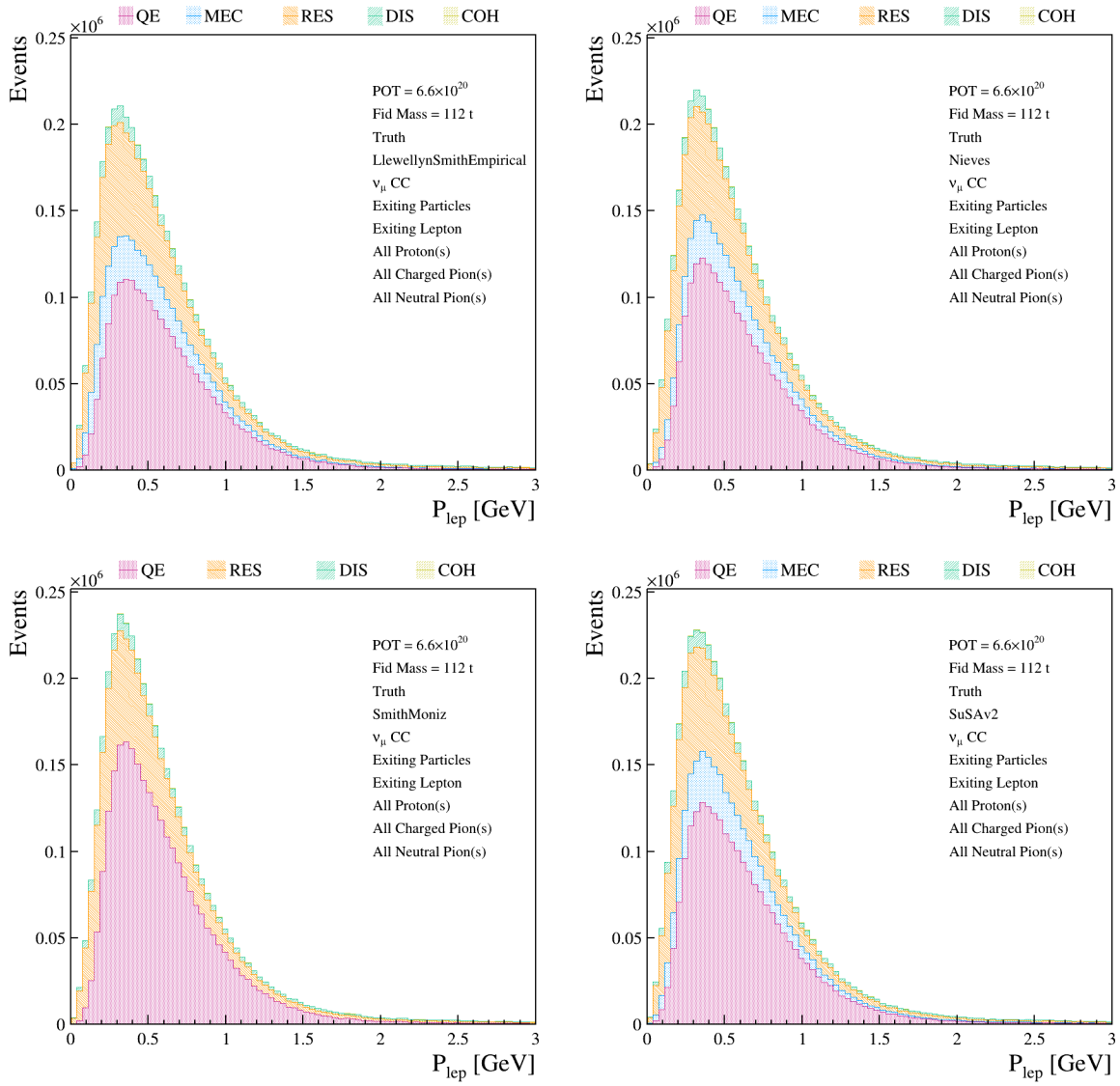

Figure A.9.: SBND p_μ-dependent CC Inclusive event rate distributions for the 4 GENIE model configurations based on G18_10a_02_11a. From top-left to bottom-right are Llewellyn Smith-Empirical, Nieves, Smith-Moniz, SuSAv2. All distributions are stacked with a breakdown of the true interaction type which took place between a muon neutrino and the argon.

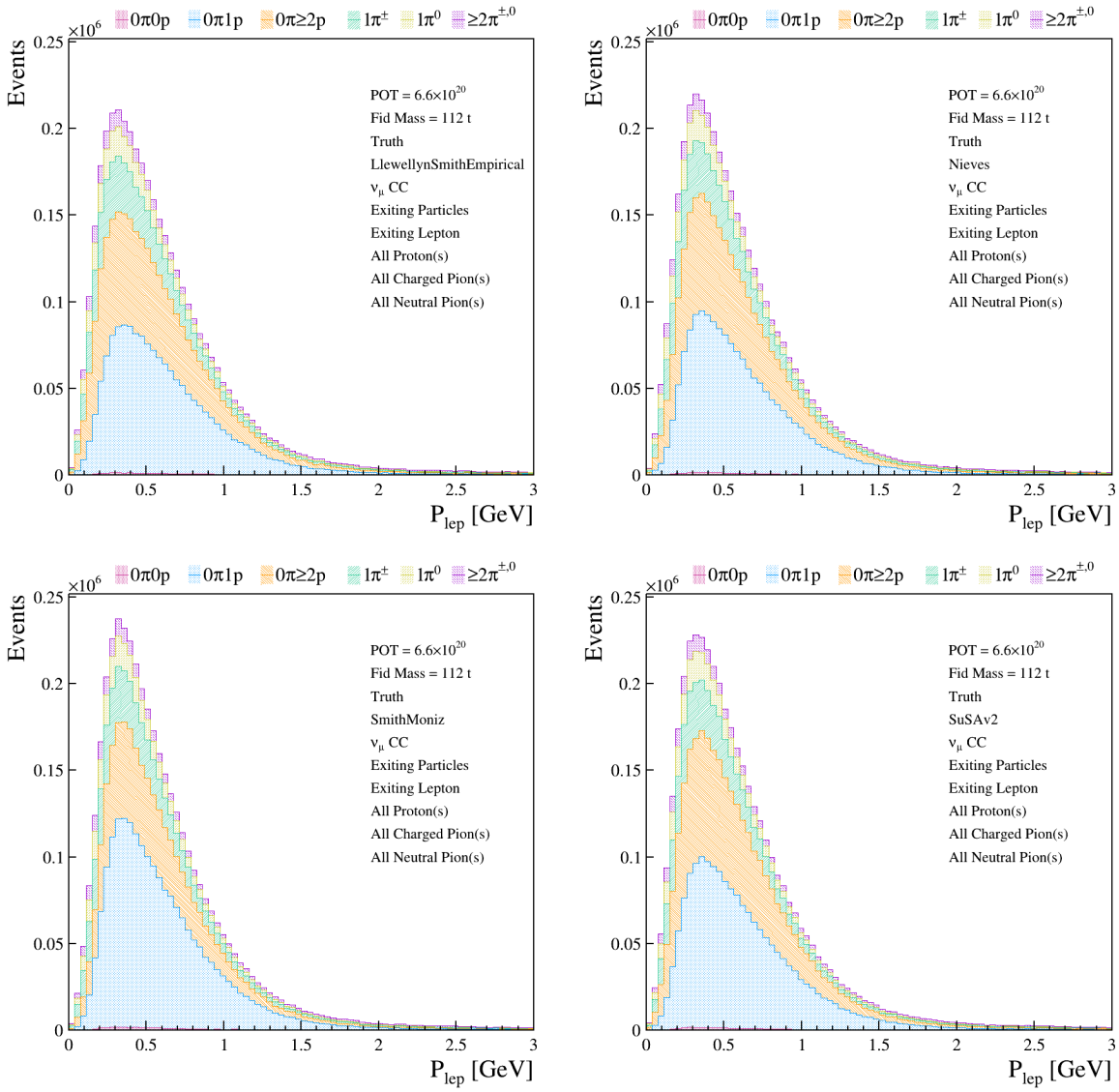

Figure A.10.: SBND p_μ-dependent CC Inclusive event rate distributions for the 4 GENIE model configurations based on G18_10a_02_11a. From top-left to bottom-right are Llewellyn Smith-Empirical, Nieves, Smith-Moniz, SuSAv2. All distributions are stacked with a breakdown of the true final state topology which emerged following the ν_μ-Ar interaction.

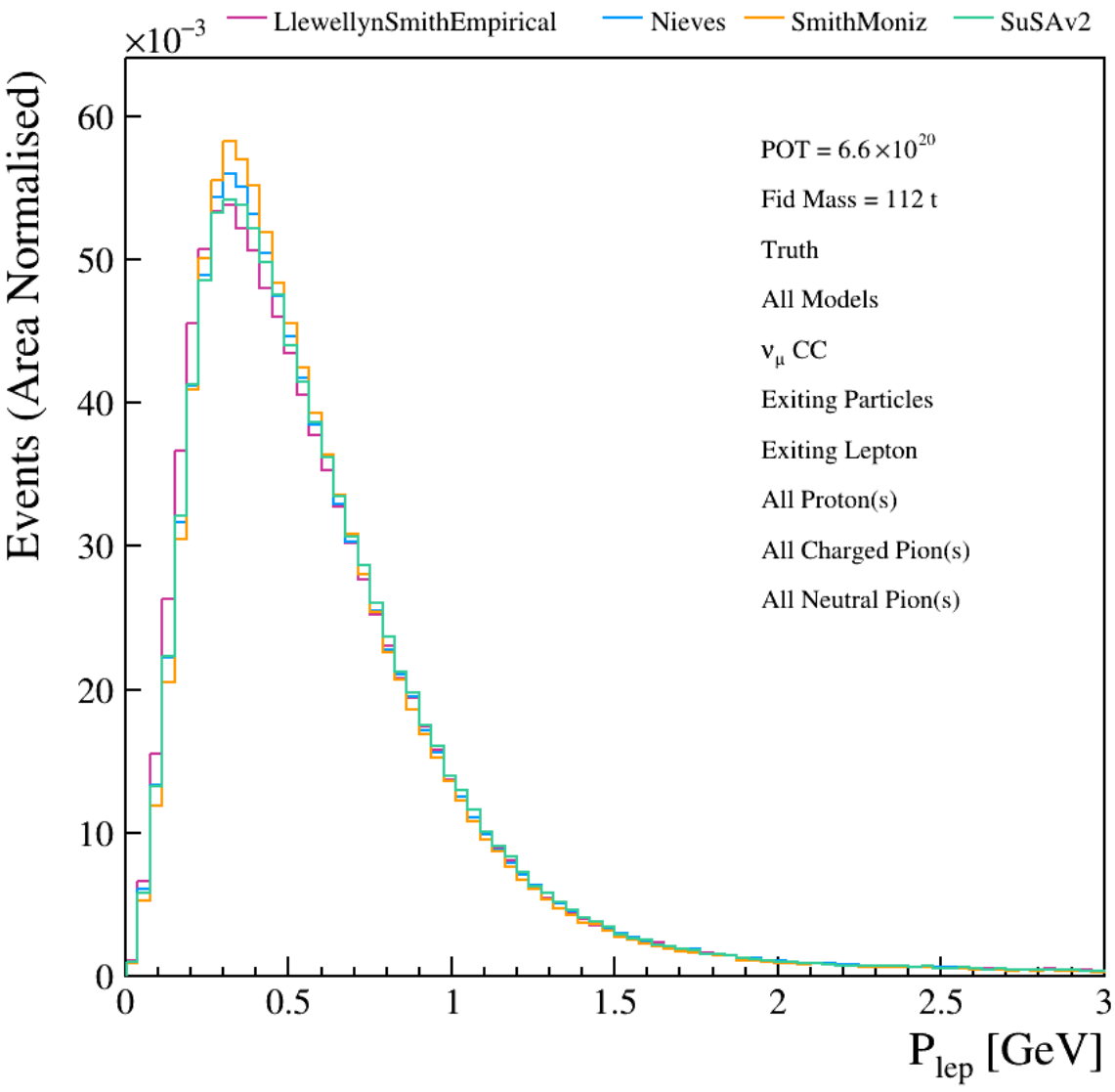

Figure A.11.: SBND p_μ-dependent CC Inclusive event rate distributions for the 4 GENIE model configurations based on G18_10a_02_11a. The integrated event rates for all 4 model configurations are overlaid and normalised to their respective event rates such that shape differences can be determined.

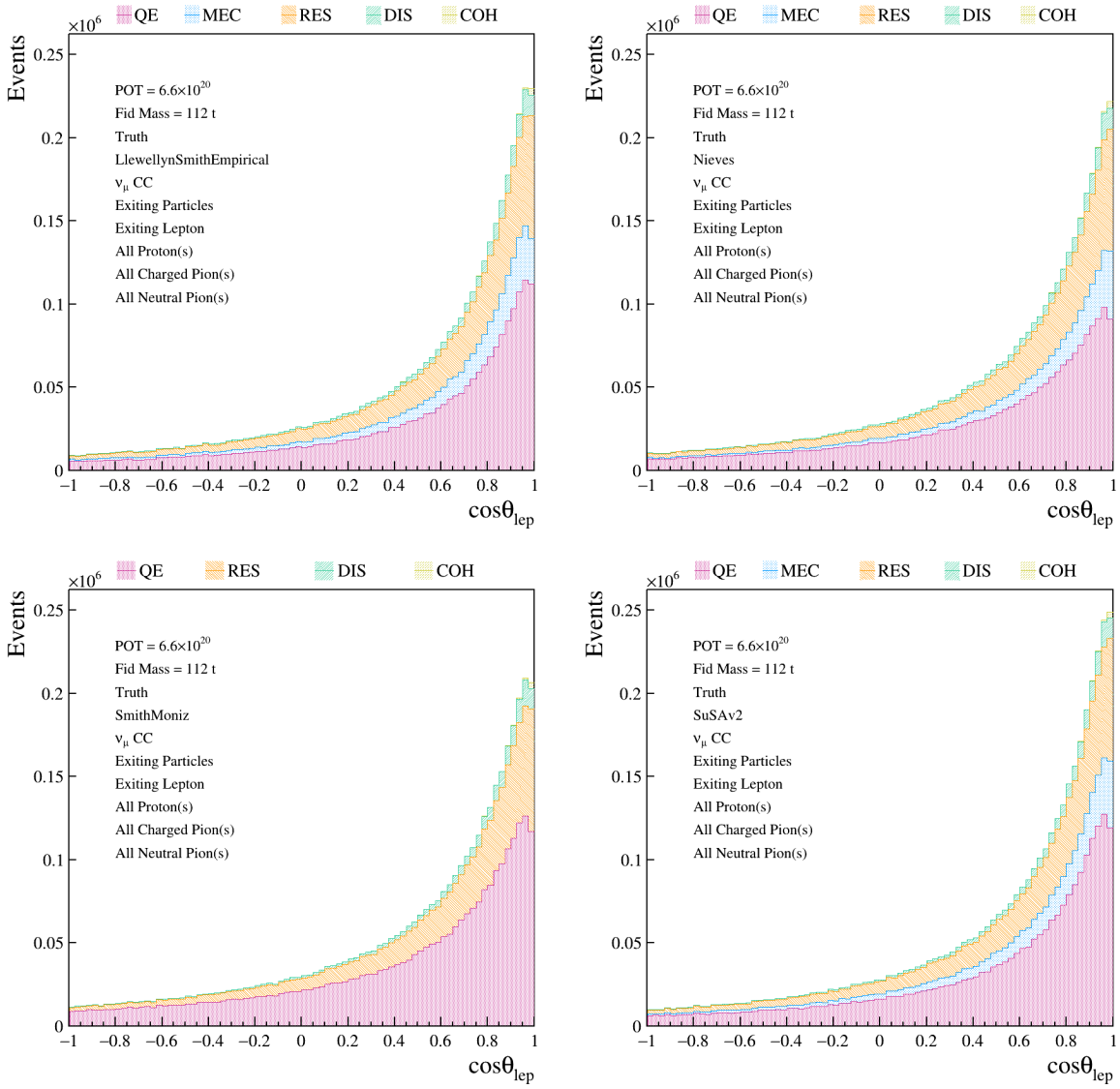

Figure A.12.: SBND $\cos\theta_\mu$-dependent CC Inclusive event rate distributions for the 4 GENIE model configurations based on G18_10a_02_11a. From top-left to bottom-right are Llewellyn Smith-Empirical, Nieves, Smith-Moniz, SuSAv2. All distributions are stacked with a breakdown of the true interaction type which took place between a muon neutrino and the argon.

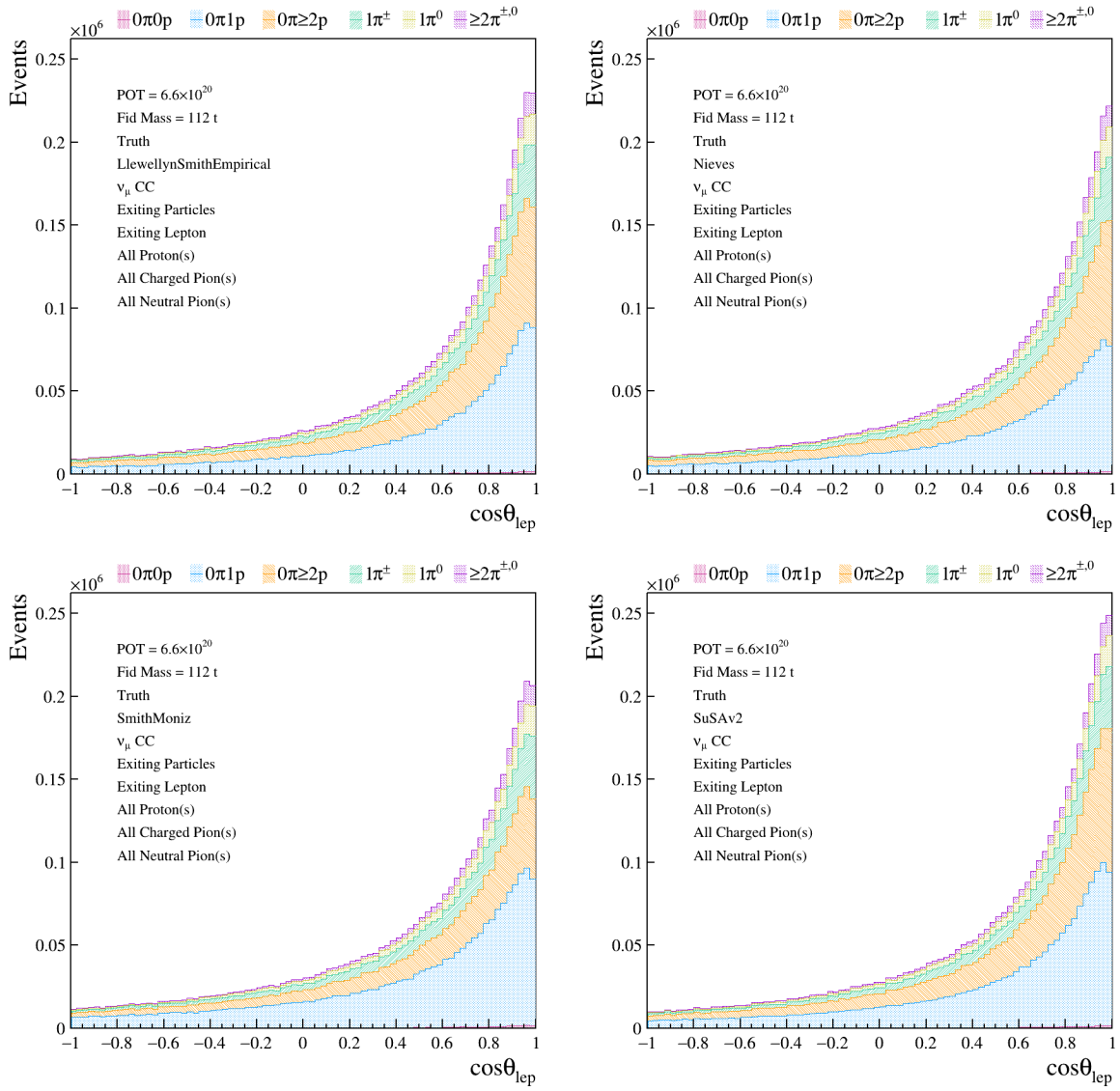

Figure A.13.: SBND $\cos\theta_\mu$-dependent CC Inclusive event rate distributions for the 4 GENIE model configurations based on G18_10a_02_11a. From top-left to bottom-right are Llewellyn Smith-Empirical, Nieves, Smith-Moniz, SuSAv2. All distributions are stacked with a breakdown of the true final state topology which emerged following the ν_μ-Ar interaction.

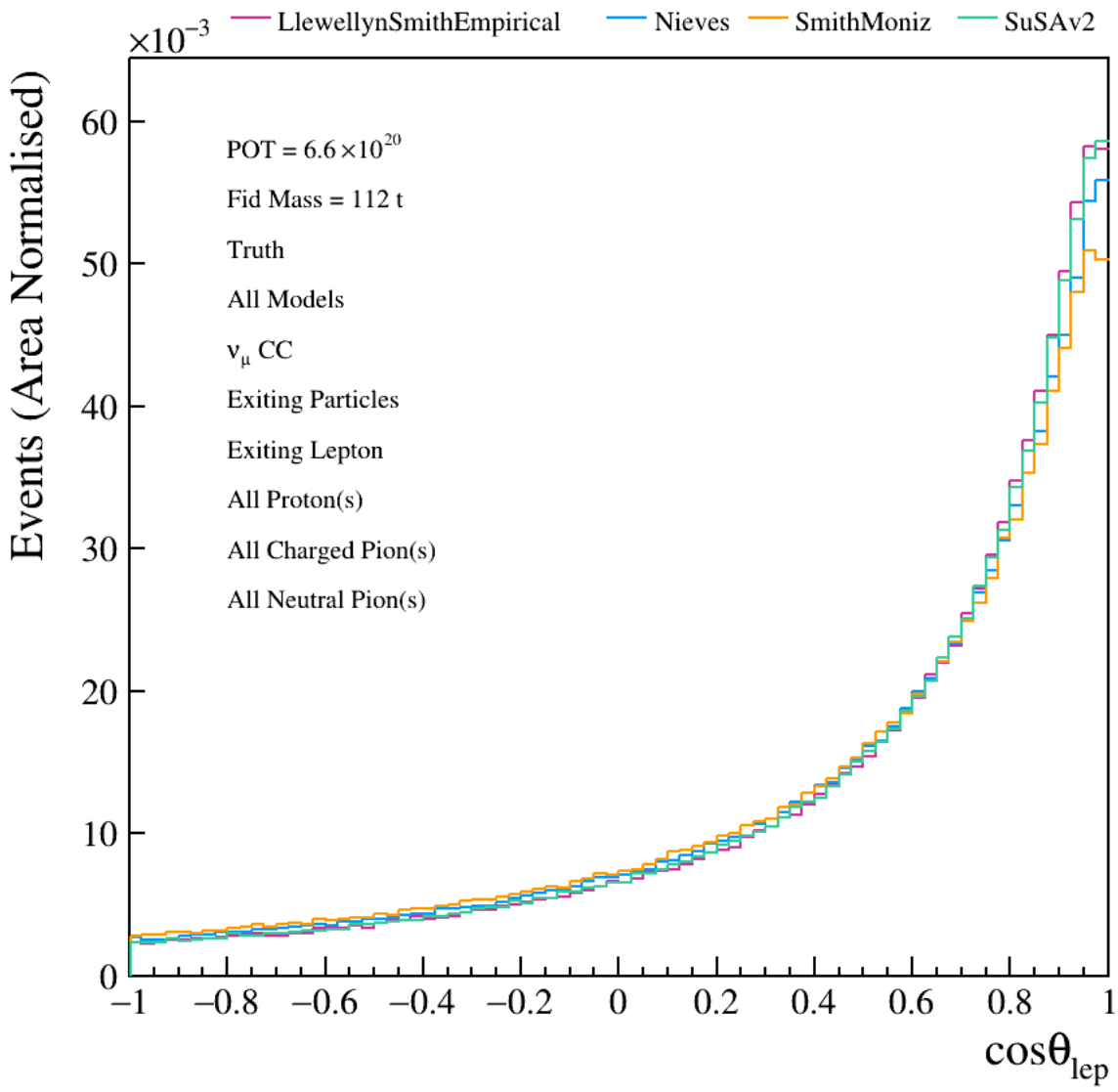

Figure A.14.: SBND $\cos\theta_\mu$-dependent CC Inclusive event rate distributions for the 4 GENIE model configurations based on G18_10a_02_11a. The integrated event rates for all 4 model configurations are overlaid and normalised to their respective event rates such that shape differences can be determined.

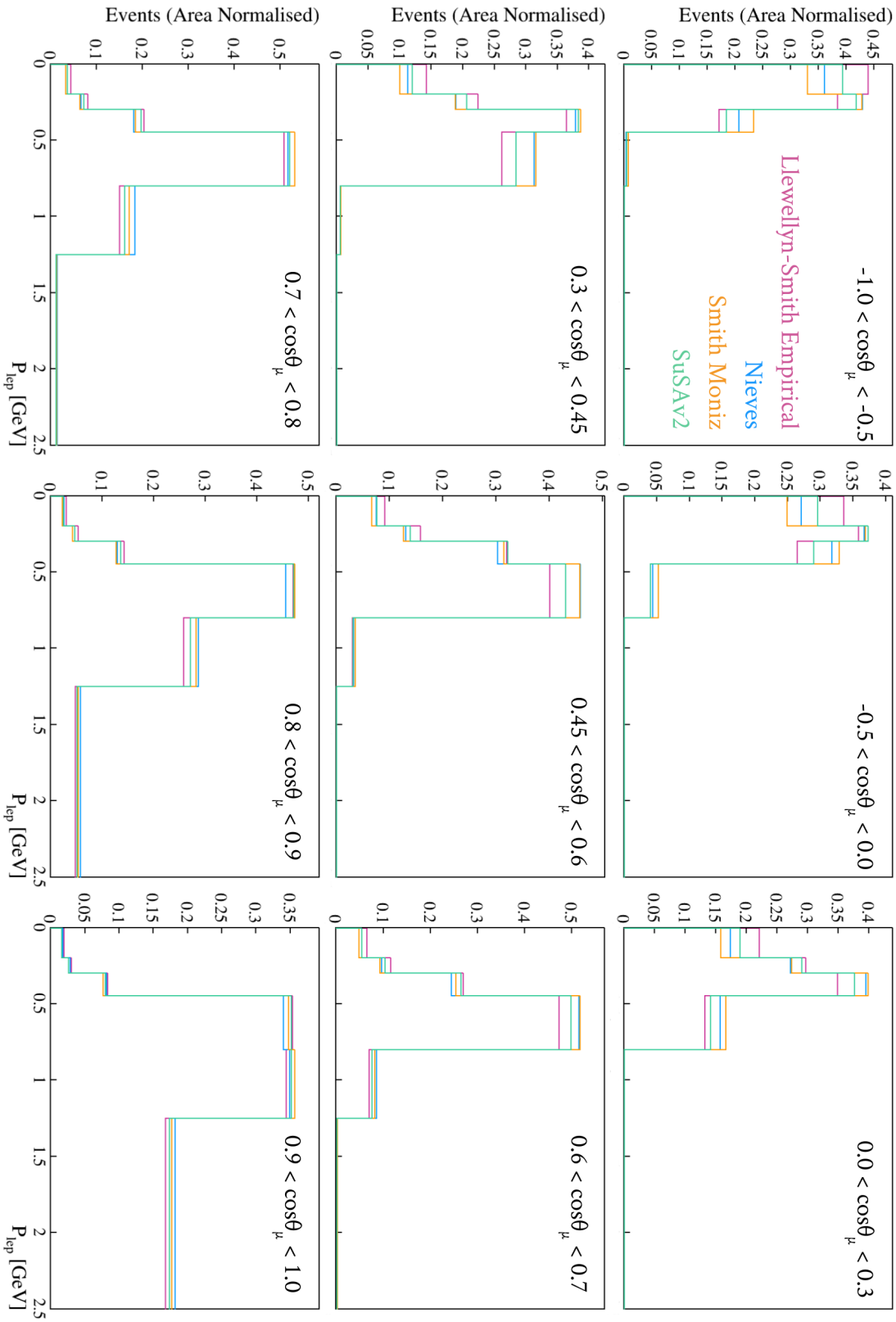

Figure A.15.: SBND $\cos\theta_\mu$ slices of the p_μ-dependent CC Inclusive event rate distributions for the 4 GENIE model configurations based on G18_10a_02_11a. The integrated event rates for all 4 model configurations are overlaid and normalised to their respective event rates such that shape differences can be determined.

Appendix B.

Systematics and validation

B.1. Flux systematic parametrisation and validation

Figure B.1 contains examples of the splines constructed for two flux unisim parameters, the Skin Effect and the total nucleon interaction cross-section in the Beryllium target and Aluminium horn. The examples show how the systematic variations change with energy and reaction mode. As is the case for all flux parameters, they behave independently of which neutrino interaction took place, therefore all differences observed in the single-parameter response functions are due to the variations in the energy bins presented.

In order to validate whether each parameter is well-defined by the splines, comparisons are made between the total MC event rates following $n\sigma$ variations from the input files and the rates following variations applied using the splines. This is done for every parameter in all of the 7 knots, k, defined above. Figure B.2 shows that for the same two example flux unisim parameters, any disagreement between the spline-based and input 1σ variations is negligible.

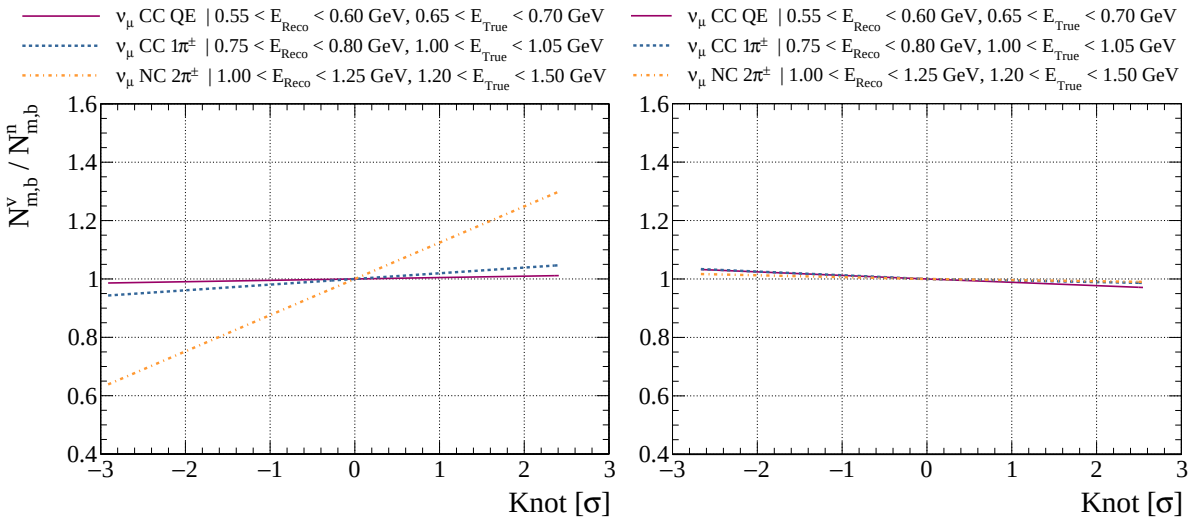

Figure B.1.: Flux response functions. The ratio of the event rate when each parameter is varied by $n\sigma$ to the nominal rate with no variations. On the left is the Skin Effect parameter and on the right is the total nucleon cross-section flux parameter. The variations are shown for events in 3 reaction modes, ν_μ CC QE, ν_μ CC $1\pi^\pm$ & ν_μ NC $2\pi^\pm$ and simultaneously in 3 2D energy bins.

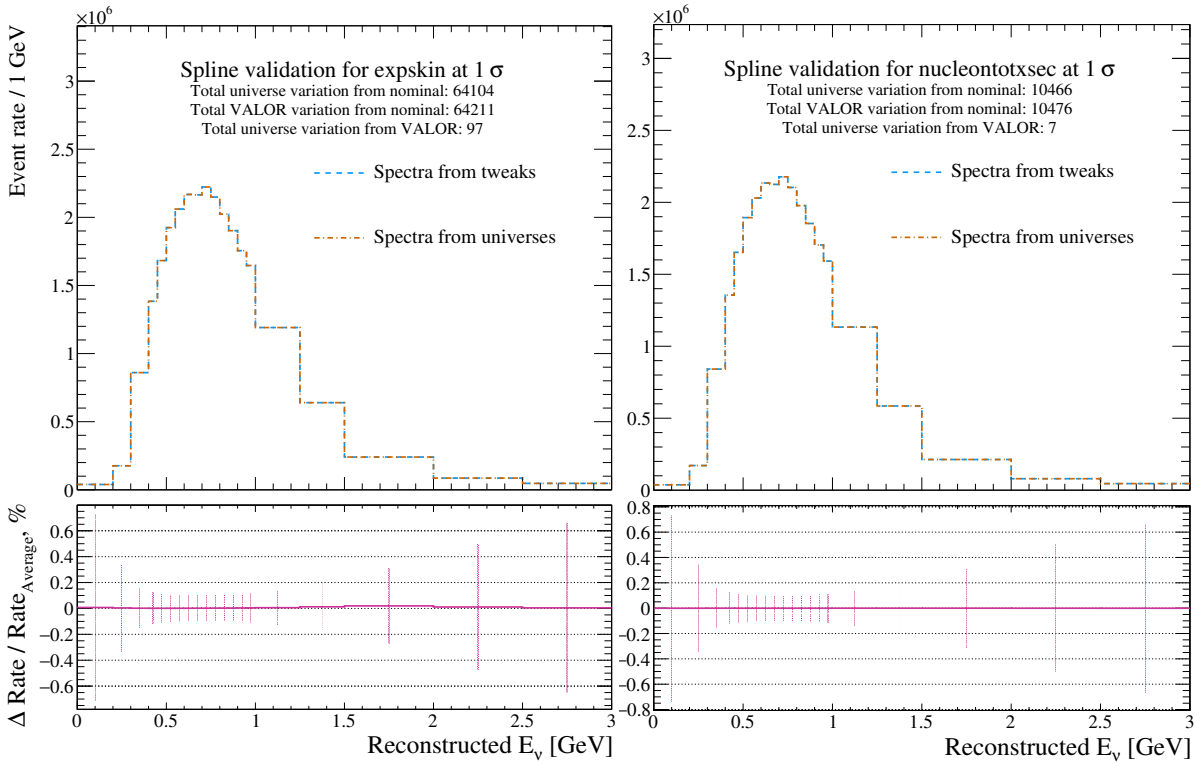

Figure B.2.: Comparing the 1σ variations of the integrated CC Inclusive event rate between the input 'universe' variations and the spline-based 'tweaks'. On the left is the Skin Effect parameter, and on the right is the total nucleon cross-section flux parameter.

B.2. Interaction systematic parametrisation and validation

Examples of the interaction response functions are shown in Figure B.3 for the cross-section parameters which were used at the time of the SBN propsal oscillation analysis. As expected, the CC QE parameter only impacts CC QE events, and the NC 2π parameter similarly only affects those involving those with NC 2π initial state interaction products.

Figure B.5 gives examples of modern parameter splines, including both cross-section and FSI parameters. The CC Res_V parameter naturally only impacts charged-current reactions modes which produces a pion, whereas the FSI parameter affects all reaction modes and the impact may vary based on both initial interaction and energy bin.

Given the similarities in the parameter construction with that of the flux unisim parameters, the same validation method was also utilised for the two interaction parameter subsets. The 1σ variations from the input universes and the response-function application are shown for the same two proposal-era parameters in Figure B.4 for which the splines were shown previously. This is repeated for the modern-era parameters and the analogous validation is shown in Figure B.6.

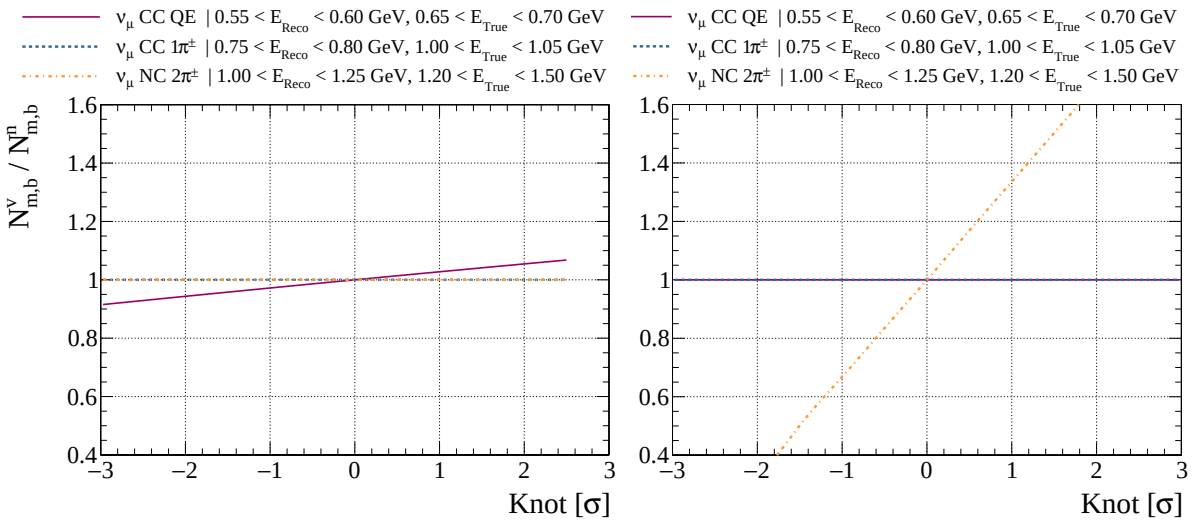

Figure B.3.: Cross-section response functions from the SBN proposal era. The ratio of the event rate when each parameter is varied by $n\sigma$ to the nominal rate with no variations. On the left is the CC QE M_A parameter and on the right is the Non-Resonant νp NC 2π background normalisation parameter. The variations are shown for events in 3 reaction modes, ν_μ CC QE, ν_μ CC $1\pi^\pm$ & ν_μ NC $2\pi^\pm$ and simultaneously in 3 2D energy bins.

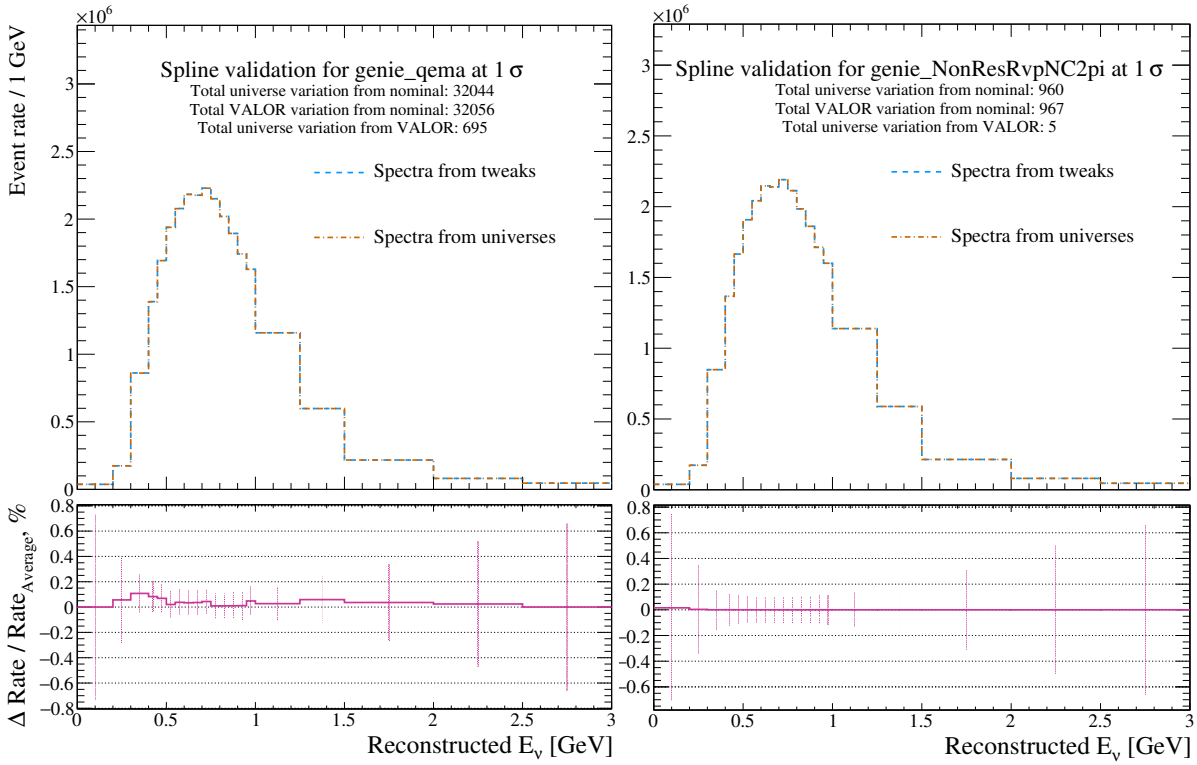

Figure B.4.: Comparing the 1σ variations of the integrated CC Inclusive event rate between the input 'universe' variations and the spline-based 'tweaks'. On the left is the CC QE M_A parameter, and on the right is the Non-Resonant νp NC 2π background normalisation parameter. Both are interaction cross-section parameters used at the time of the SBN proposal-era of the analysis.

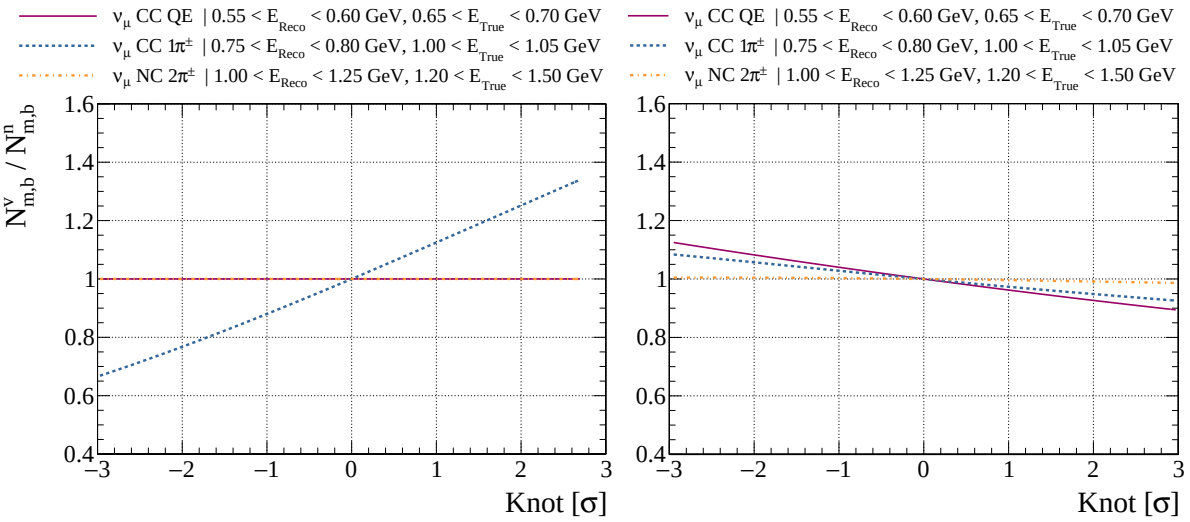

Figure B.5.: The ratio of the event rate when each parameter is varied by $n\sigma$ to the nominal rate with no variations. On the left is the CC Res$_V$ (interaction cross-section) parameter and on the right is the IntraNukeNmfp (FSI) parameter. The variations are shown for events in 3 reaction modes, ν_μ CC QE, ν_μ CC $1\pi^\pm$ & ν_μ NC $2\pi^\pm$ and simultaneously in 3 2D energy bins.

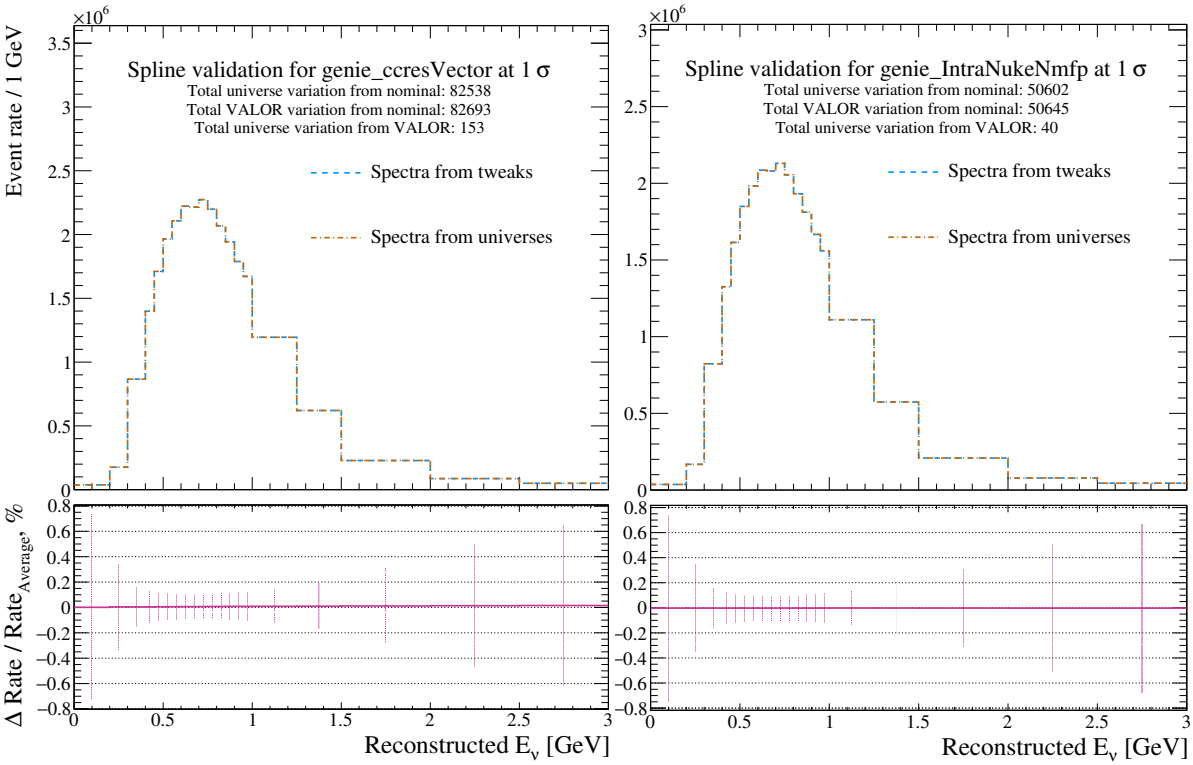

Figure B.6.: Comparing the 1σ variations of the integrated CC Inclusive event rate between the input 'universe' variations and the spline-based 'tweaks'. On the left is the CC Res$_V$ (interaction cross-section) parameter, and on the right is the IntraNukeNmfp (FSI) parameter. Both are taken from the modern interaction parameters.

B.3. Detector systematic parametrisation and validation

Figure B.7 shows the comparison between true (universe) 1σ variations and those taken from applying tweaks of the response functions to the nominal spectra. In this case, the variations are assessed when applied to the relevant exclusive sample definitions, as these systematic parameters do not affect the inclusive sample as a whole.

Note, there is a requirement that all splines must be constructed in bins with greater than 4 reconstructed events. This occurs more often in the lowest-energy bin of the CC Other sample than in the CC Inclusive and CC 0π samples such that the agreement between the true and parametrised systematics appears to be slightly worse. The integrated difference in the variations does not exceed 1% of the true 1σ variation in either sample.

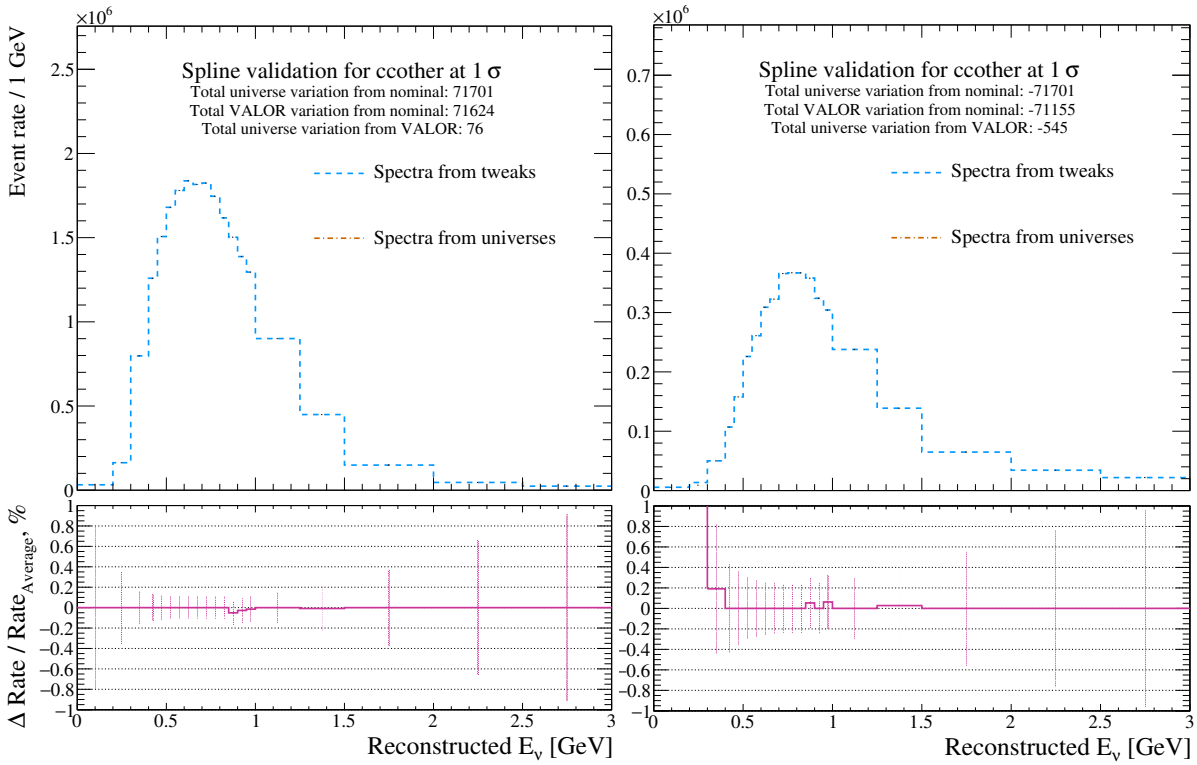

Figure B.7.: Comparing the 1σ variations each of the semi-exclusive samples involved in the SBN oscillation analysis, ν_μ CC 0π (left) and ν_μ CC Other (right) between the input 'universe' variations and the spline-based 'tweaks'. The migrations are anti-correlated, such that a 1σ increase in one would result in a 1σ decrease in the other.

Appendix C.

Mock Data Analysis

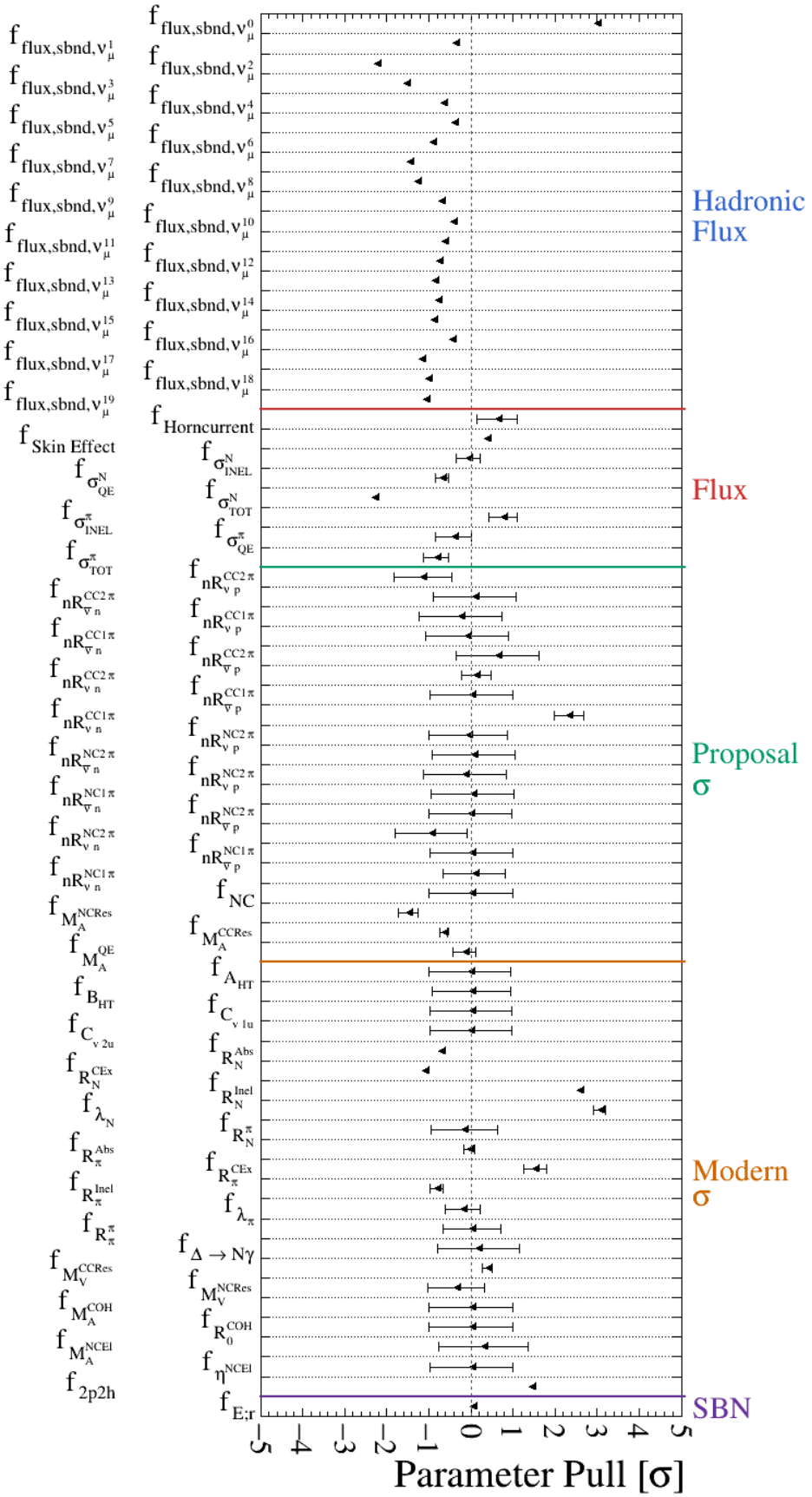

Figure C.1.: The parameter pulls and corresponding uncertainties assigned when fitting the inclusive MC sample to the inclusive GENIE v2, Default+MEC mock dataset with additional, analysis-driven systematic parameters.

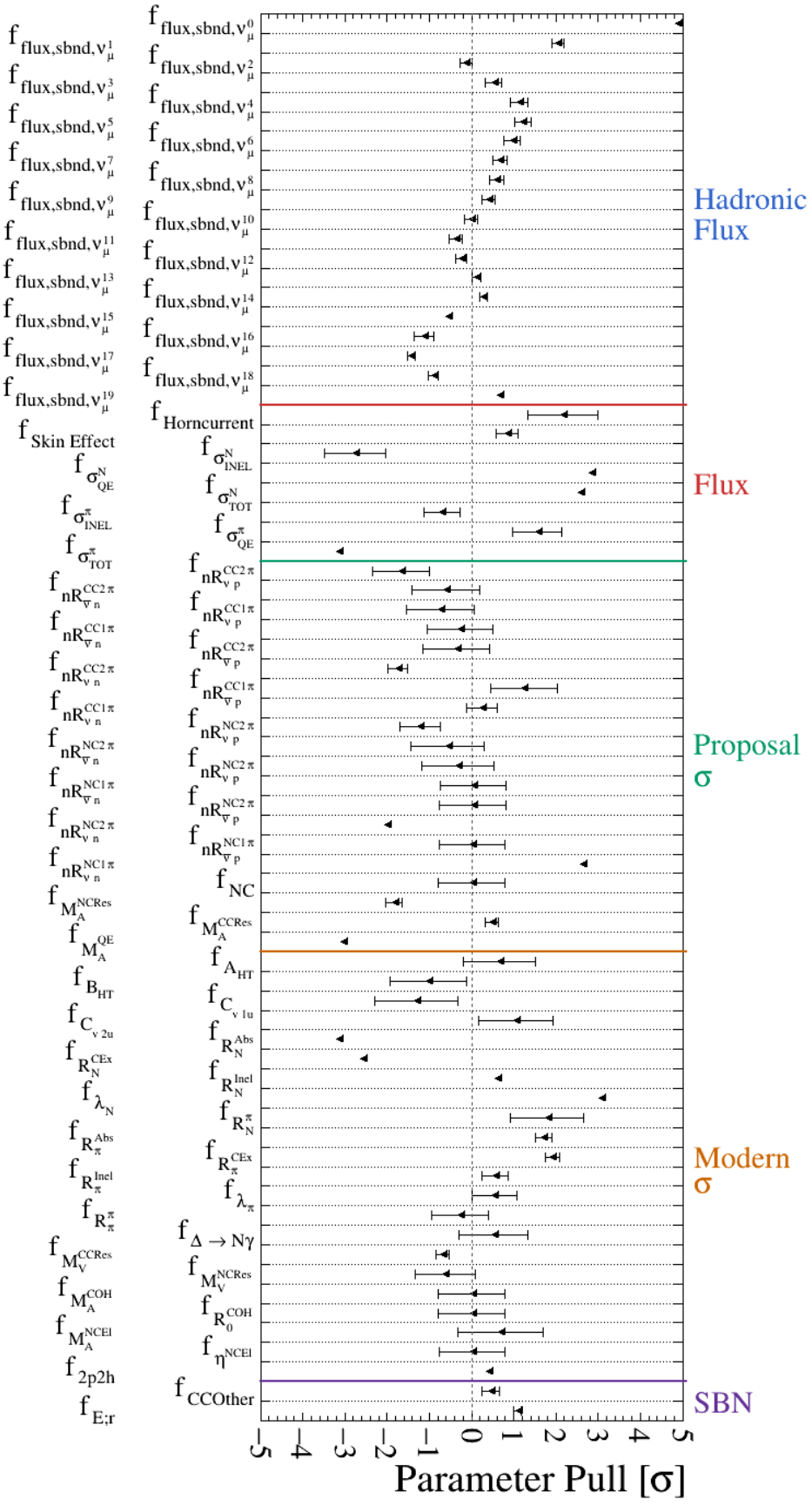

Figure C.2.: The parameter pulls and corresponding uncertainties assigned when fitting the exclusive MC sample to the exclusive GENIE v2, Default+MEC mock dataset with additional, analysis-driven systematic parameters.

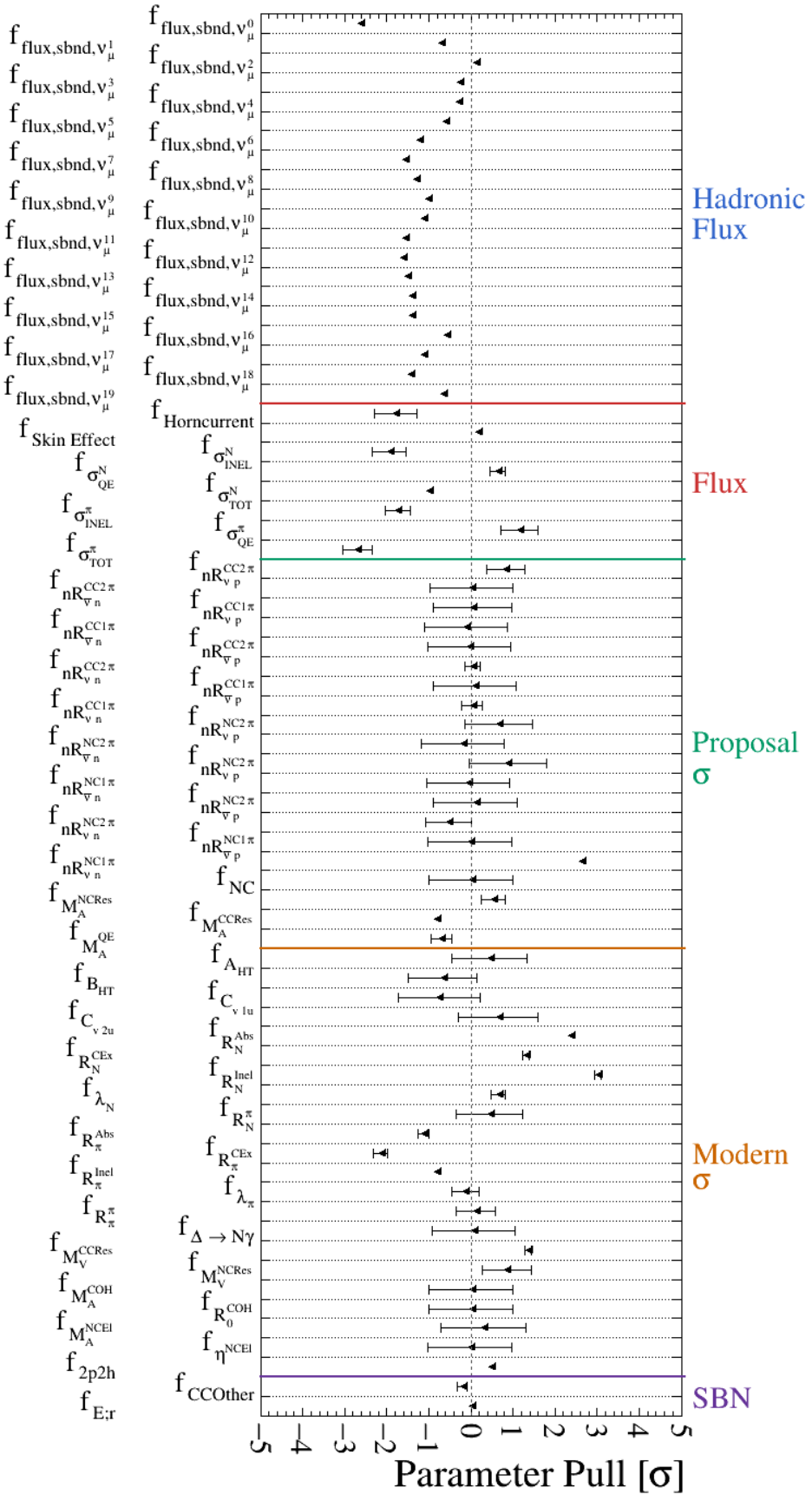

Figure C.3.: The parameter pulls and corresponding uncertainties assigned when fitting the exclusive MC sample to the exclusive GENIE v3, SuSAv2 mock dataset.

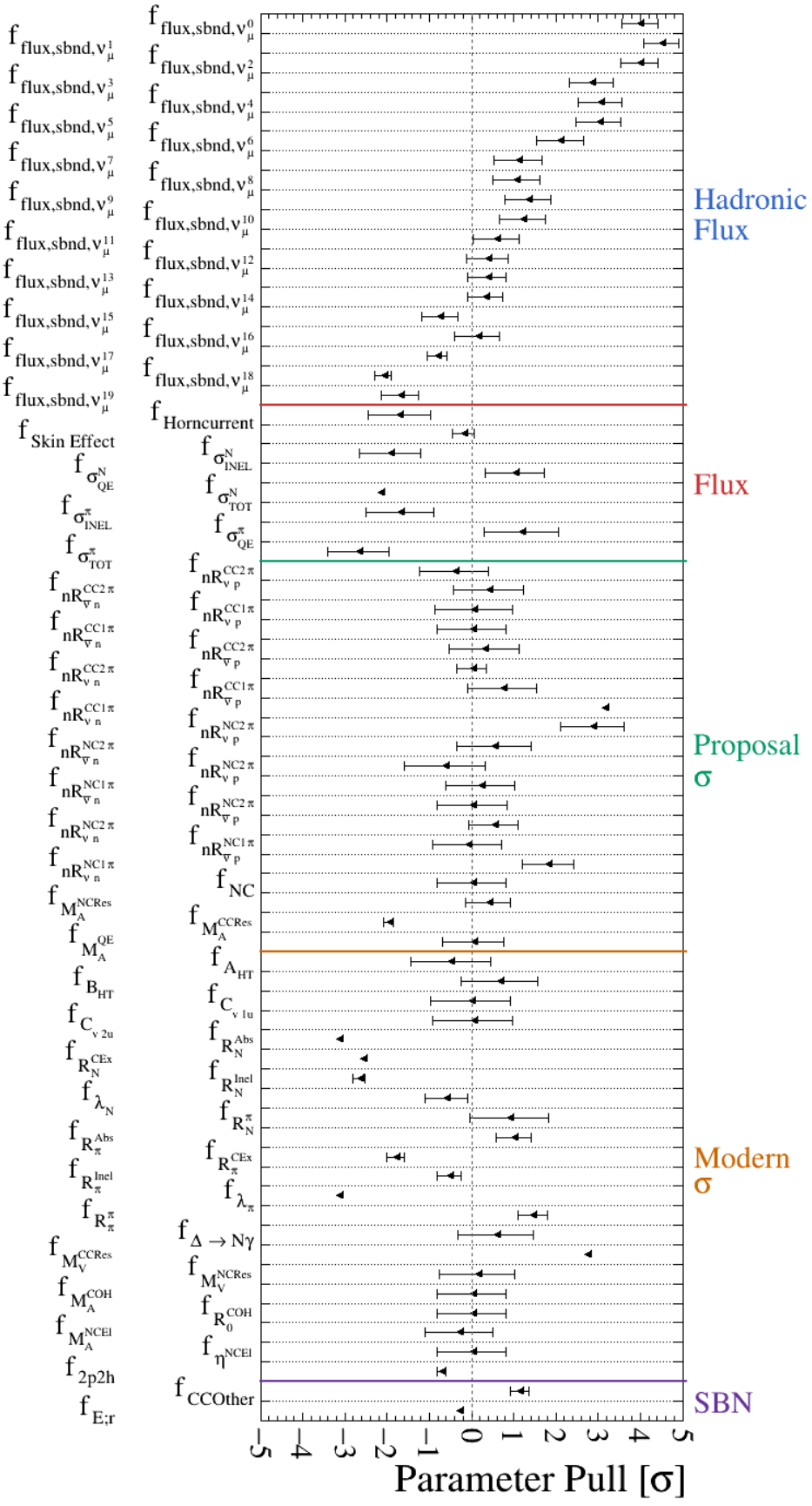

Figure C.4.: The parameter pulls and corresponding uncertainties assigned when fitting the exclusive MC sample to the exclusive GENIE v3, Smith-Moniz mock dataset.

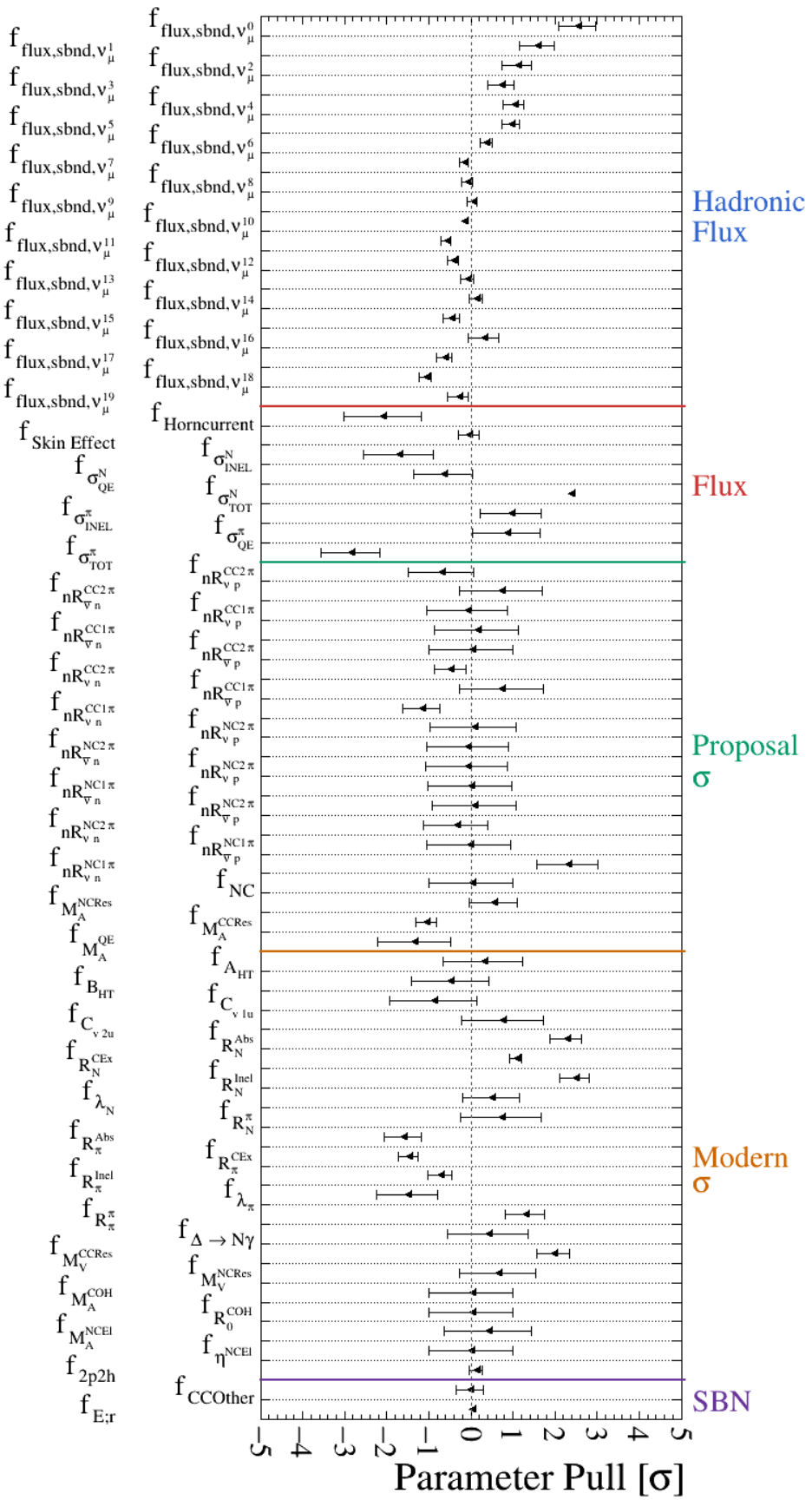

Figure C.5.: The parameter pulls and corresponding uncertainties assigned when fitting the exclusive MC sample to the exclusive GENIE v3, Llewellyn Smith-Empirical mock dataset.

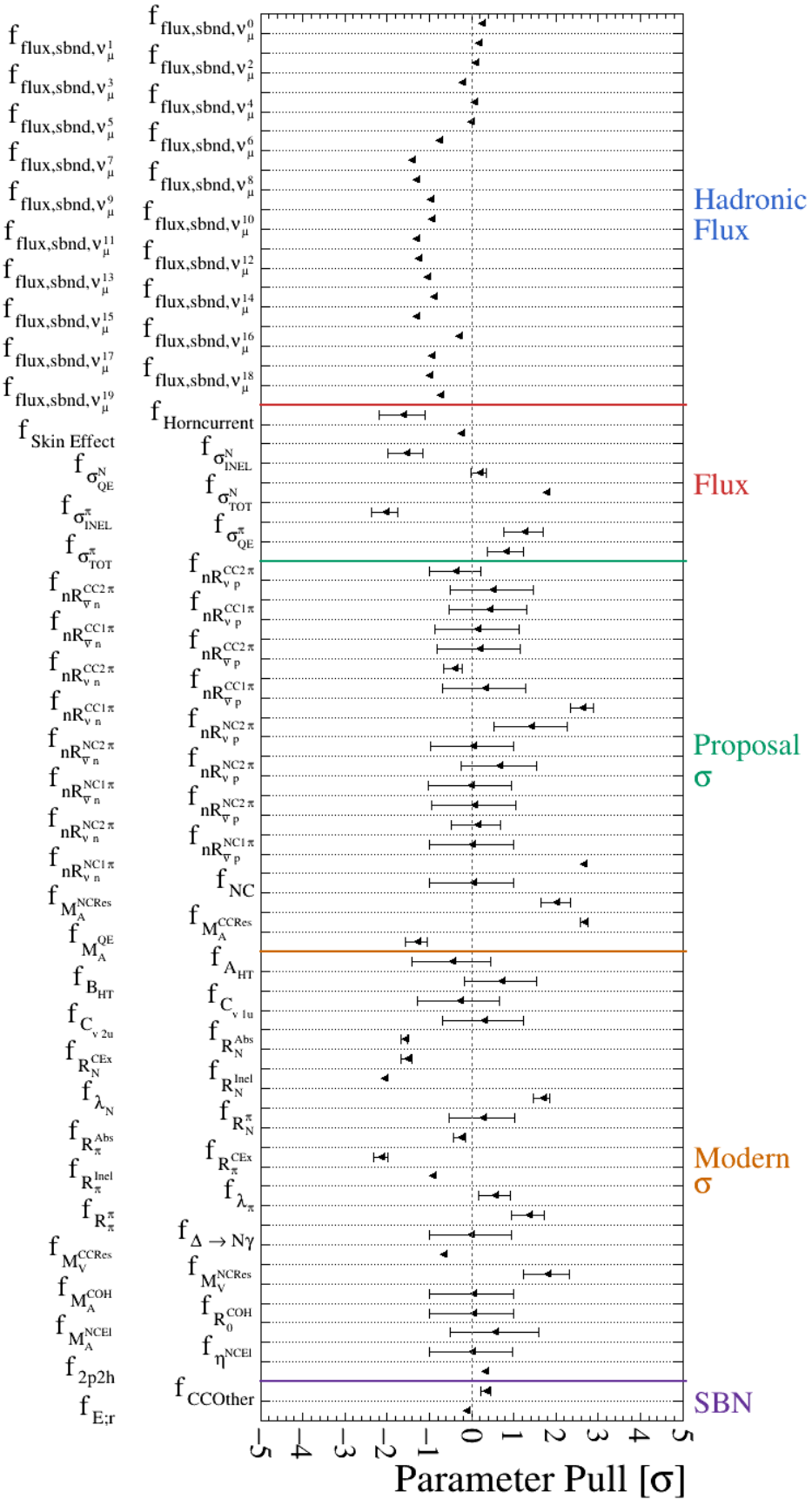

Figure C.6.: The parameter pulls and corresponding uncertainties assigned when fitting the exclusive MC sample to the exclusive GENIE v3, G18_10a_02_11a +50% BE mock dataset.

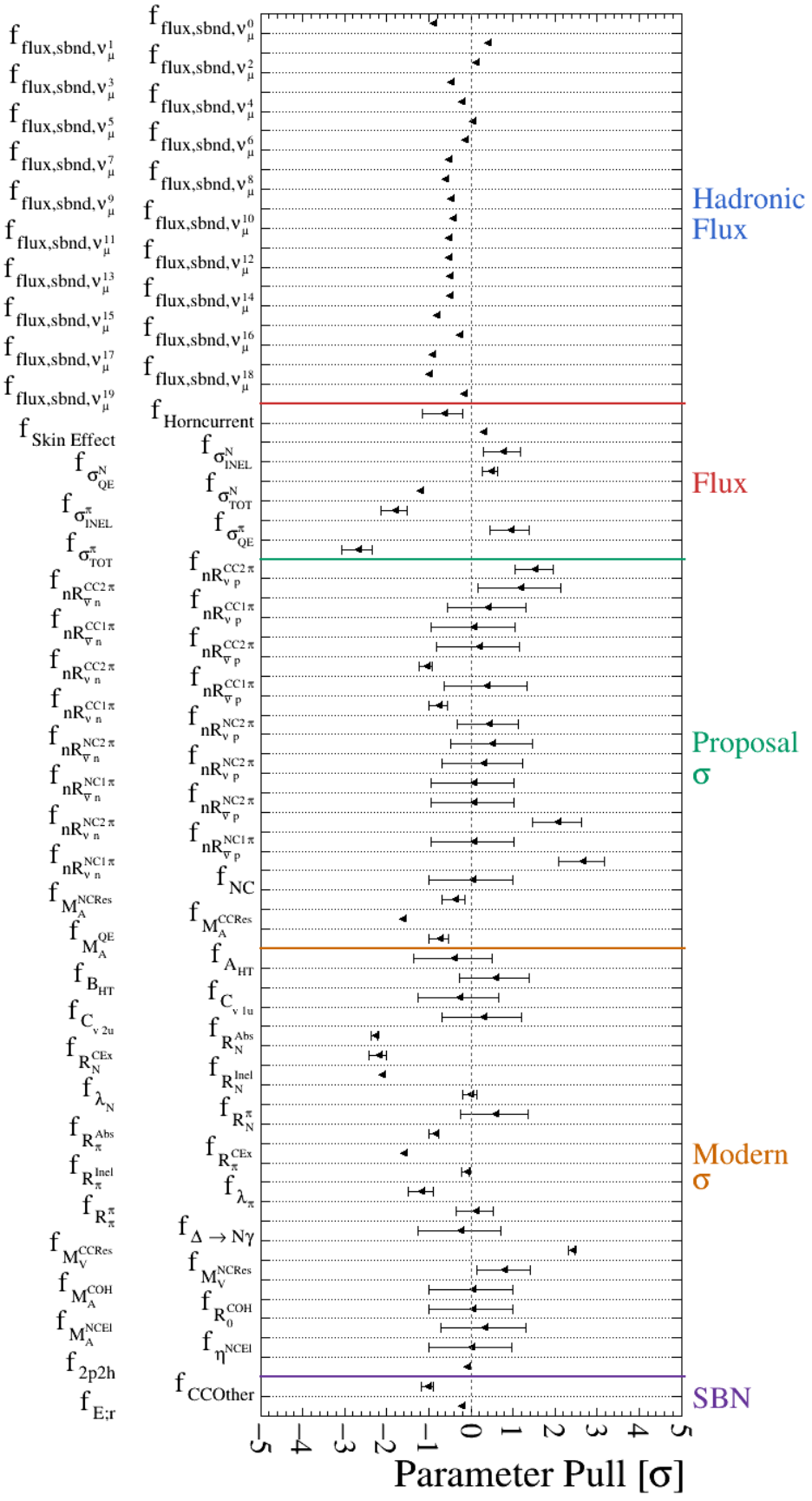

Figure C.7.: The parameter pulls and corresponding uncertainties assigned when fitting the exclusive MC sample to the exclusive GENIE v3, G18_10a_02_11a -50% BE mock dataset.

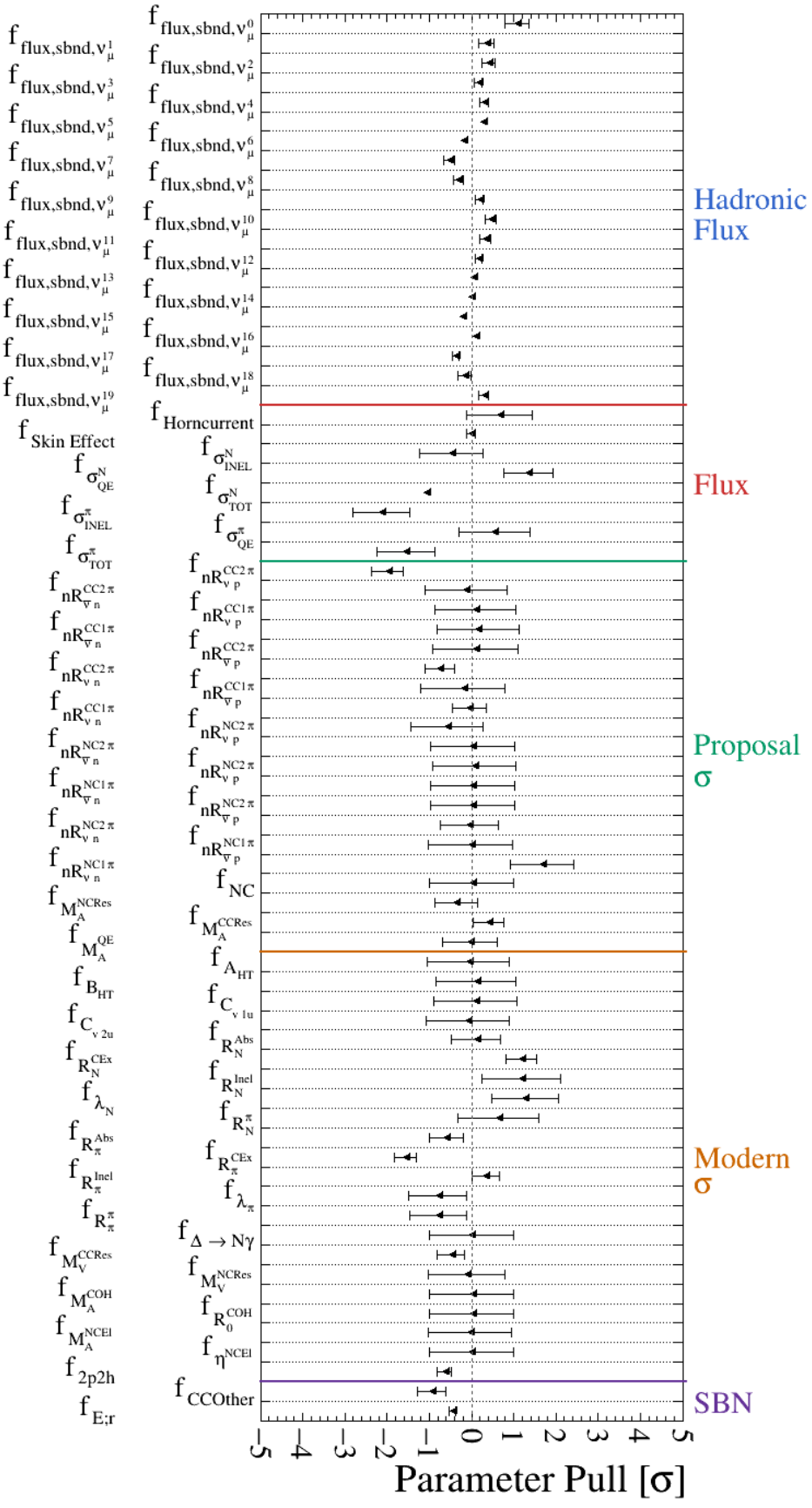

Figure C.8.: The parameter pulls and corresponding uncertainties assigned when fitting the exclusive MC sample to the exclusive GENIE v3, G18_10a_02_11a +50% 2p2h mock dataset.

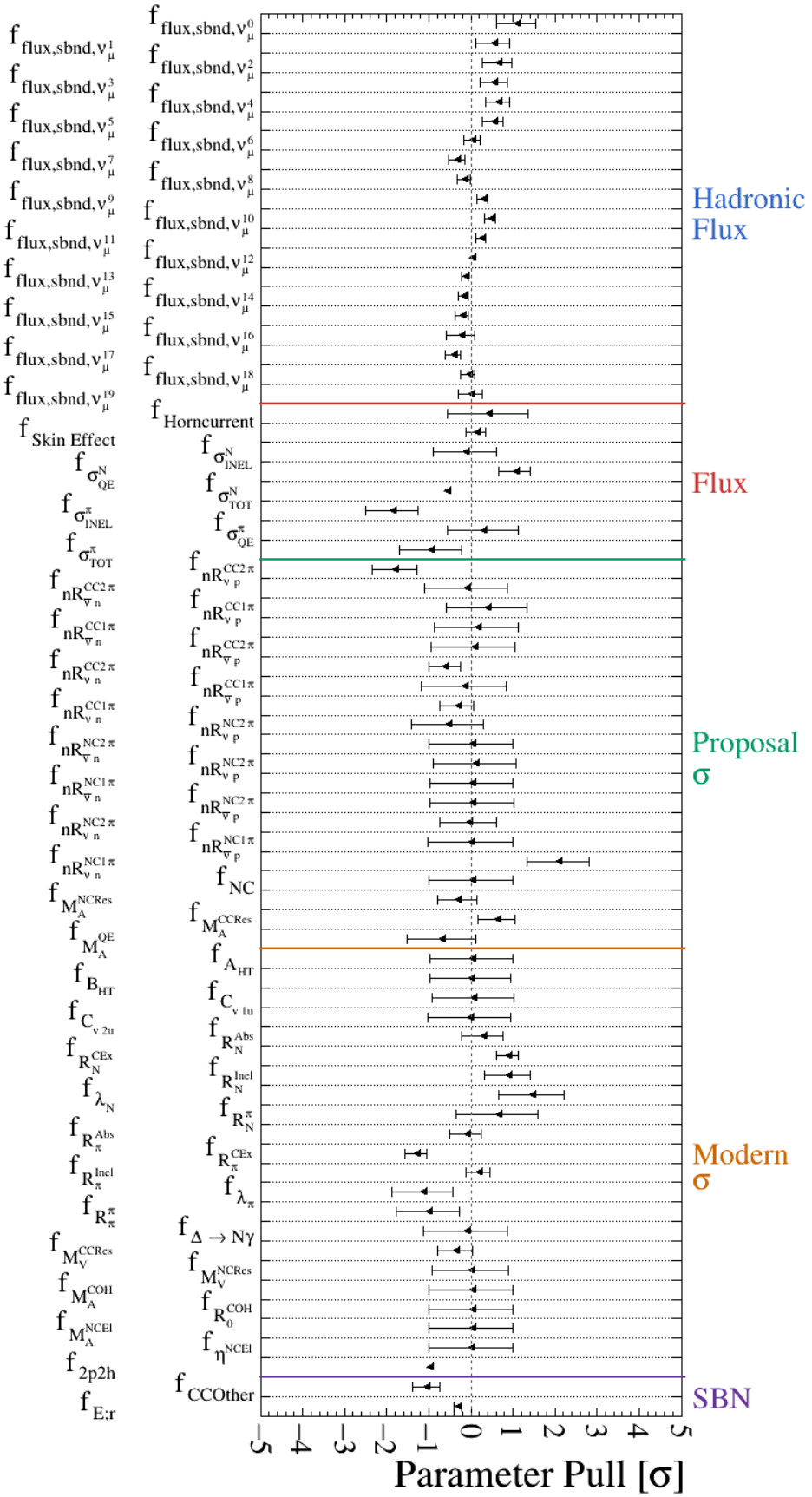

Figure C.9.: The parameter pulls and corresponding uncertainties assigned when fitting the exclusive MC sample to the exclusive GENIE v3, G18_10a_02_11a -50% 2p2h mock dataset.

Appendix D.

Cut definitions post-inclusive selection

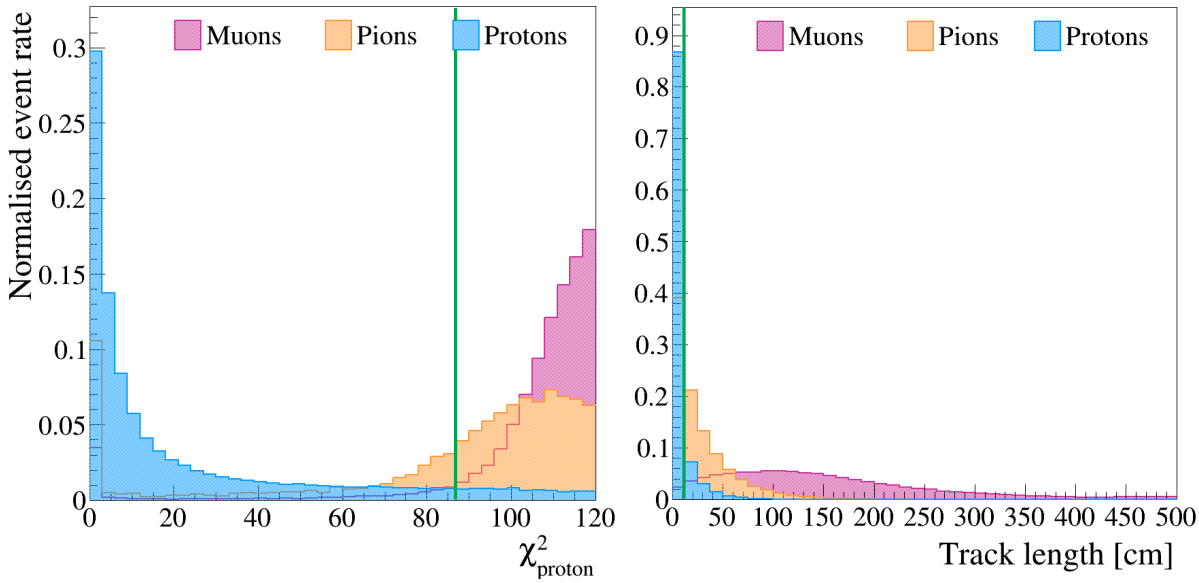

Figure D.1.: Parameters used to separate clear protons from candidate muons, χ^2_{proton} (left) and χ^2_{μ} (right) for muons protons and pions in the SBND ν_μ CC Inclusive-selected sample. The green lines indicates the cut location defined to maximise the purity of selecting muon candidates from protons. Pions are not being considered at this stage.

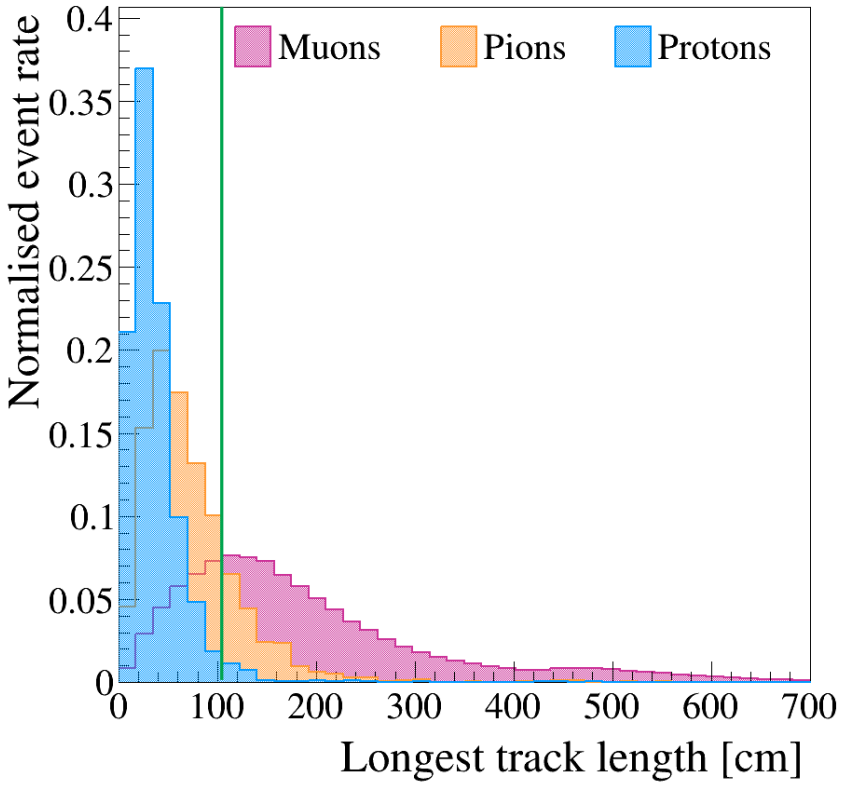

Figure D.2.: Longest track lengths for muons protons and pions in the SBND ν_μ CC Inclusive-selected sample. The green line indicates the cut location defined to maximise the purity of the muon candidate list.

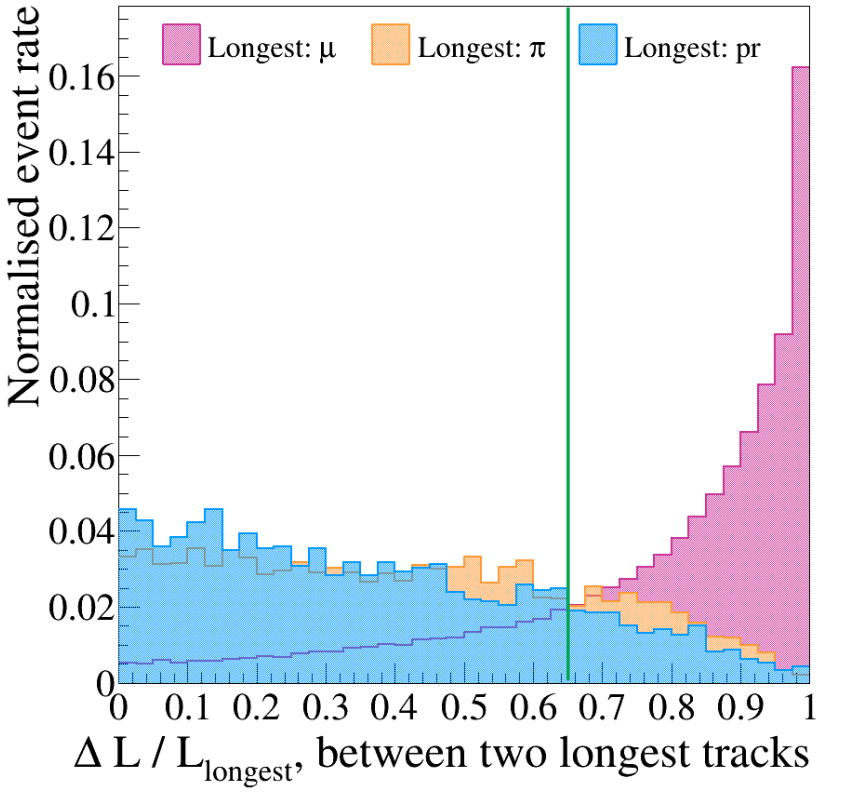

Figure D.3.: Fractional difference between the two longest tracks lengths in events with >1 reconstructable `Track` for muons protons and pions in the SBND ν_μ CC Inclusive-selected sample. The green line indicates the cut location defined to maximise the removal of events with a leading proton or pion.

Colophon

This thesis was made in LaTeX using the "hepthesis" class [211].

Bibliography

[1] C. L. Cowan, F. Reines, F. B. Harrison, H. W. Kruse, and A. D. McGuire, *Detection of the Free Neutrino: a Confirmation*, Science **124**, 103 (1956), https://science.sciencemag.org/content/124/3212/103.full.pdf.

[2] Super-Kamiokande, Y. Fukuda *et al.*, *Evidence for oscillation of atmospheric neutrinos*, Phys. Rev. Lett **81**, 1562 (1998), arXiv:hep-ex/9807003.

[3] SNO, Q. R. Ahmad *et al.*, *Measurement of the rate of* $\nu_e + d \rightarrow p + p + e^-$ *interactions produced by* ^8B *solar neutrinos at the Sudbury Neutrino Observatory*, Phys. Rev. Lett **87**, 071301 (2001), arXiv:nucl-ex/0106015.

[4] N. M. A. 2020, *The Nobel Prize in Physics 2015*, 2015, https://www.nobelprize.org/prizes/physics/2015/summary/.

[5] T. Barratt and L. Poffenberger, *Symmetry Magazine, Sterile Neutrino Sleuths*, https://www.symmetrymagazine.org/article/sterile-neutrino-sleuths.

[6] LAr1-ND, ICARUS-WA104, MicroBooNE, M. Antonello *et al.*, *A Proposal for a Three Detector Short-Baseline Neutrino Oscillation Program in the Fermilab Booster Neutrino Beam*, (2015), arXiv:1503.01520.

[7] P. A. Machado, O. Palamara, and D. W. Schmitz, *The Short-Baseline Neutrino Program at Fermilab*, Ann. Rev. Nucl. Part. Sci **69** (2019), arXiv:1903.04608.

[8] T. Katori, *Meson Exchange Current (MEC) Models in Neutrino Interaction Generators*, (2013), arXiv:1304.6014.

[9] W. Pauli, *Dear radioactive ladies and gentlemen*, Phys. Today **31N9**, 27 (1978).

[10] W. A. W. Charles Drummond Ellis and E. Rutherford, *The average energy of disintegration of radium E*, Proc. R. Soc. Lond. A117109–123 **117** (1927).

[11] F. L. Wilson, *Fermi's Theory of Beta Decay*, Am. J. Phys **36**, 1150 (1968).

[12] H. Bethe and R. Peierls, *The neutrino*, Nature **133**, 689 (1934).

[13] F. Reines and C. L. Cowan, *Detection of the Free Neutrino*, Phys. Rev **92**, 830 (1953).

[14] C. S. Wu, E. Ambler, R. W. Hayward, D. D. Hoppes, and R. P. Hudson, *Experimental Test of Parity Conservation in Beta Decay*, Phys. Rev **105**, 1413 (1957).

[15] M. Goldhaber, L. Grodzins, and A. W. Sunyar, *Helicity of Neutrinos*, Phys. Rev **109**, 1015 (1958).

[16] S. H. Neddermeyer and C. D. Anderson, *Note on the Nature of Cosmic Ray Particles*, Phys. Rev **151,884** (1937).

[17] B. Pontecorvo, *Electron and Muon Neutrinos*, Sov. Phys. JETP **10**, 1236 (1960).

[18] G. Danby *et al.*, *Observation of High-Energy Neutrino Reactions and the Existence of Two Kinds of Neutrinos*, Phys. Rev. Lett **9**, 36 (1962).

[19] DONUT, K. Kodama *et al.*, *Observation of tau neutrino interactions*, Phys. Lett **B504**, 218 (2001), arXiv:hep-ex/0012035.

[20] ALEPH, D. Decamp *et al.*, *Determination of the Number of Light Neutrino Species*, Phys. Lett. B **231**, 519 (1989).

[21] L3, O. Adriani *et al.*, *Determination of the number of light neutrino species*, Phys. Lett. B **292**, 463 (1992).

[22] M. Thomson, in *Modern particle physics*, Cambridge University Press, New York, 2013.

[23] A. De Angelis and M. Pimenta, *Interactions and Field Theories*, pp. 265–391.

[24] J. A. Formaggio and G. P. Zeller, *From eV to EeV: Neutrino cross sections across energy scales*, Reviews of Modern Physics **84**, 1307–1341 (2012).

[25] M. S. Athar and S. K. Singh, *Neutrino and Electron Scattering from Point Particles*, p. 362–384.

[26] B. Pontecorvo, *Inverse Beta Processes and Nonconservation of Lepton Charge*, JETP **7** (1957).

[27] B. Pontecorvo, *Neutrino Experiments and the Problem of Conservation of Leptonic Charge*, JETP **26** (1967).

[28] A. Diaz, C. Argüelles, G. Collin, J. Conrad, and M. Shaevitz, *Where Are We With Light Sterile Neutrinos?*, (2019), arXiv:1906.00045.

[29] R. Davis, D. S. Harmer, and K. C. Hoffman, *Search for Neutrinos from the Sun*, Phys. Rev. Lett **20**, 1205 (1968).

[30] SAGE, J. Abdurashitov *et al.*, *Measurement of the response of the Russian-American gallium experiment to neutrinos from a Cr-51 source*, Phys. Rev. C **59**, 2246 (1999), arXiv:hep-ph/9803418.

[31] J. N. Bahcall, P. Krastev, and E. Lisi, *Limits on electron-neutrino oscillations from the GALLEX Cr-51 source experiment*, Phys. Lett. B **348**, 121 (1995), arXiv:hep-ph/9411414.

[32] *Solving the mystery of the missing neutrinos*, NobelPrize.org. Nobel Media AB 2021 , https://www.nobelprize.org/prizes/themes/solving-the-mystery-of-the-missing-neutrinos.

[33] IMB, T. J. e. a. Haines, *Calculation of Atmospheric Neutrino-Induced Backgrounds in a Nucleon-Decay Search*, Phys. Rev. Lett **57**, 1986 (1986).

[34] e. a. Nakahata, *Atmospheric Neutrino Background and Pion Nuclear Effect for KAMIOKA Nucleon Decay Experiment*, Journal of the Physical Society of Japan **55**, 3786 (1986), https://doi.org/10.1143/JPSJ.55.3786.

[35] T. Kajita, *Atmospheric Neutrinos and Discovery of Neutrino Oscillations*, Proc. Japan Acad. B **86**, 303 (2010).

[36] Super-Kamiokande Collaboration, Y. e. a. Fukuda, *Evidence for Oscillation of Atmospheric Neutrinos*, Phys. Rev. Lett **81**, 1562 (1998).

[37] KamLAND Collaboration, K. e. a. Eguchi, *First Results from KamLAND: Evidence for Reactor Antineutrino Disappearance*, Phys. Rev. Lett **90**, 021802 (2003).

[38] SNO, A. Bellerive, *Constraints on neutrino mixing parameters with the SNO data*, eConf **C030908**, TUIT003 (2003), arXiv:hep-ex/0401018.

[39] C. Kim, *Neutrino physics: Fundamentals of neutrino oscillations*, J. Korean Phys. Soc **29**, 157 (1996), arXiv:hep-ph/9607391.

[40] A. De Angelis and M. Pimenta, *The Properties of Neutrinos*, pp. 543–574.

[41] C. Giunti, *Theory of neutrino oscillations*, in *16th Conference on High Energy Physics*, pp. 427–438, 2004, hep-ph/0409230.

[42] P. Hernandez, *Neutrino physics*, in *5th CERN - Latin American School of High-Energy Physics*, 2010, 1010.4131.

[43] C. Giunti, C. Kim, and O. U. Press, *Fundamentals of Neutrino Physics and Astrophysics*, OUP Oxford, 2007.

[44] X. Qian and P. Vogel, *Neutrino Mass Hierarchy*, Prog. Part. Nucl. Phys **83**, 1 (2015), arXiv:1505.01891.

[45] P. F. de Salas *et al.*, *2020 global reassessment of the neutrino oscillation picture*, Journal of High Energy Physics **2021** (2021).

[46] G. Drexlin, V. Hannen, S. Mertens, and C. Weinheimer, *Current direct neutrino mass experiments*, Adv. High Energy Phys **2013**, 293986 (2013), arXiv:1307.0101.

[47] P. F. de Salas, S. Gariazzo, O. Mena, C. A. Ternes, and M. Tórtola, *Neutrino Mass Ordering from Oscillations and Beyond: 2018 Status and Future Prospects*, Frontiers in Astronomy and Space Sciences **5**, 36 (2018).

[48] K. Abe *et al.*, *Atmospheric neutrino oscillation analysis with external constraints in Super-Kamiokande I-IV*, Physical Review D **97** (2018).

[49] M. Aartsen *et al.*, *Measurement of Atmospheric Neutrino Oscillations at 6–56 GeV with IceCube DeepCore*, Physical Review Letters **120** (2018).

[50] M. Aartsen *et al.*, *Measurement of atmospheric tau neutrino appearance with IceCube DeepCore*, Physical Review D **99** (2019).

[51] M. Jiang *et al.*, *Atmospheric neutrino oscillation analysis with improved event reconstruction in Super-Kamiokande IV*, Progress of Theoretical and Experimental Physics **2019** (2019).

[52] R. e. a. Abbasi, *The design and performance of IceCube DeepCore*, Astroparticle Physics **35**, 615–624 (2012).

[53] B. T. Cleveland *et al.*, *Measurement of the Solar Electron Neutrino Flux with the Homestake Chlorine Detector*, The Astrophysical Journal **496**, 505 (1998).

[54] J. N. e. a. Abdurashitov, *Measurement of the solar neutrino capture rate with gallium metal. III. Results for the 2002–2007 data-taking period*, Physical Review C **80** (2009).

[55] F. Kaether, W. Hampel, G. Heusser, J. Kiko, and T. Kirsten, *Reanalysis of the Gallex solar neutrino flux and source experiments*, Physics Letters B **685**, 47–54 (2010).

[56] B. e. a. Aharmim, *Combined analysis of all three phases of solar neutrino data from the Sudbury Neutrino Observatory*, Physical Review C **88** (2013).

[57] G. e. a. Bellini, *Precision Measurement of theBe7Solar Neutrino Interaction Rate in Borexino*, Physical Review Letters **107** (2011).

[58] G. e. a. Bellini, *Final results of Borexino Phase-I on low-energy solar neutrino spectroscopy*, Physical Review D **89** (2014).

[59] A. e. a. Gando, *Constraints on θ_{13} from a three-flavor oscillation analysis of reactor antineutrinos at KamLAND*, Physical Review D **83** (2011).

[60] T. K. Collaboration, *Reactor On-Off Antineutrino Measurement with KamLAND*, 2013, 1303.4667.

[61] Y. Nakajima, *Recent results and future prospects from Super- Kamiokande*, 2020.

[62] G. e. a. Bak, *Measurement of Reactor Antineutrino Oscillation Amplitude and Frequency at RENO*, Physical Review Letters **121** (2018).

[63] The Daya Bay Collaboration, D. e. a. Adey, *Measurement of the Electron Antineutrino Oscillation with 1958 Days of Operation at Daya Bay*, Phys. Rev. Lett **121**, 241805 (2018).

[64] J. Yoo, *RENO*, 2020, https://doi.org/10.5281/zenodo.4123573.

[65] Double Chooz, F. Ardellier *et al.*, *Double Chooz: A Search for the neutrino mixing angle theta(13)*, (2006), arXiv:hep-ex/0606025.

[66] Double Chooz, H. de Kerret *et al.*, *Double Chooz θ_{13} measurement via total neutron capture detection*, Nature Phys **16**, 558 (2020), arXiv:1901.09445.

[67] P. Dunne, *Latest Neutrino Oscillation Results from T2K*, 2020, https://doi.org/10.5281/zenodo.3959558.

[68] A. Himmel, *New Oscillation Results from the NOvA Experiment*, 2020, https://doi.org/10.5281/zenodo.3959581.

[69] P. e. a. Adamson, *Combined Analysis of ν_μ Disappearance and $\nu_\mu \rightarrow \nu_e$ Appearance in MINOS Using Accelerator and Atmospheric Neutrinos*, Physical Review Letters **112** (2014).

[70] M. H. e. a. Ahn, *Measurement of neutrino oscillation by the K2K experiment*, Physical Review D **74** (2006).

[71] K. e. a. Abe, *T2K measurements of muon neutrino and antineutrino disappearance using 3.13×1021 protons on target*, Physical Review D **103** (2021).

[72] K. e. a. Abe, *Constraint on the matter–antimatter symmetry-violating phase in neutrino oscillations*, Nature **580**, 339–344 (2020).

[73] M. Acero *et al.*, *First measurement of neutrino oscillation parameters using neutrinos and antineutrinos by NOvA*, Physical Review Letters **123** (2019).

[74] e. a. D.G. Michael, *The magnetized steel and scintillator calorimeters of the MINOS experiment*, Nuclear Instruments and Methods in Physics Research Section A: Accelerators, Spectrometers, Detectors and Associated Equipment **596**, 190 (2008).

[75] GALLEX, P. Anselmann *et al.*, *First results from the Cr-51 neutrino source experiment with the GALLEX detector*, Phys. Lett. B **342**, 440 (1995).

[76] C. Giunti and M. Laveder, *Statistical significance of the gallium anomaly*, Physical Review C **83** (2011).

[77] J. Kostensalo, J. Suhonen, C. Giunti, and P. Srivastava, *The gallium anomaly revisited*, Physics Letters B **795**, 542–547 (2019).

[78] P. Huber, *On the determination of anti-neutrino spectra from nuclear reactors*, Phys. Rev. C **84**, 024617 (2011), arXiv:1106.0687, [Erratum: Phys.Rev.C 85, 029901 (2012)].

[79] T. Mueller *et al.*, *Improved Predictions of Reactor Antineutrino Spectra*, Phys. Rev. C **83**, 054615 (2011), arXiv:1101.2663.

[80] LSND, C. Athanassopoulos *et al.*, *Evidence for nu(mu) —> nu(e) neutrino oscillations from LSND*, Phys. Rev. Lett **81**, 1774 (1998), arXiv:nucl-ex/9709006.

[81] LSND, A. Aguilar-Arevalo *et al.*, *Evidence for neutrino oscillations from the observation of $\bar{\nu}_e$ appearance in a $\bar{\nu}_\mu$ beam*, Phys. Rev. D **64**, 112007 (2001), arXiv:hep-ex/0104049.

[82] MiniBooNE, A. Aguilar-Arevalo *et al.*, *Significant Excess of ElectronLike Events in the MiniBooNE Short-Baseline Neutrino Experiment*, Phys. Rev. Lett **121**, 221801 (2018), arXiv:1805.12028.

[83] J. Kopp, P. A. N. Machado, M. Maltoni, and T. Schwetz, *Sterile Neutrino Oscillations: The Global Picture*, JHEP **05**, 050 (2013), arXiv:1303.3011.

[84] M. Dentler *et al.*, *Updated Global Analysis of Neutrino Oscillations in the Presence of eV-Scale Sterile Neutrinos*, JHEP **08**, 010 (2018), arXiv:1803.10661.

[85] J. M. Berryman and P. Huber, *Sterile neutrinos and the global reactor antineutrino dataset*, Journal of High Energy Physics **2021** (2021).

[86] A. A. Kuvshinnikov, L. A. Mikaelyan, S. V. Nikolaev, M. D. Skorokhvatov, and A. V. Etenko, *Measuring the anti-electron-neutrino + p —> n + e+ cross-section and beta decay axial constant in a new experiment at Rovno NPP reactor. (In Russian)*, Yad. Fiz **52**, 472 (1990).

[87] Z. D. Greenwood *et al.*, *Results of a two position reactor neutrino oscillation experiment*, Phys. Rev. D **53**, 6054 (1996).

[88] Y. Declais *et al.*, *Search for neutrino oscillations at 15-meters, 40-meters, and 95-meters from a nuclear power reactor at Bugey*, Nucl. Phys. B **434**, 503 (1995).

[89] Y. Declais *et al.*, *Study of reactor anti-neutrino interaction with proton at Bugey nuclear power plant*, Phys. Lett. B **338**, 383 (1994).

[90] Y. Ko *et al.*, *Sterile Neutrino Search at the NEOS Experiment*, Physical Review Letters **118** (2017).

[91] I. Alekseev *et al.*, *Search for sterile neutrinos at the DANSS experiment*, Physics Letters B **787**, 56–63 (2018).

[92] T. D. C. Collaboration, *Search for Signatures of Sterile Neutrinos with Double Chooz*, 2020, 2009.05515.

[93] RENO Collaboration, J. H. e. a. Choi, *Search for Sub-eV Sterile Neutrinos at RENO*, Phys. Rev. Lett **125**, 191801 (2020).

[94] F. An *et al.*, *Measurement of electron antineutrino oscillation based on 1230 days of operation of the Daya Bay experiment*, Physical Review D **95** (2017).

[95] J. Abdurashitov *et al.*, *Measurement of the response of a Ga solar neutrino experiment to neutrinos from an Ar-37 source*, Phys. Rev. C **73**, 045805 (2006), arXiv:nucl-ex/0512041.

[96] K. e. a. Abe, *Search for light sterile neutrinos with the T2K far detector Super-Kamiokande at a baseline of 295 km*, Physical Review D **99** (2019).

[97] G. Bellini *et al.*, *New limits on heavy sterile neutrino mixing inB8decay obtained with the Borexino detector*, Physical Review D **88** (2013).

[98] J. M. Conrad and M. H. Shaevitz, *Limits on electron neutrino disappearance from the KARMEN and LSND ν_e-carbon cross section data*, Physical Review D **85** (2012).

[99] M. e. a. Andriamirado, *Improved short-baseline neutrino oscillation search and energy spectrum measurement with the PROSPECT experiment at HFIR*, Physical Review D **103** (2021).

[100] A. P. S. et al, *Experiment Neutrino-4 search for sterile neutrino and results of measurements*, 2021, 2005.05301.

[101] H. e. a. Almazán, *Improved sterile neutrino constraints from the STEREO experiment with 179 days of reactor-on data*, Physical Review D **102** (2020).

[102] J. M. Conrad and M. H. Shaevitz, *Limits on electron neutrino disappearance from the KARMEN and LSND ν_e-carbon cross section data*, Physical Review D **85** (2012).

[103] MiniBooNE Collaboration, A. A. e. a. Aguilar-Arevalo, *Improved Search for $\overline{\nu}_\mu \to \overline{\nu}_e$ Oscillations in the MiniBooNE Experiment*, Phys. Rev. Lett **110**, 161801 (2013).

[104] M. Collaboration, *A Combined $\nu_\mu \to \nu_e$ and $\bar{\nu}_\mu \to \bar{\nu}_e$ Oscillation Analysis of the MiniBooNE Excesses*, 2012, 1207.4809.

[105] A. e. a. Aguilar-Arevalo, *Updated MiniBooNE neutrino oscillation results with increased data and new background studies*, Physical Review D **103** (2021).

[106] R. Seto, *BNL E776: A Search for neutrino oscillations*, AIP Conf. Proc **176**, 957 (1988).

[107] P. Astier *et al.*, *Search for $\nu_\mu \to \nu_e$ oscillations in the NOMAD experiment*, Physics Letters B **570**, 19–31 (2003).

[108] M. Antonello *et al.*, *Experimental search for the "LSND anomaly" with the ICARUS detector in the CNGS neutrino beam*, The European Physical Journal C **73** (2013).

[109] N. Agafonova *et al.*, *Final results on neutrino oscillation parameters from the OPERA experiment in the CNGS beam*, Physical Review D **100** (2019).

[110] S. A. et al, *Technical Design Report (TDR): Searching for a Sterile Neutrino at J-PARC MLF (E56, JSNS2)*, 2017, 1705.08629.

[111] M. Aartsen *et al.*, *eV-Scale Sterile Neutrino Search Using Eight Years of Atmospheric Muon Neutrino Data from the IceCube Neutrino Observatory*, Physical Review Letters **125** (2020).

[112] M. Aartsen *et al.*, *Searching for eV-scale sterile neutrinos with eight years of atmospheric neutrinos at the IceCube Neutrino Telescope*, Physical Review D **102** (2020).

[113] M. H. Moulai *et al.*, *Combining Sterile Neutrino Fits to Short Baseline Data with IceCube Data*, Phys. Rev. D **101**, 055020 (2020), arXiv:1910.13456.

[114] F. Dydak *et al.*, *A Search for Muon-neutrino Oscillations in the Delta Δm^2 Range 0.3 eV^2 to 90 eV^2*, Phys. Lett. B **134**, 281 (1984).

[115] I. E. e. a. Stockdale, *Limits on Muon-Neutrino Oscillations in the Mass Range 30$<\Delta m^2 <$ 1000 eV^2/c^4*, Phys. Rev. Lett **52**, 1384 (1984).

[116] P. Adamson *et al.*, *Search for active-sterile neutrino mixing using neutral-current interactions in NOvA*, Physical Review D **96** (2017).

[117] MINOS+ Collaboration, P. e. a. Adamson, *Search for Sterile Neutrinos in MINOS and MINOS+ Using a Two-Detector Fit*, Phys. Rev. Lett **122**, 091803 (2019).

[118] T. Ohlsson, *Status of non-standard neutrino interactions*, Reports on Progress in Physics **76**, 044201 (2013).

[119] J. Asaadi, E. Church, R. Guenette, B. J. P. Jones, and A. M. Szelc, *New light Higgs boson and short-baseline neutrino anomalies*, Phys. Rev. D **97**, 075021 (2018).

[120] MiniBooNE, A. A. Aguilar-Arevalo *et al.*, *The Neutrino Flux prediction at MiniBooNE*, Phys. Rev **D79**, 072002 (2009), arXiv:0806.1449.

[121] V. Shiltsev, *Fermilab Proton Accelerator Complex Status and Improvement Plans*, Mod. Phys. Lett **A32**, 1730012 (2017), arXiv:1705.03075.

[122] M. G. Catanesi *et al.*, *Particle identification algorithms for the HARP forward spectrometer*, Nucl. Instrum. Meth **A572**, 899 (2007).

[123] Particle Data Group, Tanabashi, M. and others, *Review of Particle Physics*, Phys. Rev. D **98**, 030001 (2018).

[124] D. Pocanic, E. Frlez, and A. van der Schaaf, *Experimental study of rare charged pion decays*, J. Phys **G41**, 114002 (2014), arXiv:1407.2865.

[125] C. Rubbia, *The Liquid Argon Time Projection Chamber: A New Concept for Neutrino Detectors*, (1977).

[126] ICARUS, L. Bassi *et al.*, *ICARUS I: an optimized, real time detector of solar neutrinos*, (1989).

[127] ICARUS, F. Arneodo *et al.*, *The ICARUS experiment: A Second generation proton decay experiment and neutrino observatory at the Gran Sasso Laboratory*, (2001), arXiv:hep-ex/0103008.

[128] C. Anderson *et al.*, *The ArgoNeuT Detector in the NuMI Low-Energy beam line at Fermilab*, JINST **7**, P10019 (2012), arXiv:1205.6747.

[129] P. Adamson *et al.*, *The NuMI Neutrino Beam*, Nucl. Instrum. Meth **A806**, 279 (2016), arXiv:1507.06690.

[130] B. Baller *et al.*, *Liquid Argon Time Projection Chamber Research and Development in the United States*, JINST **9**, T05005 (2014), arXiv:1307.8166.

[131] MicroBooNE, R. Acciarri *et al.*, *A Measurement of the Attenuation of Drifting Electrons in the MicroBooNE LArTPC*, MICROBOONE-NOTE-PUB-1026 (2017).

[132] Y. Li *et al.*, *Measurement of Longitudinal Electron Diffusion in Liquid Argon*, Nucl. Instrum. Meth **A816** (2016), arXiv:1508.07059.

[133] *Liquid Argon Properties (Tables and Calculators)*, 2021, https://lar.bnl.gov/properties/#refs.

[134] MicroBooNE, R. Acciarri *et al.*, *Design and Construction of the MicroBooNE Detector*, JINST **12**, P02017 (2017), arXiv:1612.05824.

[135] D. Garcia-Gamez, *Developing Scintillation Light Readout Simulation for the SBND experiment*, JINST **11**, C01080 (2016), arXiv:1511.04611.

[136] R. e. a. Acciarri, *Construction of precision wire readout planes for the Short-Baseline Near Detector (SBND)*, Journal of Instrumentation **15**, P06033–P06033 (2020).

[137] R. Hahn, *Fermilab Creative Services*, https://vms.fnal.gov/asset/advanced-photo.

[138] A. Machado and E. Segreto, *ARAPUCA a new device for liquid argon scintillation light detection*, Journal of Instrumentation **11**, C02004 (2016).

[139] A. A. Machado *et al.*, in *The X-ARAPUCA: An improvement of the ARAPUCA device*, 2018, 1804.01407.

[140] M. Auger *et al.*, *A Novel Cosmic Ray Tagger System for Liquid Argon TPC Neutrino Detectors*, Instruments **1**, 2 (2017), arXiv:1612.04614.

[141] SBND, S. Gao, *Low Noise Cold Electronics System for SBND LAr TPC*, in *Meeting of the Division of Particles and Fields of the American Physical Society (DPF2019) Boston, Massachusetts, July 29-August 2, 2019*, 2019, 1910.06434.

[142] H. Chen *et al.*, *Lifetime Study of COTS ADC for SBND LAr TPC Readout Electronics*, in *21st IEEE Real Time Conference (RT2018) Williamsburg, Virginia, June 11-15, 2018*, 2018, 1806.09226.

[143] MicroBooNE, C. Adams *et al.*, *Design and construction of the MicroBooNE Cosmic Ray Tagger system*, JINST **14**, P04004 (2019), arXiv:1901.02862.

[144] ICARUS, P. Cennini *et al.*, *ICARUS II - A Second Generation Proton Decay Experiment and Neutrino Observatory at the GRAN SASSO Laboratory: Proposal by the ICARUS Collaboration*, (1993).

[145] ICARUS Collaboration, C. Rubbia and C. S. Montanari, CERN Report No. CERN-SPSC-2017-012. SPSC-SR-207, 2017 (unpublished).

[146] S. Gariazzo, C. Giunti, M. Laveder, and Y. F. Li, *Updated global 3+1 analysis of short-baseline neutrino oscillations*, Journal of High Energy Physics **2017** (2017).

[147] NuSTEC, L. Alvarez-Ruso *et al.*, *NuSTEC White Paper: Status and challenges of neutrino–nucleus scattering*, Prog. Part. Nucl. Phys **100**, 1 (2018), arXiv:1706.03621.

[148] MicroBooNE, C. Adams *et al.*, *First measurement of ν_μ charged-current π^0 production on argon with the MicroBooNE detector*, Phys. Rev. D **99**, 091102 (2019), arXiv:1811.02700.

[149] MicroBooNE, P. Abratenko *et al.*, *First Measurement of Inclusive Muon Neutrino Charged Current Differential Cross Sections on Argon at E_ν ∼0.8 GeV with the MicroBooNE Detector*, Phys. Rev. Lett **123**, 131801 (2019), arXiv:1905.09694.

[150] C. Andreopoulos *et al.*, *The GENIE Neutrino Monte Carlo Generator*, Nucl. Instrum. Meth **A614**, 87 (2010), arXiv:0905.2517.

[151] G. D. Megias and T. W. e. a. Donnelly, *Meson-exchange currents and quasielastic predictions for charged-current neutrino-^{12}C scattering in the superscaling approach*, Phys. Rev. D **91**, 073004 (2015).

[152] E. Snider and G. Petrillo, *LArSoft: toolkit for simulation, reconstruction and analysis of liquid argon TPC neutrino detectors*, Journal of Physics: Conference Series **898**, 042057 (2017).

[153] S. A. et. al, *Geant4—a simulation toolkit*, Nuclear Instruments and Methods in Physics Research Section A: Accelerators, Spectrometers, Detectors and Associated Equipment **506**, 250 (2003).

[154] C. Andreopoulos *et al.*, *The GENIE Neutrino Monte Carlo Generator: Physics and User Manual*, (2015), arXiv:1510.05494.

[155] MicroBooNE, R. Acciarri *et al.*, *The Pandora multi-algorithm approach to automated pattern recognition of cosmic-ray muon and neutrino events in the MicroBooNE detector*, Eur. Phys. J **C78**, 82 (2018), arXiv:1708.03135.

[156] A. De Angelis and M. Pimenta, *Introduction to Particle and Astroparticle Physics: Multimessenger Astronomy and its Particle Physics Foundations*.

[157] J. Hewett *et al.*, *Fundamental Physics at the Intensity Frontier*, 2012, 1205.2671.

[158] MicroBooNE, P. Abratenko *et al.*, *First Measurement of Inclusive Muon Neutrino Charged Current Differential Cross Sections on Argon at E_ν ∼0.8 GeV with the MicroBooNE Detector*, Phys. Rev. Lett **123**, 131801 (2019), arXiv:1905.09694.

[159] C. Llewellyn Smith, *Neutrino reactions at accelerator energies*, Physics Reports **3**, 261 (1972).

[160] J. Nieves, I. R. Simo, and M. J. V. Vacas, *Inclusive charged-current neutrino-nucleus reactions*, Phys. Rev. C **83**, 045501 (2011).

[161] G. Megias *et al.*, *Meson-exchange currents and quasielastic predictions for charged-current neutrino-^{12}C scattering in the superscaling approach*, Phys. Rev. D **91**, 073004 (2015), arXiv:1412.1822.

[162] R. Smith and E. Moniz, *NEUTRINO REACTIONS ON NUCLEAR TARGETS*, Nucl. Phys. B **43**, 605 (1972), [Erratum: Nucl.Phys.B 101, 547 (1975)].

[163] H. Hassanabadi, A. Armat, and L. Naderi, *Relativistic Fermi-Gas Model for Nucleus*, Found. Phys **44**, 1188 (2014).

[164] L. Alvarez-Ruso, *Neutrino interactions: Challenges in the current theoretical picture*, Nuclear Physics B - Proceedings Supplements **229-232**, 167 (2012), Neutrino 2010.

[165] L. Ahrens *et al.*, *Measurement of Neutrino - Proton and anti-neutrino - Proton Elastic Scattering*, Phys. Rev. D **35**, 785 (1987).

[166] D. Rein and L. M. Sehgal, *Neutrino-excitation of baryon resonances and single pion production*, Annals of Physics **133**, 79 (1981).

[167] C. Berger and L. M. Sehgal, *Lepton mass effects in single pion production by neutrinos*, Phys. Rev. D **76**, 113004 (2007).

[168] D. Rein and L. M. Sehgal, *Coherent π^0 production in neutrino reactions*, Nuclear Physics B **223**, 29 (1983).

[169] C. Berger and L. Sehgal, *PCAC and coherent pion production by low energy neutrinos*, Phys. Rev. D **79**, 053003 (2009), arXiv:0812.2653.

[170] A. Bodek and U. Yang, *Higher twist, xi(omega) scaling, and effective LO PDFs for lepton scattering in the few GeV region*, J. Phys. G **29**, 1899 (2003), arXiv:hep-ex/0210024.

[171] C. Andreopoulos *et al.*, *GENIE Event Generator, Naming Conventions*, https://hep.ph.liv.ac.uk/c̃ostasa/genie/naming_conventions.html.

[172] M. S. Athar and S. K. Singh, *Weak Quasielastic $\nu(\bar{\nu})$-nucleus Scattering*, p. 561–602.

[173] A. Bodek and J. Ritchie, *Further Studies of Fermi Motion Effects in Lepton Scattering from Nuclear Targets*, Phys. Rev. D **24**, 1400 (1981).

[174] D. Rohe *et al.*, *Correlated strength in nuclear spectral function*, Phys. Rev. Lett **93**, 182501 (2004), arXiv:nucl-ex/0405028.

[175] O. Benhar, P. Huber, C. Mariani, and D. Meloni, *Neutrino–nucleus interactions and the determination of oscillation parameters*, Physics Reports **700**, 1–47 (2017).

[176] K. S. Kuzmin, V. V. Lyubushkin, and V. A. Naumov, *Quasielastic axial-vector mass from experiments on neutrino-nucleus scattering*, Eur. Phys. J. C **54**, 517 (2008), arXiv:0712.4384.

[177] L. D. Kolupaeva, K. S. Kuzmin, O. N. Petrova, and I. M. Shandrov, *Some uncertainties of neutrino oscillation effect in the NOνA experiment*, Modern Physics Letters A **31**, 1650077 (2016).

[178] A. Gil, J. Nieves, and E. Oset, *Many body approach to the inclusive (e, e-prime) reaction from the quasielastic to the Delta excitation region*, Nucl. Phys. A **627**, 543 (1997), arXiv:nucl-th/9711009.

[179] S. Dolan, G. Megias, and S. Bolognesi, *Implementation of the SuSAv2-meson exchange current 1p1h and 2p2h models in GENIE and analysis of nuclear effects in T2K measurements*, Phys. Rev. D **101**, 033003 (2020), arXiv:1905.08556.

[180] S. Dolan, G. D. Megias, and S. Bolognesi, *Implementation of the SuSAv2-meson exchange current 1p1h and 2p2h models in GENIE and analysis of nuclear effects in T2K measurements*, Phys. Rev. D **101**, 033003 (2020).

[181] R. P. Feynman, M. Kislinger, and F. Ravndal, *Current Matrix Elements from a Relativistic Quark Model*, Phys. Rev. D **3**, 2706 (1971).

[182] BEBC WA59, W. Wittek *et al.*, *Production of π^0 Mesons and Charged Hadrons in Anti-neutrino Neon and Neutrino Neon Charged Current Interactions*, Z. Phys. C **40**, 231 (1988).

[183] S. Gollapinni, *Neutrino Cross section Future*, in *Prospects in Neutrino Physics*, 2016, 1602.05299.

[184] E. Snider, *Introduction to LArSoft*, https://indico.fnal.gov/event/9928/sessions/12927/attachments/75529/90601/larsoft-class-intro-2015-08-07.present.pdf.

[185] M. collaboration, *Measurement of Space Charge Effects in the MicroBooNE LArTPC Using Cosmic Muons*, 2020, 2008.09765.

[186] Y. Coadou, *Boosted Decision Trees and Applications*, EPJ Web of Conferences **55**, 02004 (2013).

[187] ArgoNeuT, R. Acciarri *et al.*, *A Study of Electron Recombination Using Highly Ionizing Particles in the ArgoNeuT Liquid Argon TPC*, JINST **8**, P08005 (2013), arXiv:1306.1712.

[188] S. Collaboration, *Cosmic Background Removal with Deep Neural Networks in SBND*, 2021, 2012.01301.

[189] D. Garcia-Gamez, *Developing scintillation light readout simulation for the SBND experiment*, Journal of Instrumentation **11**, C01080–C01080 (2016).

[190] MicroBooNE, R. Acciarri *et al.*, *Michel Electron Reconstruction Using Cosmic-Ray Data from the MicroBooNE LArTPC*, JINST **12**, P09014 (2017), arXiv:1704.02927.

[191] R. Acciarri *et al.*, *Demonstration of MeV-scale physics in liquid argon time projection chambers using ArgoNeuT*, Physical Review D **99** (2019).

[192] R. Acciarri *et al.*, *First observation of low energy electron neutrinos in a liquid argon time projection chamber*, Physical Review D **95** (2017).

[193] ArgoNeuT, R. Acciarri *et al.*, *Detection of Back-to-Back Proton Pairs in Charged-Current Neutrino Interactions with the ArgoNeuT Detector in the NuMI Low Energy Beam Line*, Phys. Rev. D **90**, 012008 (2014), arXiv:1405.4261.

[194] G. Collaboration, J. Tena-Vidal, and Others, *Neutrino-Nucleon Cross-Section Model Tuning in GENIE v3*, 2021, 2104.09179.

[195] G. Collaboration, J. Tena-Vidal, and Others, *AGKY Hadronization Model Tuning in GENIE v3*, 2021, 2106.05884.

[196] MicroBooNE, P. Abratenko *et al.*, *Measurement of differential cross sections for ν_μ -Ar charged-current interactions with protons and no pions in the final state with the MicroBooNE detector*, Phys. Rev. D **102**, 112013 (2020), arXiv:2010.02390.

[197] MicroBooNE, P. Abratenko *et al.*, *First Measurement of Differential Charged Current Quasielastic-like ν_μ-Argon Scattering Cross Sections with the MicroBooNE Detector*, Phys. Rev. Lett **125**, 201803 (2020), arXiv:2006.00108.

[198] K. Abe *et al.*, *Simultaneous measurement of the muon neutrino charged-current cross section on oxygen and carbon without pions in the final state at T2K*, Physical Review D **101** (2020).

[199] F. a. James, *MINUIT: Function Minimization and Error Analysis Reference Manual*, (1998), CERN Program Library Long Writeups.

[200] e. a. Ankowski, *Measurement of through-going particle momentum by means of multiple scattering with the ICARUS T600 TPC*, The European Physical Journal C **48**, 667–676 (2006).

[201] (MicroBooNE Collaboration), R. e. a. Acciarri, *Booster Neutrino Flux Predicion at MicroBooNE*, (2018).

[202] O. Palamara, *Exclusive Muon Neutrino Charged Current Pion-less Topologies. ArgoNeuT Results and Future Prospects in LAr TPC Detectors*, , https://journals.jps.jp/doi/pdf/10.7566/JPSCP.12.010017.

[203] G. Cowan, K. Cranmer, E. Gross, and O. Vitells, *Asymptotic formulae for likelihood-based tests of new physics*, The European Physical Journal C **71** (2011).

[204] SciBooNE, MiniBooNE, K. Mahn *et al.*, *Dual baseline search for muon neutrino disappearance at $0.5eV^2 < \Delta m^2 < 40eV^2$*, Phys. Rev. D **85**, 032007 (2012), arXiv:1106.5685.

[205] A. Bodek, *High-Energy Neutrino Interactions with Two Muons in the Final State*, in *3rd SLAC Summer Institute on Particle Physics: Deep Hadronic Structure and the New Particles (Topical Conference last 3 days) (SSI 75)*, p. 315, 1975.

[206] MicroBooNE, P. Abratenko *et al.*, *Selection of numu charged–current induced interactions with $N > 0$ protons and performance of events with $N = 2$ protons in the final state in the MicroBooNE detector from the BNB*, (2018).

[207] R. Acciarri *et al.*, *First measurement of the cross section for ν_μ and $\bar{\nu}_\mu$ induced single charged pion production on argon using ArgoNeuT*, Physical Review D **98** (2018).

[208] MicroBooNE, P. Abratenko *et al.*, *Determination of muon momentum in the MicroBooNE LArTPC using an improved model of multiple Coulomb scattering*, Journal of Instrumentation **12**, P10010–P10010 (2017).

[209] P. D. Group, *Muons in Liquid argon (Ar)*, https://pdg.lbl.gov/2012/AtomicNuclearProperties/MUON_ELOSS_TABLES/muonloss_289.pdf.

[210] N. I. of Standards and Technology, *Stopping-Power & Range Tables for Electrons, Protons, and Helium Ions*, https://www.nist.gov/pml/stopping-power-range-tables-electrons-protons-and-helium-ions.

[211] A. Buckley, *The hepthesis LaTeX class*.